WAVS - the Wide Area Varability Survey

Thesis

UNRESTRICTED.

Faculty of Science, The Open University

WAVS - The Wide Area Variability Survey

David Andrew Lott MPhys.

Submitted for the degree of Doctor of Philosophy

11/08/03

Submission date: 8 August 2003
Award date: 29 November 2004

CONTENTS

LIST OF FIGURES

LIST OF TABLES

WAVS - The Wide Area Variability Survey

David Andrew Lott MPhys.
11/08/03

Faculty of Science, The Open University
Submitted for the degree of Doctor of Philosophy

The Wide Area Variability Survey (WAVS) project used the CFH12k mosaic camera as the world's largest time series photometer to obtain images of a 0.33 square degree galactic field with a time resolution of 3 minutes over 2 nights of observations. The main aim of the WAVS project was to try and differentiate between the current competing models of cataclysmic variable (CV) population and evolution by obtaining an unbiased sample using a characteristic that all known CVs exhibit. All CVs show 'flickering' in their lightcurves, that is stochastic variations in luminosity with an amplitude of tenths of a magnitude on timescales of minutes to hours, and it is this characteristic that the WAVS project exploits. Lightcurves for each of the 52000 objects in the WAVS field were created and searched for variability. Spectroscopic observations using the Nordic Optical Telescope (NOT) were carried out to further investigate candidate objects.

In searching for variability on this timescale it was apparent that the WAVS project would also discover many variables of other types which may also be of great interest. Thus, the secondary goal of the WAVS project was to investigate these objects and obtain population statistics wherever possible.

This thesis gives an introduction to various types of stellar variability and covers the observable characteristics of CVs in some depth. Competing models of CV evolution are considered and the goals and strategies of the WAVS programme are outlined in more detail. An account of the process of obtaining high quality photometry and spectroscopy is given, both in the general case and in the more specific case applicable to the WAVS data and the methods used to search for variability in the WAVS sample are discussed.

The WAVS project has currently discovered 229 new variable objects and the lightcurves of these systems are presented in Appendices A to C. Some of these objects are discussed in detail, but for others accurate classification is difficult without more data, although a tentative classification is made.

Currently the WAVS project has not discovered any new CVs and the relevance of this null result is considered. However, 30 possible flickering objects have been identified.

The author acknowledges...

The Open University for my studentship and for their continued support. My supervisor Carole Haswell for her help, advice and persistence over the last five years. Members of the Department of Physics and Astronomy, particularly my second supervisor Andy Norton for their input on various topics. Fred Ringwald for collecting the CFHT data. Tim Abbott for his collaboration and help at NOT and Jackie Abbott for her hospitality. Andrew Conway for his friendship, understanding and introducing me to my wife. Ben Eves, for cheeriness, Craig Powell and Dan Rolfe for lots of IDL help (among other things) and John Barker for letting me help him build a robot. My office mates and good friends Chris Brockwell and Lisa Blake for their love, encouragement and various memorable times. Joe Shawcross for wrestling, pot noodle and tea in times of crisis. My family for their unending understanding and support and most of all my wife Natasha without whose nagging, cajoling, correcting, self sacrifice and above all love, this thesis is unlikely to have been completed.

Chapter 1

Stellar Variability

1.1 History

For over two millennia humanity has recorded examples of stellar variability. Were it not for library burnings throughout history, even earlier records of the phenomenon would probably still exist. As it stands the earliest surviving records of changes in stellar brightness or of the apparent appearance of a new stellar body come from China and date back to several centuries B.C. Not valued for their astronomical interest, but rather for their astrological importance, new stars were considered to be powerful omens by the Imperial astrologers of the time. Some of these sightings were indeed instances of true stellar variability, whilst others can be better attributed to the passage of comets and so were actually solar system based phenomena (Petit, 1987). The appearance of 'new stars' is caused by eruptive behaviour in novae and supernovae which can result in a change in brightness of many magnitudes, making previously invisible stars obvious to the naked eye. These were the only types of variable star observed until the 16th century as other types of brightness variation are nowhere near as dramatic. The first pulsating variable to be detected was Mira ('the Wonderful', today often called Omicron Ceti) which was discovered by Fabricius in 1596. Although Mira is in fact a periodic variable with a period of approximately 330 days it was originally thought to be a nova outburst. The discovery of Mira's variability was followed 73 years later by that of Algol (the Demon) in 1669. The period of Algol was determined by Goodricke in 1782, and by the start of the nineteenth century 13 variable stars were known (Table 1.1). Interestingly, throughout the 1700s speculation about the mechanism driving variability included eclipsing binaries, transient

Table 1.1: Variables known at the end of the 18th century (Petit, 1987, p14)

Star	Date	Observer
o Ceti (Mira)	1596	Fabricius
β Persei (Algol)	1669	Montanari
χ Cygni	1687	Kirch
R Hydrae	1704	Maraldi
R Delphini	1751	Hencke
R Leonis	1782	Koch
μ Cephei	1782	Herschel
β Lyrae	1784	Goodricke
δ Cephei	1784	Goodricke
η Aquilae	1795	Pigott
R Coronae Borealis	1795	Pigott
R Scuti	1795	Pigott
α Herculis	1795	Herschel

spots on rotating stars and distorted stars to name but a few. Whilst all of these do occur in some types of variable, the idea of stellar pulsation was not advocated until much later. The discussion was unfortunately held back by a feeling that all types of variability should be accounted for by a single type of mechanism, which, as will be shown later, is far from the case.

The publication of stellar catalogues in the 1800s greatly assisted the search for stellar variability, and by the end of the century nearly 400 variables were known (Petit, 1987). However, it was not until the advent of astronomical photography that the number of discovered variables increased dramatically. By 1958 Kukarkin's 'General Catalogue' contained the positions of 10912 variable stars and by 1988 the number published in the General Catalogue of Variable Stars (GCVS) (Petit, 1987) had risen to 37470. Today this number has risen further and the total number of stars known or suspected to be variable is well in excess of 50000 (Samus & Durlevich, 1998), although in many cases their individual population statistics are poorly known.

In contrast to the 18th century belief, variable stars come in many different forms with their variability driven by a variety of different mechanisms including thermal instabilities, magnetic interactions or the gravitational effects of a binary pair. Examples of variables driven by each of these mechanisms will be given in the subsequent sections.

1.2 Single Star Variability

1.2.1 Short Period Pulsating Variables

Many stars go through a stage of short period pulsation at one or more points in their lifetime. When plotted on a Hertzsprung-Russell diagram such stars appear in the region known as the instability strip (Figure 1.1).

These variables come in many subtypes, some of which will be discussed later, but all of them vary due to radial pulsations. The pulsations occur due to a resonant effect in the outer layers of the star which does not affect the energy generating core. The instability strip on the HR diagram represents the locus of points where a He^{+} He^{++} ionization layer exists at the right depth to drive the oscillation. If the star becomes compressed for any reason, the higher density results in a higher level of ionization, and not a higher temperature. The opacity (κ) of the layers varies approximately according to Equation 1.1 and so increases if a density (ρ) increase at constant temperature (T) occurs.

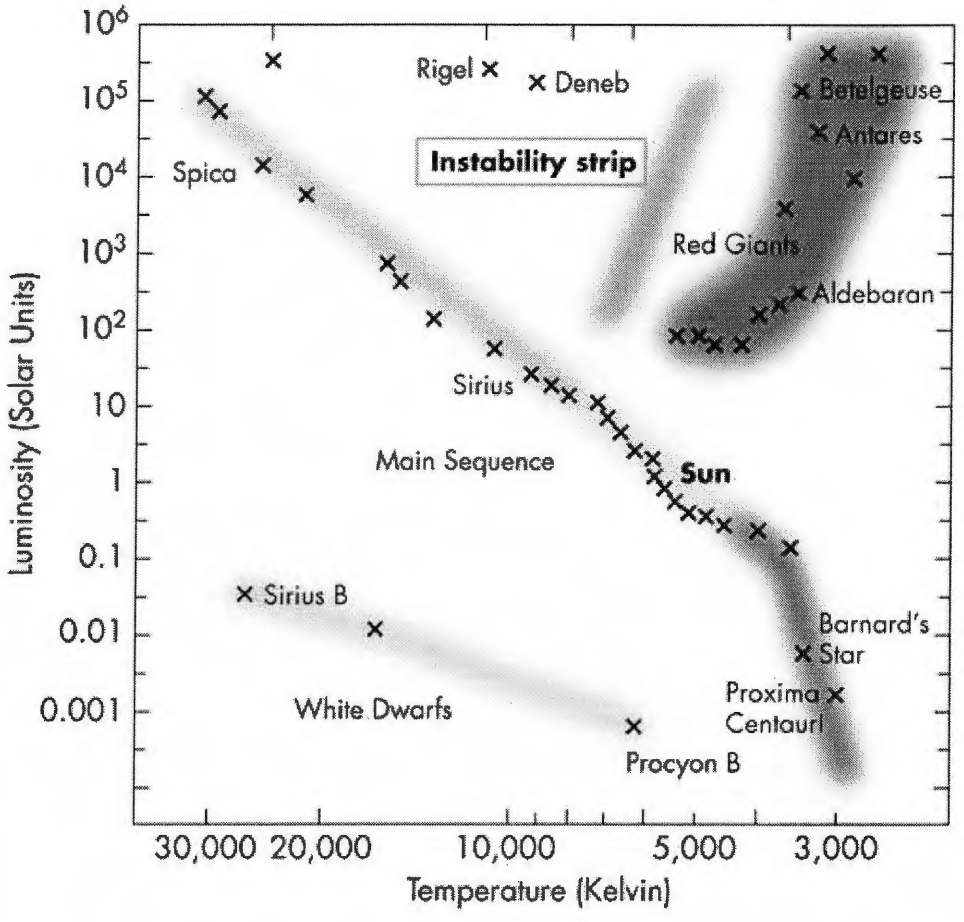

Figure 1.1: A Hertzsprung-Russell Diagram. Note the instability strip clearly labeled towards the top of the diagram, (Arny, 2000, Ch.12)

$$\kappa \propto \rho/T^3 \tag{1.1}$$

Due to the increased opacity during the contraction phase, energy is trapped by the ionization layer. When the contraction is reversed the energy is released, driving the layer past its original starting point and causing another contraction which results in an undamped oscillation of the stellar surface. The change in radius of the pulsating star causes a change in its surface area which in turn alternately increases and decreases the brightness of the source. There are many different types of pulsating variable dependent upon the mass and chemical composition of the star when it evolves onto the instability strip. All of these are interesting in their own right, but due to the constraints of their nature some are also of great use as cosmological distance finders. Classical Cepheids are a good example of this as they display a fundamental relationship between their period

and luminosity. The period of the pulsations in a Cepheid is determined by the density of the star, which is in turn determined by its mass. Since luminosity is also determined by mass a linear relationship exists. For this reason the Cepheid variable population has long been used as a 'standard candle' for distance measurement.

Cepheid Variables

The first Cepheid variable to be discovered (and the star from which this class of pulsator takes its name) was δ Cephei, which although included in Hipparchus' 126 B.C. star catalogue, was not found to be variable until 1784. In fact Cepheid variables can be split further into two categories, the classical Cepheids and the W Virginis type stars. For many years these stars were considered to be part of the same group, but were later discovered to have significantly different lightcurves and also a significantly different period-luminosity relationship (Figure 1.2 below).

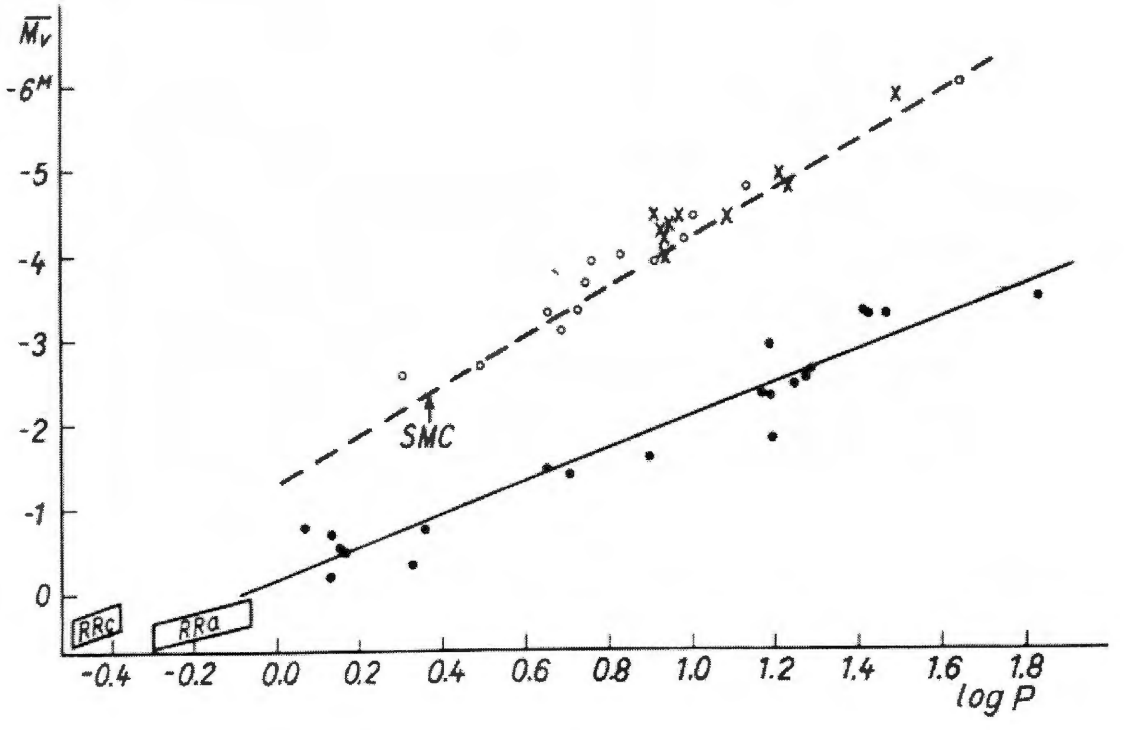

Figure 1.2: Period Luminosity relation for Cepheid (dashed line) and W Virginis stars (filled line) (Hoffmeister *et al*, 1985, p28)

In fact the classical Cepheids are all Population I stars whereas the W Virginis type

tend to be much older and can belong to Population II. All Cepheids are supergiants of spectral class F-K (Hoffmeister *et al.*, 1985) and both types display a similar range of variation. The pulsation amplitude is generally quite large (between 1 and 2 magnitudes) although amplitudes as small as 0.1 magnitudes have also been observed.

Lightcurves of a typical classical Cepheid and W Virginis star are displayed in Figure 1.3. Typically both types of Cepheid have periods between 1 and 70 days; periods below 2 days and above 50 days are rare and longer periods are generally associated with a later spectral type and a larger amplitude. As can be seen in Figure 1.3, the shape of the lightcurve is distinctly different between the two sub-types. Classical Cepheids display a saw toothed curve with a fast rise and slow decline, whereas the older W Virginis stars tend to show more complex brightness variations.

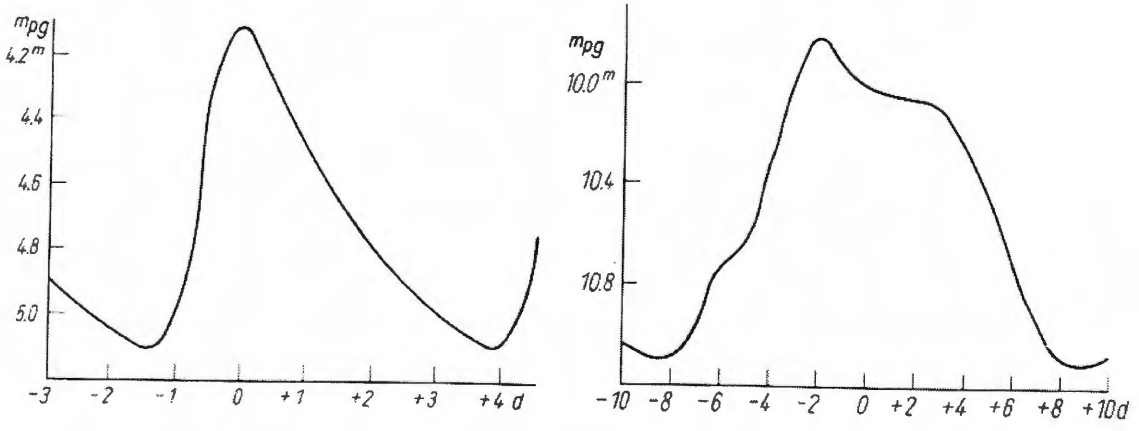

Figure 1.3: Comparison of classical Cepheid (left) and W Virginis (right) lightcurves (Hoffmeister *et al*, 1985, p27)

RR Lyrae stars

Like W Virginis stars, RR Lyraes are older stars and can often be found in globular clusters. They have shorter periods than Cepheids (0.2-1 day) and an earlier spectral type (late A to early F). RR Lyrae stars occupy a region of the HR diagram known as the RR Lyrae gap, where the horizontal branch intercepts the instability strip. These stars do not have a period luminosity relationship, but due to their position on the horizontal branch, all RR Lyrae stars have an absolute magnitude of +0.6 with some variation due to chemical composition and mass (Petit, 1987). RR Lyraes come in three types dependent

upon the behaviour of their lightcurves. RRa and RRb types have classical Cepheid like lightcurves with periods of around 0.5 days whereas RRc types display smaller amplitude, nearly sinusoidal lightcurves with periods of around 0.3 days (Figure 1.4). Only about 10% of RR Lyraes are type c and the difference in their behaviour is thought to be due to their higher metallicity.

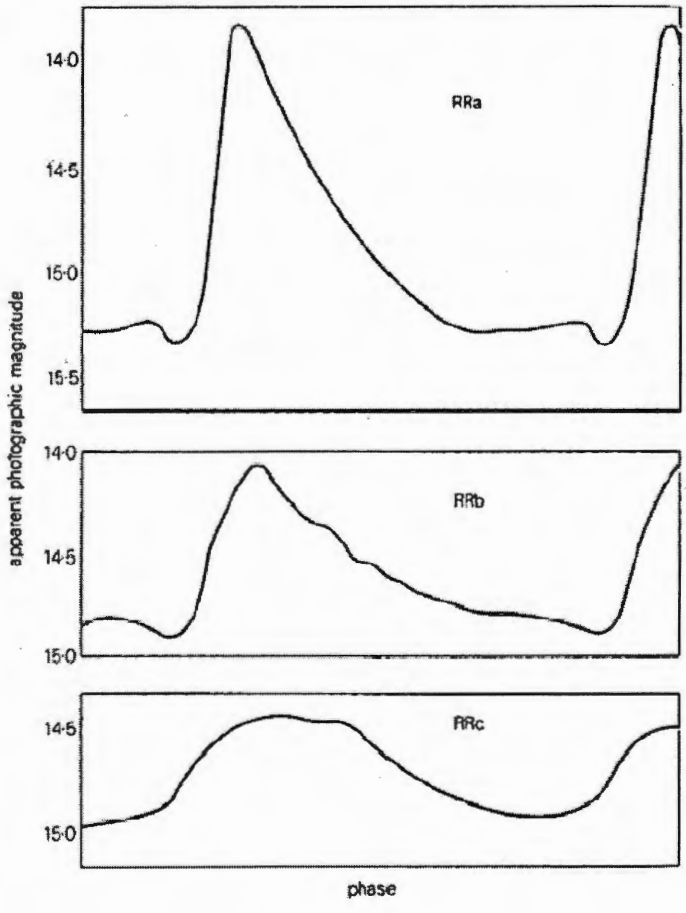

Figure 1.4: Lightcurve for RR Lyrae systems, for subclasses RRa, RRb, RRc (respectively top, middle and bottom) (Hoffmeister *et al*, 1985, p40)

δ Scuti Stars

δ Scuti stars lie in a similar position to RR Lyrae stars on the HR diagram, but have a normal heavy element abundance (RR Lyraes are low in heavy elements as they are generally globular cluster stars). They often have amplitudes of less than a tenth of a

magnitude (Petit, 1987) and periods between 0.02 and 0.25 days (Figure 1.5). These stars tend to show superimposed periods and in some cases modulation periods some 20-50 times the original period have been found. δ Scuti stars are young Population I stars with spectral types from approximately A5 to F5.

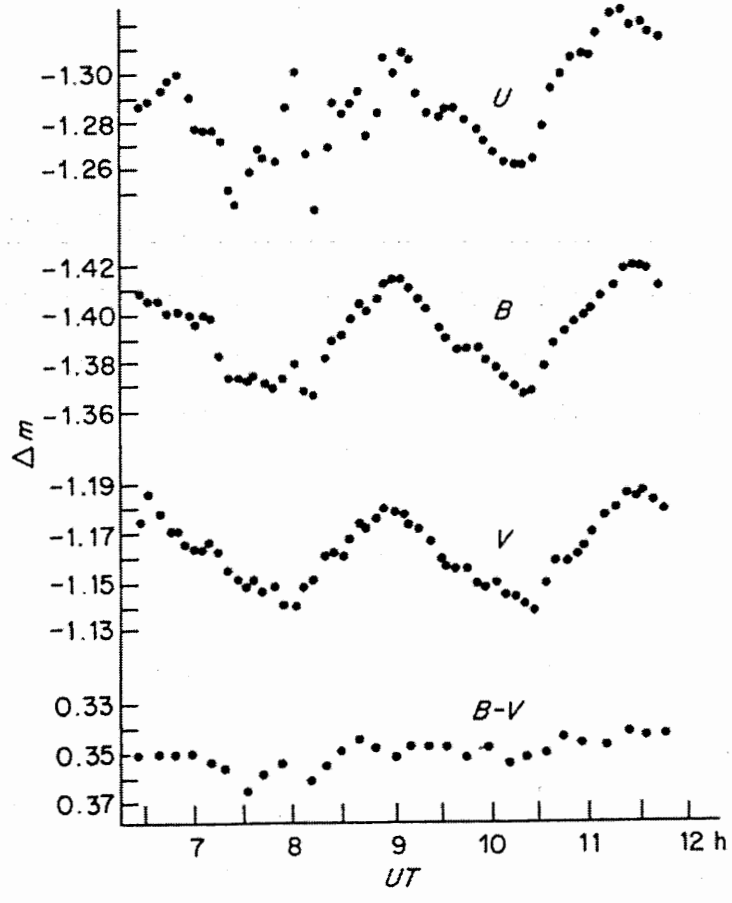

Figure 1.5: Lightcurve for a δ scuti system in U, B and V filters, y-axis is amplitude with respect to comparison star. The B-V colour variation is also displayed (Petit, 1987, p80)

Other types of short period pulsating variables do exist but they are rarer and have many properties in common with those stars already considered. These stars will not be discussed further here.

1.2.2 Long Period Pulsating Variables

Long period variables such as Mira have a typical period of around a year or more. These stars lie on the right of the HR diagram away from the instability strip, but their pulsation

is also thought to be driven by a change in opacity. In this case though, the opacity change does not come from helium ionization but instead from the dissociation and subsequent recombination of various molecules (including oxides of titanium, carbon and cyanogen) and also dust composed of metallic silicates (Petit, 1987). It is thought that the pulsation begins in the deepest layer of the star and then propagates to the surface over time. Once it reaches the surface layers of the star the pulsation creates a shock wave that heats and dissociates the molecules and dust. After the shock wave has passed the temperature falls, allowing the molecules to recombine and the opacity increases again. Long period variables are categorised as either type M,C or S dependent upon their spectra. Type M is by far the most common and encompasses over 90% of the population. The lightcurve of a Mira type variable is displayed in Figure 1.6.

The appearance of the stellar spectrum changes completely over the cycle with the hydrogen Balmer series and lines of iron and silicon being prominent at maximum but almost invisible near the minimum of the cycle. The periods of these stars also vary considerably; in the case of Mira from observed extremes of 310 to 370 days.

Other types of pulsating variable classed as semi-regular and irregular also exist. Semi-regular variables are red pulsating stars with more complex periods and smaller amplitudes than long period variables, whilst the luminosity fluctuations of irregular variables are too random to define a period at all. A typical lightcurve for an irregular variable is displayed in Figure 1.7.

1.2.3 Magnetic Effects and Variability

From the study of our own Sun it is clear that magnetic fields can play an important role in the behaviour of a star. Sunspots, plages, solar flares and Coronal Mass Ejections (CMEs) are all thought to be related to or caused by the solar magnetic field. Although these effects can be viewed in the Sun with current technology, they cannot be said to make the Sun variable in the sense that is being discussed here. However, in cases where the magnetic field is higher or the inherent luminosity of the star is lower, magnetic fields can cause significant stellar variability.

Flare stars

Flare stars come in two types. UV Ceti type stars (which will be the main topic of this discussion) show shorter but more frequent flares, whilst flare stars in galactic clusters

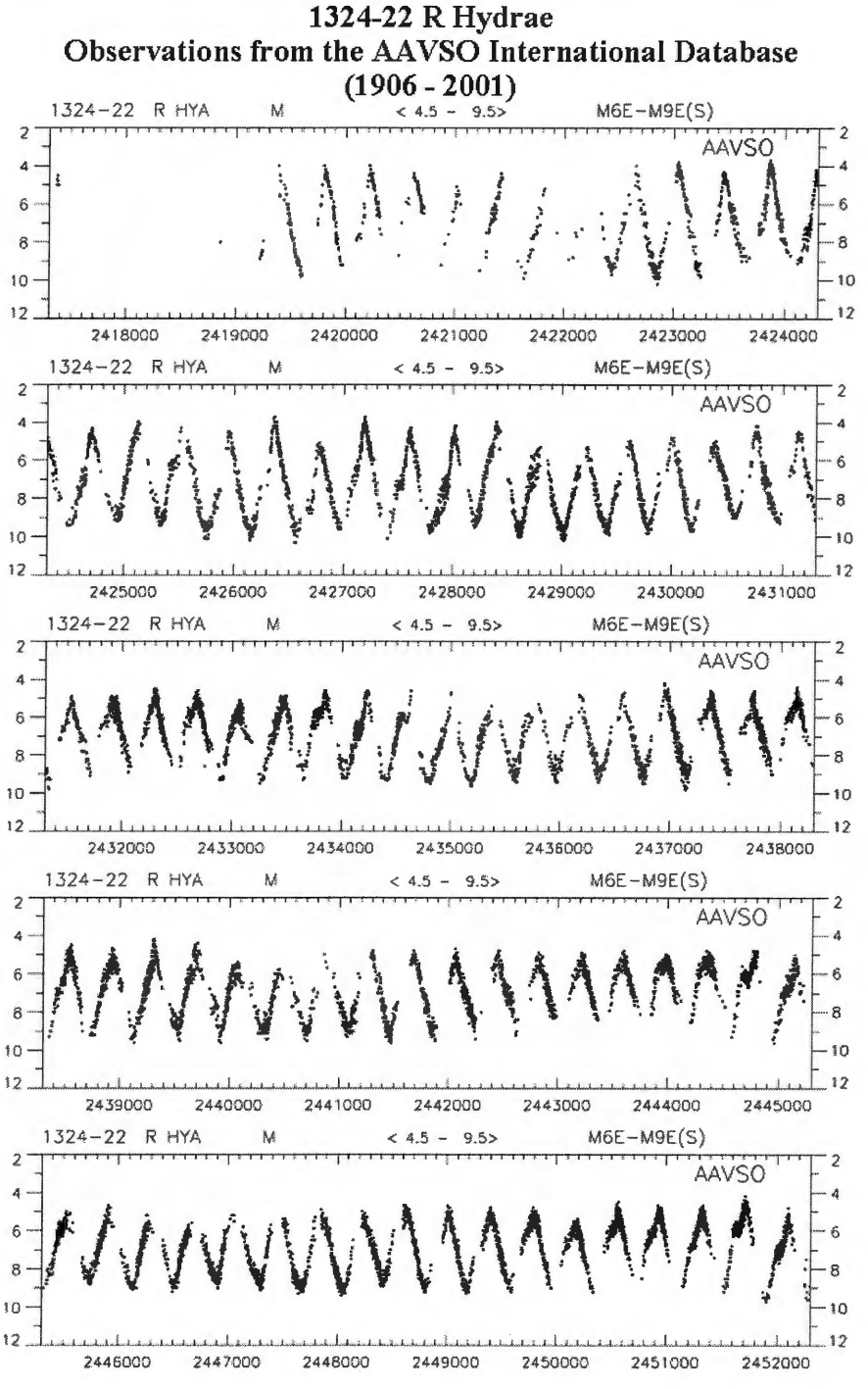

Figure 1.6: Long term lightcurve for R Hydrae, a Mira type variable, courtesy of the AAVSO.

tend to show longer less frequent flares (Mirzoian, 1984). Flare stars are all red dwarfs. In particular, they tend to have a spectral classification of dMe although this is not always the case. The mechanism driving the flares is probably related to the reconnection of

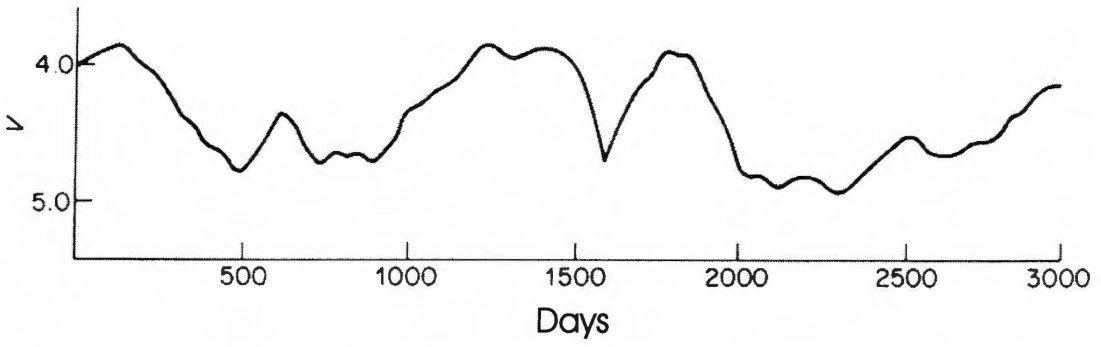

Figure 1.7: A typical irregular variable (Petit, 1987, p71)

magnetic field lines (in a similar way to solar flares) but the actual flare morphology and the plasma heating mechanism are not well known. The total energy released during a stellar flare can be as much as 2-3 orders of magnitude greater than a large solar flare, even though red dwarf masses range from approximately 0.08 to 0.51 solar masses and have corresponding luminosities of between around 0.001 and 0.08 solar (Mirzoian, 1984). The difference in this outburst behaviour may be related to the fact that the interiors of red dwarfs tend to be between 60% and 100% convective, in contrast to the Sun which is convective only in its outer layers.

UV Ceti type stars tend to show two distinctly different types of outburst behaviour. Type I flares rise to maximum brightness in a few seconds or minutes (generally with amplitudes of a few magnitudes) and the decline may last between about 10 minutes and 2 hours. In Type II events the rise and fall of the flare occurs about an order of magnitude more slowly (Hoffmeister *et al.*, 1985). In some cases a 'pre flare dip' is observed and occasionally anti-flares resulting in an abrupt decrease in brightness are seen (Mirzoian, 1984). Some of this behaviour is displayed in Figure 1.8.

Spotted stars

Spotted or BY Draconis stars are another type of variable associated with magnetic fields. Like the UV Ceti stars they are red dwarfs and in fact often also show flares, leading some astronomers to class them together (as some stars classified as UV Ceti also show BY Draconis-like variations). BY Draconis stars show periodic luminosity variations with variable amplitudes, typically up to 0.5 magnitudes. Periods range from hours to days and sample lightcurves for BY Draconis stars are shown in Figure 1.9. The variability of BY

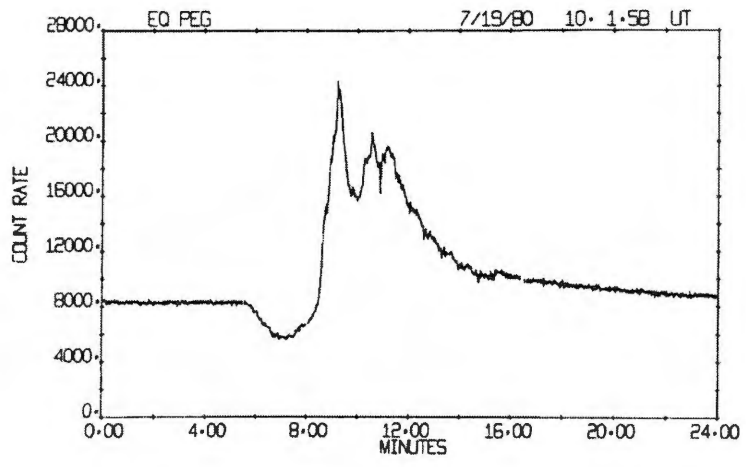

Figure 1.8: Type I stellar flare displaying a pre-flare dip (Mirzoian, 1984).

Draconis stars is thought to be caused by hot and/or cold spots on the stellar surface, not dissimilar to sunspots but much greater in size. Some success has been found by modelling lightcurves with spots covering 5-20% of the visible hemisphere with a temperature approximately 500-1500K less than the surrounding photosphere (Hoffmeister *et al.*, 1985). Again the explanation for this behaviour is thought to be magnetic and similar to that which forms sunspots. As yet the phenomenon is not thoroughly understood.

1.3 Binary Variability

Many types of variable star are not individual stars at all but rather are members of a binary pair. Binary interactions give rise to a host of variations both through accretive and non-accretive processes which will be covered in the next section. In fact, more stars exist in binary systems than exist singly in the galaxy, and the types of star involved in the pairing (from black holes and neutron stars to brown dwarfs) obviously has a huge effect on the variability that is exhibited. However, the basic physics governing the behaviour of all binary systems is the same.

1.3.1 Basic Binary Physics

Binary systems are composed of two stars which orbit a common centre of mass. The mass of the more massive or primary star is denoted M_1 and that of the less massive or

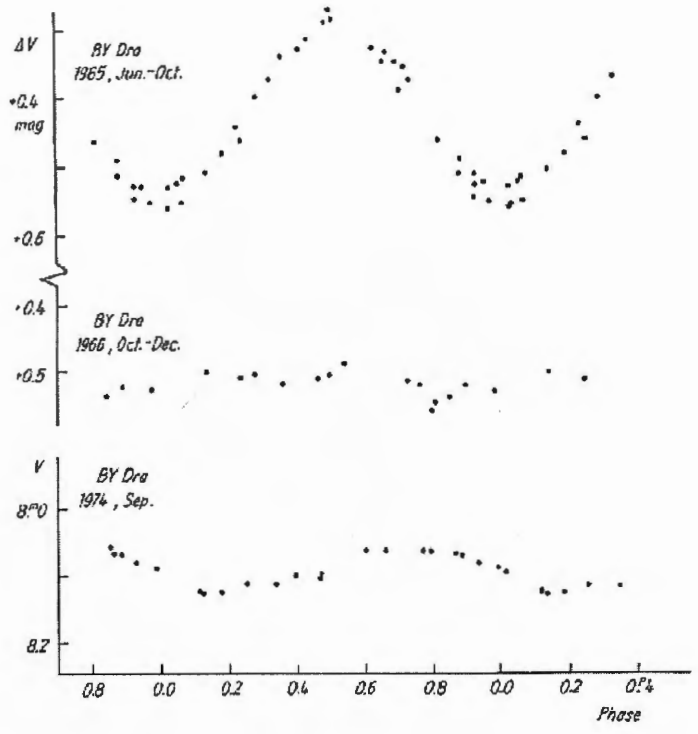

Figure 1.9: Typical lightcurves of BY Draconis at different epochs (Hoffmeister *et al.*, 1985, p190)

secondary star M_2. Thus a mass ratio q can be defined as

$$q = M_2/M_1 \tag{1.2}$$

The main parameters governing the evolution of a binary system are the mass ratio, separation, magnetic field and angular momentum of the pair. For each star in a binary pair a Roche lobe can be defined. This marks the largest closed equipotential which can contain the mass of the star (Figure 1.10).

The shape of the Roche equipotentials is a function only of the mass ratio q, and the scale is defined by the binary separation, a (Warner, 1995). L_1 marks the inner Lagrange point, at which the gravitational and centrifugal forces felt by a test mass exactly balance. Binary systems can be defined as detached, semi-detached or contact dependent upon whether zero, one or both of the stars fill their Roche lobes. In the case of semi-detached systems when the secondary star overfills its Roche lobe, mass will be transferred through the inner Lagrange point on to the primary star. This is the major process which drives eruptive binary systems and will be discussed in detail later. However, accretive behaviour is not essential for variability in binaries.

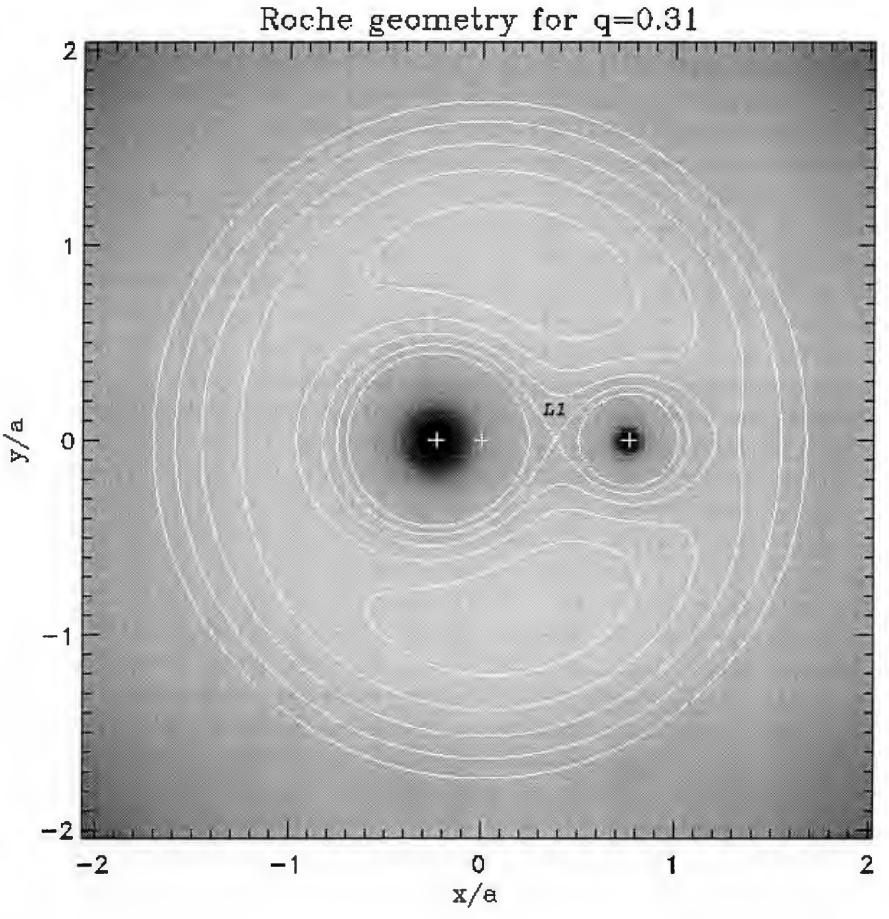

Figure 1.10: Roche equi-potentials for a binary system (Rolfe, 2001)

1.3.2 Variability in Non-accreting Binaries

Eclipsing Binaries

In a binary system an eclipse occurs when one member of the binary passes between the observer and the other star of the pair, reducing the total amount of light received. The variation in brightness this causes can take many forms, dependent upon the viewing angle and the size and separation of the components. The GCVS (Samus & Durlevich, 1998) describes three categories of binary star. EA or Algol systems are binaries with spherical or only slightly tidally distorted components. Between eclipses the light remains almost

constant and an extremely wide range of periods may be observed. Contact systems in which the binary components have very different luminosities are known as EB or Beta Lyrae type. These systems display no period of constant brightness and show primary and secondary minima which are distinctly different. Periods tend to be longer than a day and amplitudes are generally <0.2 magnitudes in V. The final classification is EW or W Ursae Majoris type eclipsing systems. These are contact systems which show equal primary and secondary minima. No period of constant light is observed and light amplitudes are generally <0.8 magnitudes in V. Many other factors can also affect the shape of the lightcurve, including relative size and surface brightness of the stellar disk, the ratio between orbital and stellar radii and the viewing angle of the system (Figure 1.11).

Ellipsoidal variations

A less obvious type of variation that can occur in non-accreting binaries is ellipsoidal variation. Ellipsoidal variations occur in systems that are not eclipsing but are close enough together and massive enough that the stars are distorted into ellipsoids by their mutual gravitation. Thus, when the shortest axes of the ellipsoids are parallel to the line of sight the brightness will be at its greatest and when the longest axes are aligned with the line of sight then the opposite will be true (Figure 1.12). In some cases, stronger limb darkening effects at the pointed end of the more extended star may cause one of the minima to be significantly deeper than the other (Hall, 1990). Systems which undergo ellipsoidal variations tend to have amplitudes of around 0.1 magnitudes and are designated Ell by the GCVS.

1.3.3 Accreting Binary Systems

If one of the stars in a binary pair over-fills its Roche lobe then it will begin to lose mass to the other member of the pair. This can occur either because the separation of the binary components has become smaller, or because one of the stars has undergone a period of expansion in the course of its evolution. In either case, a period of accretion will then occur which will either be stable and result in either a symbiotic star or the formation of a long lived accreting binary, or unstable, possibly resulting in the destruction of the donor star.

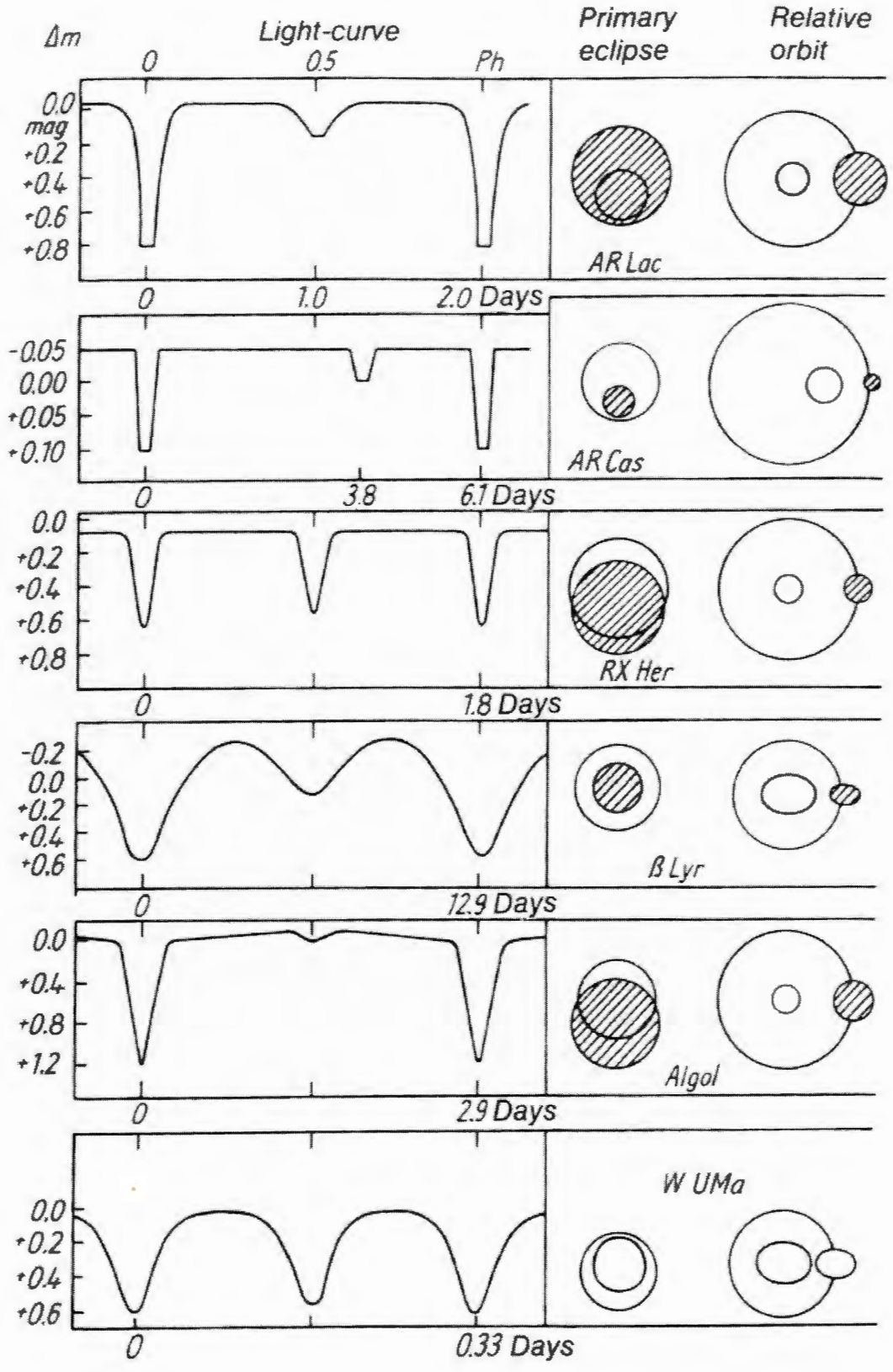

Figure 1.11: Some possible eclipse orientations (right) and the resultant light curve variations (left) (Hoffmeister *et al.*, 1985, p201)

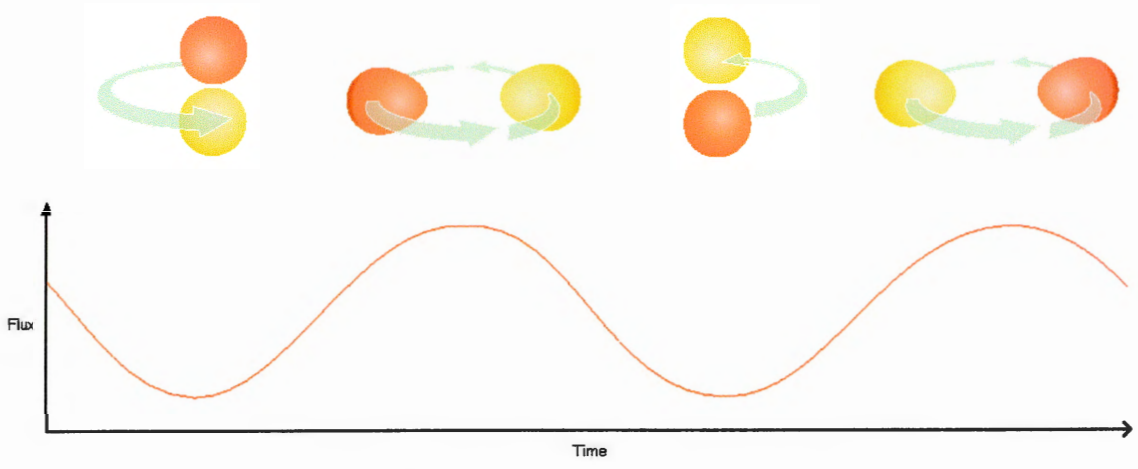

Figure 1.12: Ellipsoidal variation in a non-eclipsing binary system.

Unstable Mass Transfer

Unstable accretion can occur when the mass of the donor star is almost equal to or greater than the mass of the primary. More specifically it occurs when $q \geq \frac{5}{6}$ although this does depend slightly upon the mass-radius relation of the star (Frank *et al.*, 2001). If the star does not manage to contract rapidly enough to stay within its Roche lobe the process can become very violent. Unstable accretion occurs on either the thermal or dynamic timescale of the secondary, dependent upon whether the core is radiative or convective and will continue until the mass ratio becomes less than the critical value. This phase of binary evolution occurs on a very short timescale and so is very difficult to observe. The same cannot be said about binaries undergoing stable accretion though, and many different varieties of these systems have been discovered.

Stable Mass Transfer

In cases where the mass ratio is less than $\frac{5}{6}$ then stable mass transfer can occur. The physics of this process will be discussed in detail in the next chapter. In cases where the magnetic field is low, matter from the secondary will form into a disk or torus around the primary star. In the high magnetic field regime, mass will be funnelled along the field lines into an accretion column which impacts the primary star at its magnetic pole. The behaviour of an accreting binary system, and so its classification, is dependent upon the types of the component stars. The primary in such a system is a compact object, generally either a white dwarf (in the case of cataclysmic variable stars (CVs)) or a neutron star

or black hole (in the case of low and high mass X-ray binaries). The secondary is most commonly a main sequence star. The outburst characteristics of these systems are many and varied from low amplitude flickering to high amplitude nova outbursts, with the more energetic members of this class (the LMXBs and HMXBs) emitting most of their energy in the X-ray and γ-ray regimes. However, it is the members of the accreting binary group which emit primarily at lower energies that are of interest to this project. Cataclysmic variables are responsible for the nova outbursts which were one of man's first detections of stellar variability, and are still of great scientific interest today.

Chapter 2

Introduction to Cataclysmic Variables

Cataclysmic variables (CVs) are binary systems composed of a white dwarf (WD) primary star and generally a low mass main sequence secondary star (normally a G,K, or M class dwarf) which is filling its Roche lobe. In some instances the main sequence star can be replaced by an evolved star (eg. GK Per) or another white dwarf in the case of AM CVn or double degenerate systems. The accretion geometry of the system depends upon the strength of the WD magnetic field, with an accretion disc being formed in the low field case and an accretion column in the high field case. Both of these states will be discussed in detail below.

Apart from scientific curiosity there are many other reasons to study cataclysmic variables. Firstly they are binary systems, and as previously stated, binary systems account for a large fraction of the stars in the Galaxy. Thus we must be able to understand the behaviour of their various subtypes if we are to really understand our Galaxy. Secondly it is thought that Type Ia supernovae (by far the most energetic events we ever see in the Galaxy) could be caused by the explosion of an accreting white dwarf, and the study of CVs may help us understand this phenomenon better also. Thirdly, CVs provide a laboratory in which we can locally view phenomena that are important in other areas of astrophysics, such as active galactic nuclei (which may undergo accretion in a very similar way to CVs although on a much larger scale) and also situations in which disk formation is important i.e. at the birth of stellar systems. Finally, due to the energetic nature of their interactions and eruptions, cataclysmic variables provide a test bed for theoretical physics that is currently impossible to replicate in the laboratory.

CVs have been observed and monitored for many years, originally because of the high amplitude outburst behaviour that some of these systems undergo and more recently because of interest in their detailed physics. In fact, complete lightcurves for some CVs exist which have a base-line of over 100 years (Figure 2.1).

Although great progress has been made in understanding the physics that governs the outburst behaviour and accretion geometry of individual systems, the current population of cataclysmic variables and their evolutionary paths remain poorly known. This chapter will discuss the physics of accretion in both magnetic and non magnetic CVs and the observable characteristics that this implies. CV population densities will be discussed in more detail later.

2.1 The Physics of cataclysmic variables

2.1.1 Some Physical Parameters

As stated previously, the mass ratio, q, of a CV must be less than $\frac{5}{6}$ for accretion to be stable, with a typical value of around 0.64 for CVs above the period gap (this will be discussed later) (Webbink, 1990). Primary masses tend to range between 0.5 and 1.0 $M_{\odot}$ (the maximum white dwarf mass of 1.44 $M_{\odot}$ is given by the Chandresekhar limit) (Warner, 1995). Mass transfer generally occurs at a rate between $10^{-11} \leq \dot{M} \leq 10^{-8} M_{\odot} yr^{-1}$. The upper limit on $\dot{M}$ is due to the behaviour of the white dwarf, as at greater values of $\dot{M}$ the WD will become a giant star and the system will become symbiotic, rather than remaining as a CV. The lower limit on $\dot{M}$ is imposed by gravitational waves which remove angular momentum from the system, forcing the secondary to remain in contact with its Roche lobe (Smak, 1999). CVs typically have periods between around 80 minutes and about 15 hours (Wade & Ward, 1985) which implies through Kepler's third law that a, the binary separation between the stars, is small. Using Equation 2.1 below yields a value for the binary separation that is comparable to the radius of the Sun (Wade & Ward, 1985), where P is the orbital period in hours and M the total mass of the binary system in units of solar mass.

$$a = (3.5 \times 10^{10} cm) P^{\frac{2}{3}} M^{\frac{1}{3}} \tag{2.1}$$

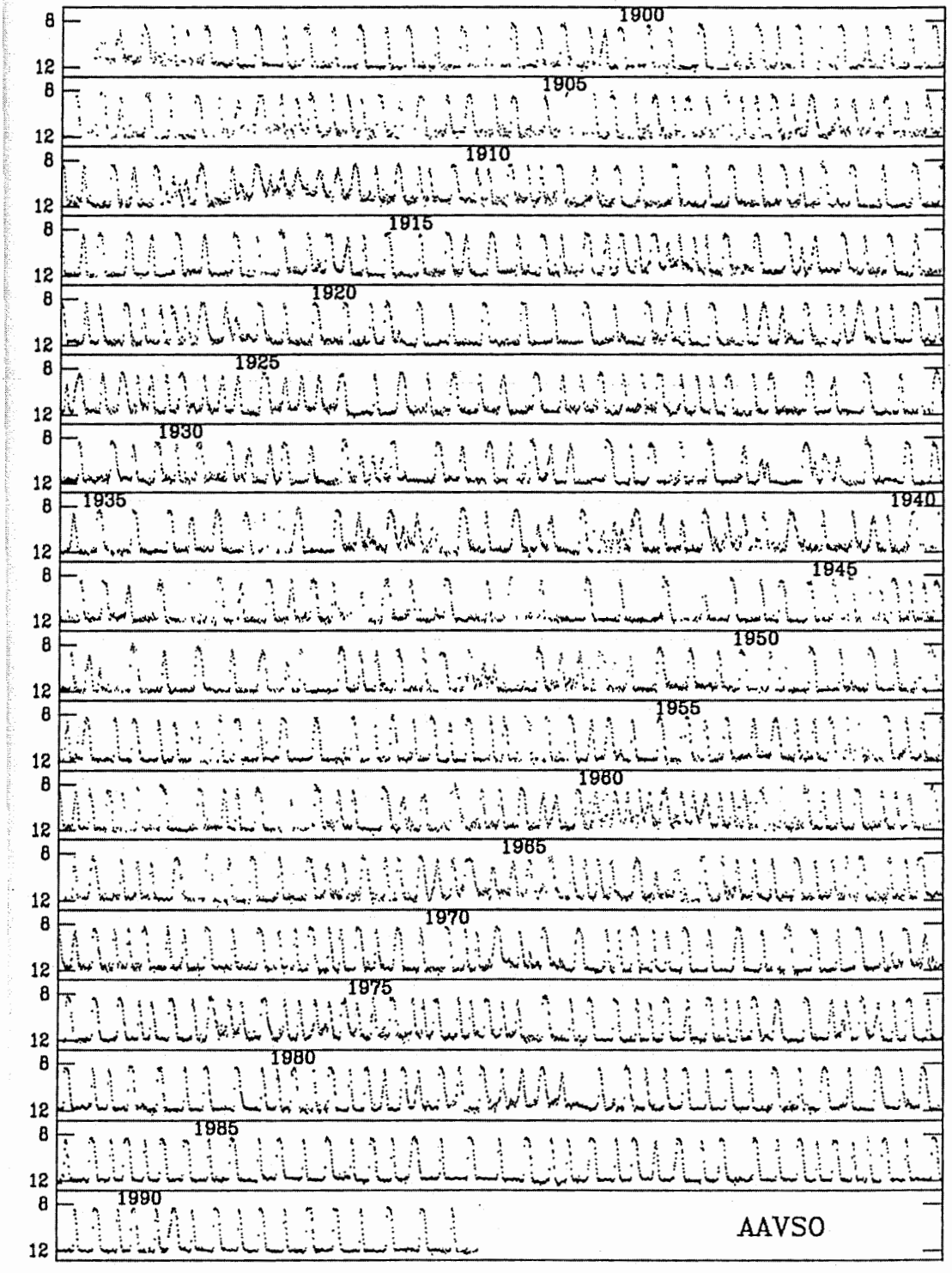

Figure 2.1: Lightcurve of CV SS Cyg from the American Association of Variable Star Observers (AAVSO) (Warner, 1995, p51).

2.1.2 Angular Momentum Loss

Angular momentum loss is the main driving force in the evolution of cataclysmic variables. In general for a system without angular momentum loss ($\dot{J}$), accretion onto the primary star causes mass to move closer to the centre of mass of the system. In order to conserve angular momentum this would result in the donor star moving away from the white dwarf, resulting in a period increase and eventually, when the Roche lobe of the secondary ceases to shrink, a cessation of mass transfer. This may be avoided if the secondary is an evolved star which is expanding on a nuclear timescale (Warner, 1995), but for most CVs this is not the case. Instead a mechanism is needed which can remove angular momentum (but not mass) from the system. Two mechanisms can be invoked to cause this effect and both are probably important at some stage in the evolution of a cataclysmic variable.

Magnetic Braking

Magnetic braking occurs in all stars in which an ionized stellar wind and a magnetic field interact. At any given time an ionized particle in a stellar wind will attempt to travel in a straight line. However, the magnetic field of a star out to the Alfvén radius co-rotates with the star. As ionized particles will not cross field lines, a braking torque due to Maxwell stresses will be felt by the central body that will be sufficient to slow it down resulting in a loss of angular momentum to the stellar wind.

This effect can be seen in our own solar system and accounts for the slowness of the solar rotation (Warner, 1995). However, in a system which is tidally locked such as a close binary system, spin-orbit coupling stops the secondary star from losing rotational angular momentum via a magnetic wind, and instead angular momentum is lost from the orbit. As the strength of a stellar magnetic field can change over the lifetime of the object (magnetic fields are often associated with the depth of the convective zone in the star) magnetic braking can become more or less important over the lifetime of the star. The cessation and continuation of magnetic braking has several implications for the evolution of cataclysmic variables which will be discussed in subsequent chapters.

Gravitational Radiation

General relativity predicts that binary stars will emit gravitational waves and in CVs with short enough periods this may become a significant angular momentum loss mechanism. Gravitational braking is not efficient enough to account for the accretion rate in high

$\dot{M}$ systems but it may be the dominant mechanism for lower accretion rate systems and probably dominates CV evolution at some stages (notably in the period gap, cf. chapter 4). Also, as was mentioned previously, gravitational radiation is responsible for the minimum accretion rate in CVs.

2.2 Non-Magnetic CVs

A schematic of a non-magnetic CV is shown below (Figure 2.2).

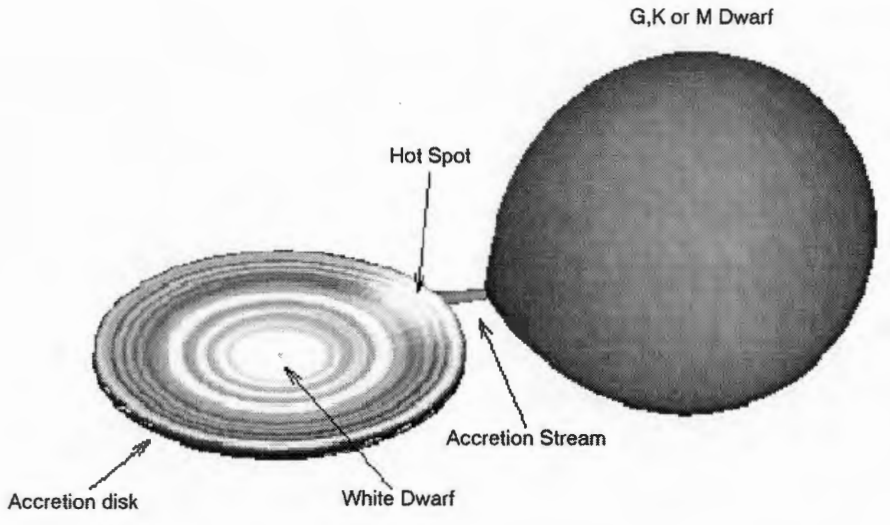

Figure 2.2: Schematic of a non-magnetic CV (Rolfe, 2001).

The main components of the system are the primary and secondary star, the accretion disc and the hot spot (the hot spot is formed at the point where the accretion stream impacts the disc). The disc has a profound effect on the observational characteristics of the system and its outburst behaviour, and it is easy to see why a disc such as this is formed in the case of a non-magnetic accreting system. Assuming that the mass of a stream element is negligible compared to the two stars, the trajectory of the accretion flow can be treated as a restricted three body problem (Smak, 1999). After passing the primary the stream element moves in a rapidly precessing elliptical orbit due to the influence of the secondary star. In the case of an accretion stream rather than a single element, collisions

between stream elements dissipate energy resulting in the formation of a torus. Viscosity effects eventually expand the torus into a disc and material from the disc is then accreted onto the surface of the WD where a boundary layer (BL) is formed. At high mass transfer rates the disc luminosity can dominate the total flux of the system. Conversely, at low accretion rates, the hot spot can account for as much as 50% of the quiescent flux with the disc making only a small contribution (Smak, 1999). If a CV has an orbital inclination, i, larger than around 65-70 degrees (at 90 degrees the system is viewed completely side-on) then eclipses can be observed. These can reveal much information about the geometry and relative brightness of individual components in the system. A schematic of an eclipse is shown in Figure 2.3

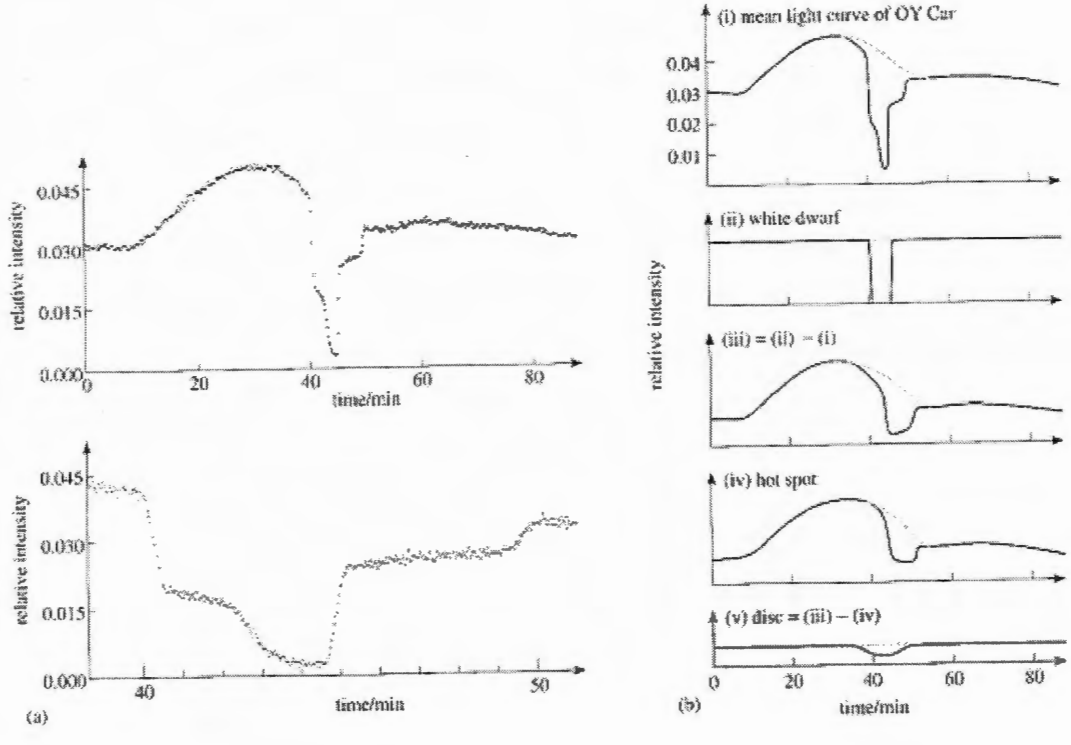

Figure 2.3: An eclipse of the disk, hot spot and primary (Schoembs, 1987).

The figure shows an optical lightcurve for OY Car displaying a hot spot bump, followed by the eclipsing of the disc, hot spot and white dwarf. The panel on the right hand side displays each of these features individually. It is important to note that the disks in cataclysmic variables are not infinitely thin, but in many cases have significant thickness.

Thus, for systems viewed at high inclination, the side of the disc will partially obscure the surface of the disc and the primary star to a varying degree (Figure 2.4)

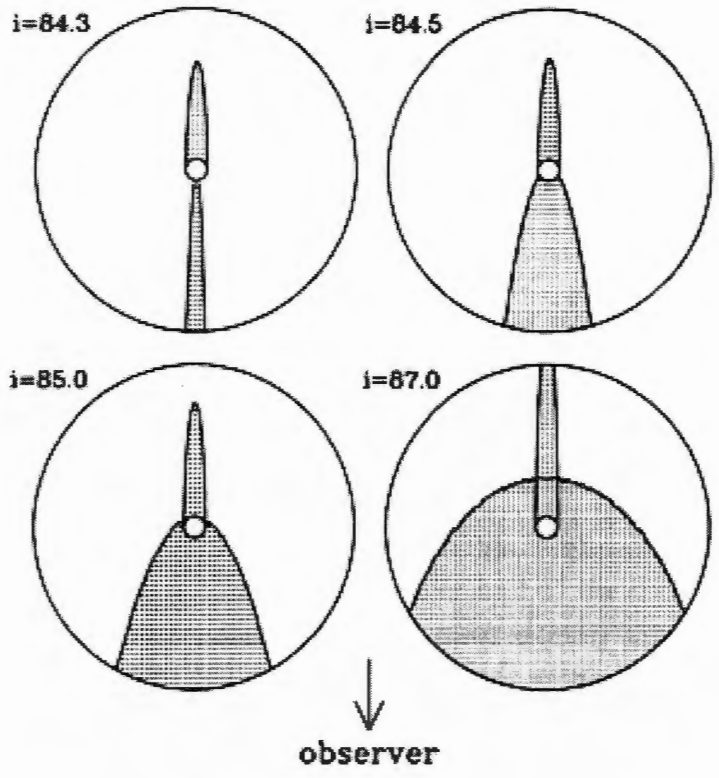

Figure 2.4: Obscuration of the disc surface and the primary by the disc edge for varying inclination i. The shadow caused by the primary itself is also displayed (Smak, 1999).

2.2.1 Variability Mechanisms in Non-Magnetic CVs

Within the subclass of the cataclysmic variable stars, there is still a variety of different brightness variations which can be observed. The observational characteristics of these variations will be described shortly. The physics which drives the variations also differs from type to type however and this will be covered first.

Thermonuclear Runaway

If the accretion rate is high enough (but not too high) thermonuclear runaway can occur on the surface of the white dwarf primary star. As the amount of material accreted onto the primary increases, a boundary between the non-degenerate accreted material and

the degenerate core forms. The equation of state for degenerate matter is temperature insensitive (Equation 2.2) (where P is period ρ is density and α is $\frac{5}{3}$ in the non-relativistic and $\frac{4}{3}$ in the relativistic case)

$$P \propto \rho^{\alpha} \tag{2.2}$$

Thus, if the temperature is high enough for nuclear reactions to occur, a small increase in temperature causes increased energy generation but does not lead to an increase in pressure (Warner, 1995). This process is amplified into a thermonuclear runaway which only subsides when the Fermi temperature is reached and results in the ejection of a substantial shell. To begin with, the nuclear reactions occur according to the proton-proton chain, but as the temperature at the base of the envelope rises, the CNO cycle also becomes important and the layer begins to convect on a timescale of approximately 100s. $\beta+$ particles formed in the reaction network are brought to the surface where they annihilate and deposit large amounts of energy, resulting in the expansion of the envelope and a large increase in luminosity. Eventually the inertia of the envelope causes the temperature to overshoot the Fermi temperature resulting in expansion, followed by cooling and a cessation of nuclear reactions (Warner, 1995). It is interesting to note that in the case of very high $\dot{M}$, thermonuclear runaway is replaced by the steady burning of accreted material upon the surface of the white dwarf (Hernanz & Jordi, 2000).

Disk Instability model

The detailed physics of accretion disks is too long and complex to be described in great depth here. However, we must take time to consider the stability conditions of the accretion disk, as this is responsible for another type of CV outburst. The vertical structure of the disk can be modelled by one independent variable, z (the disk thickness in the vertical direction) and four dependent variables, namely T,F,ρ and Σ respectively the Temperature, Flux, Density and Surface Density. Numerical integration of the four equations governing vertical structure yields the characteristic S-shape of the Σ-T_e relationship (Figure 2.5).

It can be shown by further calculation (Smak, 1999) that the middle branch of this relation is thermally unstable. On the upper and lower branches of the relation an increase in temperature will produce a reaction of opposite sign and vice versa. However, on the middle branch a positive perturbation in T will result in further heating which causes an instability. This instability can drive outburst behaviour.

For many CVs, accretion occurs within the limits of the stable hotter and colder branches of the Σ-T_e relation. However, for those with accretion rates corresponding to the middle branch, steady state accretion is replaced by a limit cycle which alternates between the stable branches.

Locally, at any point in the disk, the limit cycle can be envisaged by Figure 2.5.

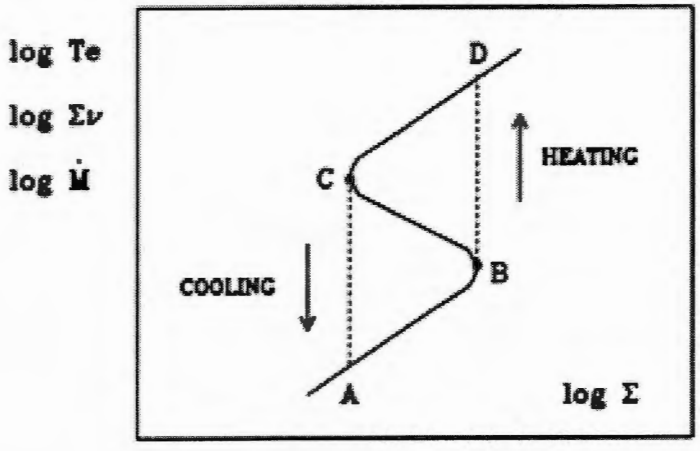

Figure 2.5: Thermal instability S-wave (Smak, 1999).

On branch A-B, the rate of accretion onto the WD ($\dot{M}_{acc}$) is less than the mass transfer rate into the disk ($\dot{M}_{tr}$) and so Σ increases. Once the critical surface density is exceeded at point B, the thermal instability results in an increase in temperature and a rapid transition to branch C-D (this corresponds to the outburst maximum). Now $\dot{M}_{acc}$ is greater than $\dot{M}_{tr}$ and the surface density decreases until point C where a transition to the lower branch occurs again. However, for an outburst to occur this behaviour must propagate throughout the entire disk. Models of the global effects of the limit-cycle mechanism have shown that such an instability can propagate, either from the inside to the outside of the disk or vice versa, resulting in slightly different observable characteristics (Smak, 1999).

Flickering

Two other mechanisms that cause variability in CVs both produce low level stochastic variations in luminosity, or flickering. All CVs show flickering and it is thought to originate both at the hot spot due to inhomogeneities in the accretion stream and in the

turbulent inner region of the accretion disk. The two mechanisms are thought to occur simultaneously with the relative importance of each contribution varying between systems (Warner, 1995) (Figure 2.6).

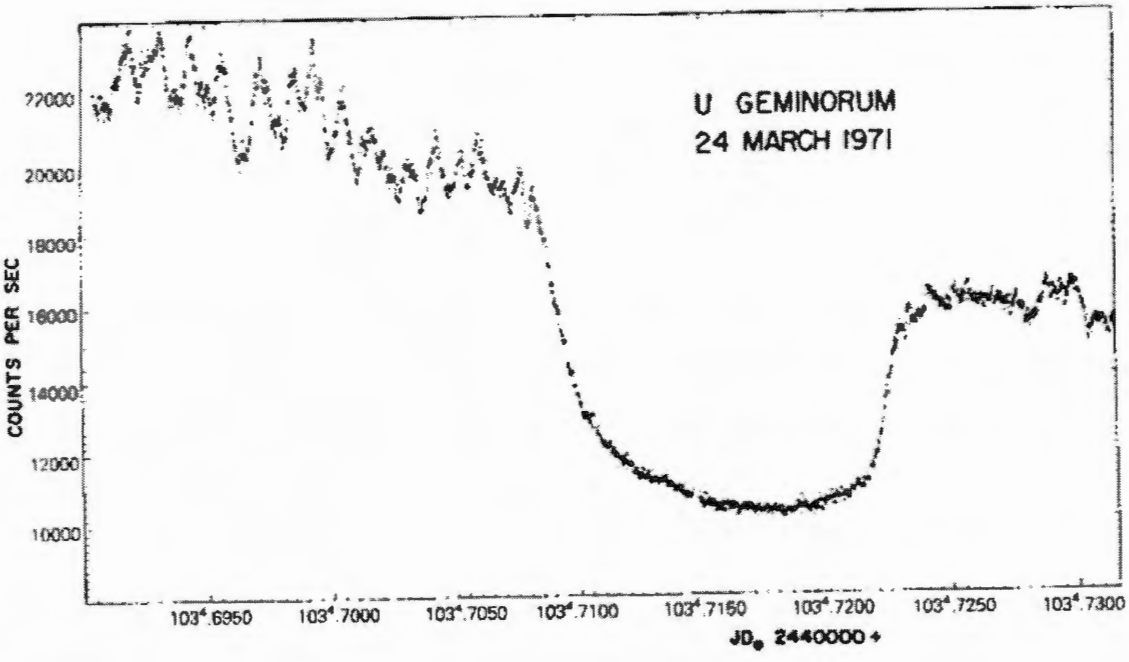

Figure 2.6: Flickering in UGem. Note that the flickering stops once the hot spot is eclipsed in this case (Warner, 1995, p11)

2.2.2 Observational Properties of Non-Magnetic CVs

Although non-magnetic CVs all have a similar basic structure of primary, secondary and accretion disk, there are many subtypes within the group which exhibit distinctly different photometric or spectroscopic properties. There are also some properties that most if not all of these systems have in common. Flickering is one of these, resulting in stochastic variations in luminosity of up to tenths of magnitude with timescales of tens of seconds to many minutes. Generally CVs tend to have blue spectra, which show prominent hydrogen emission lines - although this can vary depending on the current accretion state. Helium absorption lines can also sometimes be seen, along with the various spectral lines associated with a main sequence dwarf star. However, it is the outburst behaviour of cataclysmic variables that originally attracted the attention of observers. Non-magnetic

CVs are firstly classified into four groups based on their general outburst behaviour, with further subgroups within these categories.

Classical novae

Classical novae (CNe) were the first type of CV to be recorded, as the amplitude of their variation is by far the highest of the CV subgroups. In fact, CNe can occur in both magnetic and non-magnetic systems. They are powered by the thermonuclear runaway mechanism that was described in the previous section and have outburst amplitudes ranging from 6 to 19 magnitudes. Classical novae are classed as either fast or slow dependent upon their decay time (Figure 2.7). This ranges from 10 days in the case of very fast novae to around 150 days in the case of slow novae. CNe are reasonably common phenomena occurring with an observed rate of around 3yr^{-1}. Compensating for incompleteness and interstellar extinction, the mean CNe rate in the Galaxy is much higher (estimates range from 73 to 260yr^{-1} (Warner, 1995)). During the nova a substantial shell of material is ejected from the star which can be detected by the Doppler shift of the expanding matter. By definition CNe have only been seen to occur once, although this may be due to the relatively short baseline of modern observations. During quiescence (the period between eruptions) CNe tend to return to their pre-outburst brightness, except in some cases where high magnetic fields are present.

Dwarf Novae

Unlike CNe, dwarf novae (DNe) are not powered by thermonuclear runaway but rather by the disk instability mechanism described earlier. During a dwarf nova outburst the brightness of the system typically increases by between 2 and 5 magnitudes although up to 8 has been observed (Warner, 1995). Most of this luminosity comes from the disk which becomes thermally unstable as described above. Outbursts tend to last between 2 and 20 days and recur on timescales between 10 days and 10s of years, with shorter outbursts related to shorter recurrence times. Generally these timescales are well defined, but some exceptions have been noted, (cf. WZ Sge (Kuulkers, 2002)). Dwarf novae can easily be distinguished from classical novae by their lower amplitude and lack of ejecta.

Dwarf novae can also display DNOs or Dwarf Novae Oscillations with periods from seconds to over a minute and relatively small amplitudes. They are observed during dwarf nova outbursts and are thought to occur in situations where the magnetic field of the

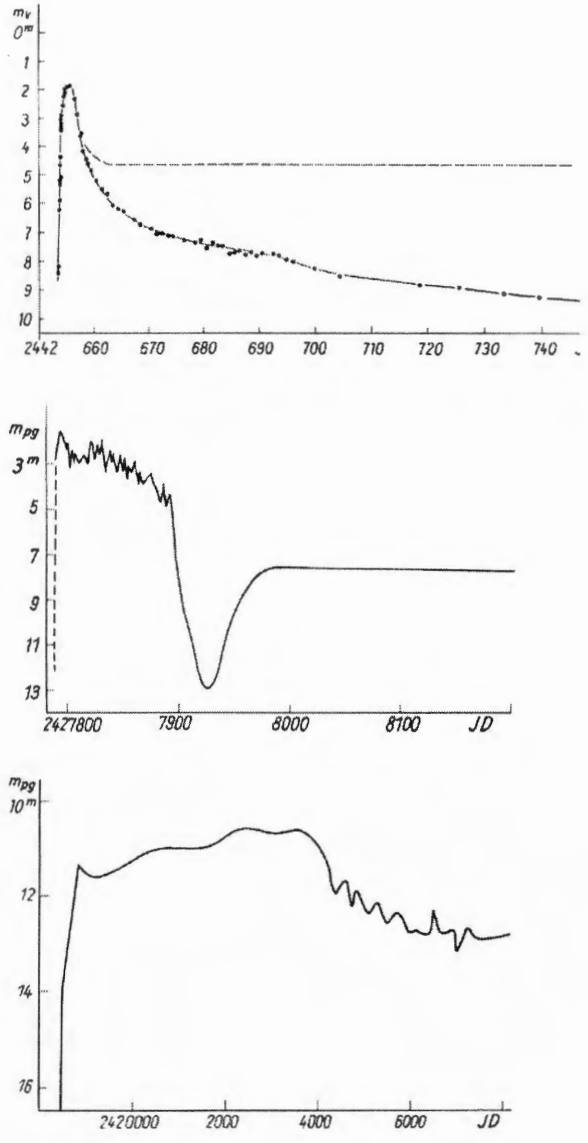

Figure 2.7: Fast, slow and very slow classical novae (Hoffmeister *et al.*, 1985, p83)

primary is low enough to allow differential rotation of its outer layers (Warner, 1995). This causes pulsations on the gravitationally determined timescale of the white dwarf which is generally of the order of a few seconds (Figure 2.8).

The behaviour of individual DNe varies greatly across the group and a variety of subclasses have been defined.

- U Gem: These systems undergo the simple outbursts that can be explained by the disk instability model. All DNe that cannot be classified as Z Cam or SU UMa are classified as U Gem. A typical outburst is shown in (Figure 2.9).

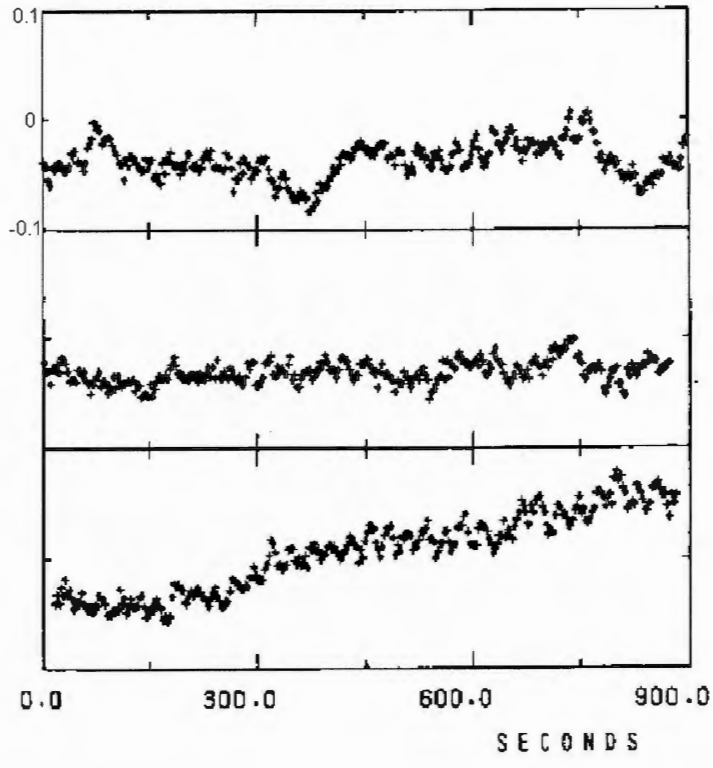

Figure 2.8: Dwarf Nova Oscillations in TY PsA during outburst. The vertical scale is fractional intensity (Warner *et al.*, 1989).

- Z Cam: In addition to classical DNe outbursts, these systems show extended periods of standstill at constant brightness (approximately 0.7 magnitudes below maximum brightness). During these periods, which may last for tens of days to years, no outbursts are seen. Z Cam behaviour only occurs in DNe with recurrence times $\leq$ 30 days but more often in those below 20 days. Z Cam systems probably represent a borderline case where the mass transfer rate is almost sufficient to satisfy the stability requirement.

- SU UMa: The SU UMa subclass are dwarf novae which occasionally display super outbursts with amplitudes around 0.7 magnitudes higher than normal and durations approximately five times average. These super outbursts occur alongside normal outbursts and often seem to be triggered by them. (Figure 2.10).

All SU UMa stars also show super humps during the decline of their outburst (Figure 2.11). These are prominent periodic humps that appear around maximum light and persist until the end of the outburst. No star has been observed which undergoes superoutburst

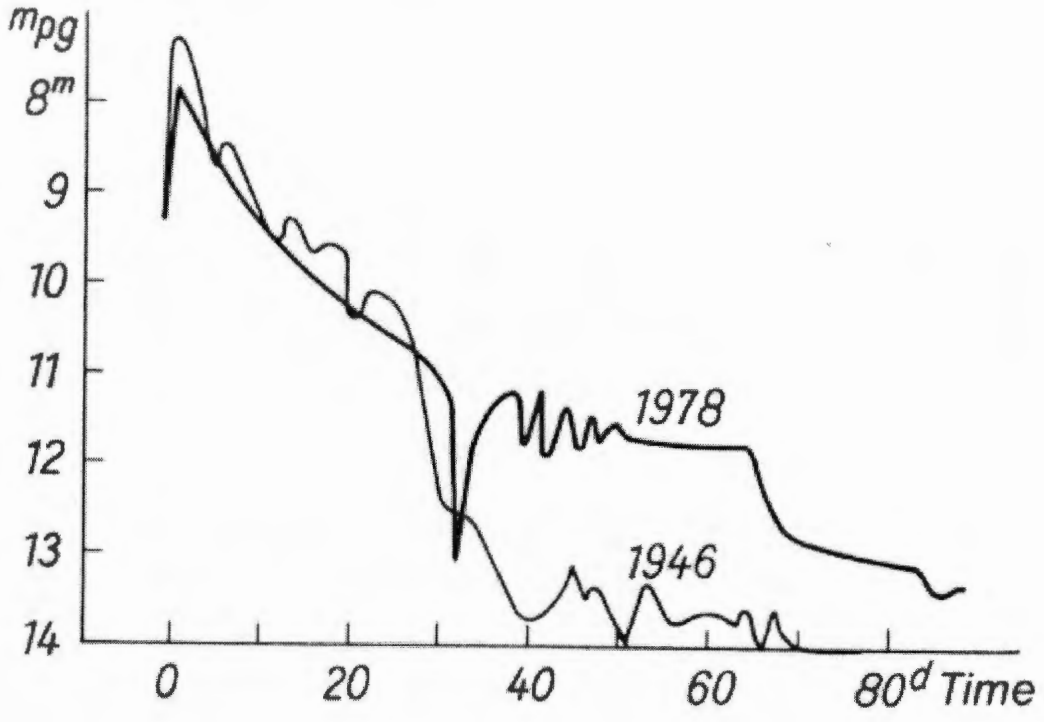

Figure 2.9: Typical lightcurve of a U Gem type DN (Hoffmeister *et al.*, 1985, p99)

but does not display superhumps. It is assumed that the phenomena are causally linked.

Superhumps are thought to be driven by eccentricities in the accretion disc caused by a tidal instability. They can occur for systems in the range $0.03 \leq q \leq 0.33$ with high mass transfer rates and viscosities. The superhumps are mainly caused by viscous energy dissipation from the disk which is distorted from a nearly circular shape to an elongated shape during the course of the oscillation (Wood *et al.*, 2000).

Recurrent Novae RNe

By definition recurrent novae are classical novae that have been seen to occur more than once. They can be easily differentiated from DNe spectroscopically, as like classical novae, RNe eject a substantial shell.

Nova-Likes NL

This category includes all cataclysmic variables that have not been seen to display eruptive behaviour. That is, objects which are photometrically and spectroscopically similar to eruptive CVs except for their lack of high amplitude variability. This class is thought to

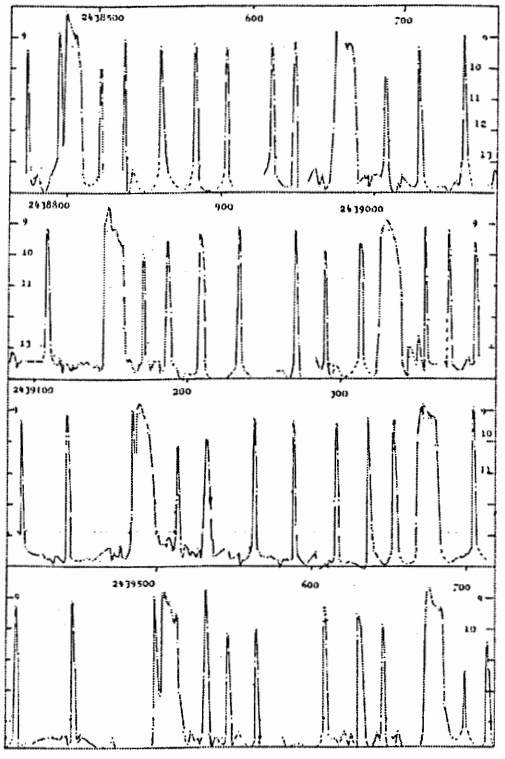

Figure 2.10: Lightcurve of an SU UMa type variable showing super outbursts. Note how super outbursts appear to be triggered by normal outbursts (Warner, 1995, p189).

include both pre and post-novae which have not been observed to outburst due to the short length of the observational baseline. Some NLs display persistent bright discs, similar to Z Cam stars in permanent standstill (Warner, 1995).

VY Scl stars are also included in the nova-like category. These are objects that are spectroscopically similar to other CVs but show occasional reductions in brightness, thought to be due to a reduction in $\dot{M}$ (Figure 2.12).

2.3 Magnetic CVs

At this point it is important to make clear the distinction between magnetic and non-magnetic CVs. In fact all cataclysmic variables display some magnetic field, the distinction made here is between systems in which the magnetic field of the WD is strong enough to govern the accretion geometry and those in which it is not (Warner, 1995). The first magnetic CV to be discovered was AM Her (later to give its name to a whole subclass of stars) which had been previously classed as a NL. In 1976 Tapia discovered that the

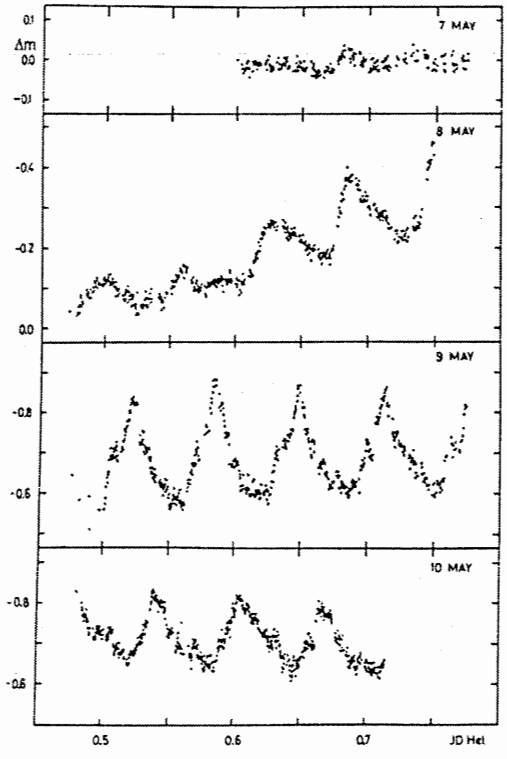

Figure 2.11: The onset of superhumps during a super outburst (Warner, 1995, p195)

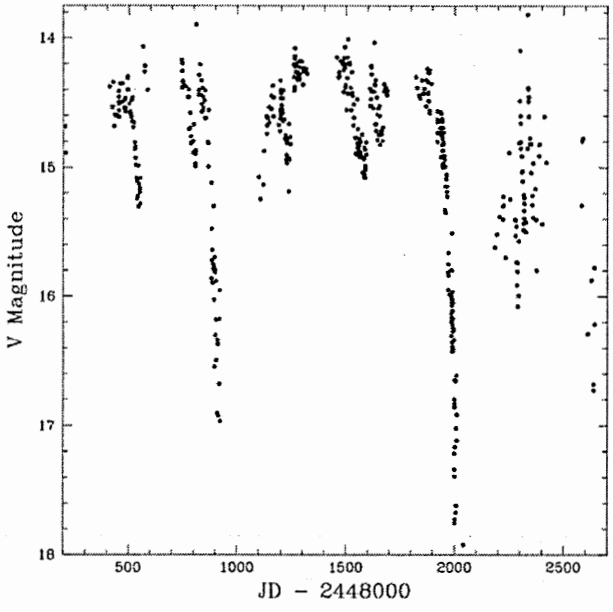

Figure 2.12: Lightcurve of the VY Scl star V794 Aquilae (Honeycutt & Robertson, 1998)

light from AM Her is both linearly and circularly polarised at optical wavelengths (Tapia, 1976). The linear polarisation varied from 0 to 7% and the circular polarisation from -9% to 3% over the ≈3h period of the system (magnitudes never before seen except in the case of magnetic white dwarfs). The fact that the period of this change in polarisation was identical to the orbital period of the system, implied that the rotation of the white dwarf and the orbit of the system were phase locked together. Applying the formula for non-relativistic cyclotron radiation gave a magnetic field strength of 4×10^7G (the solar magnetic field is around 10G).

2.3.1 Magnetic Accretion

The accretion physics in magnetic CVs is governed by the interaction of partially or completely ionised material from the secondary star falling into the increasing magnetic field density of the primary. At some point the motion of the particles under gravity will begin to be resisted by the magnetic field (B). This defines the magnetosphere of the accreting body. For spherically symmetric infall with velocity $v_{in}(r)$ and density $\rho(r)$, the radius of the magnetosphere can be calculated from the balance of the ram pressure of the infalling gas and the magnetic pressure exerted by the white dwarf (Warner, 1995).

$$B^2(r)/8\pi = \rho(r)v_{in}^2(r) \tag{2.3}$$

Assuming a dipole field $B(r)=BR^3/r^3$ (where R is the radius of the WD) and steady state accretion $\dot{M}=4\pi\rho(r)\nu_{in}(r)r^2$ and recognising that the infall velocity of the accretion flow will be comparable to its free fall velocity, the equilibrium or Alfvén radius (r_μ) is given by Equation 2.4, where $\mu=BR^3$, M is the mass of the primary and G is the gravitational constant.

$$r_\mu = 2^{-3/7}\mu^{4/7}(GM)^{-1/7}\dot{M}^{-2/7} \tag{2.4}$$

However, for a stream this is modified to include σ, the radius of the stream. Analysis by Lubow and Shu (Lubow & Shu, 1975) showed that for a given $\dot{M}$ an accretion stream will be able to penetrate much closer to the primary than in the spherically symmetric case. More recent and sophisticated treatments of the above yield a minimum r_μ that is sufficient to prevent the formation of a disk in the high field case as a disk can only exist in cases where the stream can pass completely around the primary star and collide with itself. In fact, 2 separate cases exist and both have been observed. If r_μ is less than the distance between inner Lagrange point L_1 and the primary, then the stream will follow the non-magnetic trajectory until it reaches the critical radius. In the case of r_μ greater than L_1, a stream element will follow the field lines of the primary for its entire trajectory. The action of the magnetic field on the accretion stream results in accretion onto the WD via a column rather than a disk, causing a shock front where the cool, supersonic accretion flow impacts the hot photosphere of the WD. As the gas below the shock front does not cool as quickly as it is heated by the shock, expansion results, moving the front away from the surface (Figure 2.13).

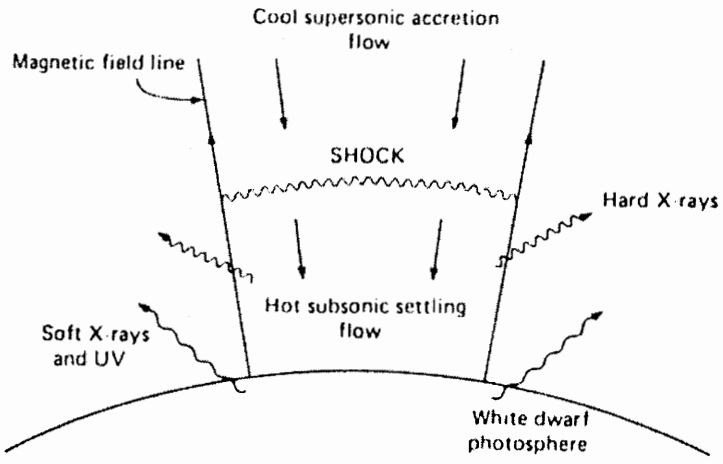

Figure 2.13: Schematic of the impact of the accretion column with the primary star (Smak, 1999).

This results in cyclotron emission at optical/IR wavelengths and in the emission of hard and soft X-rays through the process of bremsstrahlung.

2.3.2 Observational Properties of Magnetic CVs

Magnetic cataclysmic variables are catagorised in two ways depending on their accretion geometry, which is in turn dependent upon the strength of the field in the system. High field systems are classified as Polars and lower field systems as Intermediate Polars (IPs) (Patterson, 1984).

Polars

Polars exhibit no disk but rather have an accretion column as described above. A schematic of a typical polar is pictured in Figure 2.14.

Typical field strengths for this subclass range from 10-100MG causing the white dwarf to rotate synchronously with the orbit of the system. The lightcurves of both polars and intermediate polars can undergo long term brightness modulations over periods of years, probably due to variations in the accretion flow. AM Her itself has ranged between magnitude 12.0 and 15.5 over the course of the last century (Warner, 1995). Short term observations also show significant modulation in intensity and both linear and circular polarisation due to the displacement between the rotational and magnetic poles. As the

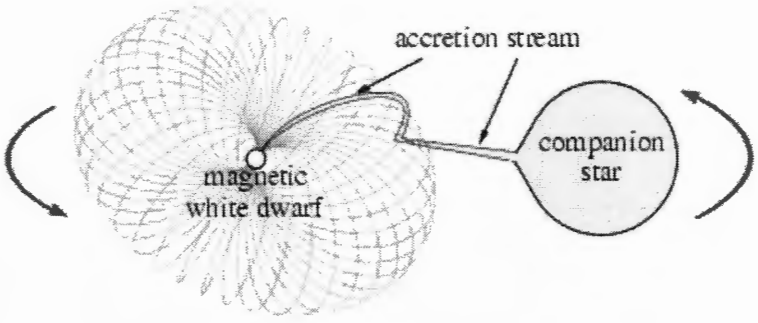

Figure 2.14: Schematic of a polar system (Frank *et al.*, 2001)

system rotates, the observer sees the magnetic pole from a range of different angles. This results in a maximum of circular polarisation when looking almost down the field lines and a maximum in linear polarisation when the field lines are viewed at their most transverse (Figure 2.15).

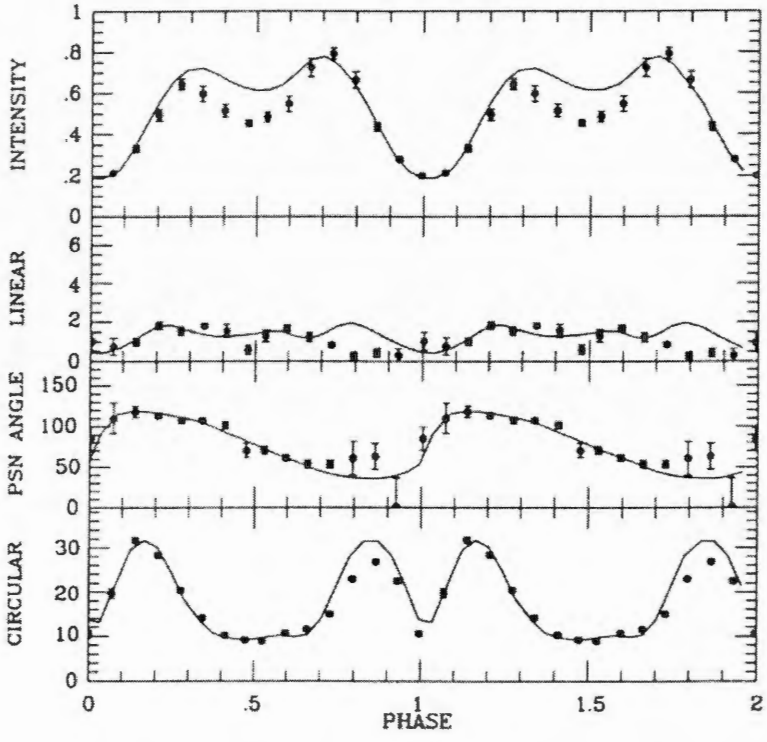

Figure 2.15: Comparison of total intensity, polarisation angle and intensity of linear and circular polarization for a polar system (Warner, 1995, p329)

Combined with this, and also with the flickering displayed by all CV systems, some polars demonstrate short but intense flares and also Quasi-Periodic Oscillations (QPOs) that are probably associated with the cyclotron emission region Figure 2.16.

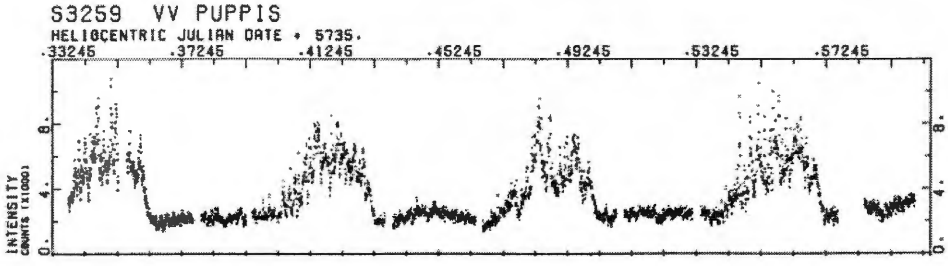

Figure 2.16: Flares from a polar type CV. (Cropper & Warner, 1986).

Intermediate Polars

Intermediate polar (IP) systems have a less intense field than their polar cousins and synchronization of the WD with the orbit of the system is not achieved. Due to their asynchronous rotation they display many different periods caused by interaction of the orbital and photometric periods. The photometric period is caused either by the periodic irradiation of the disk or secondary star by the X-ray emitting region of the primary, or by the rotation of the WD itself . Their geometry is substantially different to the polar case, in that both an accretion disk and column are thought to be present (Figure 2.17).

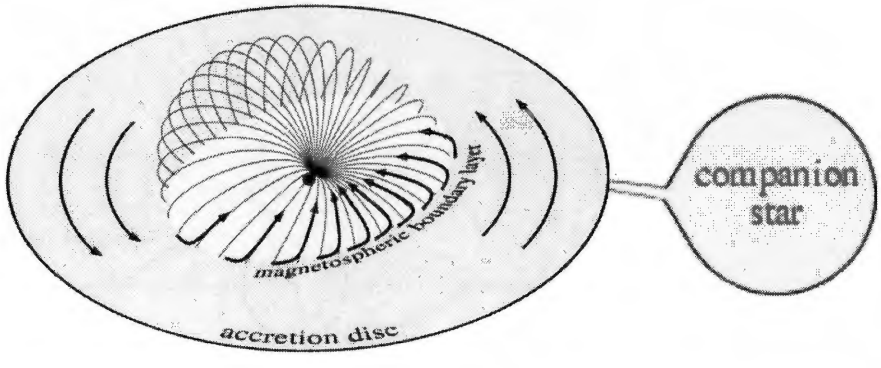

Figure 2.17: Schematic of an intermediate polar (Frank *et al.*, 2001)

The boundary between magnetic and disk behaviour occurs at the edge of the magnetosphere where material from the disk begins to flow along field lines. Perturbations of the disk by the field can cause instabilities which may carry the field into the disk, the physics of this transitional region are complex. As well as orbital and rotational modulations of the luminosity, some IPs undergo changes in both their orbital and rotational periods.

Chapter 3

CV Population and Evolution

Having looked into the physics of individual CV systems, we will now turn to the observed population of CVs as a whole. From considering this distribution and recalling the physical mechanisms discussed previously, various models of CV evolution can be developed. The problem of CV evolution is one that is currently under much debate in the community with current observations unfortunately biased and unable to differentiate between competing models. The strategy and goals of the WAVS programme, which was begun in an attempt to solve some of these problems, will be discussed at the end of this chapter.

3.1 The Observed Population of Cataclysmic Variables

3.1.1 History

Classical novae have been observed and recorded in the East for many millennia, but it was not until 1670 that the first true nova (i.e. not a supernova) was studied in Europe (Warner, 1995). A Carthusian monk named Pere Dom Anthelme observed the second magnitude nova in the constellation of Vulpecula (this later became known as CK Vul) (Shara & Moffat, 1982). No novae were noted throughout the 18th century and indeed only one was observed in the first part of the 19th. Like all types of variable star, it was the advent of photographic plates that had a real impact on the discovery rate of CVs. The first dwarf nova was discovered by J.R. Hind on 15 December 1855. Hind discovered a blue star of 9th magnitude whilst searching for minor planets. As he had been observing this patch of sky for many years, Hind could confidently state that he had discovered

a new kind of variable star 'of a very interesting description, inasmuch as the minimum brightness appears to extend over a great part of the whole period'. This behaviour was noted as unusual compared to the constantly changing lightcurves of previously discovered Algol and Mira type variables. Hind also noticed the blue colour of the new variable in comparison to the redder colours of these other stars and this first DN was designated as U Geminorum. Three months after its discovery, Pogson found U Gem to be back at maximum light proving the fact that this star was not an ordinary nova and confirming its status as a favourite object among amateur astronomers due to its fast rise and and unevenly spaced maxima. Soon after came the discovery of SS Cygni and T Leonis (in fact the first member of the SU UMa group to be discovered) and then that of Z Cam. Since then CVs have been discovered by both amateurs and professionals at an increasing rate, although the observational bias still lies with those systems which undergo frequent or violent outburst or have high accretion luminosities. Today there are around 320 systems that are classed as cataclysmic variables and many more which are also probably members of that class (Ritter & Kolb, 2003).

3.1.2 CV Period Distribution

For many CV systems, the orbital period is the best (and sometimes the only) known physical parameter. It is fortunate then that the orbital period distribution (Figure 3.1) is such a useful tool in deducing the evolutionary history of CVs (Kolb, 2001).

The CV period distribution is essentially a combination of the true evolutionary effects and those caused by observational selection. In the local area the sample of CVs is essentially magnitude limited (to the first order), but at greater distances the population is heavily biased by outburst behaviour. For the most part of their evolution CVs can be considered to be moving from right to left on the diagram, that is from longer to shorter periods. This reduction in period is driven by the angular momentum loss mechanisms discussed previously which will be revisited when evolution is covered in more detail. There are three major points about the CV period distribution that need to be mentioned at this time. Two of these are obvious on Figure 3.1 whilst the other is notable by its absence.

The Period Gap

Cataclysmic variables typically have periods between around 80 mins and 8 hours (Howell *et al.*, 2001). However it is clear from the period distribution that there is a dearth of

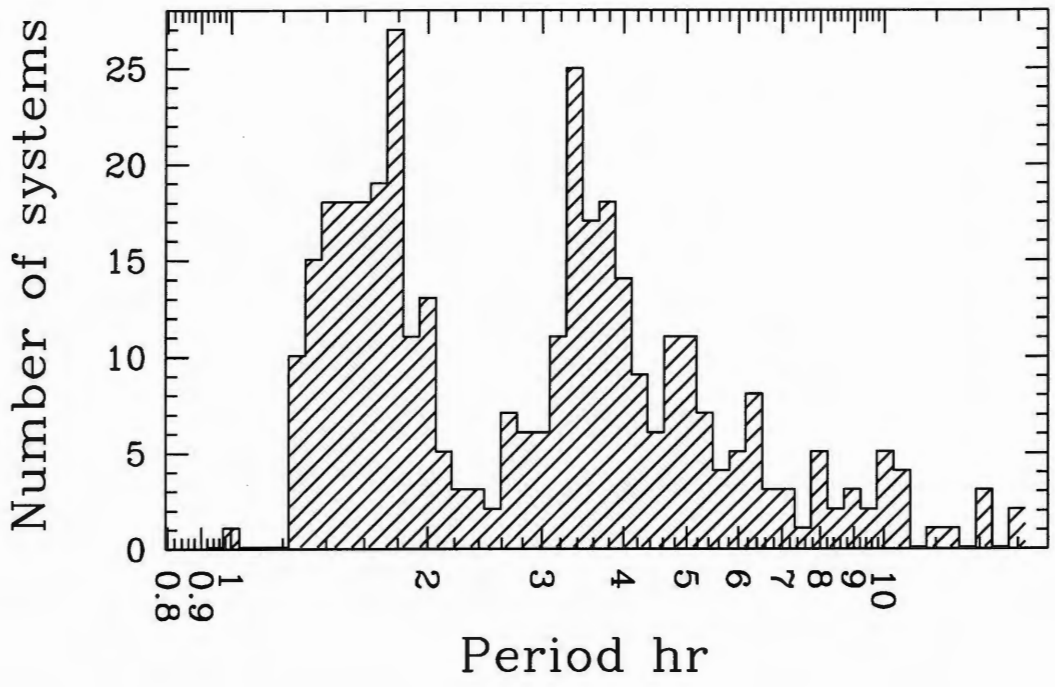

Figure 3.1: Orbital period distribution of cataclysmic variables (Barker & Kolb, 2003).

systems with orbital period (P_{orb}) between 2 and 3 hours. Clearly there are two possible explanations for this phenomenon, either CVs are very difficult to observe at this time in their life cycle and so the gap is essentially a selection effect, or that CVs evolve through this period range very quickly and so population numbers within the gap are actually less. It is generally thought that the first of these premises is true, and that CVs become less observable during this stage of their evolution. This of course implies that the accretion luminosity and so the accretion rate during this phase must be greatly reduced. In the currently accepted model, the interior of the secondary star becomes fully convective when its mass approaches $0.23M_{\odot}$. A near cessation of magnetic braking occurs, which reduces the mass transfer rate and allows the secondary to shrink towards its thermal equilibrium radius (Howell *et al.*, 2001). This causes a period of essentially zero accretion, until gravitational radiation removes sufficient angular momentum from the system for the secondary to reconnect with its Roche lobe and begin mass transfer once again.

The Minimum Period

Another obvious aspect of the CV period distribution is the sharp cut off at periods of around 80 minutes. In fact the minimum period P_{min} is ~78 minutes and is understood in terms of the evolution of the secondary star. For donor stars on the hydrogen burning main sequence, mass loss results in an increase in the density of the star. The orbital period of a cataclysmic variable is determined almost uniquely by the density of the secondary star through the equation

$$P \sim \kappa/\rho^{1/2} \tag{3.1}$$

where κ is only a weak function of the mass ratio (Kolb & Baraffe, 1999). Therefore as the density increases, the period is reduced. However, once the minimum mass for hydrogen burning is reached, the secondary star effectively becomes a brown dwarf (BD). Structural changes caused by electron degeneracy mean that further mass loss reduces ρ and causes an increase in P. Thus, during the transition from main sequence to brown dwarf secondary, the rate of change of period becomes positive and the system undergoes a 'period bounce' at the minimum period. Unfortunately there is a large discrepancy between the observed period (78min) and that calculated from models, which is on average around 10% shorter (Kolb & Baraffe, 1999). This discrepancy will be discussed in more detail shortly.

The Period Spike

A third aspect of the CV period distribution, worthy of note not for its presence but rather for its absence, is the Period Spike. The discovery probability for cataclysmic variables *p(P)*can be written as:

$$p(P) \propto (-\dot{M}^2)^{\alpha}/|\dot{P}| \tag{3.2}$$

where α is a positive power describing selection effects (King *et al.*, 2002). Since $\dot{P}$=0 at P_{min}, the period distribution should show a significant maximum unless there is a severe drop in $\dot{M}$ at this point. However, theory predicts that $\dot{M}$ is almost constant as P_{min} is approached and thus the lack of an accumulation of CVs at this point is puzzling. Different theories attempt to solve the period spike problem in a variety of different ways and some of these will be discussed in the following sections.

3.2 CV Evolution

Opinion is divided on the evolutionary paths of cataclysmic variables and the various theories will be discussed later in this section. However, it is generally agreed that CVs must reach contact after a common envelope or CE period.

3.2.1 Pre-Cataclysmic Evolution

Most systems which evolve into CVs probably begin their lives as reasonably wide binaries with $a \geq 50R_{\odot}$ (Warner, 1995). For the binary separation to shrink to CV distances a very efficient force (more so than gravitational or magnetic braking) must remove angular momentum from the system. This is thought to occur when the more massive primary star evolves into a giant with an essentially degenerate core. The primary expands far beyond its Roche lobe and the system becomes two stars rotating within a single envelope. The frictional drag this causes results in massive angular momentum (AM) loss from the orbit of the pair until the thermal energy of the envelope exceeds its binding energy and is ejected from the system, forming a planetary nebula. The ejection of the nebula leaves a main sequence dwarf orbiting a white dwarf companion at a greatly reduced separation (although the system is still detatched). Over time magnetic and gravitational forces bring the pair into contact and a cataclysmic variable is born.

3.2.2 Competing Theories

Once the binary pair come into contact and begin to evolve, the lifecycle of the pair must be such that when this is repeated by many CVs, the CV population in Figure 3.1 is replicated. The three main features that the lifecycle of an individual system must encompass are essentially those that have been discussed previously. In the next section, competing theories of CV evolution will be described and their merits and failings evaluated.

The Standard Model

In the standard evolutionary model, once the binary pair have come into contact, the system evolves due to angular momentum loss under the influence of magnetic braking and gravitational radiation. Mass is transferred from the secondary to the primary star resulting in various types of eruptive behaviour depending upon the physical parameters of the system. Once the mass of the secondary is sufficiently reduced its interior becomes completely convective, magnetic braking ceases and accretion is halted until such a time

as gravitational radiation brings the pair back into contact again (this occurs during the period gap). The system then continues to evolve under the influence of gravitational radiation until the secondary star becomes a brown dwarf and period bounce occurs. After this point the system evolves to slowly increasing periods with a diminishing accretion rate until accretion stops completely and the system essentially becomes a post-CV. The standard model explains well the general features of the period distribution and also the period gap. However it falls short in both the discrepancy between the observed and theoretical period minimum and in the theoretical prediction of a period spike. The period minimum problem may just be due to an over simplification of the input physics - specifically a difference between the true and spherically approximated radius of the secondary may account for most of the disagreement (Kolb & Baraffe, 1999). The absence of a period spike has proved a more persistent problem, but recent work by Barker and Kolb (Barker & Kolb, 2003) as well as King *et al.* (King *et al.*, 2002), may be beginning to provide an answer. By introducing a distribution rather than a single minimum period it is possible to flatten the spike (from the effect of many smaller individual period spikes) whilst retaining the sharp cut off at the observed minimum period. To do this it is necessary to add a second controlling parameter, probably in the form of varying magnetic stellar wind braking to create the spread (King *et al.*, 2002). Although this idea is in its infancy, current results are encouraging.

Binary Age Postulate

To overcome the problems of the standard model, King and Shenker proposed a new evolutionary model for the CV population (King *et al.*, 2002). In their new model the problems of the minimum period discrepancy and the lack of period spike are solved by postulating that even the oldest CVs have not yet evolved to the minimum period. The timescale for the secular evolution of CVs is considerably shorter than the age of the Galaxy and so this can only be true if the time to shrink a pre-CV into contact is considerably longer than previously assumed, or specifically that $t_{contact} \geq t_{Gal}$-t_{evol}. For this to be the case, either CE evolution must be more efficient than previously thought (so that pre-CVs emerge from the CE phase at greater separations) or the degree of magnetic braking assumed before the pair make contact must be drastically reduced. However, the normal value of magnetic braking must be assumed once contact is achieved. This Binary Age Postulate (BAP) does remove the problems associated with the CV period minimum

but the fine tuning of the models is worrying.

Hibernation and Cyclic Evolution

The hibernation scenario is unlike the other two theories of CV evolution in that it does not really attempt to explain the features of the observed CV period distribution. Proposed by Shara *et al.* in 1986, the hibernation scenario postulates that there is a vast population of low accretion rate systems with low accretion luminosities that do not display outbursts and so have not yet been observed (Shara *et al.*, 1986). These systems would have $\dot{M} \leq 10^{-12} M_{\odot}\ yr^{-1}$ and individual systems could go into periods of hibernation lasting between 10^3 and 10^6 years.

During a nova outburst both mass and angular momentum are lost from the binary system. If angular momentum loss were the dominant factor, this would lead to a decrease in the binary separation. However, if mass loss dominates (as Shara postulated), this leads to an increase in the orbital separation of the pair and also an expansion of the Roche lobe. These effects convert the semi-detached system into what is essentially a detached white dwarf-red dwarf binary pair. Whilst the pair are detached, previously accreted material can spread over the surface of the WD and provide fuel for the next outburst, removing concerns that a persistently high $\dot{M}$ can result not in a thermonuclear runaway but in either weak flashes or steady burning. Contact is not made again until the effects of magnetic or gravitational braking bring the two stars closer once more.

Obviously the effects of this reduced accretion rate should be observable immediately after a nova outburst and this has not been the case. However, Shara *et al.* introduce increased irradiation of the secondary by the primary during and immediately after the outburst which serves to expand the surface of the secondary and keep it in contact with its Roche lobe for approximately 100 years, thus the current observational baseline is not really long enough to have observed this drop in luminosity (Shara *et al.*, 1986). Calculations based on nova recurrence times and the observed frequency of nova outbursts in the bulge of M31 caused Patterson (Patterson, 1984) to comment that 100 times more inactive than presently active novae should exist in the solar neighborhood and Shara cites these nova as being in a state of hibernation. Adding to this, hibernation became incorporated into a 'Cyclic Evolution' scenario for cataclysmic variables (Livio, 1992), based upon the premise that some classical novae had been seen to undergo dwarf novae like behaviour either a long time before or after outburst (surprising as CN are thought

to be on the stable branch of the Σ-T_e relationship). A scheme in which CVs evolved through the different types of outburst behaviour at different times in their evolution was proposed. Many of these schemes involved a period of hibernation, although not always (Figure 3.2).

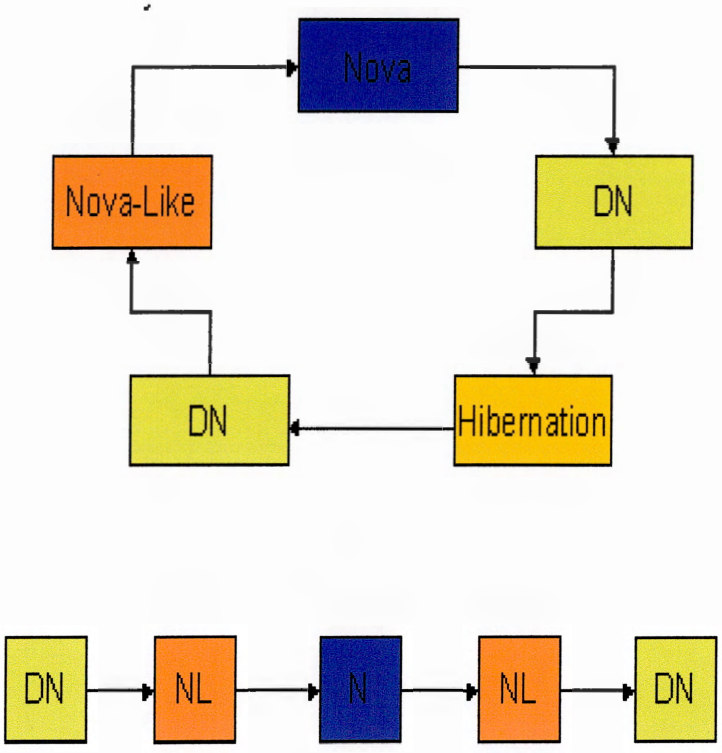

Figure 3.2: Possible cyclic evolution scenarios

However, the only real evidence for the hibernation scenario lay in the lack of evidence against it (due to the shortness of the observational baseline) and in the apparent reduction in accretion luminosity in old novae CK Vul and WY Sge. More recent observations (Naylor *et al.*, 1992) showed that CK Vul had been misidentified, making the measured decline meaningless. Also when corrections were made for inclination, it was shown that WY Sge had remained at almost constant brightness for 200 years after eruption. Due to these findings and others, the hibernation scenario has fallen out of favour in recent times (whilst not being disproved).

3.2.3 The Missing CV Population

Regardless of whether there are unobserved systems at short periods that would account for the theoretical period spike, or whether CVs spend a large percentage of their lifetime in a detached, hibernating state, there are many good reasons to believe that there are a great number of CV systems that remain undiscovered. One reason for this is that CVs are discovered largely through their outbursts, thus objects with more frequent and/or larger amplitude outbursts dominate. Also, novae with more massive primaries have shorter recurrence times, introducing a bias towards high mass primaries, while systems with short orbital periods have larger nova outbursts (Diaz & Bruch, 1997). Combined with this, a low mass transfer rate produces a lower accretion luminosity, thus deselecting for such systems.

Simulations of CV formation rate estimate that the known sample of CV progenitors is incomplete by a factor of 10-100 (de Kool & Ritter, 1993) and simulations by Kolb and Baraffe (Kolb & Baraffe, 1999) predict many unobserved CVs below the period gap.

It was due to these inconsistencies and differences of opinion that the WAVS programme was born. WAVS intended to provide an unbiased sample of the CV population in an effort to finally resolve these issues and to generate an observationally accurate view of CV populations and evolution. If an unbiased survey could discover a large number of previously unobserved short period CVs, this would bring observations much more in line with standard model theoretical predictions and could go some way to solving the period spike problem. Conversely, if no CVs were detected then this would reinforce the problems of the standard and hibernation models and further promote a rethink of current theory, along with encouraging other, alternate theories such as the BAP. The WAVS survey was sensitive to CVs down to around apparent magnitude 22.5 (this limit will be discussed in detail in chapter 4, section 4.4). Using the empirical relationship between absolute magnitude ($M_v(2)$) and period (P_{orb}) of a secondary star developed by Warner (1995) Equation 3.3, a donor star with a two hour orbital period would have an absolute magnitude of 13.4. This would mean that the WAVS survey could detect CVs at this period up to a distance of approximately 660 parsecs, allowing us to deduce the population statistics in a volume limited sample.

$$M_v(2) = 16.7 - 11/1 log P_{orb}(h) \tag{3.3}$$

3.3 WAVS - the Wide Area Variability Survey

3.3.1 Aims

WAVS set out to gain an unbiased sample of CVs by utilizing a characteristic that all CVs have in common. Rather than being based on outburst behaviour or on the spectral characteristics of sources, WAVS uses flickering to identify CV candidates. These are then followed up spectroscopically to verify their nature. As mentioned previously, flickering is the one characteristic that all currently observed CVs exhibit, and is thought to arise both from the impact of the accretion stream of the hot spot and at the boundary layer between the disk and the surface of the white dwarf. Although unobserved CVs may be in a low accretion state it was assumed that some flickering should still occur. The aim of WAVS then is to photometrically search for variability of amplitude tenths of magnitudes on a timescale of minutes to hours. These statistics can then be used to really confine CV densities and give an unbiased basis for theoretical models.

3.3.2 Methods

WAVS used the 12k mosaic on the Canada-France-Hawaii Telescope on July 12-13th 1999 to take images of a 0.33sq.deg. Galactic field with an integration time of 120s and a time resolution of 3 minutes. The field was selected such that it would contain a large number of stars (but not so many that overcrowding would be a serious problem), would be in a region of the sky where interstellar reddening was not too severe and would contain at least one known cataclysmic variable that could be used for comparison. The chosen field was centered around the eclipsing CV QU Vul at Right Ascension 20:26:45.94 and Declination +27:50:42.2.

The CFHT is a 3.6m telescope situated on Mauna Kea some 4200m above sea-level and is a high quality instrument for both optical and infrared work (Figure 3.3).

The 12k mosaic is an arrangement of 12 2048×4096 pixel Charge Coupled Devices (CCDs) which when mosaiced yields a massive 12288×8198 pixel imaging device (over 100,000,000 pixels in total) (Figure 3.4).

The CFH12k mosaic saw first light in 1999 and is currently the largest close-packed CCD mosaic camera in use today. It covers an area of 42×28 arc minutes on the sky and can read out the entire array in around a minute. Each full image has a size of 412Mb resulting in 160Gb of data over the two night run.

Figure 3.3: The CFHT telescope on Mauna Kea. CFHT Website (2003).

The data reduction methods used will be covered in subsequent sections, suffice to say that the lightcurve for each of the stars imaged with the 12k Mosaic (some 66000) was plotted over the two nights of the run with 3 minute time-resolution. Candidates were selected on the basis of their variability and follow-up spectroscopy was performed on 3 occasions using the Andalusia Faint Object Spectrograph and Camera (ALFOSC) at the 2.4m Nordic Optical Telescope (NOT) on La Palma.

3.3.3 Secondary Goals

As well as investigating the population of cataclysmic variables in the Galaxy, the WAVS survey has also uncovered a large number of other variable stars, many of them of types discussed in Chapter 2. Some spectral followup has been undertaken on these objects and it is hoped that the WAVS survey can add something to these areas of variable star research, both in the discovery of new and interesting objects and in calculating their unbiased population densities.

A detailed discussion of the methods employed by the WAVS survey, and the ways in which WAVS data was reduced to give the most accurate and valuable results will be

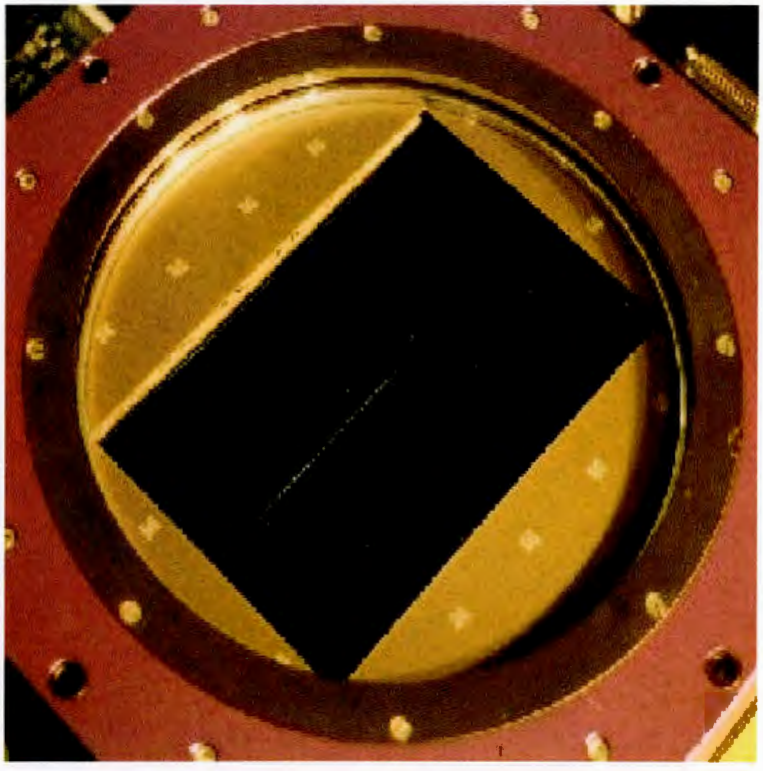

Figure 3.4: The CFHT 12k mosaic camera. CFHT Website (2003).

discussed in the subsequent chapters. Following this, example variables will be considered and populations for the various types of variable star will be discussed. Full lightcurves (and where appropriate spectra) for all variable WAVS objects are given in Appendices (A)to (C).

Chapter 4

Photometric Data Reduction and Analysis

The essence of photometry is to measure the total amount of light coming from a source. The practice of this is somewhat more complicated. No detector is ever 100% efficient, from the human eye to the latest Charge Coupled Device (CCD), and all detectors have differing responses to radiation and display various artifacts that must be removed before the photometry process can even be started. The process of photometry itself is not trivial, and there are many problems that must be dealt with, especially in cases where the field is crowded by many stars. This chapter attempts to address these issues, firstly in the general case, and secondly in the specific case of the WAVS data.

4.1 CCD Photometry

The CCD is by far the most useful detector in astronomy today. It shows a linear response up to very high count rates and has a quantum efficiency which far exceeds any competing detectors over most wavelength regimes. Figure 4.1 shows an illustration of this.

However, the CCD is not without its problems. Detectors must be severely cooled to reduce thermal noise (to -85C in the CFHT case (Cuillandre *et al.*, 1999)) and in general have been restricted to domains of lower time resolution due to their finite readout time. Recent work using frame transfer technology is lessening this restriction (Dhillon & Marsh, 2001) but it is currently still a factor in most circumstances. CCD images also require a substantial amount of reduction before photometry can take place.

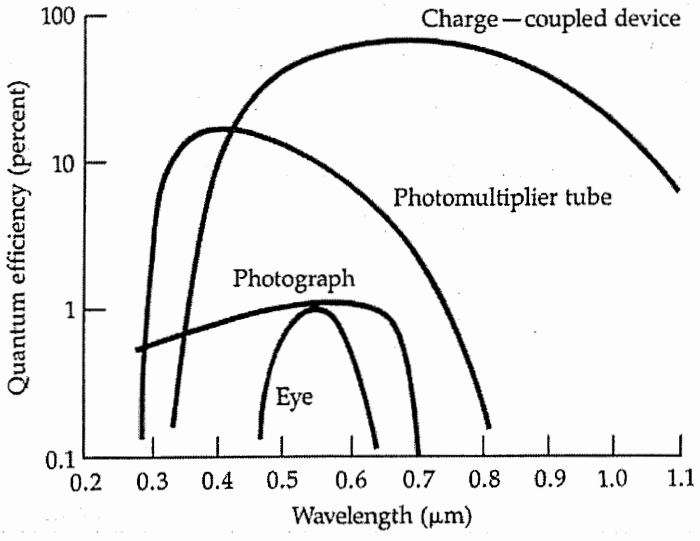

Figure 4.1: Typical Wavelength dependent quantum efficiency for various detectors (Zelik *et al.*, 1992, p190)

4.1.1 Reducing CCD Data

Data taken with a CCD will be subject to various sources of noise (such as the thermal and read-out noise of the chip) and also to various artifacts (such as the differing response across the chip to incident radiation). The pre-photometry procedure endeavours to remove as many of these artifacts as possible, although some sources of noise will always remain.

Bias subtraction

In order to measure noise in the electronics, the CCD frame can be read out with a zero integration time. In this case, any counts that are recorded are due only to the bias voltage and the read-out noise. The bias or offset voltage is applied to the CCD to so that the readout noise can be measured properly. Without this, the Gaussian distribution of the noise would be truncated as negative counts will not be recorded (Figure 4.2). However, applying a bias voltage means that all of the frames taken during the night have an 'extra' amount of counts which must be subtracted before accurate photometry can be performed.

Multiple bias frames are generally taken both at the beginning and end of a night of observations. These are then checked to ensure that none show any obvious deviations and combined to reduce noise. The combined bias frame is then subtracted from each of the image exposures from the same night, removing the bias voltage and also any artifacts due to the readout electronics.

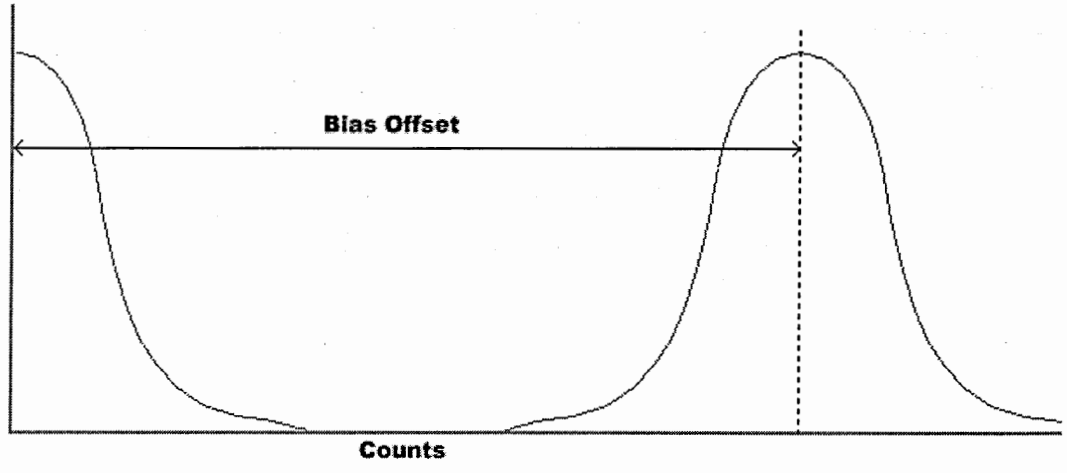

Figure 4.2: Readout noise profile before and after bias offset

Overscan

It is possible that changing conditions may cause a change in the level of the bias over the course of a night's work. To account for this effect, several columns of unexposed virtual pixels are read from the CCD after the image transfer has been completed, i.e. the clock voltages are applied to step the charge more times than there are pixels on the chip. These form a strip along the side of the image which can be used to account for changes in the bias level. The overscan strip is generally composed of a few tens of columns on one side of the image and after bias subtraction, contains very few counts. These columns are averaged and then fitted with a simple function. The function should be of high enough order that it accounts for any gradient in the strip but not so flexible that random deviations are included in the fit. The fit to the overscan strip is then subtracted across the chip removing any image to image variation in the bias level. An aspect to note when specifying the overscan region is the effect that blooming can have on a CCD chip. It is possible that some pixels will be so over exposed that during frame transfer, not all of the charge will be moved across in the correct pixel bin. Thus when clock voltages are applied to read the virtual overscan pixels, some charge may still be in the chip causing the appearance of bright patches in the overscan region. The effect of including this in the overscan section used for subtraction will be a dark stripe across the image and very inaccurate photometry. Thus the overscan strip should always be specified so that it does not include effects of this kind.

Flat Field

The reaction of a CCD chip to incident radiation is often not completely consistent across its surface. In fact CCDs generally show some kind of gradient in the way they respond to light and in some cases, display distinct patterns on their surface. The optics and construction of the telescope can also add to these effects. To remove these artifacts a flat field frame is used. Flat field frames are made by exposing the CCD chip to a source of uniform radiation either in the form of sky flats (in which the detector is exposed to the sky during twilight) or dome flats (in which the telescope is exposed to a uniformly illuminated surface inside the dome). Generally sky flats are preferred, as the way in which the camera is illuminated in this case is similar to that which will occur for the image exposures and any artifacts are more likely to have the same form.

The flat field frames are treated in the same way as the object exposures and undergo both bias and overscan subtraction. They are then checked for any random variations (such as shooting stars which crossed the field during the exposure). Combination of the flat field frames using a suitable algorithm removes the effects of cosmic rays, and the combined flat is then normalized. Object exposures are divided by the final flat field to remove any gradients caused by changes in sensitivity. Unlike the bias and overscan parts of the reduction, flat field frames are sensitive to the type of filter (if any) that is being used. In cases where object exposures will be taken in a number of filters, separate flat field exposures must be created for each and care must be taken that the correct flat field is applied to each object exposure.

4.1.2 Photometric Techniques

Accurate measurement of fluxes is a complex task, as the instrumental brightness of a single star is really a composite of several factors. What is actually measured is a combination of the stellar flux at a given bandpass, the flux from the sky at the same bandpass, the sensitivity function of the detector and a number of atmospheric effects. There are two main methods used to determine the number of counts received from a source and to remove the effects of sky brightness. Both of these methods are useful in different circumstances and will be discussed shortly.

Although stellar sources are at sufficient distance that no terrestrial telescope could resolve them as anything more then a point source, this is not how they appear when imaged. Variable refraction effects, mainly from the Earth's atmosphere, act to smear the

point into a disk (Figure 4.3).

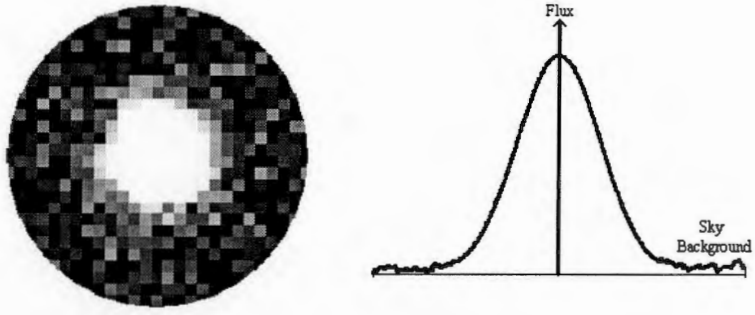

Figure 4.3: Brightness profile of an imaged star

The seeing conditions are measured in terms of the Full Width at Half Maximum (FWHM) of this disk and sub-arc second seeing is generally considered to be good. The extended nature of astronomical images is another thing that must be accounted for when performing photometry.

Aperture Photometry

Aperture photometry is by far the simplest type of photometry to perform, although it is not the best kind in all circumstances. To measure the total flux in this case, a ring or aperture is placed around the star to be measured at a radius where the counts from the source can no longer be distinguished from the sky brightness (Figure 4.4). All the counts within this aperture are then added together. A second, larger aperture is placed around the first, and the counts in between these two apertures are then measured, allowing calculation of an average sky value. The total number of counts due to sky brightness within the original aperture can then be subtracted from the observed flux. The result is the total number of counts due to the source. Aperture photometry is very useful in situations where the stellar field is not crowded. However, in the case where many stars appear next to each other on the image, aperture photometry becomes severely limited. Figure 4.4 shows two possible outcomes if aperture photometry is used in the crowded field case. Either the aperture is made large enough to encompass most of the light from the object being measured but also encompasses its companions, or the aperture is made too small, and contains only a fraction of the incident flux. To overcome this problem, a different method must be employed.

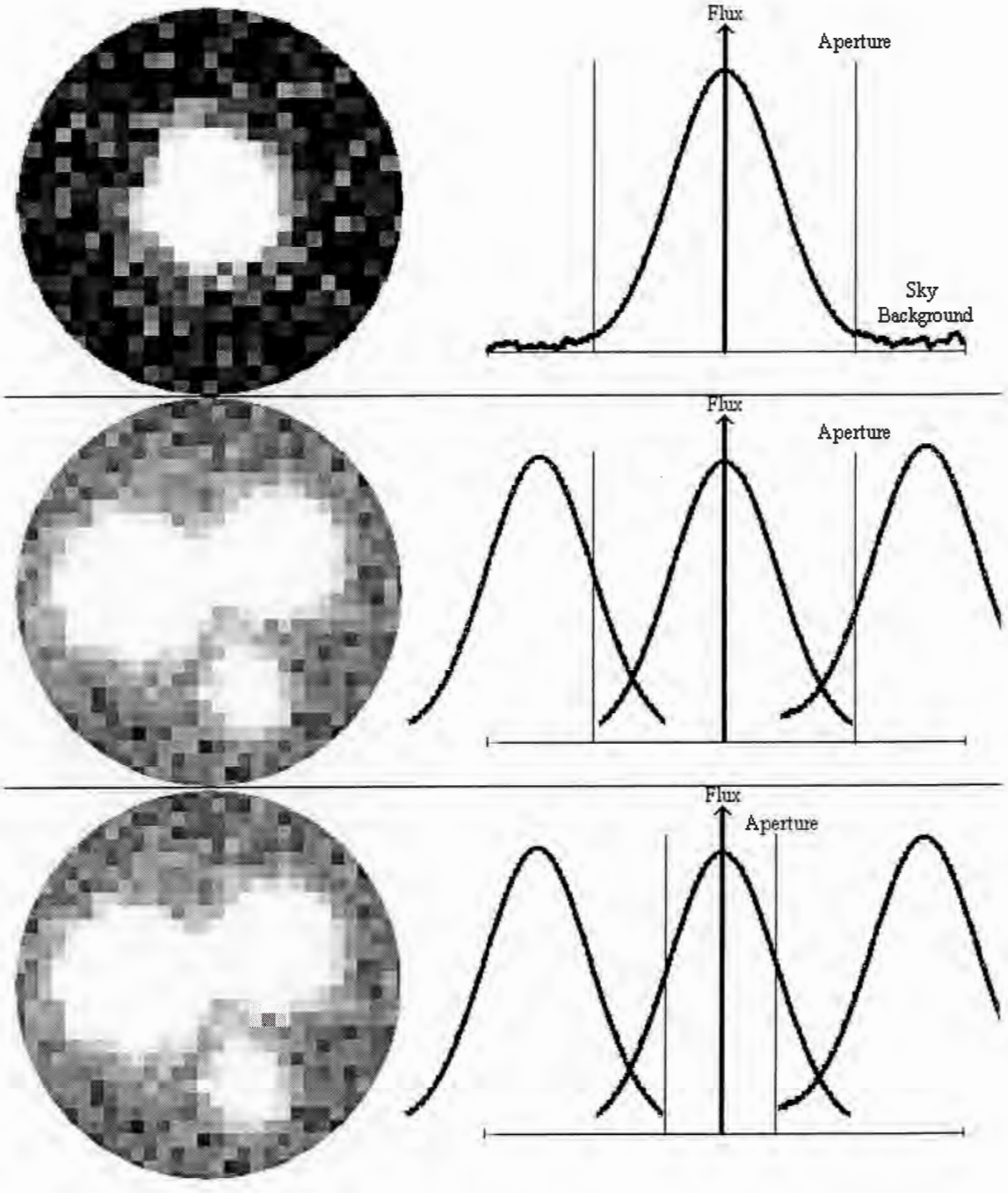

Figure 4.4: Top: Placement of aperture in the ideal case. Middle: The crowded field case, large aperture. The aperture now encompasses light from more than one object. Bottom: The crowded field case, small aperture. The total brightness of the source is not measured.

Point Spread Function Fitting

Point Spread Function (PSF) fitting can be used to measure stellar brightness in cases where the field is crowded. The PSF is a function which traces the brightness profile of a

star, and in the simple case for a given CCD, its shape is dependent only on the central flux of the source over a large range of intensity. A PSF can be formed by taking a number of isolated stars (from the same chip) and fitting their overall shape with a function. In the most basic case of a radially symmetrical image and a Gaussian point spread function, the intensity at any given point I_{xy} is given by

$$I_{xy} = I_0 e^{-r^2/\sigma^2} \tag{4.1}$$

where I_0 is the central intensity, r is the radial distance and σ is the width of the Gaussian. In practice, more complex point spread functions than this are often used but the principle is the same. Once the function which best described the data has been calculated, it can be fit to objects in the crowded area, providing that their centre can be found. These objects can then be subtracted, removing only their own flux and often revealing fainter objects that were previously hidden in the seeing disk of the brighter star. It is easy to tell if the fitting procedure has been successful in individual cases, as stars for which the PSF was a poor fit yield significant residuals.

There are several circumstances in which PSF fitting will fail. Stars which have become saturated due to over exposure will obviously not be subtracted correctly by the PSF fitting procedure. However due to their saturation they would not have yielded useful photometry anyway. A more serious failure occurs when a well sampled star gains extra counts in its centre from a source which cannot be subtracted. For example, if charge from a saturated star bleeds across the centre of another star, the central intensity of the second star will be erroneously high, causing the PSF to be scaled incorrectly (Figure 4.5). The effect of the saturated star cannot be subtracted easily as its true central intensity is not available. A fit to the wings of the saturated star could be used to remove the excess brightness from its neighbour, but this may not be possible as the saturation is unlikely to have radial symmetry and so any fit to the wings would be complex. Similar problems occur for stars which have been affected by bad rows or columns.

Over the course of a night's observing, such effects can become more or less important as the telescope is dithered and the seeing conditions vary. This can give erroneous results in variability analysis and so should always be considered.

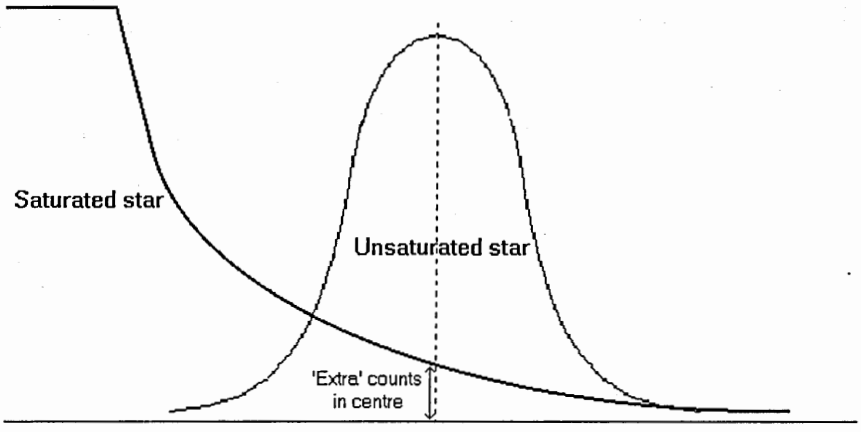

Figure 4.5: Effect of a saturated star on PSF function fitting.

Conversion to the Standard System

Any photometric procedure yields results only in terms of instrumental magnitude. To convert this into a true apparent magnitude a comparison with standard stars is necessary. These are objects which have been observed repeatedly and have well known and calibrated magnitudes in different filters. By imaging a number of standard stars in three different filters at varying airmass, it is possible to calibrate the sensitivity of the detectors and to make a fit to the extinction correction for the observing conditions on a given night. Applying this fit to the instrumental magnitudes, true apparent magnitudes for the programme objects can be obtained.

4.2 Reduction of the WAVS Data

The photometry for this project was performed using the CFH12k mosaic camera by Fred Ringwald on the 15th and 16th of July 1999. The details of these observations are displayed in Tables 4.1 and 4.2. Object exposures on 15.07.99 began at 8.40UT and ended at 14.29UT. Exposure times of 200, 300 and 120 seconds were used for the R, B and V filters respectively. On 16.07.99 object exposures began at 8.15UT and comprised 120 second exposures in the V filter only, ending at 14.41UT. Johnson-Kron-Cousins B,V,R filters were used in these observations as they were the only broadband filters available for use with CFH12k. This was acceptable for the survey, as at the time this filter set was used in most published CV work (although the Sloan filter set is now becoming increasingly common in the field of variable star observations). On both nights, seeing conditions were

Table 4.1: CFH12k exposures for 15.07.99

Type	Filter	No. of Exposures
Calibration		
Bias	NA	9
Flat	B	0
Flat	V	8
Flat	R	4
Standard Star		
PG 1657+078	B	7
PG 1657+078	V	7
PG 1657+078	R	7
Object		
QU Vul	B	6
QU Vul	V	65
QU Vul	R	6

around 0.7" to begin with but deteriorated over the course of the night to 1.5" at some stages.

The 12k mosaic was chosen for this project due to its wide field of view, good resolution and sensitive detectors. The massive amount of information gathered in this process did not come without a price however, the 160GB of data gathered created severe data storage demands (two large disks respectively 70 and 180Gb were used in this project) and also put a severe strain on the computer doing the reduction. Although this work was performed on a dedicated Dec Alpha it was still necessary to carefully consider the format of the data being reduced.

4.2.1 Data Format and Reduction Suite

Essentially the data from the CFH12k mosaic can be treated as one image in MEF (Multi Extension Fits) format, or can be divided into the twelve separate images that make up the mosaic. The pros and cons of each of these methods were considered in detail and the main points of the decision making process are outlined in the subsequent subsections. The reduction was carried out almost totally within IRAF (the Image Reduction and

Table 4.2: CFH12k exposures for 16.07.99

Type	Filter	No. of Exposures
Calibration Exposures		
Bias	NA	10
Flat	B	0
Flat	V	7
Flat	R	6
Standard Star Exposures		
PG 1657+078	B	0
PG 1657+078	V	0
PG 1657+078	R	0
Object Exposures		
QU Vul	B	0
QU Vul	V	109
QU Vul	R	0

Analysis Facility) except for times when bespoke IDL (the Interactive Data Language) code was preferred. However, other data reduction suites (FLIPS, ISIS, SExtractor) were considered also, and the reasons why IRAF was selected will be discussed shortly.

MEF or Split files

A multi extension fits file consists of a global image header and (in the CFH12k case) 12 image extensions each with its own image headers. Thus, using the IRAF display or mscdisplay commands (within the **mscred** mosaic reduction package) either the entire mosaic or a single segment can be displayed. This can be achieved by typing mscdisplay imagename.fits

To display the entire mosaic or

display imagename[#]

to display a single segment (where # is a number between 0 and 11).

At the time this project was begun, the software for dealing with mosaic files was in its infancy, but more importantly, the sheer size of CFH12k images made dealing with the mosaics as a whole incredibly intensive in terms of processor time. For these reasons it was decided that the mosaics would be split into individual sections. This strategy had two benefits, firstly that the files were much easier to deal with, and secondly, that more tried and tested data reduction packages could be employed.

Why IRAF?

The decision to use the Image Reduction and Analysis Facility was made for several reasons. Firstly and probably most importantly, a level of expertise in the use of IRAF packages existed among the WAVS team members and among other members of the Physics and Astronomy Department. Also, the level of help available by email from the software's developers NOAO (the National Optical Astronomy Observatory) has always been found to be excellent. It was thought that these would be important factors when dealing with such emerging technology. For this reason IRAF was chosen over FLIPS (the Fits Large Image Processing System). Once the image reduction had been completed, it would have been possible to undertake the photometry using another package such as the recent ISIS and SExtractor programs. However, it was felt that the proven abilities of the IRAF daophot package would be well up to the task, and bringing in less tested (although perhaps more efficient) software could add further complications and confusion to the results.

For tasks where the IRAF Packages were not found to be sufficient, IDL (the Interactive Data Language) scripts were written which easily compensated for any deficiencies.

4.2.2 WAVS CCD Reduction

For the WAVS data each of the reduction operations had to be performed 22 times (11 × 2), CCD 6 suffered from so many defects at this time that it was not usable for the project (Figure 4.6). In the following write up, average parameter values for the CCDs as a whole will be given as appropriate and any special cases will be mentioned where necessary.

Figure 4.6: Unusable CCD6

Ccdproc

The IRAF task which governs the reduction of CCD exposures is called **ccdproc** (Figure 4.7).

Ccdproc is capable of controlling CCD reduction for both photometry and spectroscopy and the two cases are slightly different. Only those parameters relevant to the

```
      images = "@objectfile"   List of CCD images to correct
      (output = "")            List of output CCD images
     (ccdtype = "")            CCD image type to correct
   (max_cache = 0)             Maximum image caching memory (in Mbytes)
      (noproc = no)            List processing steps only?\n
      (fixpix = no)            Fix bad CCD lines and columns?
    (overscan = yes)           Apply overscan strip correction?
       (trim = no)             Trim the image?
     (zerocor = yes)           Apply zero level correction?
     (darkcor = no)            Apply dark count correction?
     (flatcor = no)            Apply flat field correction?
    (illumcor = no)            Apply illumination correction?
   (fringecor = no)            Apply fringe correction?
     (readcor = no)            Convert zero level image to readout correction
     (scancor = no)            Convert flat field image to scan correction?\n
    (readaxis = "line")        Read out axis (column|line)
     (fixfile = "")            File describing the bad lines and columns
     (biassec = "[2070:2080,1:4128]") Overscan strip image section
     (trimsec = "")            Trim data section
        (zero = "Zero.fits")   Zero level calibration image
        (dark = "")            Dark count calibration image
        (flat = "")            Flat field images
       (illum = "")            Illumination correction images
      (fringe = "")            Fringe correction images
  (minreplace = 1.)            Minimum flat field value
    (scantype = "shortscan")   Scan type (shortscan|longscan)
       (nscan = 1)             Number of short scan lines\n
 (interactive = yes)           Fit overscan interactively?
    (function = "legendre")    Fitting function
       (order = 1)             Number of polynomial terms or spline pieces
      (sample = "*")           Sample points to fit
    (naverage = 1)             Number of sample points to combine
    (niterate = 1)             Number of rejection iterations
  (low_reject = 3.)            Low sigma rejection factor
 (high_reject = 3.)            High sigma rejection factor
        (grow = 0.)            Rejection growing radius
       (flpar = no)            flush pfile on assign?
        (mode = "ql")
```

Figure 4.7: Ccdproc parameters

current discussion will be mentioned here. **Ccdproc** can be run multiple times to complete each of the reduction steps separately (bias subtraction, overscan subtraction, flat fielding and trimming of the image), or can be run once to complete all of these tasks in sequence. In the WAVS data set each of the steps was completed separately so that the results could be monitored more closely for any problems.

Bias Subtraction

The average value of the bias frame in the WAVS data was around 450 ADU (Analogue to Digital Unit). Unfortunately many of the chips on the 12k mosaic display a number of bad rows and columns in the bias frame which are also present on the image exposures (Figure 4.8).

Bias frames from the start and end of the evening showed similar counts and so were checked and combined using the IRAF task **zerocombine**. The parameters for the **zerocombine** task are shown in Figure 4.9.

The most important of these parameters (apart from the obvious *input* and *output* keywords) are the *combine* and *reject* keywords which control the type of operation used to create the bias frame and the algorithm used to reject bad pixels. In this case we select *average* rather than *median* for the *combine* operation and *minmax* for the rejection

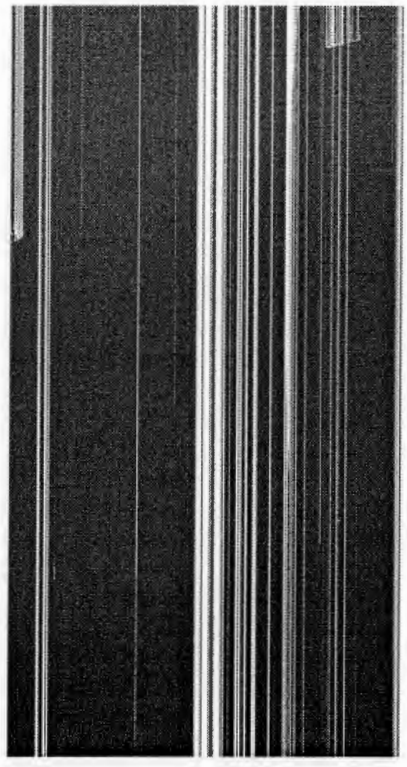

Figure 4.8: A bias image showing bad columns

algorithm. Choosing *minmax* means that when averaging the exposures for any given pixel, the highest and lowest pixel values from the set can be rejected. This is defined by the *nhigh* and *nlow* keywords and specifying these as 1 and 0 respectively should mean that any high pixel values due to cosmic rays will be excluded. *Minmax* is a simple rejection method which is fast and effective at removing bad data values in cases where there are plenty of available frames (Massey, 1997). Many of the other parameters displayed in Figure 4.9 control the actions of other types of rejection algorithm (such as *avsigclip* and *crreject*) which will be discussed shortly in the context of combining flat fields. Setting the *zerocor* switch in **ccdproc** to 'yes' and defining the name of the combined bias frame allows the task to perform bias subtraction on a list of images.

Overscan Subtraction

The overscan strip for the WAVS data is described in the image header under the keyword BIASSEC. However, experience showed that this section was in general too close to the exposed area of the chip and often suffered from the effects of overexposure as described previously. To remedy this, a thinner but leakage free region of the overscan strip was

```
                    Image Reduction and Analysis Facility
PACKAGE = ccdred
   TASK = zerocombine

input   =            @zerolist  List of zero level images to combine
(output =                 Zero) Output zero level name
(combine=              average) Type of combine operation
(reject =               minmax) Type of rejection
(ccdtype=                    ) CCD image type to combine
(process=                   no) Process images before combining?
(delete =                   no) Delete input images after combining?
(clobber=                   no) Clobber existing output image?
(scale  =                 none) Image scaling
(statsec=                    ) Image section for computing
statistics
(nlow   =                    0) minmax: Number of low pixels to
reject
(nhigh  =                    1) minmax: Number of high pixels to
reject
(nkeep  =                    1) Minimum to keep (pos) or maximum to
reject (neg)
(mclip  =                  yes) Use median in sigma clipping
algorithms?
(lsigma =                   3.) Lower sigma clipping factor
(hsigma =                   3.) Upper sigma clipping factor
(rdnoise=                   0.) ccdclip: CCD readout noise
(electrons)
(gain   =                   1.) ccdclip: CCD gain (electrons/DN)
(snoise =                   0.) ccdclip: Sensitivity noise (fraction)
(pclip  =                -0.5) pclip: Percentile clipping parameter
(blank  =                   0.) Value if there are no pixels
(flpar  =                   no) flush pfile on assign?
(mode   =                   ql)
```

Figure 4.9: Zerocombine parameters

defined under the *biassec* parameter in **ccdproc**. The *function* and *order* parameters control the fit to the overscan region. Tests performed with the *interactive* switch on lead to a third order legendre polynomial being selected for the bulk data reduction (Figure 4.10).

Flat field

In the WAVS data set, sky flat fields were taken in V, B and R filters. The time-series data were reduced using the V flat field, but B and R were necessary for reducing the calibration frames. Several of the CCDs on the 12k mosaic show strong gradients in the flat field frame, whilst others show more complex structure such as 'brick wall patterns' (Figure 4.11).

All the flat field frames were checked carefully before combination for transient events such as shooting stars. They were then passed through **ccdproc** for bias and overscan subtraction.

Flat field frames were combined using the IRAF task **flatcombine**, the parameters for this are displayed in Figure 4.12 and are not dissimilar to those of **zerocombine**.

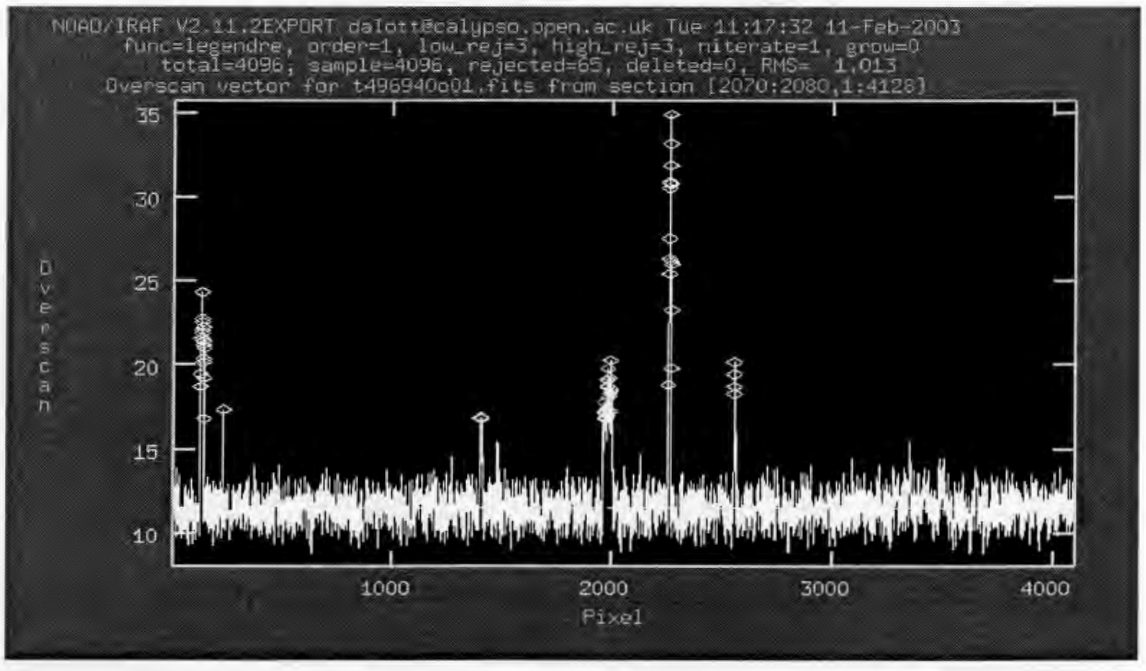

Figure 4.10: Interactive overscan fitting procedure. Circles mark rejected points.

There are several important differences between the chosen parameters for **zerocombine** and **flatcombine**, most notably that the rejection algorithm has now changed from *minmax* to *crreject*. The *crreject* keyword is chosen here as does a good job of removing any radiation events (caused by cosmic rays etc.) in cases where exposures are less plentiful. *Crreject* assumes that Poisson statistics apply and calculates an expected σ using the known gain and readout noise of the chip (as specified in the *rdnoise* and *gain* parameters). Pixel values that are above the average value by a number of sigma specified by the *hsigma* keyword are rejected.

Once the final flat field is constructed a final pass through **ccdproc** can be used to apply the flat field to the images and then trim off the overscan strip. The CCD reduction is now complete, and photometry can begin.

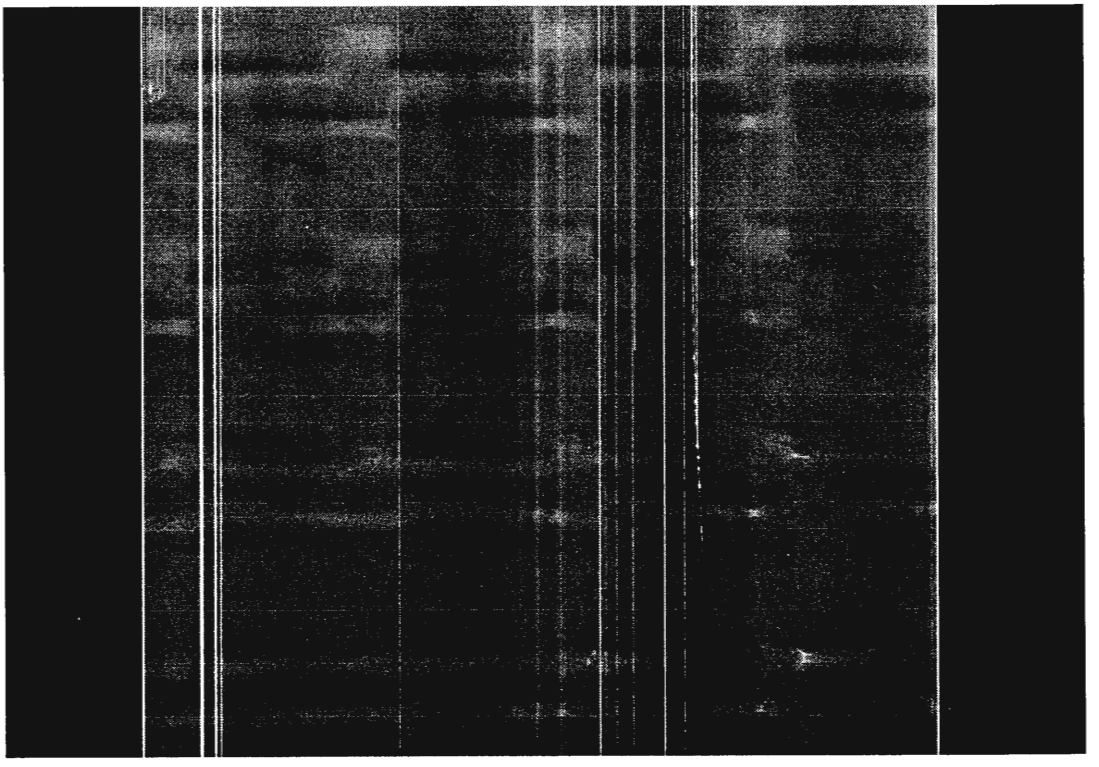

Figure 4.11: Section of a flat field image showing brick wall pattern. Image intensity is scaled such that the variations are actually around 10% of the total counts.

```
                    Image Reduction and Analysis Facility
PACKAGE = ccdred
   TASK = flatcombine

input   =             @flatlist  List of flat field images to combine
(output =                 Sflat) Output flat field root name
(combine=               average) Type of combine operation
(reject =              crreject) Type of rejection
(ccdtype=                      ) CCD image type to combine
(process=                    no) Process images before combining?
(subsets=                   yes) Combine images by subset parameter?
(delete =                    no) Delete input images after combining?
(clobber=                    no) Clobber existing output image?
(scale  =                  mode) Image scaling
(statsec=                      ) Image section for computing
statistics
(nlow   =                     1) minmax: Number of low pixels to
reject
(nhigh  =                     1) minmax: Number of high pixels to
reject
(nkeep  =                     1) Minimum to keep (pos) or maximum to
reject (neg)
(mclip  =                   yes) Use median in sigma clipping
algorithms?
(lsigma =                    3.) Lower sigma clipping factor
(hsigma =                    3.) Upper sigma clipping factor
(rdnoise=                    6) ccdclip: CCD readout noise
(electrons)
(gain   =                    1.) ccdclip: CCD gain (electrons/DN)
(snoise =                    0.) ccdclip: Sensitivity noise (fraction)
(pclip  =                  -0.5) pclip: Percentile clipping parameter
(blank  =                    1.) Value if there are no pixels
(flpar  =                    no) flush pfile on assign?
(mode   =                    ql)
```

Figure 4.12: Flatcombine parameters

4.2.3 WAVS Photometry

Each of the WAVS time-series images contains around 6000 stars per CCD, detected at 5 sigma above sky. Typical seeing is 0.8" with a pixel size of 0.2"/pixel. Sky values vary between around 250 and 350 counts per pixel from CCD to CCD. In places the field is very crowded and simple aperture photometry is not viable (Figure 4.13).

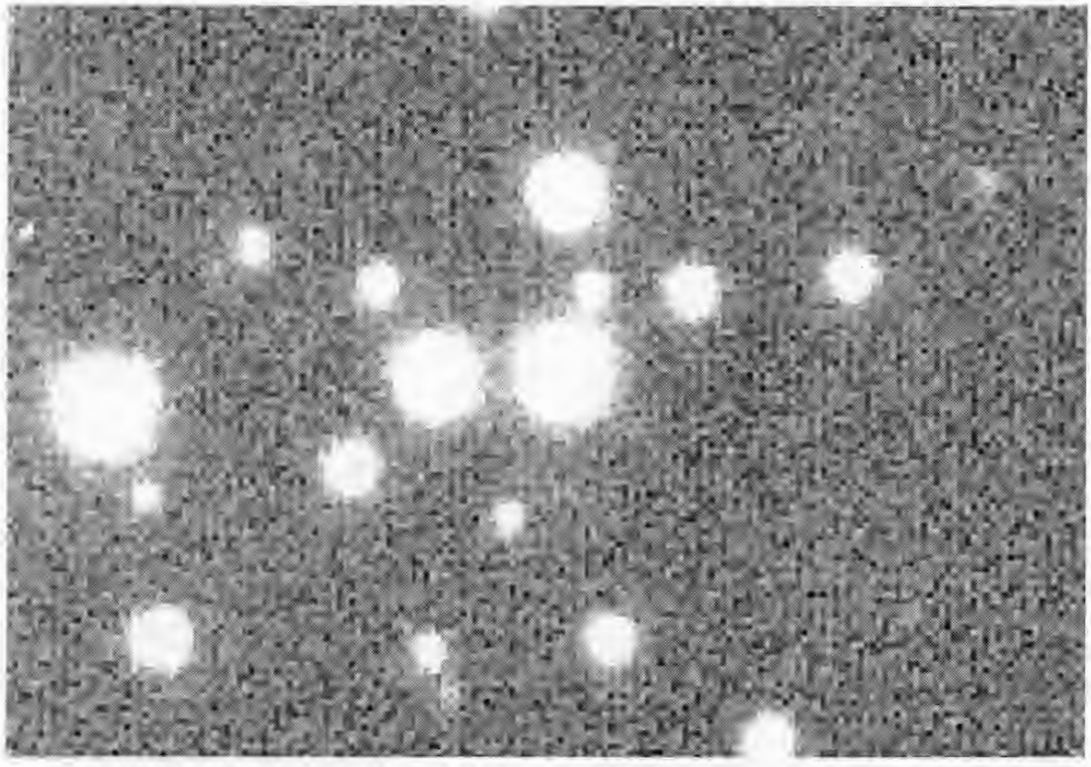

Figure 4.13: A crowded field from the WAVS dataset

The following section describes the process of achieving good photometry in the case of the WAVS data.

4.2.4 Parameters

The IRAF package which controls both aperture photometry and PSF fitting is **daophot**. Within the **daophot** environment there are several parameters which must be set up before photometry can begin. Most of these are found within the **datapars** and **daopars** parameter files (Figure 4.14 and 4.15).

```
                    Image Reduction and Analysis Facility
PACKAGE = daophot
   TASK = daopars

(functio=                  auto) Form of analytic component of psf
model
(varorde=                     0) Order of empirical component of psf
model
(nclean =                     0) Number of cleaning iterations for
computing psf
(saturat=                    no) Use wings of saturated stars in psf
model comput
(matchra=                    3.) Object matching radius in scale units
(psfrad =                   12.) Radius of psf model in scale units
(fitrad =                    4.) Fitting radius in scale units
(recente=                   yes) Recenter stars during fit ?
(fitsky =                    no) Recompute group sky value during fit
?
(groupsk=                   yes) Use group rather than individual sky
values ?
(sannulu=                    0.) Inner radius of sky fitting annulus
in scale uni
(wsannul=                   11.) Width of sky fitting annulus in scale
units
(flaterr=                 0.75) Flat field error in percent
(proferr=                    5.) Profile error in percent
(maxiter=                     50) Maximum number of fitting iterations
(clipexp=                      6) Bad data clipping exponent
(clipran=                    2.5) Bad data clipping range in sigma
(mergera=                INDEF) Critical object merging radius in
scale units
(critsnr=                    1.) Critical S/N ratio for group
membership
(maxnsta=                 20000) Maximum number of stars to fit
(maxgrou=                    60) Maximum number of stars to fit per
group
(flpar  =                    no) flush pfile on assign?
(mode   =                    ql)
```

Figure 4.14: The daopars parameter file

Full Width at Half Maximum (FWHM)

The Full Width at Half Maximum is a term used to measure the PSF on an image. If the brightness profile of a stellar source is represented as a two dimensional image, then the FWHM is the distance from one side to the other of the profile (the full width) when the brightness falls to half its maximum value. This is essentially a measure of how 'spread out' the image has become due to atmospheric effects. The FWHM of an individual star can be easily measured using the IRAF command *imexam* (Figure 4.16).

Having measured a number of stars across the image, an average FWHM is found and this is inserted under the heading *fwhmpsf* in the **datapars** parameter set. This value will be used by the star finding routine **daofind** (see later). It is important to note that for a long series of exposures the FWHM may change over the course of time (even from frame to frame), and so it may be necessary to mirror this variation within the parameter files. However, this is only really necessary if the variation is large (Massey & Davis, 1992).

```
                                  I R A F
                       Image Reduction and Analysis Facility
PACKAGE = daophot
   TASK = datapars

(scale  =                   1.) Image scale in units per pixel
(fwhmpsf=                  3.2) FWHM of the PSF in scale units
(emissio=                  yes) Features are positive ?
(sigma  =                 12.6) Standard deviation of background in
counts
(datamin=                240.) Minimum good data value
(datamax=              62000.) Maximum good data value
(noise  =              poisson) Noise model
(ccdread=                    ) CCD readout noise image header
keyword
(gain   =                    ) CCD gain image header keyword
(readnoi=                  5.2) CCD readout noise in electrons
(epadu  =                  2.1) Gain in electrons per count
(exposur=              EXPTIME) Exposure time image header keyword
(airmass=              AIRMASS) Airmass image header keyword
(filter =                    ) Filter image header keyword
(obstime=              UTC-OBS) Time of observation image header
keyword
(itime  =                120.) Exposure time
(xairmas=              INDEF) Airmass
(ifilter=              INDEF) Filter
(otime  =              INDEF) Time of observation
(flpar  =                 no) flush pfile on assign?
(mode   =                 ql)
```

Figure 4.15: The datapars parameter file

Table 4.3: Gain, readout noise and max counts for linearity parameters for the 12k mosaic

CCD	00	01	02	03	04	05	06	07	08	09	10	11
Gain (e^-)/ADU	1.5	1.5	1.6	1.5	1.3	1.7	1.8	1.7	1.4	1.5	1.8	1.5
Rdns (e^-)	4.2	3.0	5.4	5.1	10.5	3.4	5.0	5.1	5.9	3.9	3.4	5.2
Lin (kADU)	62	65	51	65	60	65	52	53	65	54	61	55

Gain and Readout noise

The gain and readout noise of the individual detector (Note, the 12 detectors each have different qualities) are represented in the parameter files by the keywords *epadu* and *readnoi* respectively. These values can either be input by hand (from the image header) or referenced by their image header keywords. Gain is measured in electrons per ADU (Analogue to Digital Unit), and readout noise in electrons. Values for each of the 12 CFH12k mosiac CCDs are shown in Table 4.3 along with the maximum counts for linearity for each of the CCDs.

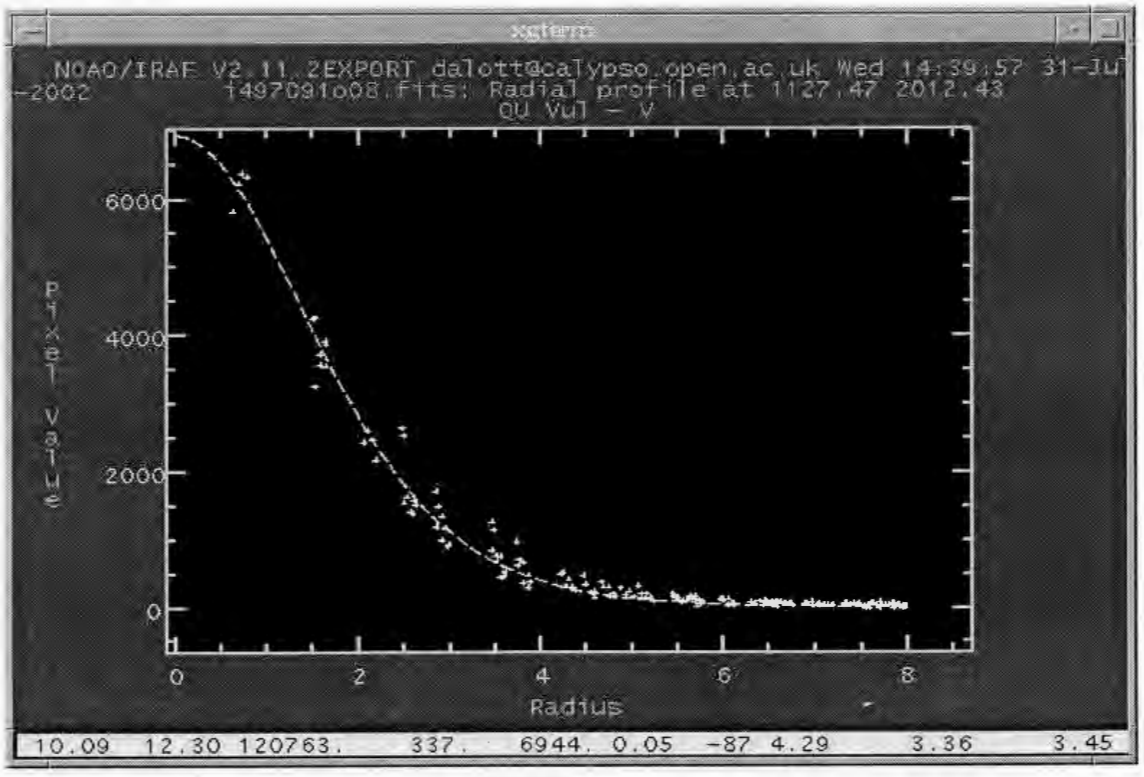

Figure 4.16: Plot used in calculating the FWHM. Last number on the bottom right gives the FWHM of this particular object

Sky and 1σ sky variation

Before accurate photometry of faint sources can be calculated it is necessary to know how many counts per unit area are coming from the diffuse sky background. The sky value of the data can be found easily by once again using *imexam* and this time producing an histogram of the pixel values in a region of the sky (Figure 4.17).

Calculating the 1σ sky variation is slightly more complex and is given by

$$1\sigma = (\sqrt{(s \times p + r^2)})/p \tag{4.2}$$

where s is the mean sky value, p is the gain and r is the readout noise (Massey & Davis, 1992). This should be of the order of the half width half maximum (HWHM) of Figure 4.17.

Maximum and Minimum good data values

Also important to the photometry procedure is defining the maximum and minimum good data values (so that pixels with values outside these limits will be counted as 'bad' and

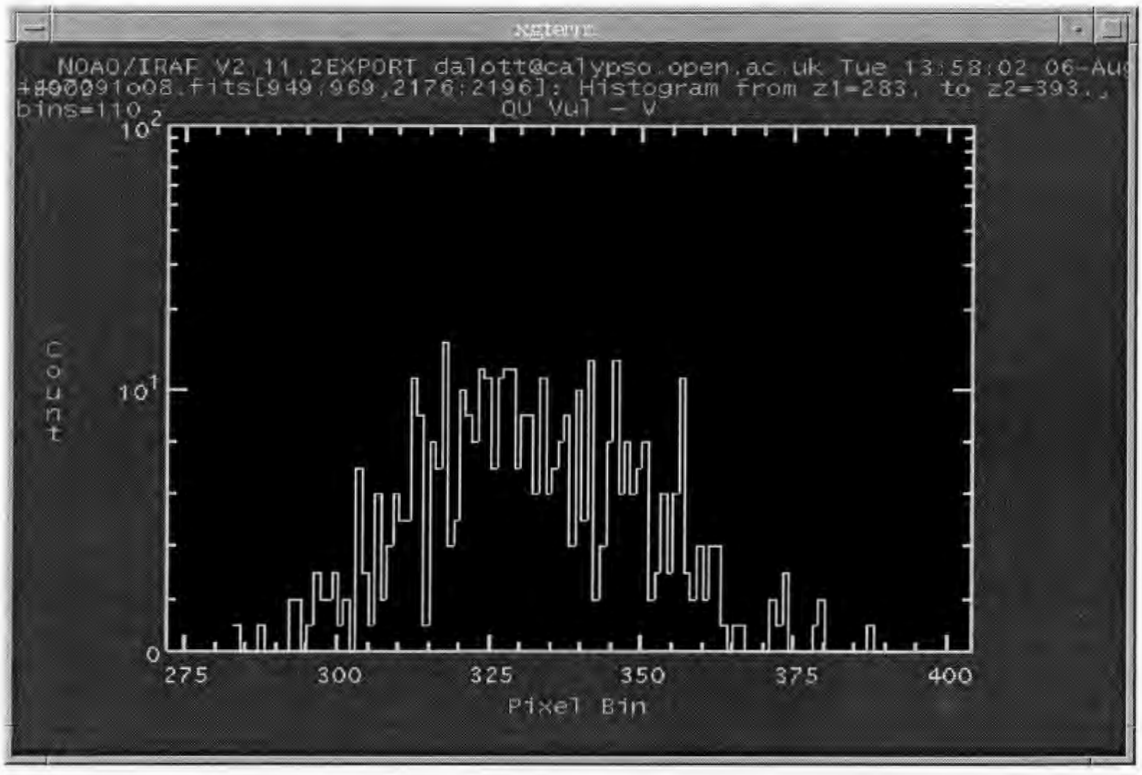

Figure 4.17: An histogram representing the average of sky pixel values. The 1 σ sky variation is of the order of the HWHM

not included in the process). The maximum good data value (represented by *datamax* in the **datapars** file) is easy enough to find. It is limited by either the saturation limit of the CCD, or more often, by the limit of its linearity. A reasonable value for the minimum good data value *datamin* can be calculated by multiplying the 1σ sky variation by 3.5 and subtracting it from the value of the sky (Massey & Davis, 1992).

There are a selection of other parameters in **daopars** that are used in only a few of the necessary tasks and these will be discussed as and when appropriate.

4.2.5 Preparation for Photometry

To include as many stars as possible in the photometry it is necessary to locate the image (for each night of observations) which has the best seeing conditions. In this case the stars are better defined (having a smaller FWHM) and so it will be easier to distinguish them from their neighbours.

daofind, imcentroid and lintran

To locate and measure the positions of the (some 6000) stars on each chip, the IRAF task **daofind** must be run on the 'best' image (the image which has the best seeing). The 'best' image is chosen by running **daofind** on all the time-series images and selecting the one in which the highest number of objects are found. This process should reveal the image with the best seeing conditions, but this can be checked by examining the image and measuring the FWHM as described previously. Before this is possible there are some other parameters that must be checked within the parameter file **findpars**. The parameter of interest here is *thresho* which controls the detection threshold above which a signal will be considered to be real and not noise. The actual value for this parameter is decided by an iterative process in which *daofind* is run and the found objects are overlayed upon the image using the IRAF task **tvmark**. Dependent upon whether there are stars remaining undetected, or if noise is being included as stars, the value of *thresho* can be altered and the task re-run.

Once **daofind** has been run in such a way that all relevant objects are being detected with the minimum amount of spurious detections (i.e. all stars, but not all galaxies, hot pixels etc) then the process is complete. In cases such as this where there are thousands of objects on an individual CCD chip, it is not sensible to run the **daofind** task on all of the images separately. As the 'best' image has been chosen, not all of the stars found here will be detected on images with poorer seeing conditions. Even if the same number of stars were relocated on the other images, spurious detections would mean that the numbering system of the detected objects would be confused, making building lightcurves for individual objects almost impossible. Using the relative coordinates of objects from the 'best' image as a template also helps to avoid systematic errors in measuring fluxes from close neighbours on images where the seeing conditions are worse. Instead, the IRAF task **imcentroid** is used to calculate the shifts between exposures.

During the course of the night, the telescope was moved in a dithering pattern so that the same object did not appear on the same pixels all the time - this practice increases the chance of being able to spot incorrect photometry due to bad pixels, but also means that the objects found by the **daofind** task do not lie at the same image co-ordinates on each of the exposures. The **imcentroid** task calculates the shifts between an image specified by the *reference* keyword (in this case the previously selected 'best' image) and a number of other exposures using the co-ordinates of registration objects specified by the

coords parameter. The coordinates file specified is generally a coordinate list created by the **daofind** task. However, using a coordinate file containing thousands of objects makes the process unnecessarily long and more likely to fail. This can be avoided by running **daofind** again and increasing the value of the detection threshold until only a hundred or so bright stars that are common across the frames are included. An important parameter controlling the **imcentroid** process is *bigbox*. Unless an estimate of the shifts between each image and the reference image is to be supplied, then *bigbox* must be large enough to encompass the largest shift between reference image and exposure. Once the parameters are set correctly, using the command

imcentr > shifts

will create a file called 'shifts' which contains the list of exposure names accompanied by x and y pixel shifts from the reference image. By amending this file somewhat a script can be created (Figure 4.18) that uses the IRAF lintran task to shift the original daofind coordinate list into the reference frame of each individual image exposure.

```
lintran i497091o02.fits.coo.1 x1=13.70 y1=0.74 > 165.coo
lintran i497091o02.fits.coo.1 x1=13.77 y1=0.75 > 166.coo
lintran i497091o02.fits.coo.1 x1=13.83 y1=0.61 > 167.coo
lintran i497091o02.fits.coo.1 x1=13.66 y1=0.59 > 168.coo
lintran i497091o02.fits.coo.1 x1=13.72 y1=0.62 > 169.coo
lintran i497091o02.fits.coo.1 x1=14.08 y1=0.69 > 170.coo
lintran i497091o02.fits.coo.1 x1=14.06 y1=0.75 > 171.coo
lintran i497091o02.fits.coo.1 x1=14.05 y1=0.64 > 172.coo
lintran i497091o02.fits.coo.1 x1=13.87 y1=0.57 > 173.coo
```

Figure 4.18: Lintran script

Having done this, the shifted coordinates can be checked by plotting them onto the relevant image using the task **tvmark**. Generally this was done for the images which showed the greatest shift from the reference to check that the process was working correctly (Figure 4.19).

Once all these stages are complete there should exist both a number of reduced image exposures and an equal number of coordinate files in the form *.coo. With these sets of files it is now possible to begin aperture photometry.

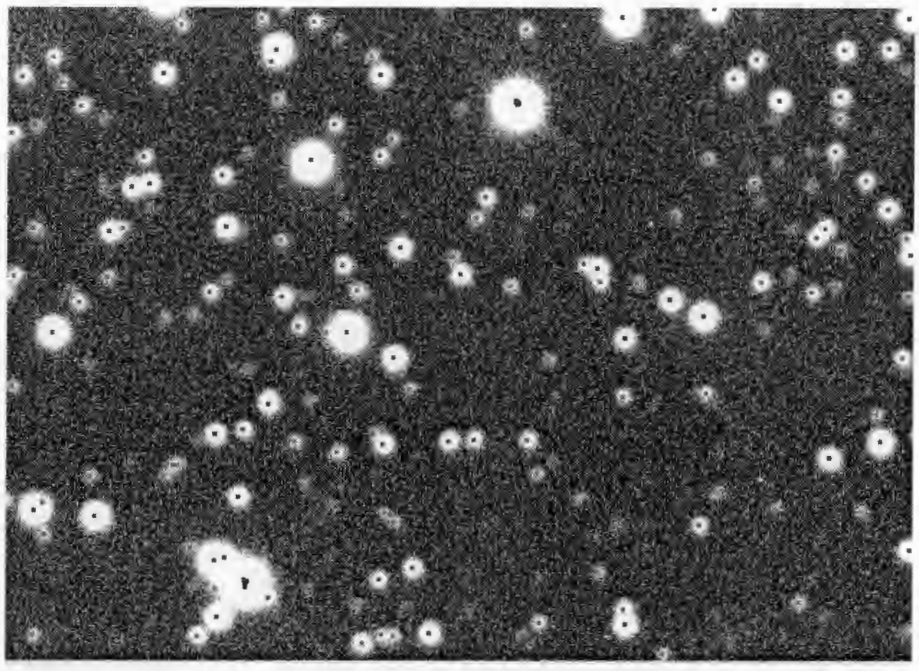

Figure 4.19: Results of the co-ordinate shifting procedure. This image is one of the furthest away from the reference, shifted co-ordinates are shown by the grey dots.

4.3 Photometry and PSF fitting

4.3.1 Aperture Photometry

Although the WAVS field is too crowded to rely on aperture photometry to give reliable magnitudes, it is still necessary to run this procedure as the files created here will later be input into the PSF fitting procedure. Aperture photometry in IRAF is controlled by the package **phot**, and its parameter files **centerpars**, **photpars** and **fitskypars** (as well as the **datapars** parameter set used by most **daophot** tasks). The most important parameters here are *apertur* (the aperture radius in pixels) and the *annulus* and *dannulus* parameters which control the inner radius and the width of the sky annulus respectively. Another important point to note for crowded field photometry is that the centering algorithm, *calgori*, is set to none. As the co-ordinates are already centered on the individual frames a centering algorithm is not necessary and may cause the **phot** task to blur separate objects together.

4.3.2 PSF Fitting

The PSF fitting procedure is in several parts, controlled respectively by the **psf**, **nstar**, **substar** and **allstar** tasks. The **psf** task creates the point spread function for each image exposure, **nstar** and **substar** are both packages used in refining that PSF, whilst **allstar** is used to finally apply the PSF to individual objects and create a list of accurate magnitudes. Obviously, the validity of the results created by **allstar** depends upon the accuracy of the PSF, and several factors must be taken into account.

What constitutes a good PSF star?

A good PSF star must be bright and obviously must have no close neighbours, also any stars in the surrounding area must be fainter than the chosen star. Bad columns should be avoided, as must bad lines and areas of the chip where blooming has occurred. Stars too close to the edge of the chip must also be avoided. An important factor to realise in choosing PSF stars is that they must be good on all frames taken on that night. As the telescope is dithered, bad lines and columns move relative to the star field, thus a star which appears to be a 'good' PSF star at the start of the night may be very bad by the end of the night or indeed may have disappeared from the image altogether. It would be possible to interactively choose different PSF stars that were good on each of the frames, but this process would be incredibly time consuming. Therefore it is important to have a good idea of the magnitude of the largest shift between the reference image and the other exposures when making this decision.

Creating the PSF

The parameters for the **daophot** task **psf** are displayed below in Figure 4.20.

Other parameters that affect the fitting of the point spread function can be found in the parameter set **daopars**. Two of the most important are the *psfrad* and *fitrad* parameters which respectively describe the radius of the PSF model that will be constructed, and how much of this function will be used in making a fit to a star. *Psfrad* is set to a value similar to the radius of the largest star that will be used in defining the PSF (the radius here is the distance from the centre of the star to a point where it cannot be differentiated from the sky). A good value for the fitting radius (used later by the **allstar** and **substar** tasks) is something like the same as the FWHM (Massey & Davis, 1992). Another important parameter in **daopars** is *functio* which defines the type of function

```
PACKAGE = daophot
   TASK = psf

image   =              @allist  Input image(s) for which to build PSF
photfile=             @maglist  Input photometry file(s) (default:
image.mag.?)
pstfile =             @pstlist  Input psf star list(s) (default:
image.pst?)
psfimage=              default  Output PSF image(s) (default:
image.psf.?)
opstfile=              default  Output PSF star list(s)
(default:image.pst.?)
groupfil=              default  Output PSF star group file(s)
(default: image.ps
(plotfil=                     ) Output plot metacode file
(datapar=                     ) Data dependent parameters
(daopars=                     ) Psf fitting parameters
(matchby=                 yes) Match psf star list to photometry
file(s) by id
(interac=                  no) Compute the psf interactively ?
(showplo=                 yes) Show plots of PSF stars?
(plottyp=                mesh) Default plot type
(mesh|contour|radial)
(verbose=                  no) Print psf messages ?
(verify =                  no) Verify critical psf parameters ?
(update =                 yes) Update critical psf parameters ?
(graphic=          )_.graphics) Graphics device
(display=           )_.display) Display device
(icomman=                     ) Image cursor: [x y wcs] key [cmd]
(gcomman=                     ) Graphics cursor: [x y wcs] key [cmd]
(flpar  =                  no) flush pfile on assign?
(mode   =                  ql)
```

Figure 4.20: Parameters for the psf task

that will be used to fit the PSF. Setting this to 'auto' means that a number of different functions will automatically be tried and the best one chosen. In the first instance the *image* and *photfile* keywords are set to the relevant filenames for the reference image, and the *interactive* switch is set to 'yes'. In this mode, a mesh plot of potential PSF stars is created (Figure 4.21). By rotating this profile it is possible to see if the star is contaminated in any manner (such as by a faint companion). The star is then selected or rejected by the user. This procedure is repeated until some 60 stars are selected across the chip. At this point the PSF can be fitted by quitting the application, and the best fit to the profiles (the one with the least scatter) will be chosen.

In general the PSF was created using bright objects to increase the signal to noise ratio of the fit. However, to make sure that same fit could be applied successfully to the fainter program objects, a test fit using only fainter objects was created. The residuals for a bright and faint PSF fit constructed from stars on the same CCD are displayed in Figure 4.22. Although the residuals of the faint fit contain considerably more noise, the overall pattern is clearly consistent. This can be seen in Figure 4.23 which shows the residuals from the bright fit divided by those from the faint.

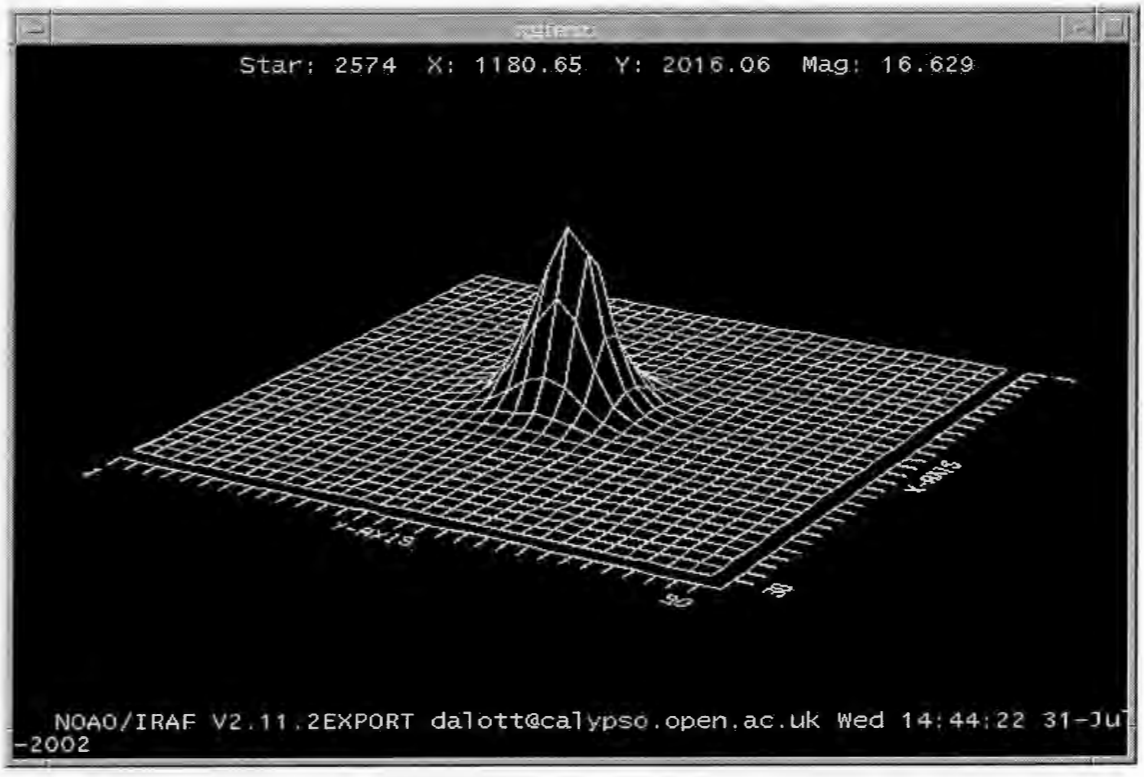

Figure 4.21: Mesh plot of of an object brightness profile in psf

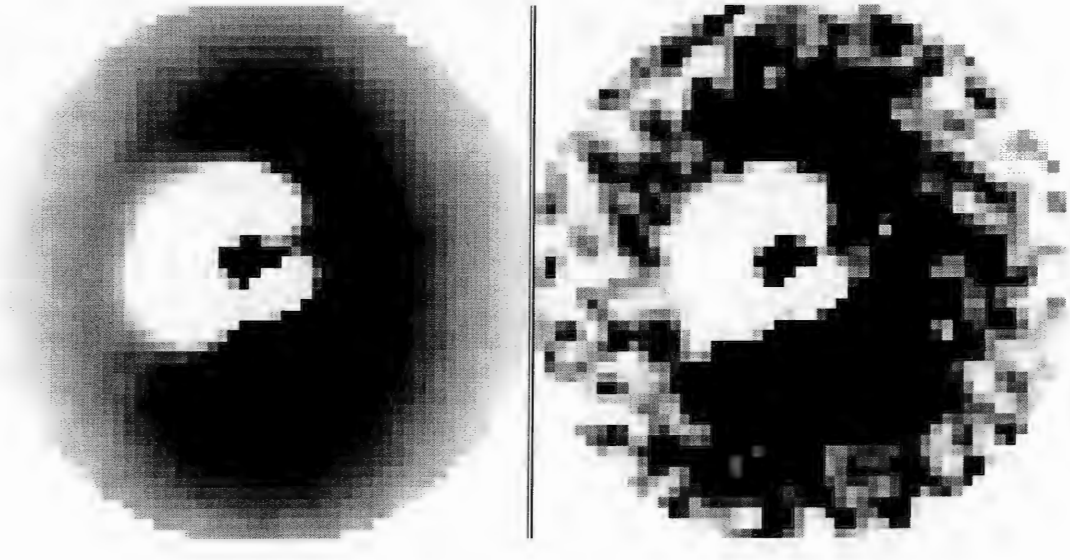

Figure 4.22: Residuals for both the bright (left) and faint (right) PSF fits

Refining the PSF

The two tasks used to refine the PSF are **nstar** and **substar**. The **substar** task is used to fit the calculated PSF to the selected PSF stars and to subtract them from the image.

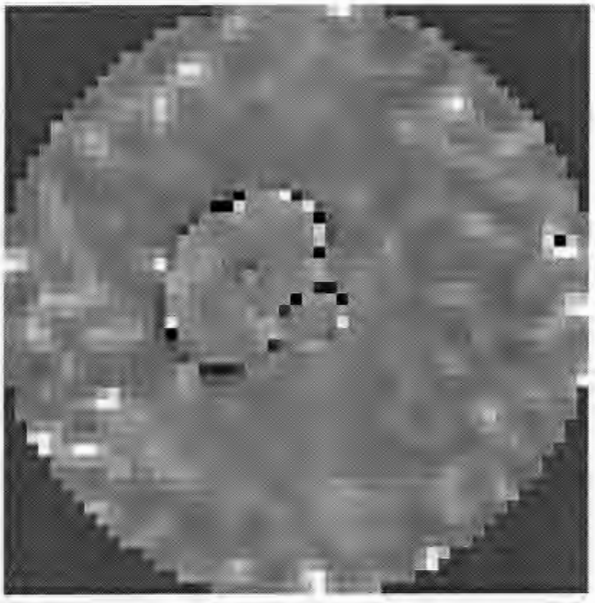

Figure 4.23: bright residuals divided by faint residuals

Once this is complete it is easy to see if any of these stars had serious problems as the subtraction will be poor, and the shape of any residuals is often inverted with respect to the other stars (Figure 4.24)

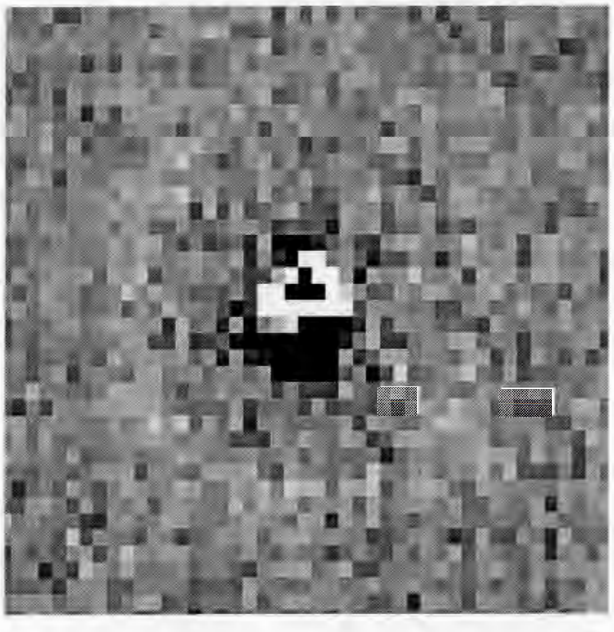

Figure 4.24: Example of bad subtraction

If any of the selected stars do fall into this category then they should be removed from the PSF star list and the process repeated. The **nstar** task is used for simultaneously fitting PSFs to any stars considered to be in a group with the chosen PSF stars (as may be the case in a very crowded field). By checking the PSF group file (the file with extension .psg) it is possible to see if IRAF considers the individual PSF stars to have neighbours which must be subtracted separately to get a good fit. In this case the **nstar** task can be used to fit and subtract the neighbouring stars before re-fitting the PSF star to gain more accurate results. Although the WAVS field was very crowded in places, due to the sheer number of stars on each chip, it was often possible to find completely isolated stars. For this reason the **nstar** process was not always necessary.

Having calculated the PSF, the task **allstar** is used to fit the PSF to the program objects defined in the .coo and .mag files created previously by the **daofind** and **phot** tasks. The output of **allstar** is a list of fitted stars and their magnitudes, a list of rejected stars (after a number of fitting iterations with a user defined tolerance) and an image of the field with the program objects removed (Figure 4.25). A closeup of the subtracted stars is also shown (Figure 4.26). Objects that cannot be subtracted (a diffuse galaxy and cosmic ray) are also visible in this image.

If subtracting the program objects has revealed a number of other stars that were previously hidden, then these stars should be appended to the co-ordinates list and the process repeated (generally two iterations were sufficient for the WAVS data). Once the field is almost blank (apart from cosmic rays, bad pixels, galaxies and saturated stars) then the PSF fitting process is completed and the next stage is to calibrate the photometry correctly.

4.3.3 Converting to the Standard System

Although the results of **phot** and **allstar** are given in terms of magnitudes, these are not necessarily the correct apparent magnitudes of the program objects. As a first approximation, IRAF calculates instrumental magnitudes defined as -2.5*log((Counts above sky)/(Exposure time))+Constant, where the constant is the magnitude assigned to a star that has a total of 1 ADU per second within the measuring aperture (Massey & Davis, 1992). To properly convert these magnitudes to the standard system it is necessary that both standard and program stars were observed in at least three filters. For most of the CCDs on the CFH12k mosaic (1,2,3,4,7,8,9), this was the case, and observations were

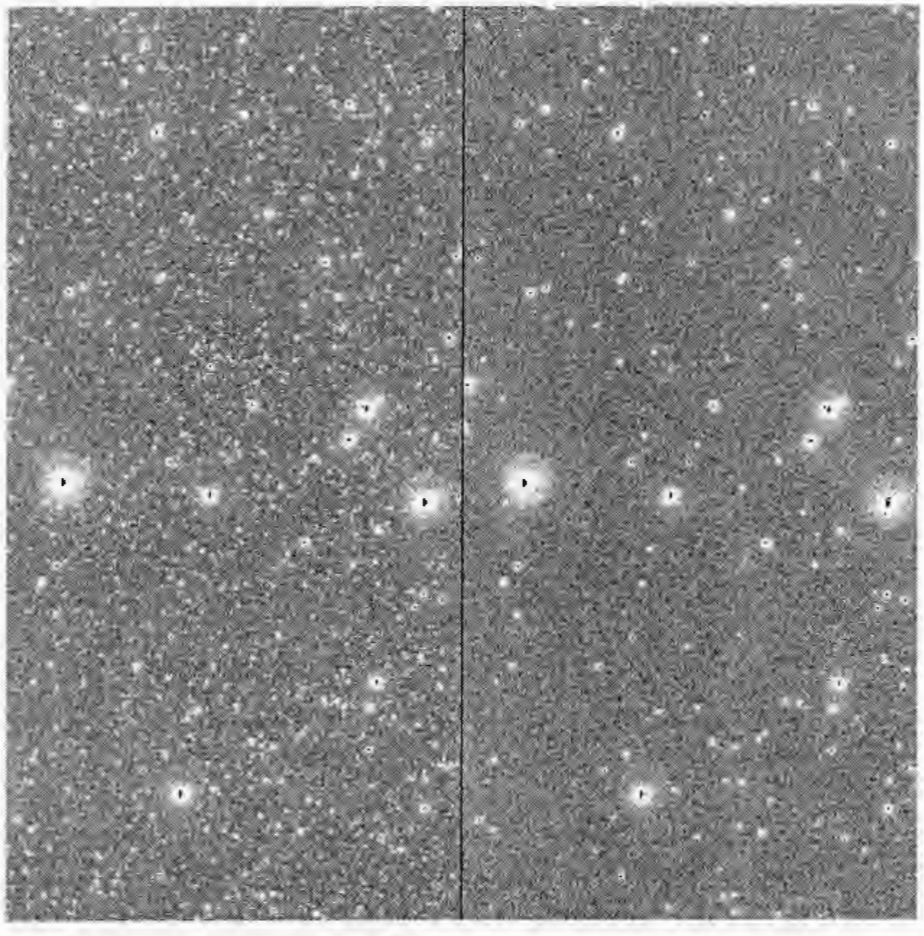

Figure 4.25: Before and after PSF subtraction. The stars remaining on the right hand side are all saturated (the resolution in this image is greatly reduced meaning that some saturated points cannot be seen)

made using B,V and R filters (this took place on the first night of observations). For those CCDs which were omitted (mainly due to technical problems) another, less accurate method must be used and this will be discussed later.

Obtaining the standard star solutions

The standard stars used in the WAVS survey were all from the Landolt field PG1657+178 (Figure 4.27). These are all bright stars in an uncrowded field with well known apparent magnitudes and so serve well for calibration purposes. The CCD reduction for the B and R filters proceeds in much the same way as it did for the V filter exposures. Obvious exceptions to note are that various input parameters (*sky*, FWHM etc.) must be changed, and also that the correct flat field frame must be used for each filter. Once the frames

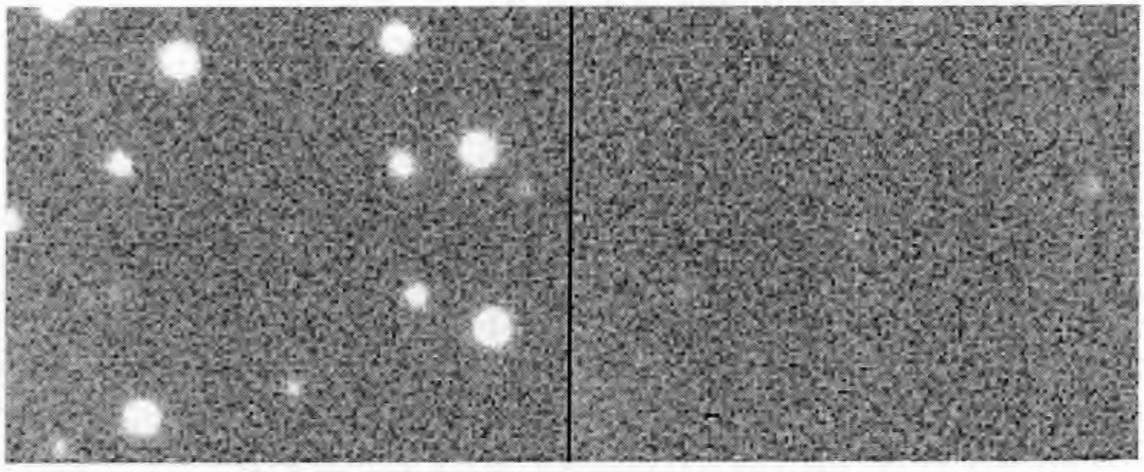

Figure 4.26: Closer view of subtracted stars

have had instrumental artifacts removed, photometry of the standard stars can proceed using the aperture method described previously as the field is sparse. By changing the *interactive* switch in **photpars** to 'yes' it will be possible to measure the standard stars individually, rather than creating coordinate files (this would be unnecessary due to the limited number of stars that need to be measured).

Colour information for the stars in PG1657+078 is already stored in the IRAF catalogue. Once the photometry is completed a standard star observations file is created using the task **mknobsfile**. The inputs to this task are the instrumental magnitude files created by the **phot** task, and also a file which assigns which individual exposures go with which standards. The output of **mknobsfile** is a file of instrumental magnitudes and positions which are now clearly associated with the filter ID and standard star name for each object. Next the **mkconfig** task is used to create a configuration file for fitting the observed colour information. **Mkconfig** allows editing of this file so that irrelevant transformation equations (in this case those relating to U and I filters) can be removed. An example of the equations used in the fit is displayed below.

$$B = B_i + b_1 + b_2 X_B + b_3 (B - V) \tag{4.3}$$

In this case B is the apparent magnitude, B_i is the instrumental B magnitude, X_B is the airmass and V is the apparent V magnitude. The coefficients b_1 and b_3 will be solved for by the IRAF task **fitparams**. If standard star observations had been taken at a number of different airmasses over the course of the night, then it would also be

Figure 4.27: Landolt field PG1657+078. The central 'triangle' formation are PG1657+078, PG1657+078A, PG1657+078B and PG1657+078C

possible to solve for the extinction coefficient b_2. In this case however, a literature value for the extinction coefficient must be used. Extinction coefficients were obtained from the Mauna Kea website for the central wavelengths of each of the filters used (Puxley, 2001). Second order terms (such as $b_4(B-V)X_B$) are not included in the fit as they are assumed to be small and are hard to calculate without more calibration exposures. **Fitparams** is run interactively with the standard star observations and configuration files as input parameters. **Fitparams** displays a plot of the residuals for each fit and any points that appear discrepant can be interactively removed. Once the fit is acceptable the process is repeated for the next filter. The output of this procedure (called CFHT.ans) will be used later in applying the fit to the program objects.

Calibrating the Program Objects

To calibrate the program objects the process that was run on the V frames previously (aperture photometry, co-ordinate matching, psf fitting), must now be run on the object exposures in the other two filters. Again, parameters such as the FWHM must be measured

and changed accordingly. Once this is done the task **mkobsfile** (no 'n') is used to generate a file, similar to the one generated previously for the standard stars, but this time for the program objects. **Mkobsfile** requires as input parameters both the shifts between the frames (calculated as described previously) and the aperture correction. The aperture correction needs to be defined if a larger aperture was used when fitting the standard stars than the program stars as it affects the zero point of the magnitude scale. It can easily be calculated by running **phot** once again on an object exposure, this time using the larger aperture and only using stars with no close neighbours. The average difference between the magnitude values can then be calculated and input into **mkobsfile** (Massey & Davis, 1992).

Finally the task **invertfit** can be used to apply the transformation equations to the stars in the object exposures for each of the filters. The output of **invertfit** contains the x and y positions of program objects as well as the apparent magnitudes and errors given in terms of V, B-V and V-R.

Applying the **invertfit** task to each of the object exposures in a time series allows the effect of extinction to be removed from the lightcurve (Figures 4.28 and 4.29). At this stage the extinction corrected lightcurve of this (non-variable) object still seems to show some variations. These variations are due to changing seeing and atmospheric extinction throughout course of the night which cause similar brightness variations in all of the lightcurves. A much better insight can be gained by using differential photometry in which a bright and non-variable star is subtracted from each program object, hopefully removing the effects of these global variations. Plotting a differential lightcurve removes these remaining effects (Figure 4.30).

Calibration without the correct colour exposures

Unfortunately during the observing run, some problems with the computer script used for taking the standard star exposures meant that on CCDs 0,5,6,10 and 11, insufficient exposures were taken for calibration to be achieved properly. Also, no object exposures in B and R filters were imaged on the second night of observations. Little could be done about gaining correct colour information for the night two observations, but a method was developed to apply colour corrections to those CCDs from night one for which sufficient standard star observations were not available. Although this method is less accurate than if the standard star observations were present, the results are considerably better

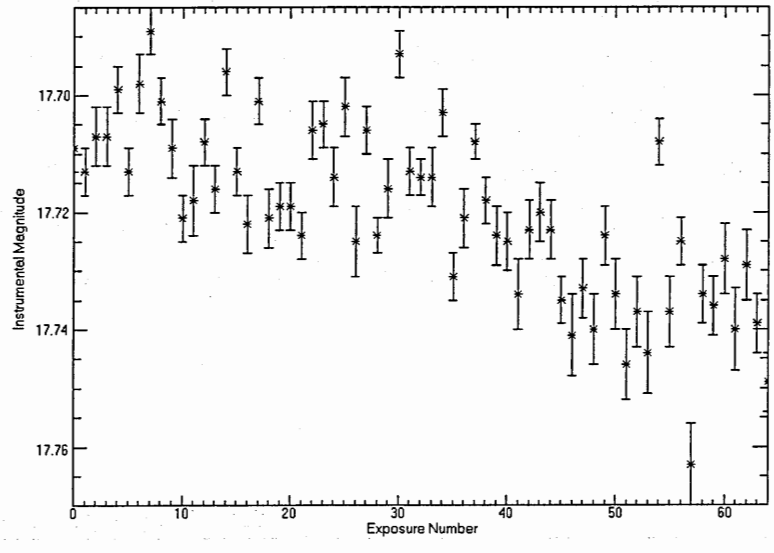

Figure 4.28: Uncalibrated lightcurve

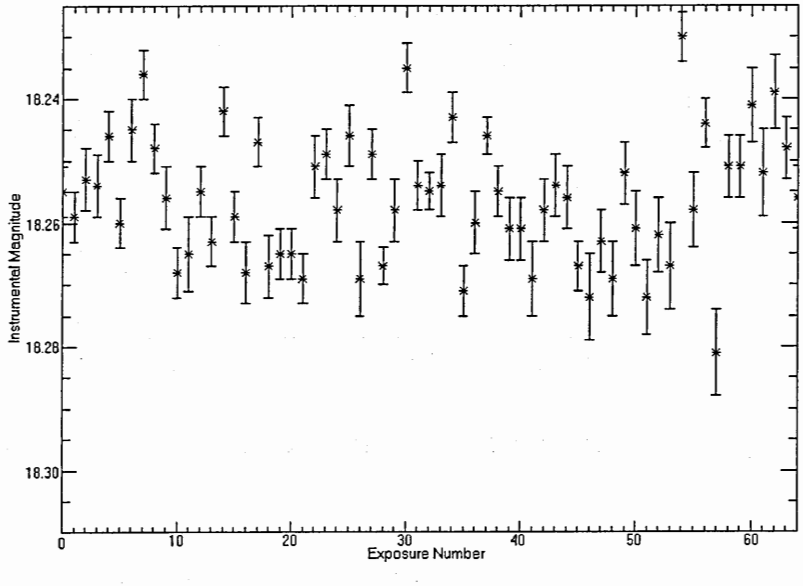

Figure 4.29: Calibrated and extinction-corrected lightcurve

than if no calibration were applied at all. Figure 4.31 shows graphs of the parameter b_1 plotted against gain for each of the CCDs for which correct calibration could be obtained, the values are tabulated in Table 4.4. A least squares fit to these points was then used to calculate approximate b_1 values for each of the filters on the remaining uncalibrated CCDs.

Using values of b_1 calculated in the above manner and the literature values of b_2 for

Table 4.4: *b1* values for calibrated CCDs

CCD	b1B	b1V	b1R
9	-0.78	-1.16	-1.17
8	-0.82	-1.10	-1.16
7	-0.06	-0.91	-1.00
4	-0.46	-1.23	-1.24
3	-0.49	-1.30	-1.33
2	-0.27	-0.68	-0.79

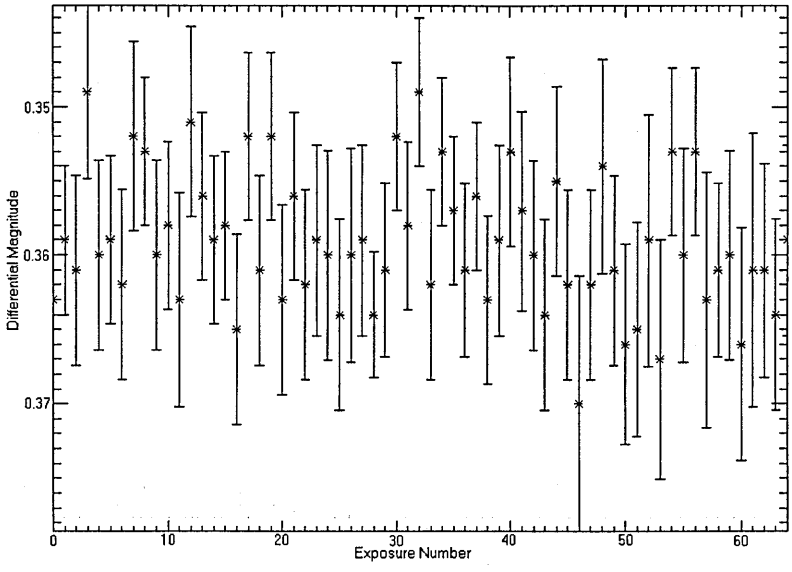

Figure 4.30: Differential calibrated lightcurve

each of the filters, it is possible to perform a rough calibration on the program objects. This calibration will of course not be perfect due to the lack of information about the parameter b_3. This parameter is the colour term, and as such will have a greater effect on stars which are either very red, or very blue. However, as b_3 is generally an order of magnitude less than b_1, this calibration will be roughly correct.

CCD Response

Having calibrated all of the CCDs, it became apparent that in some cases (namely CCDs 3,4 and 5) the average B-V and V-R values were anomalous (Table 4.5).

As can be seen, the 3 CCDs in the lower panel of the table all show spurious values. Further investigation revealed that this was not due to mistakes during the calibration process, but rather was inherent in the CCDs themselves. Most of the CCDs on the 12k mosaic are made from epitaxial silicon (EPI), but CCDs 3,4, and 5 are made from high resistivity bulk silicon (HiRho) (CFHT Website, 2003). Although the HiRho chips have an up to 20% higher Q.E. in the red part of the spectrum, their response in the B band varies strongly with wavelength, Figure 4.32 (CFHT Website, 2003)(in fact this effect is also present in the EPI chips but it is considerably less severe).

The calibration process described above only works correctly if the response of the CCD is constant across the pass band. If this is not the case then stars with the same

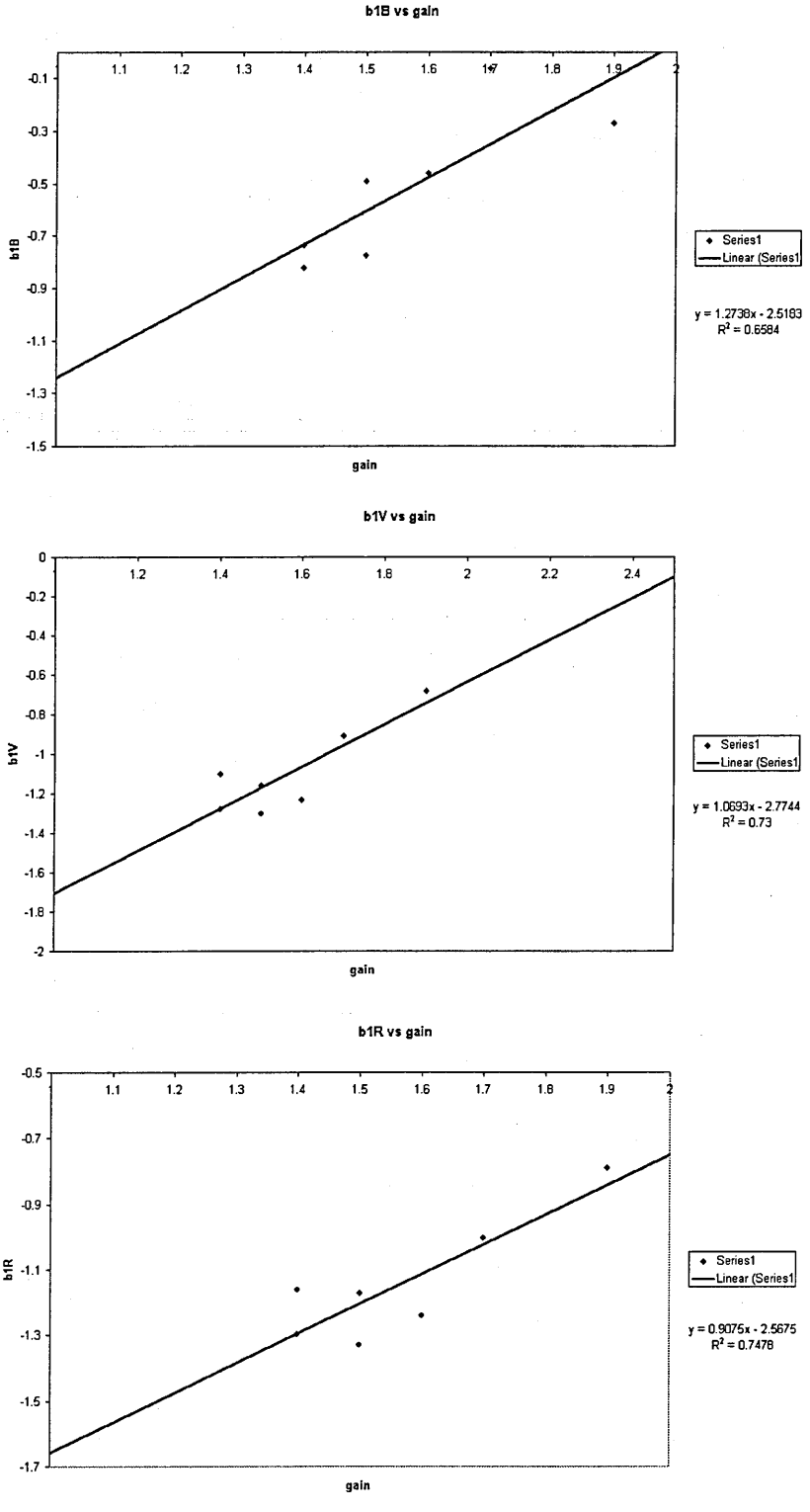

Figure 4.31: Plots of b_1 against gain for B, V and R filters

Table 4.5: Calculated average B-V values for WAVS CCDs. *s mark those CCDs which were calibrated using standard stars

CCD	B-V	V-R
0	1.04	0.7
1	1.2	1.04
2	1.52	0.87*
7	1.47	0.83*
8	1.39	0.85*
9	1.39	0.86*
10	1.38	0.82
11	1.21	0.82
3	0.83	1.21*
4	0.79	1.77*
5	1.04	0.95

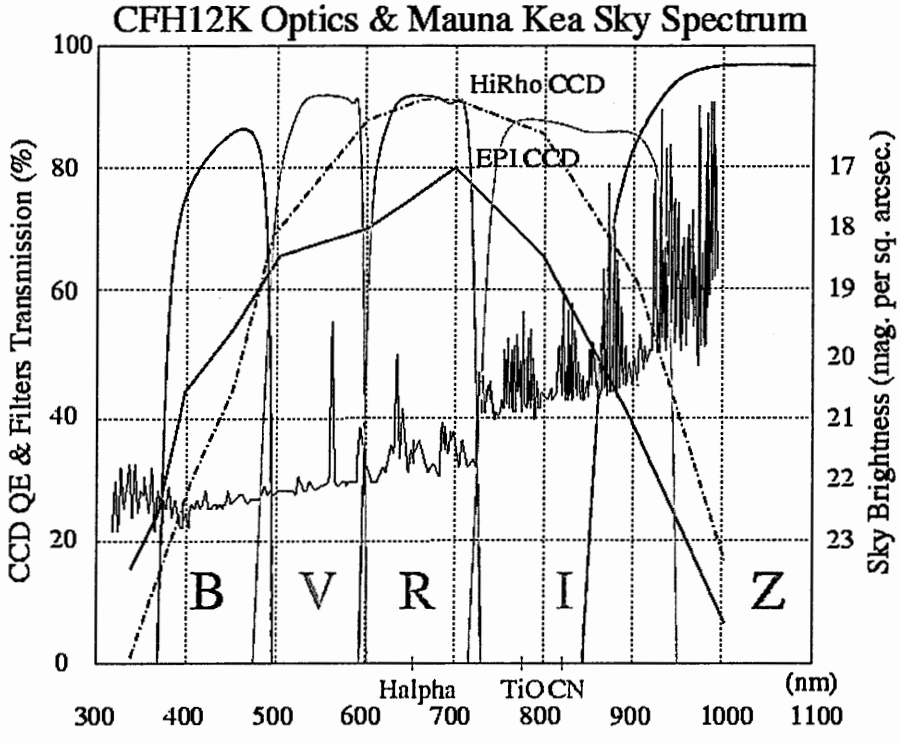

Figure 4.32: Filter transmission and CCD efficiency for CFHT optics. Solid Line EPI CCD, Dashed Line HiRho CCD. Mauna Kea sky spectrum is also shown (CFHT Website, 2003) .

total brightness within the band, but with different spectral characteristics will have their magnitudes estimated very differently.

The IRAF package **synphot** was employed to perform synthetic photometry using the combined total efficiency of the CCD and filter combination in each pass band. Figures 4.33, 4.34 and 4.35 show spectra of O5, F5 and K4 type stars along with the amount of flux that would actually be received by each of the CCD types.

Clearly the amount of flux received in each pass band is heavily dependent upon the spectrum of the star being measured. In the B band (where this effect is particularly prominent) the amount of flux received from a red K4 class star is almost identical between the HiRho and Epi filters. However, in the case of a blue O5 class star, there is a 20% difference in received counts. Using the task **calcphot** it is possible to calculate synthetic observational magnitudes for each of the star and filter combinations. Using the EPI efficiency curves yields a B-V value of -0.31 for the O5 class star, this compares favourably with the literature value of B-V=-0.35 (on the Johnson system) (Ridpath, 1998). However, performing the same calculation for the HiRho CCD returns a value of B-V=0.06, clearly inaccurate.

Of the four standard stars used in the calibration process 3 had predominantly red spectra (being of types K0, K4 and G3) whilst the fourth was a bluer (B6) type star. For the HiRho CCDs that were calibrated using IRAF packages this star was generally rejected in the fit as its value appeared spurious. Without creating an individual solution for each of the stellar types (which would require a great many more standard stars) there is little that can be done to solve this problem. Even with such data, obtaining correct magnitudes for the program objects would still be very difficult. It is unfortunately necessary to conclude that at this time it is not feasible to correctly calibrate the stars on CCDs 3, 4 and 5. However, the data from these CCDs is still usable for variability analysis.

4.4 Analysis

The remaining part of this chapter describes how the lightcurves were plotted and the methods which were used to search for variability. It also describes how the images from the two nights of observations are rectified and transformed to the correct world co-ordinate system (WCS).

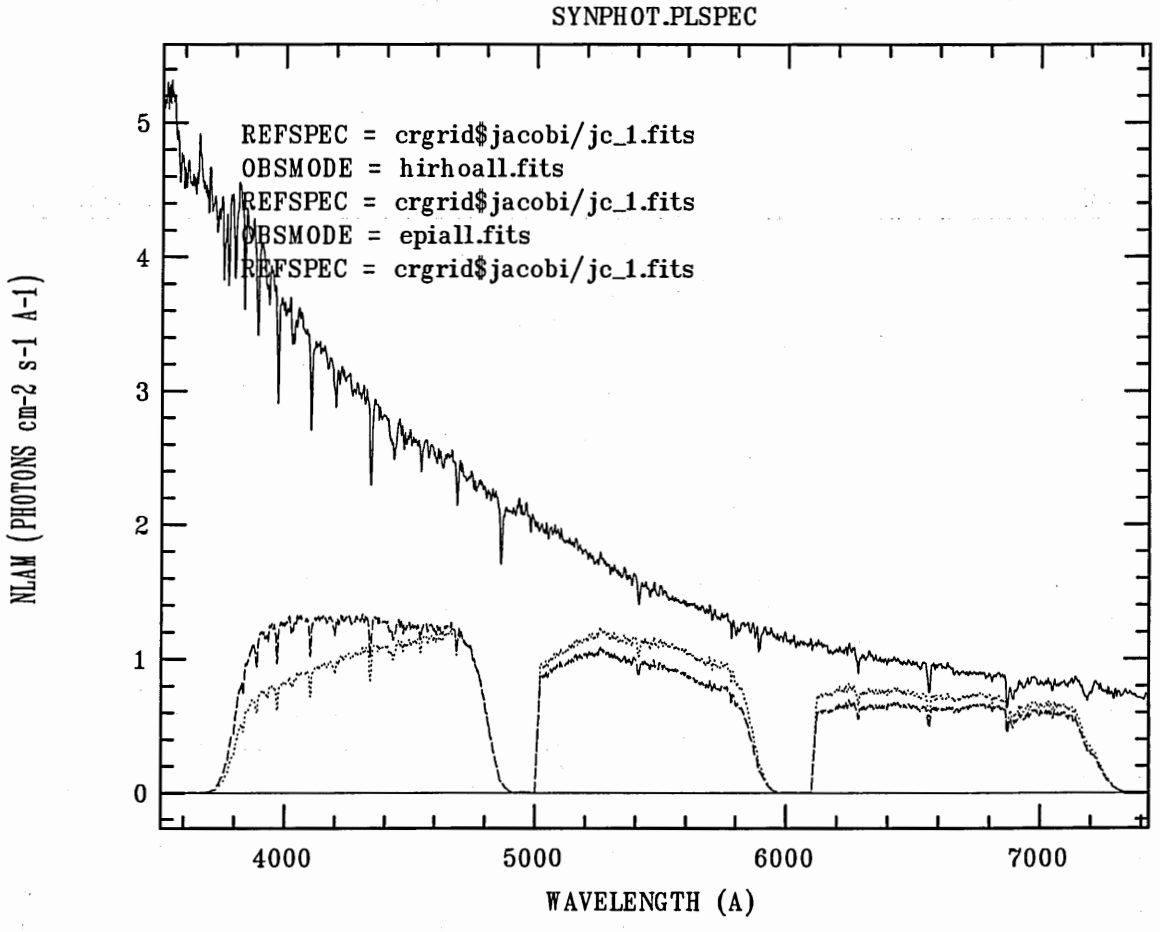

Figure 4.33: O5 type spectrum with over plotted HiRho (dotted) and EPI (dashed) efficiencies for B,V and R filters

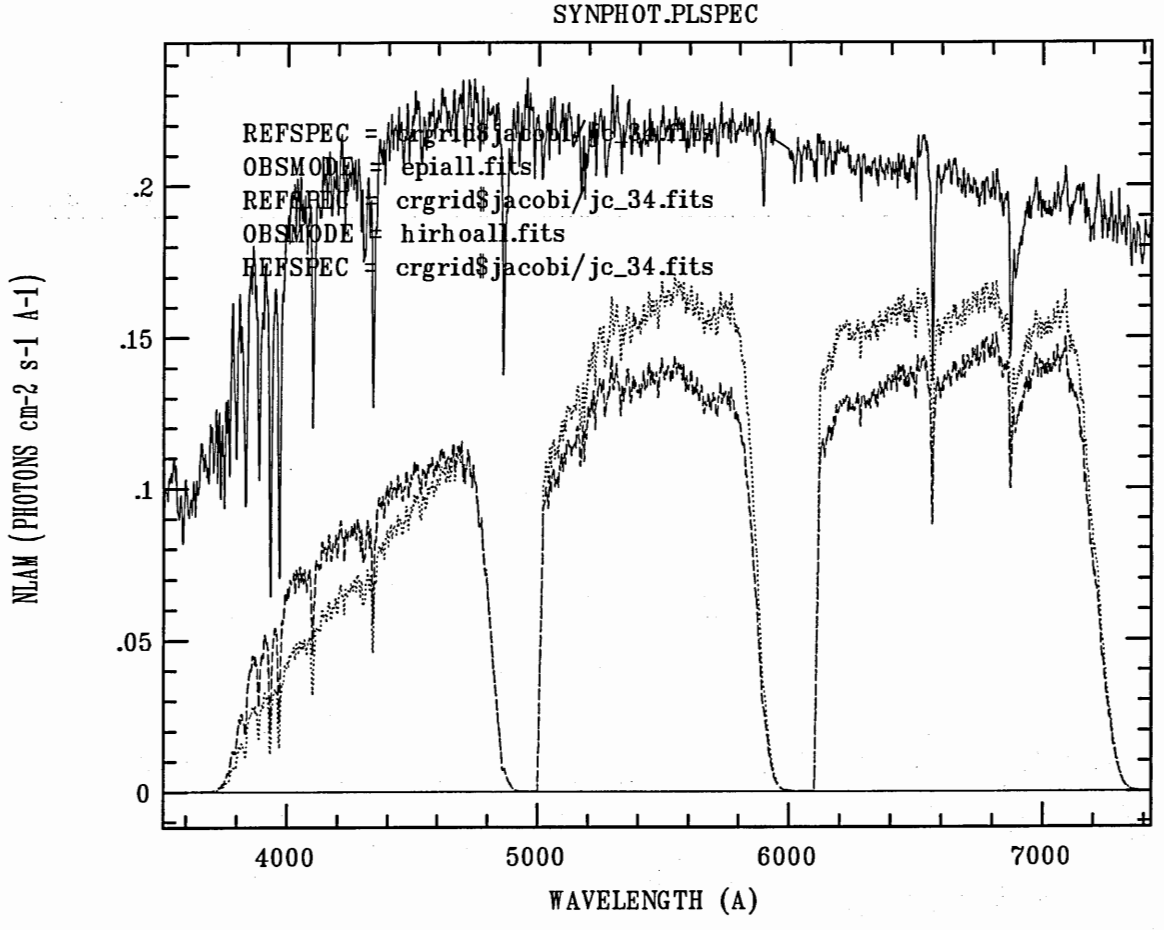

Figure 4.34: F5 type spectrum with over plotted HiRho (dotted) and EPI (dashed) efficiencies for B,V and R filters

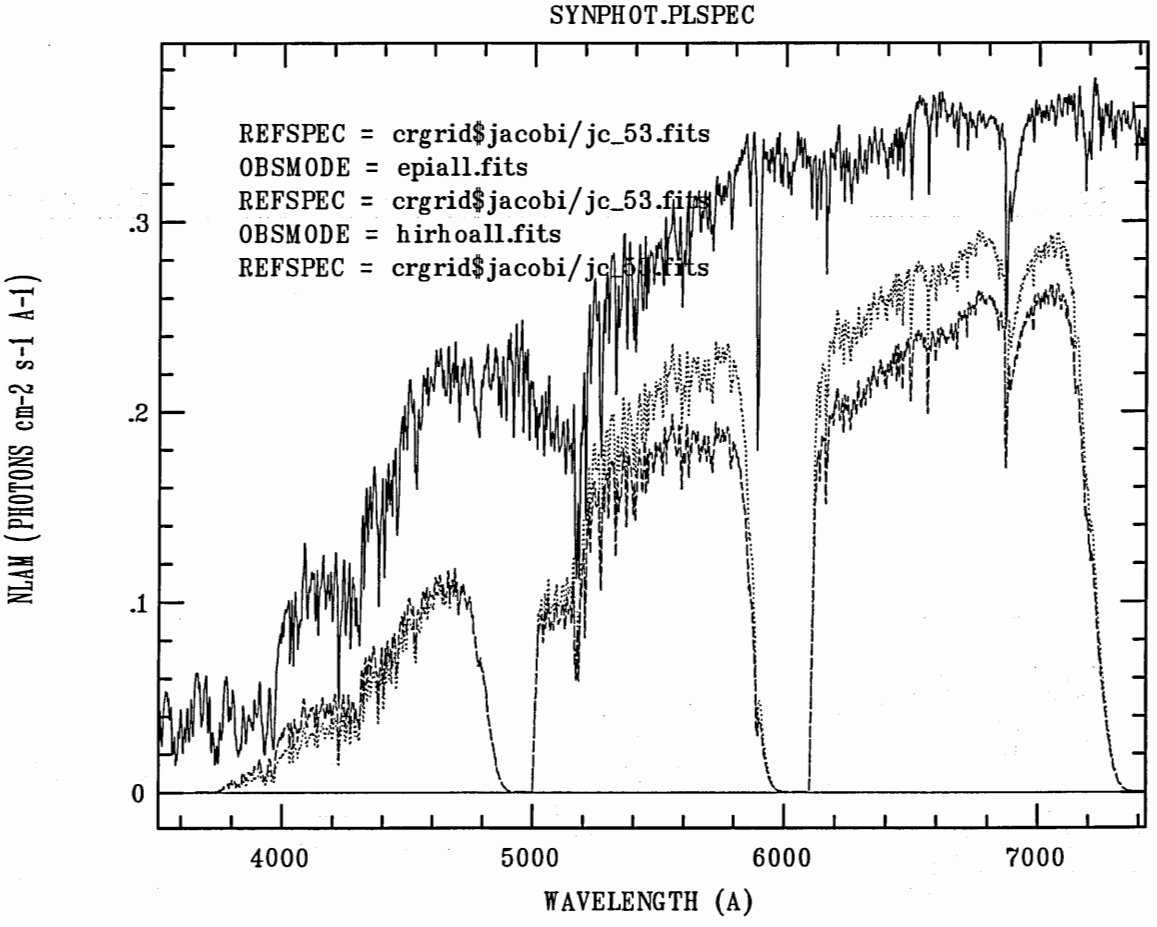

Figure 4.35: K4 type spectrum with over plotted HiRho (dotted) and EPI (dashed) efficiencies for B,V and R filters

4.4.1 Creating the Lightcurves

The output of the **allstar** task contains more information than is necessary for plotting the lightcurves, thus the task **txdump** was used in a script called makals.cl to create files in the form als## which contained the object id, calculated magnitude and the magnitude error for each of the exposures (Figure 4.36).

```
txdump i497162o08.fits.als.1 ID,MAG,MERR headers+ parameters+ > als162
txdump i497163o08.fits.als.1 ID,MAG,MERR headers+ parameters+ > als163
txdump i497164o08.fits.als.1 ID,MAG,MERR headers+ parameters+ > als164
txdump i497165o08.fits.als.1 ID,MAG,MERR headers+ parameters+ > als165
txdump i497166o08.fits.als.1 ID,MAG,MERR headers+ parameters+ > als166
txdump i497167o08.fits.als.1 ID,MAG,MERR headers+ parameters+ > als167
txdump i497168o08.fits.als.1 ID,MAG,MERR headers+ parameters+ > als168
txdump i497169o08.fits.als.1 ID,MAG,MERR headers+ parameters+ > als169
txdump i497170o08.fits.als.1 ID,MAG,MERR headers+ parameters+ > als170
```

Figure 4.36: Makals script

Once this was complete, these files were read into an IDL script (called curve.pro, see Appendix D) which created an array for each of the program objects containing magnitudes, errors and ID numbers. The modified Julian date for each of the time-series exposures was then extracted from the image header and written out into a list.

Due to changes in the fit of the PSF over the course of the night, some magnitude variation is present that is consistent across all of the lightcurves. This can be removed by subtracting the magnitude of a template lightcurve constructed from a number of non-variable stars from each of the time series exposures.

Differential lightcurves were created from the time-series data using the script differential.pro (Appendix D). Lightcurves with greater than 30 points in them were placed into magnitude bins and averaged, creating template lightcurves for each magnitude between 15 and 24. These were then applied to individual lightcurves on the basis of magnitude to account for the variation of the PSF effects with intensity. Lightcurves from each of the nights were then stored in files with the naming convention n#diff.dat where # represents the night (either 1 or 2) and the CCD number.

In order to check that the effects of second order colour terms were not biasing the differential lightcurves unfairly, differential.pro was modified to include colour information and run on one of the fully calibrated CCDs. In this case template curves were created on the basis of both magnitude and B-V colour with three colour bins created for each

magnitude increment (B-V<1, 1≤B-V≤1.8 and B-V>1.8). The results of these tests showed little if any improvement over the previous differential lightcurves (Figure 4.37).

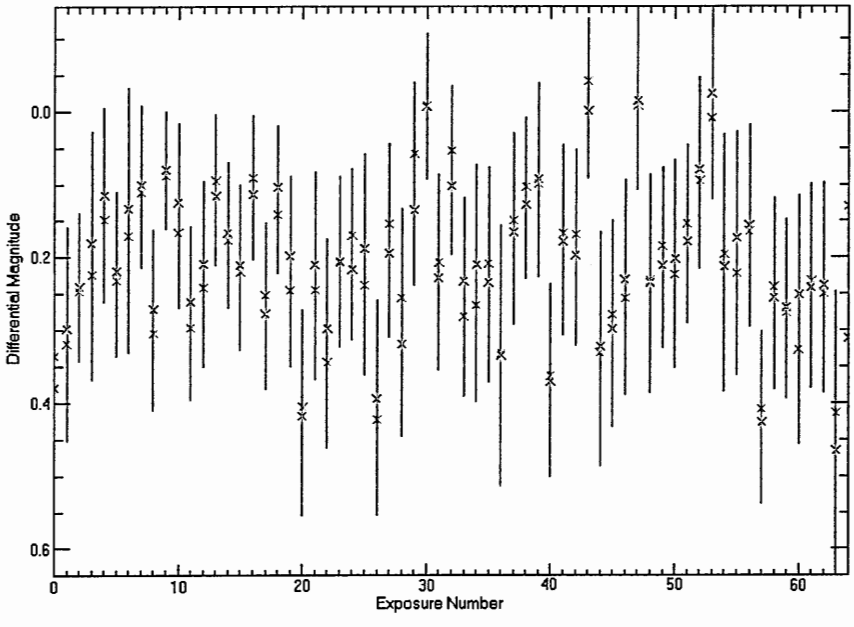

Figure 4.37: Standard differential lightcurve (red points) and colour corrected differential lightcurve (black points) for star 124078.

As the process would have been difficult to repeat on CCDs with less calibration information, differential lightcurves created using the original differential.pro script were used in the variability analysis.

4.4.2 Finding Variability

Once the differential lightcurves were created it was possible to begin searching for variability. This was done for each night individually as the poorer calibration of exposures from night 2 created difficulties in detecting true night by night variations. The time-series were combined later and this will be discussed towards the end of the chapter.

4.4.3 Finding Variability: Problems

Finding true variable stars from the WAVS sample was nowhere near as simple as it might first appear. In an ideal world, performing a χ^2 test on the data using a flat (i.e. non variable lightcurve) as the standard, and creating a plot of χ^2 against magnitude should have shown a number of outliers - all of which would be variable stars. However, once this was put into practice it was apparent that most of the outliers were not truly variable, but were due to situations where the photometry had been compromised. These effects occurred for a variety of reasons, the most important of which will be discussed below.

Edge effects

Edge effects occur due to the dithering of the telescope over the course of the nights observing. Some stars that were not originally entirely on the chip will move onto the frame, thereby undergoing an increase in brightness and stars that were on the chip but near the edge may move until only a portion of their luminosity is recorded. As these effects occur along the four edges of the CCD a surprising amount of stars can be affected over the course of the night (Figure 4.38). During the dithering process, an average WAVS CCD moves 15 pixels in the x direction. Considering this direction alone and assuming a PSF radius of 12 pixels, any star that has its centre within 27 pixels of the trailing edge of the CCD will undergo a brightness variation on account of this process. A similar situation will occur for any star within 12 pixels of the leading edge at the start of the night. Thus, an area of the chip equal to (12+27)$\times$ 4128 or 160992 pixels will be affected. This amounts to almost 2% of the entire chip or approximately 112 stars (if the chip is assumed to contain 6000)

Severe blooming

Most of the WAVS CCD frames contain several stars that are much brighter than the majority of the stars on the chip. As WAVS exposures are relatively long (it is faint stars that we are most interested in) the bright stars can become severely over exposed, leading to a great deal of charge bleeding across the chip (Figure 4.39).

As this effect can cover such a large area and include a considerable number of other objects, it is unwise to dismiss all the affected stars out of hand. However it is not possible to simply subtract a constant amount of 'extra' brightness, as the amount of bleeding varies dependent upon several factors (including the seeing conditions). Thus

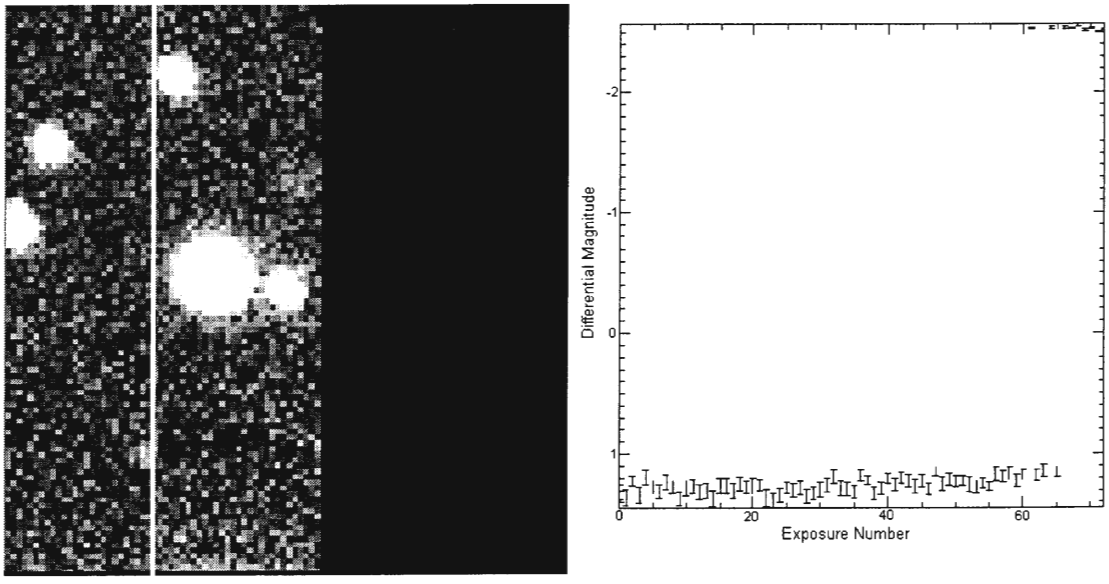

Figure 4.38: Left Panel: Any star with any part of its disk to the right of the line will be affected, either by a drop in brightness or by a loss and substitution of the PSF. Right Panel: High χ^2 lightcurve. x-axis is exposure number, y-axis differential magnitude.

over the course of the night, stars in the affected region can undergo considerable pseudo brightness variations, which makes them outliers on a χ^2 plot whilst not being truly variable (Figure 4.40). For an average saturated object with an apparent radius of 150 pixels (this is by no means large for the sample) 1% or approximately 60 stars are affected. Many of the WAVS CCDs contained several of these objects, some of them with effective areas much larger than this.

Bad pixels and bad columns

A bad column, row or pixel crossing the region of a star (again due to dithering) is also a cause of confusion in the χ^2 plot (Figure 4.41).

Dependent upon whether the column is bright or dark, the motion of a bad column can cause either considerable dimming or brightening of a source (the case of dimming is particularly bad as the resultant lightcurve can look much like that of an eclipsing system). Bright or dark pixels can also cause similar effects although this problem is not as severe due to their smaller area of effect. The number of objects affected by a bad column can be calculated in a similar way to those affected by the edge of the chip (Figure 4.42). For a bad column just one pixel across, an area equal to 2% of the total area of the CCD is

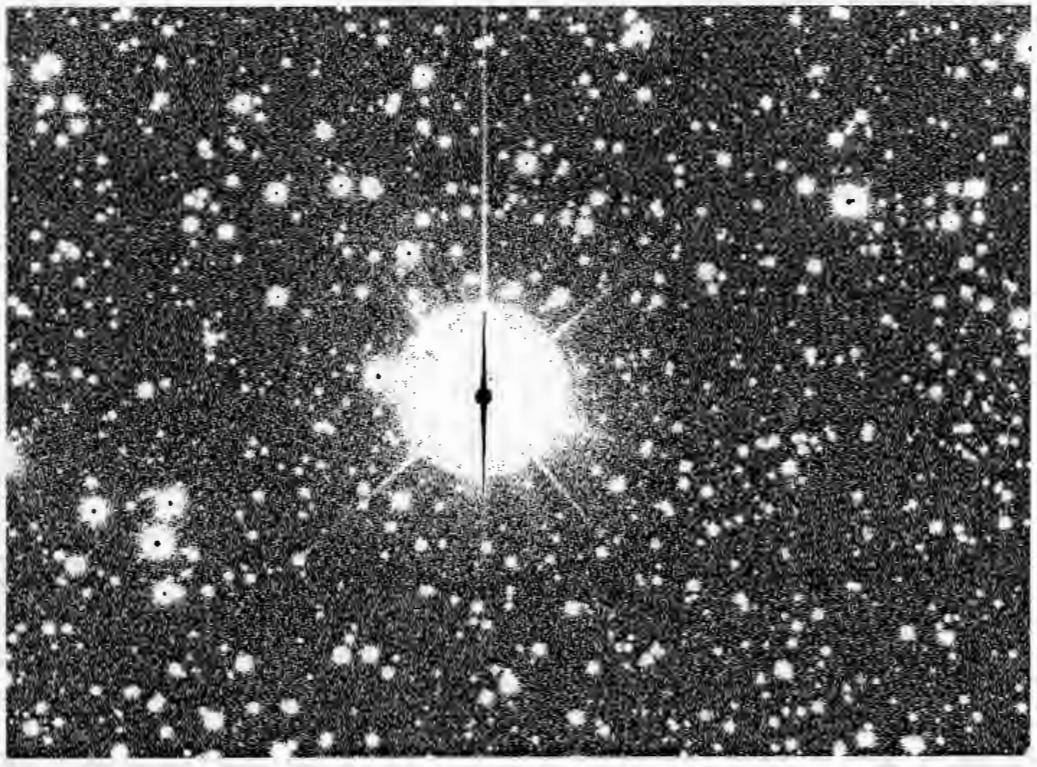

Figure 4.39: A saturated star and contaminated surrounding area

disrupted, again accounting for around 112 stars in an average field. Many of the CCDs on the CFH12k mosaic contain more than one bad column, leading to a further increase in these figures.

Extreme seeing variations

Another source of confusion in the WAVS time-series data comes from a severe change of seeing towards the end of the night. In cases where there is a bright star next to a faint star, deterioration in seeing conditions can cause the task to incorrectly identify the fainter companion, causing a sudden brightness increase in its lightcurve. Figure 4.43 represents such a case.

Comparison with Figure 4.44 clearly shows the decline in seeing conditions which causes the problem.

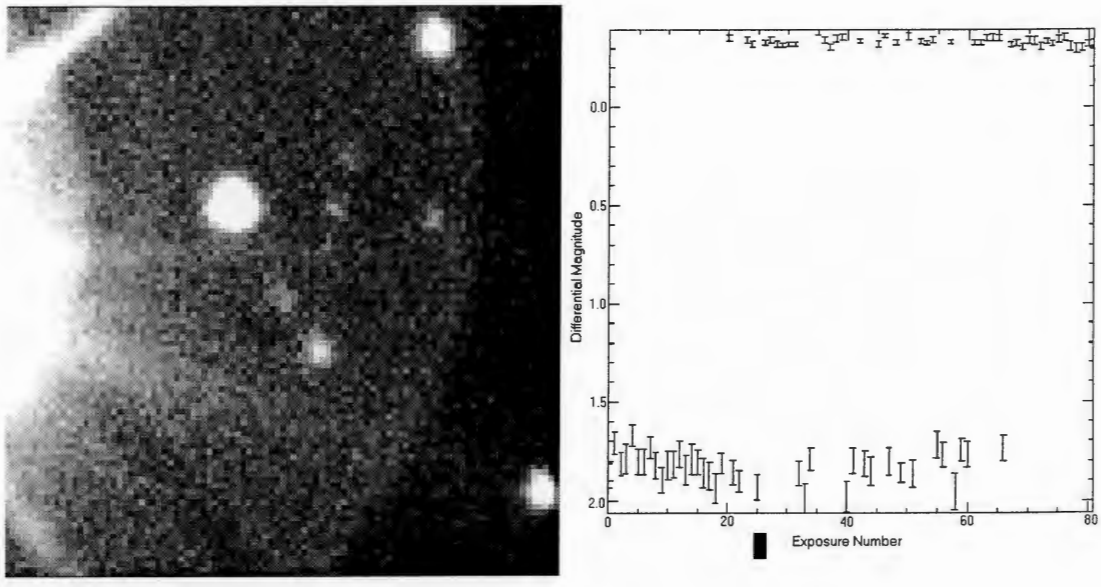

Figure 4.40: Left Panel: Large saturated object affecting nearby companions. Right Panel: High χ^2 lightcurve of star in centre of image.

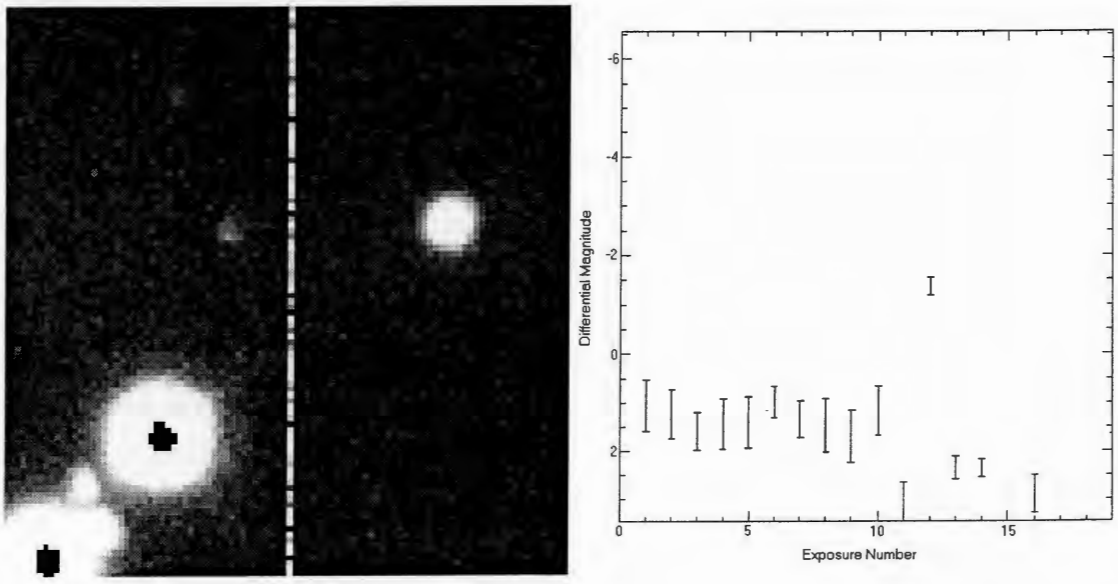

Figure 4.41: Left Panel: Bad column affecting star in centre left. Right Panel: High χ^2 lightcurve

4.4.4 Finding Variability: Solutions

Chi Squared Method

In order to solve these problems, a script was written that would discard useless lightcurves and remove spurious points from those which would otherwise be useful in the variability

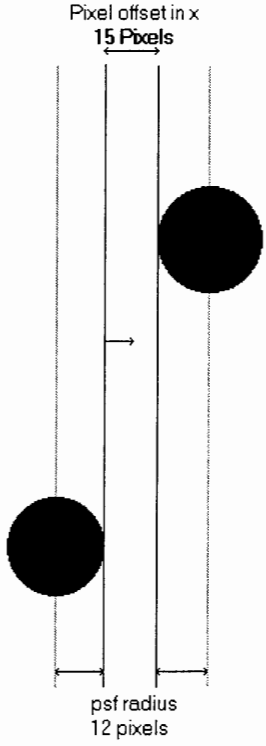

Figure 4.42: Effect of bad column on psf fitting

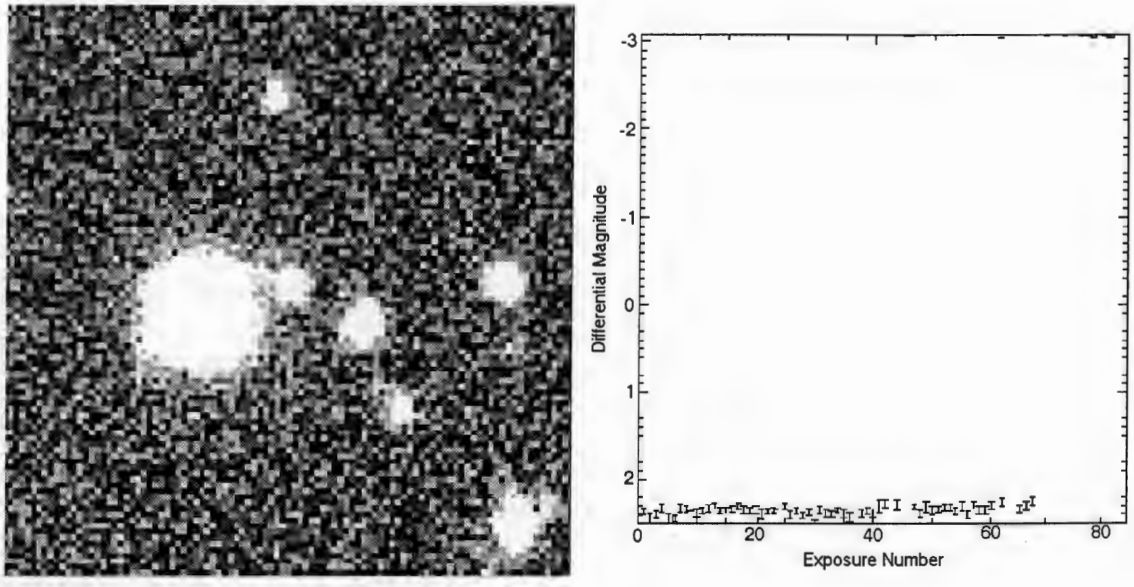

Figure 4.43: Left Panel: Good seeing image The star in the centre is lost when seeing deteriorates. Right panel: Differential lightcurve showing effects of PSF confusion (lower values equal greater brightness.)

Figure 4.44: Same field in bad seeing

analysis. It would then output the χ^2 values in a format that could be sorted by IRAF. The script (diffchi.pro, Appendix D) has three different rejection methods for contaminated lightcurves. The first of these is the most simple. The complete data sets for the

night 1 and 2 time-series comprise 67 and 106 points respectively. The first rejection method removes those lightcurves that have less than 30 points in them from the process. The second rejection method is aimed specifically at those curves which show a bimodal distribution due to PSF loss. This is detected by essentially splitting the lightcurve into 3 sections, top, middle and bottom. If the top and bottom contain data points but the middle section is empty, then the curve is considered to be bimodal and the brighter points (those where psf loss is likely to have occurred) are rejected.

The final rejection method takes each point in turn and calculates the difference between its value and the value of the points previous and subsequent to it. These two differences are then summed and the absolute value taken. This absolute value is then compared to a preset tolerance and points whose sum was greater than this tolerance are rejected. The rejection value was determined by trial and error so that a balance could be struck between removing as many spurious points as possible and not rejecting stars that are truly varying rapidly. A value of 0.5 magnitudes was found to strike the best balance. A corrected lightcurve is displayed in Figure 4.45

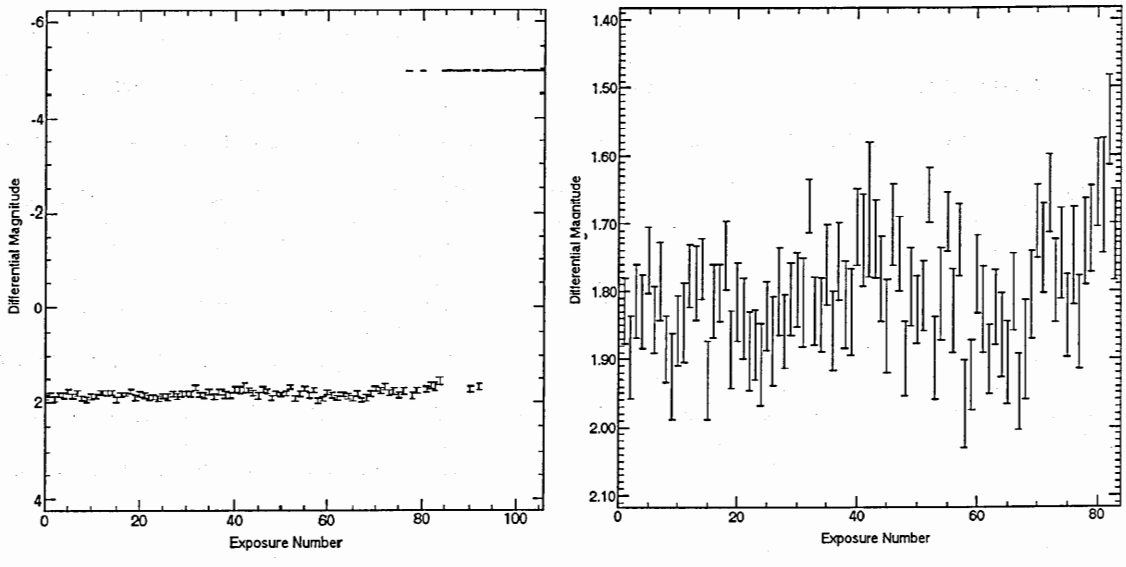

Figure 4.45: Lightcurve before and after spurious points are removed

Once this process was complete the remaining lightcurves were ordered so that those with the highest χ^2 values came first and were inspected visually to determine if they were true variables.

Visual Determination of Variability

Although the χ^2 method was very successful in detecting variables in the WAVS sample, it is possible that some true variables may have been rejected by the process described previously. For this to be the case, severe variations must be occurring on timescales of less than three minutes and this is highly unlikely to account for a large percentage of the detectable variables in the sample. However, for the sake of completeness, all the uncorrected lightcurves were checked visually using the plotcurves.pro script (Appendix D). Lightcurves were checked at least twice to ensure that variables were not missed, and then classified as either non-variable, variable, contaminated or unusual. A contaminated star is one which is suffering from one of the problems mentioned above and an unusual star is one which looks variable, but not in an easily classifiable way (eg. not an eclipse, pulsation or flare etc.). After this selection process, stars within 3 of these groups were investigated further. In the variable case the stars were checked to make sure that they appeared truly variable and were not contaminated in any of the ways mentioned above. This was done using the script whyvar.pro to display the lightcurve of the object alongside the section of the image from which it came. Stars in the unusual group were also treated in this way and any appearing in contaminated regions were discarded. Finally, using the IRAF task **tvmark**, the contaminated stars were plotted back onto the original CCD image. Any of these stars that did appear in openly contaminated areas were set aside for further study and included in the list of variable stars if applicable.

Success of the variability search

Figure 4.46 shows a plot of reduced chi squared (χ^2_r) against magnitude for CCD2 on night 2 before the rejection process was applied. Clearly not all of the high χ^2_r points relate to variable objects and the many spurious points are caused by the problems described previously.

Figure 4.47 shows the same objects after the rejection methods have been applied. In this case many of the spurious points have been removed leaving only true variables or noisy lightcurves that are not rejected by the process described above. As can be seen, the method is quite successful, for example, although many spurious high χ^2_r points have been rejected, a true variable (WAVS221850) with an χ^2_r of nearly one thousand is still present (Figure 4.47).

In order to assess how well flickering would be detected by the WAVS survey, data from

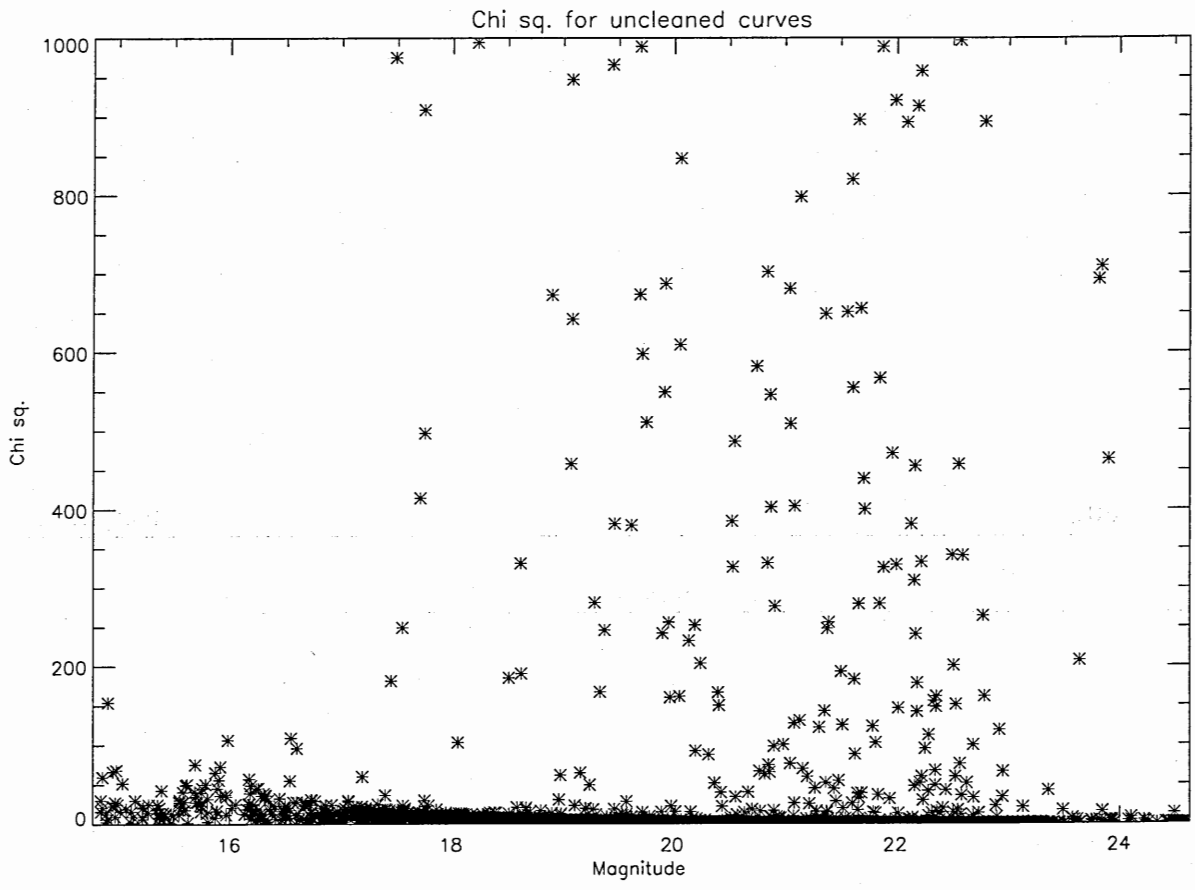

Figure 4.46: χ_r^2 against magnitude before rejection methods applied.

the control CV in the sample (QU Vul) was taken and combined with increasing amounts of noise. As QU Vul is also an eclipsing source it was necessary to first remove the eclipses from the data. The lightcurve for QU Vul with eclipses removed is shown in the top panel of Figure 4.49, at this stage the χ_r^2 of this plot is 41.2. This would place the star within the top ten stars the list of sorted χ_r^2 values for this CCD - certain to be picked up by the survey. The QU Vul curve was normalized and the error bars removed. This normalized data was then added (as the data is in magnitudes) to random non-variable lightcurves of different average magnitudes to simulate the effect of noise on the detection process. The results are displayed in the other three panels of Figure 4.49, error bars are those of the original non-variable lightcurve points.

The simulated data at 20.6 magnitude has a χ_r^2 of 26.1, placing it within the top 20 stars, again - certain to be detected by the survey. Simulated data at 21.6 magnitude has an χ_r^2 of 8.12, placing it within the top 100 stars on the list. At this level the object

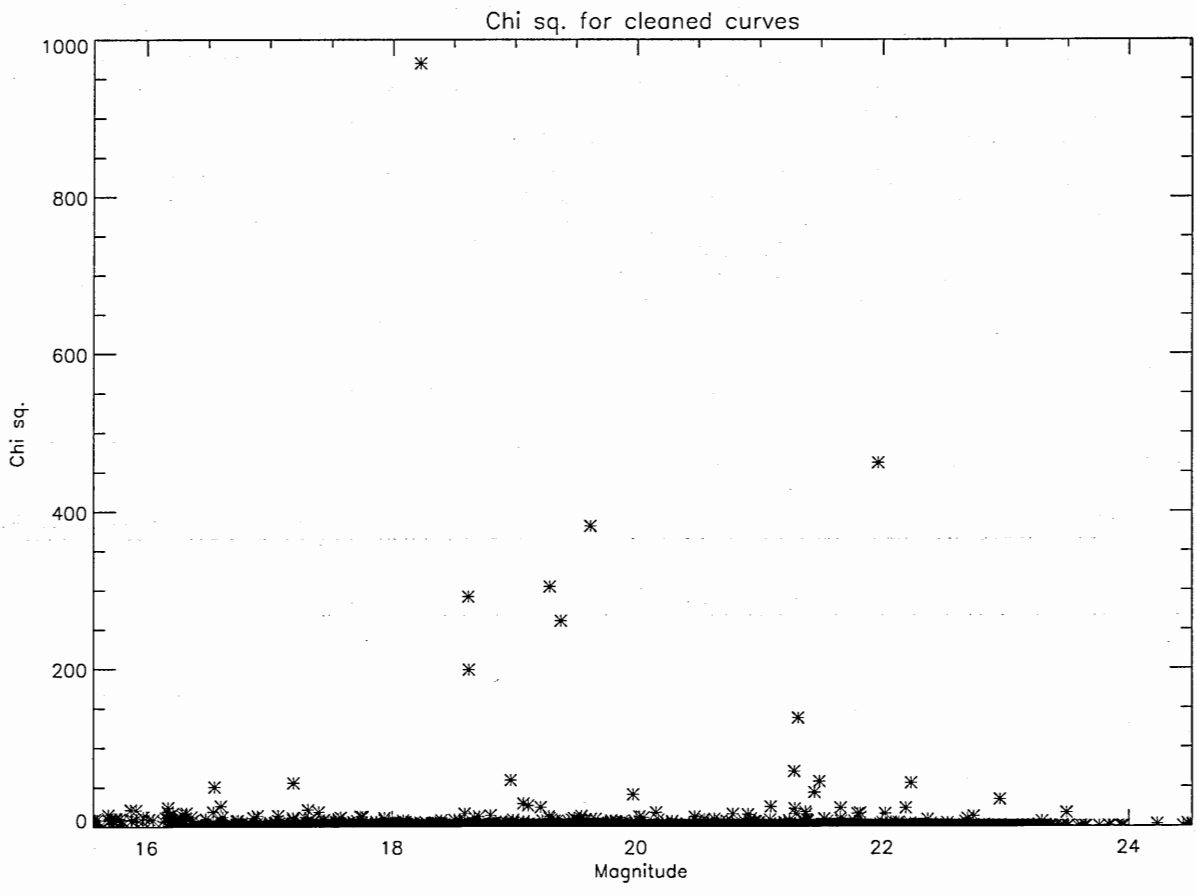

Figure 4.47: χ^2_r against magnitude after rejection methods applied.

would be followed up from the χ^2_r list and would also have been detected in the visual survey. The χ^2_r of the of the simulated data at 22.6 magnitude is 2.77. This still places the star within the top 500 on the sorted χ^2_r list but does mean that it would not have been followed up from this part of the testing. However, the object would still have been part of the visual survey and as such it is likely to have been detected. As an illustration, Figure 4.50, shows a number of the lower χ^2_r stars selected by the survey, displayed alongside the simulated point.

In order to further establish the detection limits of WAVS, the variable star population discovered by the survey was split by apparent magnitude into 0.1 magnitude bins. The lowest amplitude variable in each of these bins was then selected and plotted on a graph of variability amplitude against apparent magnitude. The results are shown in Figure 4.51.

The number of variable stars discovered by the survey was not sufficient for each of the magnitude bins to contain an object at the limits of detection. Therefore the plot does

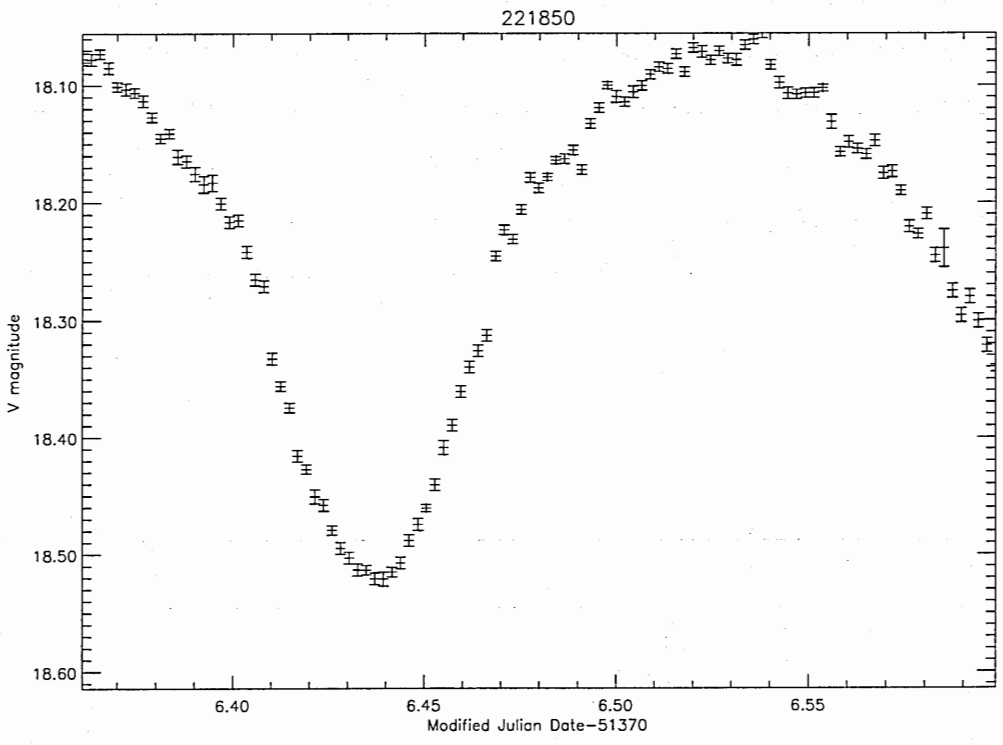

Figure 4.48: The high χ_r^2 lightcurve of WAVS221850

not yield a smooth curve showing the sensitivity limit. However, there are sufficient points at the limit to make the general trend clear. For magnitudes up to approximately 21.5 the detection threshold for variability amplitude is below 0.1 magnitudes (as low as 0.05 for brighter objects). However, as magnitude increases beyond this point, the detection threshold drops off rapidly. For objects with apparent magnitude of 22, only those showing variations of 0.2 magnitudes or more will be detected, by 23rd magnitude, variations of almost a magnitude must occur if they are to be detected by the survey.

Considering these populations as percentages of the total number of stars detected by WAVS yields 0.1 magnitude variability detectable in 60% of the WAVS sample, 0.2 magnitude variability detectable in 71% and 0.3 magnitude variability detectable in 91% of the WAVS sample. Obviously the types of variables detected will also depend upon the timescale of the variation, and this is considered in more detail later.

4.4.5 Adjusting to the World Co-ordinate System

Although the image headers created at the CFHT do contain world co-ordinate information, it is not accurate enough to provide correct astrometry for the program objects.

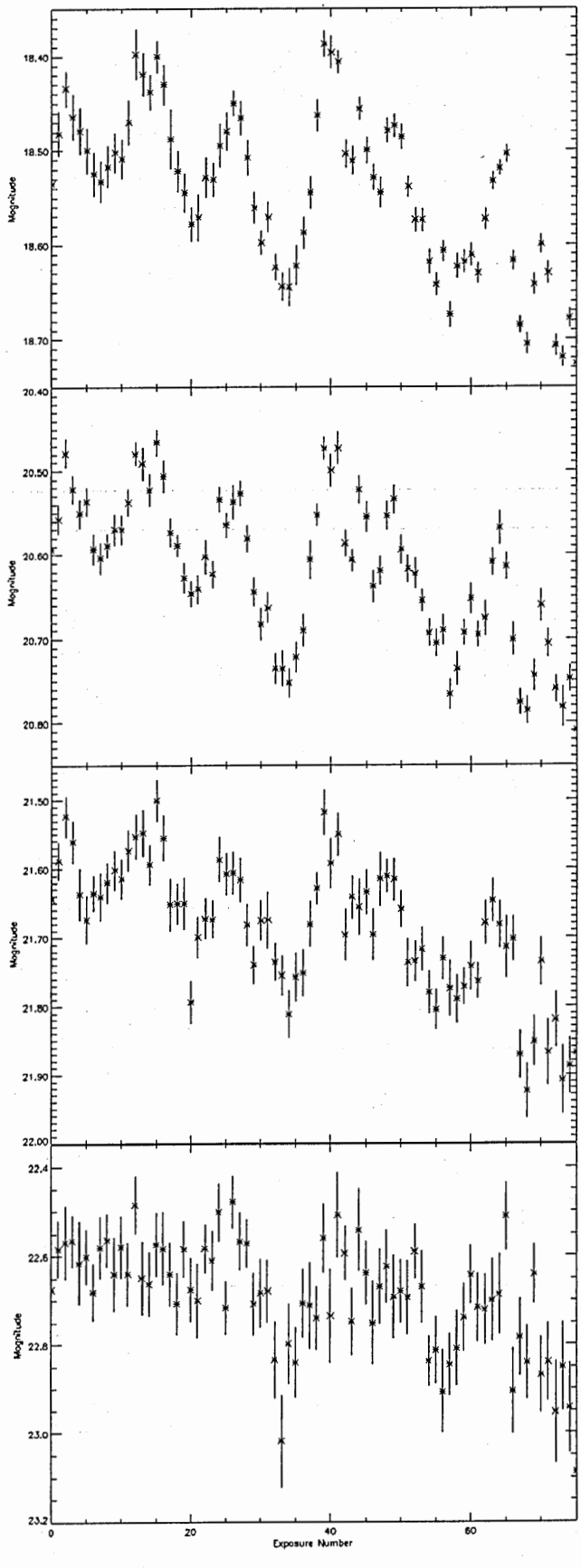

Figure 4.49: Top Panel: QU Vul data with eclipses removed. Second Panel: Simulated data of flickering at 20.6 magnitude. Third Panel: Simulated data of flickering at 21.6 magnitude. Bottom Panel: Simulated data of flickering at 22.6 magnitude.

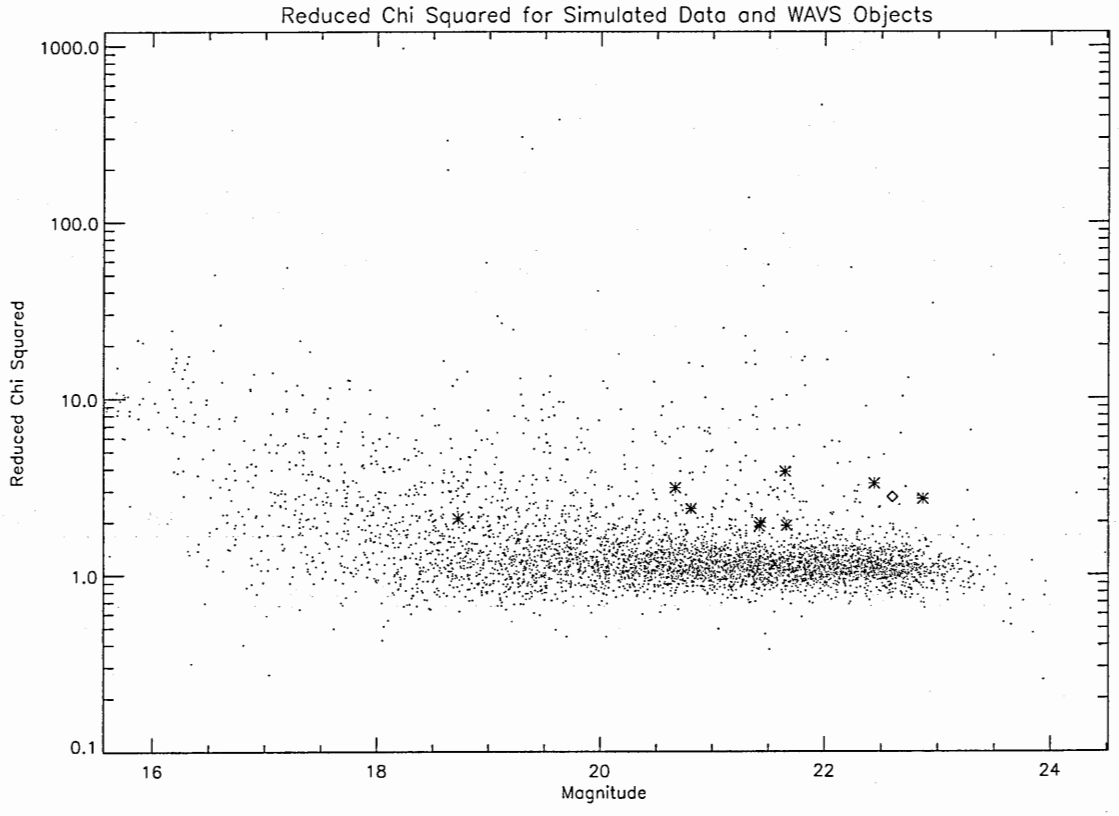

Figure 4.50: χ_r^2 against magnitude on a logarithmic scale. The diamond marks the simulated data at 22.6 magnitude whilst the crosses represent stars identified as variable in the WAVS sample. The lightcurves of these stars (WAVS22584, 992398, 823925, 722455, 1020614, 95132, 712878, 517964 and 9910756) can be found in the Appendices to this thesis.

Comparison with a correctly calibrated HST image showed clear deviations.

To remedy this, images can be registered using the accurately determined positions of stars in the field from another source. If this is not done then it will not only mean that these stars are harder to find for follow up observation, but also that it will be very difficult to match up objects imaged on the two nights of observations as they have different identifiers (assigned by the **allstar** task) and different pixel coordinates.

Calculating the transformation

Although the WCS information in the fits image headers is not completely accurate it is roughly correct. After loading the image into an image viewer such as SaoImage DS9 the centre can be found using the cursor. Taking the values of RA and DEC, along with the

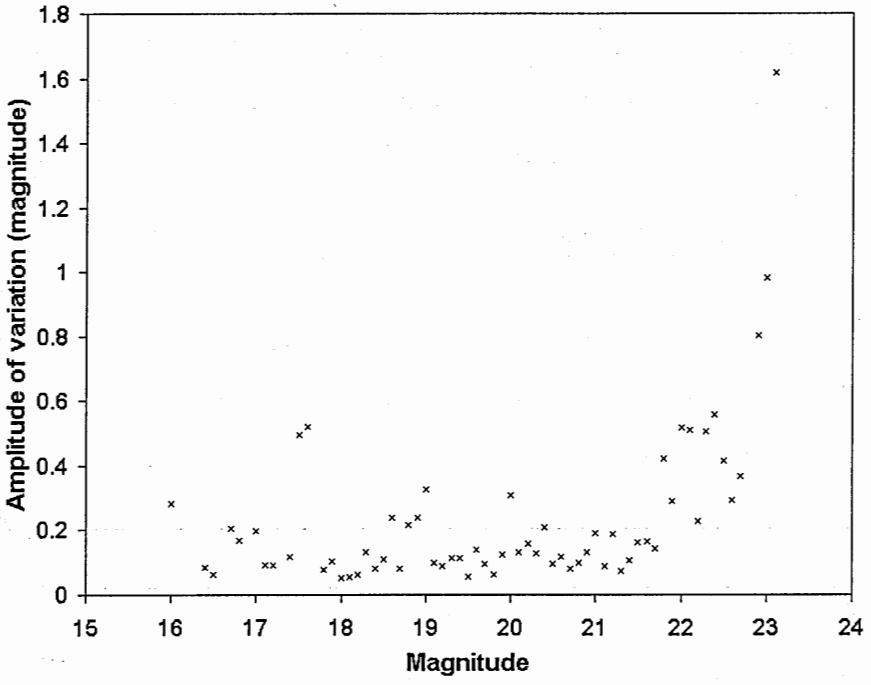

Figure 4.51: Plot of variability amplitude against apparent magnitude for the lowest amplitude WAVS variable found per 0.1 magnitide bin.

approximate dimensions of the WCS in degrees from here and inputting it into the USNO finding chart program (USNO, 1997) a list can be created which contains the accurate positions of many of the stars in a given field. Using the DSS sky survey website (STScI, 1997) it is also possible to create a fits image which shows the same star field as the object image. This will only contain the brightest stars that are in the object image but that is enough for the next stage of the process. With both images displayed in DS9, a list can be created which contains the image pixel coordinates of some of the brighter objects, along with the correct RA and DEC of the same objects taken from the DSS image. This list can then be used as an input into the IRAF task **ccmap** which calculates the plate solution based on the matched celestial and pixel co-ordinate list. The tasks **cctran** and **setwcs** can then be used to update the image header WCS parameters. This first pass through **ccmap** should have made a considerable correction to the image WCS, however, as there are few data points, the plate solution will not be correct all over the image. A better fit can be achieved by repeating the process again, this time using the task **ccfind** to create the input file. Using the USNO co-ordinate file along with the roughly corrected image will allow **ccfind** to generate a list of matched celestial and pixel co-ordinates, this time

containing many hundreds of objects. Putting this into **ccmap** and increasing the order of the fit allows an accurate plate solution to be calculated (Figure 4.52). This solution can now be applied to the image using **cctran** and **setwcs** to rectify the images correctly and give individual objects their correct WCS co-ordinates.

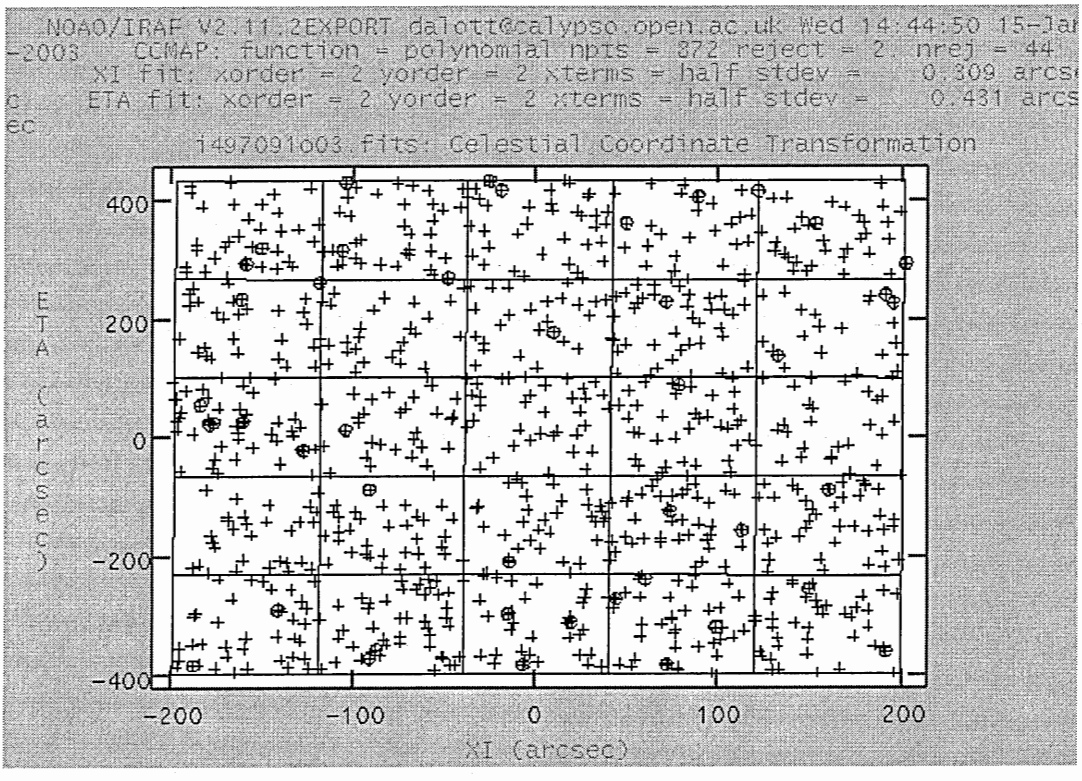

Figure 4.52: The ccmap WCS fitting task

In order to assess the accuracy of the WCS transformation, a number of objects with well known positions were identified in the WAVS field. Their coordinates as calculated in the WAVS survey were then compared with those available on the SIMBAD website. Table 4.6 shows the results of this comparison. In all but one of the objects measured the offset was less than one arc second and in general, it was much lower than this.

4.4.6 Matching the Stars

Between the two nights of observations the field of the telescope was offset considerably, meaning that only around 70% of the stars that were observed on the first night were also observed on the second. The direction of the offset meant that a star which has previously appeared on one CCD, could either be on the same CCD or any of three others (its

Table 4.6: Comparison of WAVS and SIMBAD coordinates

Star	WAVS RA	WAVS Dec	SIMB RA	SIMB Dec	ΔRa"	ΔDec"	Offset"
HD341077	20:25:51.16	+27:53:02.80	20:25:51.20	+27:53:02.2	0.53	0.60	0.80
HD340175	20:27:12.63	+27:57:40.06	20:27:12.62	+27:57:40.1	0.13	0.04	0.14
HD340309	20:28:07.33	+27:52:50.80	20:28:07.34	+27:52:51.2	0.13	0.44	0.46
HD340185	20:25:54.01	+27:40:48.34	20:25:53.96	+27:40:47.9	0.67	0.66	0.94
HD340819	20:27:12.67	+27:40:18.33	20:27:12.61	+27:40:17.8	0.90	0.53	1.04
HD340313	20:27:35.24	+27:44:00.19	20:27:35.24	+27:43:59.6	0.00	0.25	0.25
HD340172	20:26:29.94	+27:57:21.47	20:26:29.91	+27:57:21.4	0.40	0.07	0.41

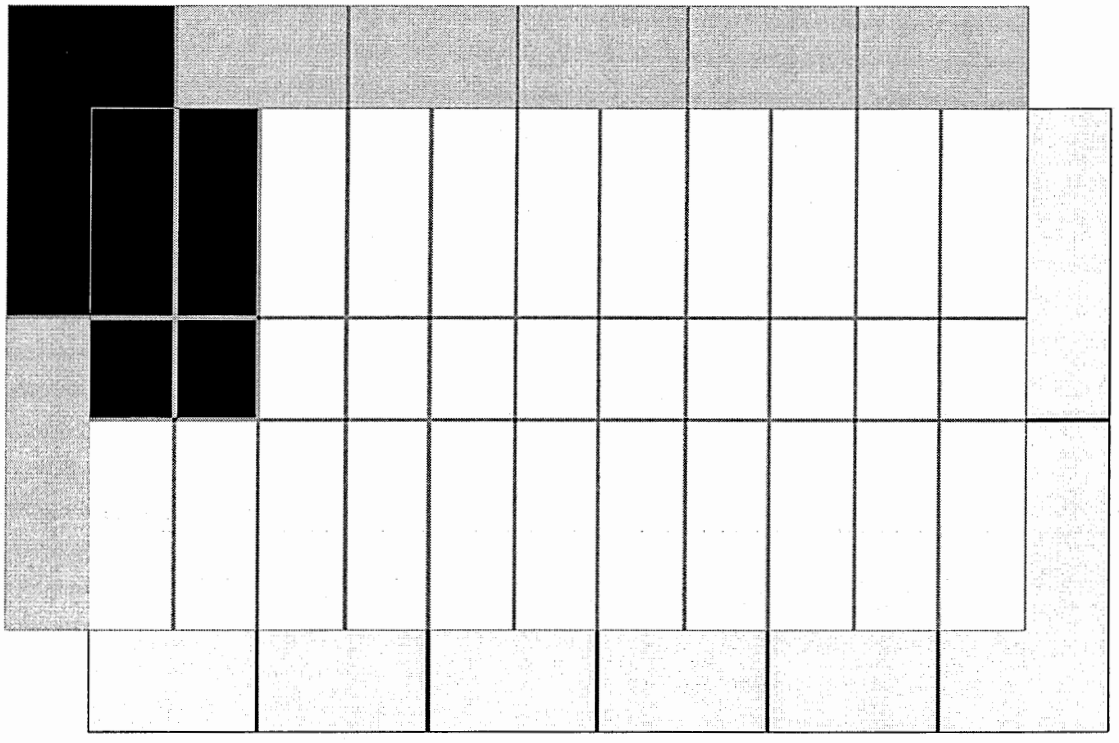

Figure 4.53: Image shows a schematic of the 12k mosaic displaying the effect of the offset between nights one and two. The lines between CCDs represent true blank regions of the mosaic and the dark panel CCD6 which was not used due to its poor condition. The effect of dithering is not included and would serve to further reduce the area of the CCD available on both nights (the white region in the centre).

neighbour above, to the left, or above-left (Figure 4.53). Unfortunately this offset meant that not only were around 30% of the stars from the night 1 field lost completely, but that many stars which were in clear regions of the CCD were moved into gaps, saturated areas and bad columns (of course as many stars were moved out of these areas between nights also, but in this case there is no data from night 1). Figure 4.53 is drawn to scale and as such the thickness of the lines that delimit the CCDs show true blank regions in the mosaic.

The black region represents CCD6 which was unusable in this project and the dark and light gray areas represent those areas gained and lost to the survey respectively. The only portions of the mosaic in which usable two night lightcurves could be obtained are those represented by white. However, this diagram contains none of the bad columns or rows which appear on the real CCDs, and indeed, were they drawn on they would all be

duplicated, reducing still further the white areas available on the diagram. Finally, the effect of dithering must also be introduced. As this cycle was different on each of the two nights the blank areas also move with respect to each other over the course of the night further reducing the effective area in which a star must exist if it is to have a lightcurve which spans two nights without contamination. However, even considering these effects there are many objects that were clearly visible on both nights and for which a lightcurve with a longer time base could be created. To do this a variety of code was written in IDL to take the .dat files saved from the individual nights and CCDs and combine them using the now correct WCS information. Objects in the .dat files were renamed using a simple naming convention based on the CCD and night of exposure. Thus star 1254 from ccd3 on night2 became 231254 (where necessary zeros were added so that the object number always consisted of 4 digits and for ease of programming objects from ccd00 have the prefix 99). These data were now stored in two arrays (one for each night) named allnight1.dat and allnight2.dat. A script was then written that would take the calibrated position of an object on the second night and locate the object whose coordinates fell within the closest radius of this point on night1 (matchstars.pro, dix D). This method was generally successful, as the WCS for both the images was sufficiently well calibrated that if the closest object fell outside a specified radius then it could be assumed that the object had not been detected on both occasions. Finally, this list of matched ids was used to generate a new array (allcurves.dat) which contained the combined lightcurves of the objects which had been successfully located on both nights. These could then be used to calculate more accurate periods for some of the objects. This will be discussed later in the analysis chapter. Next we will consider the reduction of the spectroscopic data.

Chapter 5

Spectroscopic Data Reduction and Analysis

Having photometrically identified candidate objects, the WAVS programme used spectroscopic techniques to attempt to classify them. This chapter gives a brief introduction to astronomical spectroscopy, followed by an in depth look at the process of reducing the WAVS spectroscopic data.

5.1 Introduction to Astronomical Spectroscopy

5.1.1 History

The dispersal of white light into its component colours by some sort of prism had been known for some time when its first astronomical use was found. It was in 1666 that Newton performed experiments in which he discovered that '...Whiteness is the usual colour of light;for, Light is a confused aggregate of Rays imbued with all sorts of colours...' (Newton, 1671). The first known use of astronomical spectroscopy was the discovery of dark lines in the solar spectrum by William Wollaston. Wollaston interpreted these lines as 'gaps' separating the colour of the Sun. It was not until 1817 that Joseph Fraunhofer observed the Solar absorption spectrum and compared this with spectra of other stars. Having ascertained that some stellar lines were not present in the Sun and some Solar lines were not present in the other spectra, Fraunhofer correctly concluded that the lines were not all of terrestrial origin (Fraunhofer, 1817). Herschel later suggested that they were due to absorption by a cool gas in the Sun's atmosphere. As astronomical spectroscopy progressed it became apparent just how useful a tool it could be in determining information about

stars, from chemical composition to temperatures and radial velocities. In the early 20th century a stellar classification system, based on spectral characteristics was established (the Harvard system). Although it has changed over time and some sub-types have been added and removed, it is still in use today (Figure 5.1)

5.1.2 Origin of Spectral Lines

Spectral lines occur in both emission and absorption and are due to transitions between energy levels of atoms in the stellar atmosphere. Emission lines, such as the prominent hydrogen Balmer emission series often observed in cataclysmic variables, are caused when an excited atom relaxes to a lower energy state releasing a photon of energy $E=h\nu$. Conversely absorption lines are caused when a photon of energy $h\nu$ is absorbed by an atom, promoting it to a higher energy state. Table 5.1 shows a list of some prominent spectral characteristics for main sequence stars.

Spectral lines both in emission and absorption can undergo a number of effects which will serve to widen and blur the line shape. These can occur in the form of rotational Doppler broadening, Stark and Zeeman effects due to electric and magnetic fields, or thermal Doppler broadening caused by the random velocities of individual particles.

Spectral line strengths tend to be given in terms of equivalent widths. The equivalent width of a spectral line is displayed in Figure 5.2. The strength of the line is proportional to the area it removes from the continuum spectrum, and the equivalent width is the width

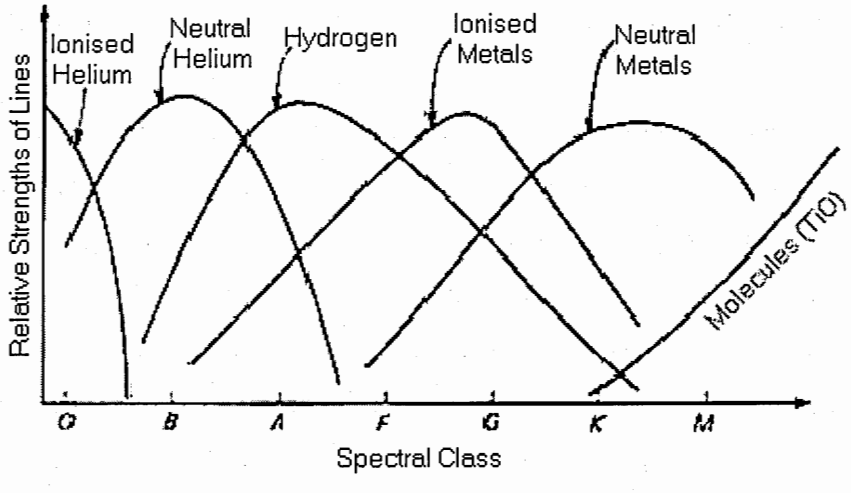

Figure 5.1: Spectral classes in the Harvard system (Zelik *et al.*, 1992, p258)

Table 5.1: Common spectral lines for main sequence stars. Prepared from various sources.

Type	Colour	Approx. Surface Temp.	Main Characteristics	Examples
O	Blue	$\geq$ 25,000 K	Singly ionized helium lines either in emission or absorption. Strong ultraviolet continuum.	10 Lacerta
B	Blue	11,000 - 25,000	Neutral helium lines in absorption.	Rigel, Spica
A	Blue	7,500 - 11,000	Hydrogen lines at maximum strength for A0 stars, decreasing thereafter.	Sirius, Vega
F	Blue to White	6,000 - 7,500	Metallic lines become noticeable.	Canopus, Procyon
G	White to Yellow	5,000 - 6,000	Solar-type spectra. Absorption lines of neutral metallic atoms and ions (e.g. once-ionized calcium) grow in strength.	Sun, Capella
K	Orange to Red	3,500 - 5,000	Metallic lines dominate. Weak blue continuum.	Arcturus, Aldebaran
M	Red	$\leq$ 3,500	Molecular bands of titanium oxide noticeable.	Betelgeuse, Antares

of a rectangle placed between the zero point and the continuum which has the same area as the line profile.

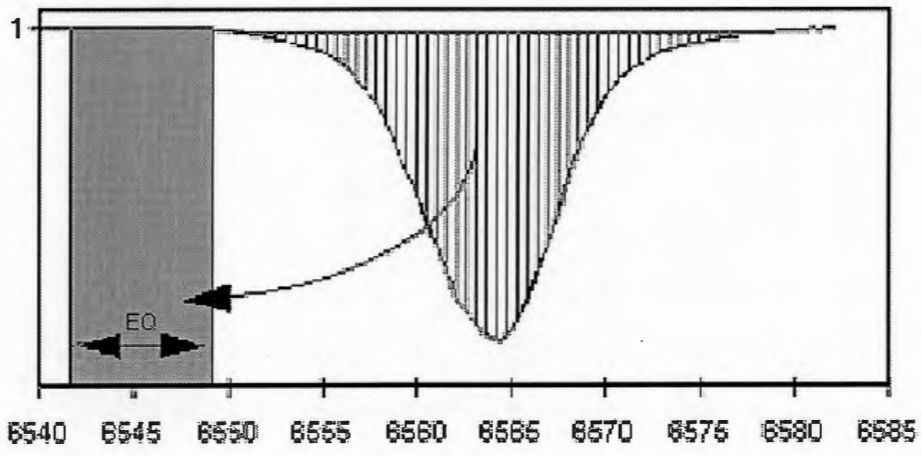

Figure 5.2: The definition of equivalent width

5.1.3 Reducing Spectroscopic Data

In long slit spectroscopy, light from a distant source is passed through a single slit and a collimator before being dispersed by a diffraction grating or prism. Camera optics then re-image the slit onto a detector (generally a CCD). The resultant image shows the stellar spectrum running almost vertically whilst lines from the night sky are apparent across the chip (Figure 5.3). The dispersed light does not follow a straight line down the centre of the chip for three reasons, firstly, because the camera optics introduce distortions which are worse along the longer axis, secondly, because the gratings do not sit exactly square in their cells and thirdly, because differential atmospheric effects will cause the blue end of the spectrum to be shifted along the slit closer to the zenith than the red (Massey *et al.*, 1992).

The higher the resolution of a spectrograph, the more dispersion is needed and so a greater exposure time is necessary. For this reason, high resolution spectroscopy is not always the best choice. WAVS spectroscopic followup was done using the Andalusia Faint Object Spectral Camera (ALFOSC) on the NOT which allowed for a reasonable range of resolutions and wavelength coverage. Most of the WAVS follow-up was done using a

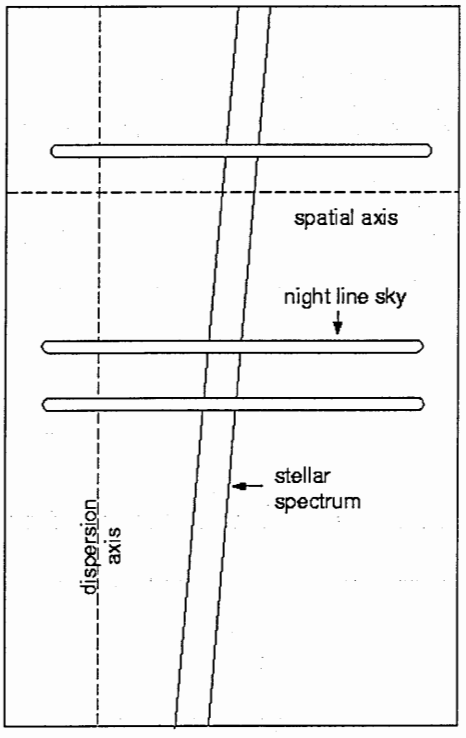

Figure 5.3: Schematic of a stellar spectrum

1 arcsecond slit and grism number 7 which covers a wavelength range from 3850-6850 Angstroms.

Reduction of spectroscopic data is basically the process of turning an exposed CCD image (Figure 5.4) into a plot of calibrated flux against wavelength (Figure 5.5). In some ways it is similar to the photometric case in that it involves the reduction of a CCD image, however, there are differences in the reduction process. Spectroscopic images also require calibration not only in flux but also in wavelength.

Flux calibration in the spectroscopic case is applied using spectroscopic standard stars that were observed with the same slit and grism combination as the object exposures. Wavelength calibration is calculated from comparison with exposures of lamps taken on the same night. The spectra of these standard lamps (generally helium, neon or argon) show easily identifiable emission features which can be used to calibrate the wavelength axis of the exposure (Figure 5.6).

The remainder of this chapter discusses how these tasks were performed in the specific case of the WAVS data.

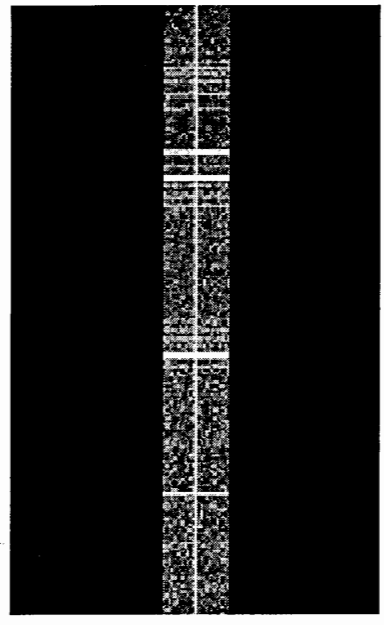

Figure 5.4: A raw CCD image showing both the object spectrum and some prominent sky lines.

5.2 Reduction of WAVS Spectroscopic Data

WAVS spectroscopic followup observations were undertaken by Tim Abbott, Carole Haswell and David Lott on the nights of the 12th to the 15th of July 2002 on the Nordic Optical Telescope. Details of these observations are displayed in Tables 5.2 to 5.5.

Although for the most part reducing a spectroscopic image is similar to reducing a CCD image that will be used for photometry, there are two additional factors that need to be considered. These are controlled by the IRAF routines **response** and **illumination**.

5.2.1 Response

In photometric data reduction the combined flat field is normalized by division with the average flat field (Massey, 1997). In the spectroscopic case it is also a good idea to remove any large scale wavelength dependent structure of the flat field lamp along the dispersion axis. The task used to do this is called **response**. The **response** task allows the interactive fitting of a function along the flat field in the dispersion direction which can then be used for normalization. It is important that the order of this fit is not too high as only structure which is found in the lamp but not found in stellar or sky spectra should be removed. Fringes and suchlike artifacts should not be fit (Figure 5.7). The output flat

Table 5.2: NOT spectral followup 12.07.02

Type/Object	Slit Width	Grism No.	No. of Exps	UT start	Exp. time (s)
Calibration					
Bias	NA	NA	10	NA	NA
HeNe	1.0"	7	14	Various	2
ThAr	1.0"	7	2	Various	30
Standard Star					
BD+332642	1.0"	7	3	Various	60
BD+332642	10.0"	7	6	Various	30
HZ44	1.0"	7	2	Various	180
HZ44	10.0"	7	3	Various	120
BD+824211	10.0"	7	2	Various	30
BD+824211	1.0"	7	1	Various	60
Object					
WAVS126212	1.0"	7	1	22.34	1800
WAVS126212	1.0"	7	1	23.05	1800
WAVS126212	1.0"	7	1	23.50	600
WAVS126212	1.0"	7	1	00.37	600
WAVS126212	1.0"	7	1	00.48	600
WAVS120861	1.0"	7	1	01.22	1800
WAVS120861	1.0"	7	1	02.31	1800
WAVS120861	1.0"	7	1	03.20	1800
WAVS120861	1.0"	7	1	03.52	1800
WAVS120861	1.0"	7	1	04.26	1800
WAVS120861	1.0"	7	1	04.57	1800

Table 5.3: NOT spectral followup 13.07.02

Type/Object	Slit Width	Grism No.	No. of Exps	UT start	Exp. time (s)
Calibration					
Bias	NA	NA	30	NA	NA
Twilight Flat	1.0"	open	8	Various	Various
Flat Lamp	1.0"	open	3	Various	10
HeNe	1.0"	7	15	Various	2
ThAr	10.0"	7	1	21:28	30
Standard Star					
BD+332642	1.0"	7	2	Various	60
BD+332642	10.0"	7	3	Various	60
HZ44	1.0"	7	2	Various	180
HZ44	10.0"	7	2	Various	120
Object					
WAVS323426	1.0"	7	1	22.07	1800
WAVS323426	1.0"	7	1	23.12	1800
WAVS124251	1.0"	7	1	23.54	1800
WAVS124251	1.0"	7	1	00.24	1800
WAVS124251	1.0"	7	1	00.55	1800
WAVS820051	1.0"	7	1	01.40	1200
WAVS820051	1.0"	7	1	02.23	1800
WAVS820051	1.0"	7	1	02.57	1800
WAVS324886	1.0"	7	1	03.40	1800
WAVS324886	1.0"	7	1	04.10	1800
WAVS324886	1.0"	7	1	04.45	1800

Table 5.4: NOT spectral followup 14.07.02

Type/Object	Slit Width	Grism No.	No. of Exps	UT start	Exp. time (s)
Calibration					
Bias	NA	NA	9	NA	NA
Twilight Flat	1.0"	open	10	Various	Various
Flat Lamp	1.0"	open	4	Various	10
HeNe	1.0"	7	15	Various	2
HeNe	1.8"	7	1	22.04	1
ThAr	1.0"	7	2	Various	180
Standard Star					
BD+332642	1.0"	7	1	Various	60
BD+332642	10.0"	7	9	Various	60
HZ44	1.0"	7	1	Various	180
HZ44	10.0"	7	1	Various	120
Object					
WAVS120754	1.8"	7	1	22.05	1200
WAVS120754	1.0"	7	4	22.30	1800
WAVS120754	1.0"	7	4	23.00	1800
WAVS120754	1.0"	7	4	23.32	1800
WAVS120754	1.0"	7	4	00.50	1800
WAVS920239	1.0"	7	1	00.18	1800
WAVS9922720	1.0"	7	1	02.10	1800
WAVS722462	1.0"	7	1	03.04	1800
WAVS722830	1.0"	7	1	04.03	1800

Table 5.5: NOT spectral followup 15.07.02

Type/Object	Slit Width	Grism No.	No. of Exps	UT start	Exp. time (s)
Calibration					
Bias	NA	NA	26	NA	NA
Twilight Flat	1.8	open	6	Various	Various
Twilight Flat	10.0	open	10	Various	Various
Flat Lamp	1.8"	open	20	Various	6
Flat lamp	10.0"	open	20	Various	1
HeNe	1.0"	7	14	Various	2
Standard Star					
BD+332642	10.0"	7	4	Various	60
HZ44	10.0"	7	5	Various	120
BD+284211	10	7	4	Various	30
Object					
WAVS1122062	1.0"	7	1	21.41	1800
WAVS925282	1.0"	7	1	22.22	1800
WAVS925282	1.0"	7	1	22.52	1800
WAVS1123123	1.0"	7	1	23.37	1800
WAVS1123123	1.0"	7	1	00.10	1800
WAVS1123123	1.0"	7	1	00.51	1800
WAVS1123123	1.0"	7	1	01.22	1800
WAVS120754	1.0"	7	1	02.19	1800
WAVS120754	1.0"	7	1	02.55	1800
WAVS120754	1.0"	7	1	04.46	1800
WAVS1020811	1.0"	7	1	03.32	1800
WAVS102816	1.0"	7	1	04.10	1800

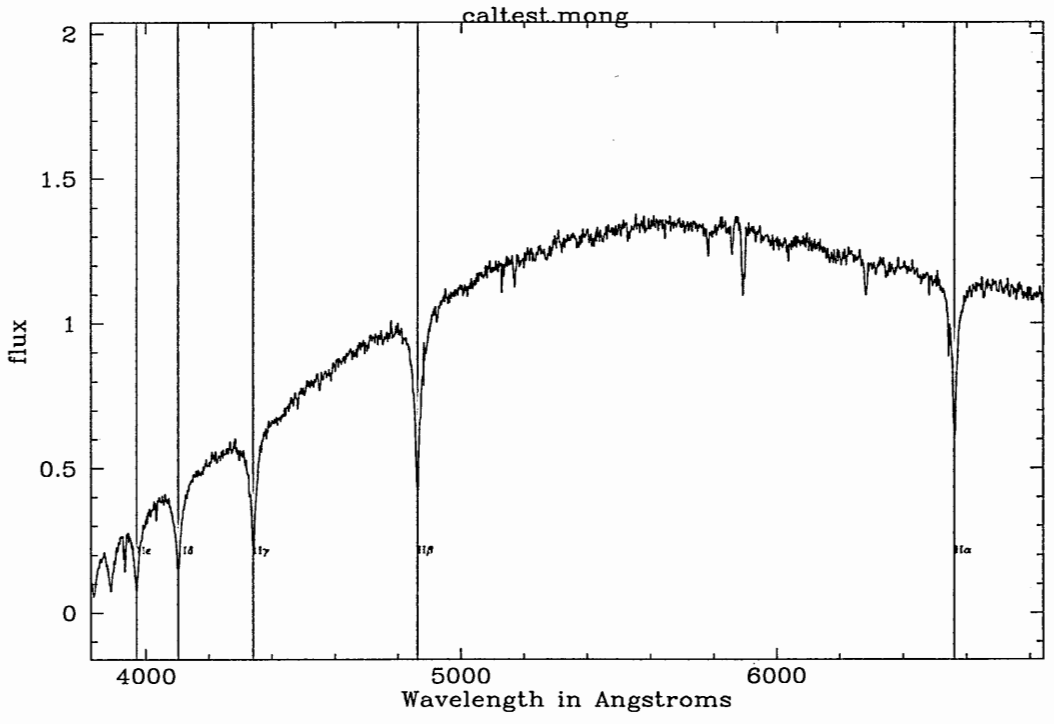

Figure 5.5: a reduced spectrum

field (called something like nFlat.fits) should be entered into the **ccdproc** parameters.

5.2.2 Illumination

To get the flat fielding completely correct, the task **illumination** is used to remove any gradients in the spatial (left - right) axis of the chip. To see if this is necessary an averaged plot across a sky flat field can be made. If there is a noticeable gradient in the spatial direction, then **illumination** can be used to remove this. As the illumination correction may vary slightly in the dispersion direction, a number of wavelength bins (in this case 5) can be defined. A fit to each of these regions is displayed and then a final spatial cut is created (Figure 5.8). The illumination correction output file (illum.fits) can then be applied to the object exposures using **ccdproc**.

5.3 Extraction and Calibration of Stellar Spectra

IRAF contains several packages capable of extracting spectra, originally tailored for use with certain instruments. However, as none of these was meant specifically for NOT data one was chosen arbitrarily (**kpnoslit**) and certain parameters (mainly those dealing with

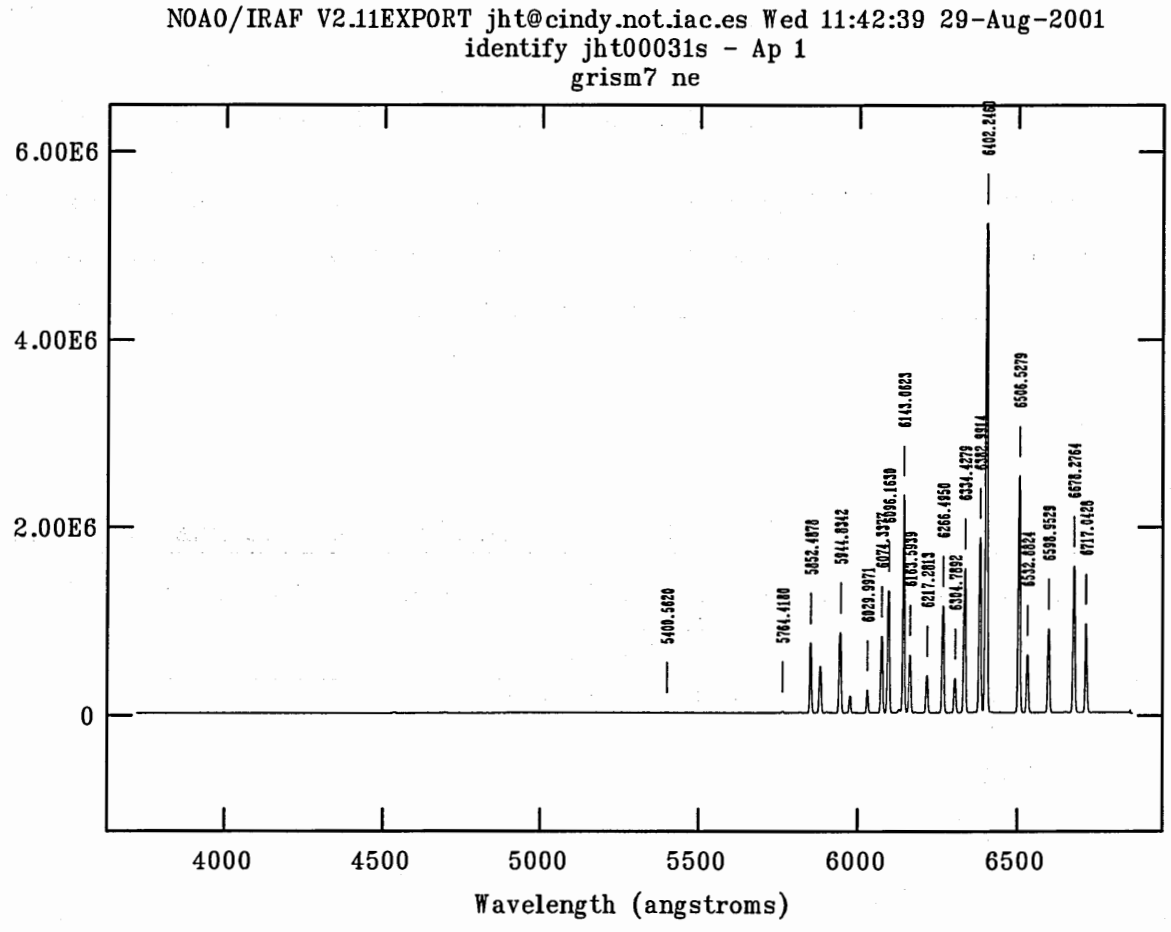

Figure 5.6: Neon lamp calibration spectra (Nordic Optical Telescope Website, 2002), y-axis is counts in arbitrary units.

airmass and other local variations) were changed accordingly.

5.3.1 Extracting the Raw Spectrum

The extraction procedure is governed by the **apall** package in IRAF. The parameters for the **apall** task are displayed in Figure 5.9 and are mainly concerned with the size and position of the aperture, the size and position of the background subtraction regions, and the type and order of function that will be used to fit the trace. Although these parameters can be set up here, for the first extraction it is better to characterise the data by turning the *interactive* switch to 'on' and changing the parameters during the procedure.

Starting **apall** gives a display similar to that shown in Figure 5.10. It is an average of a number of rows specified by the **nsum** parameter, summed in the dispersion direction.

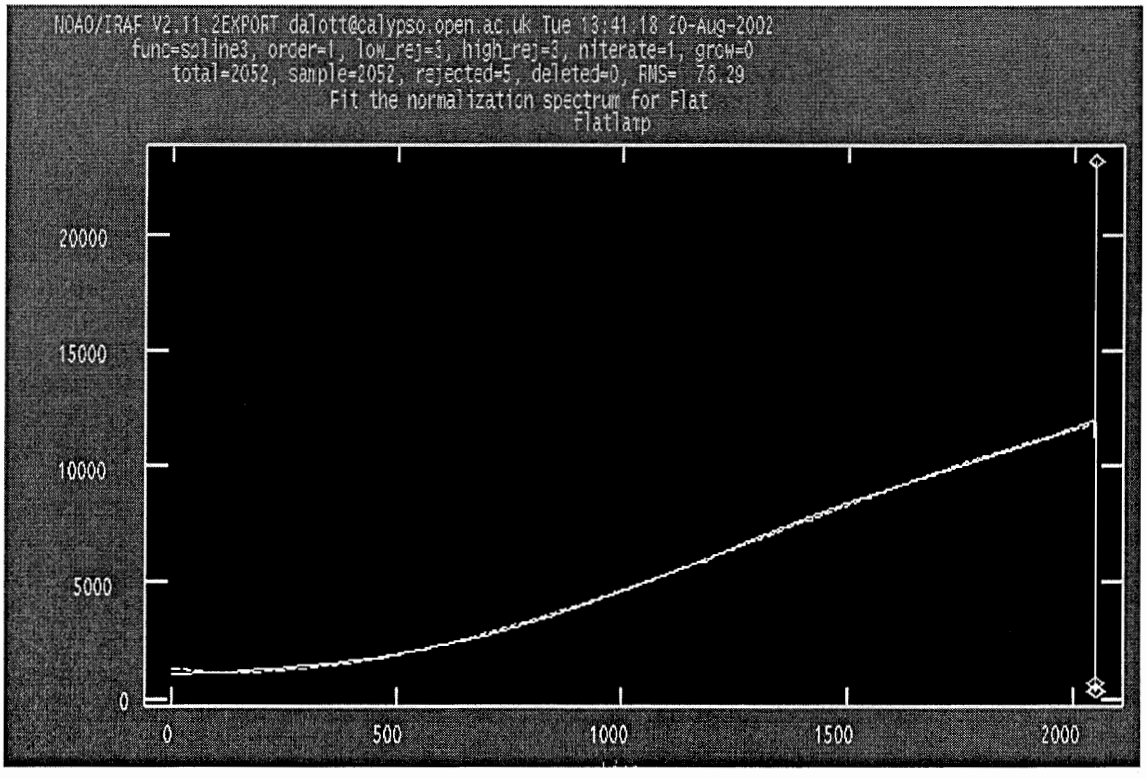

Figure 5.7: Plot of intensity against pixel number fitted using the **response** task.

The position of the aperture should have been found automatically, but if this is not the case or there is more than one star in the slit, apertures can be assigned manually.

The aperture is selected so that it encompasses all the light from the program object but as little of the background as possible. Background regions are specified and these will be used to subtract sky lines and other artifacts from the spectrum (Figure 5.11). It is necessary that these regions should contain only background, thus counts from any other objects in the slit, or from cosmic rays should be avoided.

Once the aperture and background regions are specified the spectrum can be traced. The trace is a plot of the spatial position of the spectrum against position on the dispersion axis and is used to account for the deviation of the spectrum from vertical. The commands *:funct* and *:order* can be used to control the the type of function used to fit the trace, possible options are *spline3*, *chebyshev* and *legendre*. In the case of the WAVS data, low order splines were generally used for the fit (Figure 5.12). Once the trace has been fitted satisfactorily, the spectrum can be extracted. At this stage the spectrum is still uncalibrated in both flux and wavelength.

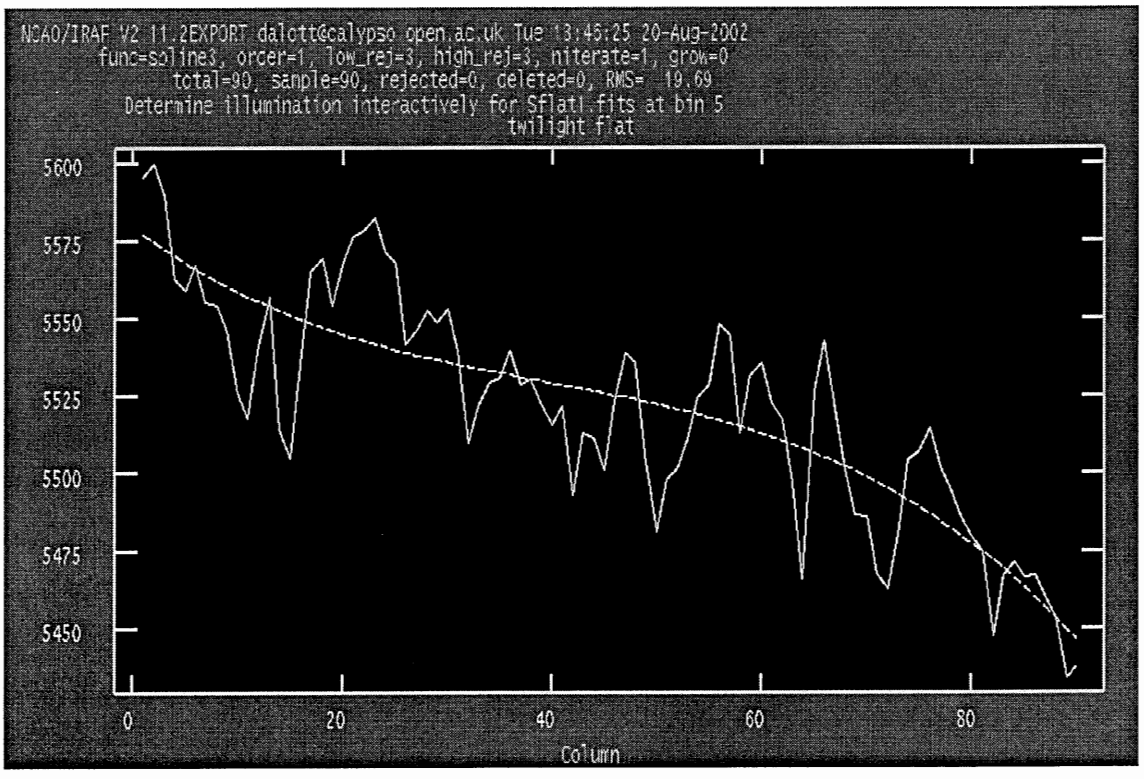

Figure 5.8: Fitting the illumination correction, y-axis is intensity in counts

5.3.2 Wavelength Calibration

The extracted spectrum can now be plotted as a graph of uncalibrated flux against pixel number. However, the conversion from pixels to angstroms is not generally linear and identification of spectral features is hence difficult.

To overcome this, calibration exposures of helium and neon lamps were taken throughout the course of the spectroscopic observing runs, generally at either side of an object exposure and with the same slit and grism combination. Using the emission lines in these spectra as a guide, it is possible to calibrate the dispersion axis of the spectrum in terms of wavelength. This calibration can then be applied to the object exposures. Firstly the calibration spectrum must be extracted. This can be done using the same parameters as were used for extracting the object exposures. The trace that was previously determined for the object exposure is also used, as the lamp spectra are composed of emission lines without continuum and as such cannot be traced. Once the helium-neon spectrum is extracted, the calibration can be undertaken using the IRAF task **identify**.

```
       input = "@standfile"    List of input images
       nfind = 1               Number of apertures to be found
automatically
      (output = "")            List of output spectra
  (apertures = "")             Apertures
      (format = "multispec")   Extracted spectra format
  (references = "")            List of aperture reference images
    (profiles = "")            List of aperture profile images\n
 (interactive = yes)           Run task interactively?
        (find = yes)           Find apertures?
    (recenter = yes)           Recenter apertures?
      (resize = no)            Resize apertures?
        (edit = yes)           Edit apertures?
       (trace = yes)           Trace apertures?
    (fittrace = yes)           Fit the traced points interactively?
     (extract = yes)           Extract spectra?
      (extras = yes)           Extract sky, sigma, etc.?
      (review = yes)           Review extractions?\n
        (line = INDEF)         Dispersion line
        (nsum = 10)            Number of dispersion lines to sum or
median\n\n
       (lower = -3.)           Lower aperture limit relative to
center
       (upper = 3.)            Upper aperture limit relative to
center
   (apidtable = "")            Aperture ID table (optional)\n\n#
DEFAULT BACKG
  (b_function = "chebyshev")   Background function
     (b_order = 1)             Background function order
    (b_sample = "-20:-8,8:20") Background sample regions
  (b_naverage = -3)            Background average or median
  (b_niterate = 0)             Background rejection iterations
(b_low_reject = 3.)            Background lower rejection sigma
(b_high_rejec = 3.)            Background upper rejection sigma
      (b_grow = 0.)            Background rejection growing radius\n
\n# APERTU
       (width = 8.)            Profile centering width
      (radius = 10.)           Profile centering radius
   (threshold = 0.)            Detection threshold for profile
centering\n\n#
      (minsep = 5.)            Minimum separation between spectra
      (maxsep = 1000.)         Maximum separation between spectra
       (order = "increasing")  Order of apertures\n\n# RECENTERING
PARAMETERS\n
  (aprecenter = "")            Apertures for recentering calculation
```

Figure 5.9: Parameters for the apall task

Line Identification

On running **identify**, the extracted helium-neon combined spectrum is displayed. The task allows the user to identify spectral features and assign wavelengths to them. The correct wavelengths can be ascertained by comparison with a calibrated template spectrum available from the NOT website (Nordic Optical Telescope Website, 2002). Once a number of features over the length of the spectrum have been identified and numbered, the task displays a wavelength calibration function which is a fit to these points. As this may not necessarily be linear, the function can be changed using the commands previously described for fitting the trace. As ever, using too high an order will result in spurious points being fit. A third order spline was generally used for the WAVS data. Once a

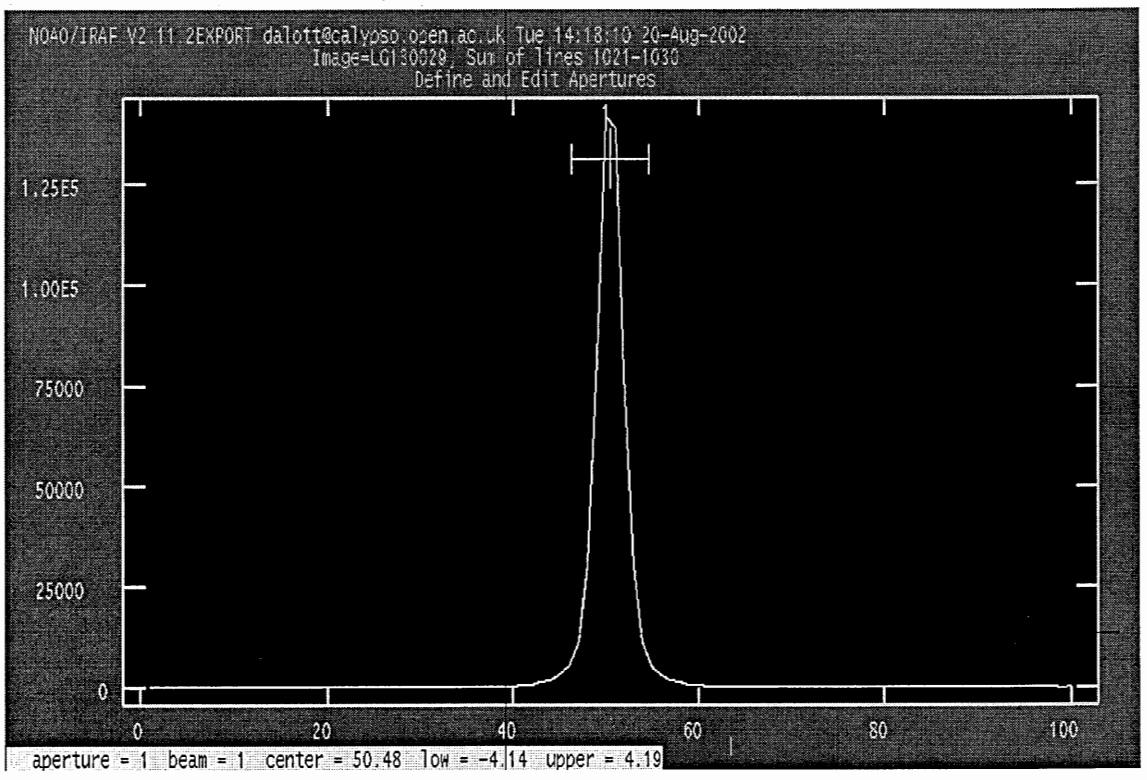

Figure 5.10: Definition of the aperture in the apall task. X-axis is column on CCD, y-axis is intensity

function has been selected and fitted, IRAF uses its database to assign wavelengths to the rest of the spectral lines. Returning to the fit and deleting any spurious points, it should be possible to get the RMS of the fit to well below 0.1.

Identifying spectral lines in other HeNe spectra is now made easy by using the task **reidentify**. By specifying the calibrated spectrum as a reference, the **reidentify** task fits the lines automatically and presents the user with the RMS of the fit. If this is unreasonably high there is an option to enter the **identify** task and improve it. Once all the lamp spectra have been calibrated, they can be assigned to the object exposures.

Assigning and Applying the Dispersion Solution

The calibration spectra were applied to the object spectra on the basis of time. To make this possible the **setjd** task was used to assign Julian dates to both the calibration and object exposures. The procedure is simple and the parameters are displayed in Figure 5.13.

There is a slight problem with the headers created at the NOT telescope in that any

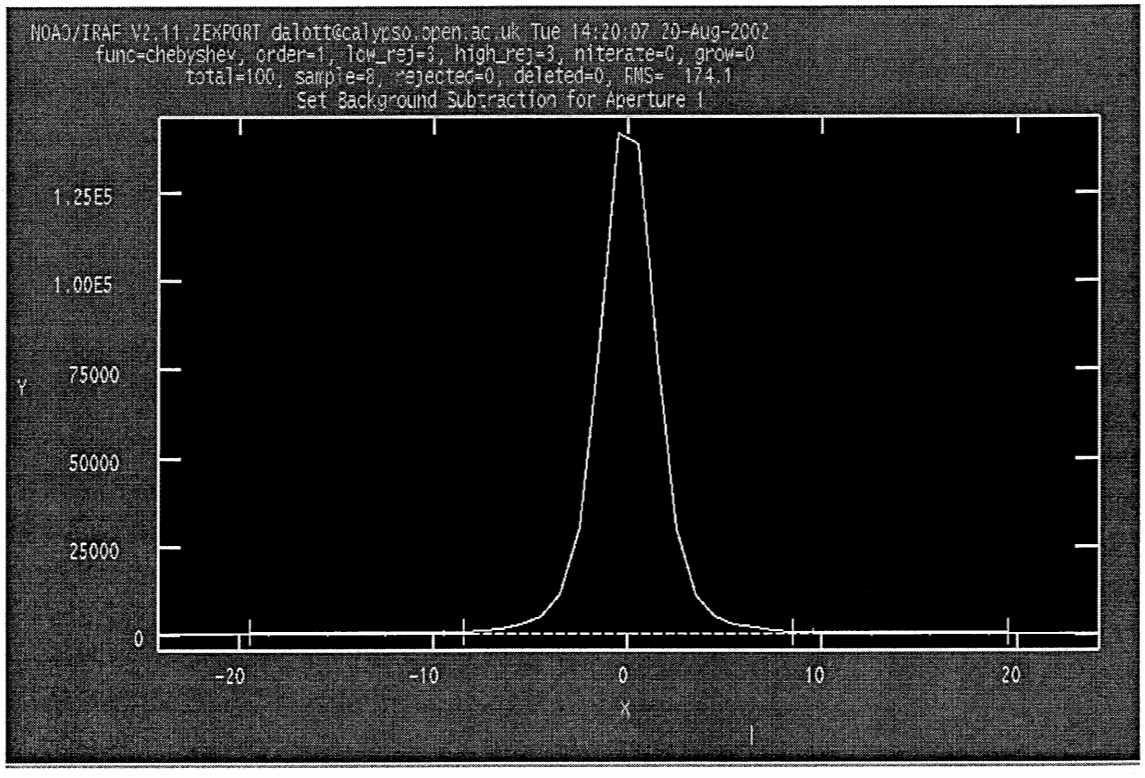

Figure 5.11: Specification of the background regions. X-axis is in columns of pixels, y-axis is intensity

exposure that was being undertaken at Universal Time (UT) midnight, will have a Local Julian date one day in advance of the rest of the exposures. However this can be easily changed by using the **hedit** task and specifying the correct date. Next the **refspec** task was used to assign the calibration spectra to the image exposures. The parameters for this are displayed in Figure 5.14.

Setting the select keyword to *interp* meant that calibration exposures could be be applied to object exposures with a weighting based on their temporal proximity. Thus those calibration images taken closer in time to the object exposure will have a higher weight.

Once the reference spectra were defined, the **dispcor** task was used to dispersion correct the object exposures. **Dispcor** runs non-interactively, and as long as the reference spectra have been correctly defined produces wavelength calibrated spectra.

It is now possible to correctly identify features in the object spectrum. However, without flux calibration it is impossible to know how strong these features really are.

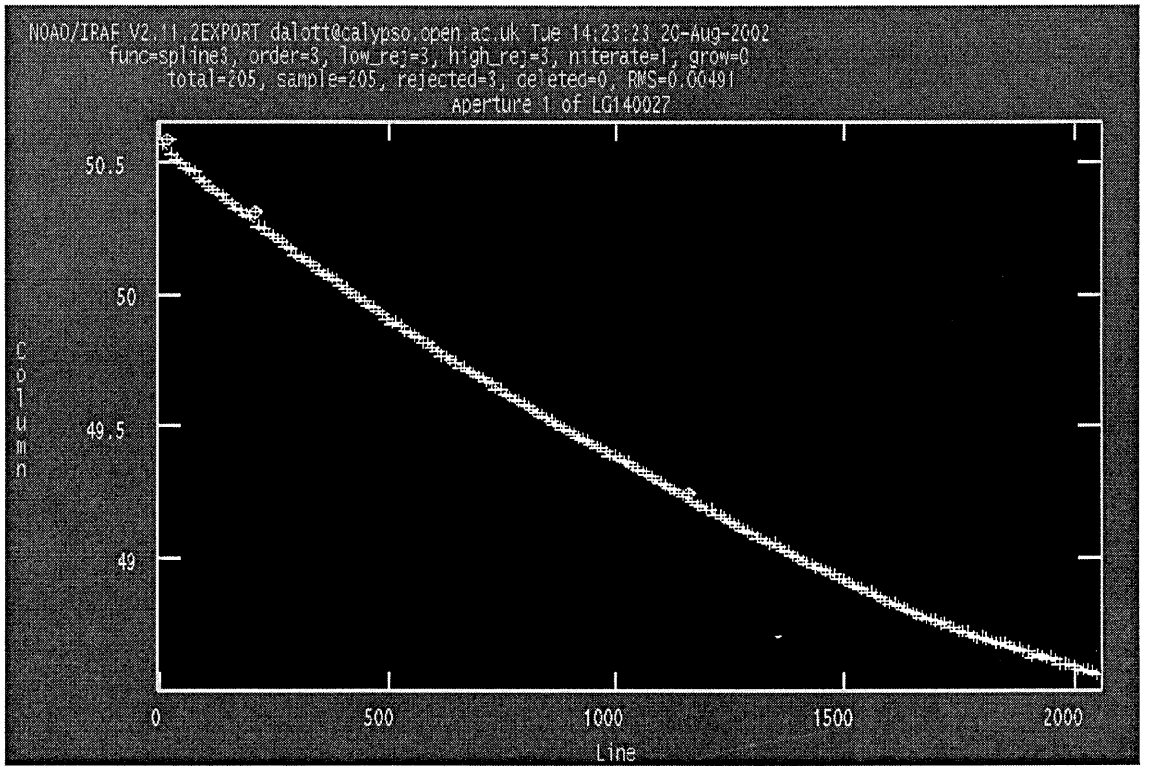

Figure 5.12: Spectral Trace

```
       images = "@standfile"     Images
 (observatory = )_.observatory)  Observatory of observation
         (date = "date-obs")     Date of observation keyword
         (time = "ut")           Time of observation keyword
    (exposure = "exptime")       Exposure time keyword
           (ra = "ra")           Right ascension (hours) keyword
          (dec = "dec")          Declination (degrees) keyword
        (epoch = "EQUINOX")      Epoch (years) keyword\n
          (jd = "jd")            Output Julian date keyword
         (hjd = "hjd")           Output Helocentric Julian date
keyword
         (ljd = "ljd")           Output local Julian date keyword\n
      (utdate = yes)             Is observation date UT?
      (uttime = yes)             Is observation time UT?
    (listonly = no)              List only without modifying images?
       (flpar = no)              flush pfile on assign?
        (mode = "ql")
```

Figure 5.13: Setjd parameters

5.3.3 Flux Calibration

Throughout the WAVS observing runs, exposures of spectroscopic standard stars were taken at varying airmasses. By comparing the program exposures of such stars with their spectra in the IRAF database it is possible to remove the varying colour response of the CCD chip and thereby obtain a more realistic value for the size of spectral features.

```
        input = "@standfile"    List of input spectra
       answer = "yes"           Accept assignment?
   (references = "@HeNefile")   List of reference spectra
   (apertures = "")             Input aperture selection list
      (refaps = "")             Reference aperture selection list
   (ignoreaps = yes)            Ignore input and reference apertures?
      (select = "interp")       Selection method for reference
spectra
        (sort = "jd")           Sort key
       (group = "ljd")          Group key
        (time = no)             Is sort key a time?
    (timewrap = 17.)            Time wrap point for time sorting
    (override = no)             Override previous assignments?
     (confirm = yes)            Confirm reference spectrum
assignments?
      (assign = yes)            Assign the reference spectra to the
input spect
    (logfiles = "STDOUT,logfile") List of logfiles
     (verbose = no)             Verbose log output?
       (flpar = no)             flush pfile on assign?
        (mode = "ql")
```

Figure 5.14: Parameters for the refspec task

The three IRAF tasks which accomplish this are **standard**, **sensfunc**, and **calibrate**. Before using any of these tasks, the standard star spectra must be reduced and wavelength calibrated in the same manner as the object exposures. The inputs to the **standard** task are both the name of the standard star exposure, and the name of the standard star as it appears in the IRAF database. The **standard** task then compares the overall continuum shape of these spectra and outputs the transformation between the two into the file *std*. Performing this operation on different standards will append the results onto the same *std* file. From here they can be plotted using the **sensfunc** task. The output of the **sensfunc** task is displayed in Figures 5.15 and 5.16. It is a plot of the detector sensitivity function calculated from each of the program standards. Although the shape of the curve is the same for each, the overall brightness is considerably different for two of the plots (Figure 5.15). This could be due to high cloud, or to the star not sitting properly in the slit during these exposures. Performing a grey-shift brings these curves in line with the others, whilst not affecting their overall shape. This reduces the residuals by a factor of ten (Figure 5.16). The curve can now be fit using the procedure outlined previously. In this case a 6th order spline tends to do the best job.

The output of the **sensfunc** task is the file *sens*, which contains both the sensitivity function and the transformation from counts into absolute flux. This is applied to the object exposures using the task **calibrate**. Having completed this final step the spectra are fully calibrated and the reduction process is complete.

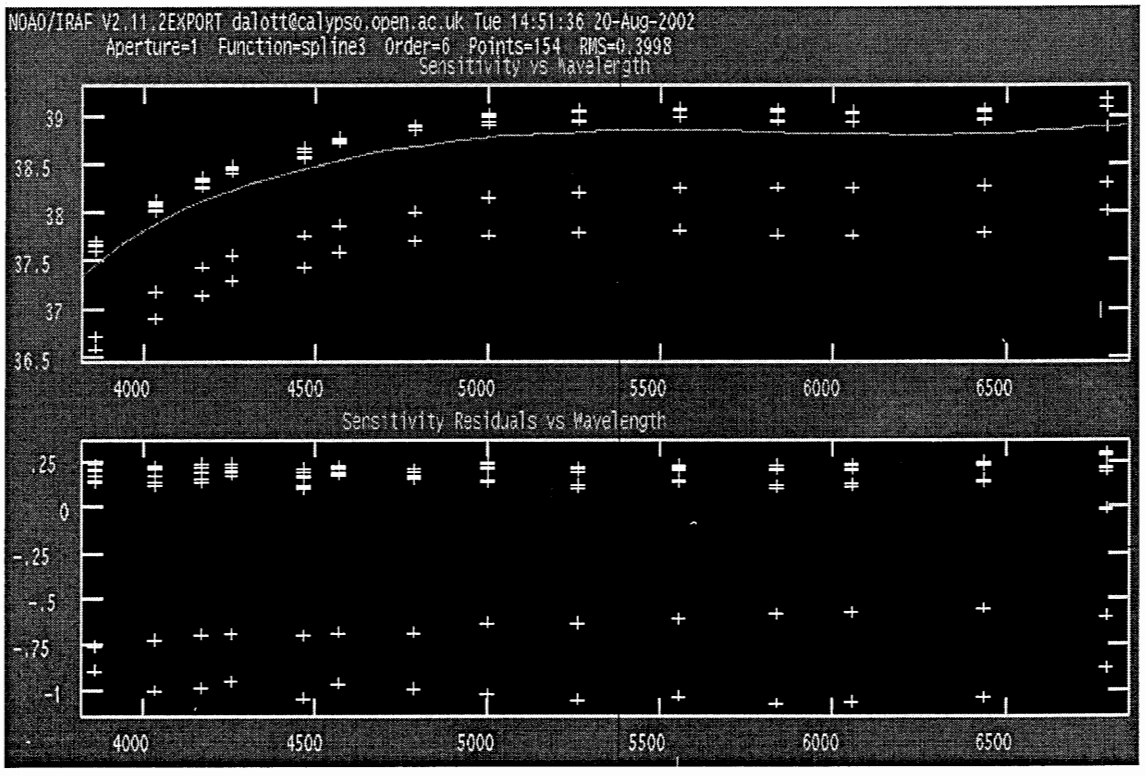

Figure 5.15: Top Panel: Sensitivity vs wavelength (in Å) for standard stars before grey-shift. Bottom Panel: Residuals (magnitude) against wavelength (in Å) for fit.

5.3.4 The Effects of Interstellar Reddening

A final caveat to this discussion of spectral reduction is to consider the effects of interstellar reddening on the spectra, a step that appears somewhere between the completion of the reduction process and the final analysis of the data. Due to the wavelength dependence of interstellar extinction, the shape of the continuum will be altered (made redder) to a varying degree dependent upon the amount of dust that lies between the Earth and the star. In the case of the WAVS field, the magnitude of this effect will vary for individual objects as it is affected both by their distance from us and by their position within the WAVS field. Figure 5.17 shows a dust map of the WAVS field created using the IDL routine DUST-GETVAL developed by Schlegel *et al.* (1998).

The reddening value E(B-V) for extra-galactic sources varies across the WAVS field from 0.6 to 0.9 magnitude. As distances to the WAVS objects are unknown, these figures represent a maximum and in practice spectra were dereddened using an iterative process alongside spectral classification with these figures as a guideline. This process will be discussed further in chapter 6.

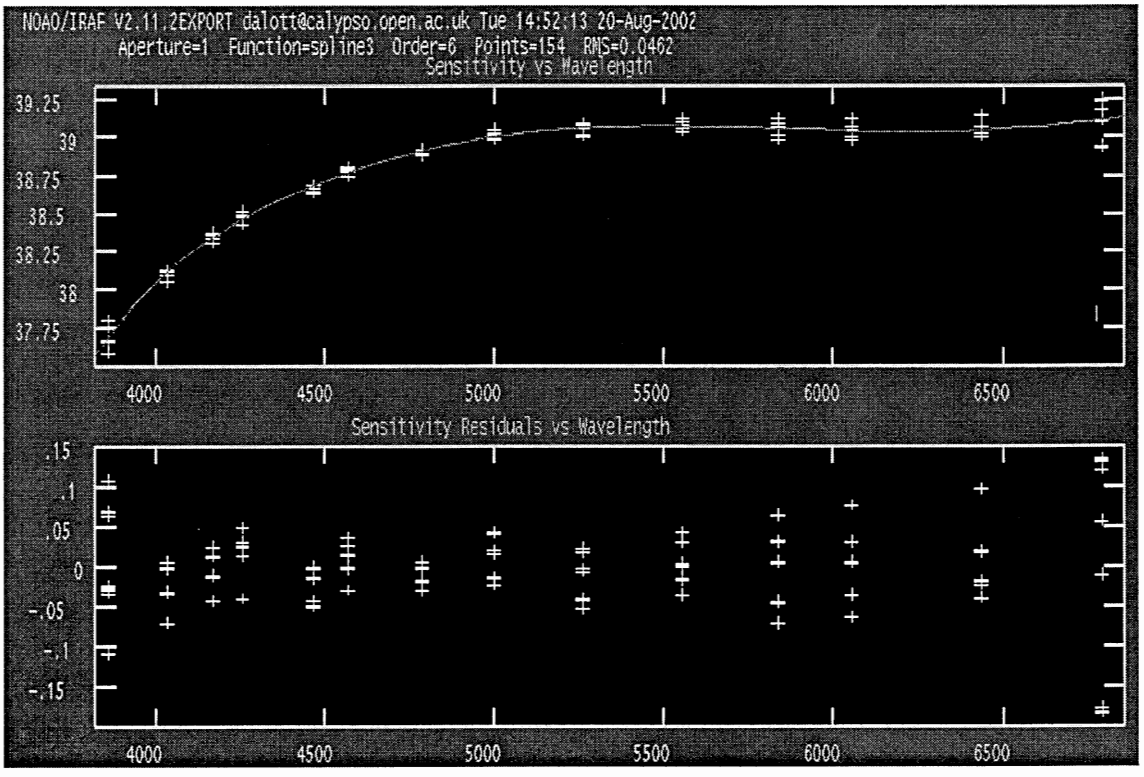

Figure 5.16: Top Panel: Grey shifted and fitted sensitivity function. Bottom Panel: Residuals against wavelength (in Å) for fit.

5.4 Examining the Final Spectra

There are several tasks within IRAF that are useful for analyzing the final spectra. **Splot** is a powerful plotting tool which allows smoothing and zooming in on sections of spectra as well as measurement of line widths and removal of cosmic rays. **Scombine** is also useful and can combine multiple spectra by simple summing, averaging or calculating the mean, thus reducing noise. However, for the most part a script (mongspec.sm) was written in the supermongo language to aid in the plotting of the data and comparison with both prominent spectral lines and also stellar spectral types (Appendix D).

5.4.1 Mongspec

The program mongspec asks for the filename of the object spectra to plot. A number of options are then available. Inputting 'H'or 'He' on the command line will plot the wavelengths of either strong hydrogen or helium lines onto the spectrum. The command 'sky' will plot the wavelengths of prominent sky lines. Mongspec can also over-plot stellar

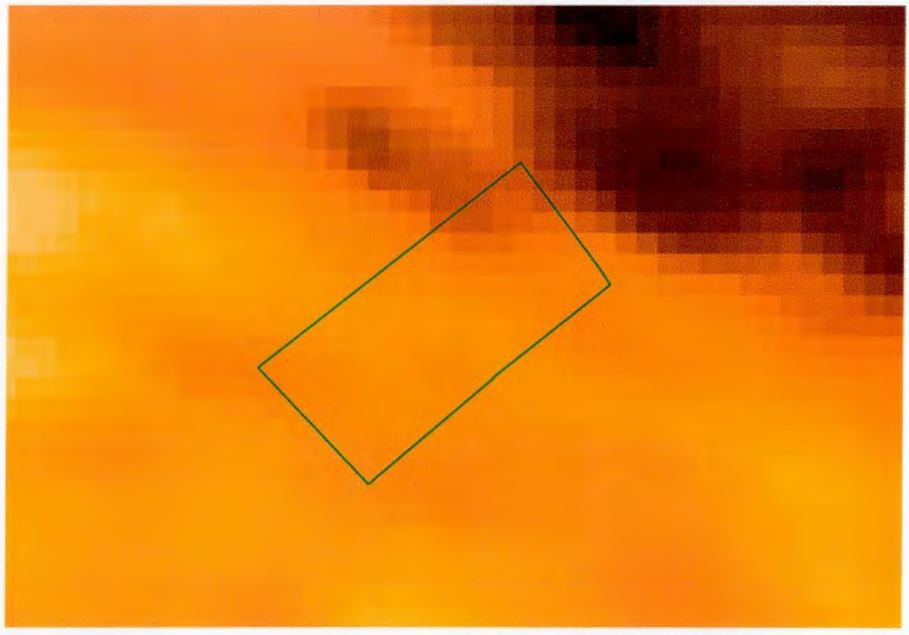

Figure 5.17: Dust map of the WAVS region (field denoted by green box) created using maps from (Schlegel *et al.*, 1998). Within box brightest parts E(B-V)$\approx$ 0.6, darkest parts E(B-V)$\approx$ 0.9

spectra, for example - typing 'a5' will give the spectrum of an a5 type star, whilst 'm3' will do the same for the m3 class. As some of the stars that have been studied are suspected binary systems a combination option is also available. Typing 'combo' enters this mode and it is then possible to enter two stellar types, along with weights (a number from 0-1) for each star so that a spectrum can be created for a system which is made up of (for example) 20 percent A3 type and 80 percent K7 type flux. This has been a useful tool in identifying and classifying spectra. Some of the results from this program will be displayed in chapter 6.

Chapter 6

Results and Analysis

The reduction of the WAVS data and the subsequent investigation of the lightcurves revealed many interesting objects, most of which fell into the types discussed in chapter 1. Population statistics for these data will be dealt with in the second half of this chapter, firstly though, individual objects that were deemed to be of particular interest will be considered.

Throughout this section and in the following appendices, apparent V magnitudes will be quoted at the observed maxima and minima as calculated on first night of observations. This is due to the superior calibration of the night one data which was discussed in chapter 4 section 3.3. In circumstances where this would be either impossible (i.e. objects observed on night two only) or misleading (eg. for objects such as flare stars which only displayed variations on the second night of observations) night two magnitudes will be quoted. Errors on the observed V magnitudes at both maxima and minima will be those calculated by **daophot** during the photometry process. The B and R colours will be quoted either as calculated by **daophot** or as calculated by the method described earlier in chapter 4 section 3.3. As only one B and one R exposure was taken on each of the CCDs, absolutely no variability information is available in these bands. Unfortunately this makes classification more difficult and also means that errors quoted on these values would be formal errors only, not taking into account the variability of the object which is expected to be manifest in all optical bandpasses. Any error quoted would only represent the error on the measurement at that time and would not give any information on the range of variation, also, as B,V and R band observations were not simultaneous, measurements

could be made at maximum brightness in one band, and at minimum in another. In the most extreme (and admittedly unlikely) case, a single B or R measurement taken when a flare star was erupting could be very misleading if compared to the average V value during the rest of the cycle.

Although it can by no means be expected that variations in other bands will mirror those observed in the V band, in most if not all, cases some correlation could be expected. For the variable stars discovered in this sample, differences due to variation are likely to be much greater than the error in calibration (at least for those calibrated using **daophot**), B and R magnitudes are quoted in the text with errors equal to the amplitude of the observed V band variations. Although this is by no means expected to be accurate - it at least gives some idea of the scale of the possible deviation.

As discussed in the previous chapter, values of E(B-V) for objects with spectra were found using an iterative process alongside spectral classification. For objects for which no spectra are available, the effect of interstellar reddening on the colours is not known.

6.1 Individual Objects

As expected, the WAVS project turned up a large number of variable stars. Some of the stars considered in this section will be mentioned because they are of particular scientific interest, others will be included as they are representative of a population of similar stars found in the survey. The discussion of these objects will be split into three subsections:

- Those objects for which well defined periods can be established.
- Objects which are possibly periodic but have an insufficient baseline for an accurate period to be calculated.
- Objects which are probably inherently non-periodic but still show variability.

6.1.1 Periodic Objects with Defined Periods

This section contains examples of many of the types of short period variable discussed in the introductory chapters. In some cases it is obvious from the behaviour of the lightcurve, or from the spectra what class of object these variables belong to. In other cases the classification is uncertain without more data.

Calculating Periods

Calculating accurate periods is easiest with a long observational baseline. Thus most of the objects included here will be those that are present on both nights of observation. To calculate the periods of these stars, the starlink program PERIOD was used. PERIOD reads in the data in 3 column format (time, magnitude, error) and then allows the user to manipulate it in various ways (such as detrending or adding and subtracting sine waves etc). It also allows the calculation of periods using a variety of methods such as Fourier Transforms, the Lomb-Scargle method (Van Dongen *et al.*, 1999) and Phase Dispersion Minimization (Schwarzenberg-Czerny, 1997). In analyzing the WAVS variables, the Lomb-Scargle technique was used as it works well with unevenly sampled data. This uses a Fast Fourier Transform method but with the classical periodogram redefined to make it invariant to a shift of the origin in time. The PEAKS option in PERIOD was then used to accurately calculate the peak of the distribution and IDL was used to interactively fit the data. In some cases, data spanning both nights were detrended to remove the effects of the calibration problems discussed in chapter 4. The original lightcurves are displayed in Appendix A. In all of the plots detrended using PERIOD, the y-axis is in terms of magnitude above or below the zero point of the detrended curve with brightness increasing upwards.

Radial velocity variations

In cases where multiple spectra exist it is possible to calculate radial velocities by measuring any shift in the wavelength of spectral lines between exposures. However, this will only really prove useful in cases where the period of variation is not comparable to the integration time of the spectrum (generally 30 minutes), and also when the radial velocity variation is large enough to be detected at the spectral resolution used. The spectral resolution of ALFOSC in the 1" slit grism 7 configuration that was used during the observing run was calculated by measuring the FWHM of arc lamp lines and using Equation 6.1

$$\frac{\Delta\lambda c}{\lambda} = v \tag{6.1}$$

Where λ = wavelength, $\Delta\lambda$ = FWHM, c = speed of light and v = spectral resolution. The results of this are shown in Figure 6.1.

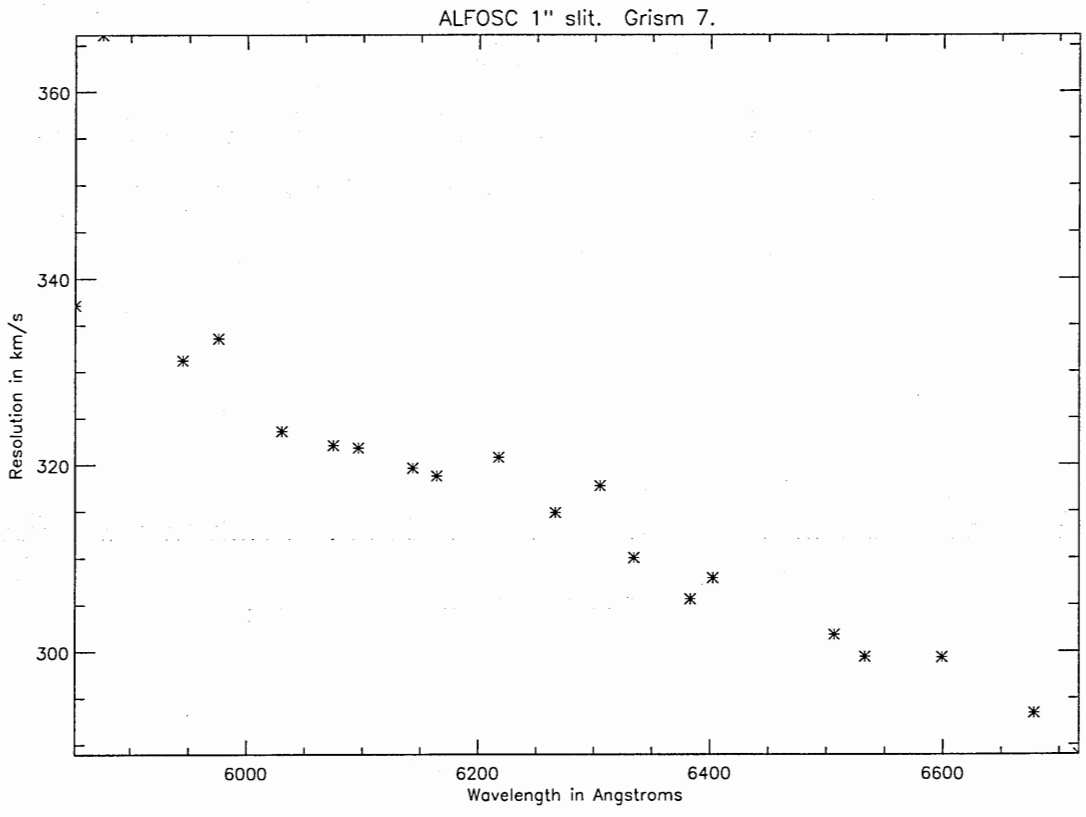

Figure 6.1: Plot of resolution in kms^{-1} against wavelength in Angstroms for ALFOSC in 1" slit, grism 7 configuration.

WAVS126212

It seems sensible to begin this section with one of the most interesting objects found in the WAVS survey. WAVS126212 is a pulsating object which seems to show a variety of interacting periods (Figure 6.2).

Clearly WAVS126212 is an object which displays the effects of two similar periods beating together where:

$$\frac{1}{P_{beat}} = \frac{1}{P_1} - \frac{1}{P_2} \tag{6.2}$$

Using PERIOD to attempt to locate these periods produced several spikes in the Lomb-Scargle periodogram (Figure 6.3). By far the largest of these (at around 40 cycles per day) is actually composed of two periods of such similarity that the resolution was not high enough to differentiate between them.

Using the value provided by PEAKS as a starting point, IDL was used to fit the curve

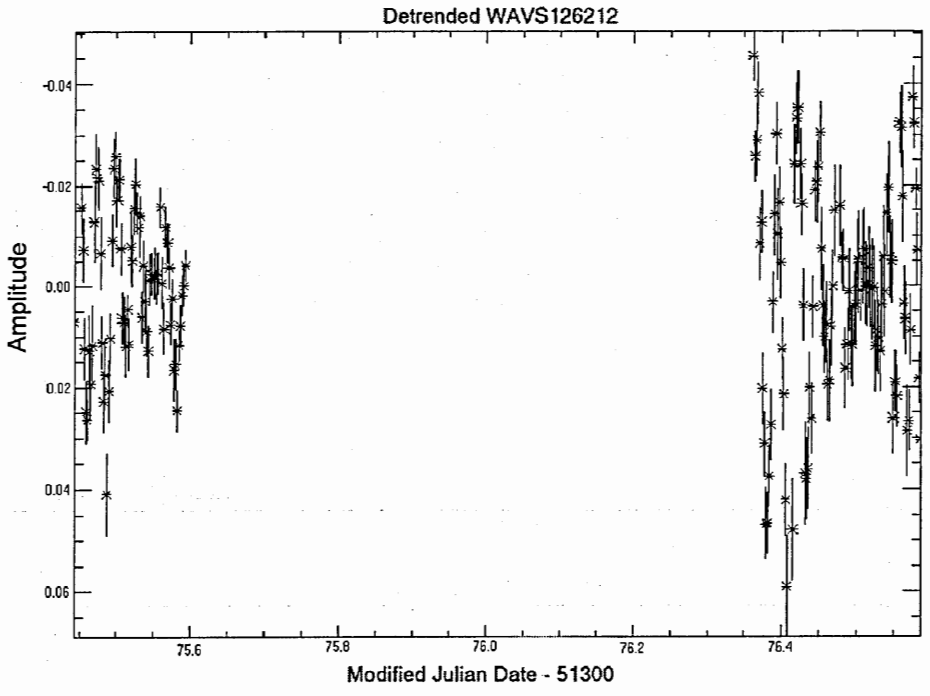

Figure 6.2: Detrended lightcurve of WAVS126212. Amplitude is in magnitudes with brightness increasing upwards

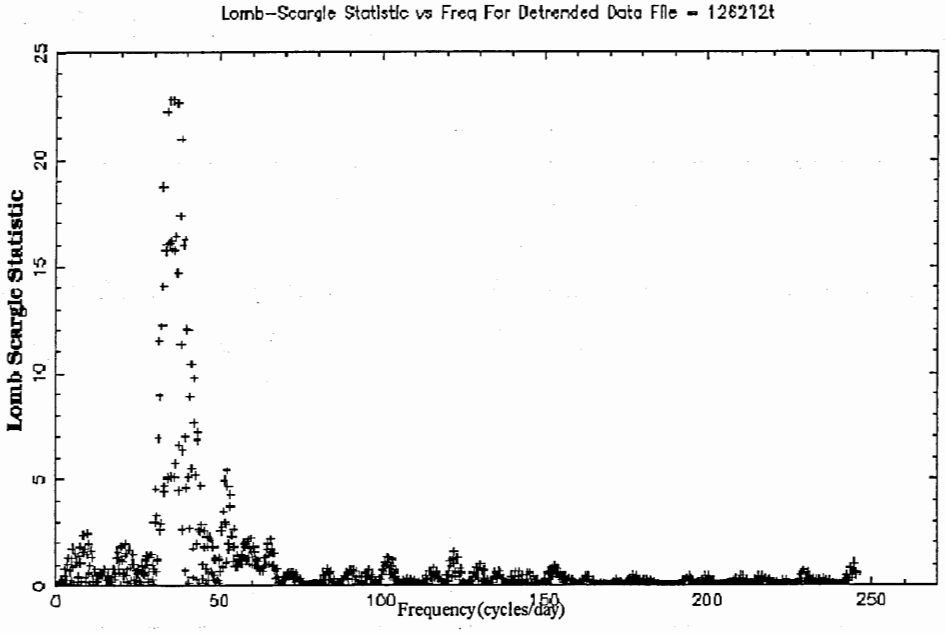

Figure 6.3: Lomb-Scargle Periodogram for WAVS 126212

with two interacting sine waves of very similar period. Eventually a fit was found and it became apparent that a third period was present that was modulating the amplitude of the beats. The final fit (Equation 6.3) is plotted in Figure 6.4.

$$fit = ((0.025\sin((2\pi/0.0270)t)) - (0.025\sin((2\pi/0.0248)t)))(\sin((2\pi/5)t)) \quad (6.3)$$

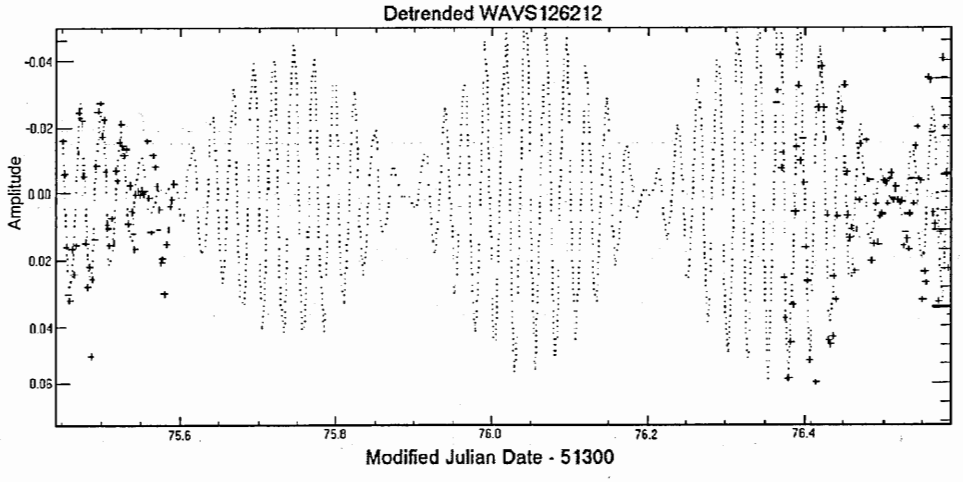

Figure 6.4: WAVS126212 fitted with three interacting periods. Amplitude is in magnitudes with brightness increasing upwards.

The fit (displayed by the dotted line) is given by the sum of two sine waves with amplitudes of 0.025 magnitudes and periods of 0.0249 days and 0.0270 days or 35.9 and 38.9 minutes respectively. This is then multiplied by a further sine wave with period 5 days. Visually the fit appears to be good, although there are clearly some incongruent points. These could be due either to inherent flickering in the object, or to extra, unaccounted for periods. The latter would appear to agree with the periodogram, which does show evidence for additional periods at higher frequencies (Figure 6.3).

The high speed, low amplitude pulsations displayed by WAVS126212 are strikingly similar to those displayed by Pre-Main Sequence (PMS) Delta Scuti stars such as V351 and V346 Ori (Figure 6.5) (Ripepi *et al.*, 2003) and (Pinheiro *et al.*, 2003). These are young stars often designated as Herbig Ae or A-emission (A-type stars which show emission lines within the hydrogen absorption lines of their spectra) (Monin *et al.*, 2003). Only around ten of these stars are known and they are particularly useful for testing PMS

evolutionary models as identification of their pulsation frequencies can lead to information about important stellar parameters such as mass, luminosity and effective temperature (Pinheiro *et al.*, 2003).

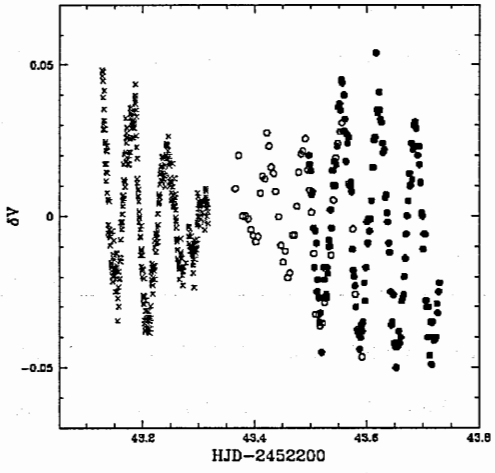

Figure 6.5: Lightcurve of V351 Ori from 3 different telescopes on the same night (Ripepi *et al.*, 2003). The meaning of δV (in magnitudes) is Variable star magnitude-Comparison star magnitude.

A composite spectrum of WAVS126212 is displayed in Figure 6.6 with the spectrum of an A3 type star over plotted in red. The dereddening correction for this object was originally set using E(B-V)=0.8 which yielded an obviously A type spectrum (lower values of E(B-V) were not consistent with spectral features). Fits of various A subtypes were then applied and the reddenning value altered slightly within the range discussed earlier. The best fit to both continuum shape and line profile was found with an A3 type spectrum and E(B-V)=0.9. In all of the fitted WAVS spectra, there is a slight deviation from the template spectra at the reddest wavelengths. This is likely due to slit losses caused by differential atmospheric refraction.

The deduced intrinsic colours of this object (V_{max}=17.077±0.005, V_{min}=17.167±0.008 B-V=0.10 ±0.05) are also consistent with an early A type star which is promising for the hypothesis that WAVS126212 is a PMS Delta Scuti. Ae stars have been shown to often exist in binary systems (Leinert *et al.*, 1997) but in this case the spectrum does not seem to show any features that point to a companion.

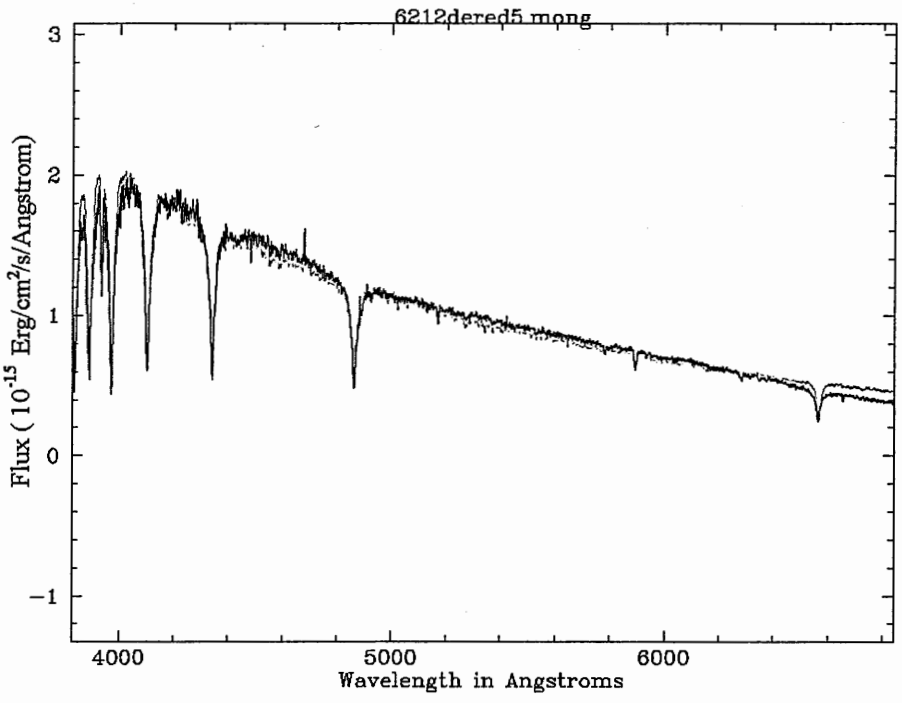

Figure 6.6: Combined spectrum of WAVS126212 dereddened with E(B-V)=0.9, over plotted in red with the spectrum of an A3 type star.

To determine if emission lines are present it is necessary to study the hydrogen lines in detail. This can be done by comparing the observed profile with a synthetic spectrum, as demonstrated by Monin *et al.* (2003) (Figure 6.7)

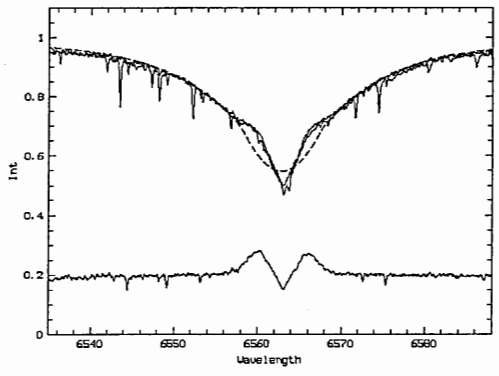

Figure 6.7: Observed (upper solid curve), Synthetic (dashed) and Observed-Synthetic (lower solid curve) Hα line profiles for Ae star κUMa (Monin *et al.*, 2003). Weak emission can be seen within the wings of the absorption profile

Unfortunately in this case, we do not have enough information available to construct a synthetic spectra for WAVS126212. However, profiles of the Hα, Hβ and Hβ lines are shown in Figure 6.8.

Due to the low resolution of the spectra and the lack of a synthetic comparison it is very difficult to say whether any emission is present or not. The Hα profile shows no sign of the central 'notch' seen in Figure 6.7, however our resolution (6Å at Hα) is insufficient to reveal such a feature. Intriguingly, Hγ hints of a central notch. This object warrants follow up study with higher spectral resolution

Although the shorter two periods of this object are comparable to the spectral integration time, measurements of radial velocities were taken as multiple spectra did exist and variations due to the longer period may still be apparent. The results of this are displayed in Figure 6.9 below.

There definitely appears to be a trend of radial velocity decreasing with time, again showing evidence of longer periods. Further observations are required (a) to test for radial velocity variations at the shorter periods and (b) to measure the period of variation producing the trend we have observed.

In summary, the available data points strongly to the classification of WAVS 126212 as a PMS Delta Scuti. Further studies of this interesting object are warranted as described above.

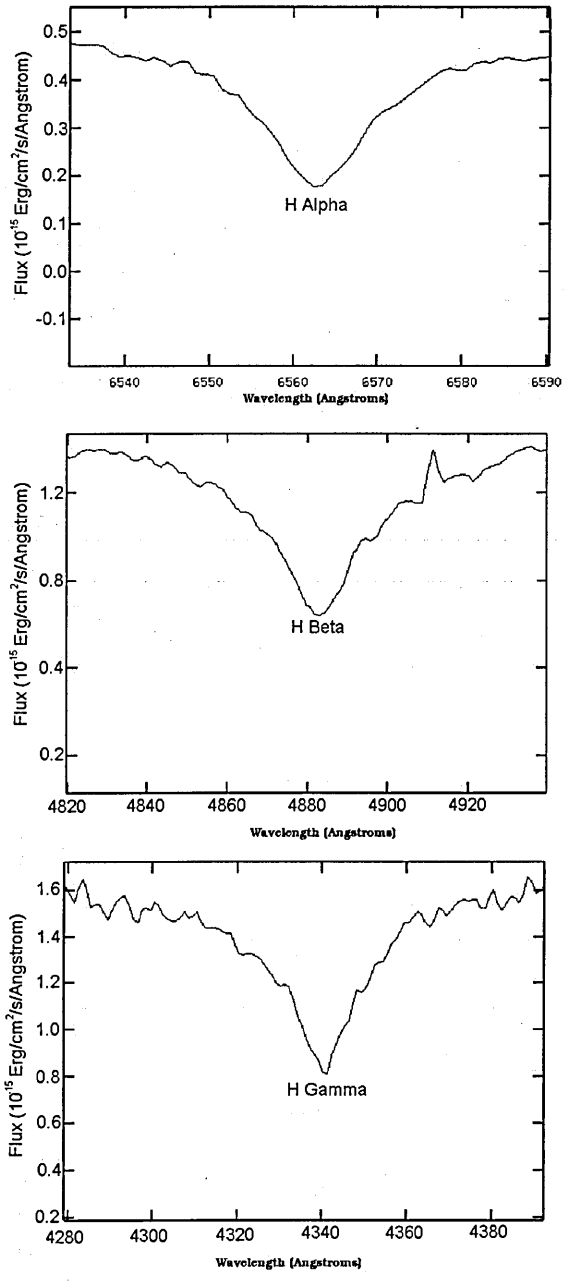

Figure 6.8: Hα, Hβ and Hγ lines in WAVS126212

WAVS120861

WAVS120861 is a periodic variable with one obvious period. The fitted lightcurve is shown in Figure 6.10.

The fitted sine wave has a period of 0.06 days or 1h 26 minutes and is consistent with either an ellipsoidal variation or a low amplitude pulsation of some kind. To check the validity of the calculated period the lightcurve of WAVS120861 was folded on 0.06 days,

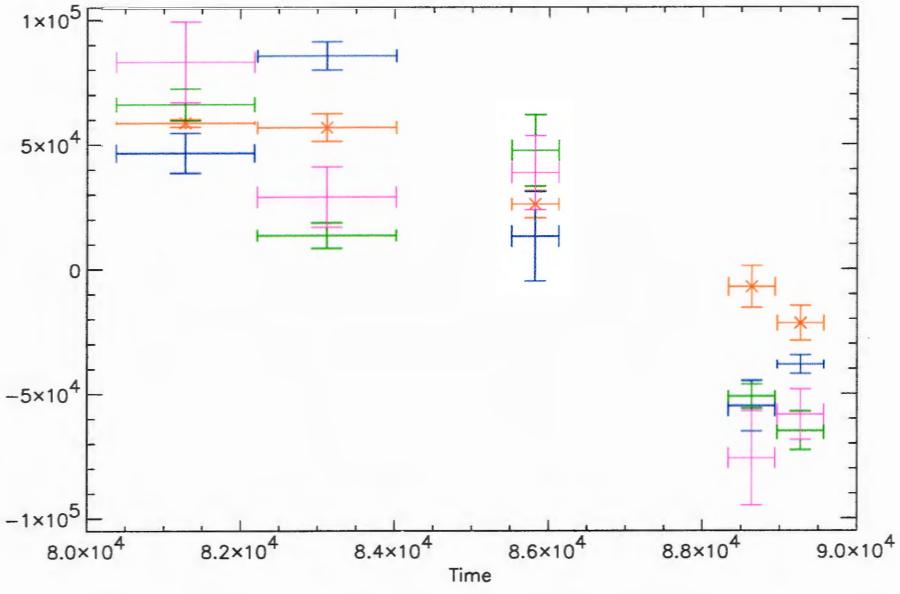

Figure 6.9: Radial velocity measurements for WAVS126212. Measurements taken using Hα, β,δ and γ are shown by red, blue, green and pink crosses respectively. The x-axis represents Universal time in seconds and the y-axis radial velocity in ms^{-1}.

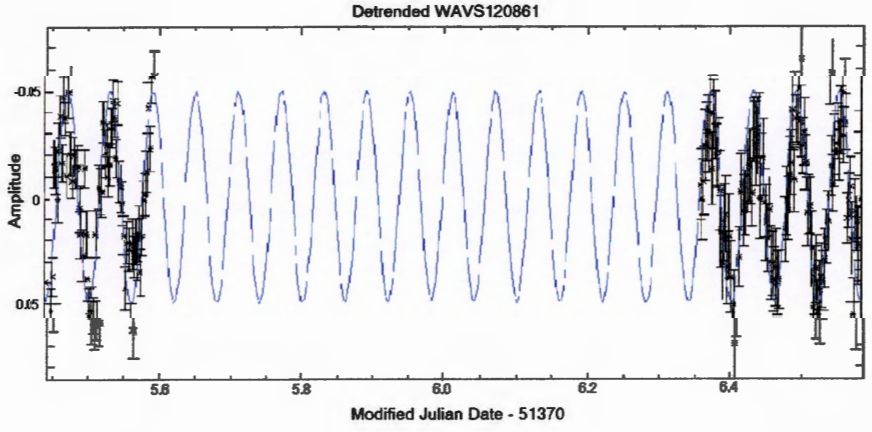

Figure 6.10: Fitted lightcurve of WAVS120861. Amplitude is in magnitudes with brightness increasing upwards.

a plot of amplitude against phase for the folded lightcurve is shown in Figure 6.11.

Radial velocity measurements for this object are limited but show a range of variation consistent with either a pulsating object or a rapidly rotating binary (Figure 6.12).

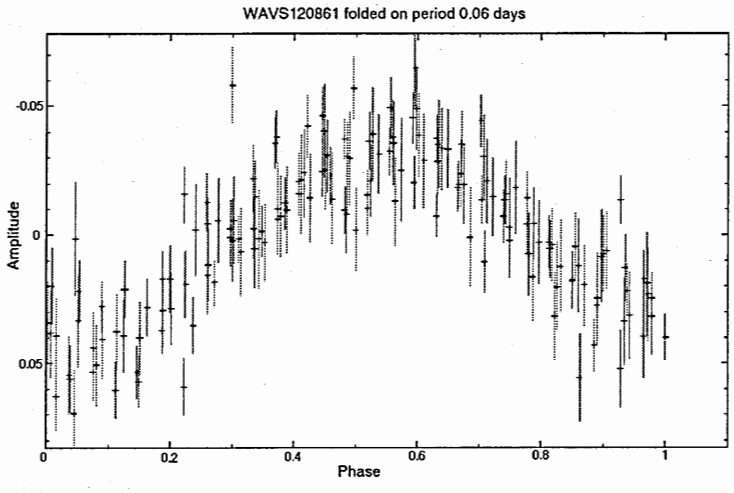

Figure 6.11: Lightcurve of WAVS120861 folded on 0.06day period. Amplitude is in magnitudes with brightness increasing upwards.

However, the scatter between the results from different spectral lines is comparable to the scatter from one time to another, highlighting the difficulties in obtaining radial velocities from these low resolution grism spectra.

The intrinsic colours of this object (V_{max} =20.242±0.012, V_{min}=20.371±0.013, B-V=0.6±0.1, V-R=0.6±0.1) indicate a late F type star but the spectrum of WAVS120861, although noisy (Figure 6.13) has more in common with a late G or early K type star. The best fit to the shape of the continuum was found with E(B-V)=0.8 and a combination of G7 and K5 spectra with the ratio 0.7/0.3, however the spectral line strengths are clearly not consistent with a simple G and K type binary. Although the Ca H and K lines are fit reasonably well with this combination, Hα, β,γ and δ lines are all clearly enhanced in the object spectrum. There is also a depression in the object spectrum between 4300 Å and 4600Å possibly due to the presence of enhanced CH, leading to the possibility that one of the objects is a CH star. This would be inconsistent however with evolutionary models of CH stars in binaries which lead to significantly longer periods than 0.06 days (Han *et al.*, 1995). It appears that HeI lines are also enhanced in the spectrum of this object. This combined with the unusual strength of the Balmer series would point to an earlier classification, but there is no evidence for this from the overall continuum shape. In short the spectrum of WAVS120861 is very difficult to classify and further work will be needed before any real conclusions can be reached about this object.

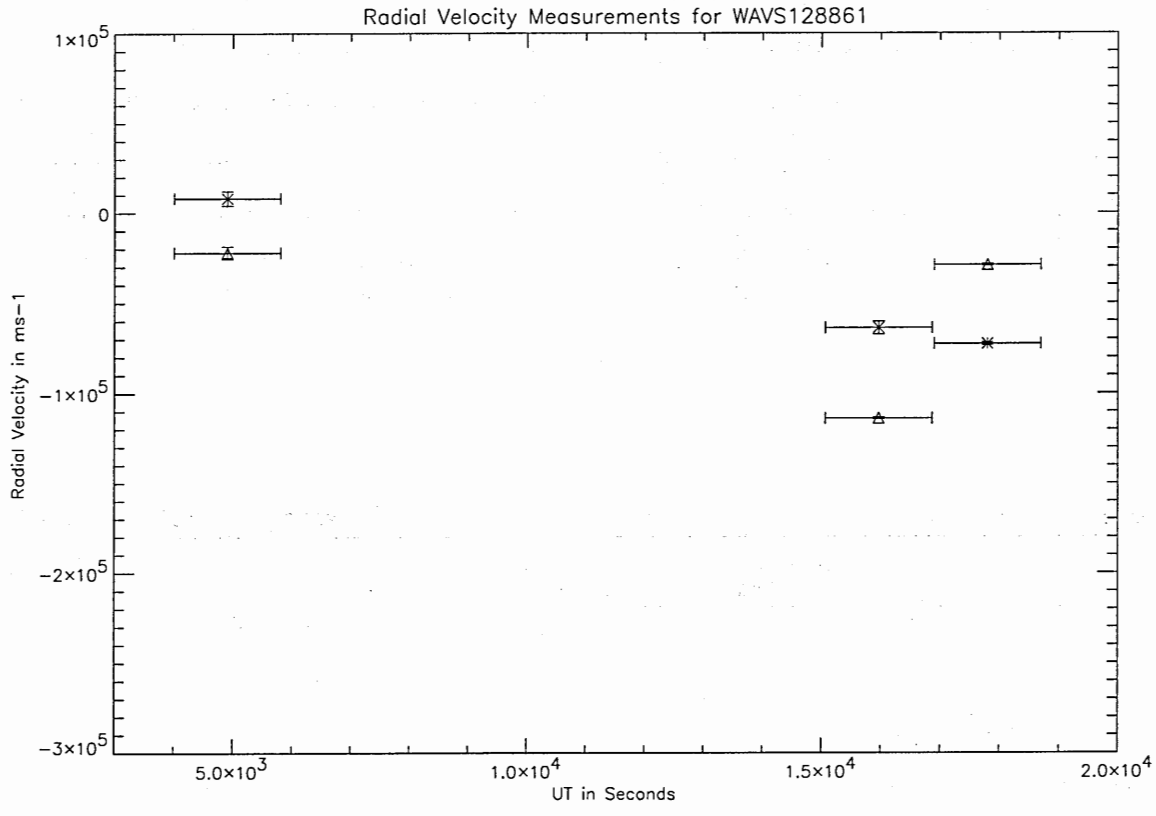

Figure 6.12: Radial velocity measurements for WAVS120861. Asterisks represent measurements taken using the Hα line, whilst triangles represent those taken using Hβ.

WAVS424709

WAVS424709 is a good example of a subset of variable objects with slightly longer periods and higher amplitude variations than WAVS120861 (Figure 6.14). A period of 0.106 days (2h 33m) is gained from the Lomb-Scargle periodogram and this produces a reasonable fit.

However, folding the lightcurve on this period is less satisfactory, revealing some amplitude variation within the data (Figure 6.15)

This object is a likely candidate for ellipsoidal variation, with the amplitude variation being due to stronger limb darkening effects on the pointed end of the more elongated star (Hall, 1990). The measured colours of this object (V_{max} =19.622±0.008, V_{min}=19.878±0.009, B-V=1.7±0.1, V-R=0.8±0.1) suggest M class components, but only spectrographic study will confirm this.

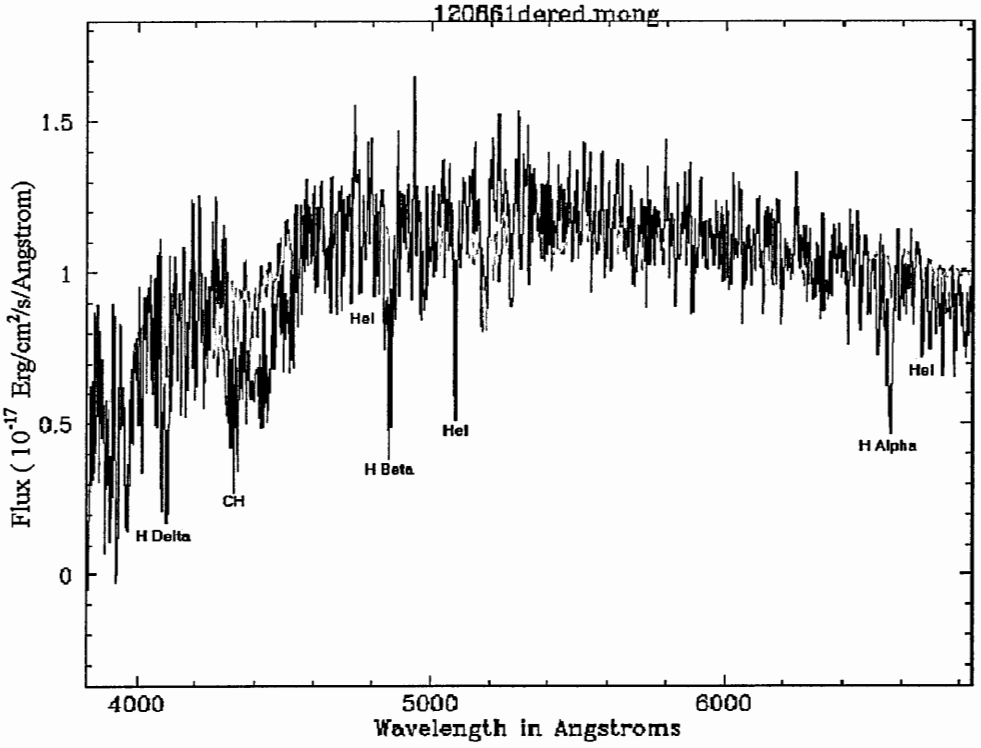

Figure 6.13: Spectrum of WAVS120861 (black) dereddened with E(B-V)=0.8. Over plotted in red is a G7-K5 combination spectrum in ratio of 0.7/0.3.

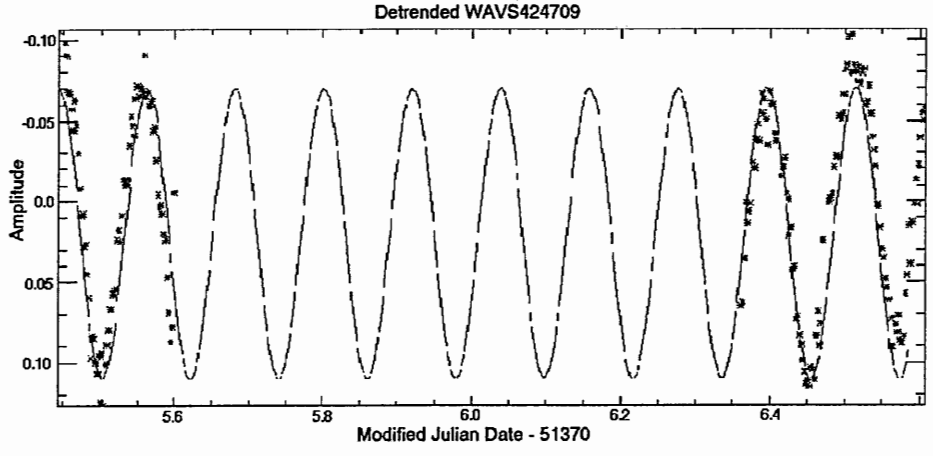

Figure 6.14: Fitted lightcurve of WAVS424709. Amplitude is in magnitudes with brightness increasing upwards.

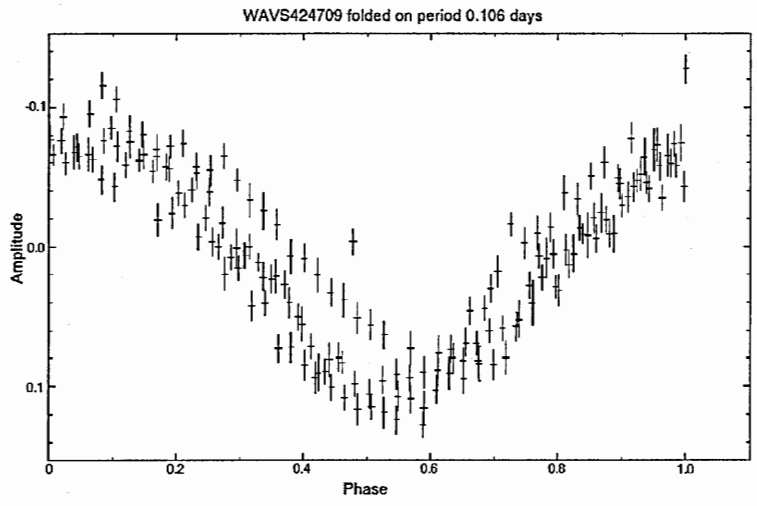

Figure 6.15: Lightcurve of WAVS424709 folded on period 1.106days. Amplitude is in magnitudes with brightness increasing upwards.

WAVS722796

WAVS722796 is also typical of several others found in the WAVS sample (Figure 6.16). The period of this system was calculated to be 0.131 days (3h 8m) and folding on this period revealed reasonable results (Figure 6.17). The lightcurve is consistent with that of an EW type binary system with an orbital period of 0.262 days (2 times the measured period). In an EW type system the components are in contact with each other and are of equal size, this leads to almost equal minima and no periods of constant light out of eclipse (Samus & Durlevich, 1998). Periods range from around 7 hours to a day, and two subclasses (A and W type) are distinguished on the basis of their period and spectral type, with the former showing earlier spectral types and longer periods (Sterken & Jaschek, 1996). The colours of this object (V_{max}=21.853±0.033, V_{min}=22.770±0.072, B-V=0.2±0.5=V-R 1.6±0.5) are compatible with a late A type star, leading to an EW-A type classification, but short period indicates a star of EW-W type. However some EW stars exist in the intermediate region and have been known to change between A and W type behaviour on periods of months or years (Sterken & Jaschek, 1996). A spectrum is not currently available for this object and while the EW classification is reasonably certain, a distinction between A and W types will have to wait for further observations.

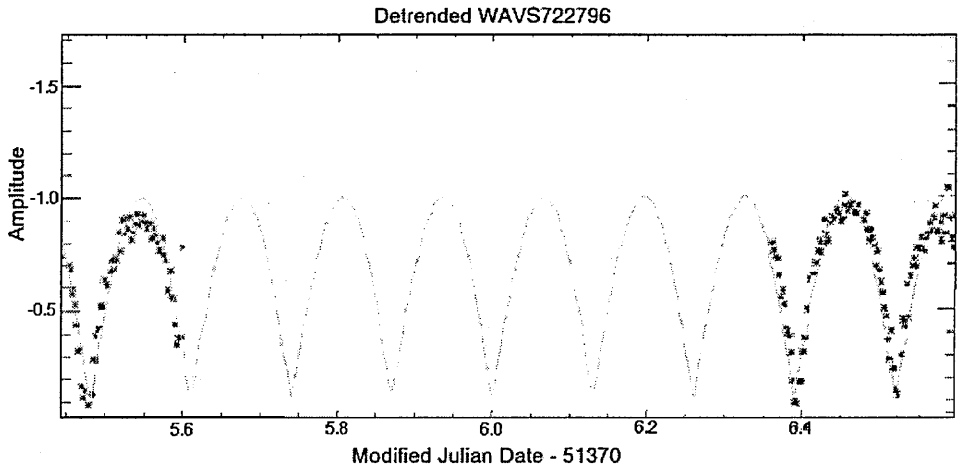

Figure 6.16: Fitted lightcurve of WAVS722796. Amplitude is in magnitudes with brightness increasing upwards.

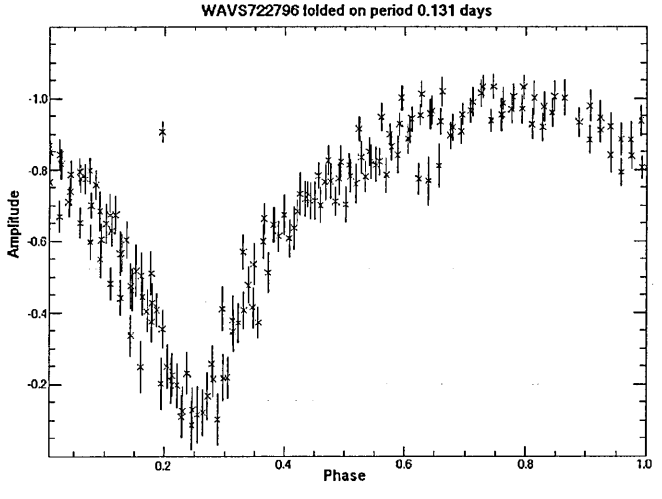

Figure 6.17: Lightcurve of WAVS722796 folded on period 0.131days. Amplitude is in magnitudes with brightness increasing upwards.

WAVS223551 (Better known as QU Vul)

Unfortunately for the project, the control star (QU Vul) slipped into one of the gaps between CCDs during the first night of observations, thus it is impossible to display the timeseries for both nights here. The night 2 timeseries is displayed in Figure 6.18.

Due to its short orbital period, the timeseries for the second night shows three eclipses, leading to a period of 0.11±0.01d which compares favorably with the literature value of

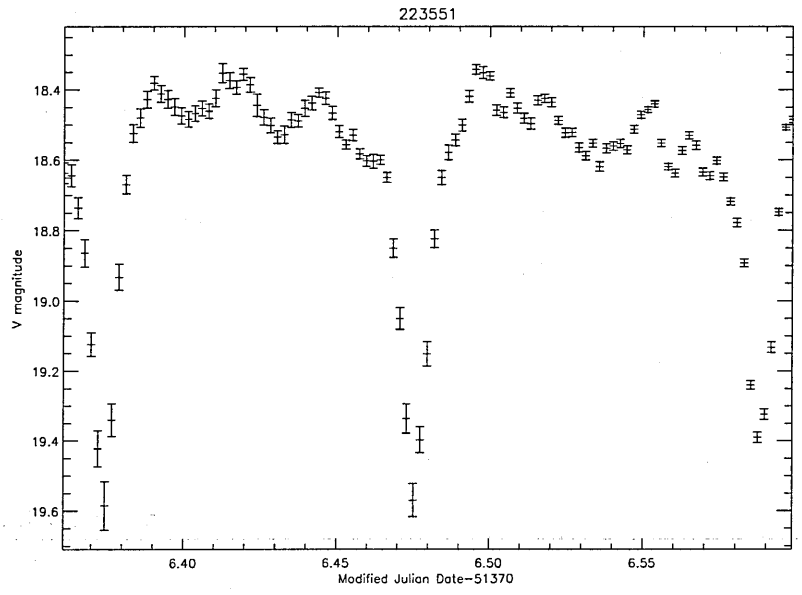

Figure 6.18: Night 2 lightcurve for QU Vul

0.111765d, especially considering the short dataset (Ritter & Kolb, 2003). Flickering is also visible in the lightcurve when the system is out of eclipse. Sadly QU Vul is not displayed here to be representative of all the eclipsing CVs in the sample as it was the only one found.

6.1.2 Possible Periodic Objects with Undefined Periods

The short timebase for the WAVS observations has meant that many systems have been found which are possibly demonstrating eclipses or longer period pulsating behaviour, but for which periods cannot be found accurately. In some cases this makes classification difficult. In this section some unique objects and some which are representative of subgroups will be discussed, although with the current lack of data, some of the groupings may be erroneous.

WAVS1020811

The lightcurve of WAVS1020811 is unfortunately only available for one of the two nights of observations, but the night 2 lightcurve shows an asymmetric variation typical of a pulsating star (Figure 6.19). The period of the pulsation is around 0.25 days with an amplitude of approximately 0.2 magnitudes. Although the curve does appear somewhat saw toothed, it may be rounded on the right hand side and an 0.25d period would make

it too short for a classical Cepheid. This is an acceptable period for an RR Lyrae type variable, specifically RRc type as RRab types generally have periods of the order of 0.4 - 1.0 days (Sterken & Jaschek, 1996). However, the decline from maximum brightness appears to be sharper than the rise which is unusual even in the more sinusoidal lightcurves of RRc type stars (Figure 6.20).

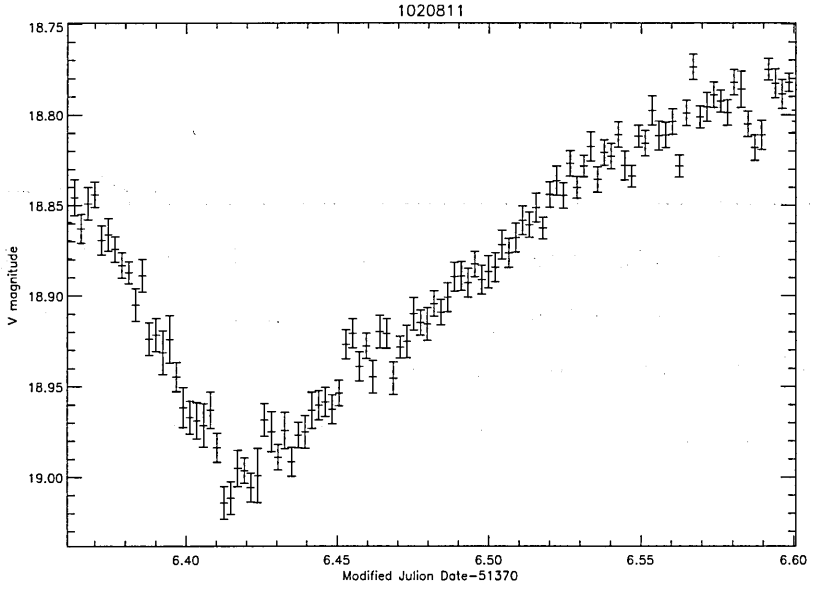

Figure 6.19: Lightcurve for WAVS1020811

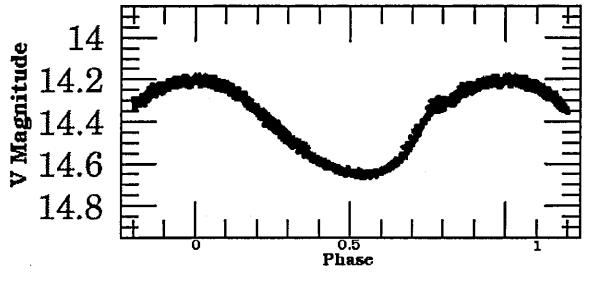

Figure 6.20: Phase Diagram for RRc Variable in M55 (Olech *et al.*, 1998)

The spectrum of WAVS1020811 (Figure 6.21) is quite noisy and contains many spectral features. At shorter wavelengths Ca, Fe and CH lines are prominent and the strength of the

Ca H and K lines relative to the CH Fe blend near 430nm lines suggests an early to mid G-Type classification (Figure 6.22). Assuming this, the best value for the dereddening correction was found to be E(B-V)=0.6. There is a strong emission feature at around 417nm which does not appear to be due to cosmic ray impact (Figure 6.23). However, the origin of this line is currently unclear and as only one spectrum was taken, it is difficult to rule out a cosmic ray origin entirely. The spectrum over plotted on Figure 6.21 is that of a G7 type star, which is inconsistent with an RR Lyrae classification (see chapter 1 section 1.2). Clearly the fit is in no way perfect but other spectral types proved worse and matching the spectral features has proved very difficult. Whilst some features such as the Ca H and K lines are fitted very well, many lines (eg the Ca I line at 422nm) are much stronger than in a standard G7 type star. There are also lines present that are not obvious in the G star spectrum at all, notable among these are the lines around 440nm and 450nm which may represent Ce and Zr respectively (it does not appear from the image that these lines are caused by bad sky subtraction). Certainly Hα absorption also appears considerably reduced pointing to an evolved star. It appears likely that this object is some kind of RR Lyrae type variable but further observations will be needed to confirm this.

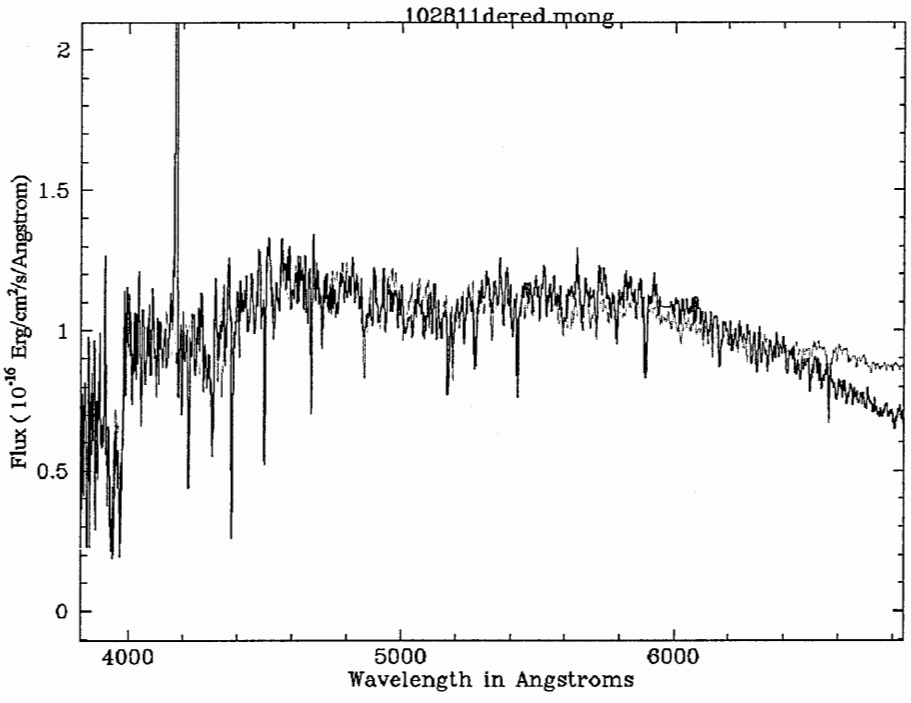

Figure 6.21: Smoothed spectrum of WAVS1020811 dereddened using E(B-V)=0.6. Over plotted in green is the spectrum of a G7 type star.

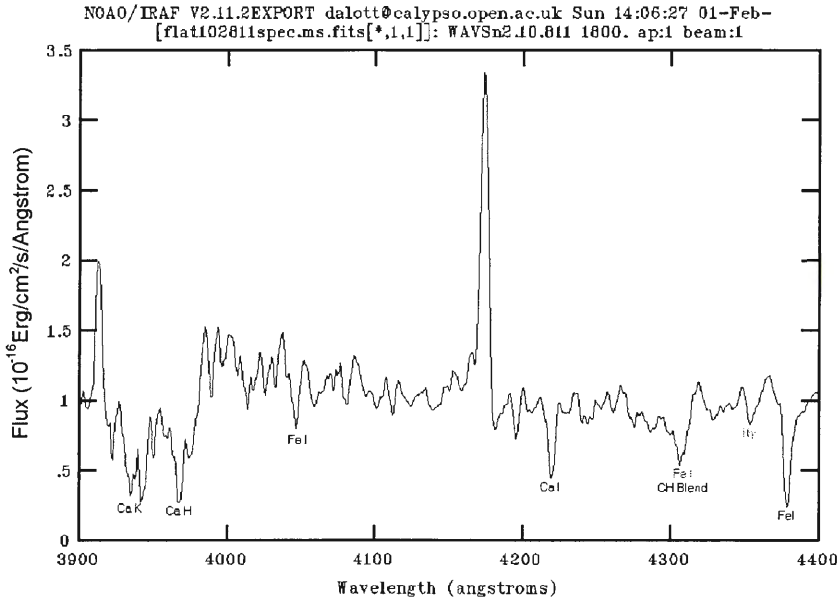

Figure 6.22: Close up of the 3900 to 4400 Angstrom region of the WAVS1020811 spectrum. Ca H and K lines are readily apparent as is the CH-Fe blend near 430 nm

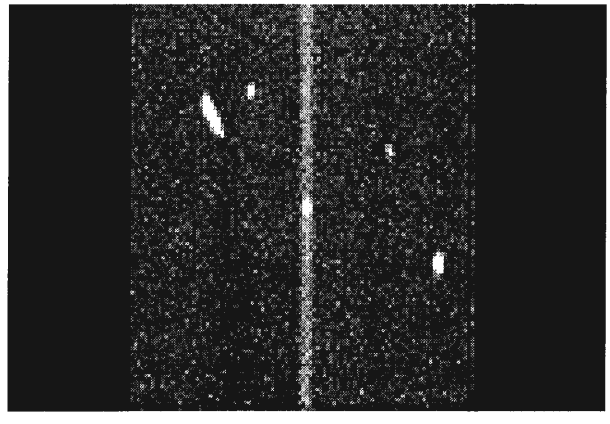

Figure 6.23: Image of the spectrum of WAVS1020811 around 417nm with possible emission line in the centre.

WAVS820318

WAVS820318 is another object which shows possible pulsations in its lightcurve (Figure 6.24). Again the period is just over 0.2 days and the amplitude is around 0.12 magnitudes. This time however, the decline from maximum brightness is less sharp than the rise and the object is most likely an RR-Lyrae star, probably type RRc. No spectra were taken for this star and unfortunately, as it was imaged only on the second night of observations, no colours are available. Once again, this object requires further study before a final classification can be made.

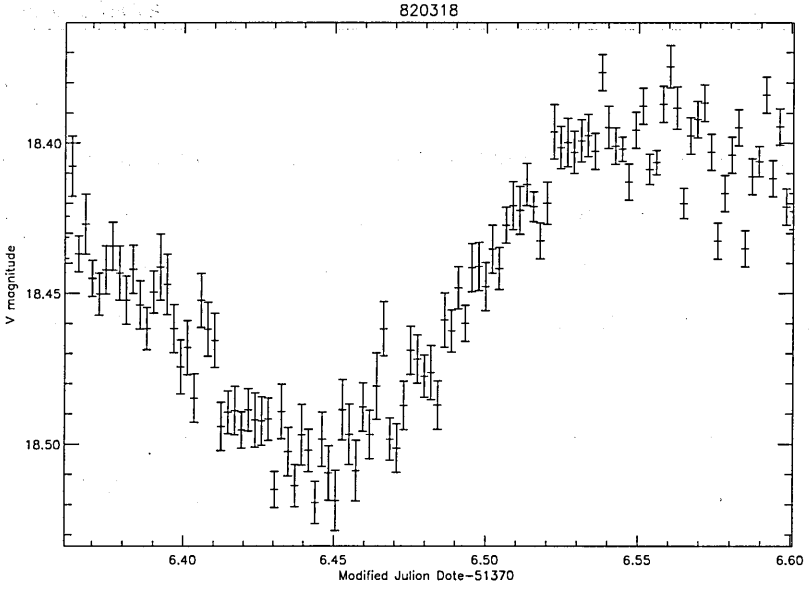

Figure 6.24: Lightcurve of WAVS820318

WAVS124251

This is another object for which only a single night's data is available. WAVS124251 appears to be an eclipsing variable, with distinctly different primary and secondary eclipses and no period of constant light (Figure 6.25). This object probably falls into the GCVS classification EB or Beta Lyrae type eclipsing systems. Stars within this classification can be in a number of different evolutionary states, from unevolved main sequence stars to semi detached binaries undergoing mass transfer, or even evolved objects with white dwarf companions (Sterken & Jaschek, 1996). The spectrum of WAVS124251 is shown

in Figure 6.26. A combination of A3 and G7 type spectra in an equal ratio, combined with dereddening of the WAVS124251 spectrum using E(B-V)=0.8 created the best fit. This combination makes a reasonable fit with the overall continuum shape and most of the major spectral lines. There are clearly more spectral features present than can be modeled by this simple method but an early and late type binary system seems the most probable classification for this object.

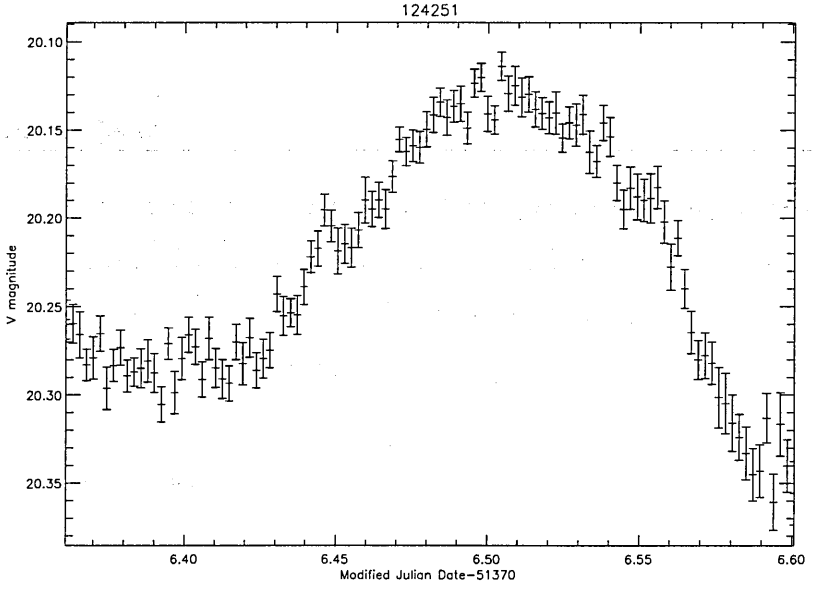

Figure 6.25: Lightcurve of WAVS124251

WAVS9921282

Like WAVS124251, WAVS9921282 shows two distinctly different minima, this time with a period around 12h. Again this star is a likely EB system, but the short period tends to suggest an EW type. There is some overlap between these two classifications however. EW stars are best modelled by assuming that both stars are in contact, with the more massive star transferring mass to its less massive companion. However, in some theoretical scenarios, thermal contact is broken from time to time and some EB systems have been observed with similar masses and periods to EW type binaries (Sterken & Jaschek, 1996). The colours of this object (V_{max}=20.896±0.018, V_{min}=21.305±0.032 B-V=1.4±0.4, V-R=0.4±0.4) suggest K type components which would be consistent with a classification

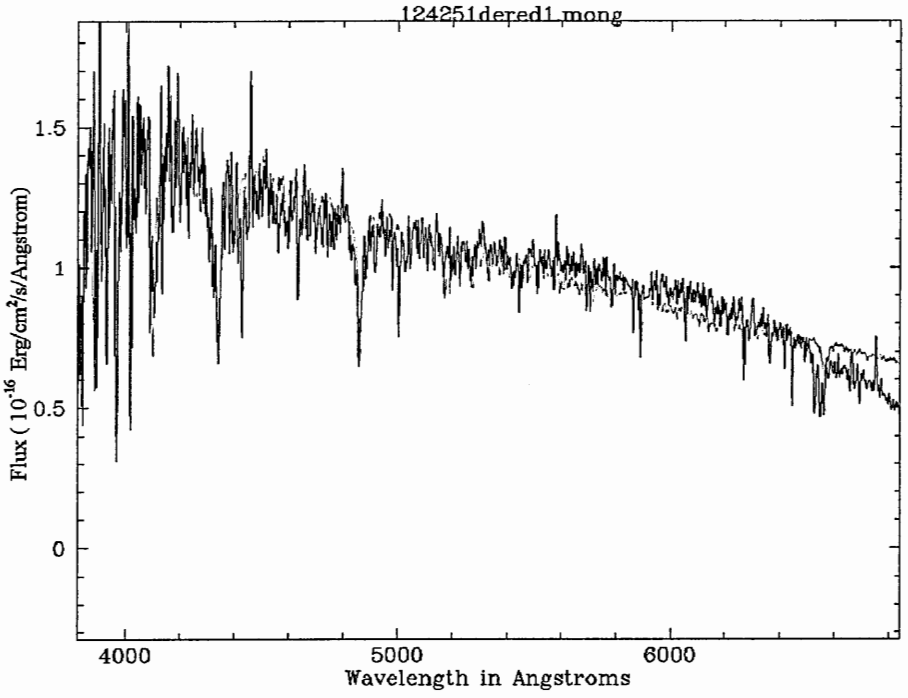

Figure 6.26: Spectrum of WAVS124251 dereddened with E(B-V)=0.8. An A3/G7 combination spectrum overplotted in red.

of a W-Type EW system.

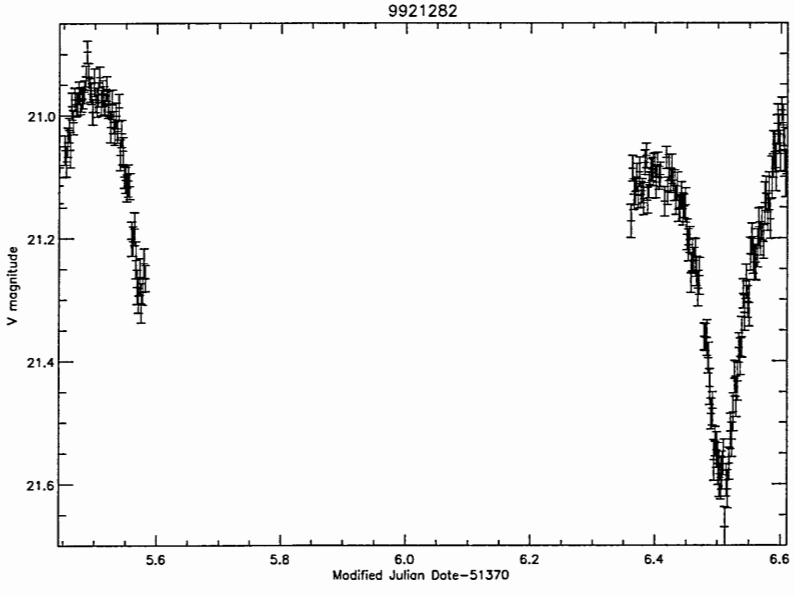

Figure 6.27: Lightcurve of WAVS9921282

WAVS120754

This object represents a class of eclipsing binary which display flat bottomed eclipses. The lightcurve of WAVS102754 shows a period of around 6h 50m and also appears to display a knee in the rising side of the primary eclipse, possibly implying that the system does not have a simple two body structure (Figure 6.28).

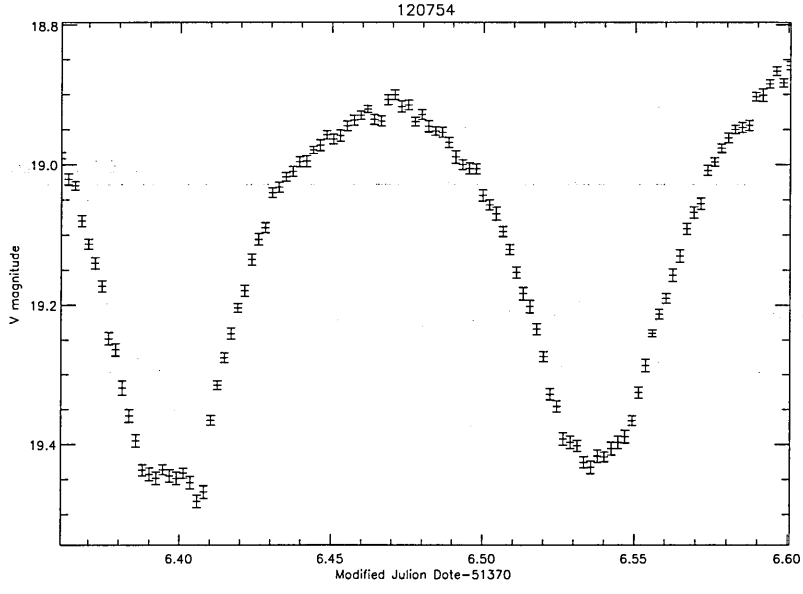

Figure 6.28: Lightcurve of WAVS120754

The flat bottom of the first eclipse necessarily means that the smaller of the two bodies is almost completely eclipsed by the larger during this interval, thus implying that the inclination of the system must be close to 90 degrees. Several spectra of this system exist, primarily because it was thought that hydrogen emission lines may have been present in the first spectrum imaged. On further examination of the WAVS120754 spectra this appeared inconclusive. However, a clear change in the spectrum (continuum shape, lines present) is apparent over the course of the orbital period (Figure 6.29).

Defining the start time of the first integration as phase 0 and using the calculated period of 410±6 minutes (with errors estimated from Figure 6.28), Figure 6.30 shows the behaviour of the Hα absorption line at various phases.

When considering this data it must be remembered that some temporal definition is liable to have been lost due to the 30 minute exposure times. That said the behaviour of

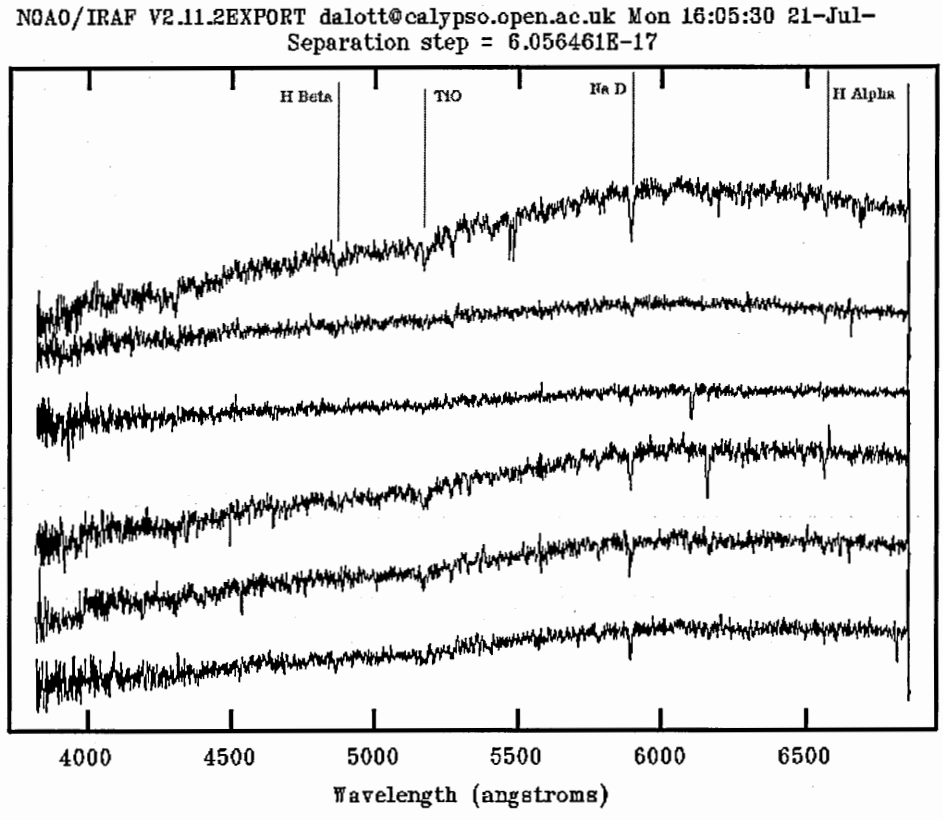

Figure 6.29: Variation of the spectra of WAVS 120754. Top four spectra taken in a 3 hour period. Bottom two spectra taken within a two hour period on the subsequent night.

the line is consistent with that of a high inclination binary, this will be discussed further below. At phase 0.15 the Hα line is no longer clearly visible. This would be consistent with the earlier type star of the pair being occluded by the later type object. Assuming that this is the case then phase 0 shows the earlier type object moving away from the observer (shifting Hα to longer wavelengths) and phase 0.28 shows the object moving towards the observer (shifting Hα to shorter wavelengths). Supporting this conclusion, at phase 4.16, Hα is again no longer clearly visible and at phase 4.43 is shifted even further to the left. Coming approximately one quarter of a cycle after minimum, this would be consistent with maximum observed radial velocity.

It is possible to obtain an order of magnitude estimate of the binary separation if several assumptions are made. Firstly that the inclination of the system is exactly 90 degrees, secondly that the stars follow circular orbits and thirdly that phases 0.15 and 0.28 represent points when the observed radial velocities are equal and opposite (Figure 6.31).

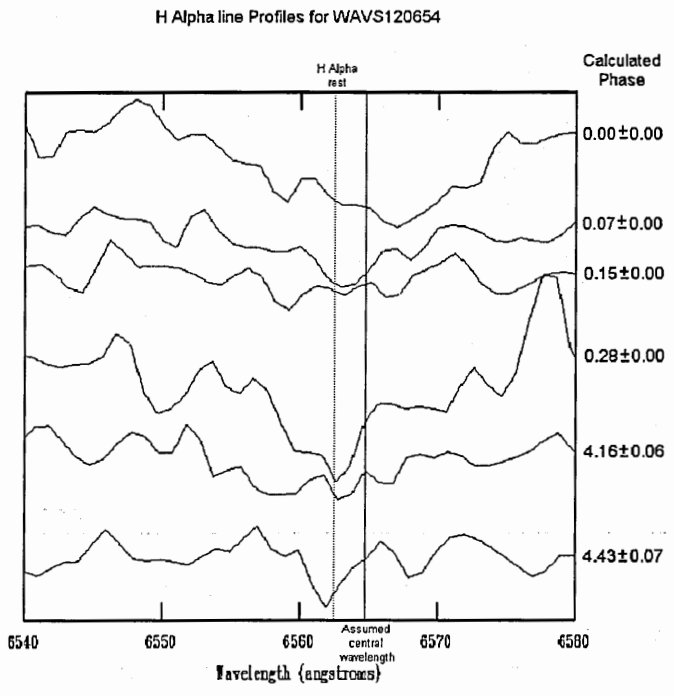

Figure 6.30: Variation of Hα line in WAVS120754. Phase is calculated from an arbitrary zero point at the start time of the first exposure using the calculated period of 410±6 minutes.

If this is true, then the point approximately between their corresponding wavelengths must not show any radial velocity variation due to the rotation of the system. Hence any offset between this value and the laboratory wavelength of Hα must be due to the velocity of the entire system relative to the observer v_γ. Using an assumed central wavelength of 6564.8Å (Figure 6.30) gives $\Delta\lambda$ equal to 2.3Å which translates to an approximate v_γ of 100kms^{-1} . To calculate the radial velocity of the system at the phase 0.28, $\Delta\lambda$ is now measured relative to the assumed central wavelength. Using an approximate $\Delta\lambda$ of 2.5 yields v_{obs} of 114kms^{-1}. At phase 0.28, the star is assumed to be one eighth of a period away from being in eclipse. Thus a rough estimate of the true velocity of the star is given by 114/(cos 45)=160kms^{-1}. The distance from the centre of the star to the centre of mass r of the system can then be calculated using $v=r\omega$ where $\omega=(2\pi/P)$, to obtain an order of magnitude estimate for r equal to 6×10^8m. This value is comparable to the Solar radius (6.96×10^8m), suggesting that this system may be a compact binary.

Comparison of the lightcurve of WAVS120754 with that of AE Phe, a W-type EW contact binary with a period of 0.36 days, shows a clear resemblance (Figure 6.32) (Sterken &

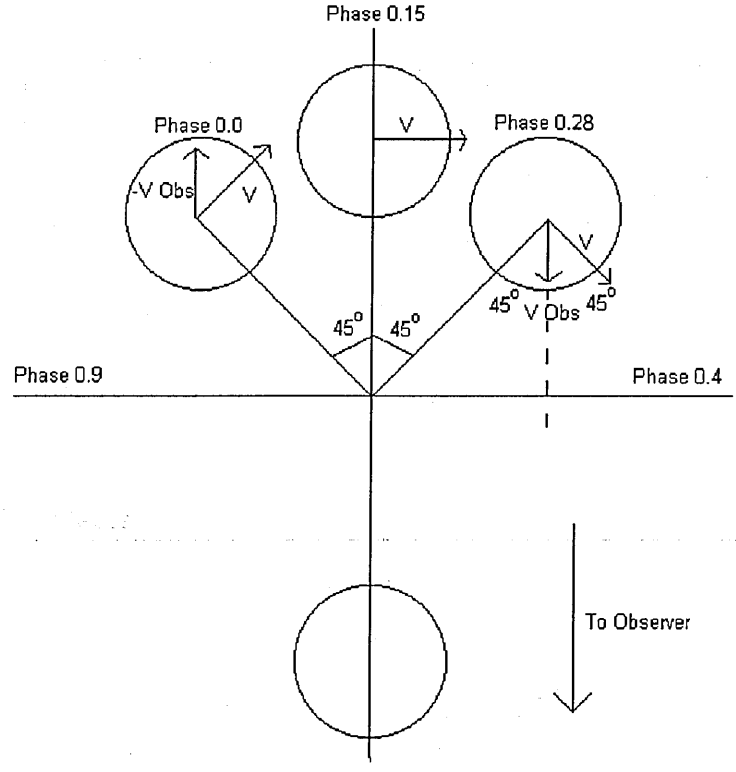

Figure 6.31: The figure describes the assumed orbital configuration of WAVS120754. All values are approximations and results are intended as an order of magnitude estimate only.

Jaschek, 1996). However, as the common envelope of a contact binary would have the same effective temperature throughout (Rucinski, 2004), this is not consistent with the spectral changes observed in WAVS120754. In conclusion, it would appear that WAVS120754 is a compact binary of some kind but that further observations are needed before a firm classification can be made.

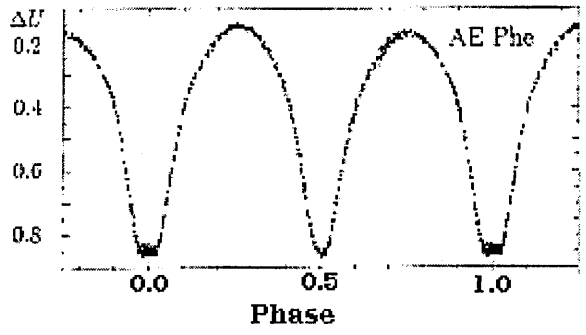

Figure 6.32: Lightcurve of AE Phe, y-axis is differential magnitude with respect to companion star HD9067 (Sterken and Jaschek, 1996, p185)

WAVS324886

Another object apparently displaying more structure than most eclipses is WAVS324886 (Figure 6.33). The night 2 lightcurve shows two distinct eclipses around 0.5 magnitudes deep. Doubling the interval between eclipses suggests $P_{orb} \approx 0.25$days . Both of the eclipses appear slightly asymmetric, particularly in the second eclipse around the point of minimum light and on the rising limb of the first eclipse. This behaviour may be consistent with a W-type EW star, possibly with an asymmetric lightcurve due to stellar spots.

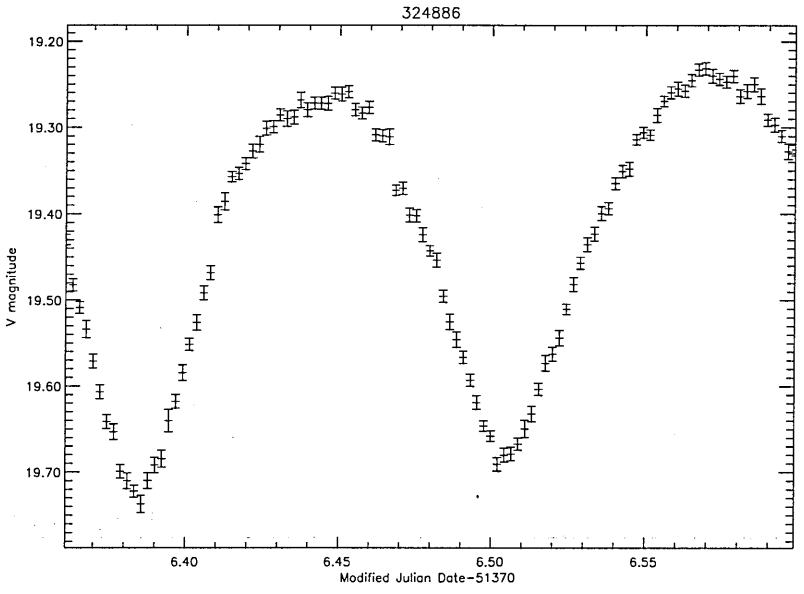

Figure 6.33: Lightcurve of WAVS324886.

The most satisfactory results for the spectrum of WAVS324886 were found by fitting with a G6 type star spectrum and dereddening using E(B-V)=0.8 (Figure 6.34). Although a two body structure is likely to be present, attempts to fit a combination spectrum were not successful. However, there are some spectral line deviations, most notably the lack of Hα and Hβ absorption and what appear to be two emission features around 450nm and 580nm. Possibly the lack of Balmer absorption could be due to evolved components, or perhaps emission features are also present and are masking the absorption lines. This may be consistent with the lightcurve of this object if asymmetries are real and are caused by the system not having a simple two body structure. In any event, WAVS324886 presents an interesting case for further study.

WAVS1020816

WAVS1020816 is another object that is clearly variable and possibly periodic, but for which no attempt can be made to discern a period. Unfortunately this object is not present in the data from the first night. The lightcurve of WAVS1020816 is displayed in Figure 6.35 and clearly shows a triangular eclipse and periods of constant brightness. The object probably belongs to the EA or Algol class in the GCVS system. It is not possible to tell whether a secondary eclipse is present but the large magnitude change (around 0.6

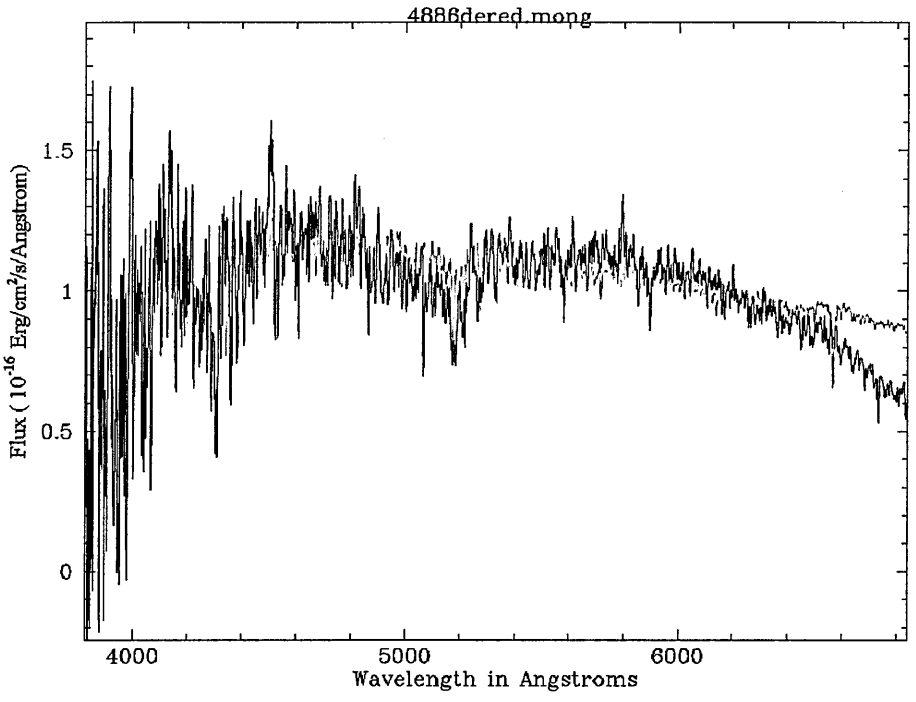

Figure 6.34: Spectrum of WAVS324886 dereddened with E(B-V)=0.8. The spectrum of a G6 type star is overplotted in red.

magnitudes) is consistent with this classification.

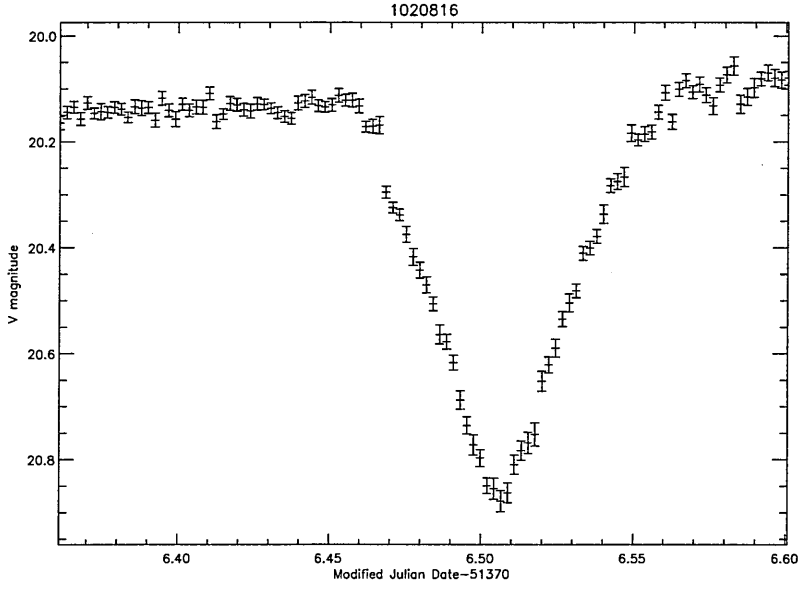

Figure 6.35: Lightcurve for WAVS1020816

The spectrum of WAVS1020816 is that of an M class star which seems to be showing some emission. A dM4e spectrum with dereddening using E(B-V)=0.1 gives a very good fit to all of the spectral features (Figure 6.36). As many as 85% of the nearest active dwarf stars are in binaries (Houdebine & Stempels, 1997) and this is consistent with the eclipsing behaviour. However, the lightcurve shows no evidence of any flaring or BY Draconis type variations when out of eclipse. Again, it will take further observations before this system can be finally classified.

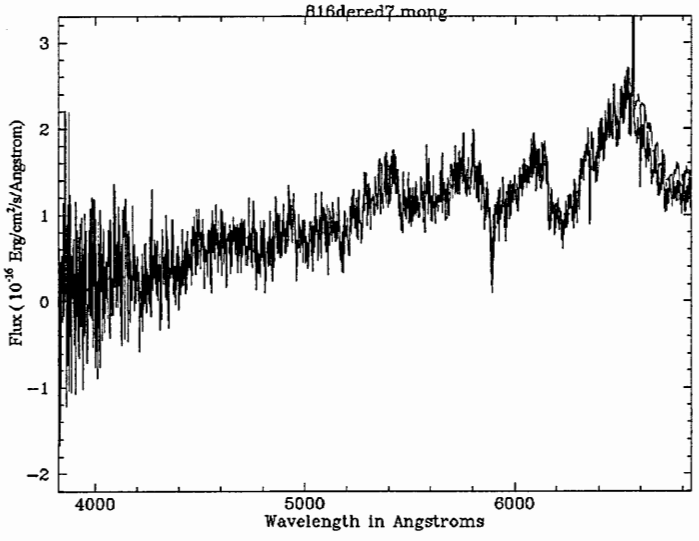

Figure 6.36: Spectrum of WAVS1020816, dM4e spectrum is overplotted in blue.

WAVS520989

The lightcurve of WAVS520989 (Figure 6.37) is interesting as it displays two of the shortest eclipses in the WAVS sample. The eclipse lasts only 36 minutes (in comparison to the 27 minute eclipse of QU Vul) and is around 0.2 magnitudes deep. The period of the object cannot be calculated from the current data, but it must at least be greater than 0.20 days (4.8 hours) and less than (or equal to) 0.95 days (22.8 hours). Unfortunately the colours for this object (V_{max}=20.265±0.013, V_{min}=20.475±0.019, B-V=1.3±0.1, V-R=1.3±0.1) were calculated using the HiRho CCDs and as such may well be spurious. No spectra have been taken at this time. The v-shaped eclipses suggest a grazing incidence binary - perhaps another EA type system, but only further observations will decide.

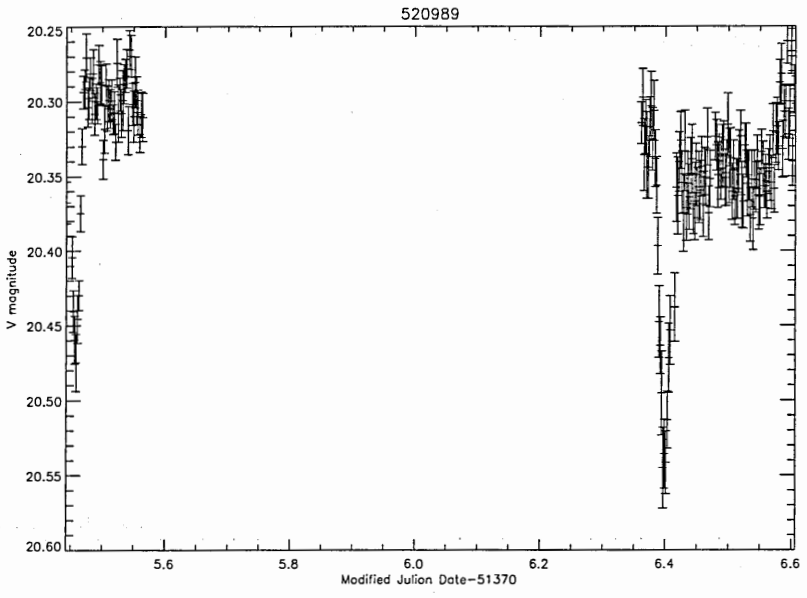

Figure 6.37: Lightcurve of WAVS520989

WAVS425674

WAVS425674 represents a group of objects discovered in the WAVS survey which are very difficult to classify. Clearly some variation is present in the lightcurve (Figure 6.38), but at present it is difficult to say what the source of the variation could be. B and R colours are not currently available for this object and without further observations there is really little that can be said about it. Frustrating as it is, objects such as these will have to wait for further observations before they can be correctly classified.

WAVS1123123

WAVS1123123 is another clearly variable object which is difficult to classify. The lightcurve shows what look like two eclipses, the first being $\approx$1 magnitude deep (Figure 6.39). However, it if this is a simple periodic object then it should have been seen to be going back into eclipse by the end of the night, instead the lightcurve seems to become increasingly noisy.

Whilst a spectrum of WAVS1123123 was taken it was unfortunately too weak to be successfully extracted. Although very little can be said about it currently, further observations of this object are certainly warranted.

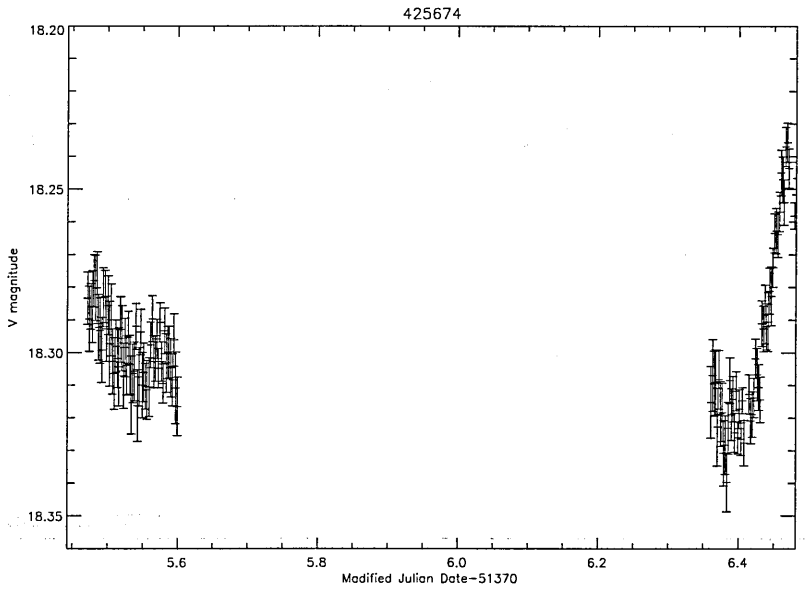

Figure 6.38: Lightcurve of WAVS425674

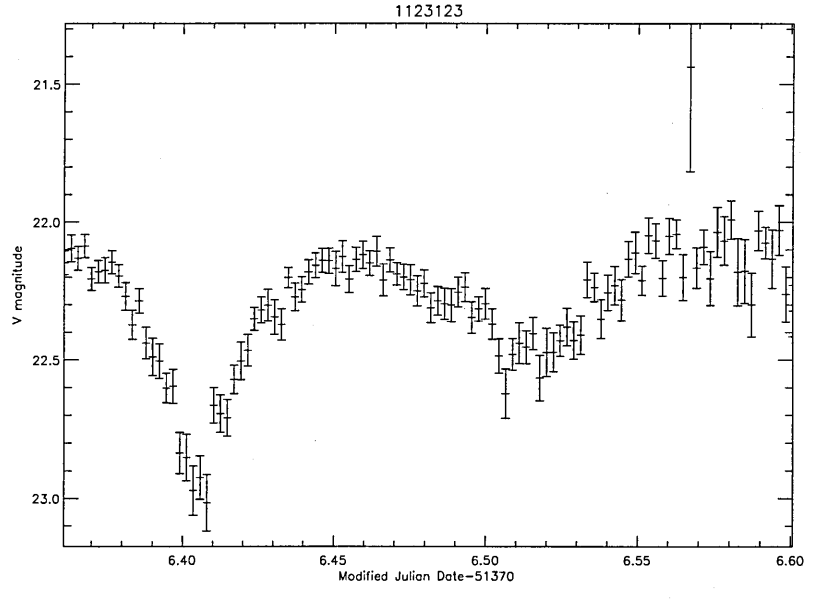

Figure 6.39: Lightcurve of WAVS1123123

WAVS710820 and other longer period objects

For some of the objects in the WAVS survey, (for example WAVS710820, Figure 6.40) it is impossible to say anything certain about the nature of their variability, except that it exists. In this case the object is most likely a longer period eclipsing system, but in

others it may be due to a pulsating star, or another type of long period variation. Only through observations with a longer baseline and spectroscopic followup will we be able to learn anything concrete about these systems and until then they will all have to be classed together as longer period variables.

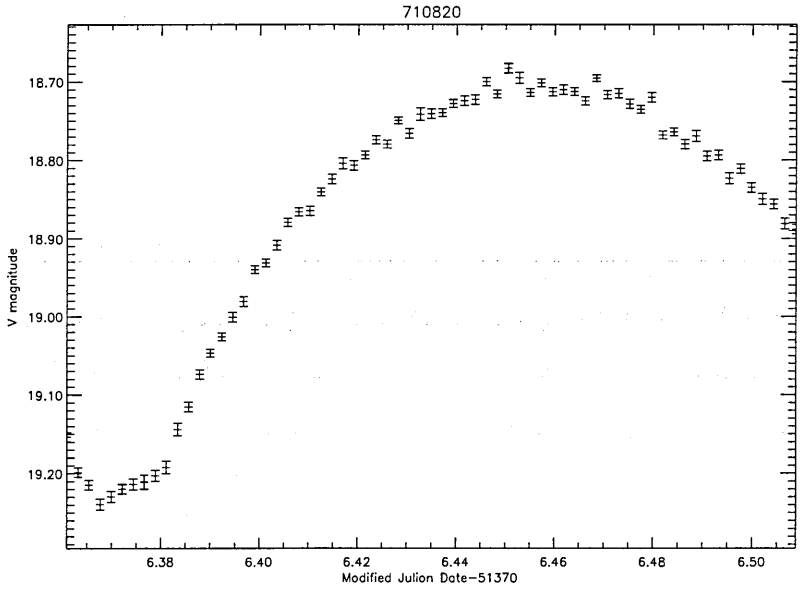

Figure 6.40: Lightcurve of WAVS710820

6.1.3 Non-Periodic Variable Objects

This section will cover those objects that are clearly variable but are not obviously periodic. The WAVS survey captured a number of these objects, although of course this cannot be considered to be a complete census of all the irregularly variable objects in the field, as it is quite possible that many of these were not in a period of eruption at this time.

WAVS323426

WAVS323426 was observed on both nights of the observing run, but only on one of these occasions did it exhibit variability. The lightcurve of this object on the second night of observations undergoes a brightening event with a variation of approximately 1 magnitude and duration under an hour (Figure 6.41). This behaviour of almost instantaneous rise and rapid fall is consistent with a fast stellar flare as displayed in the flare star EV Lac

(Figure 6.42).

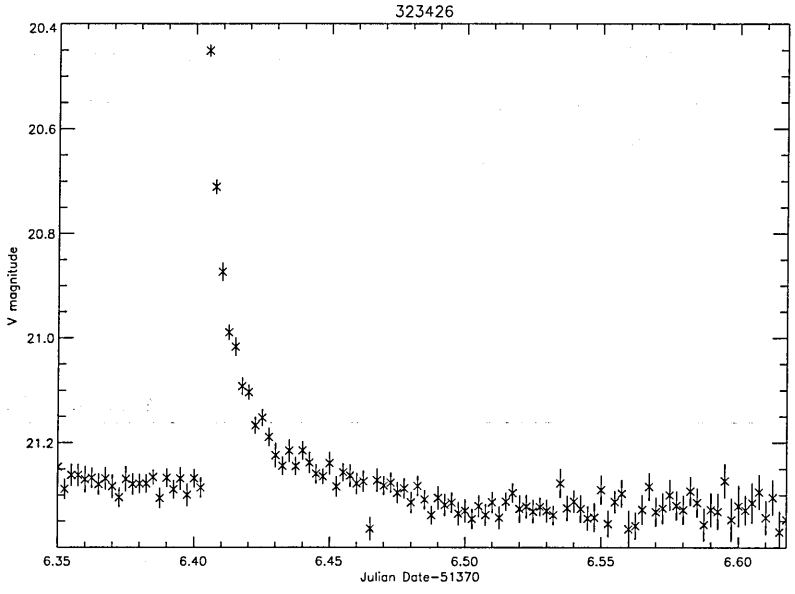

Figure 6.41: Lightcurve of WAVS323426

The spectrum of this WAVS323426 is, unfortunately, rather noisy due to the faintness of the object (V = 21.30±0.02) (Figure 6.43). However, it does appear to be reasonably similar to a K type star. Whilst most flare stars are type dMe (M-emission), K type objects are also common (Sterken & Jaschek, 1996) and as no emission lines can be seen in the spectrum, seems a reasonable classification for WAVS323426.

WAVS920239

The lightcurve of WAVS920239 also displays a flare event, but this time one which lasts for over three hours. The magnitude change in this case is around 0.2 and the rise to maximum brightness is well resolved (Figure 6.44). This behaviour is reasonably consistent with a slow flare and the spectrum of this object reveals a dMe type star with obvious emission lines from the hydrogen Balmer series (Figure 6.47). Comparison with a slow flare on EV Lac (Figure 6.45) highlights some differences between this event and a classic slow flare though, specifically it appears to have a more rounded peak and does not appear to return to its pre-flare magnitude. However, flare morphology is varied and poorly understood and it is possible that this flare has more in common with plateau dominated flares such

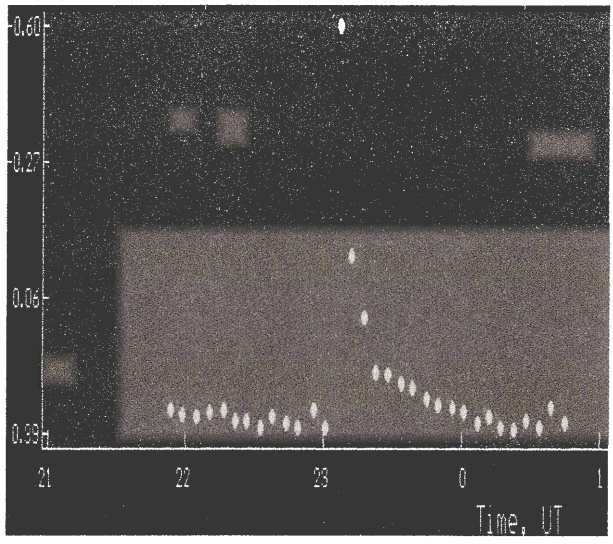

Figure 6.42: Lightcurve of EV Lac during a fast flare (Sea of Galilee Astrophysical Research team, 1995)

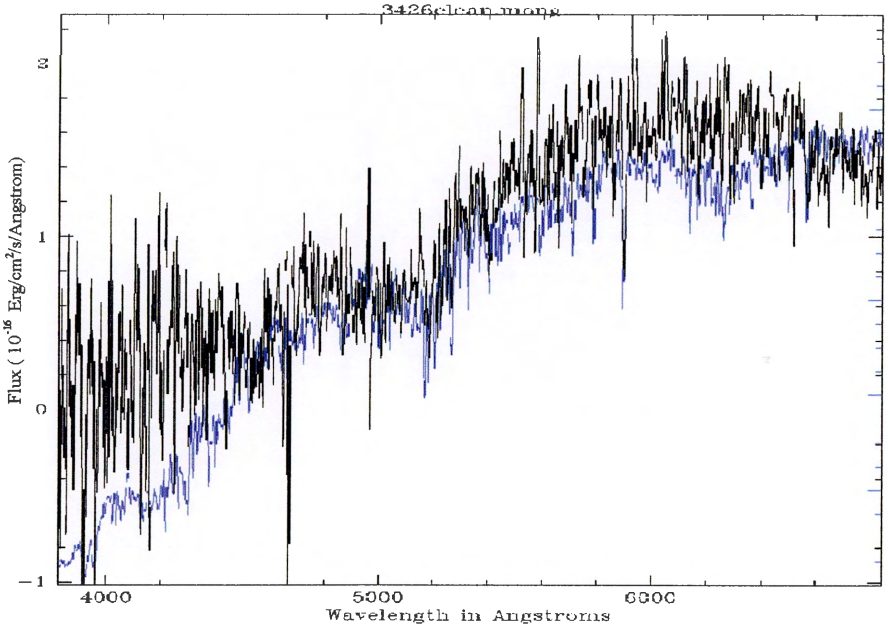

Figure 6.43: Spectrum of WAVS323426 (dereddened with E(B-V)=0.6), with a K4 type spectrum overplotted in blue (K4 spectrum is offset for clarity).

as those seen on AD Leo than the simple slow flare case, Figure 6.46 (Sterken & Jaschek, 1996).

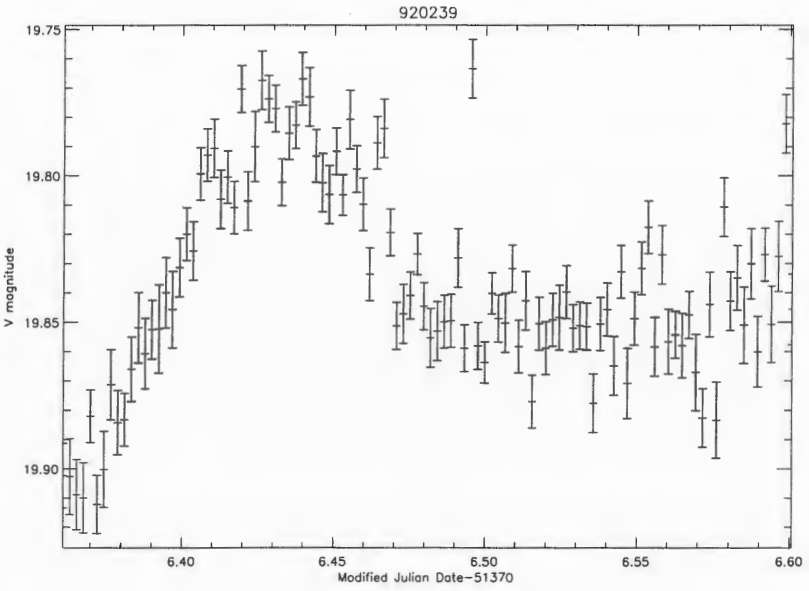

Figure 6.44: Lightcurve of WAVS920239

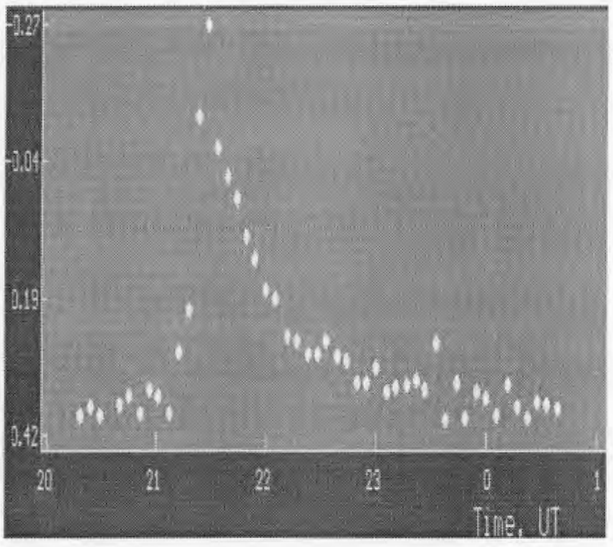

Figure 6.45: Slow Flare on EV Lac (Sea of Galilee Astrophysical Research team, 1995)

Flaring behaviour of this kind is generally associated with the interactions of magnetic fields and stars of this type are often spotted and show BY Draconis type variations. Only further study will verify whether this is the case or not in both WAVS323426 and WAVS920239

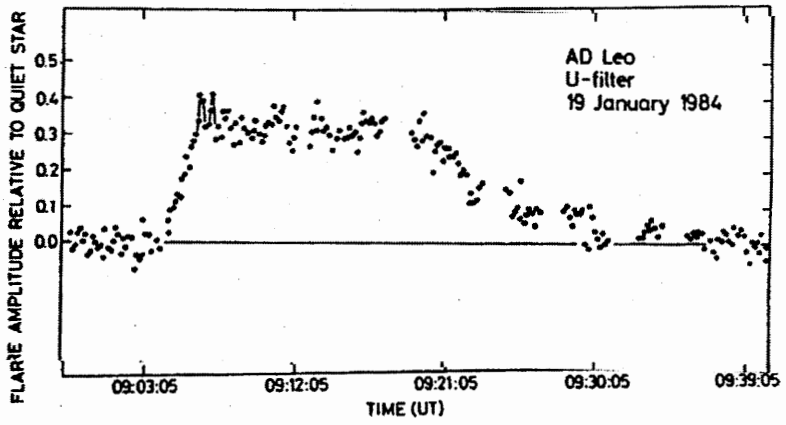

Figure 6.46: Slow Flare on AD Leo (Sterken and Jaschek, 1996, p58)

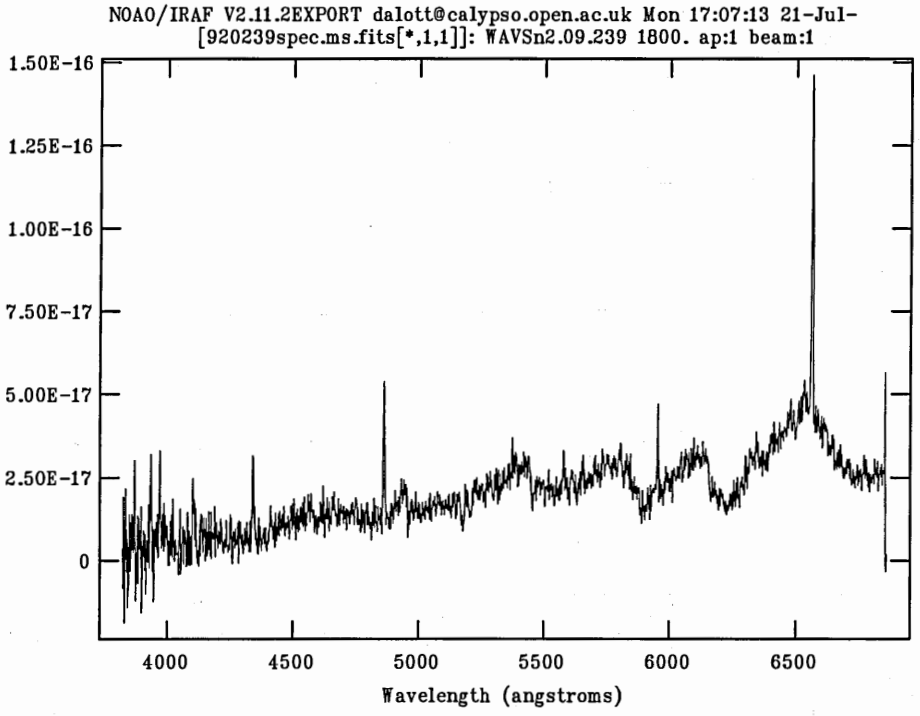

Figure 6.47: Spectrum of WAVS920239 showing prominent emission from the hydrogen Balmer series

WAVS9925398

This star is included not as it is particularly interesting in itself, but because it represents a subset of objects that were important to this survey. WAVS9925398 is one of a number

of lightcurves which were considered to be flickering by the WAVS survey. This star and others like it do appear to show stochastic variations in their lightcurves in the manner that would be expected for a CV (Figure 6.48). Unfortunately, most of these objects were extremely dim and good spectra for them could not be obtained with the NOT. In cases where a spectrum was taken the results were generally uneventful with none of the objects displaying emission, or even a particularly blue spectrum. Obviously this result was somewhat disappointing for the survey but the possible meaning and ramifications of it will be discussed in more detail later.

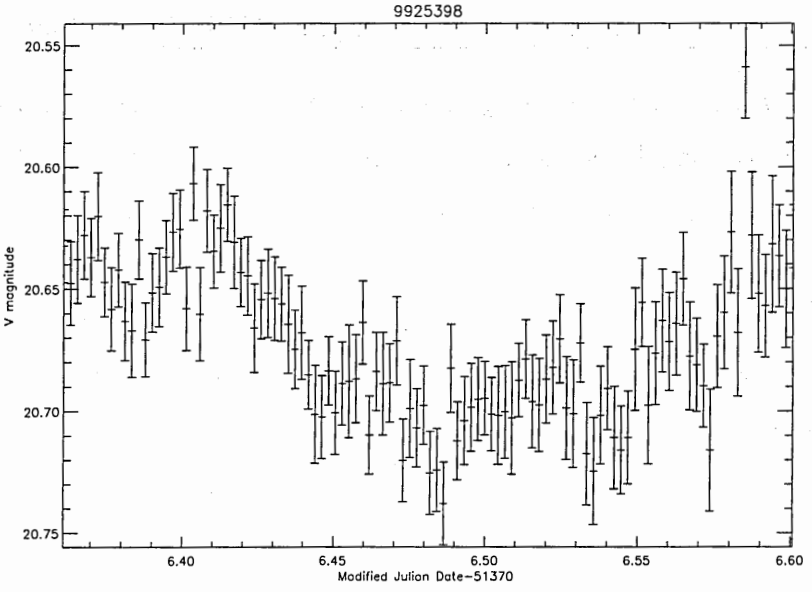

Figure 6.48: Lightcurve of WAVS9925398

6.2 Populations in the WAVS Sample

Having considered some of the individual objects discovered in the WAVS survey, attention must now be turned to the population statistics uncovered by the programme. Firstly in terms of the total population of objects, and then in terms of variables and variable subtypes.

6.2.1 Overall Population of Objects

Figure 6.49 shows two V-R vs B-V colour diagrams, one for a Galactic field (Spagna *et al.*, 1998) and the other from CCD2 of the WAVS sample.

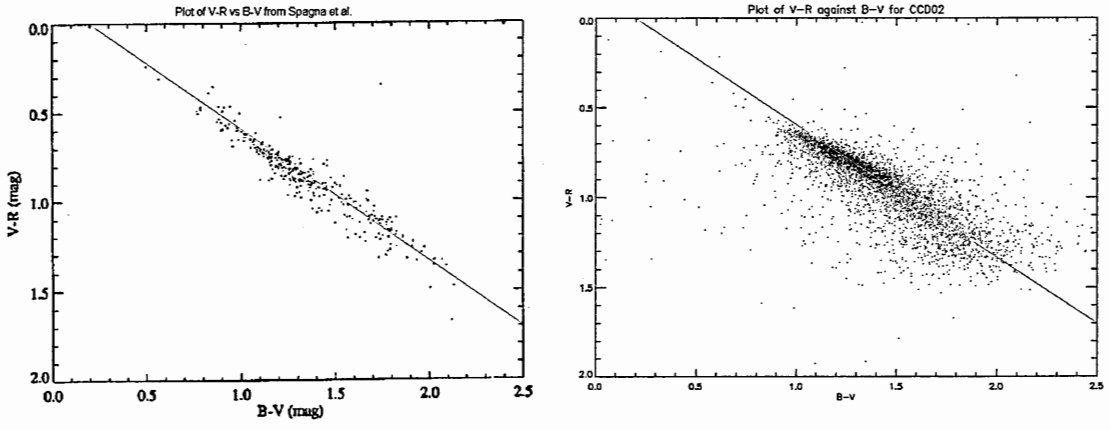

Figure 6.49: V-R vs B-V plots for WAVS sample (right) and a Galactic sample taken from literature (left) (Spagna *et al.*, 1998). The equation of the red line on both plots is the same and is included to aid comparison.

The two distributions are clearly similar, this is as expected, as the WAVS sample also covers a Galactic field. The effect of interstellar reddening on the two samples seems approximately the same, although any difference would be manifested by a translation of the distribution along the slope of the red line (Spagna *et al.*, 1998). The similarity of the two plots is confirmation that the colour calibration of the WAVS data has been done correctly.

In total the WAVS survey detected around 66000 objects down to approximately 23rd magnitude, however, many of these detections were spurious, caused by bad columns, rows and saturated stars. The true number of stars investigated by the survey was nearer 52000. A search of the SIMBAD astronomical database yielded no previously known variables within this field (other than QU Vul). The shortest variation detected by the survey was the 18 minute eclipse of QU Vul, but the limiting resolution of the survey was closer to 9 minutes i.e. two low data points may have been considered spurious, three would have been investigated further (although this also depends upon the magnitude of the variation). Unfortunately, due to the lack of calibration data on night 2 and the

offset of the field between the two nights, night to night variations have not been detected and the longest timescale covered will be on the scale of 0.25 days. In total the WAVS survey has detected 230 variable stars with a sensitivity of around 0.05 magnitudes at 18th magnitude, 0.1 magnitudes at 21.5 magnitude and 0.3 magnitudes at 22.5 magnitude. 142 of these have B,V and R colours available. This leads to 1 star in every 230 measured being variable within these limits. The positions and magnitudes of all of these variables are displayed, along with their lightcurves in Appendices A to C.

6.2.2 Individual Variable Types

Classifying the variables found in the WAVS survey has proved difficult due to the small amount of information currently available for many of the objects. However, classification has been attempted with ten main categories defined. For some types of object (such as EA systems) the classification is reasonably certain from the lightcurve behaviour, other categories however are necessarily much broader. The ten categories defined for the WAVS survey are:

- EA Type systems
- EB Type systems
- EW type systems
- Sinusoidal objects
- Asymmetric pulsating objects
- Flare stars
- Longer period systems
- Unclassifiable objects
- Flickering systems
- Confirmed CVs

EA Type objects

EA type systems have reasonably unique lightcurves (constant light between eclipses, see section 1.3.2) and as such are easy to classify when the observational baseline is long enough. However, as this is not always the case, the EA category is split into those systems

which are probably EA systems, and those for which only a more tentative classification can be made. In total 36 objects are placed in this category. The relative size of this population is discussed below.

Table 6.1: WAVS objects classified as EA systems

Probable EA systems	Possible EA systems
313606	213561 511194
410719	9911373 913919
811611	110012 1110706
911605	9922148 9920421
9922720	9925201 322568
223345	323495 324293
320673	721075 722455
520989	722785 720385
724281	823022 824798
724454	925382 1026691
1020816	1120553 1124317
1120794	1122543
1122083	

EB type objects

Again, where the observational baseline is long enough, EB systems are reasonably easy to classify from their lightcurve behaviour (no period of constant brightness - again see section 1.3.2). However, in cases where eclipses are a similar depth, there is some confusion between EB and EW types (as discussed previously) and this may lead to some misclassification of objects. The EB systems have also been split into two subgroups, with 43 objects in total.

Population statistics derived from the MACHO project (Alcock *et al.*, 1997) show a relative frequency of observation for EA and EB stars of approximately 3:1. This result is clearly inconsistent with the WAVS data which shows more possible EB type systems than EA. However, given that the period of many EA type systems is far longer the longest period that could be reliably detected by this survey, this result is not unexpected.

Table 6.2: WAVS objects classified as EB systems

Probable EB systems	Possible EB systems
1011862	210343 214524 313839
9923670	410352 515485 810308
122677	916424 1111582 9923598
124251	9924142 120858 221850
524006	123169 222899 224858
820163	422265 424393 722830
1020575	320042 723995 824576
1022130	922754 924140 925010
1021706	925282 925299 112012
1021699	1120804 1122055 1122550
1021970	1123123
1023127	

EW type objects

For the most part, the unique behaviour of the lightcurve in EW systems makes classification reasonably simple (although the same proviso which applies to EB systems also applies here). For this reason the classification is not split into subsections and contains 18 objects in total.

A population of 18 in the WAVS survey would mean that one in approximately 2900 objects was an EW type system. This is somewhat outside of the one in 500-2000 estimate given by Rucinski (Rucinski, 1993). Taking into account that a survey of this kind is likely to miss around 10-15% of this type of system due to low inclination angles (Rucinski, 2001) leads to a value of 1 in 2500, which is still outside of Rucinski's range. This however does not take account of the small statistical size of the WAVS sample. Assuming Poisson statistics gives 18±4 for the the expected number of systems or 1 per 2000-3150 which could just be consistent with Rucinski's statistics. This figure though, is obviously affected by the split of objects in the WAVS programme between EB and EW. In fact a more recent survey, again by Rucinski (Rucinski, 2002) considers both of these populations together, along with the population of systems designated as ELL or ellipsoidal variables. This results in a space density of $(1.02\pm0.24)\times10^{-5}\mathrm{pc}^{-3}$ for these EB, EW and ELL

systems giving an occurrence rate of one in 500 with an uncertainty of around a factor of 2 (Rucinski, 2002). Considering the possible EW and EB systems in the WAVS sample gives an occurrence rate of around 1 in 850 systems (assuming that all of these systems have been classified correctly). If half of the sinusoidal variables (discussed next) are ellipsoidal variables then this would mean that around 1 in 750 of the systems in the WAVS sample were EB, EW or ELL which, correcting for inclination and assuming Poisson statistics, results in a population of 1 in 570 to 730 systems, in good agreement with the Rucinski result. Obviously though, with the difficulties associated with the correct classification of these lightcurves, these results are by no means absolute.

Table 6.3: WAVS objects classified as EW systems

Probable EW systems
9921077 9921649 9921282
9922370 120732 120754
125590 321830 324886
420470 424233 524766
721327 722796 821760
1020614 1022265 924548

Sinusoidal objects

This classification contains objects which have reasonably sinusoidal lightcurves. As such it probably covers both ellipsoidal systems and some types of sinusoidal pulsating objects. Without further spectral follow-up it is difficult to separate the two however, and so for now they must be classified together. In total, this classification contains 17 objects.

Table 6.4: WAVS objects with sinusoidal lightcurves

Sinusoidal Objects
9912425 714642 120108
120861 126212 225125
323815 424709 425581
520129 520260 521176
820051 823301 1025220

continued...

Table 6.4: continued

1120387 1122602

Asymmetric pulsating objects

This classification includes all of the WAVS objects which appear to have asymmetric variations in their lightcurves indicative of pulsating objects (particularly RR Lyrae type variables). Some objects with asymmetric eclipses may have been erroneously included but there is little that can be done to remedy this without further observations. As before objects are split into probable and possible subsections, with 24 objects in total.

RR Lyrae stars constituted 20% of the variable objects discovered by the MACHO collaboration in their survey of the Large Magellanic Cloud (Cook *et al.*, 1995). The distribution of periods was such that all of the detected objects had periods of less than one day (Figure 6.50).

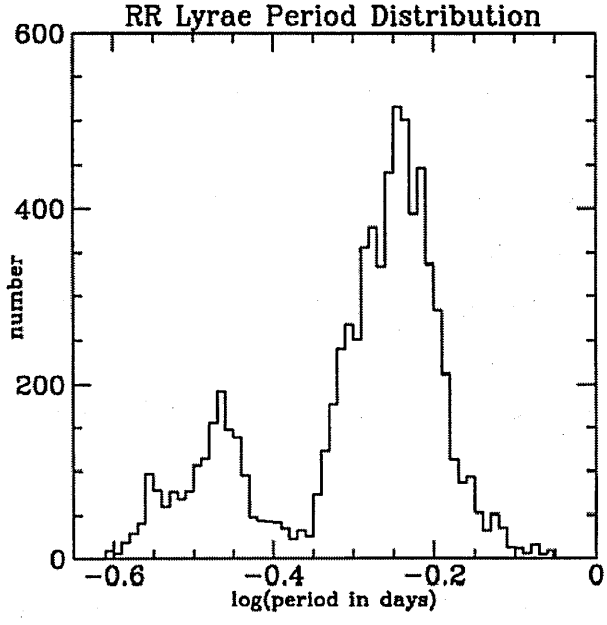

Figure 6.50: Distribution of periods for RR Lyrae stars discovered by the MACHO project (Cook *et al.*, 1995)

In this time the star has to rise to maximum amplitude and then fall again, i.e the

rise to maximum amplitude takes half of this time (0.5 days), thus, within the limits of the WAVS observations (0.25 days) we would expect to see at best an increase in brightness equal to half the total amplitude and at worst, half of this (if the object was first observed rising and then falling). At 21.5 magnitude, WAVS would be sensitive to all RR Lyrae stars with an amplitude of 0.4 magnitudes or greater, i.e. (sensitivity limit (0.1) $\times$ maximum rise time in days(0.5)) / (WAVS time detection limit as a fraction of rise time(2)). Some RR Lyrae stars do vary with amplitudes below this level, although most do not. Given the increasing sensitivity limitations of our survey at higher magnitude, a reasonable estimate would be that 75% of the MACHO sample would have been detected by WAVS, hence we would expect $\approx$ 15% of detected variables to be of RR Lyrae type. If all of the asymmetric pulsating objects discovered in the WAVS survey were of RR Lyrae type then this would represent 10% of the variable population. Whilst this is not likely, there will be some RR Lyrae stars currently classified as sinusoidal objects and still more that are currently amongst the longer period or unclassifiable systems. Once these stars are correctly identified, it is possible that to be the number of RR Lyrae stars discovered by WAVS will be comparable with that discovered by the MACHO project.

Table 6.5: WAVS objects classified as asymmetric pulsating systems

Probable asymmetric pulsating systems	Possible asymmetric pulsating systems
9910759	9911311 110517
9913058	214671 415432
312909	514059 711419
713423	713236 713294
111108	1111038 1112722
422257	424750 820318
722836	1020811 1121781
724012	1121811 1123900

Flare stars

The WAVS survey uncovered 4 possible flare stars, two of which have been reasonably confirmed (WAVS323426 (fast) and WAVS920239 (slow)) and two of which require follow-up. These two stars (WAVS921760 and WAVS912537) appear to be fast flares with much

smaller amplitude than WAVS323426 (around 0.2 magnitudes compared to 1.2 magnitudes). Further work to confirm the nature of these objects is currently being undertaken by Carole Haswell and Ben Eves.

Longer period systems

Due in part to the unfortunate loss of objects caused by the offset of the field between nights, many WAVS variables have too short an observational baseline to be classified properly. They could be longer period eclipsing systems, Cepheid variables, or objects of another kind entirely. They have currently been grouped together as longer period variables and require more photometry before they can be classified properly. There are currently 45 objects in this category.

Table 6.6: WAVS objects with longer period lightcurves

Longer period objects
1111665 214289 214356 214595
312118 312809 318450 410411
414869 411515 415423 511639
710820 711043 711848 710477
712878 711566 712650 811481
812619 911591 917017 1012756
1111037 1111626 1112342 1111648
1110575 121830 224978 424508
524898 720134 720553 720639
721329 721426 723809 720868
721429 721846 1021941 1122288
1125498

Unclassifiable objects

These are objects which clearly show variability but which cannot be easily classified into any of the other groups at this time. An example of such a system is WAVS425674 discussed earlier in the chapter. Without considerably more photometry and where necessary spectroscopy it will be difficult to say any more about these objects. However, the 9 members of this class are likely to be very interesting objects.

Table 6.7: WAVS objects which are currently hard to classify

Unclassifiable objects
322587 325367
424049 424548
425674 520528
721865 924414
1023437

Flickering Objects and Confirmed CVs

At this stage in the project the only confirmed CV discovered in the WAVS sample is QU Vul, the control object. There are however some 30 systems that remain possible CV candidates. These objects show variations in their lightcurves that may be consistent with flickering but only extensive follow-up observations will confirm or deny this.

Table 6.8: Possible flickering objects

Flickering objects
9910756 9910773 115380
310125 517946 516819
521150 915011 9920733
9925398 122458 123229
220487 222584 224129
320340 321522 421398
520714 523070 720195
720911 723193 724897
721971 723509 821344
824349 922412 925132

6.3 Discussion

6.3.1 The WAVS sample and Cataclysmic Variables

Obviously the lack of confirmed new CVs has been a disappointment to the project, but this null result may still yield useful scientific information. Considering the total number of stars covered by WAVS (52000) we can now go back to the competing population estimates and see if a conclusion can be reached. The average space density of stars in the local area is around 0.12 pc^{-3}, and the observed population of CVs has a space density of $\approx 1 \times 10^{-6} pc^{-3}$ (Patterson, 1984). Schreiber and Gänsicke (2003) calculated a lower limit of $\geq 1 \times 10^{-5} pc^{-3}$ for the CV population density based on the observed population of Pre-Common Envelope Binaries (PCEB) and Kolb (2001) gives a theoretical prediction for CVs of $\approx 1 \times 10^{-4} pc^{-3}$. Using these figures, a population of 52000 stars is likely to contain 0.43 CVs (using the observational estimate)and 43 CVs using the estimate provided by theory. Due to the detection limits of the survey however, we would not expect to be able to detect flickering in all of the 52000 objects. On the timescales observable by the WAVS project, known CVs tend to exhibit flickering with amplitudes above the 0.1 magnitude level (Bruch, 1992). This means that (using the values calculated in chapter 4) at least 61% of stars with characteristics similar to known CVs would have been detected. However, most known CVs demonstrate flickering in excess of this, with values above 0.2 or even 0.3 magnitudes reasonably common. Based on the above considerations and the number derived in chapter 4 (71% at amplitude 0.2 and 91% at amplitude 0.3) a good estimate would be that 75% of CVs with characteristics similar to the known population of CVs would have been detected by WAVS. Hence, for a population of 52000 stars we would expect to detect 0.32 CVs using the observational estimate and 32 CVs using the theoretical estimate. Although further follow-up of the WAVS sample is to be undertaken by Haswell *et al.*, it seems unlikely that all of the 30 possible flickering objects will be CVs. Of course this does not mean that the current observational population density is correct, even if only 5 of the WAVS objects are shown to be CVs then this would be within the limit of ≥ 4.3 CVs set from PCEB population density. However, this result does mean that one of several possibilities must be true, either:

- WAVS has somehow missed a large population of variables.
- Current theoretical estimates for the space density of CVs are incorrect.

- Low accretion rate CVs do not flicker with an amplitude large enough to be detected by WAVS.

It is my opinion that the first of these is unlikely to be true as the procedure for detecting variables in the WAVS sample is very thorough and robust within the limits described. Even if some stars which varied within these limits had somehow been missed, it is unlikely that they would have represented an entire population, especially not the population that the survey was originally tailored to look for. Whether or not the second statement is true or not is a difficult one to answer. Certainly there is a great deal of theoretical evidence for a higher space density of CVs and if this is not the case then the accepted evolutionary models of CVs must be revised. It is my opinion that the third of the above possibilities probably represents the truth behind the null result, as considered below.

Chapter 2 discussed flickering in CVs is due either to the impact of the accretion stream with the hotspot or to interactions at the boundary layer between the disk and the surface of the white dwarf. In a situation where the accretion rate is reduced, it is reasonable to suppose that flickering arising from the stream impact region would also be reduced accordingly. During a sustained period of low accretion, the boundary layer-WD interaction may be reduced also, possibly resulting in a cessation of flickering, or a drop in amplitude sufficient to fall under the detection threshold of the survey. If the flickering amplitudes of these systems dropped much below the 0.1 magnitude level, the possibility of WAVS detecting these systems would be greatly reduced.

A final conclusion on these matters cannot be reached without further observations of some of the objects in the WAVS sample, particularly those whose lightcurves show possible flickering.

Other Surveys

WAVS is not the only survey working in this field. A recent paper by Gänsicke discusses three new large observational projects all designed to test current theories of cataclysmic variable evolution (Gänsicke, 2004). The first of these uses data from the Hamburg Quasar Survey to attempt to discover CVs based on their spectroscopic properties rather than variability, blue colour or X-ray emission. This survey is expected to be particularly sensitive to short period systems and has already discovered 53 new CVs. The second of these new surveys attempts to increase the known number of pre-CVs thereby allowing

a better understanding of CV evolution as a whole. Previously most pre-CVs have been discovered first as a white dwarf with evidence for a faint companion arising later. This survey looks instead for red dwarf/white dwarf binaries containing cold white dwarfs using Sloan digital sky survey data as a starting point. It is already showing positive results and is expected to boost the known number of pre-CVs by a large factor over the coming years. The final survey investigates the evolutionary route of CVs with post-supersoft X-ray binaries as their progenitors. This survey uses a HST/STIS FUV spectroscopic survey of a large number of known CVs to test for non-main sequence donor stars.

As results from all of these surveys are analysed, hopefully in addition to follow-up observations on the WAVS sample, it cannot be long before puzzles of CV population densities are finally solved.

6.3.2 The WAVS sample general conclusions

In summary, although the WAVS programme has been beset by some unexpected problems due to CCD offset, lack of calibration images and the non-linear response of some of the CFH12k CCDs, it has yielded a population of 230 variable stars, 229 of which (not including QU Vul) are believed to be newly discovered variable objects. Follow up observations of these new objects by Haswell *et al.* will hopefully generate more complete time series and higher resolution spectra. In my view, further observations should be focused on the more interesting variables highlighted in this chapter and should comprise a simultaneous photometric and spectrographic study where possible. This will no doubt reveal many interesting systems and provide useful population statistics for variable star observers in a number of different fields. Confirmation of WAVS123212 as a PMS delta Scuti star for example, would be a great addition to a small observed population of stars which could lend a great deal to theories of stellar evolution. In short, although WAVS has not currently been able to answer all the questions which it set out to do, it has been a success, and will continue to yield interesting scientific results as follow up observations continue.

REFERENCES

Alcock C., Allsman R., Alves D., Axelrod T., 1997. *The MACHO Project LMC Variable Star Inventory. V. Classification and Orbits of 611 Eclipsing Binary Stars. ApJ* **114** 326

Barker J., Kolb U., 2003. *The Minimum Period Problem in Cataclysmic Variables. MNRAS* **340** 623

Bruch A., 1992. *Flickering in cataclysmic variables; its properties and origins. A&A* **266** 237

CFHT Website, 2003. *http://www.cfht.hawaii.edu/*

Cook K., Alcock C., Axelrod T., Freeman K., 1995. *Variable Stars in the MACHO Collaboration Database. ASP Conference Series* **83** 221

Cropper M., Warner B., 1986. *Polarimetry of VV Puppis. MNRAS* **220** 633

Cuillandre J.C., Luppino G., Starr B., Isani S., 1999. *CFH12k: the new CFHT wide field CCD mosaic camera. CFHT Bulletin 40*

de Kool M., Ritter H., 1993. *On the Formation Rate and Space Density of Close White Dwarf Main Sequence Star Binaries. A&A* **267** 397

Dhillon V., Marsh T., 2001. *Ultracam - Studying Astrophysics on the Fastest Timescales. New Astronomy Reviews* **45** 91

Diaz M., Bruch A., 1997. *The orbital period distribution of novae. A&A* **322** 807

Frank J., King A., Raine D., 2001. *Accretion Power in Astrophysics. Cambridge University Press*

Fraunhofer J., 1817. *Bestimmung des Brechungs- und Farbenzerstreuungs-Vermgens verschiedener Glasarten in Bezug auf die Vervollkommnung achromatischer Fernrhre. Denkschriften der kniglichen Academie der Wissenschaften zu Mnchen V.*

Gänsicke B., 2004. *Observational Studies of Cataclysmic Variable Evolution: of Samples, Biases and Suprises. RevMexAA (Serie de Conferencias)* **20** 152

Hall D., 1990. *Masses and Radii for 13 Chromospherically Active Ellipsoidal Variables. AJ* **100** 554

Han Z., Eggleton P., Podsiadlowski P., Tout C., 1995. *The formation of barium and CH stars and related objects. MNRAS* **277** 1443

Hernanz M., Jordi J., 2000. *Thermonuclear Runaways on Accreting White Dwarfs: Models of Classical Novae Explosions. Cosmic Explosions: Tenth Astrophysics Conference,AIP Conference proceedings* p. 339

Hoffmeister C., Richter G., Wenzel W., 1985. *Variable Stars. Springer-Verlag*

Honeycutt R., Robertson J., 1998. *Multiyear Photometry and a Spectroscopic Period Search for the VY Sculptoris Type Cataclysmic Variable V794 Aquilae. AJ* **116** 1961

Houdebine E., Stempels H., 1997. *Observation and modelling of main sequence stellar chromospheres. A&A* **326** 1133

Howell S., Nelson L., Rappaport S., 2001. *An Exploration of Paradigm for the 2-3 Hour Period Gap in Cataclysmic Variables. ApJ* **550** 897

King A., Schenker K., Hameury J., 2002. *Blunting the Spike: the CV Minimum Period. MNRAS* **335** 513

Kolb U., 2001. *The Population of Cataclysmic Variable Systems. The Influence of Binaries on Stellar Population (D. Vanbeveren (Ed.))* **264** 321

Kolb U., Baraffe I., 1999. *Brown Dwarfs and the Cataclysmic Variable Period Minimum. MNRAS* **309** 1034

Kuulkers E.e.a., 2002. *First results from multi-wavelength observations during the 2001 outburst of WZ Sge. The Physics of Cataclysmic Variables and related objects, ASP Conference Proceedings* **261** 443

Leinert C., Richichi A., Haas M., 1997. *Binaries among Herbig Ae/Be stars. A&A* **318** 472

Livio M., 1992. *The Cyclic Evolution-"Hibernation" Scenario of Cataclysmic Variables. ASP Conference Series* **29** 269

Lubow S., Shu F., 1975. *Gas dynamics of semidetached binaries. ApJ* **198** 383

Massey P., 1997. *A User's Guide to CCD Reduction with IRAF*

Massey P., Davis L., 1992. *A Users Guide to Stellar CCD Photometry with IRAF*

Massey P., Valades F., Barnes J., 1992. *A Users Guide to Reducing Slit Spectra with IRAF*

Mirzoian L., 1984. *Flare stars. Vistas in Astronomy* **27** 77

Monin D., Wade G., Fabrika S., 2003. *Two new bright Ae stars. A&A* **411** 197

Naylor T., Charles P., Mukai K., Evans A., 1992. *An Observational Case against Hibernation. MNRAS* **258** 449

Newton I., 1671. *Letter to Henry Oldenburg*

Nordic Optical Telescope Website, 2002. *http://www.not.iac.es/technical/astronomical /instruments/alfosc/*

Olech A., Kaluzny J., Thompson I., Pych W., Krzeminski W., 1998. *RR Lyrae Variables in the Globular Cluster M55. AJ* **118** 442

Patterson J., 1984. *The Evolution of Cataclysmic and Low-Mass X-Ray Binaries. ApJ, Supplement Series* **54** 443

Petit M., 1987. *Variable Stars. Wiley and Sons*

Pinheiro F., Folha D., Marconi M., Ripepi V., 2003. *Oscillations in the PMS Delta Scuti star V346 Ori. A&A* **339** 271

Puxley P., 2001. *Observing Constraints - Sky Transparency. http://www.gemini.edu/ sciops/ObsProcess/obsConstraints/ocTransparency.html*

Ridpath I., 1998. *Norton's Star Atlas and Reference Handbook. Longman*

Ripepi M., Marconi M., Bernabi S., Palla F., 2003. *Multisite observations of the PMS Delta Scuti star V351 Ori. A&A* **408** 1047

Ritter H., Kolb U., 2003. *Catalogue of Cataclysmic Binaries, Low mass X-ray Binaries and related objects (7th Edition). A&A* **404** 301

Rolfe D., 2001. *Accretion Flow and Precession Phenomena in Cataclysmic Variables. PhD. Thesis* pp. 3,6

Rucinski S., 1993. *The Realm of Interacting Binary Stars. ed. J. Sahade et al.* **Dordrecht: Kluwer** 111

Rucinski S., 2001. *The Photometric Amplitude and Mass-ratio Distributions of Contact Binary Stars. AJ* **122** 1007

Rucinski S., 2002. *The 7.5 Magnitude Limit Sample of Bright Short-Period Binary stars. I. How many Contact Binaries are there? PASP* **114** 1124

Rucinski S., 2004. *Contact Binaries of the W Uma type as distance tracers. New. Astron. Rev* **48** 703

Samus N., Durlevich O., 1998. *GCVS Variability Types and Distribution Statistics of Designated Variable Stars According to their Types of Variability. http://www.sai.msu.su/groups/cluster/gcvs/gcvs/*

Schlegel D., Finkbeiner D., Davis M., 1998. *Maps of Dust IR Emission for use in estimation of Reddening and CMBR Foregrounds. ApJ* **500** 525

Schoembs R., 1987. *Simultaneous multicolour photometry of OY Carinae during quiescence. A&A* **181** 50

Schwarzenberg-Czerny A., 1997. *The Correct Probability Distribution for the Phase Dispersion Minimization Periodogram. ApJ* **489** 941

Shara M., Livio M., Moffat A., Orio M., 1986. *Do Novae Hibernate During Most of the Millennia Between Eruptions? Links Between Dwarf and Classical Novae, and Implications for the Space Densities and Evolution of Cataclysmic Binaries. ApJ* **311** 163

Shara M., Moffat A., 1982. *The recovery of CK Vulpeculae (Nova 1670) - The oldest 'old nova'. ApJ, Part 2 - Letters to the Editor* **258** L41

Smak J., 1999. *Cataclysmic Variables. Binary Stars: Selected Topics on Observations and Physical Processes. EADN School XII* p. 110

Spagna A., Lattanzi M., McClean B., Massone G., Lasker B., 1998. *Faint Photometric BV Rc sequences. A&A Supplement Series* **130** 359

Sterken C., Jaschek C., 1996. *Lightcurves of Variable Stars - A Pictorial Atlas. Cambridge University Press*

STScI, 1997. *DSS Digitised Sky Survey website. http://stdatu.stsci.edu/dss/*

Tapia S., 1976. *IAUC 2987: HR 1099; AM Her; 1976g. IAU Circular* **2987**

USNO, 1997. *USNO finding chart program. http://ftp.nofs.navy.mil/projects/pmm/chart.html*

Van Dongen H., Olofsen E., Van Hartevelt J., Kruyt E., 1999. *A Procedure of Multiple Period Searching in Unequally Spaced Time-Series with the Lomb-Scargle Method. Biological Rhythm Research* **30** 149

Wade R., Ward M., 1985. *Cataclysmic Variables: An Observational Overview. Interacting Binary Stars, Cambridge University Press* p. 129

Warner B., 1995. *Cataclysmic Variable Stars. Cambridge University Press*

Warner B., O'Donoghue D., Wargau w., 1989. *High-speed photometry and spectroscopy of the dwarf nova TY Piscis Austrini. MNRAS* **238** 73

Webbink R., 1990. *Accretion-Powered Compact Binaries. Cambridge University Press*

Wood M., Montgomery M., Simpson.J.C., 2000. *Smoothed Particle Hydrodynamics Simulations of Apsidal and Nodal Superhumps. ApJ Letters* **535** L39

APPENDIX A

Variables with lightcurves spanning two nights

The lightcurves for variable stars found in the WAVS project are displayed in Appendices A,B and C. Stars for which two night lightcurves are available are displayed in Appendix A. Those which were observed on the first or second nights only are displayed in Appendices B and C respectively. As discussed previously, stars which appeared on CCD0 were given the prefix 99 for technical reasons, and as such these appear first in the lists. The naming convention CCD#, night(1 or 2), followed by the four digit star number is applied consistently. Hence 224305 corresponds to CCD2, night 2, star 4305 and 1111626 corresponds to CCD11, night 1, star 1626. Stars which were observed on both nights are referred to with their night two designation. Note: when considering which list an object will appear in it is best to start with star number as CCD number may consist of one or two digits. Errors on B and R magnitudes can be estimated from the amplitude of variability in the V band as described in chapter 6.

Table A.1: Variables with 2 night lightcurves

ID	RA	DEC	Obs. V Max	Obs. V Min	B-V	V-R
9921077	20h 25m 47.0	27h 57m 18.4	20.701 ± 0.012	21.140 ± 0.019	1.4	0.8
9921649	20h 25m 39.4	27h 55m 48.4	19.24 ± 0.005	19.390 ± 0.007	0.5	0.4
9922148	20h 25m 37.4	27h 54m 32.4	20.700 ± 0.015	20.780 ± 0.02	0.7	0.5
9920421	20h 25m 37.7	27h 59m 8.5	21.691 ± 0.039	22.209 ± 0.061	1.2	0.6
9920459	20h 25m 31.9	27h 59m 2.4	20.528 ± 0.0160	20.645 ± 0.021	0.9	0.6
9921282	20h 25m 36.5	27h 56m 42.7	20.896 ± 0.0180	21.305 ± 0.032	1.4	0.4

continued...

Table A.1: continued

9922370	20h 25m 39.6	27h 54m 1.1	19.691 ± 0.009	20.159 ± 0.011	1.1	0.3
9922720	20h 25m 26.6	27h 53m 8.5	20.549 ± 0.017	20.665 ± 0.017	1.4	0.8
9923598	20h 25m 46.8	27h 50m 58.9	21.161 ± 0.015	21.54 ± 0.022	0.7	1.3
9924142	20h 25m 48.2	27h 49m 39.4	20.125 ± 0.010	20.497 ± 0.016	0.6	0.5
9925201	20h 25m 43.7	27h 47m 6.7	19.263 ± 0.007	19.377 ± 0.007	0.8	0.8
120108	20h 26m 7.7	28h 0m 5.4	22.022 ± 0.037	22.454 ± 0.049	1.7	1.4
120732	20h 26m 7.4	27h 57m 59.4	21.115 ± 0.014	21.303 ± 0.026	0.7	0.9
120858	20h 26m 9.4	27h 57m 36.7	18.924 ± 0.005	19.196 ± 0.006	1.3	1
120861	20h 25m 59.8	27h 57m 36.0	20.242 ± 0.012	20.371 ± 0.013	0.6	0.6
122458	20h 26m 0.5	27h 53m 38.8	18.053 ± 0.004	18.116 ± 0.004	1.2	1
123140	20h 26m 8.4	27h 52m 12.0	18.199 ± 0.005	18.263 ± 0.004	1.2	1
125590	20h 26m 13.9	27h 47m 43.1	16.398 ± 0.454	22.41 ± 0.103	NA	NA
126212	20h 26m 1.0	27h 46m 43.7	17.077 ± 0.005	17.167 ± 0.008	0.1	NA
220487	20h 26m 59.0	27h 59m 3.5	21.304 ± 0.02	21.378 ± 0.013	0.7	1.3
221850	20h 26m 48.5	27h 55m 25.0	18.662 ± 0.005	19.040 ± 0.004	0.5	1.2
224305	20h 26m 27.8	27h 48m 45.7	21.589 ± 0.043	21.781 ± 0.054	1.9	1.1
225125	20h 26m 29.5	27h 46m 34.0	20.864 ± 0.015	21.056 ± 0.023	1.1	0.6
224129	20h 26m 56.9	27h 49m 12.7	20.843 ± 0.022	20.976 ± 0.017	1	0.7
220367	20h 26m 54.7	27h 59m 27.6	20.031 ± 0.017	20.166 ± 0.009	0.7	1.2
322587	20h 27m 4.8	27h 54m 15.1	20.501 ± 0.009	20.596 ± 0.010	NA	NA
325367	20h 27m 13.9	27h 47m 21.5	21.406 ± 0.028	21.663 ± 0.051	0.7	0.5
320673	20h 27m 24.2	27h 58m 52.7	22.062 ± 0.032	22.288 ± 0.033	0.7	1.3
321830	20h 27m 10.3	27h 56m 3.5	21.966 ± 0.019	22.501 ± 0.034	0.9	1.3
322568	20h 27m 14.4	27h 54m 17.3	21.363 ± 0.015	21.47 ± 0.018	0.7	1.3
323426	20h 27m 26.9	27h 52m 4.1	21.601 ± 0.016	21.744 ± 0.021	1	1.6
323815	20h 27m 7.7	27h 51m 12.6	20.79 ± 0.009	20.889 ± 0.015	0.3	1.1
320340	20h 27m 14.2	27h 59m 37.3	19.813 ± 0.007	19.877 ± 0.007	0.4	1.1
323495	20h 27m 26.6	27h 51m 54.7	21.606 ± 0.05	23.216 ± 0.061	0.9	1.5
320748	20h 27m 2.2	27h 58m 41.5	21.042 ± 0.011	21.13 ± 0.011	1.1	1.6
421398	20h 27m 38.6	27h 57m 14.8	21.402 ± 0.021	21.564 ± 0.023	0.4	1.1
422257	20h 27m 49.4	27h 55m 4.4	19.828 ± 0.008	19.961 ± 0.008	0.6	1.2

continued...

Table A.1: continued

424393	20h 27m 42.0	27h 49m 54.1	17.207 ± 0.004	17.702 ± 0.006	0.8	1.1
422265	20h 27m 53.5	27h 55m 3.0	20.142 ± 0.009	20.578 ± 0.012	0.7	0.8
424233	20h 27m 46.1	27h 50m 17.2	18.148 ± 0.006	20.917 ± 0.252	NA	NA
424548	20h 27m 49.7	27h 49m 28.6	20.109 ± 0.014	20.271 ± 0.011	NA	NA
424750	20h 27m 45.4	27h 49m 1.2	20.002 ± 0.011	20.135 ± 0.011	1.8	0.9
425581	20h 27m 55.2	27h 47m 2.8	20.097 ± 0.011	20.396 ± 0.012	0.7	0.8
425674	20h 27m 44.4	27h 46m 50.2	17.979 ± 0.005	18.03 ± 0.006	NA	NA
420470	20h 27m 43.2	27h 59m 28.3	17.744 ± 0.003	18.19 ± 0.004	NA	NA
424709	20h 27m 37.9	27h 49m 8.4	19.622 ± 0.008	19.878 ± 0.009	1.7	0.8
520129	20h 28m 10.6	28h 0m 3.2	21.192 ± 0.022	21.377 ± 0.023	0.7	0.9
523070	20h 28m 8.2	27h 52m 52.7	20.909 ± 0.026	21.180 ± 0.022	1.2	0.7
520989	20h 28m 20.6	27h 57m 54.7	20.265 ± 0.013	20.475 ± 0.019	1.3	1.3
721960	20h 26m 20.4	27h 37m 55.6	20.221 ± 0.012	20.397 ± 0.013	1	0.6
722836	20h 26m 3.6	27h 40m 18.8	19.473 ± 0.007	19.529 ± 0.006	0.6	0.6
723509	20h 26m 19.7	27h 42m 7.2	21.156 ± 0.030	21.485 ± 0.027	NA	NA
721865	20h 26m 6.0	27h 37m 39.0	18.097 ± 0.010	18.168 ± 0.021	0.9	0.9
721971	20h 26m 5.8	27h 37m 58.8	16.506 ± 0.003	16.569 ± 0.006	0.6	-1.5
722830	20h 26m 1.7	27h 40m 18.1	19.821 ± 0.007	20.03 ± 0.011	1	0.6
723995	20h 26m 2.6	27h 43m 19.2	20.958 ± 0.020	21.226 ± 0.022	0.8	0.8
724281	20h 26m 20.6	27h 43m 59.5	21.426 ± 0.027	21.641 ± 0.028	1.1	0.8
724454	20h 26m 20.6	27h 44m 26.5	22.11 ± 0.047	22.381 ± 0.068	1.8	1.1
722796	20h 26m 0.2	27h 40m 12.4	21.853 ± 0.033	22.770 ± 0.072	0.2	1.6
823301	20h 26m 32.4	27h 41m 7.4	20.768 ± 0.017	20.934 ± 0.021	1.3	0.9
824349	20h 26m 28.1	27h 43m 46.2	19.481 ± 0.007	19.607 ± 0.008	1.1	0.7
924140	20h 27m 11.3	27h 42m 58.0	18.452 ± 0.004	18.689 ± 0.005	0.9	0.8
925010	20h 27m 17.0	27h 45m 0.7	19.838 ± 0.007	20.236 ± 0.009	1.2	0.2
925282	20h 27m 27.6	27h 45m 45.4	20.37 ± 0.013	20.868 ± 0.016	1.6	0.5
924414	20h 27m 27.4	27h 43m 37.2	20.829 ± 0.023	20.967 ± 0.023	1.5	1
924548	20h 27m 8.9	27h 43m 57.4	20.269 ± 0.011	20.740 ± 0.015	1.2	0.6
1022130	20h 27m 51.8	27h 36m 36.4	17.372 ± 0.004	17.907 ± 0.006	0.7	0.8
1023437	20h 28m 2.6	27h 39m 33.5	22.473 ± 0.088	22.838 ± 0.102	2.4	0.7

continued...

Table A.1: continued

1025220	20h 27m 55.9	27h 43m 12.7	21.867 ± 0.048	22.378 ± 0.075	1.3	0.6
1022265	20h 27m 33.4	27h 36m 53.6	19.841 ± 0.01	22.589 ± 0.076	1.8	1

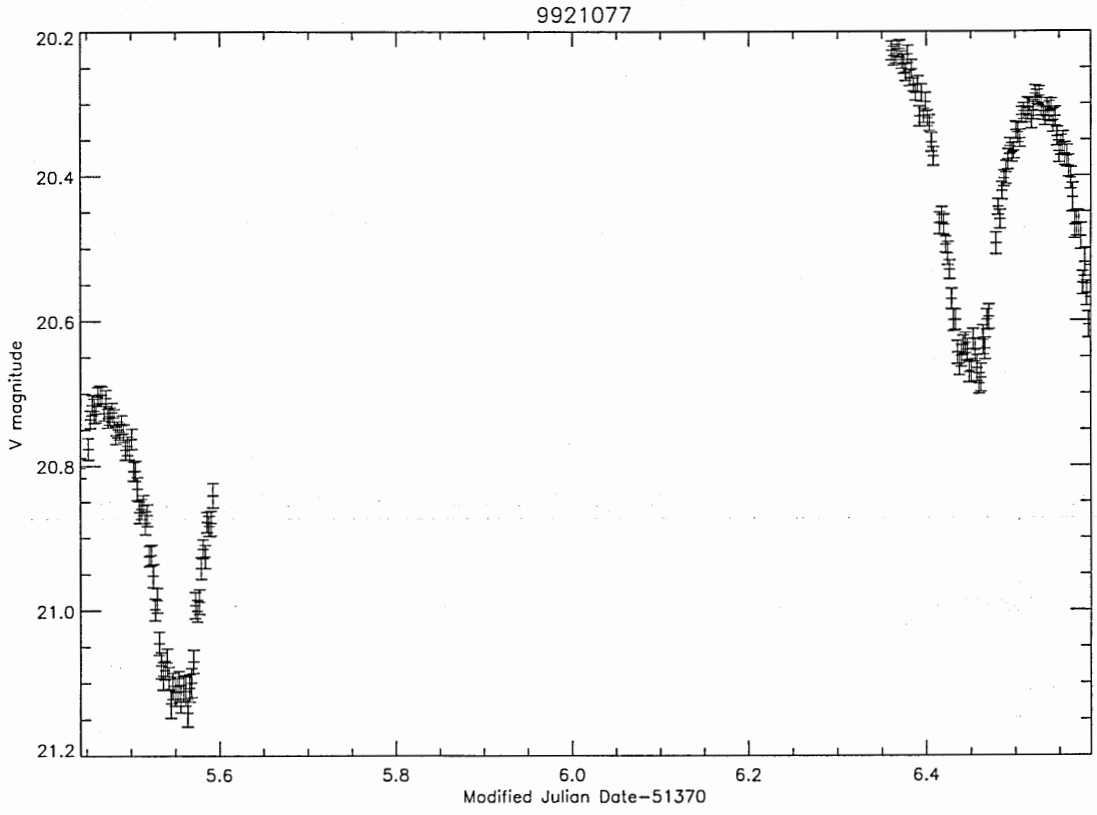
9921077
20.2
20.4
20.6
20.8
21.0
21.2
V magnitude
5.6
5.8
6.0
6.2
6.4
Modified Julian Date−51370

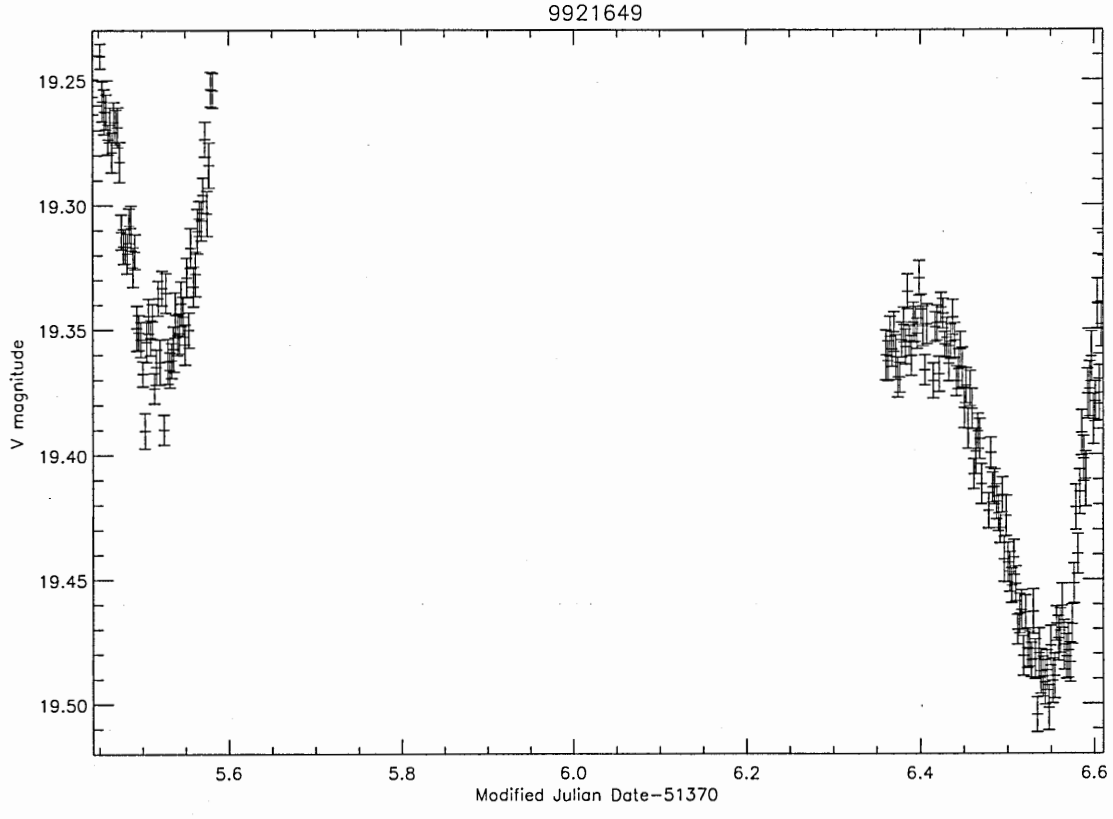
9921649
19.25
19.30
19.35
19.40
19.45
19.50
V magnitude
5.6
5.8
6.0
6.2
6.4
6.6
Modified Julian Date−51370

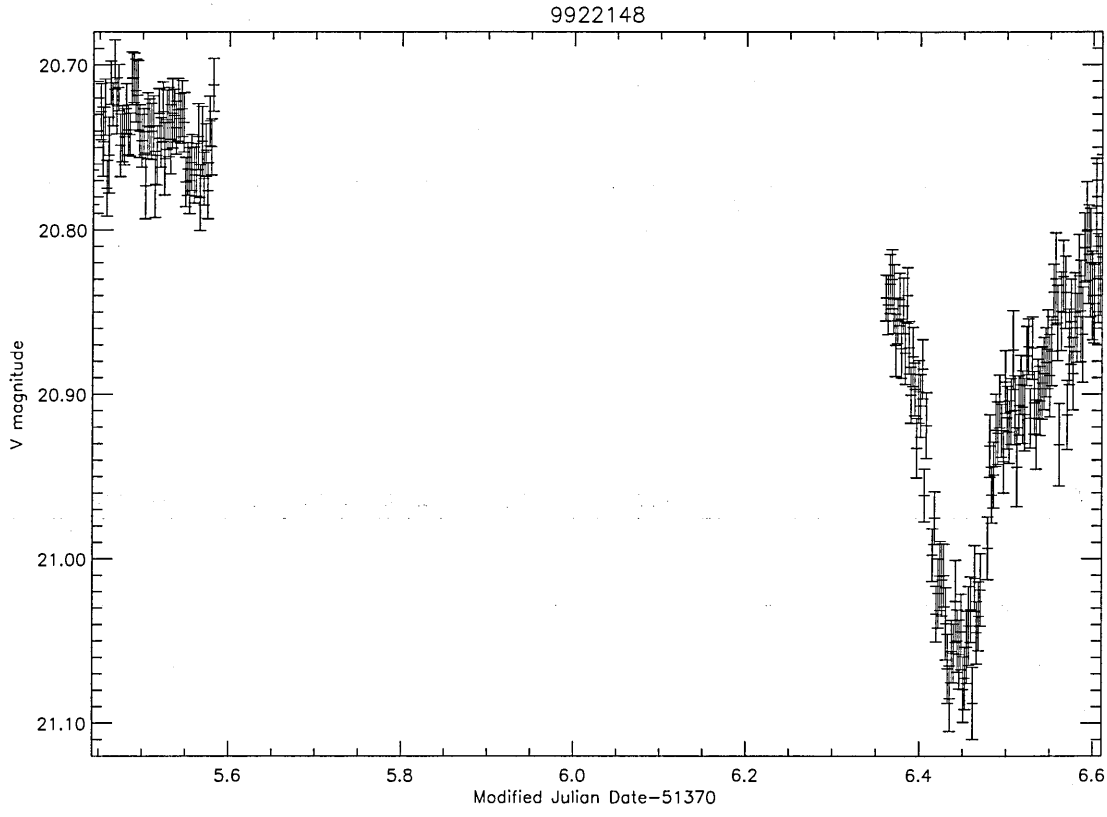
9922148
20.70
20.80
20.90
21.00
21.10
V magnitude
5.6
5.8
6.0
6.2
6.4
6.6
Modified Julian Date−51370

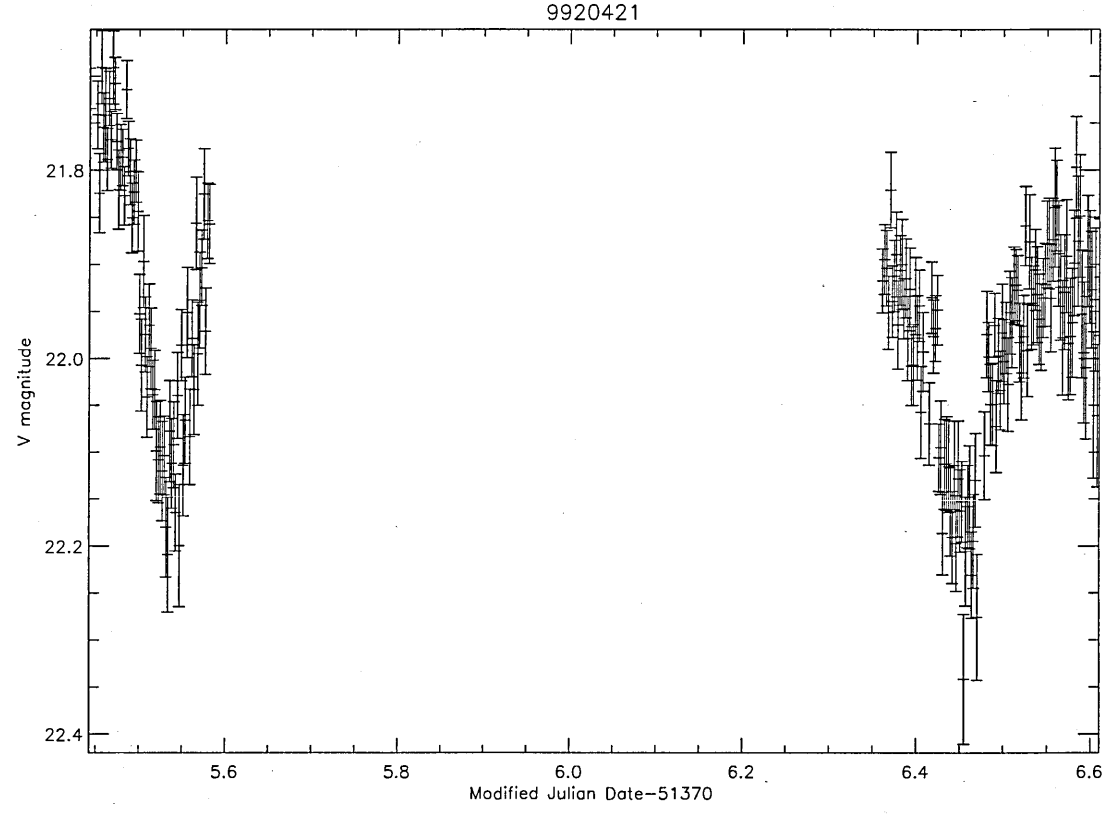
9920421
21.8
22.0
22.2
22.4
V magnitude
5.6
5.8
6.0
6.2
6.4
6.6
Modified Julian Date−51370

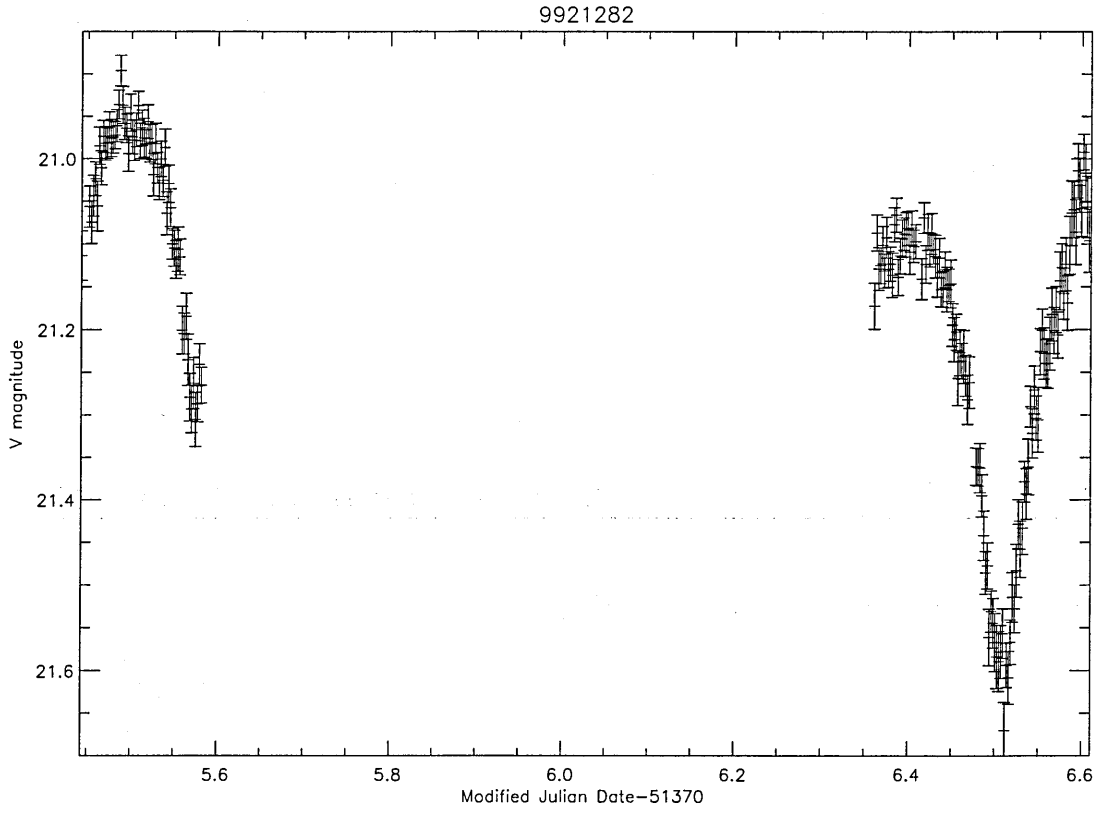
9921282
21.0
21.2
21.4
21.6
V magnitude
5.6
5.8
6.0
6.2
6.4
6.6
Modified Julian Date−51370

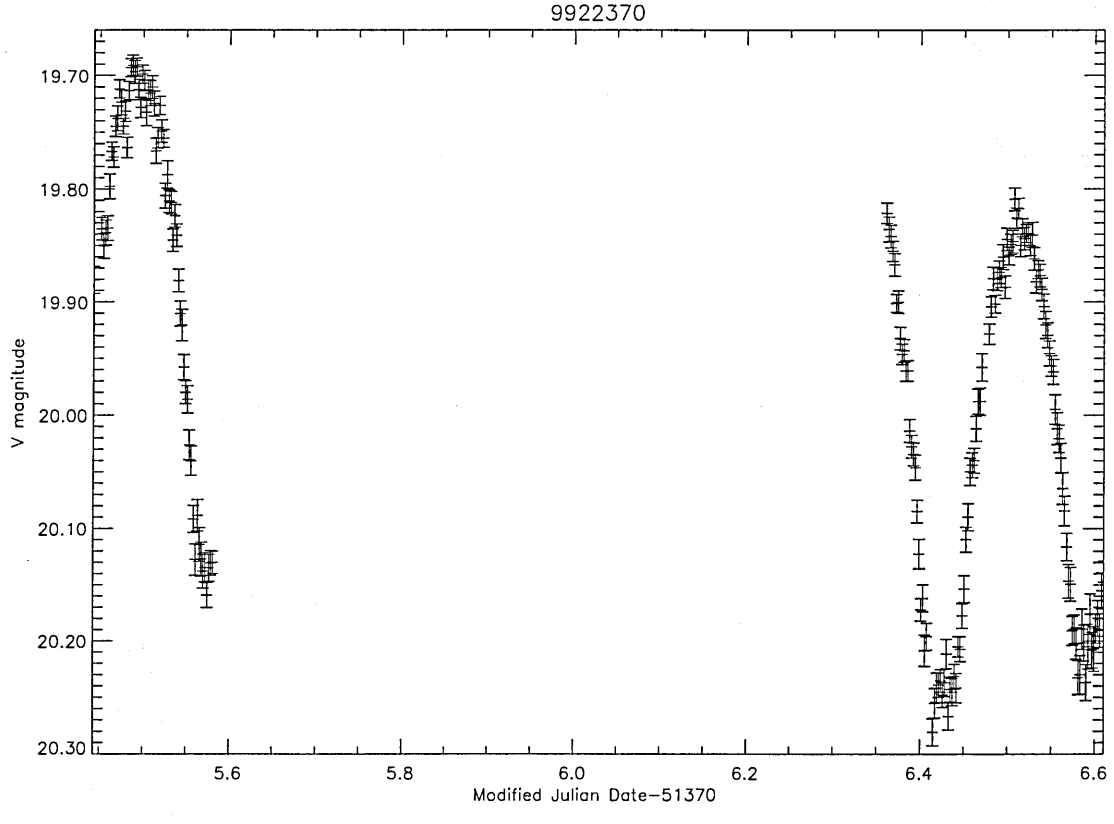
9922370
19.70
19.80
19.90
20.00
20.10
20.20
20.30
V magnitude
5.6
5.8
6.0
6.2
6.4
6.6
Modified Julian Date−51370

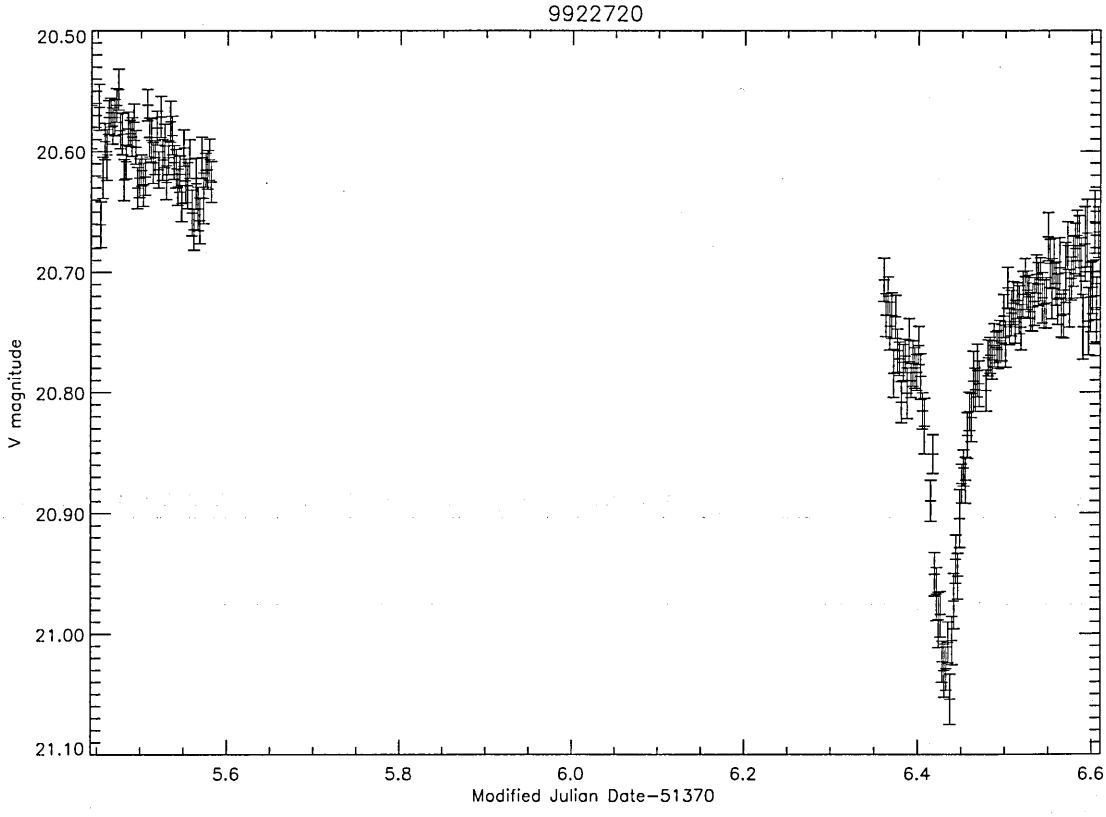
9922720
20.50
20.60
20.70
20.80
20.90
21.00
21.10
V magnitude
5.6
5.8
6.0
6.2
6.4
6.6
Modified Julian Date−51370

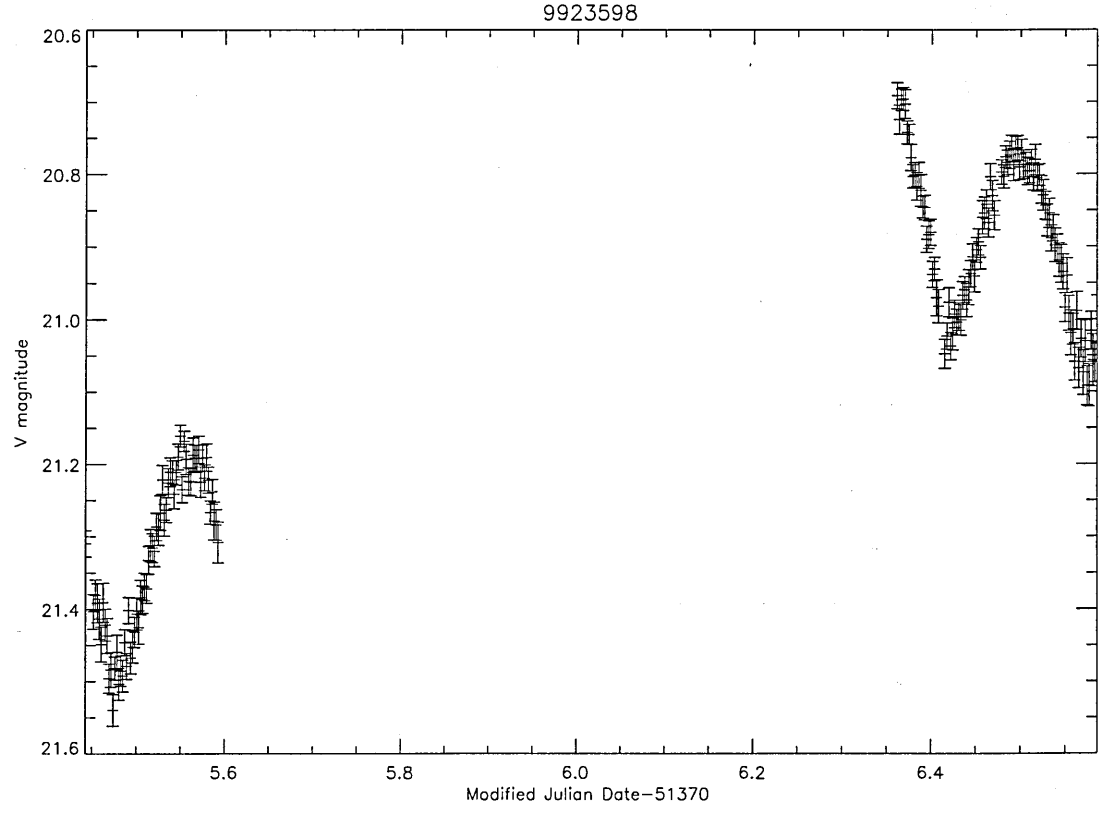
9923598
20.6
20.8
21.0
21.2
21.4
21.6
V magnitude
5.6
5.8
6.0
6.2
6.4
Modified Julian Date−51370

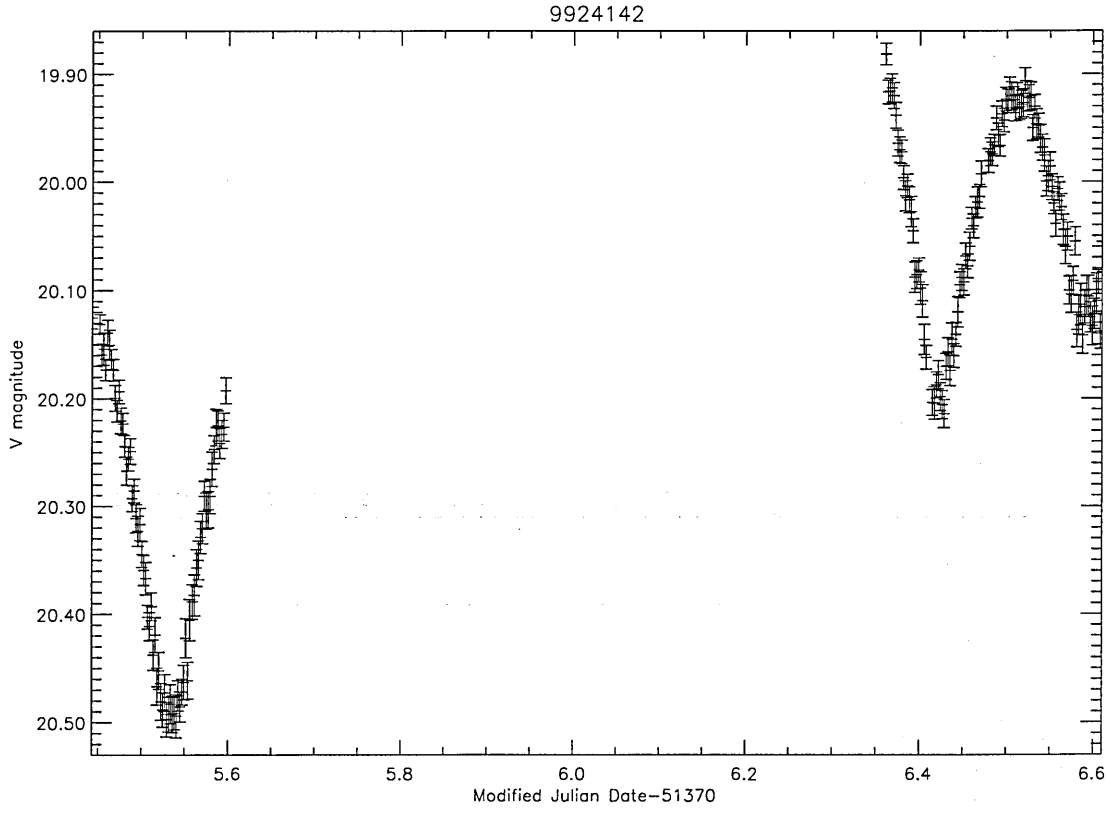
9924142
19.90
20.00
20.10
20.20
20.30
20.40
20.50
V magnitude
5.6
5.8
6.0
6.2
6.4
6.6
Modified Julian Date−51370

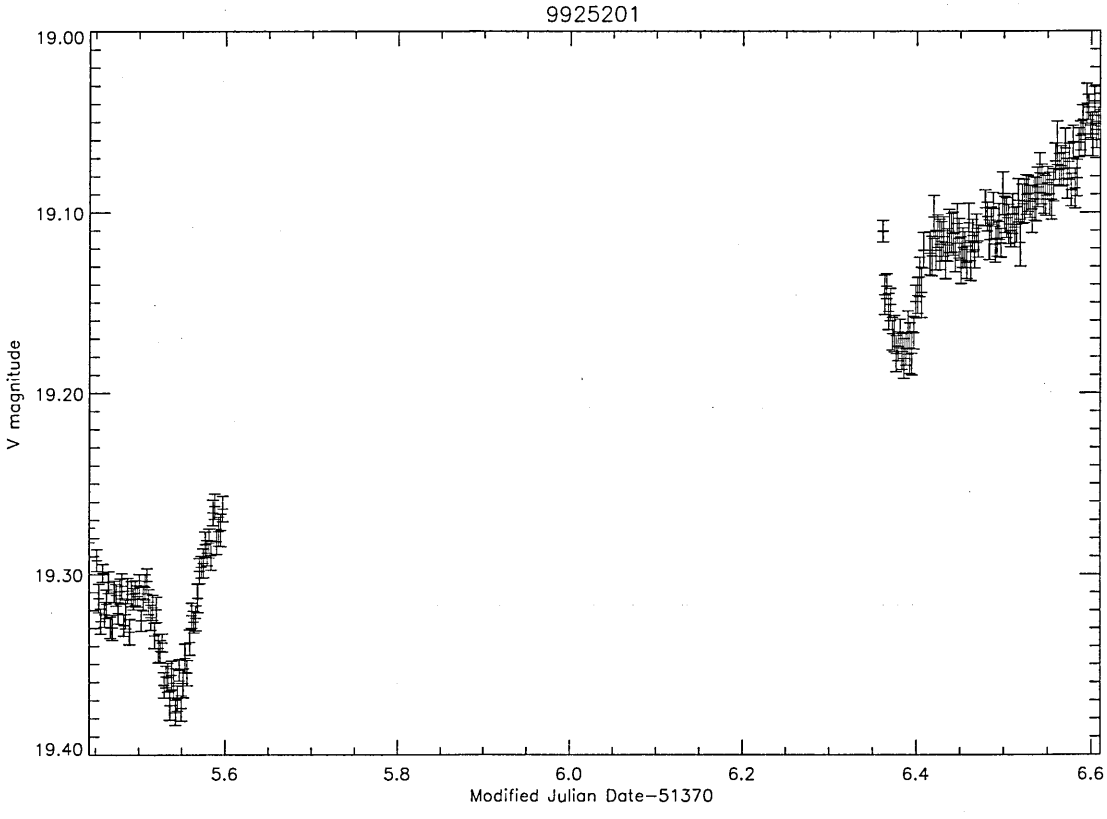
9925201
19.00
19.10
19.20
19.30
19.40
V magnitude
5.6
5.8
6.0
6.2
6.4
6.6
Modified Julian Date−51370

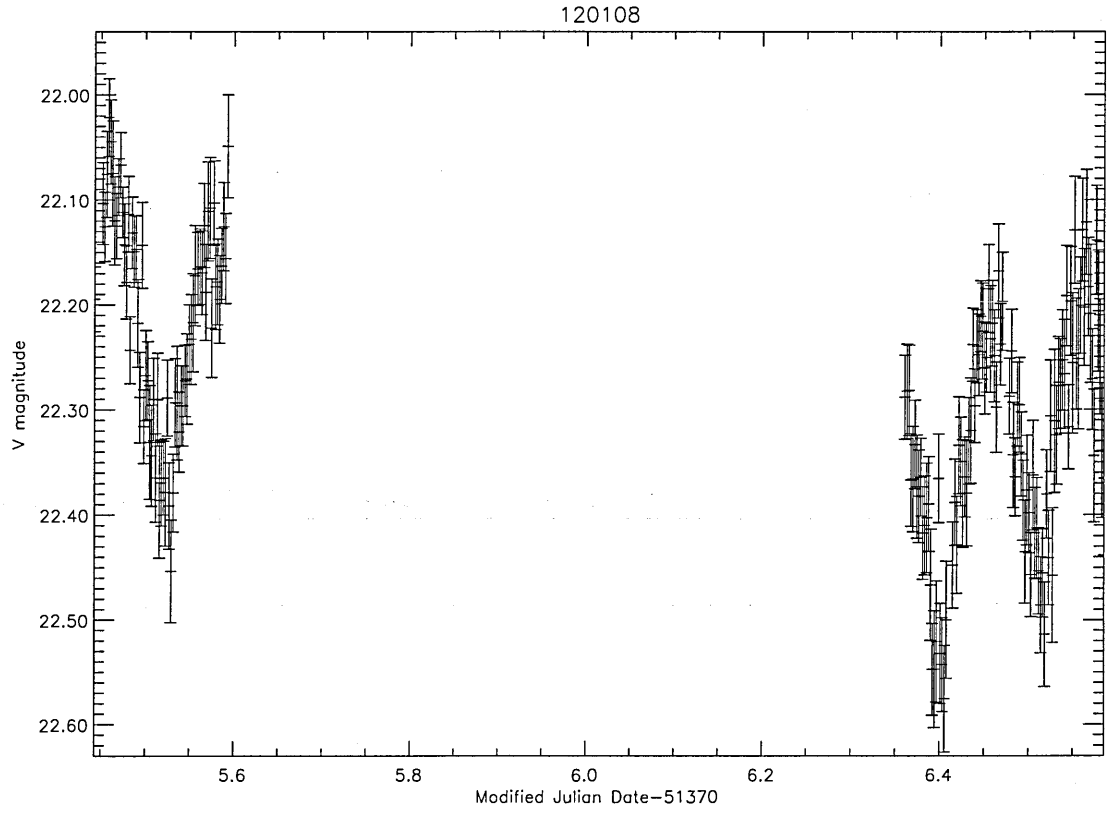
120108
22.00
22.10
22.20
22.30
22.40
22.50
22.60
V magnitude
5.6
5.8
6.0
6.2
6.4
Modified Julian Date−51370

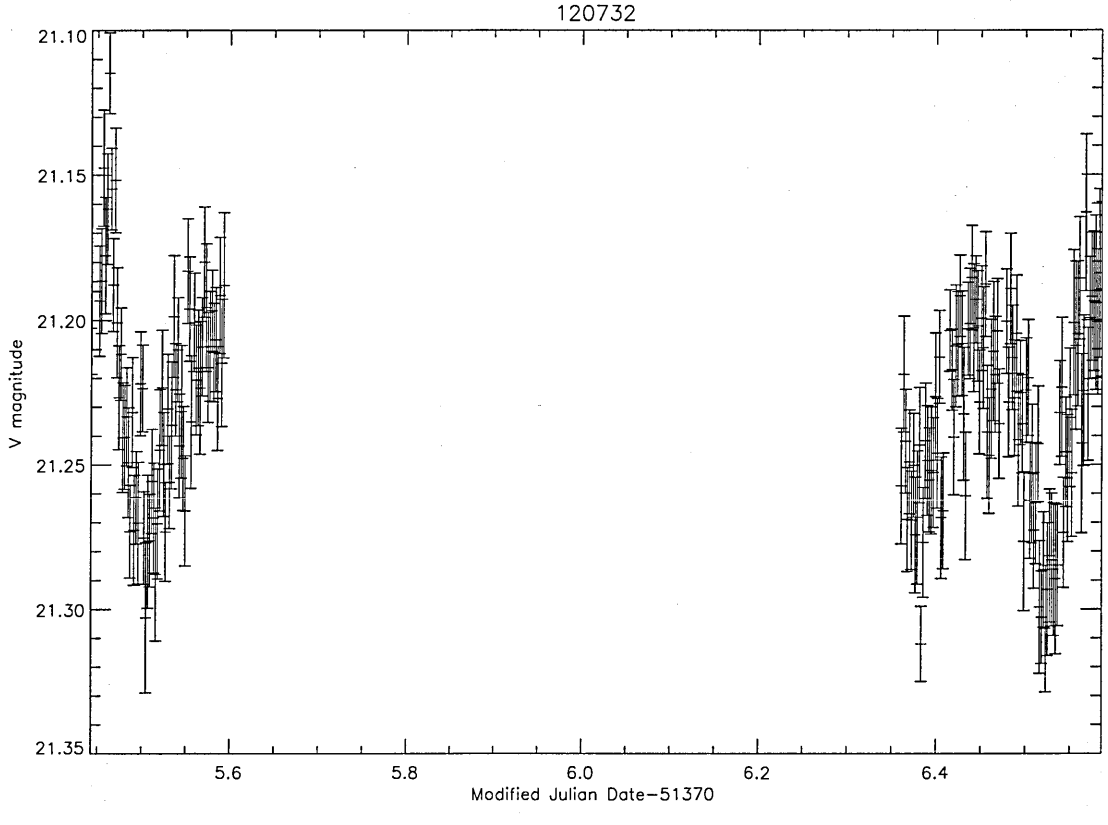
120732
21.10
21.15
21.20
21.25
21.30
21.35
V magnitude
5.6
5.8
6.0
6.2
6.4
Modified Julian Date−51370

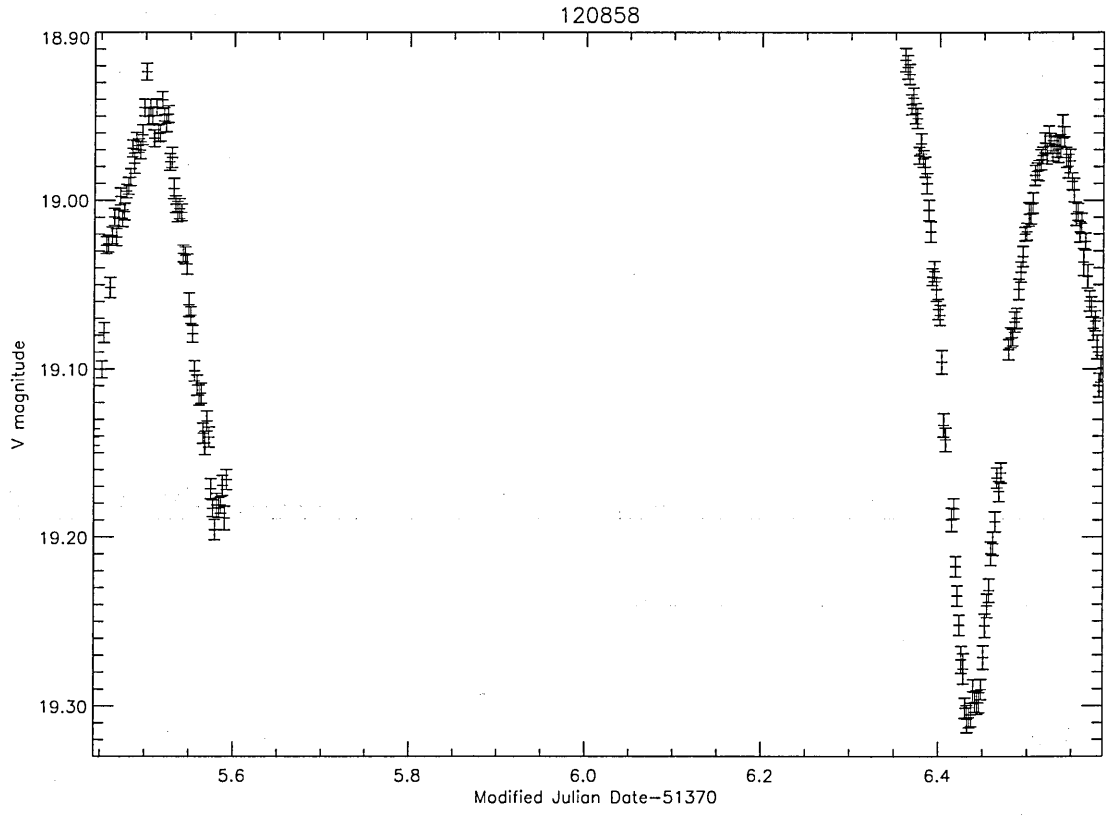
120858
18.90
19.00
19.10
19.20
19.30
V magnitude
5.6
5.8
6.0
6.2
6.4
Modified Julian Date−51370

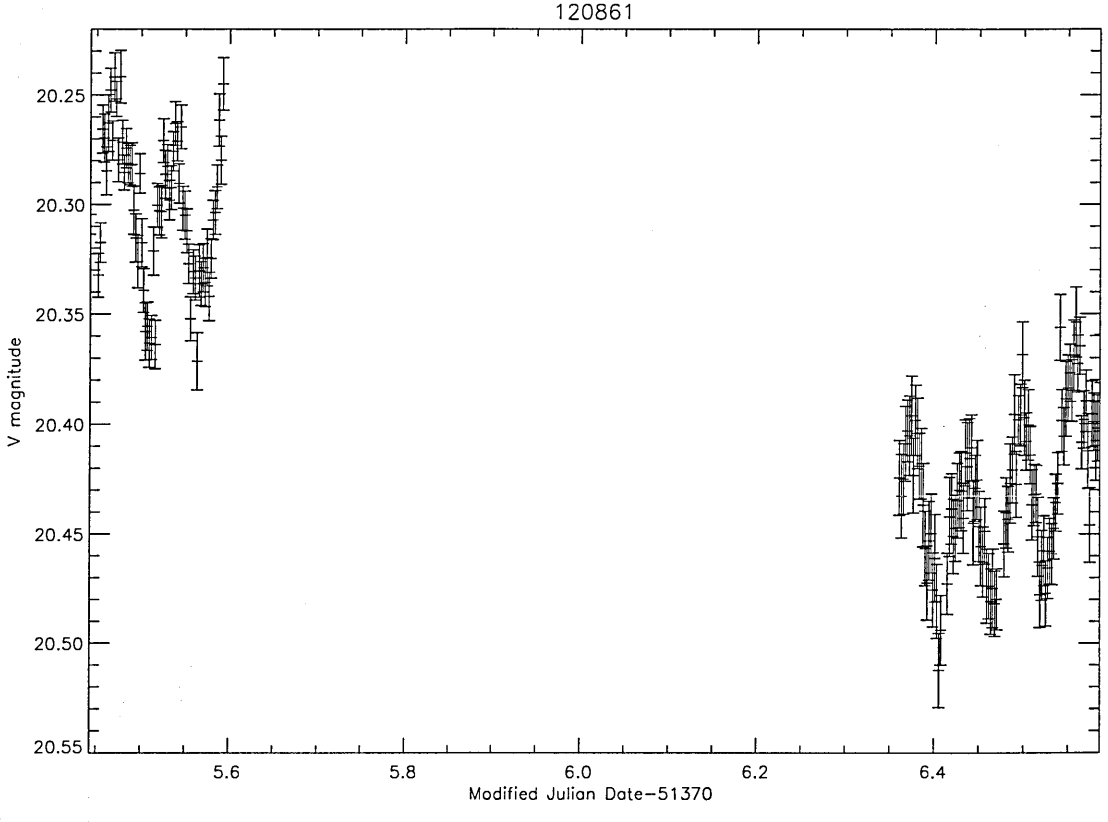
120861
20.25
20.30
20.35
20.40
20.45
20.50
20.55
V magnitude
5.6
5.8
6.0
6.2
6.4
Modified Julian Date−51370

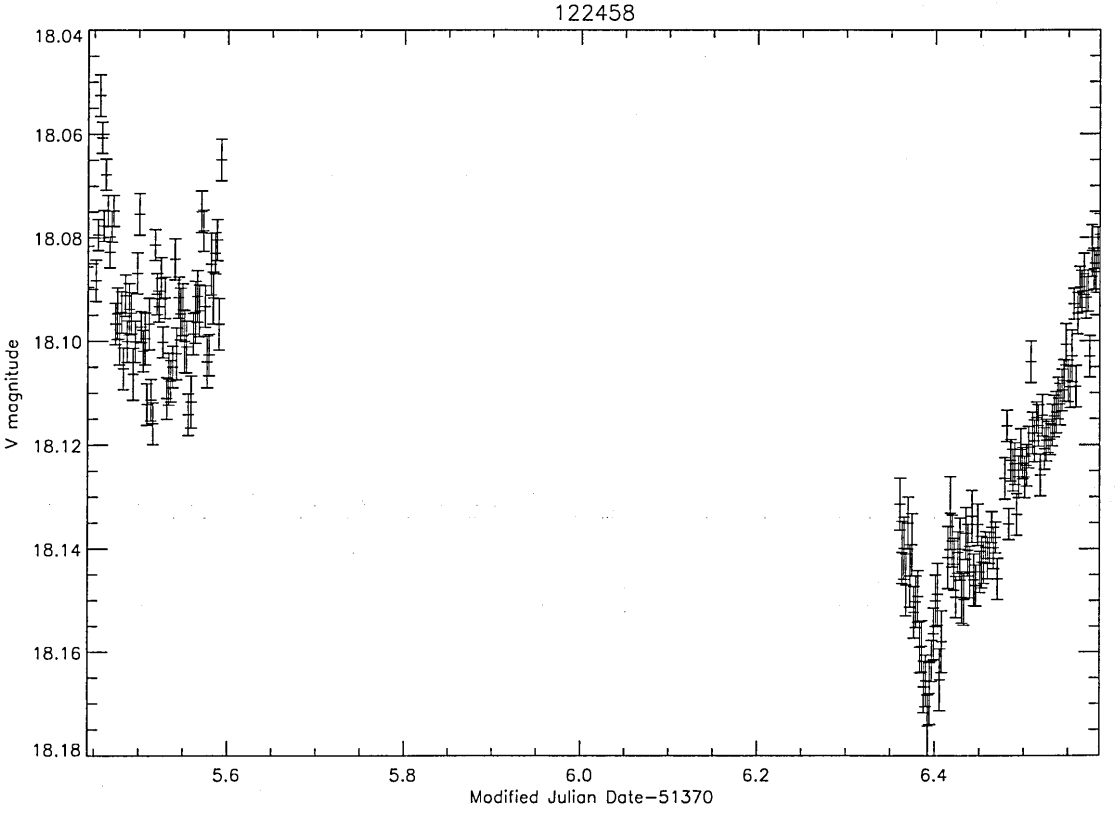
122458
18.04
18.06
18.08
18.10
18.12
18.14
18.16
18.18
V magnitude
5.6
5.8
6.0
6.2
6.4
Modified Julian Date−51370

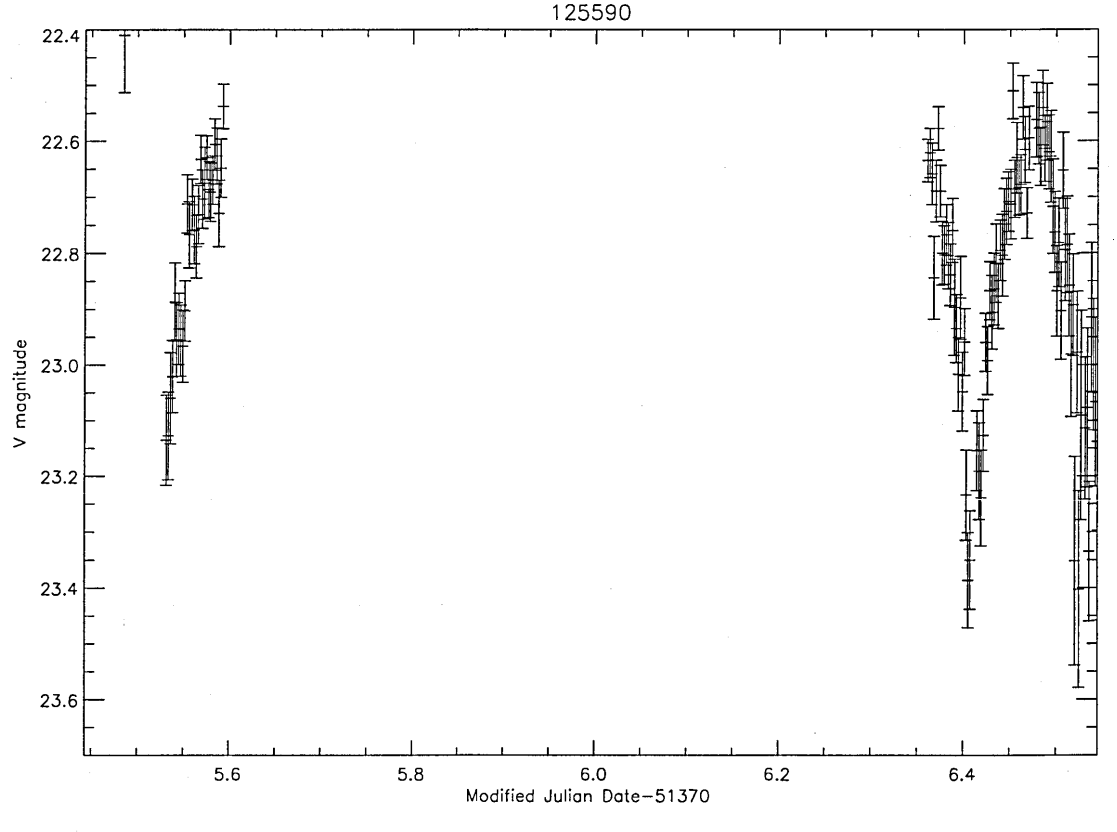
125590
22.4
22.6
22.8
23.0
23.2
23.4
23.6
V magnitude
5.6
5.8
6.0
6.2
6.4
Modified Julian Date−51370

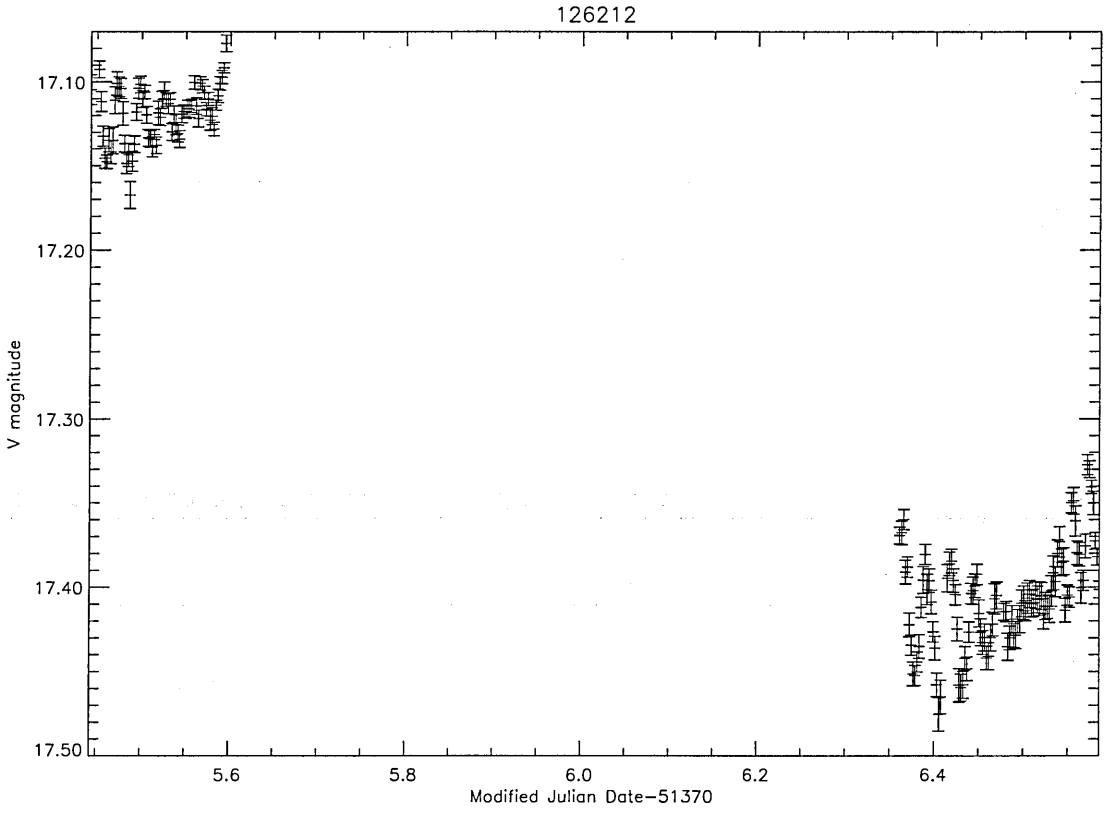
126212
17.10
17.20
17.30
17.40
17.50
V magnitude
5.6
5.8
6.0
6.2
6.4
Modified Julian Date−51370

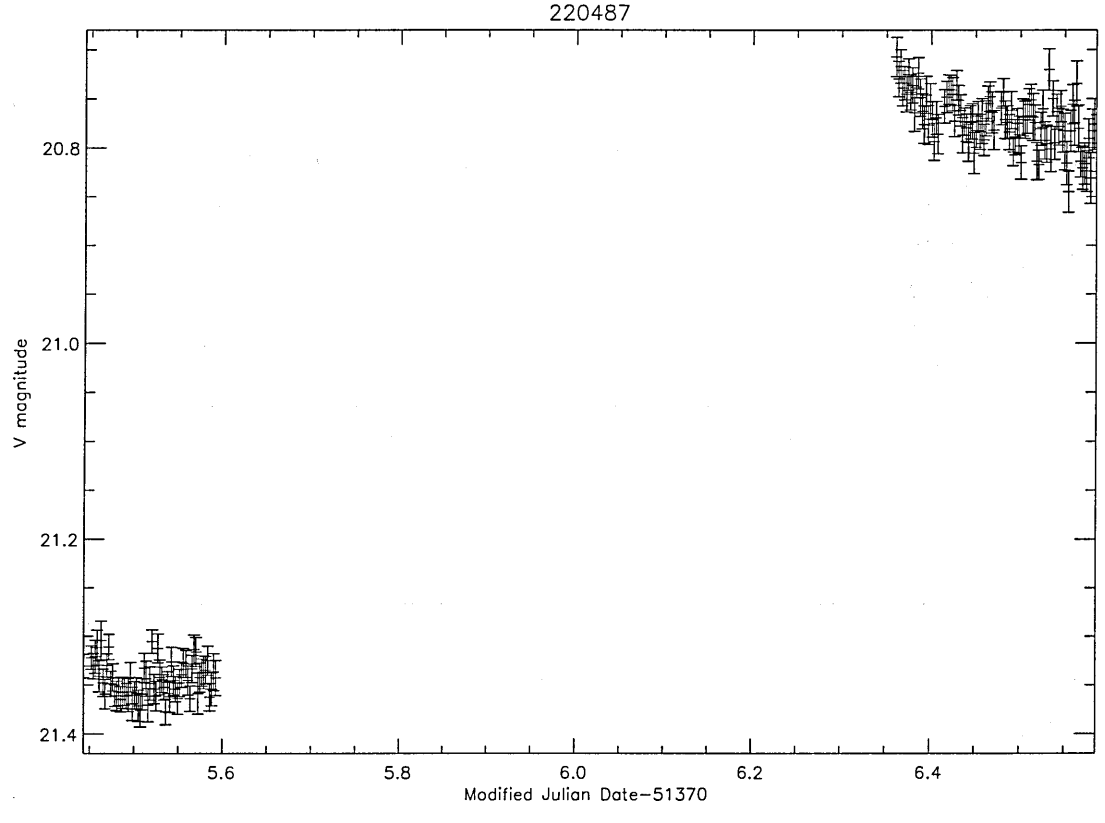
220487
20.8
21.0
21.2
21.4
V magnitude
5.6
5.8
6.0
6.2
6.4
Modified Julian Date−51370

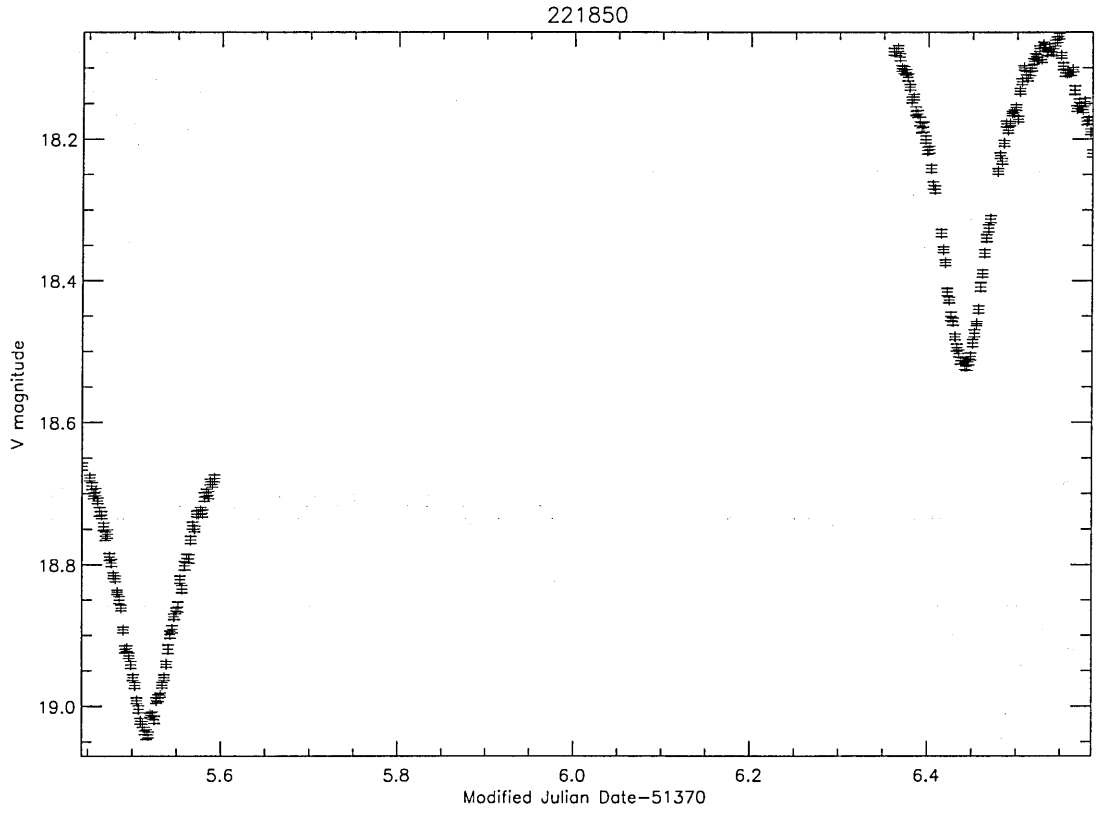
221850
18.2
18.4
18.6
18.8
19.0
V magnitude
5.6
5.8
6.0
6.2
6.4
Modified Julian Date−51370

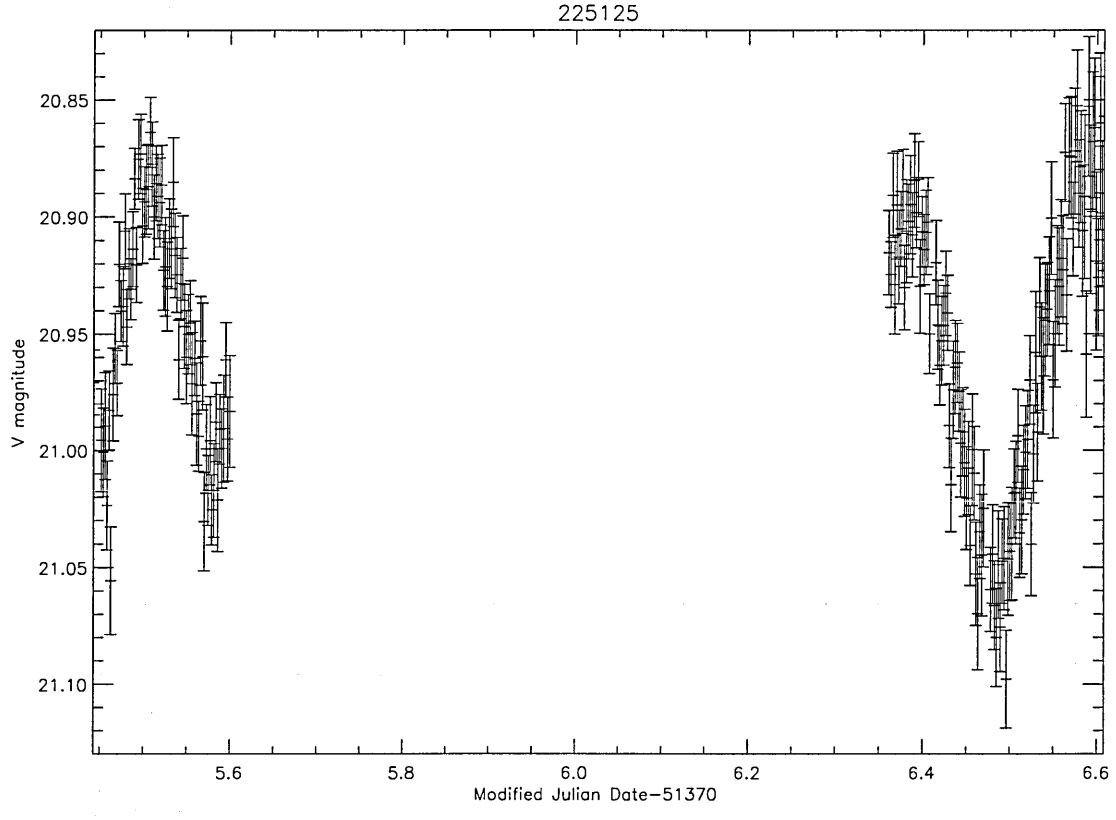
225125
20.85
20.90
20.95
21.00
21.05
21.10
V magnitude
5.6
5.8
6.0
6.2
6.4
6.6
Modified Julian Date−51370

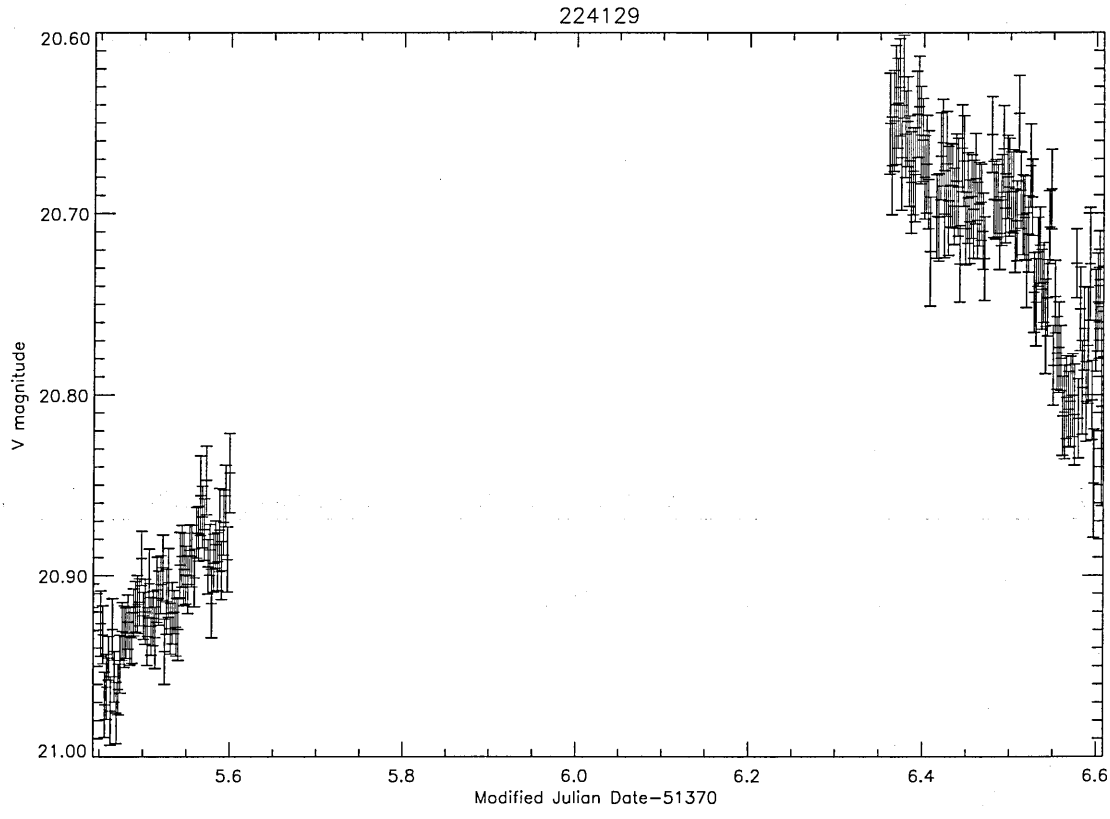
224129
20.60
20.70
20.80
20.90
21.00
V magnitude
5.6
5.8
6.0
6.2
6.4
6.6
Modified Julian Date−51370

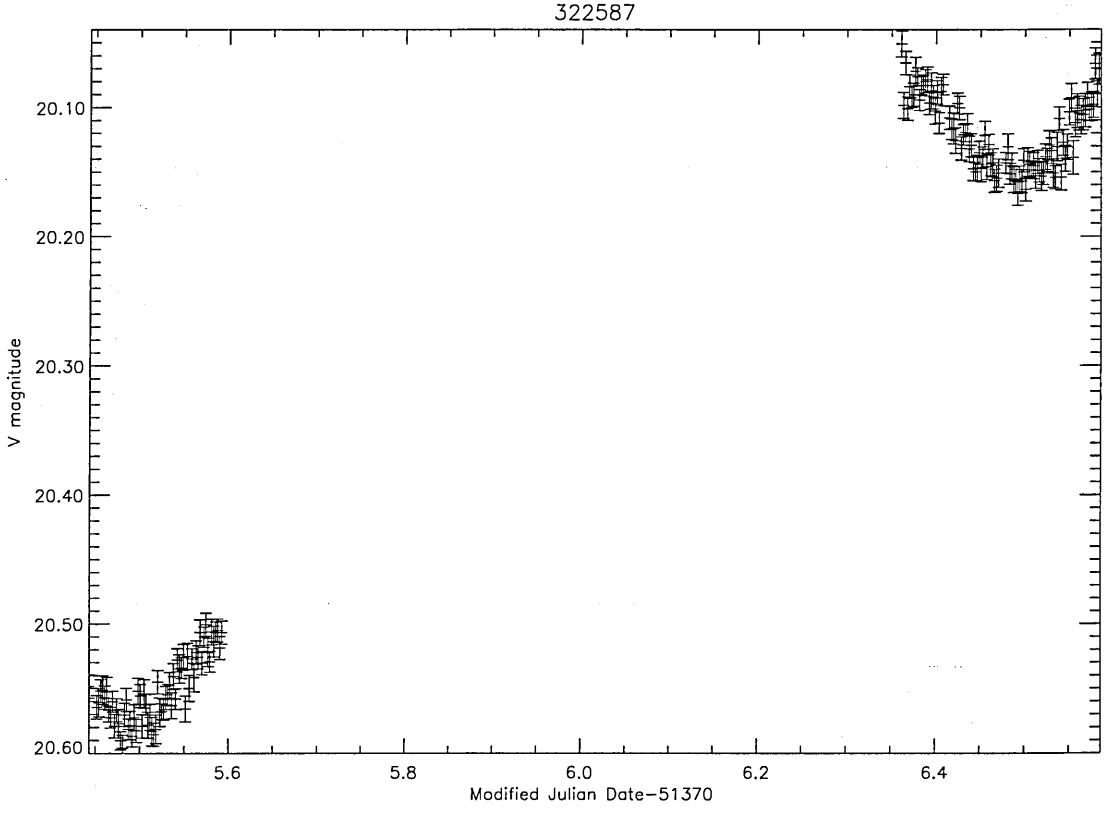
322587
20.10
20.20
20.30
20.40
20.50
20.60
V magnitude
5.6
5.8
6.0
6.2
6.4
Modified Julian Date−51370

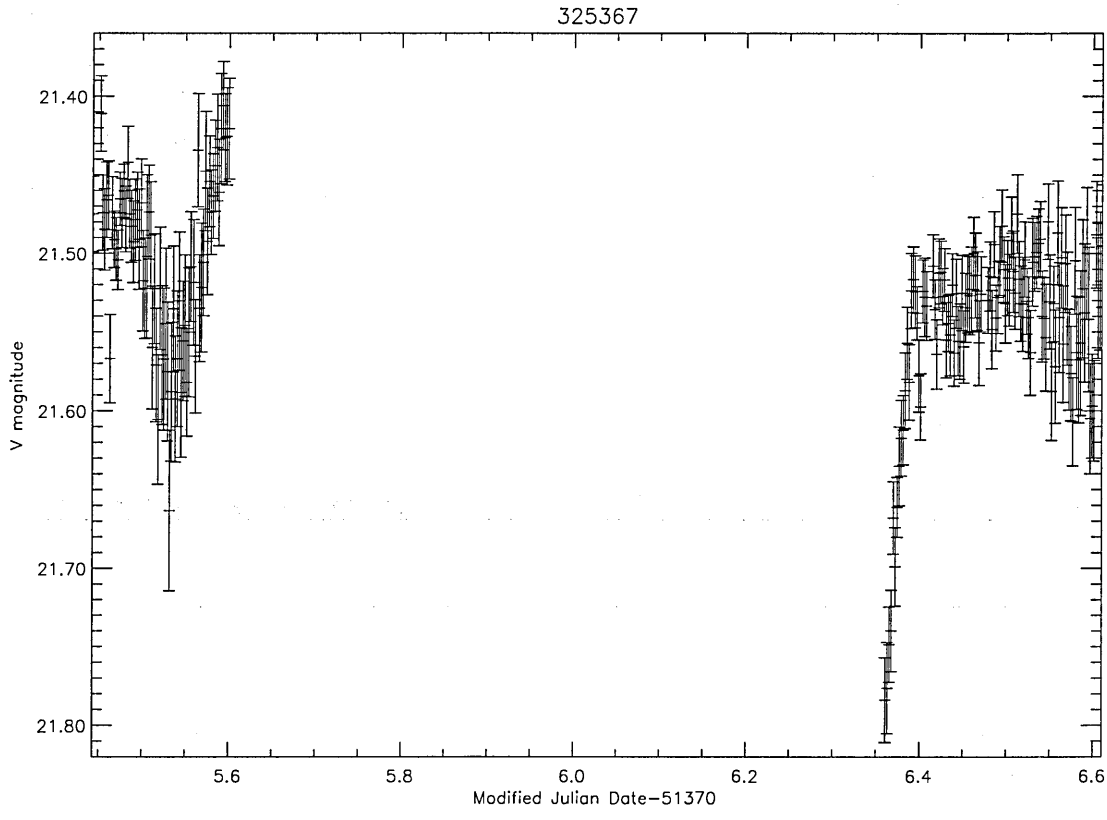
325367
21.40
21.50
21.60
21.70
21.80
V magnitude
5.6
5.8
6.0
6.2
6.4
6.6
Modified Julian Date−51370

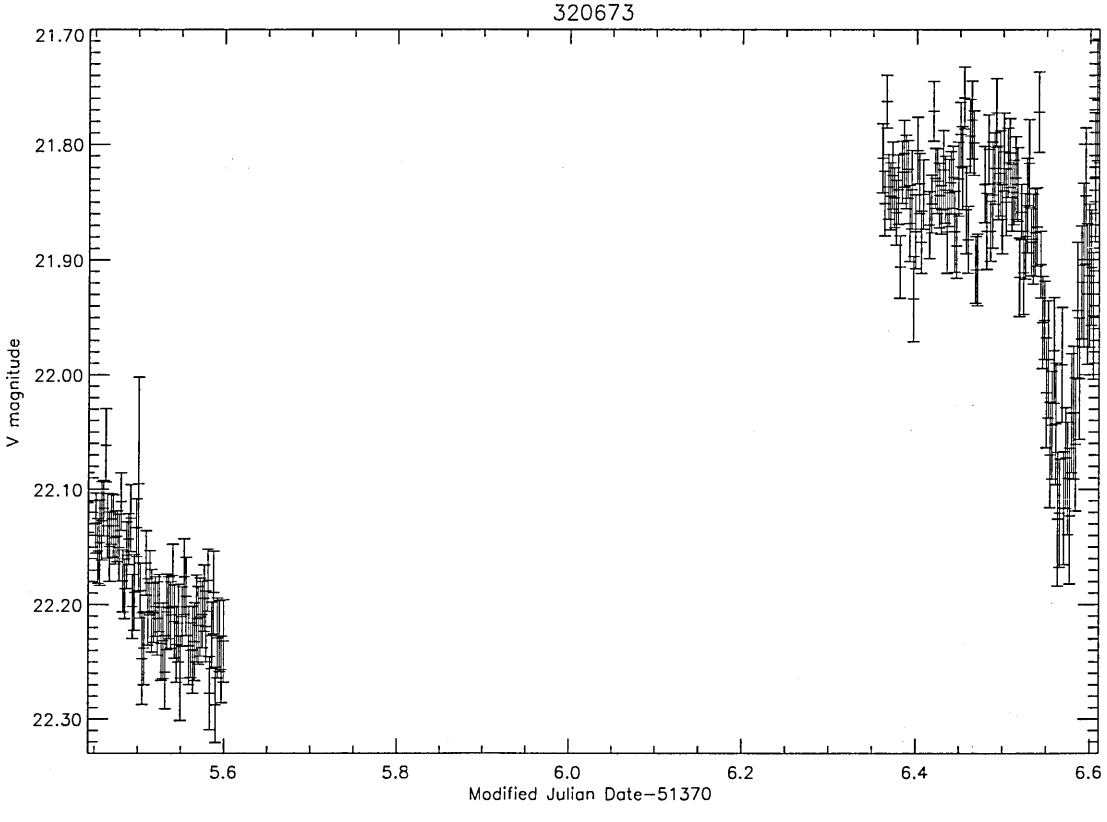
320673
21.70
21.80
21.90
22.00
22.10
22.20
22.30
V magnitude
5.6
5.8
6.0
6.2
6.4
6.6
Modified Julian Date−51370

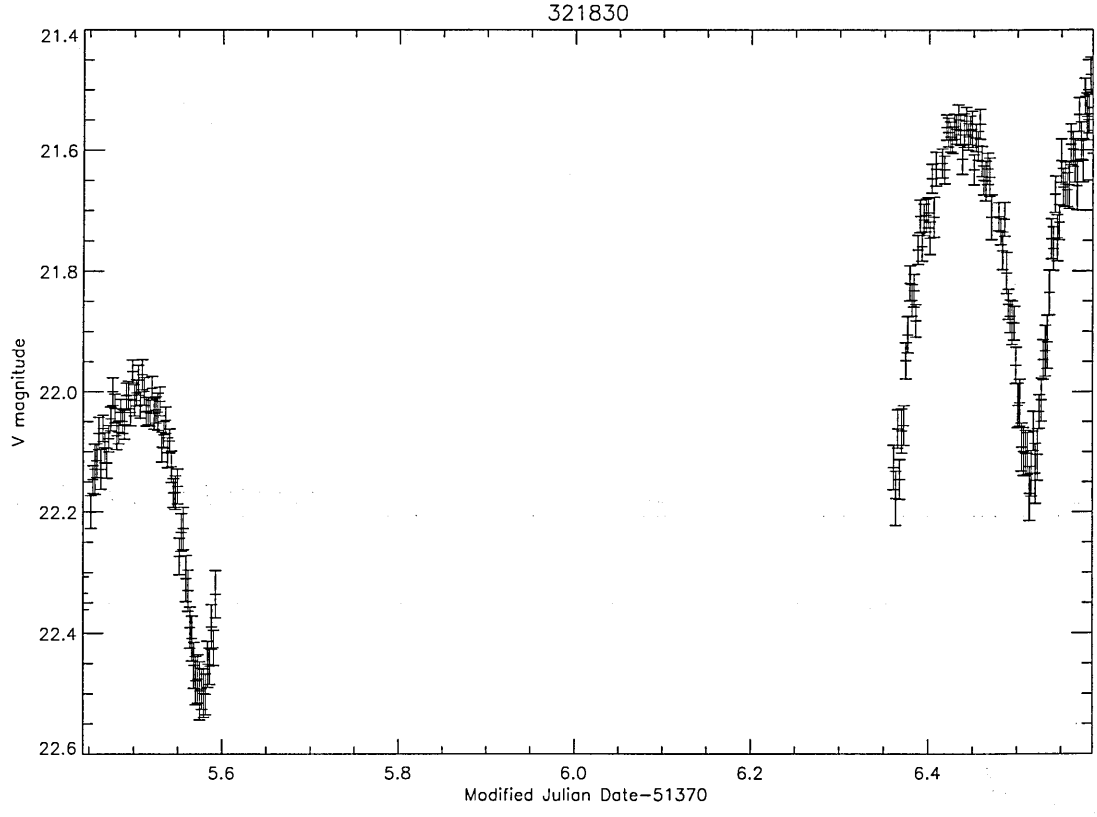
321830
21.4
21.6
21.8
22.0
22.2
22.4
22.6
V magnitude
5.6
5.8
6.0
6.2
6.4
Modified Julian Date−51370

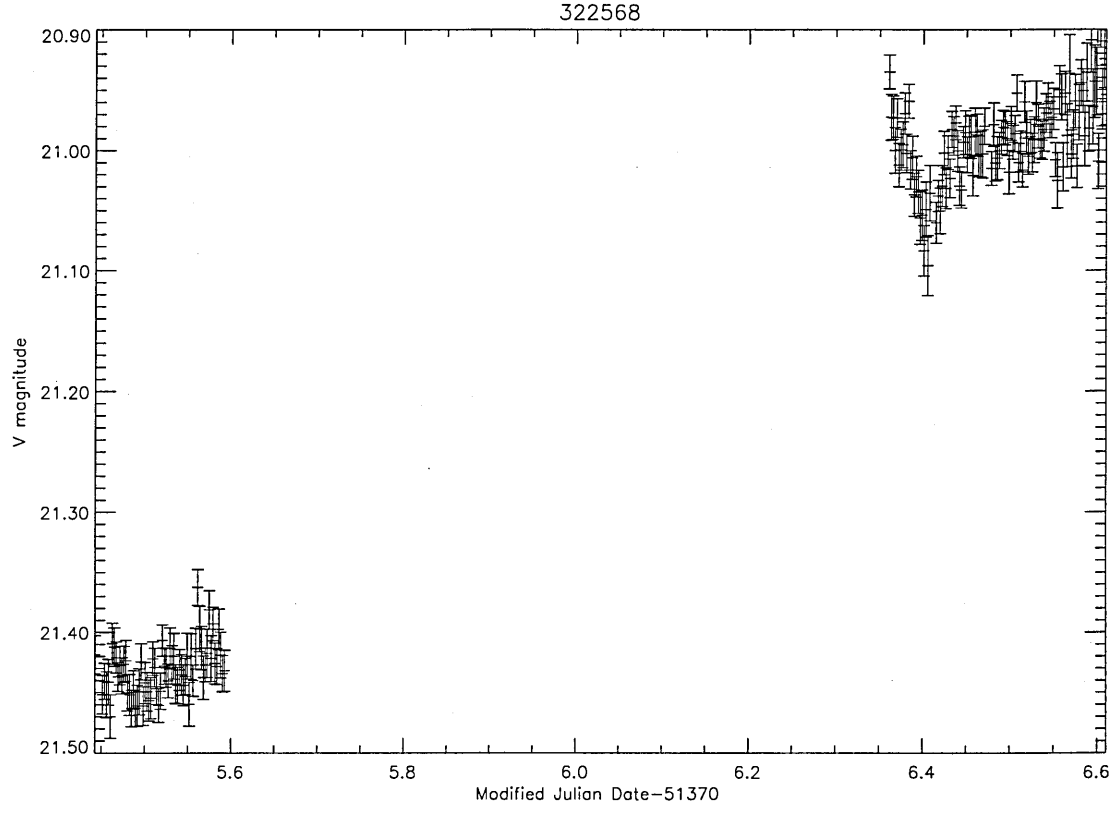
322568
20.90
21.00
21.10
21.20
21.30
21.40
21.50
V magnitude
5.6
5.8
6.0
6.2
6.4
6.6
Modified Julian Date−51370

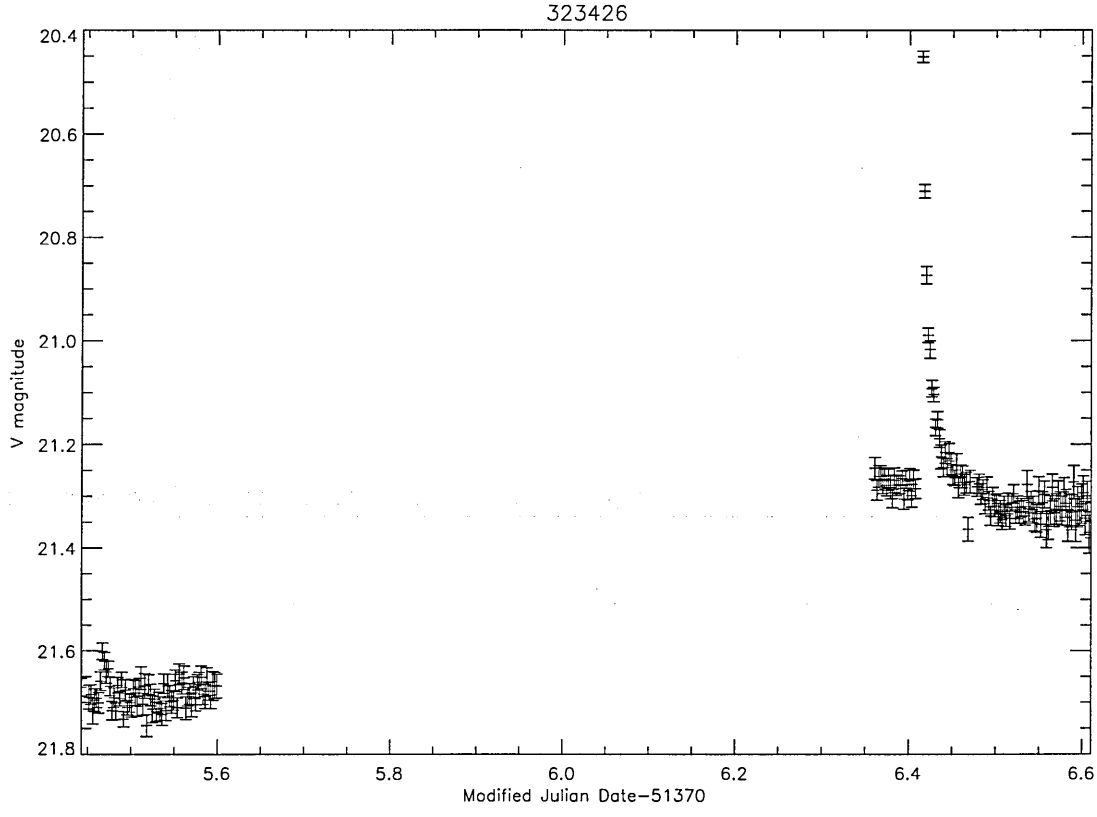
323426
V magnitude
20.4
20.6
20.8
21.0
21.2
21.4
21.6
21.8
5.6
5.8
6.0
6.2
6.4
6.6
Modified Julian Date−51370

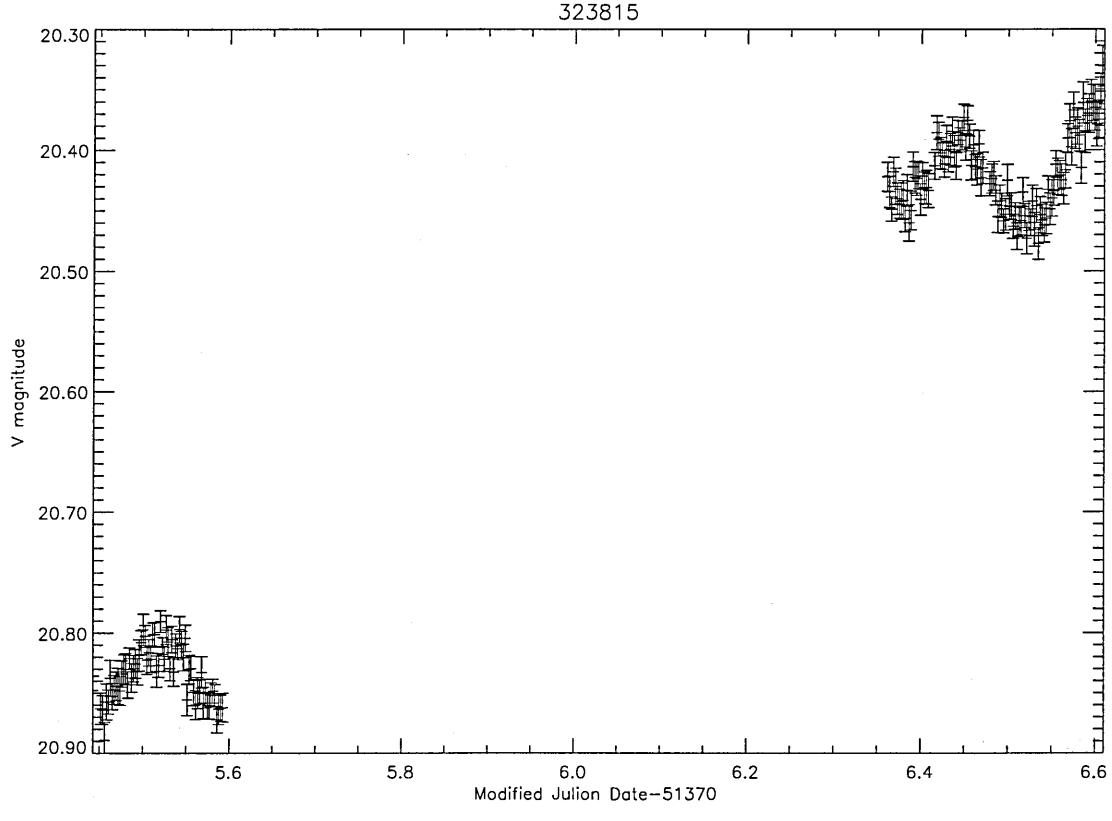
323815
V magnitude
20.30
20.40
20.50
20.60
20.70
20.80
20.90
5.6
5.8
6.0
6.2
6.4
6.6
Modified Julion Date−51370

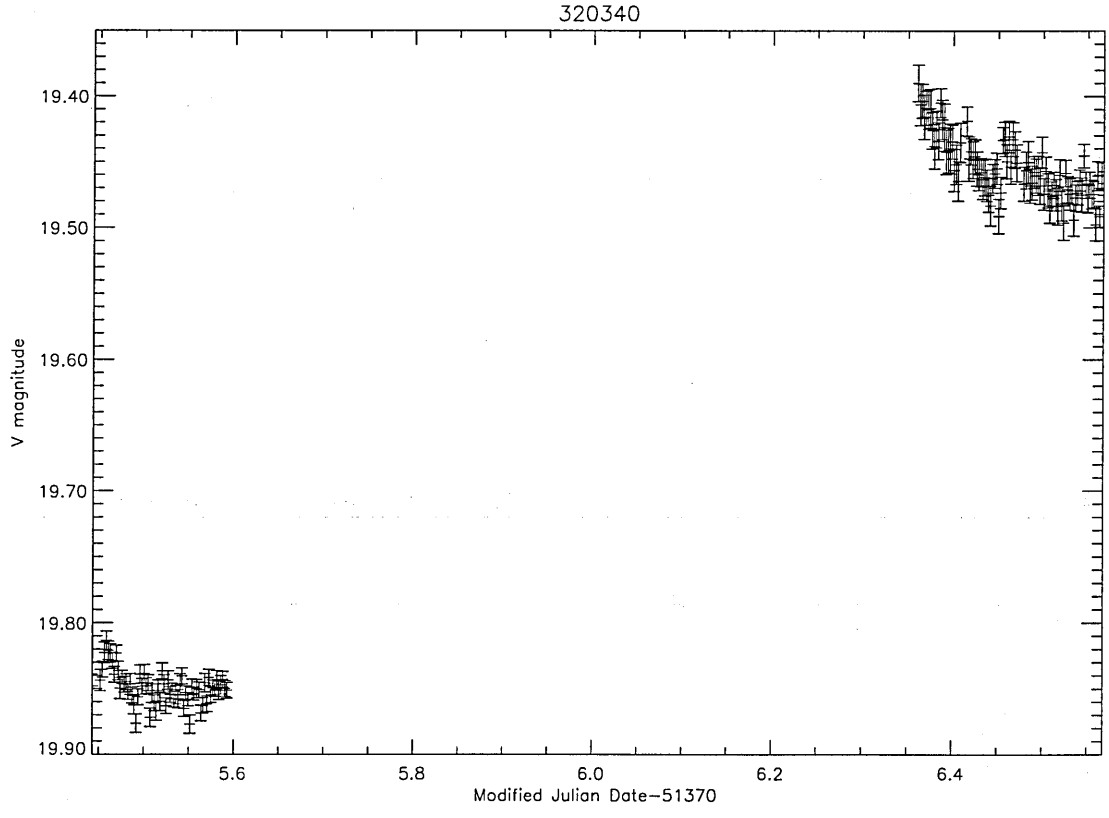
320340
19.40
19.50
19.60
19.70
19.80
19.90
V magnitude
5.6
5.8
6.0
6.2
6.4
Modified Julian Date−51370

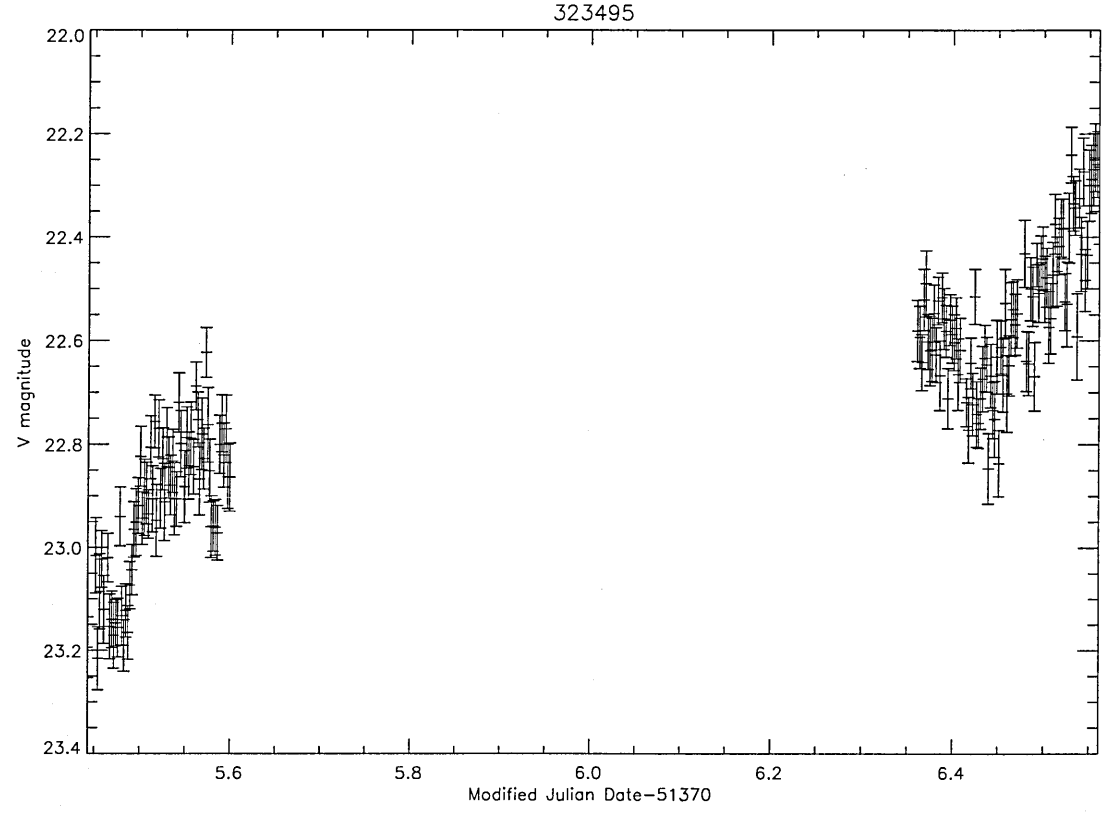
323495
22.0
22.2
22.4
22.6
22.8
23.0
23.2
23.4
V magnitude
5.6
5.8
6.0
6.2
6.4
Modified Julian Date−51370

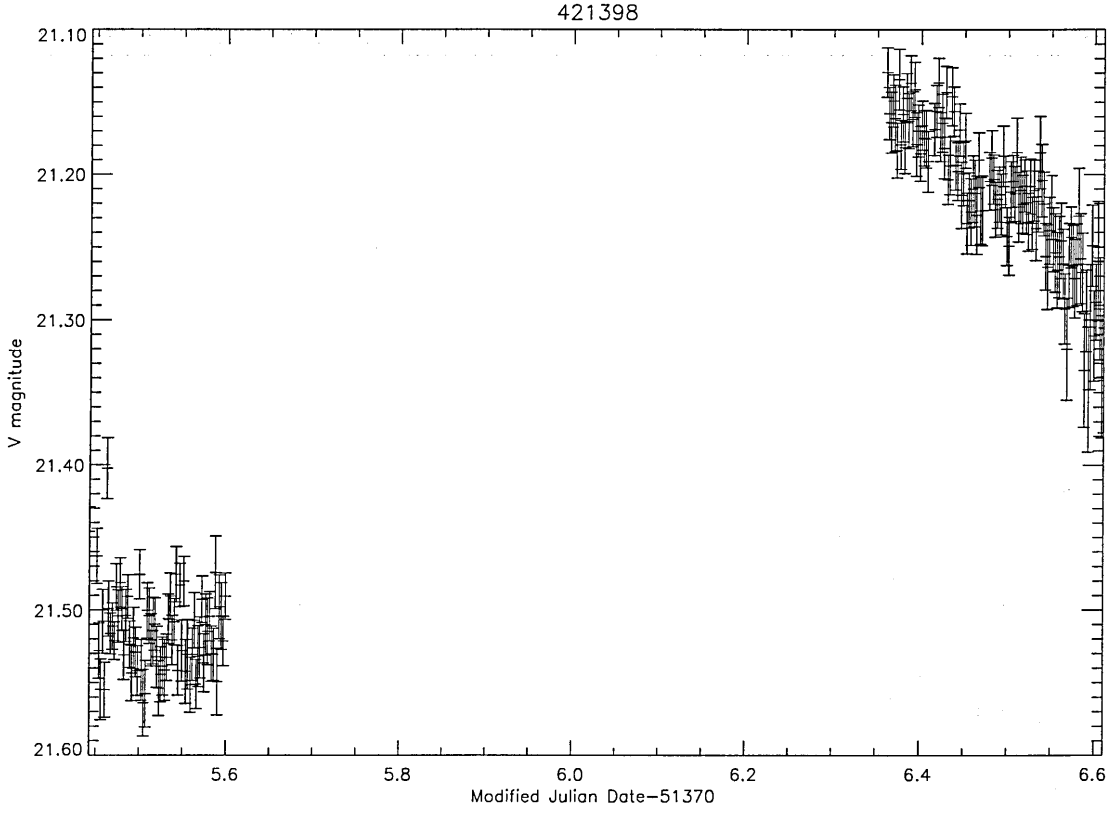
421398
21.10
21.20
21.30
21.40
21.50
21.60
V magnitude
5.6
5.8
6.0
6.2
6.4
6.6
Modified Julian Date−51370

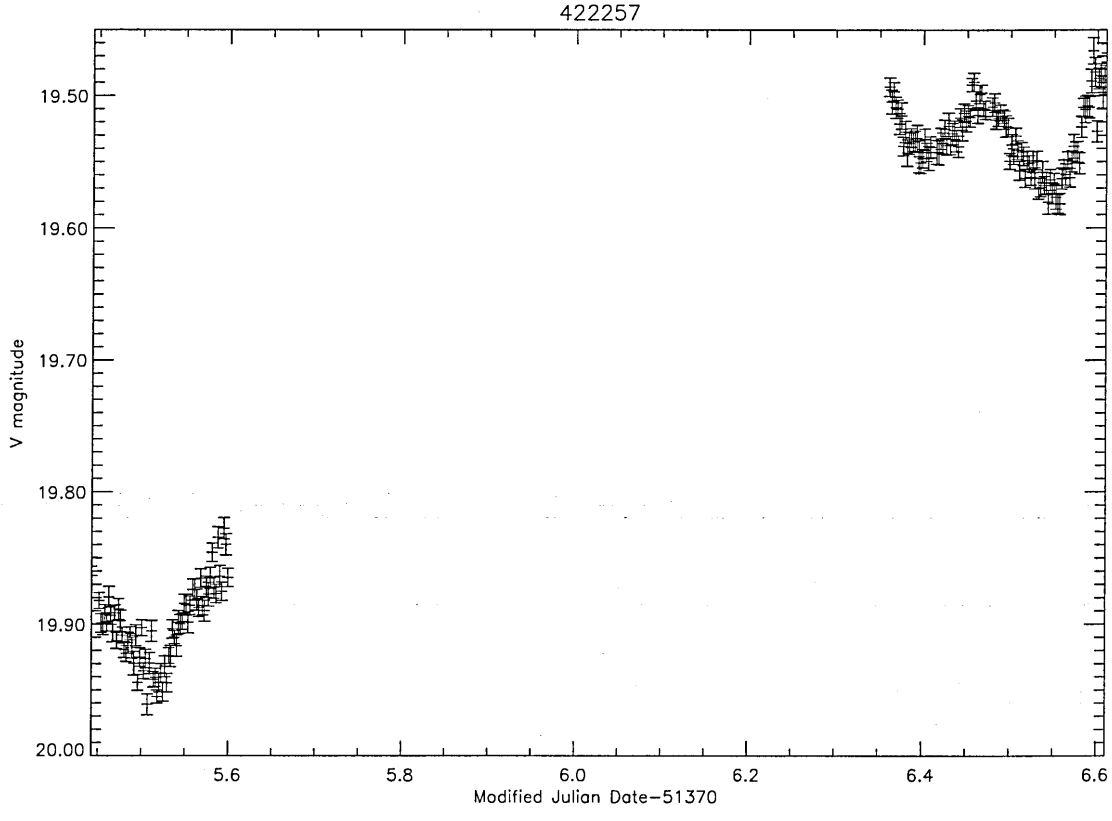
422257
19.50
19.60
19.70
19.80
19.90
20.00
V magnitude
5.6
5.8
6.0
6.2
6.4
6.6
Modified Julian Date−51370

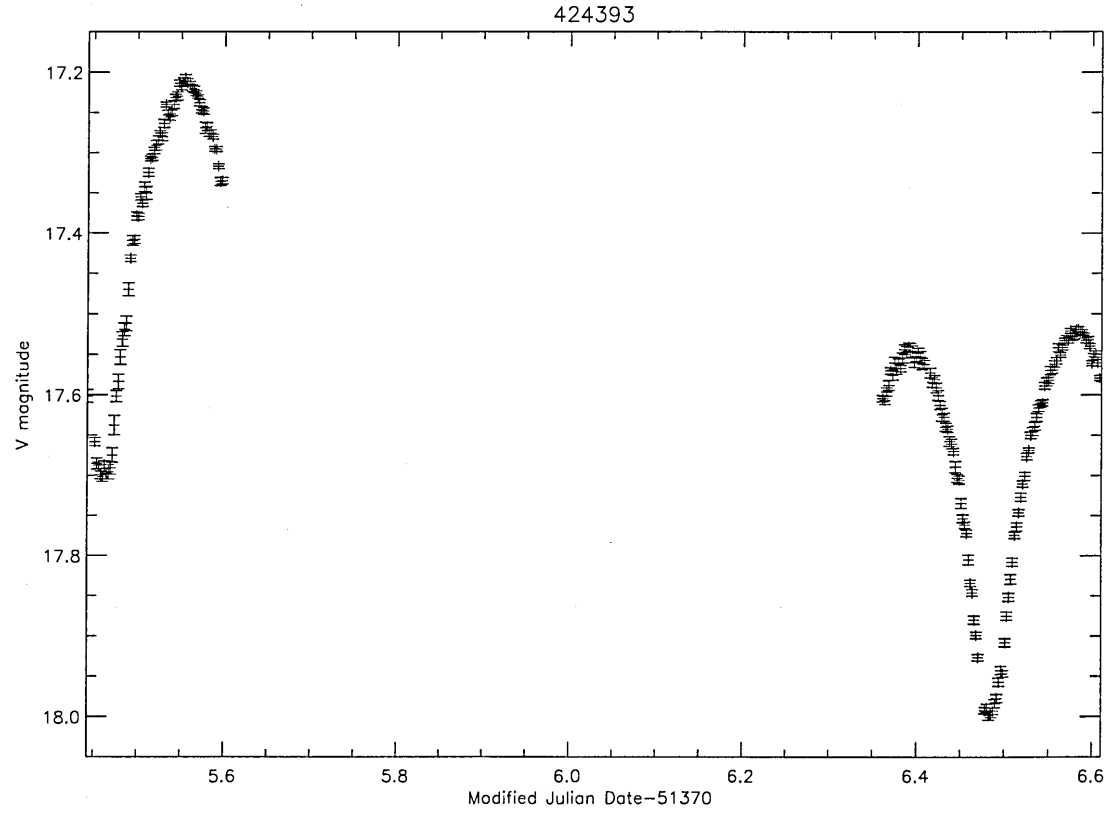
424393
17.2
17.4
17.6
17.8
18.0
V magnitude
5.6
5.8
6.0
6.2
6.4
6.6
Modified Julian Date−51370

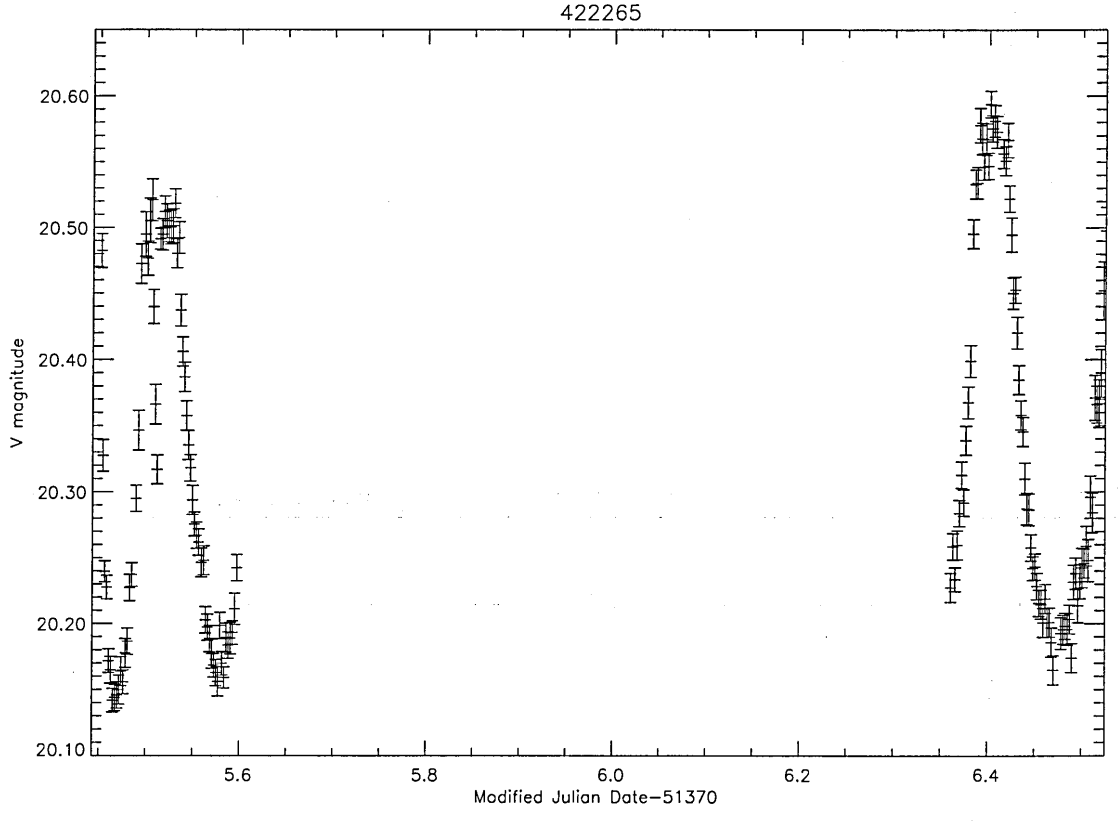
422265
20.60
20.50
20.40
20.30
20.20
20.10
V magnitude
5.6
5.8
6.0
6.2
6.4
Modified Julian Date−51370

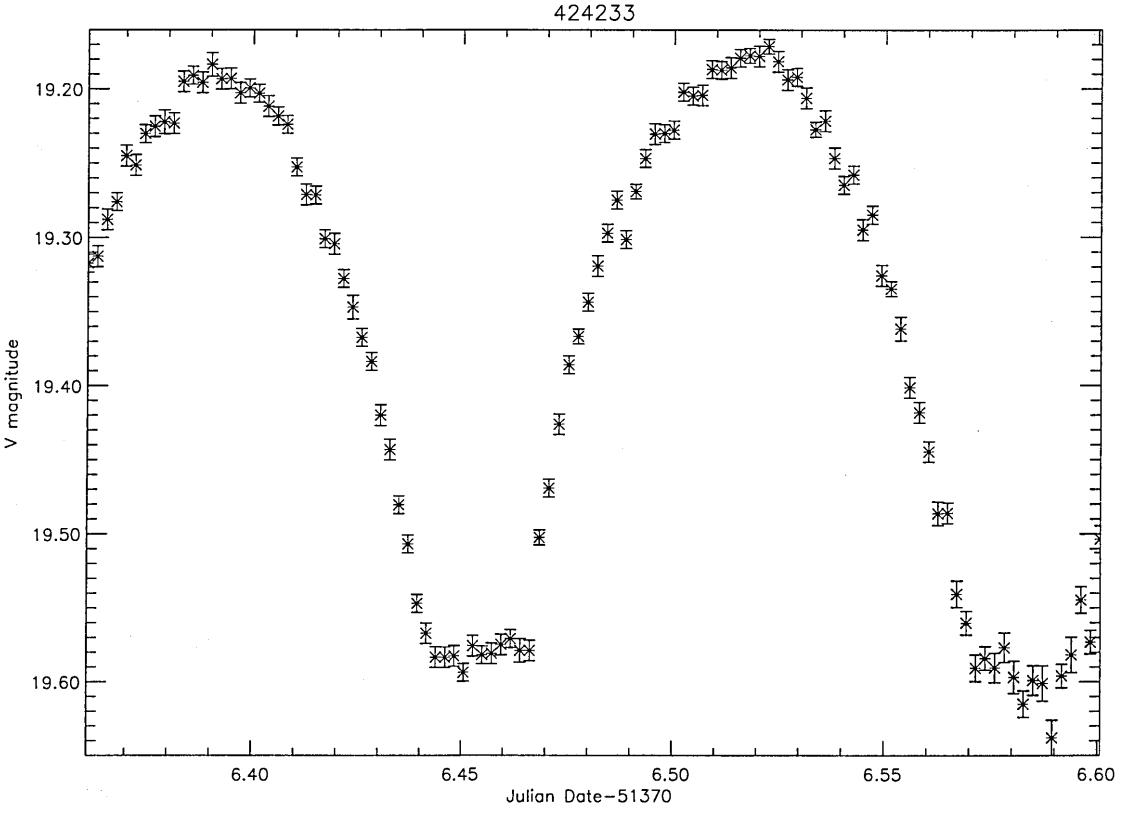
424233
19.20
19.30
19.40
19.50
19.60
V magnitude
6.40
6.45
6.50
6.55
6.60
Julian Date−51370

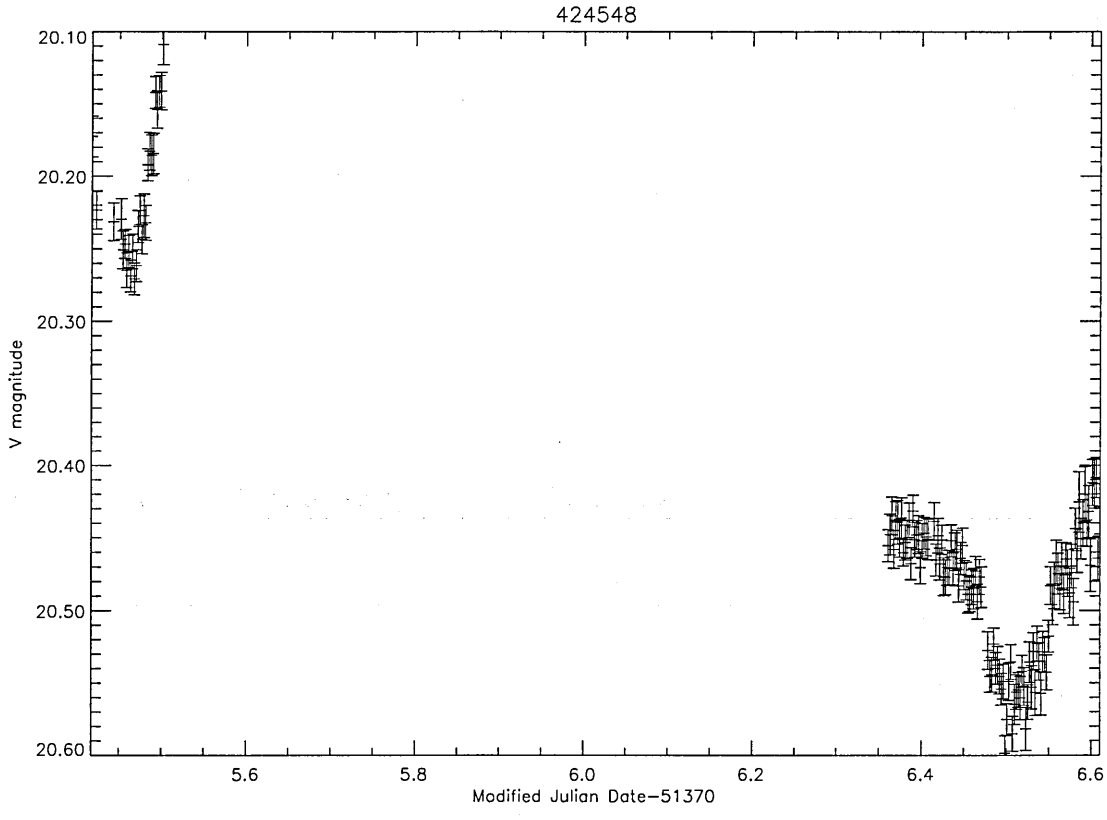
424548
20.10
20.20
20.30
20.40
20.50
20.60
V magnitude
5.6
5.8
6.0
6.2
6.4
6.6
Modified Julian Date−51370

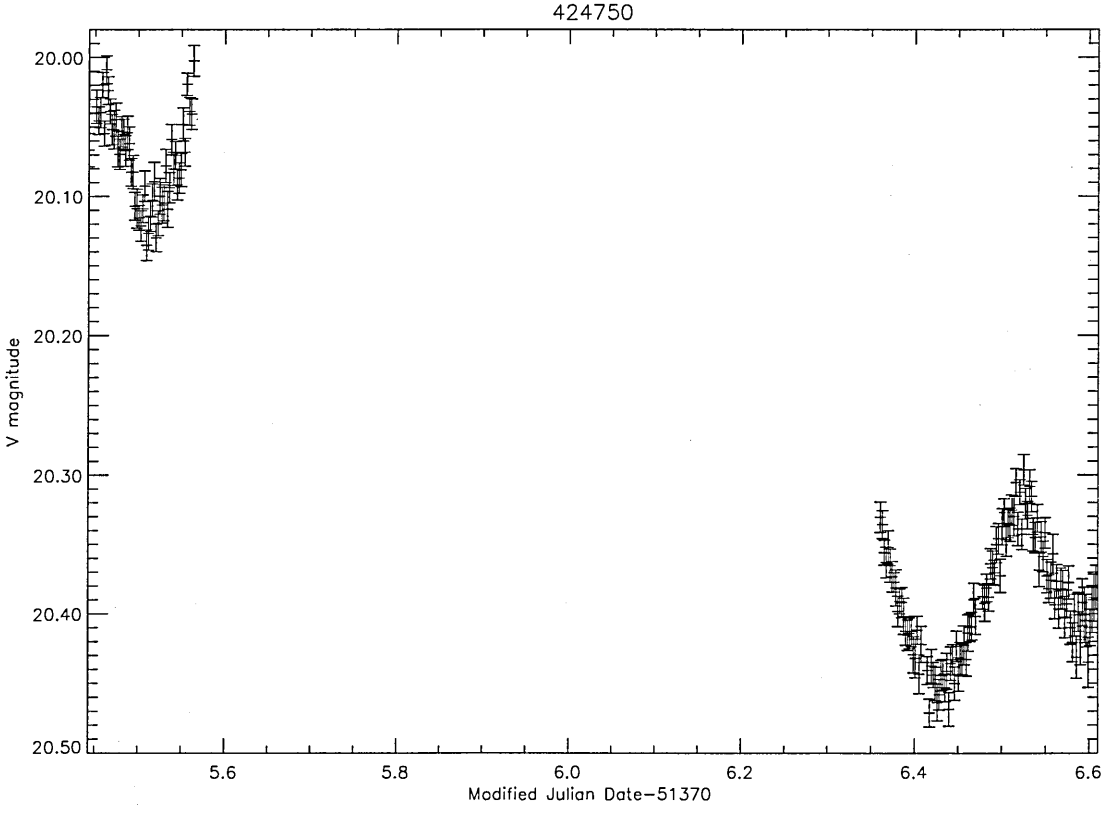
424750
20.00
20.10
20.20
20.30
20.40
20.50
V magnitude
5.6
5.8
6.0
6.2
6.4
6.6
Modified Julian Date−51370

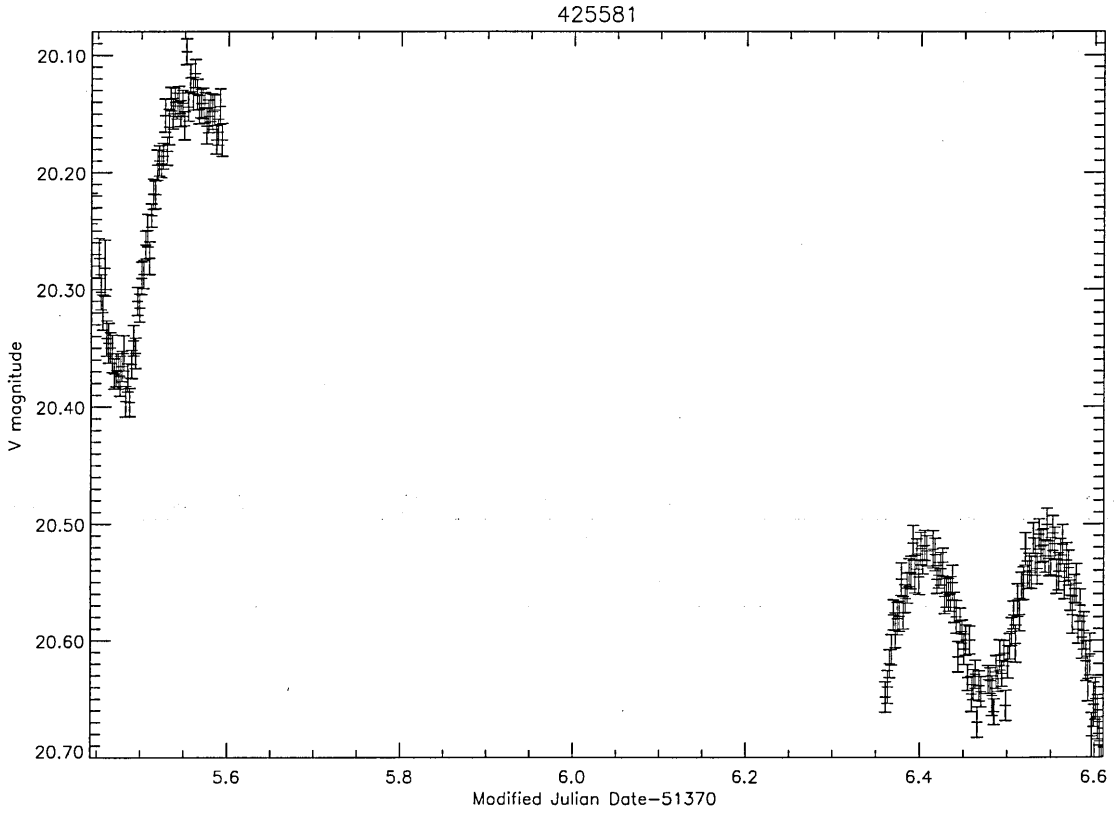
425581
20.10
20.20
20.30
20.40
20.50
20.60
20.70
V magnitude
5.6
5.8
6.0
6.2
6.4
6.6
Modified Julian Date−51370

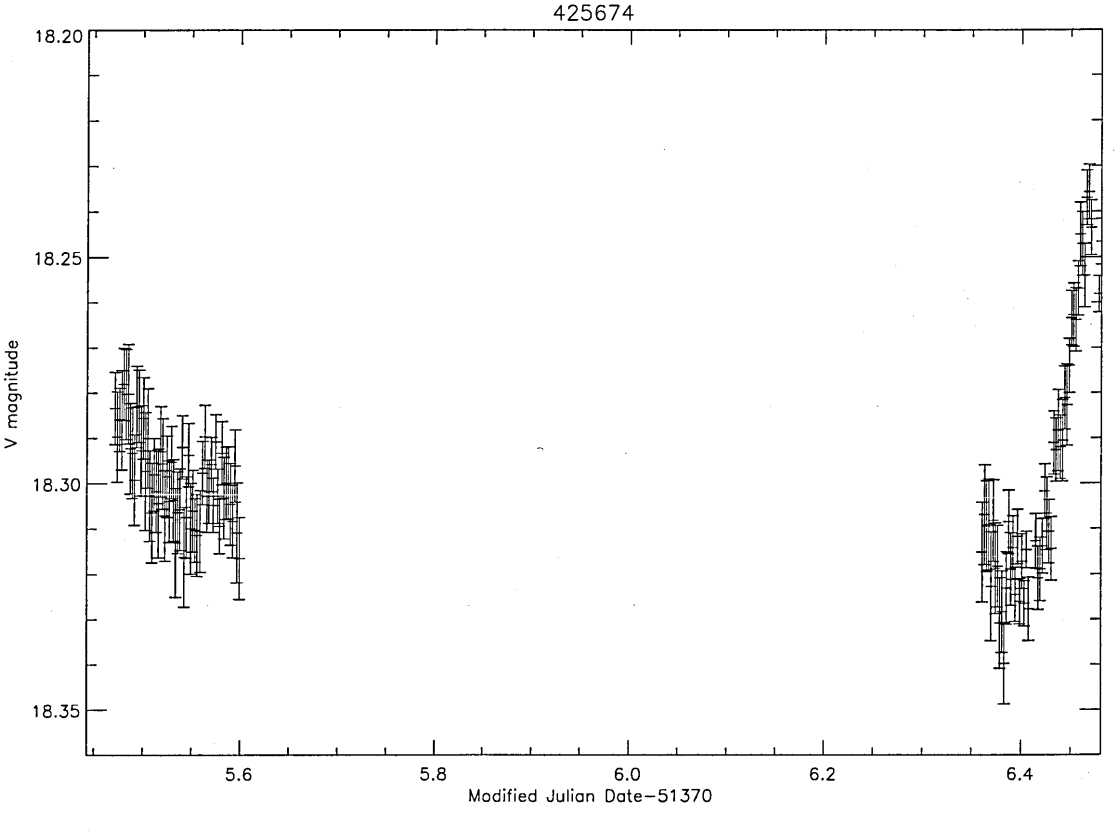
425674
18.20
18.25
18.30
18.35
V magnitude
5.6
5.8
6.0
6.2
6.4
Modified Julian Date−51370

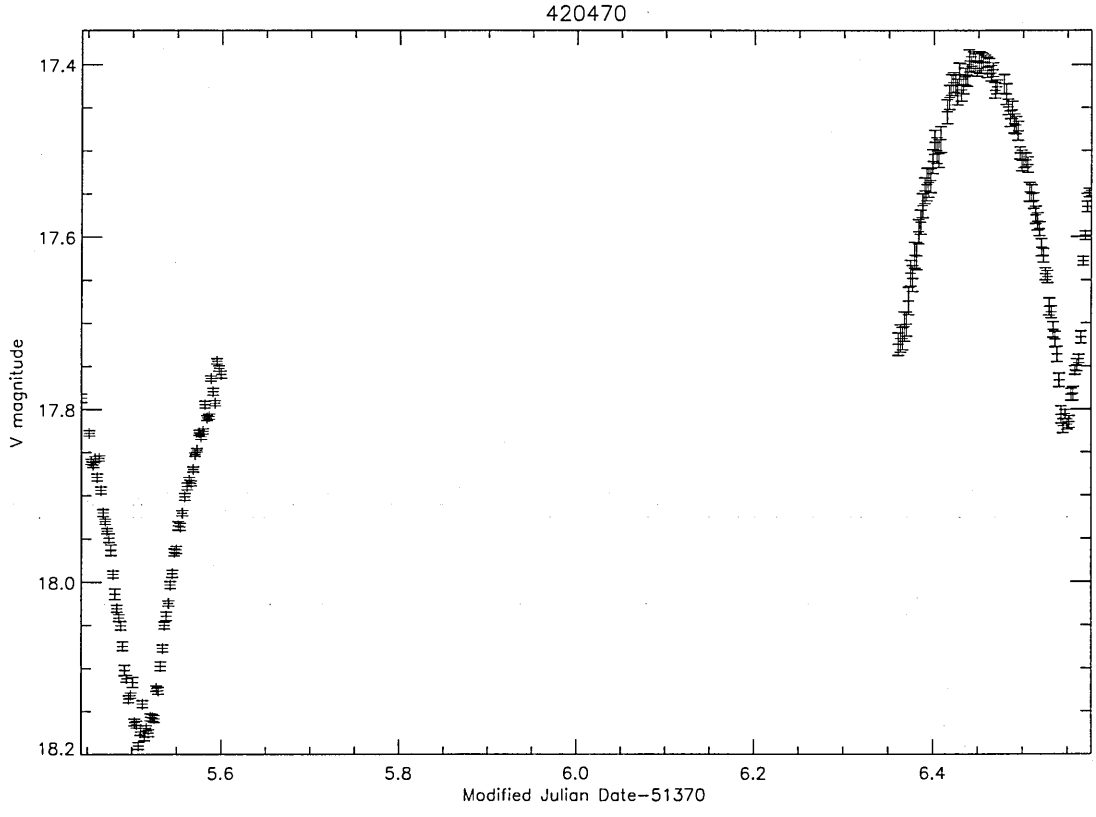
420470
17.4
17.6
17.8
18.0
18.2
V magnitude
5.6
5.8
6.0
6.2
6.4
Modified Julian Date−51370

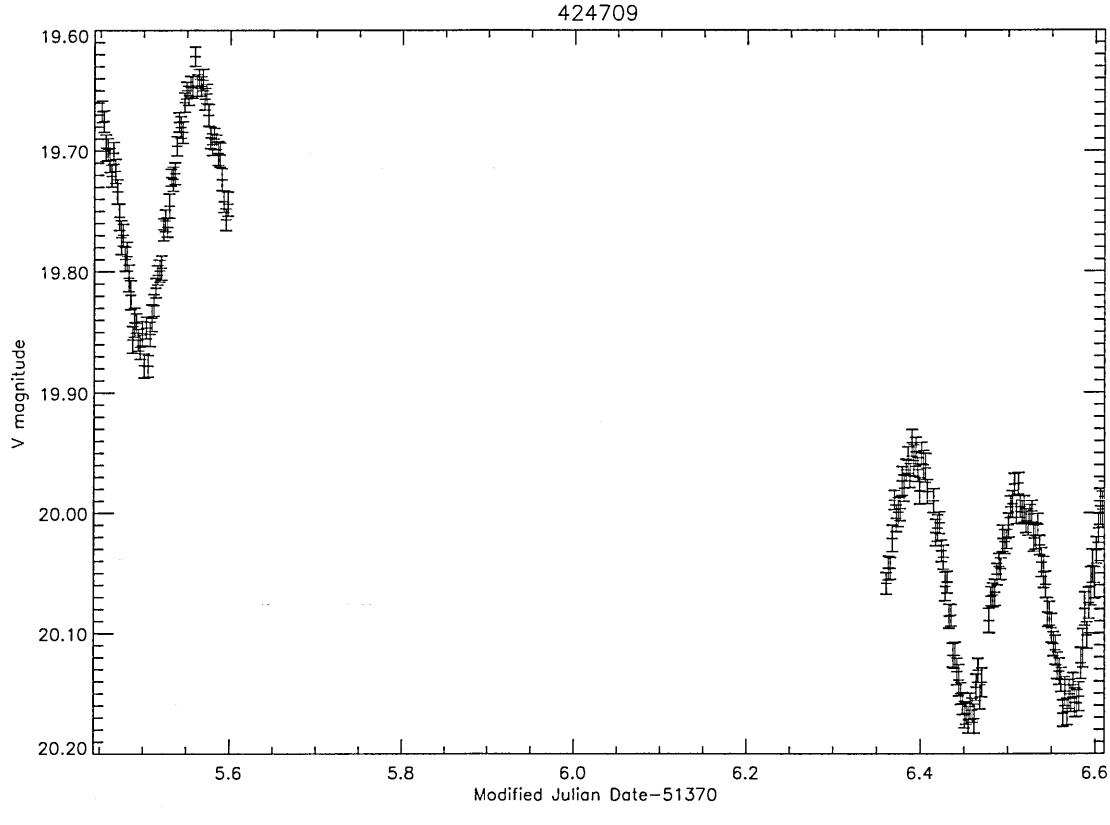
424709
19.60
19.70
19.80
19.90
20.00
20.10
20.20
V magnitude
5.6
5.8
6.0
6.2
6.4
6.6
Modified Julian Date−51370

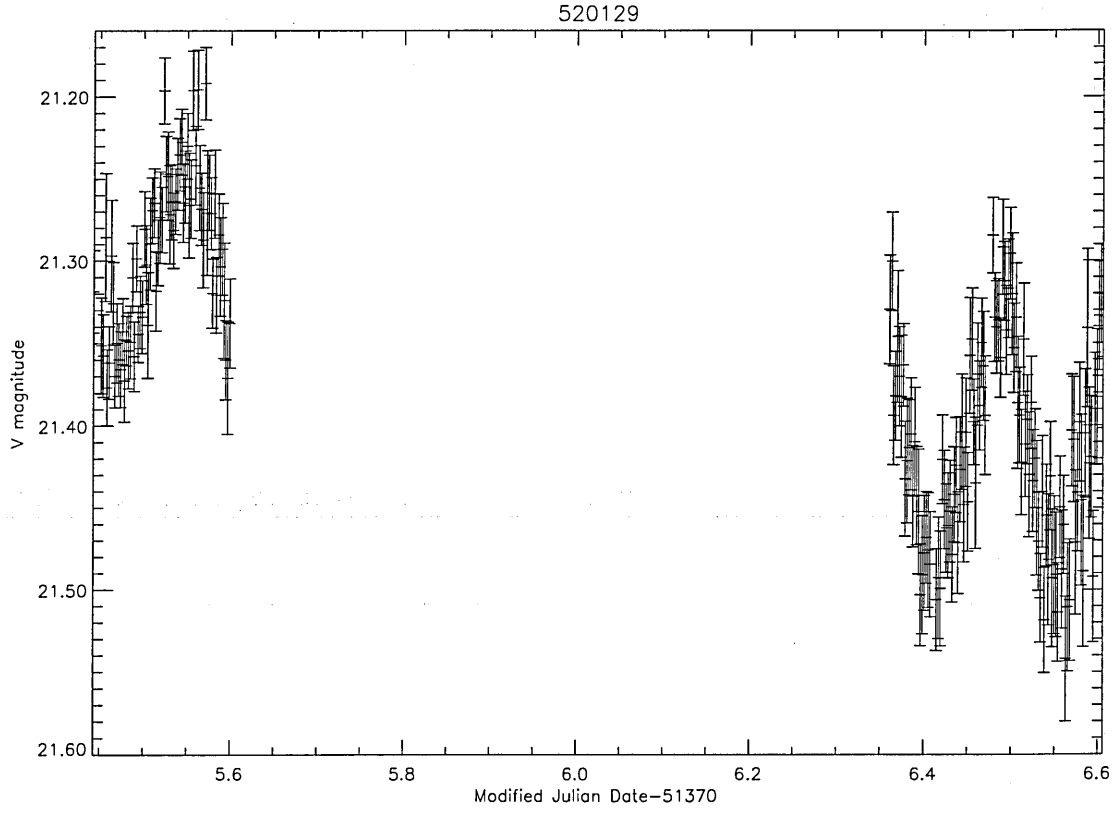
520129
21.20
21.30
21.40
21.50
21.60
V magnitude
5.6
5.8
6.0
6.2
6.4
6.6
Modified Julian Date−51370

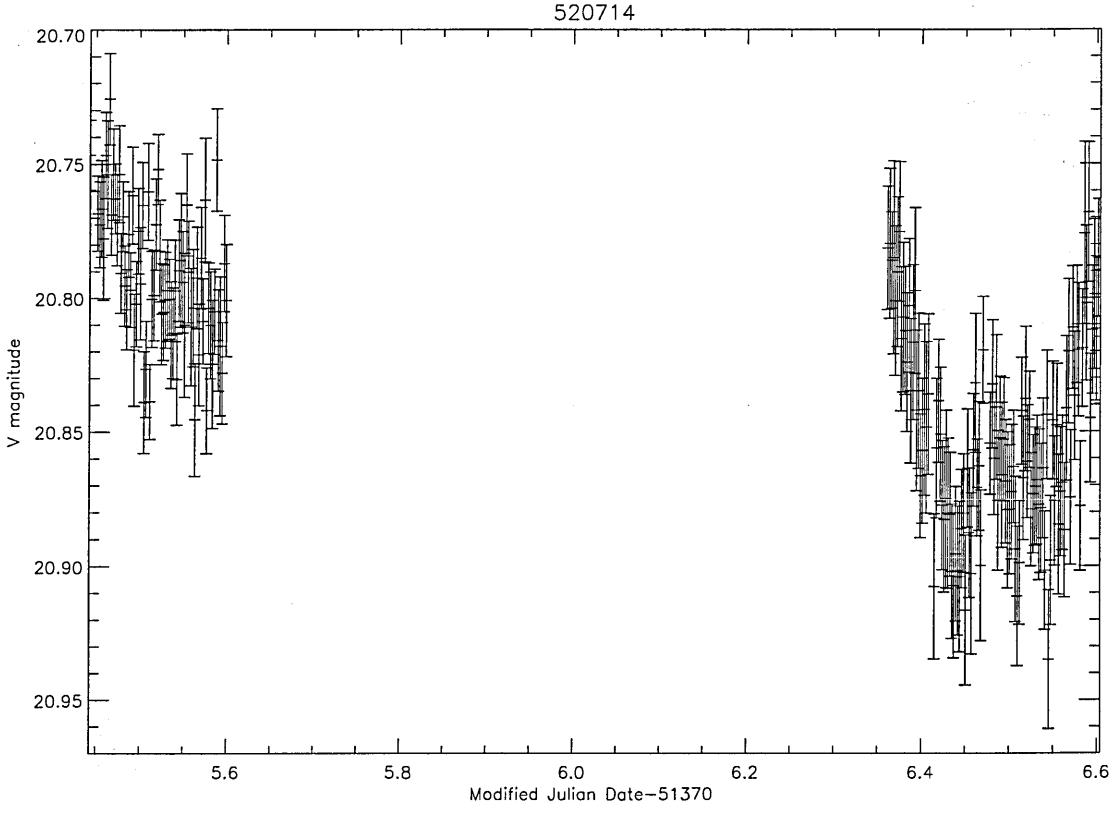
520714
20.70
20.75
20.80
20.85
20.90
20.95
V magnitude
5.6
5.8
6.0
6.2
6.4
6.6
Modified Julian Date−51370

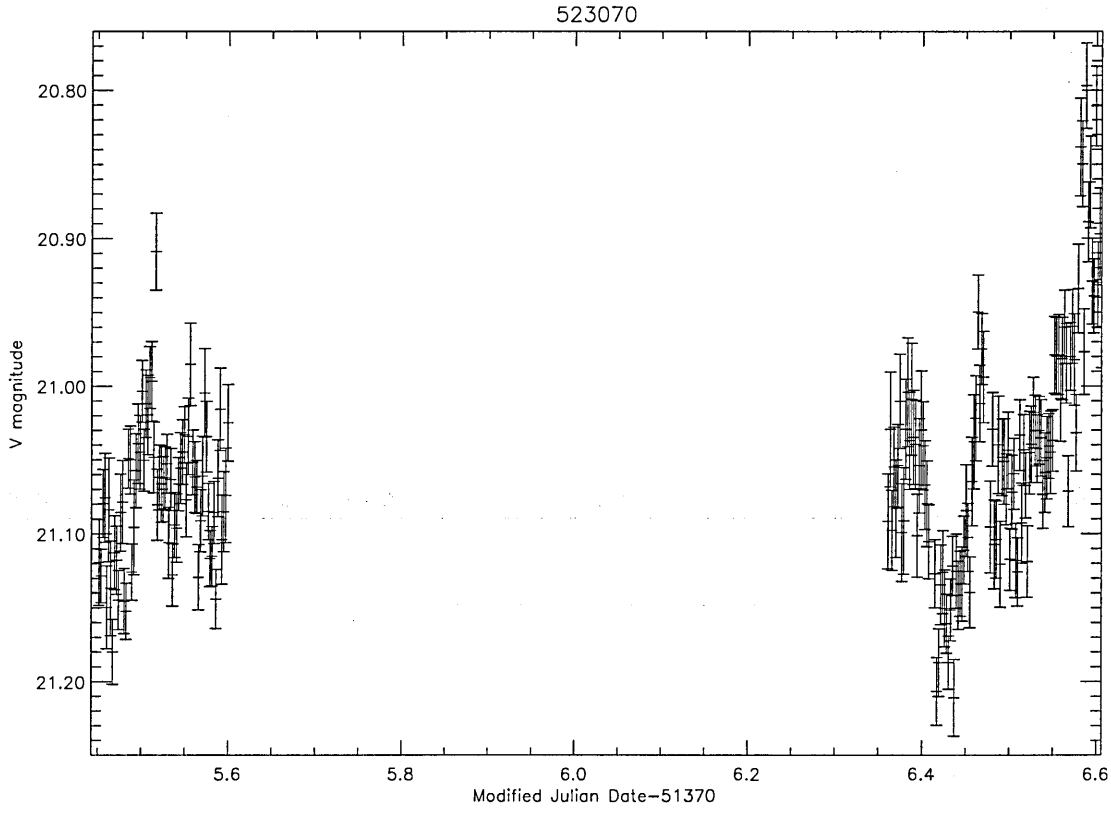
523070
20.80
20.90
21.00
21.10
21.20
V magnitude
5.6
5.8
6.0
6.2
6.4
6.6
Modified Julian Date−51370

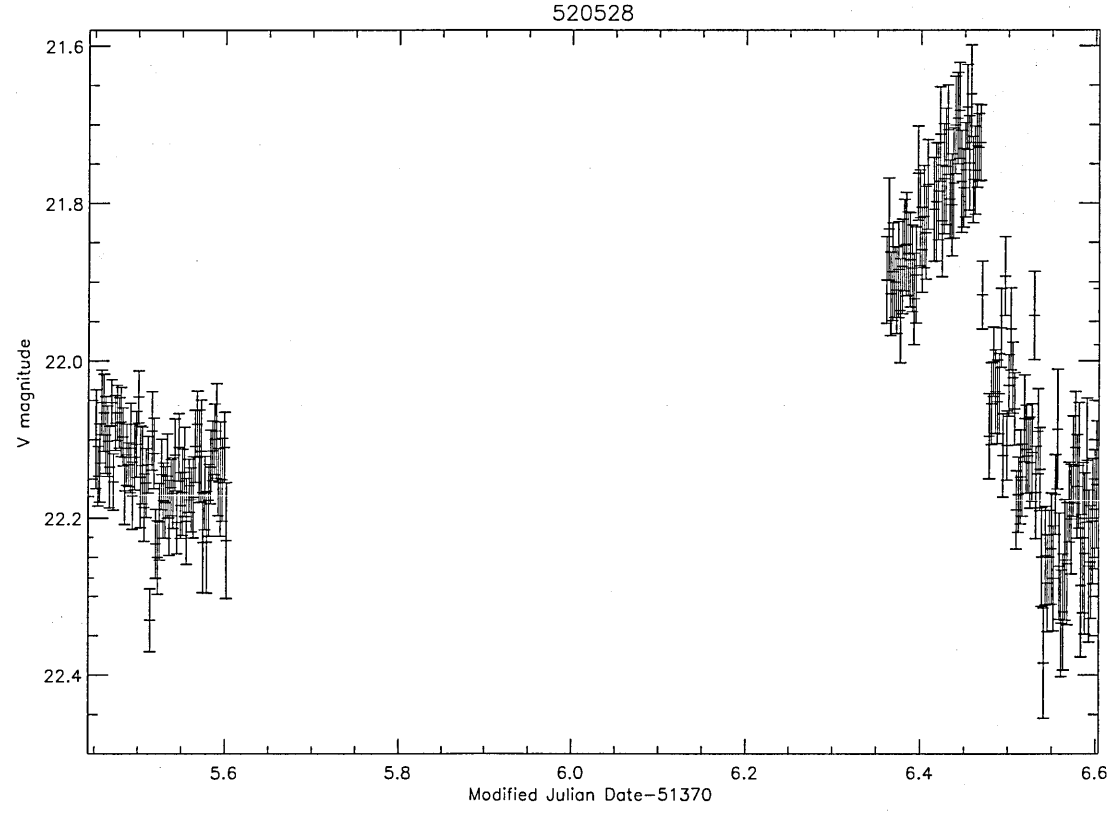
520528
21.6
21.8
22.0
22.2
22.4
V magnitude
5.6
5.8
6.0
6.2
6.4
6.6
Modified Julian Date−51370

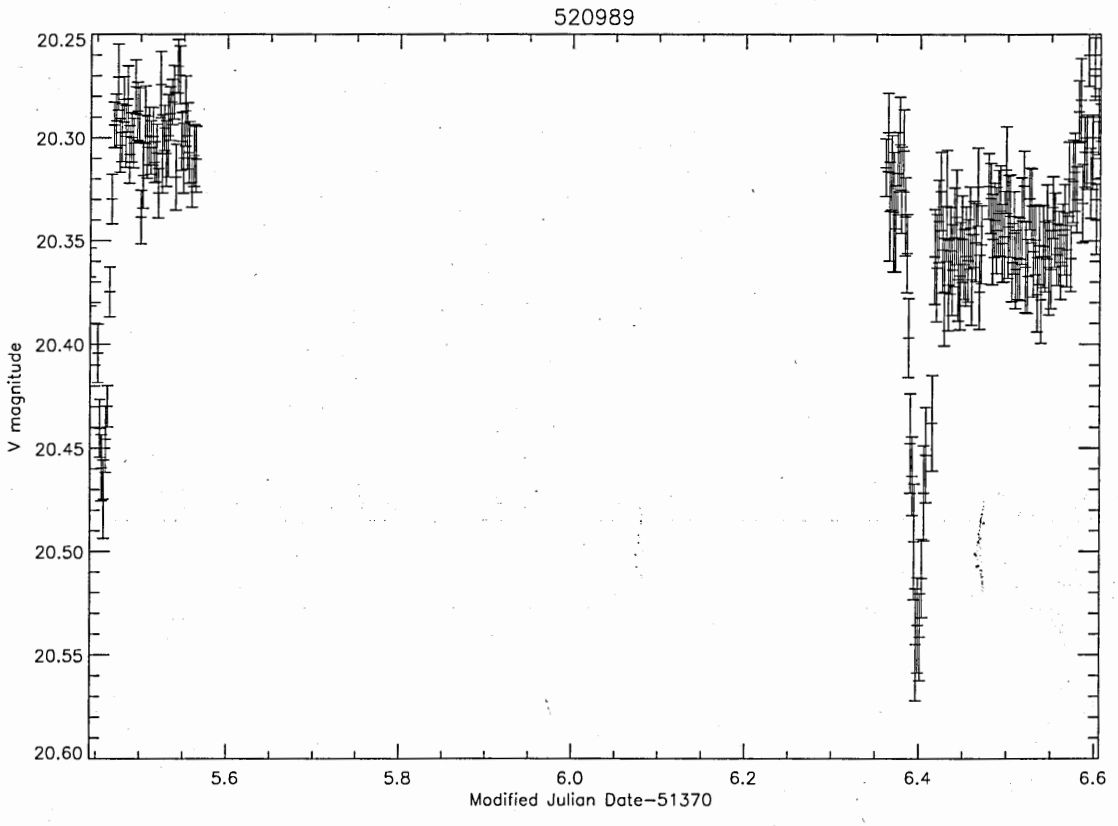
520989
20.25
20.30
20.35
20.40
20.45
20.50
20.55
20.60
V magnitude
5.6
5.8
6.0
6.2
6.4
6.6
Modified Julian Date−51370

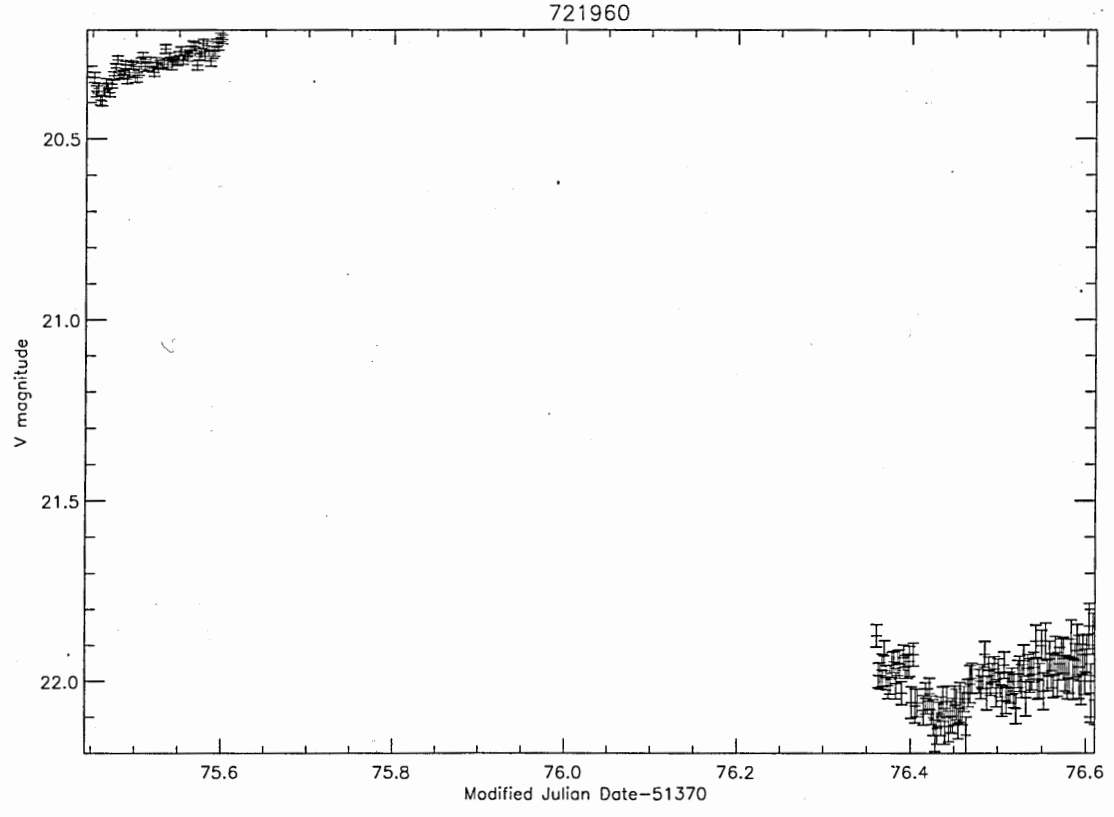
721960
20.5
21.0
21.5
22.0
V magnitude
75.6
75.8
76.0
76.2
76.4
76.6
Modified Julian Date−51370

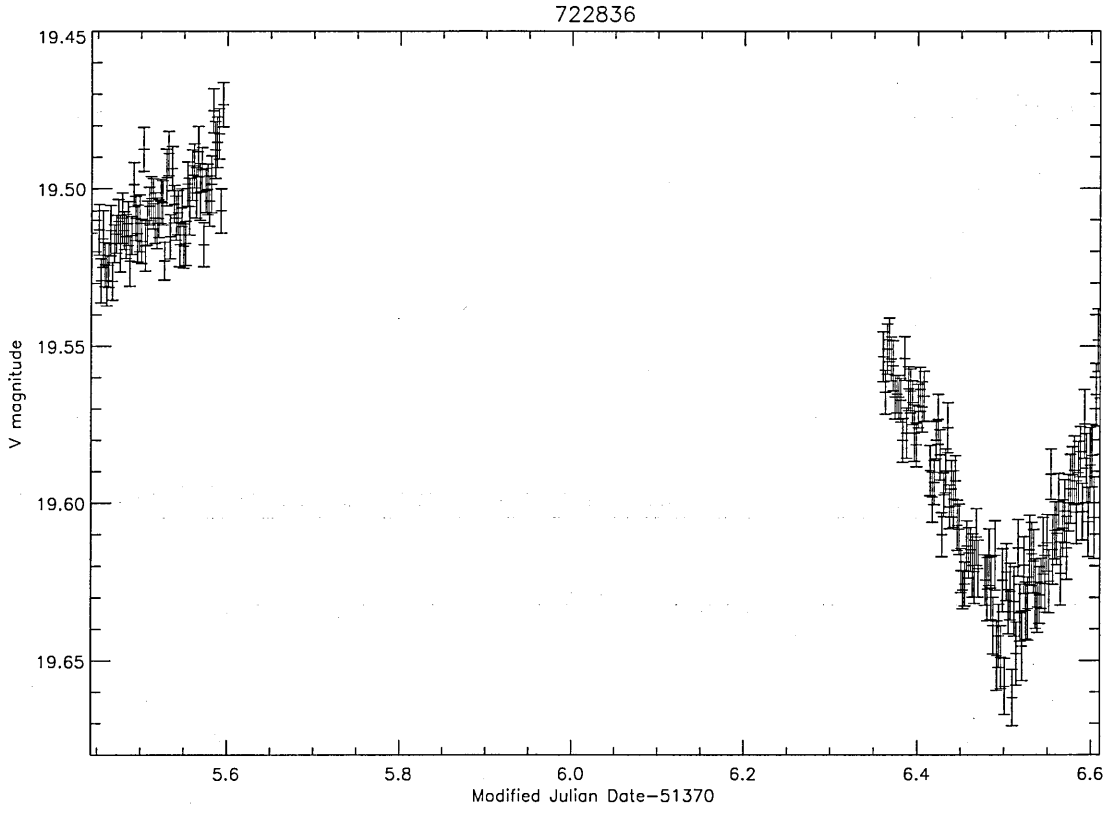
722836
19.45
19.50
19.55
19.60
19.65
V magnitude
5.6
5.8
6.0
6.2
6.4
6.6
Modified Julian Date−51370

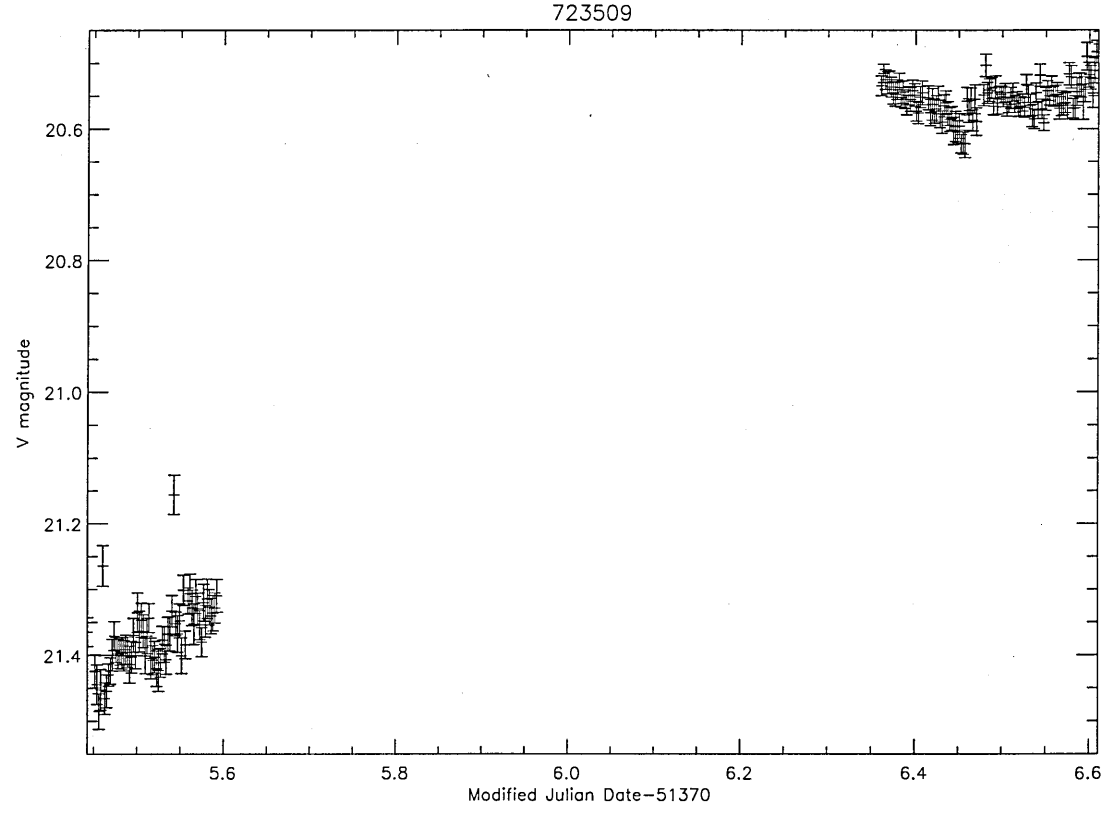
723509
20.6
20.8
21.0
21.2
21.4
V magnitude
5.6
5.8
6.0
6.2
6.4
6.6
Modified Julian Date−51370

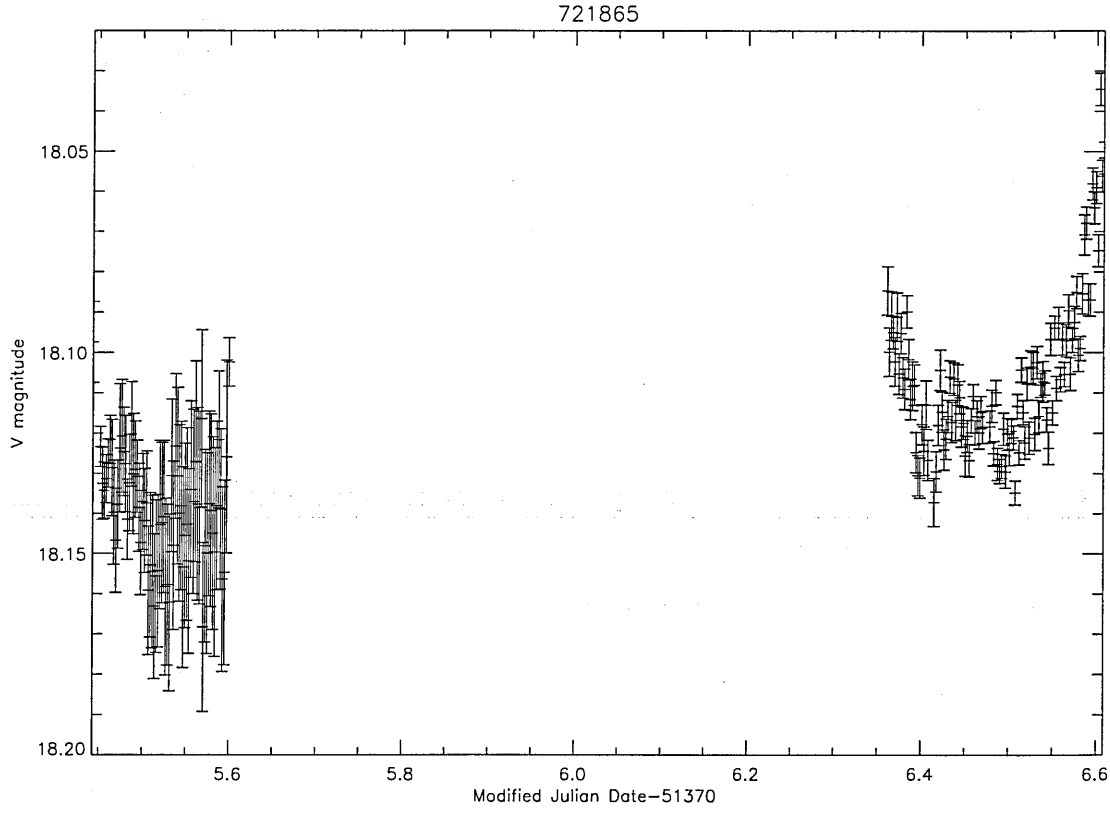
721865
18.05
18.10
18.15
18.20
V magnitude
5.6
5.8
6.0
6.2
6.4
6.6
Modified Julian Date−51370

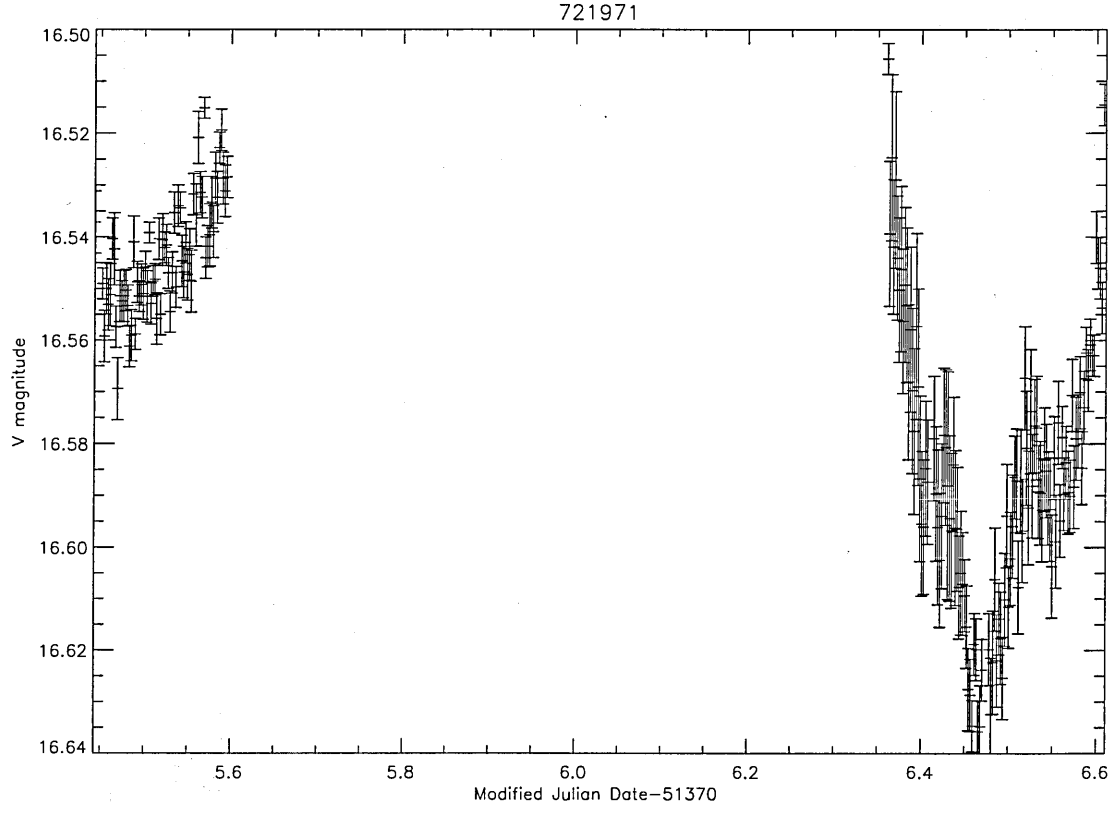
721971
16.50
16.52
16.54
16.56
16.58
16.60
16.62
16.64
V magnitude
5.6
5.8
6.0
6.2
6.4
6.6
Modified Julian Date−51370

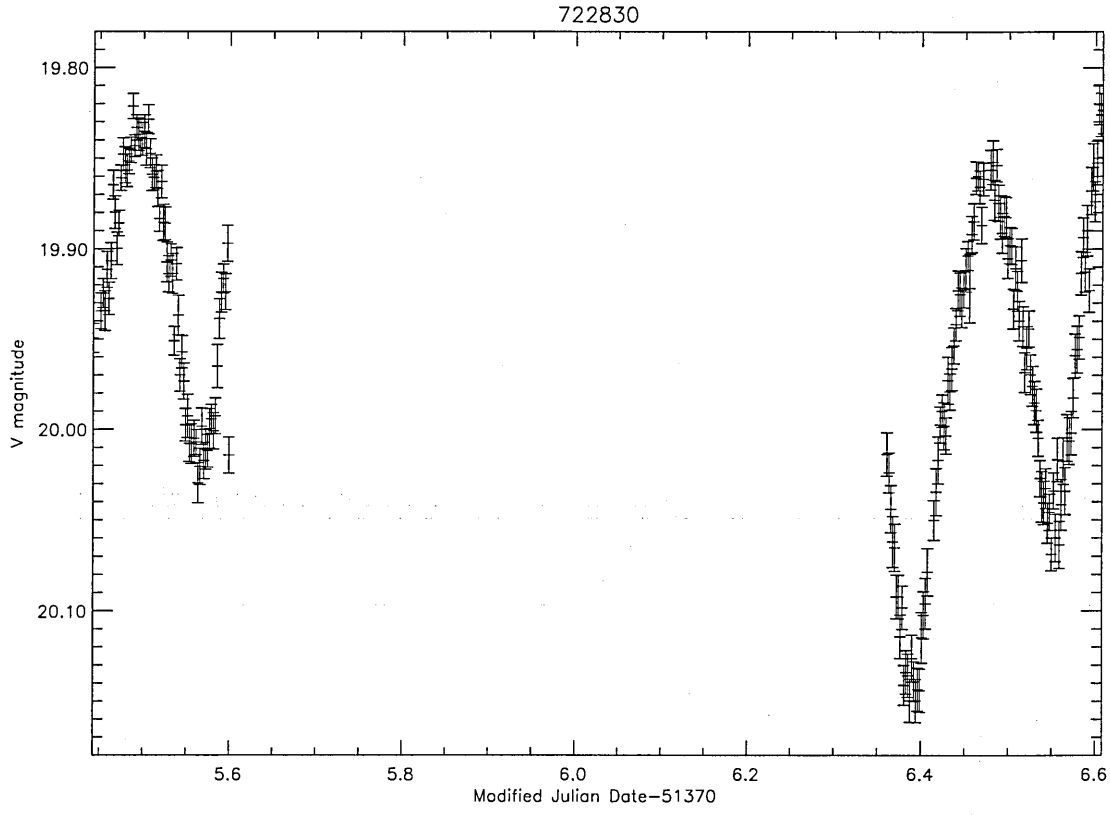
722830
19.80
19.90
20.00
20.10
V magnitude
5.6
5.8
6.0
6.2
6.4
6.6
Modified Julian Date−51370

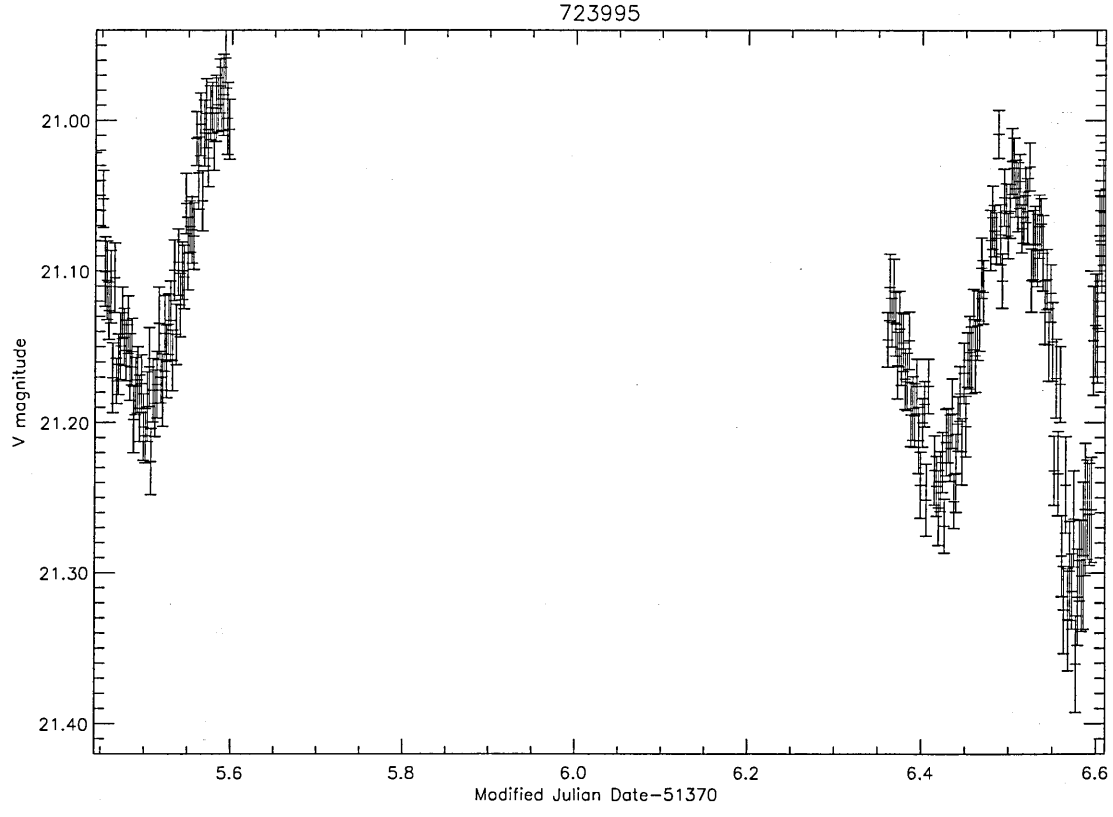
723995
21.00
21.10
21.20
21.30
21.40
V magnitude
5.6
5.8
6.0
6.2
6.4
6.6
Modified Julian Date−51370

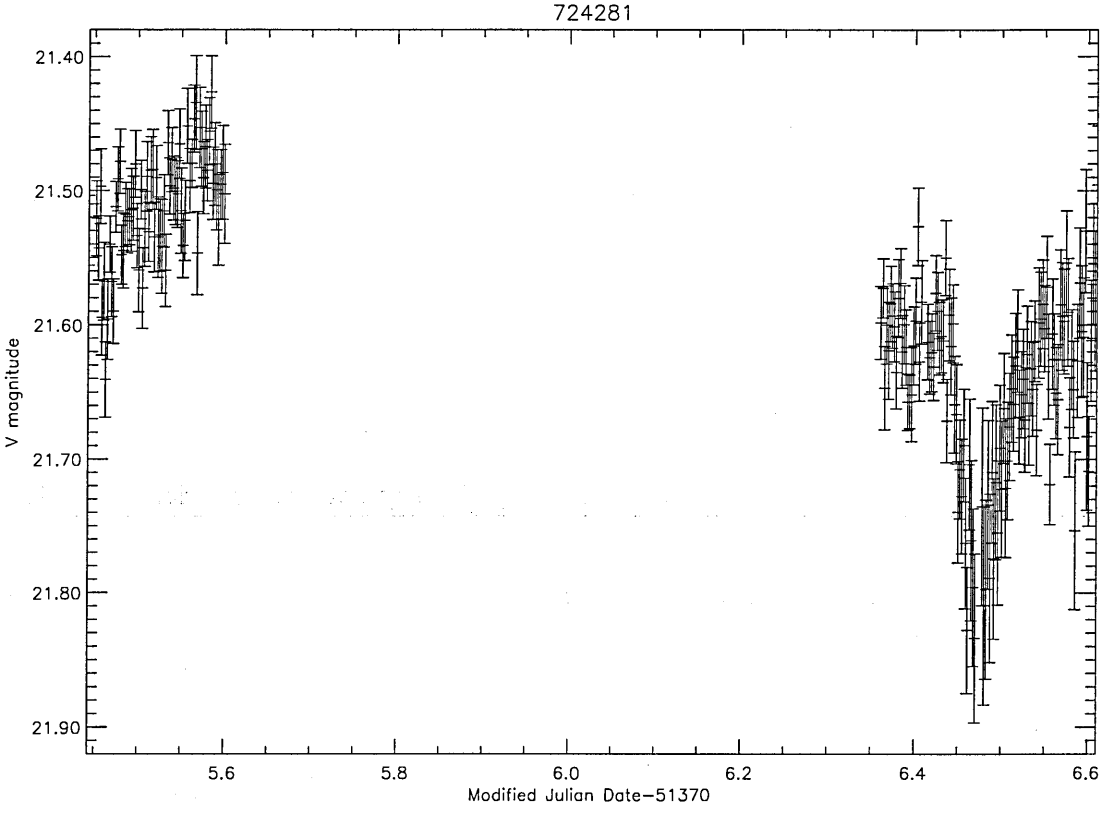
724281
21.40
21.50
21.60
21.70
21.80
21.90
V magnitude
5.6
5.8
6.0
6.2
6.4
6.6
Modified Julian Date−51370

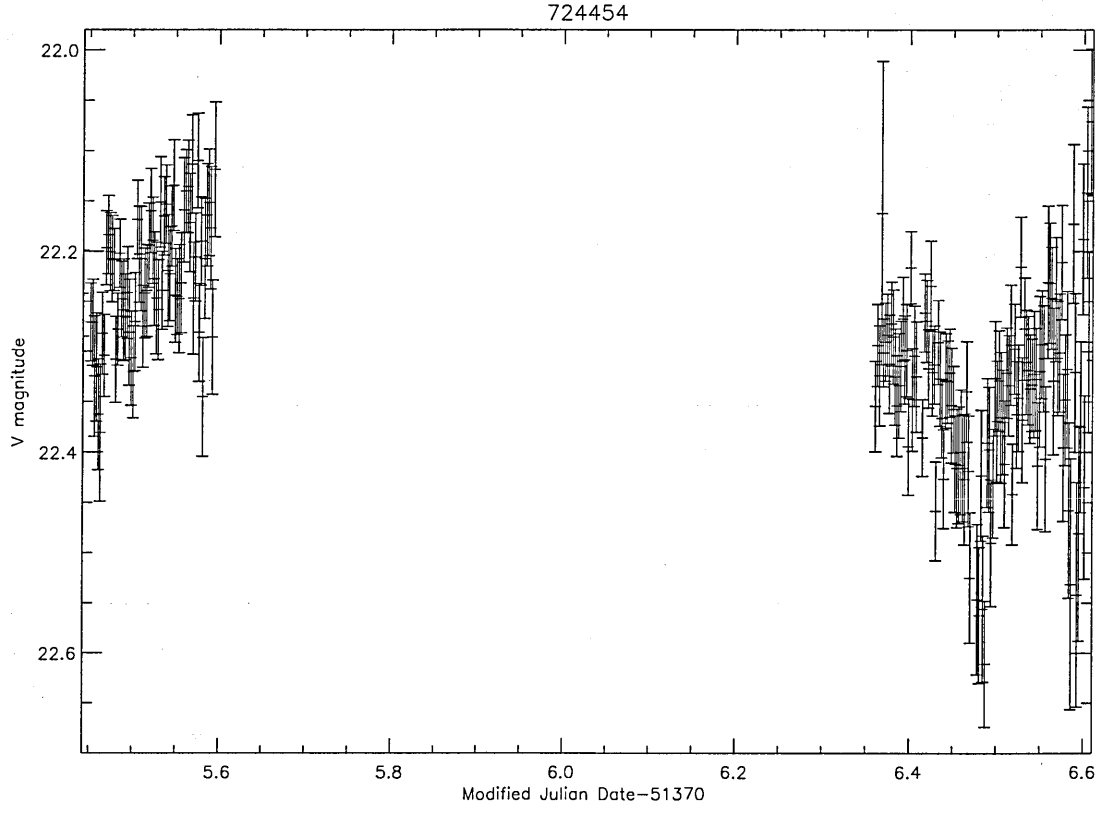
724454
22.0
22.2
22.4
22.6
V magnitude
5.6
5.8
6.0
6.2
6.4
6.6
Modified Julian Date−51370

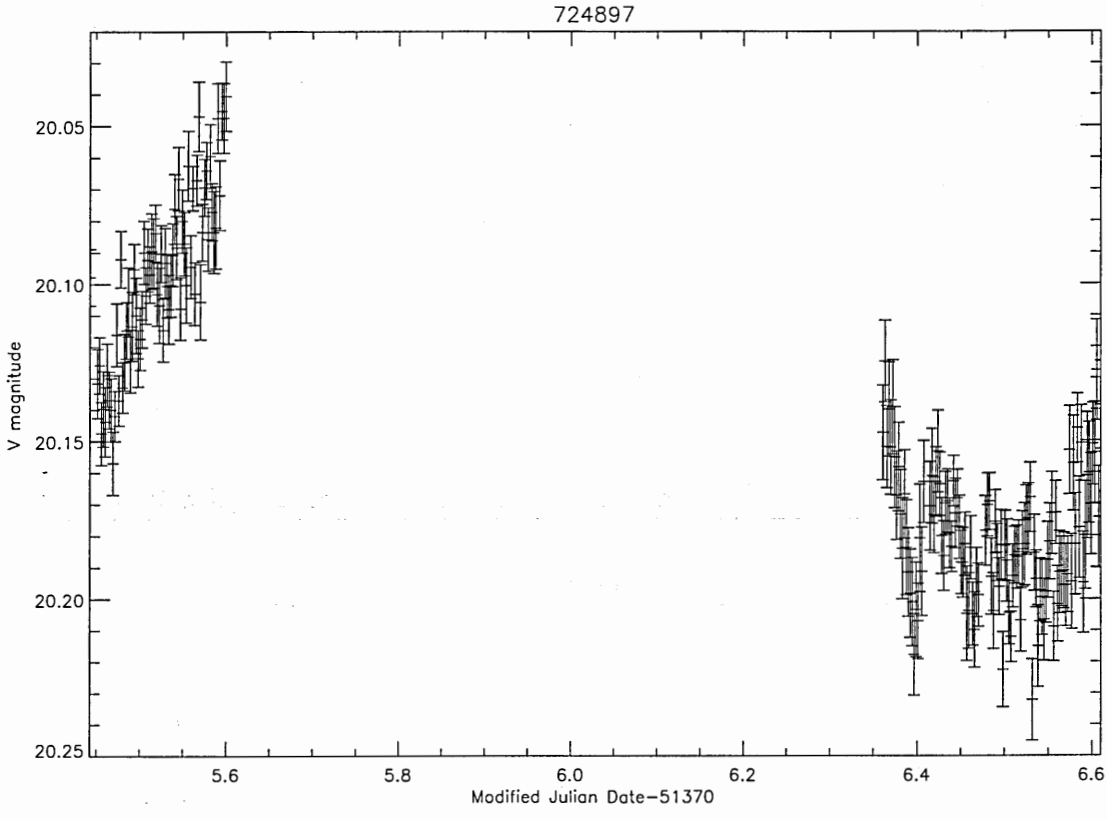
724897
20.05
20.10
20.15
20.20
20.25
V magnitude
5.6
5.8
6.0
6.2
6.4
6.6
Modified Julian Date−51370

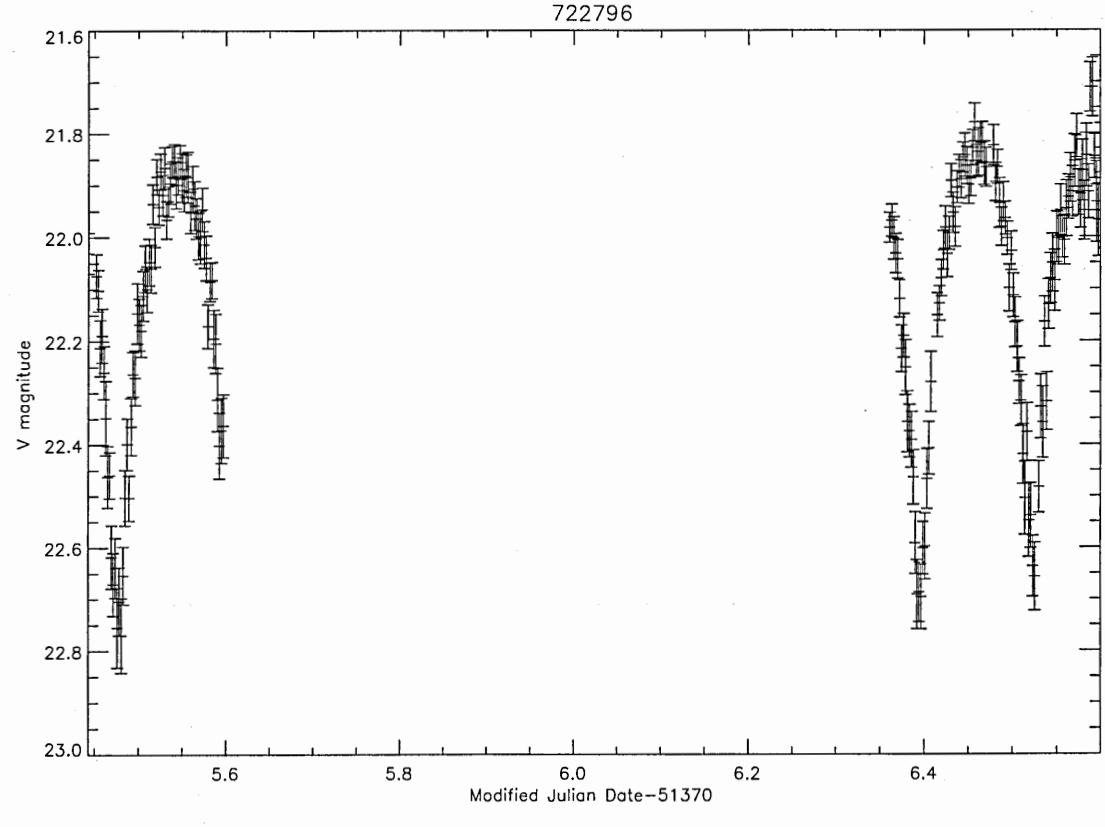
722796
21.6
21.8
22.0
22.2
22.4
22.6
22.8
23.0
V magnitude
5.6
5.8
6.0
6.2
6.4
Modified Julian Date−51370

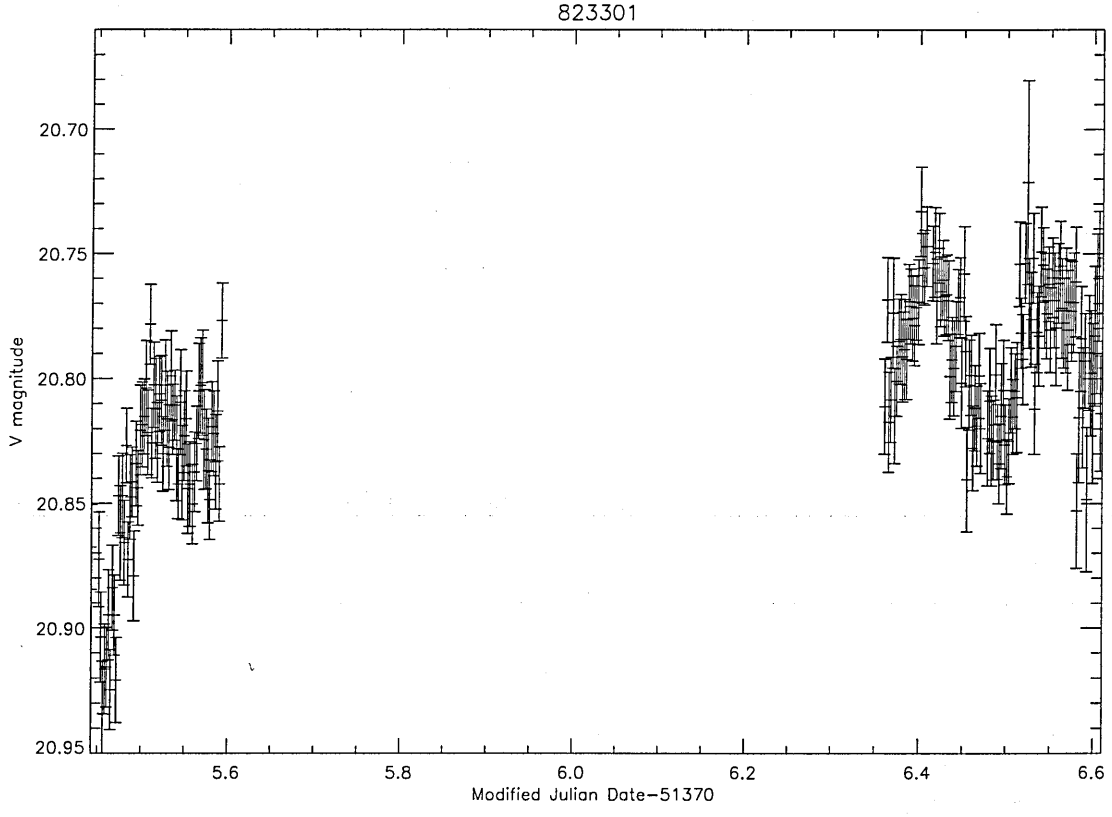
823301
20.70
20.75
20.80
20.85
20.90
20.95
V magnitude
5.6
5.8
6.0
6.2
6.4
6.6
Modified Julian Date−51370

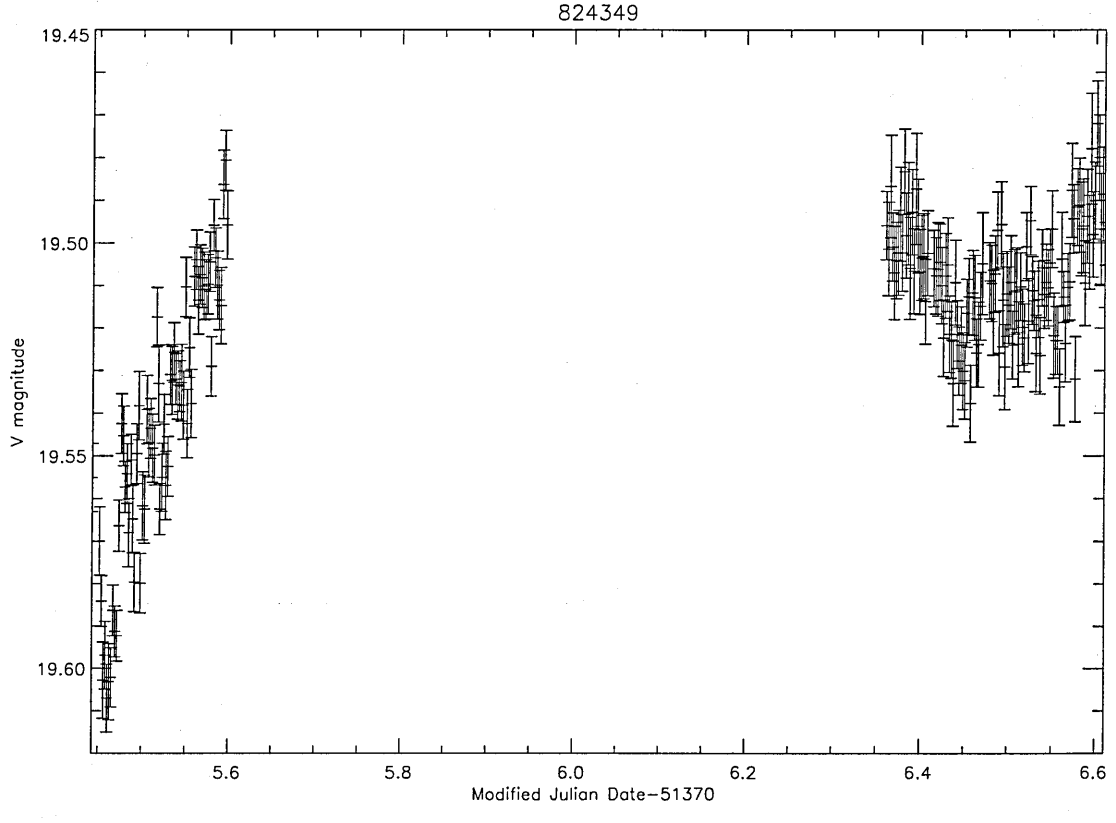
824349
19.45
19.50
19.55
19.60
V magnitude
5.6
5.8
6.0
6.2
6.4
6.6
Modified Julian Date−51370

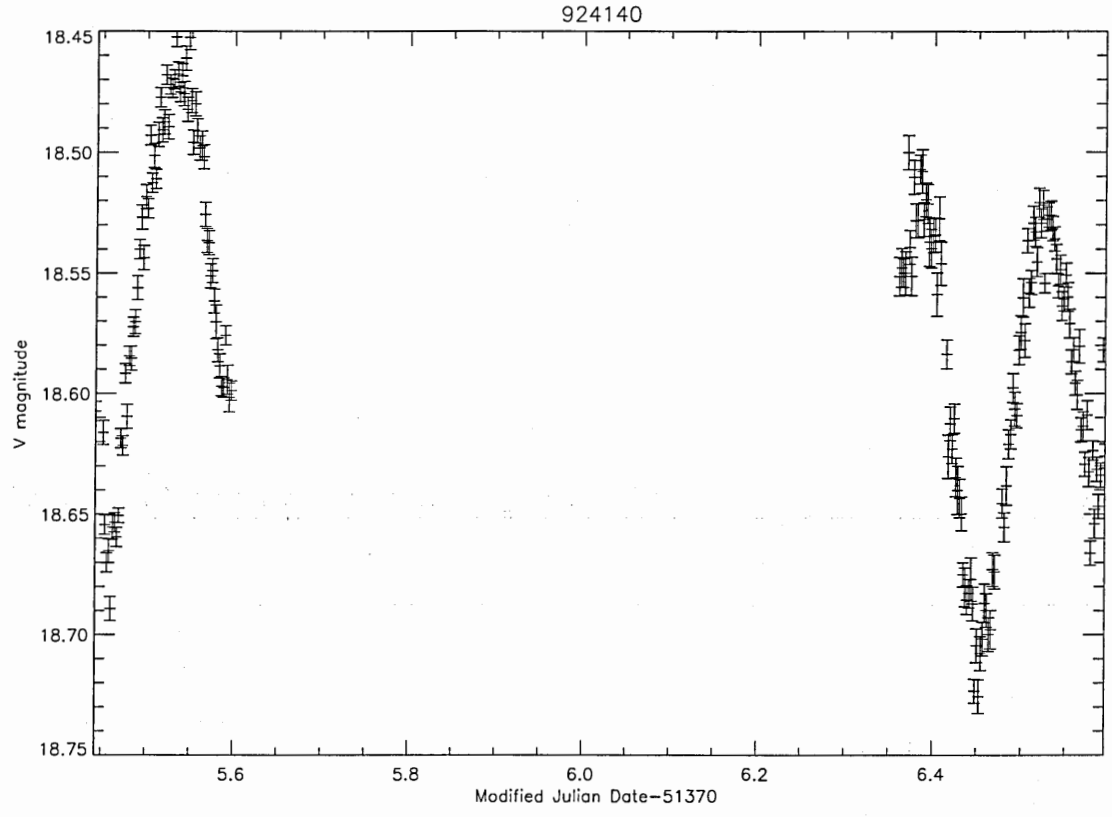
924140
18.45
18.50
18.55
18.60
18.65
18.70
18.75
V magnitude
5.6
5.8
6.0
6.2
6.4
Modified Julian Date−51370

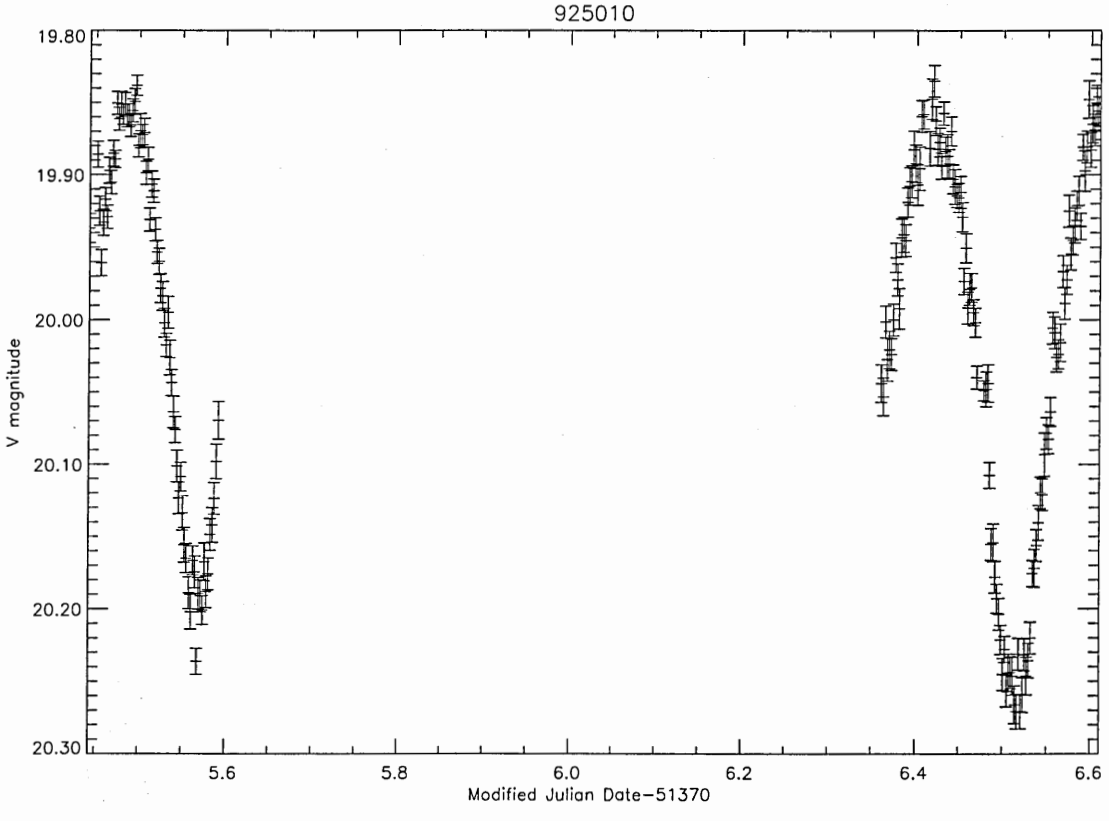
925010
19.80
19.90
20.00
20.10
20.20
20.30
V magnitude
5.6
5.8
6.0
6.2
6.4
6.6
Modified Julian Date−51370

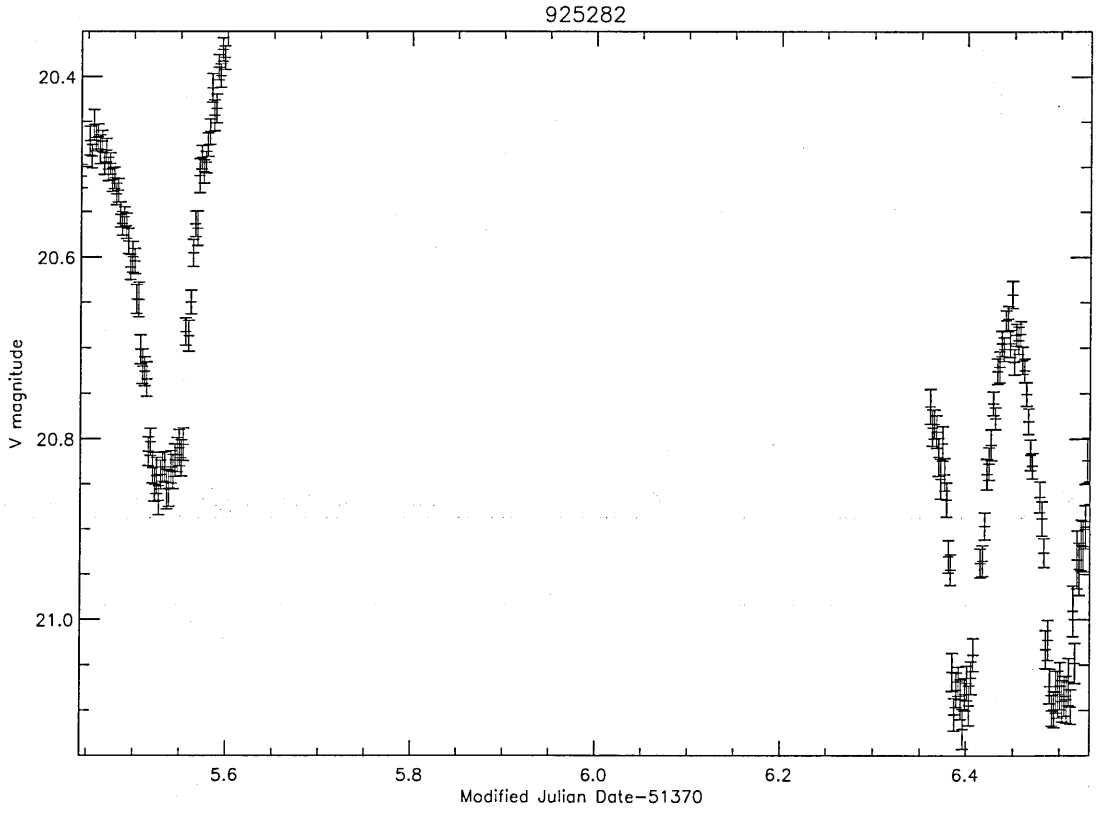
925282
20.4
20.6
20.8
21.0
V magnitude
5.6
5.8
6.0
6.2
6.4
Modified Julian Date−51370

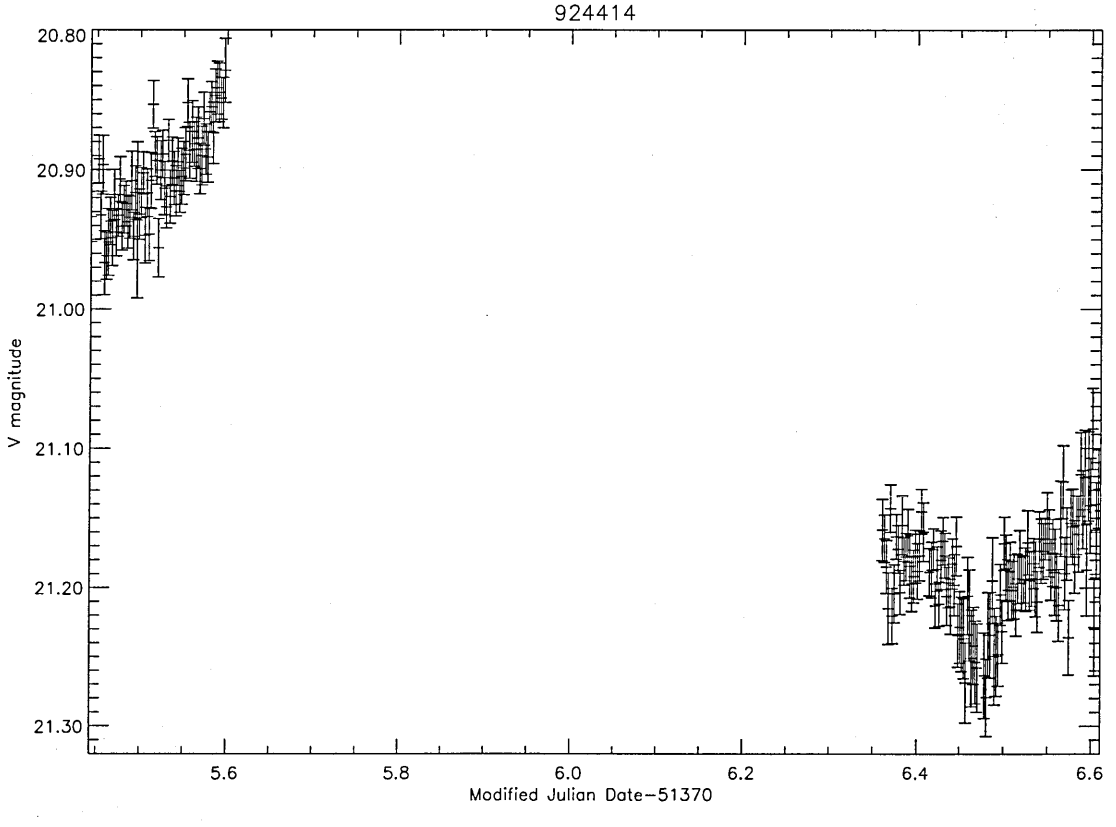
924414
20.80
20.90
21.00
21.10
21.20
21.30
V magnitude
5.6
5.8
6.0
6.2
6.4
6.6
Modified Julian Date−51370

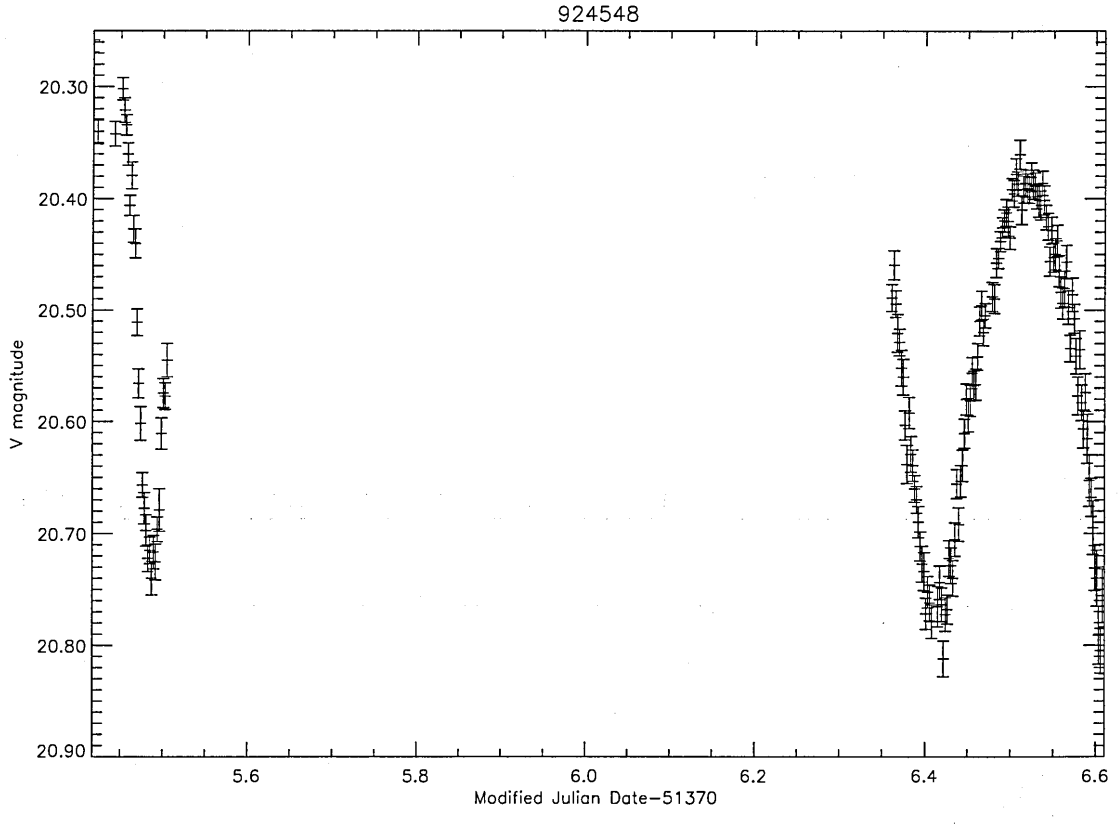
924548
20.30
20.40
20.50
20.60
20.70
20.80
20.90
V magnitude
5.6
5.8
6.0
6.2
6.4
6.6
Modified Julian Date−51370

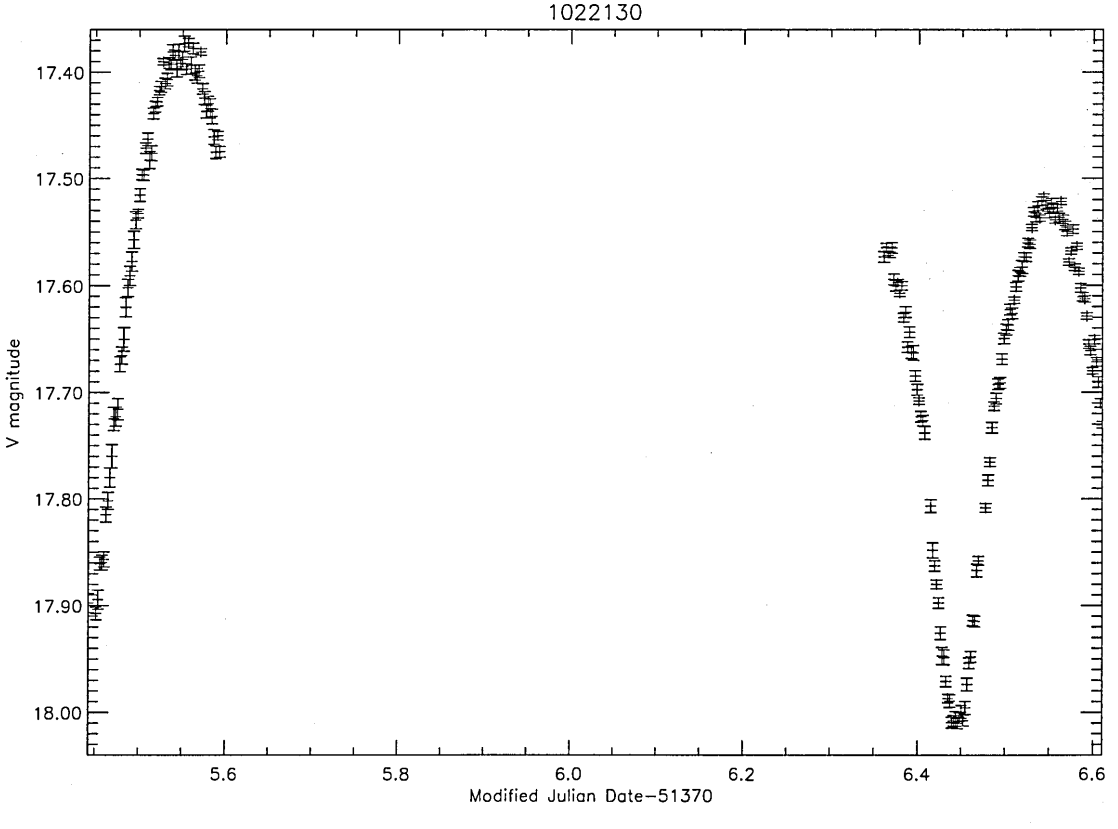
1022130
17.40
17.50
17.60
17.70
17.80
17.90
18.00
V magnitude
5.6
5.8
6.0
6.2
6.4
6.6
Modified Julian Date−51370

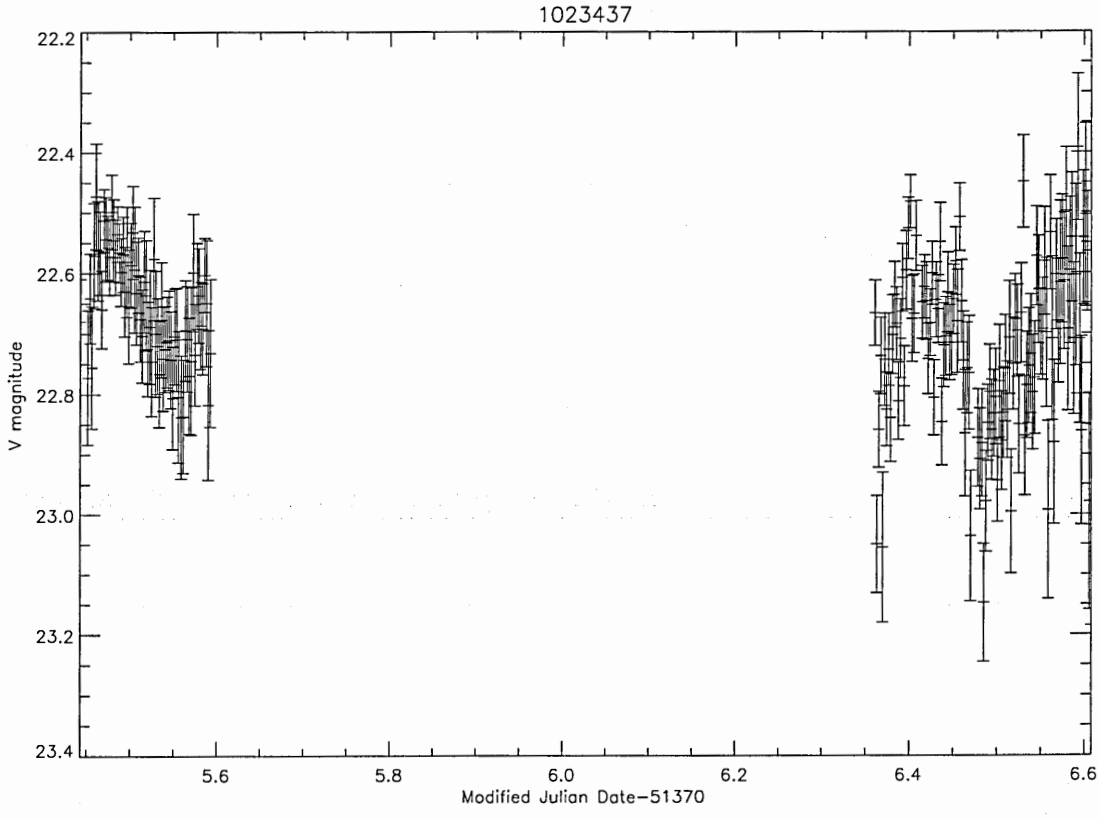
1023437
22.2
22.4
22.6
22.8
23.0
23.2
23.4
V magnitude
5.6
5.8
6.0
6.2
6.4
6.6
Modified Julian Date−51370

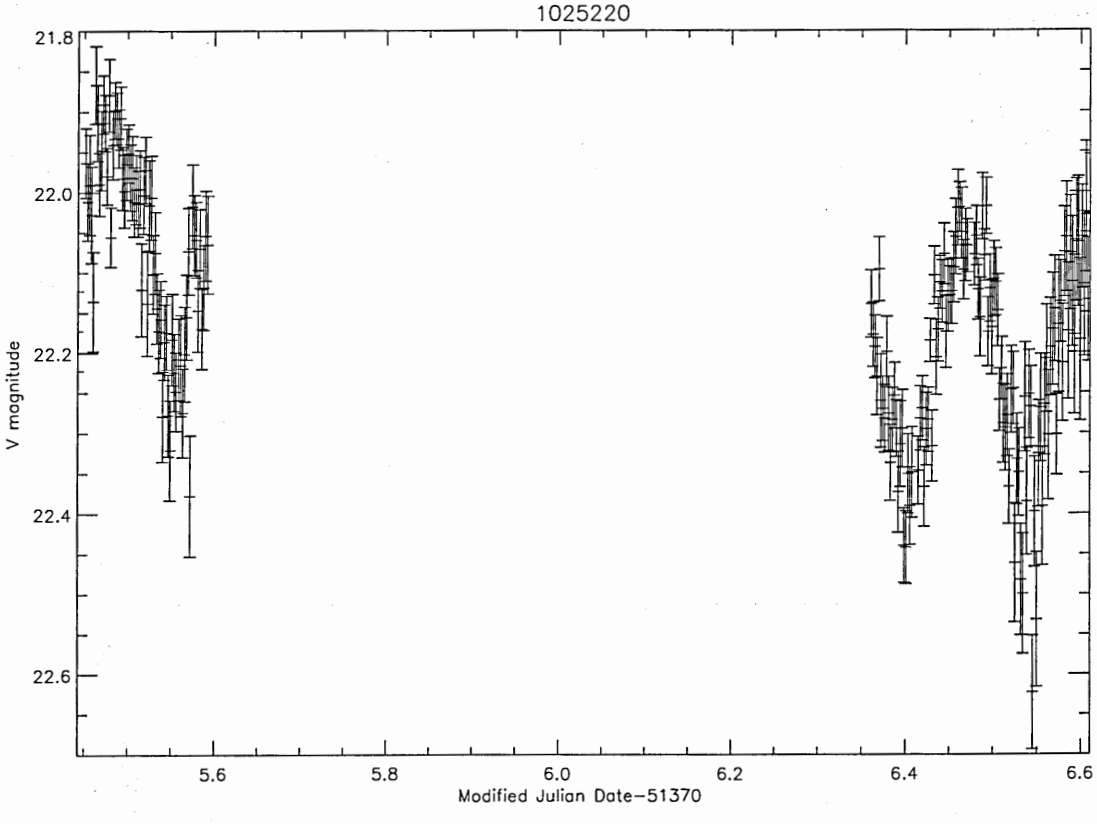
1025220
21.8
22.0
22.2
22.4
22.6
V magnitude
5.6
5.8
6.0
6.2
6.4
6.6
Modified Julian Date−51370

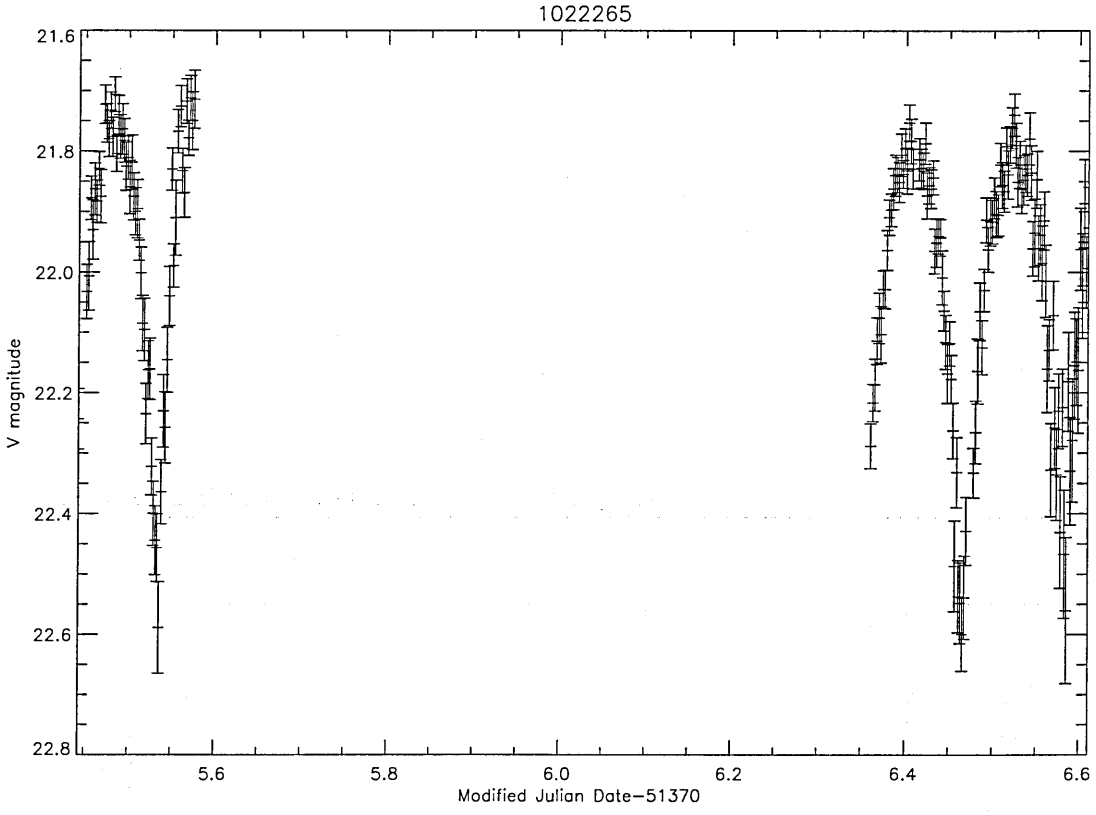
1022265
21.6
21.8
22.0
22.2
22.4
22.6
22.8
V magnitude
5.6
5.8
6.0
6.2
6.4
6.6
Modified Julian Date−51370

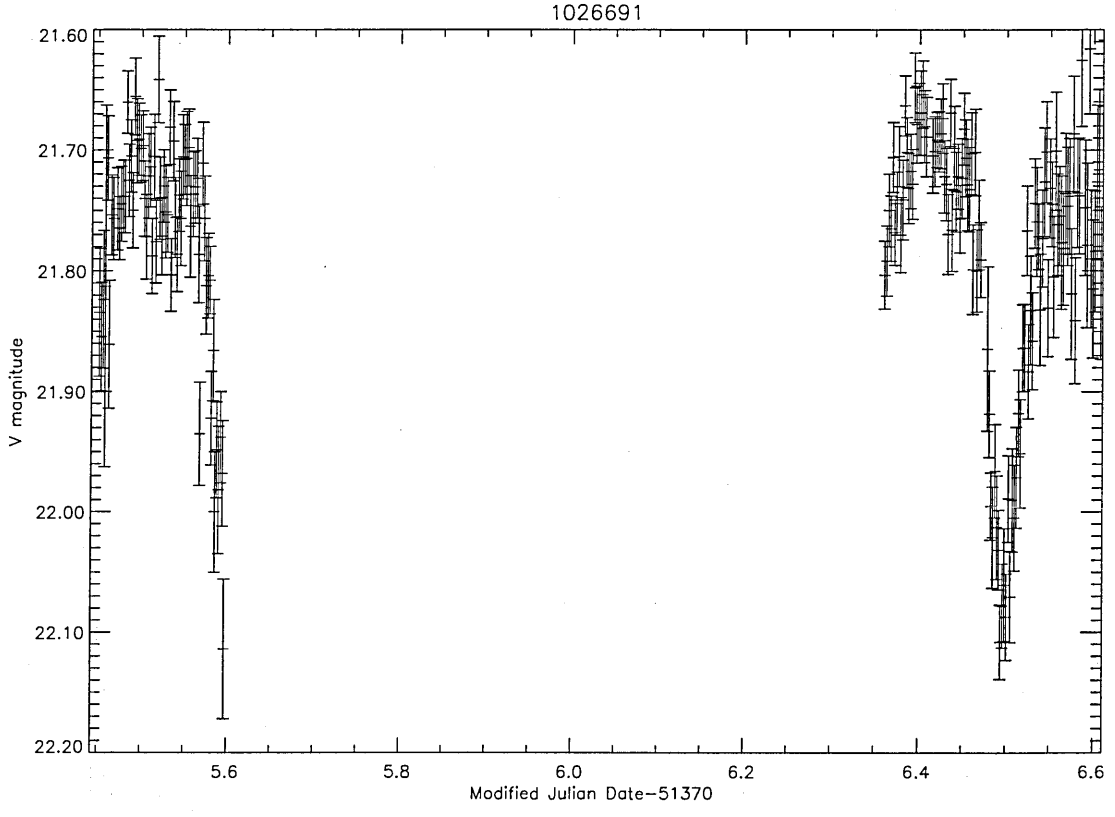
1026691
21.60
21.70
21.80
21.90
22.00
22.10
22.20
V magnitude
5.6
5.8
6.0
6.2
6.4
6.6
Modified Julian Date−51370

APPENDIX B

Lightcurves of variable objects observed on night one only

B.1 Night One Lightcurves

Table B.1: IDs and Positions of Night One Variables found by the WAVS Survey. IDs with *s represent variables calibrated using CCDs 3,4 or 5.

ID	RA	DEC	Obs. V Max	Obs. V Min	B-V	V-R
9910759	20h 25m 37.0	28h 2m 36.6	20.490 ± 0.014	20.725 ± 0.018	0.9	0.6
9911311	20h 25m 37.9	28h 1m 16.7	20.209 ± 0.013	20.596 ± 0.020	0.8	0.3
9911373	20h 25m 24.5	28h 1m 7.7	18.706 ± 0.005	19.366 ± 0.010	1.2	0.4
9912425	20h 25m 30.2	27h 58m 47.6	21.005 ± 0.019	21.254 ± 0.034	0.5	0.4
9913058	20h 25m 22.3	27h 57m 20.2	20.088 ± 0.010	20.459 ± 0.014	1.2	0.7
9910756	20h 25m 33.6	28h 2m 37.0	20.714 ± 0.027	20.898 ± 0.026	1.3	0.7
9910773	20h 25m 14.2	28h 2m 33.0	19.797 ± 0.009	19.973 ± 0.013	1.1	0.7
110517	20h 25m 46.8	28h 2m 56.8	21.339 ± 0.028	21.771 ± 0.031	1	1
111108	20h 25m 47.3	28h 1m 16.3	22.018 ± 0.042	22.592 ± 0.047	1.7	1
111665	20h 26m 2.4	27h 59m 49.9	20.102 ± 0.009	20.377 ± 0.011	1.1	1
115380	20h 25m 49.7	27h 52m 57.0	21.917 ± 0.045	22.475 ± 0.063	1.7	0.9
110012	20h 25m 47.8	28h 4m 29.6	21.436 ± 0.026	21.728 ± 0.032	NA	NA
210343	20h 26m 2.2	28h 3m 27.0	20.025 ± 0.012	20.581 ± 0.012	0.8	1.3
213561	20h 26m 17.3	27h 55m 02.2	19.382 ± 0.016	19.803 ± 0.029	NA	NA

continued...

Table B.1: continued

214289	20h 26m 15.1	27h 53m 12.2	17.370 ± 0.003	17.891 ± 0.003	NA	NA
214356	20h 26m 18.9	27h 53m 01.0	15.87 ± 0.002	16.152 ± 0.004	NA	NA
214524	20h 26m 8.9	27h 54m 25.9	18.516 ± 0.005	18.807 ± 0.006	1.3	0.5
214671	20h 25m 58.1	27h 54m 10.1	20.129 ± 0.013	20.429 ± 0.013	1.3	0.6
214595	20h 25m 46.6	27h 54m 16.9	22.468 ± 0.072	23.452 ± 0.163	1.3	1
310125*	20h 26m 57.6	28h 4m 19.6	22.427 ± 0.032	22.721 ± 0.044	0.8	1.6
312118*	20h 27m 13.2	28h 1m 24.2	17.959 ± 0.005	18.184 ± 0.008	NA	NA
312809*	20h 27m 14.4	28h 0m 26.6	19.379 ± 0.006	19.612 ± 0.007	0.5	0.9
312909*	20h 27m 10.5	28h 00m 18.9	16.999 ± 0.003	17.335 ± 0.002	NA	NA
313606*	20h 27m 1.0	27h 59m 15.7	21.463 ± 0.036	22.103 ± 0.025	1.2	1.6
313839*	20h 26m 53.8	27h 58m 54.1	21.552 ± 0.014	21.975 ± 0.028	0.7	1.1
318450*	20h 26m 57.8	27h 51m 16.9	17.719 ± 0.003	17.796 ± 0.007	0.5	1
410352*	20h 27m 28.3	28h 4m 6.2	17.836 ± 0.005	18.103 ± 0.005	NA	NA
410411*	20h 27m 35.8	28h 3m 57.6	20.763 ± 0.013	21.116 ± 0.021	0.3	1.3
414869*	20h 27m 21.6	27h 55m 10.2	18.818 ± 0.022	19.065 ± 0.009	NA	NA
410719*	20h 27m 44.4	28h 3m 27.7	21.446 ± 0.016	22.334 ± 0.041	0.7	1.3
411515*	20h 27m 36.7	28h 2m 1.3	22.228 ± 0.034	22.693 ± 0.036	0.5	1.6
415423*	20h 27m 48.0	27h 53m 54.6	22.318 ± 0.049	23.934 ± 0.200	-0.5	2.5
415432*	20h 27m 30.0	27h 53m 55.3	22.343 ± 0.036	22.756 ± 0.033	0.8	1.7
511194*	20h 28m 8.2	28h 2m 33.7	20.578 ± 0.015	20.909 ± 0.026	1	1.1
511639*	20h 28m 18.7	28h 1m 51.2	20.467 ± 0.018	21.157 ± 0.038	0.7	1
515485*	20h 27m 36.7	28h 2m 1.3	20.120 ± 0.001	20.537 ± 0.013	NA	NA
514059*	20h 28m 4.1	27h 57m 46.4	21.493 ± 0.056	22.149 ± 0.054	0.8	1
516819*	20h 28m 21.4	27h 52m 41.2	21.933 ± 0.039	22.384 ± 0.096	1.5	1.2
517946*	20h 28m 21.1	27h 50m 38.8	21.467 ± 0.045	21.961 ± 0.085	1.2	1
710820	20h 25m 54.5	27h 38m 19.7	18.683 ± 0.006	19.239 ± 0.007	0.2	1
711043	20h 25m 56.9	27h 38m 43.8	16.723 ± 0.003	16.891 ± 0.003	NA	NA
711848	20h 25m 48.0	27h 40m 34.0	19.089 ± 0.015	19.402 ± 0.008	1	0.4
713236	20h 26m 6.7	27h 43m 20.6	19.283 ± 0.014	19.586 ± 0.018	0.3	0.9
713294	20h 26m 0.7	27h 43m 28.2	17.295 ± 0.006	17.412 ± 0.007	NA	NA
713423	20h 26m 5.5	27h 43m 46.6	19.353 ± 0.006	19.468 ± 0.008	0.5	0.8

continued...

Table B.1: continued

714642	20h 26m 5.0	27h 46m 22.4	18.244 ± 0.003	18.386 ± 0.003	0.4	0.5
710477	20h 26m 7.0	27h 37m 28.6	20.835 ± 0.018	20.995 ± 0.032	0.7	0.7
711419	20h 26m 12.7	27h 39m 31.3	19.004 ± 0.007	19.163 ± 0.007	0.5	0.7
711566	20h 26m 7.0	27h 39m 51.5	21.551 ± 0.037	21.809 ± 0.046	0.7	0.7
712650	20h 26m 7.0	27h 42m 12.2	21.013 ± 0.019	21.189 ± 0.032	0.7	0.7
712878	20h 26m 7.2	27h 42m 39.6	22.518 ± 0.059	23.322 ± 0.143	1	1.1
810308	20h 26m 44.2	27h 37m 1.6	19.952 ± 0.012	20.325 ± 0.014	0.8	0.9
811611	20h 26m 14.6	27h 39m 34.9	19.841 ± 0.009	20.150 ± 0.011	1.5	0.9
812619	20h 26m 38.6	27h 41m 27.2	20.729 ± 0.019	20.927 ± 0.017	1.1	0.7
811481	20h 26m 27.8	27h 39m 20.9	22.012 ± 0.041	22.517 ± 0.059	1.4	1.5
911591	20h 27m 6.0	27h 39m 34.2	19.061 ± 0.008	19.216 ± 0.007	1.5	1
911605	20h 27m 16.3	27h 39m 34.9	22.000 ± 0.042	22.982 ± 0.099	1.7	1.3
916424	20h 27m 3.6	27h 48m 32.0	19.185 ± 0.007	19.661 ± 0.012	0.8	1.2
912537	20h 26m 55.9	27h 41m 19.0	21.086 ± 0.016	21.376 ± 0.021	NA	NA
913919	20h 27m 08.9	27h 43m 55.3	19.290 ± 0.010	19.681 ± 0.016	NA	NA
915011	20h 27m 13.9	27h 45m 57.2	21.490 ± 0.032	21.654 ± 0.041	1.1	0.7
917017	20h 26m 49.9	27h 49m 43.3	19.184 ± 0.006	19.272 ± 0.010	1.5	1.1
1011862	20h 27m 33.4	27h 38m 53.9	19.769 ± 0.009	21.546 ± 0.035	NA	NA
1012756	20h 27m 31.9	27h 40m 11.6	16.591 ± 0.004	16.798 ± 0.005	NA	NA
1110575	20h 28m 19.7	27h 37m 49.4	17.035 ± 0.011	17.247 ± 0.010	NA	NA
1111037	20h 28m 6.2	27h 39m 5.8	18.490 ± 0.007	18.979 ± 0.009	1.1	0.9
1111038	20h 28m 8.4	27h 39m 6.5	20.831 ± 0.019	21.204 ± 0.015	0.6	0.8
1111582	20h 28m 12.0	27h 40m 28.6	21.992 ± 0.045	22.993 ± 0.097	1	1.6
1111626	20h 28m 13.4	27h 40m 34.3	22.040 ± 0.056	22.738 ± 0.091	1	0.8
1111648	20h 28m 08.8	27h 40m 37.3	18.449 ± 0.010	18.927 ± 0.014	NA	NA
1112342	20h 28m 11.3	27h 42m 30.6	17.124 ± 0.003	17.296 ± 0.004	NA	NA
1112722	20h 28m 14.4	27h 43m 31.8	21.103 ± 0.029	21.435 ± 0.028	1.1	0.9
1110706	20h 27m 58.1	27h 38m 11.8	21.417 ± 0.040	22.034 ± 0.048	0.9	0.7

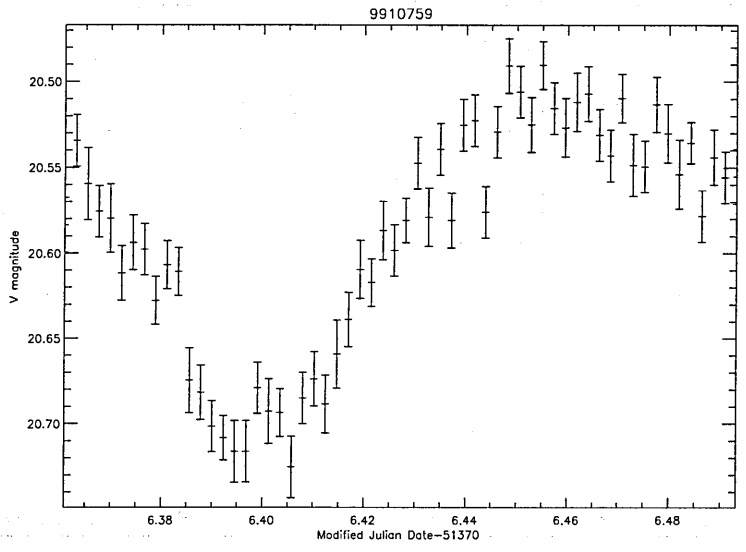
9910759
20.50
20.55
20.60
20.65
20.70
V magnitude
6.38
6.40
6.42
6.44
6.46
6.48
Modified Julian Date−51370

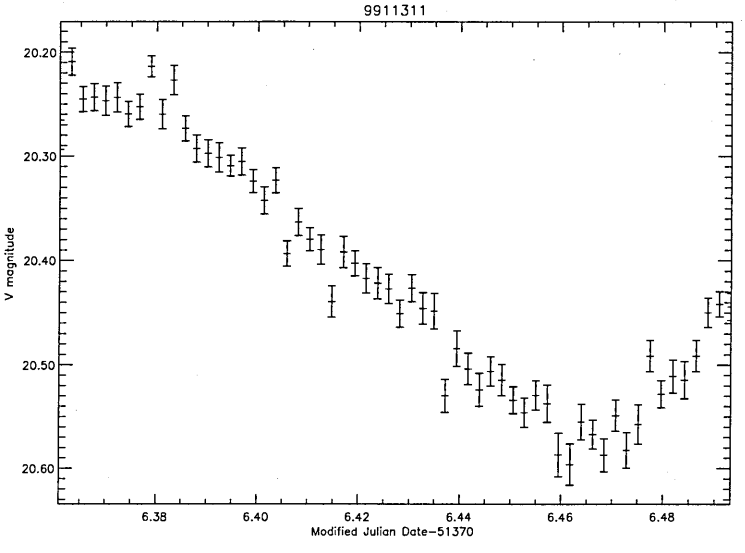
9911311
20.20
20.30
20.40
20.50
20.60
V magnitude
6.38
6.40
6.42
6.44
6.46
6.48
Modified Julian Date−51370

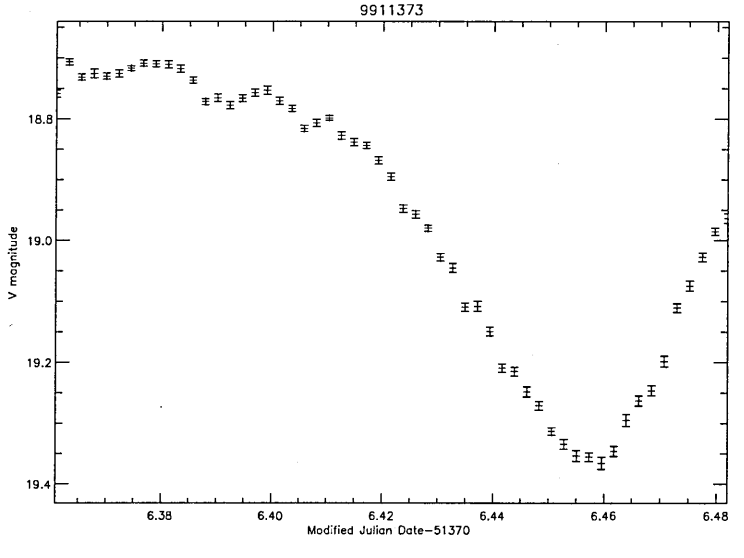
9911373
18.8
19.0
19.2
19.4
V magnitude
6.38
6.40
6.42
6.44
6.46
6.48
Modified Julian Date−51370

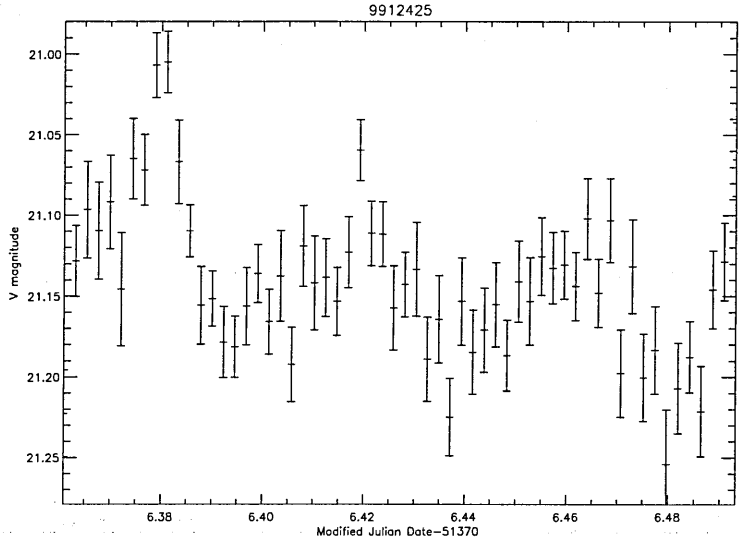
9912425
V magnitude
21.00
21.05
21.10
21.15
21.20
21.25
6.38
6.40
6.42
6.44
6.46
6.48
Modified Julian Date−51370

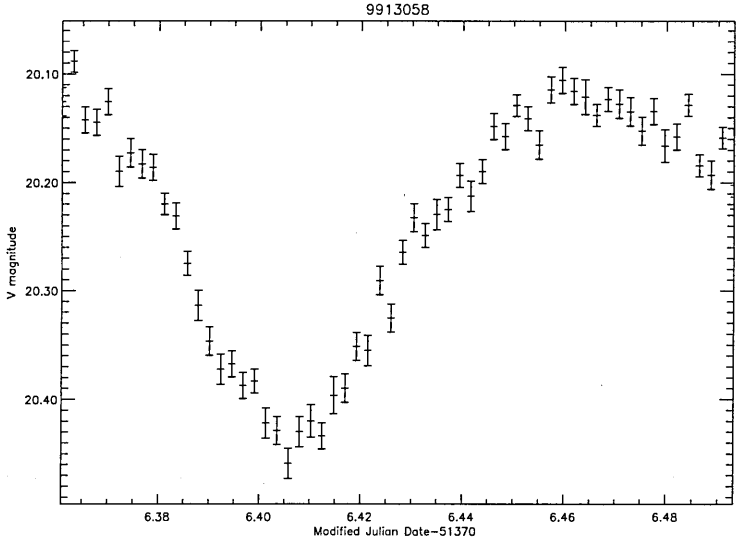
9913058
V magnitude
20.10
20.20
20.30
20.40
6.38
6.40
6.42
6.44
6.46
6.48
Modified Julian Date−51370

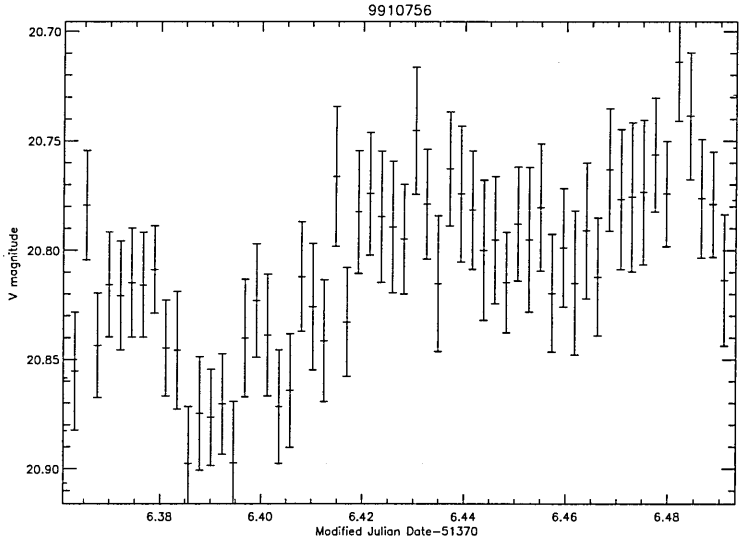
9910756
V magnitude
20.70
20.75
20.80
20.85
20.90
6.38
6.40
6.42
6.44
6.46
6.48
Modified Julian Date−51370

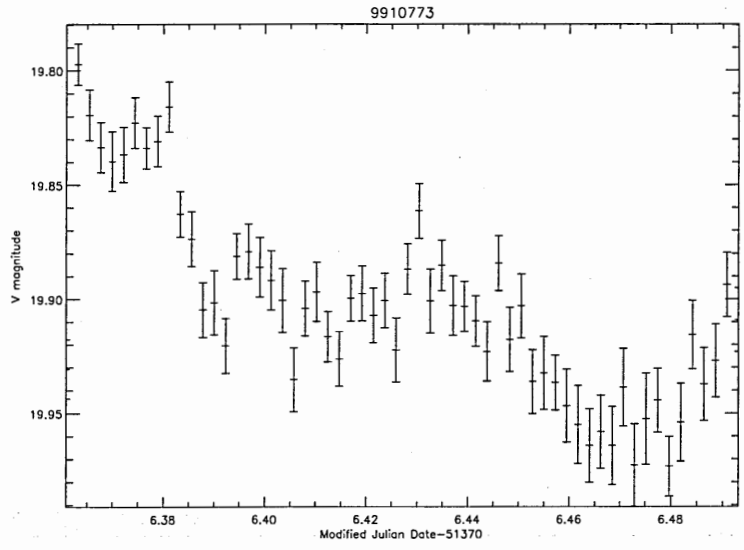
9910773
V magnitude
19.80
19.85
19.90
19.95
6.38
6.40
6.42
6.44
6.46
6.48
Modified Julian Date−51370

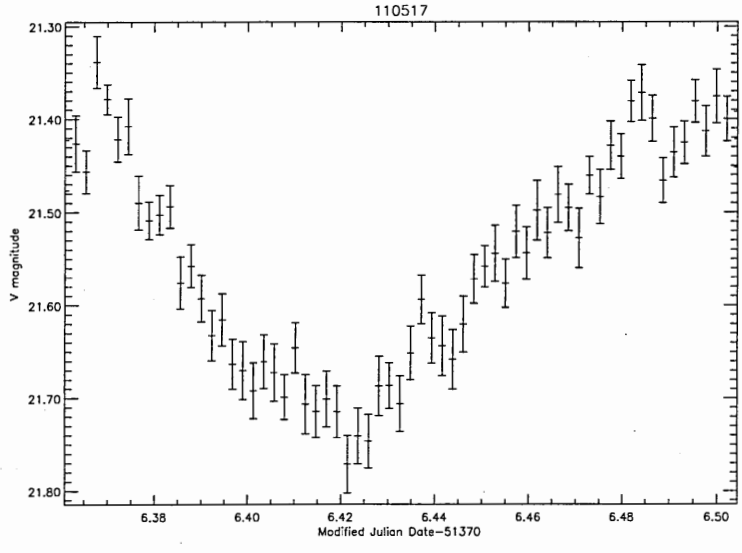
110517
V magnitude
21.30
21.40
21.50
21.60
21.70
21.80
6.38
6.40
6.42
6.44
6.46
6.48
6.50
Modified Julian Date−51370

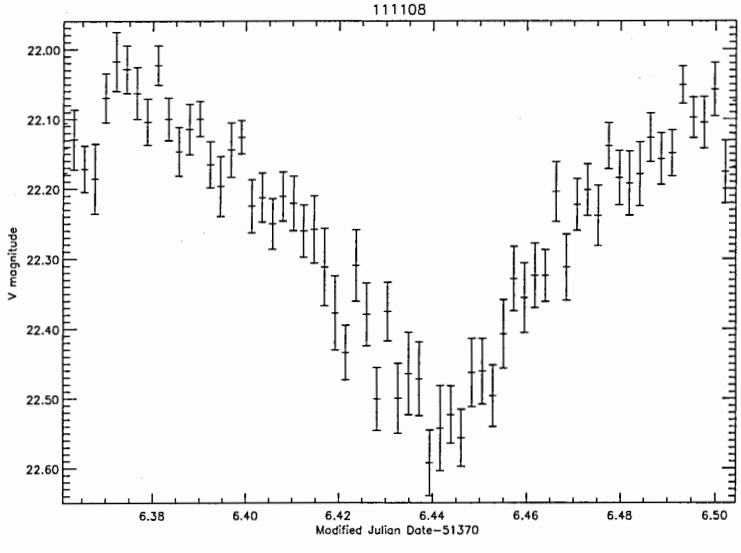
111108
V magnitude
22.00
22.10
22.20
22.30
22.40
22.50
22.60
6.38
6.40
6.42
6.44
6.46
6.48
6.50
Modified Julian Date−51370

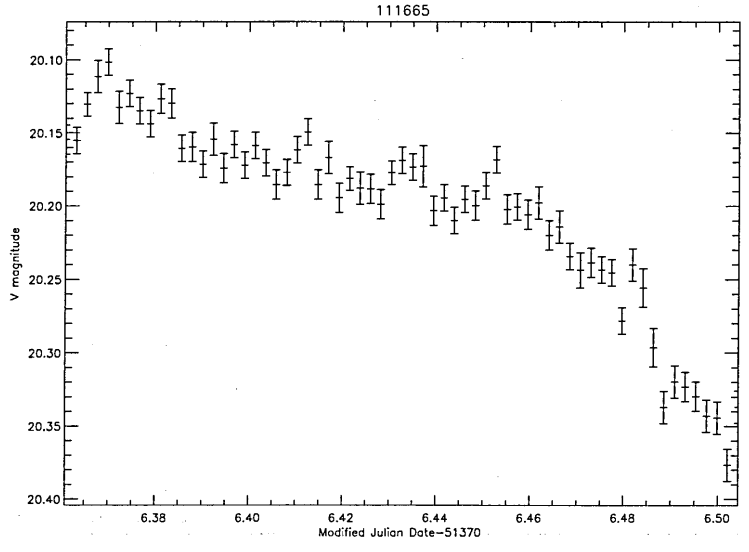
111665
V magnitude
20.10
20.15
20.20
20.25
20.30
20.35
20.40
6.38
6.40
6.42
6.44
6.46
6.48
6.50
Modified Julian Date−51370

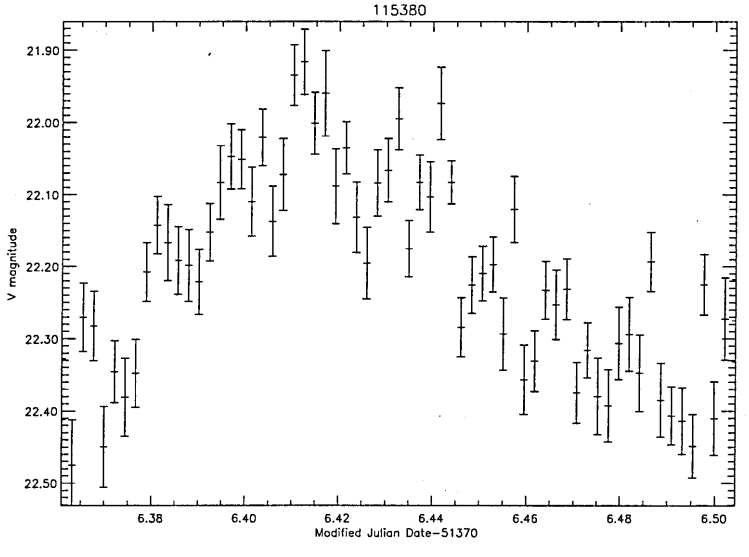
115380
V magnitude
21.90
22.00
22.10
22.20
22.30
22.40
22.50
6.38
6.40
6.42
6.44
6.46
6.48
6.50
Modified Julian Date−51370

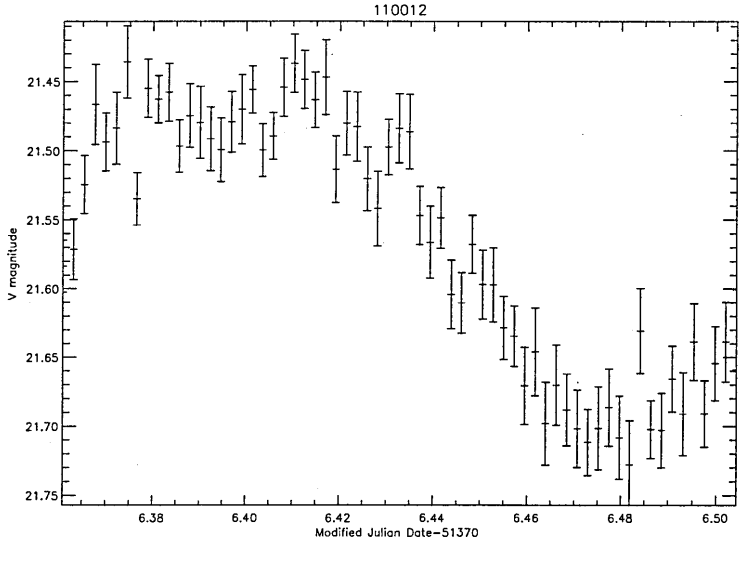
110012
V magnitude
21.45
21.50
21.55
21.60
21.65
21.70
21.75
6.38
6.40
6.42
6.44
6.46
6.48
6.50
Modified Julian Date−51370

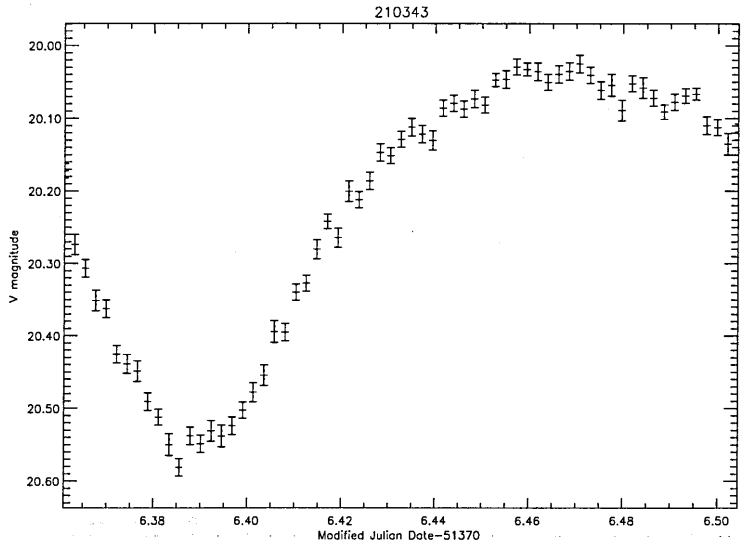
210343
20.00
20.10
20.20
20.30
20.40
20.50
20.60
V magnitude
6.38
6.40
6.42
6.44
6.46
6.48
6.50
Modified Julian Date−51370

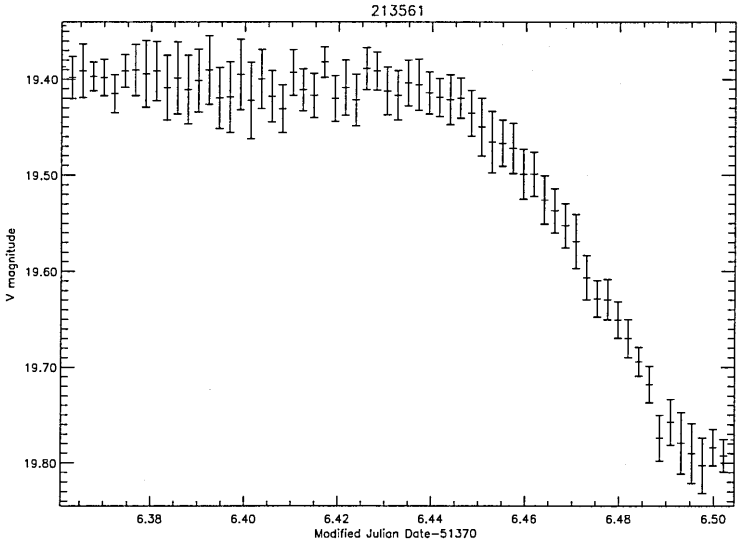
213561
19.40
19.50
19.60
19.70
19.80
V magnitude
6.38
6.40
6.42
6.44
6.46
6.48
6.50
Modified Julian Date−51370

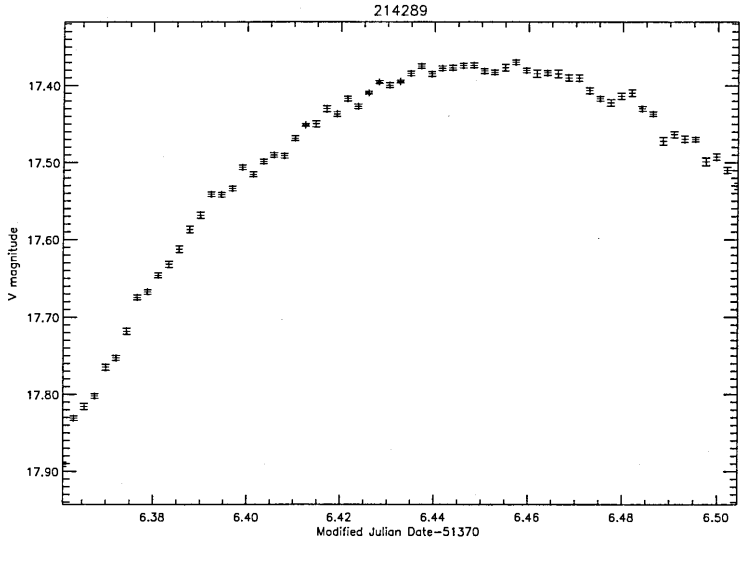
214289
17.40
17.50
17.60
17.70
17.80
17.90
V magnitude
6.38
6.40
6.42
6.44
6.46
6.48
6.50
Modified Julian Date−51370

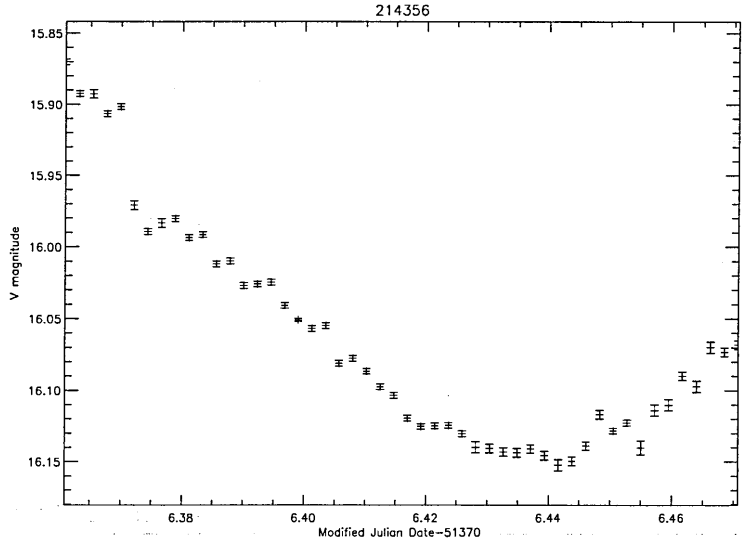
214356
15.85
15.90
15.95
16.00
16.05
16.10
16.15
V magnitude
6.38
6.40
6.42
6.44
6.46
Modified Julian Date−51370

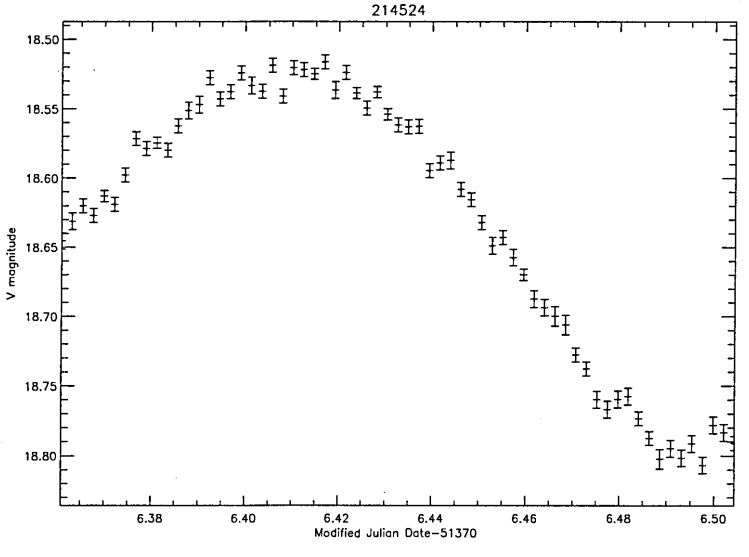
214524
18.50
18.55
18.60
18.65
18.70
18.75
18.80
V magnitude
6.38
6.40
6.42
6.44
6.46
6.48
6.50
Modified Julian Date−51370

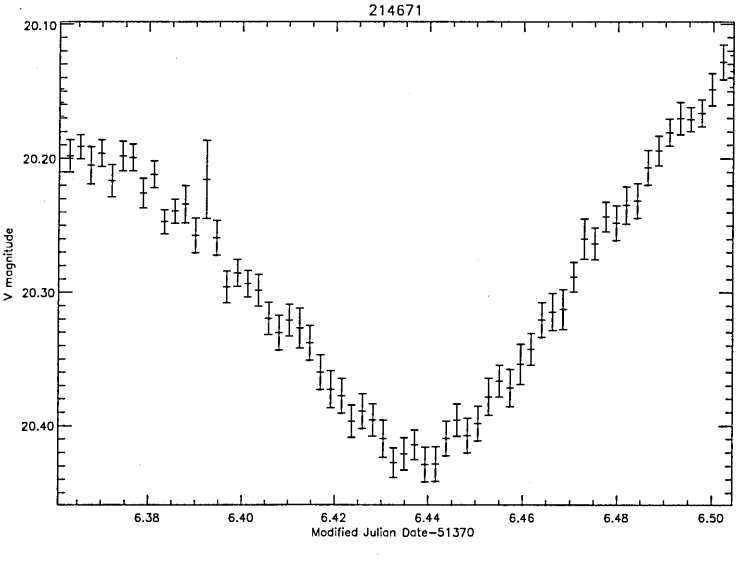
214671
20.10
20.20
20.30
20.40
V magnitude
6.38
6.40
6.42
6.44
6.46
6.48
6.50
Modified Julian Date−51370

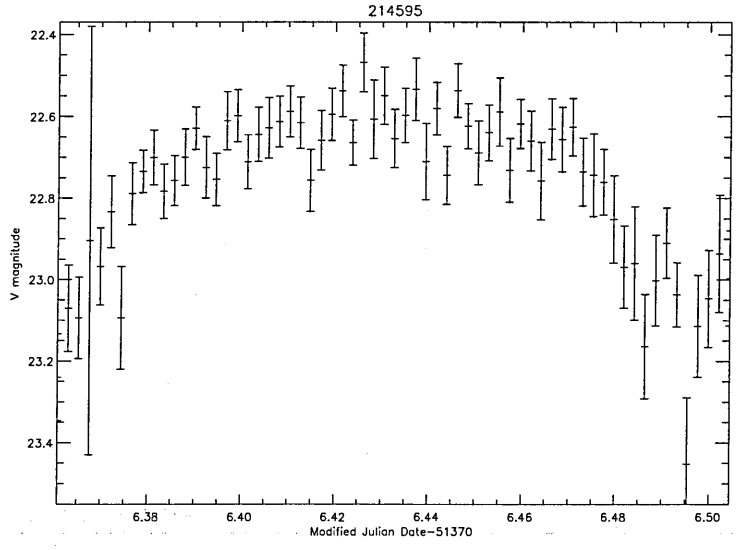
214595
V magnitude
22.4
22.6
22.8
23.0
23.2
23.4
6.38
6.40
6.42
6.44
6.46
6.48
6.50
Modified Julian Date−51370

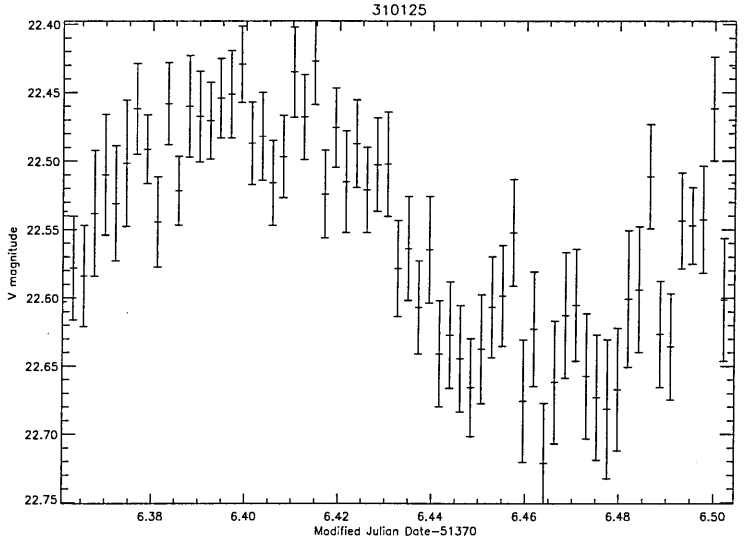
310125
V magnitude
22.40
22.45
22.50
22.55
22.60
22.65
22.70
22.75
6.38
6.40
6.42
6.44
6.46
6.48
6.50
Modified Julian Date−51370

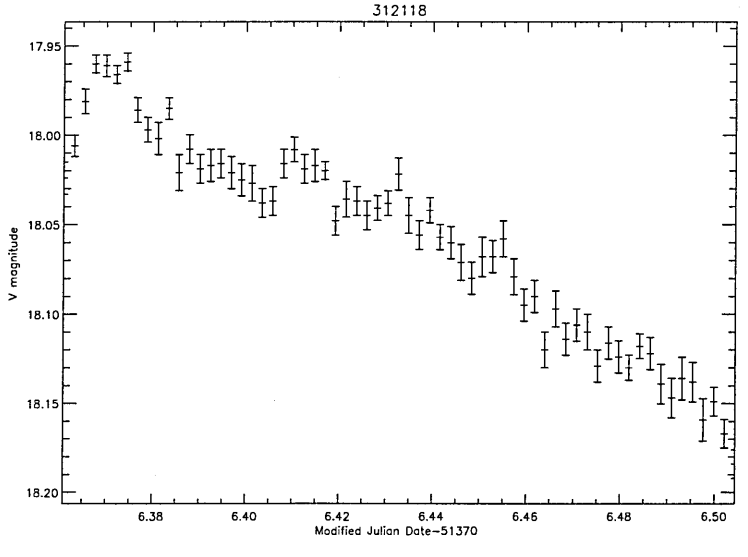
312118
V magnitude
17.95
18.00
18.05
18.10
18.15
18.20
6.38
6.40
6.42
6.44
6.46
6.48
6.50
Modified Julian Date−51370

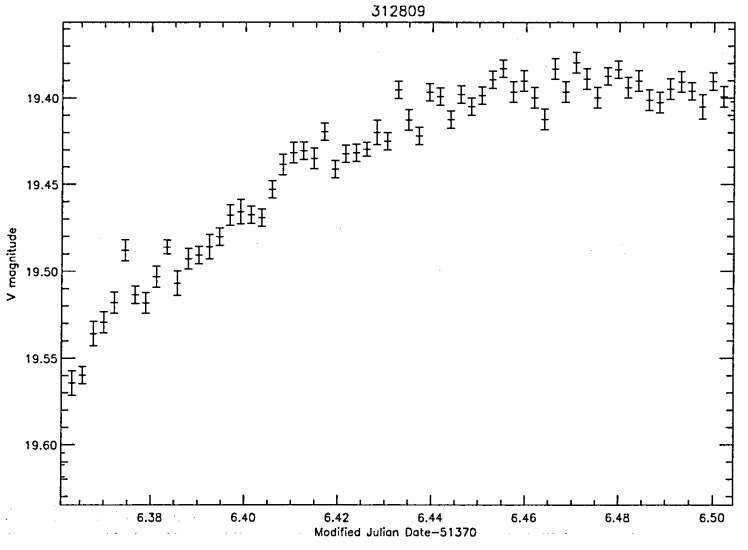
312809
V magnitude
19.40
19.45
19.50
19.55
19.60
6.38
6.40
6.42
6.44
6.46
6.48
6.50
Modified Julian Date−51370

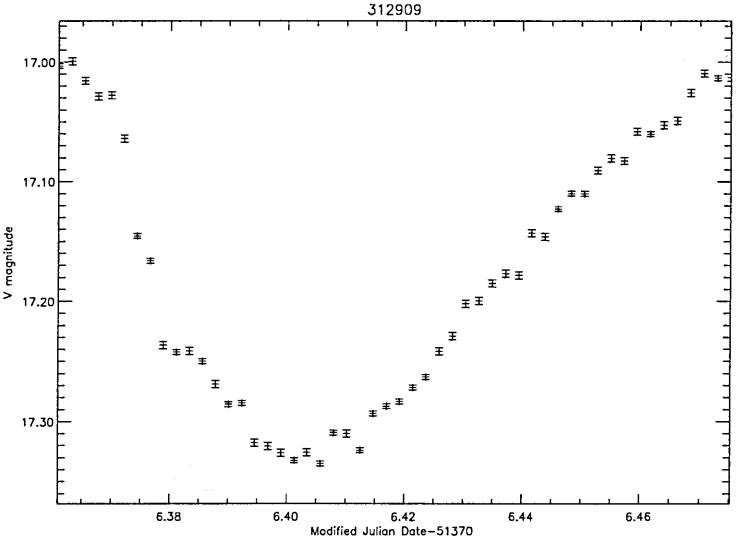
312909
V magnitude
17.00
17.10
17.20
17.30
6.38
6.40
6.42
6.44
6.46
Modified Julian Date−51370

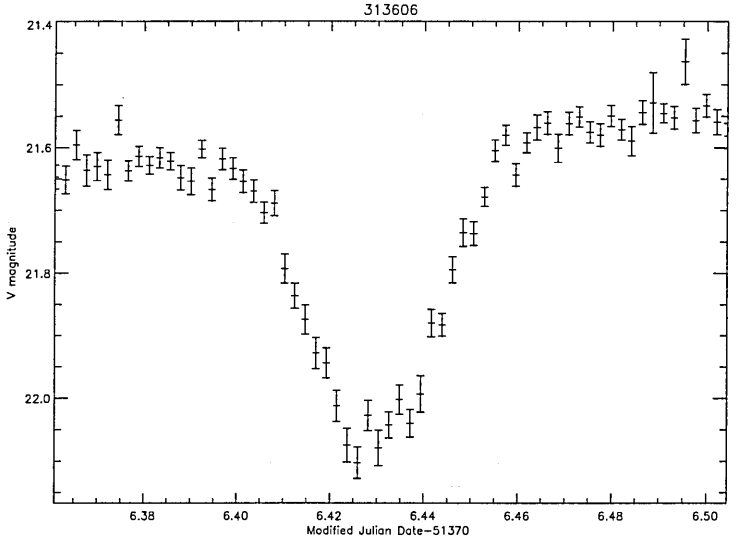
313606
V magnitude
21.4
21.6
21.8
22.0
6.38
6.40
6.42
6.44
6.46
6.48
6.50
Modified Julian Date−51370

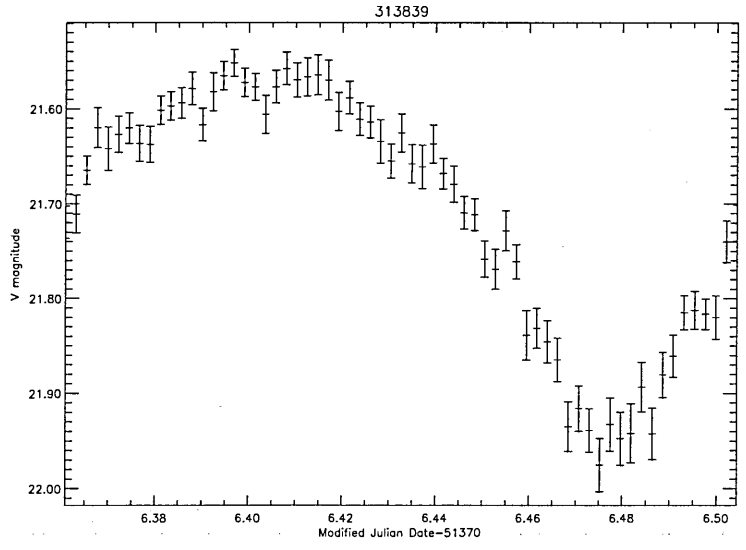
313839
V magnitude
21.60
21.70
21.80
21.90
22.00
6.38
6.40
6.42
6.44
6.46
6.48
6.50
Modified Julian Date−51370

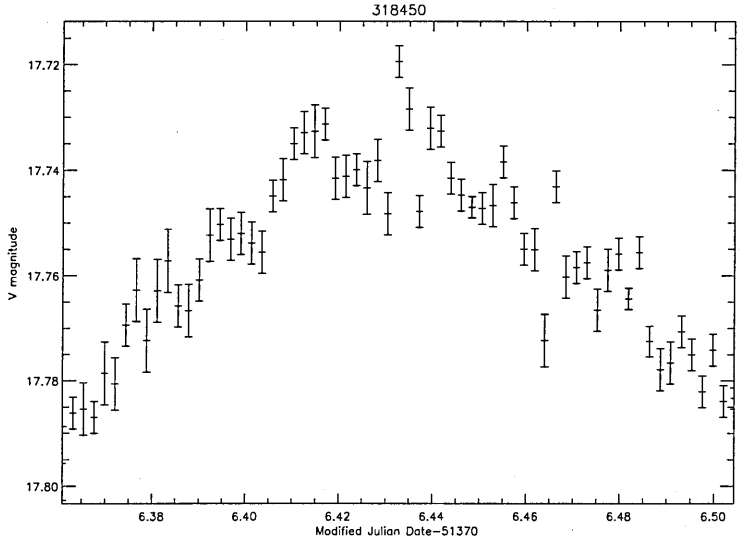
318450
V magnitude
17.72
17.74
17.76
17.78
17.80
6.38
6.40
6.42
6.44
6.46
6.48
6.50
Modified Julian Date−51370

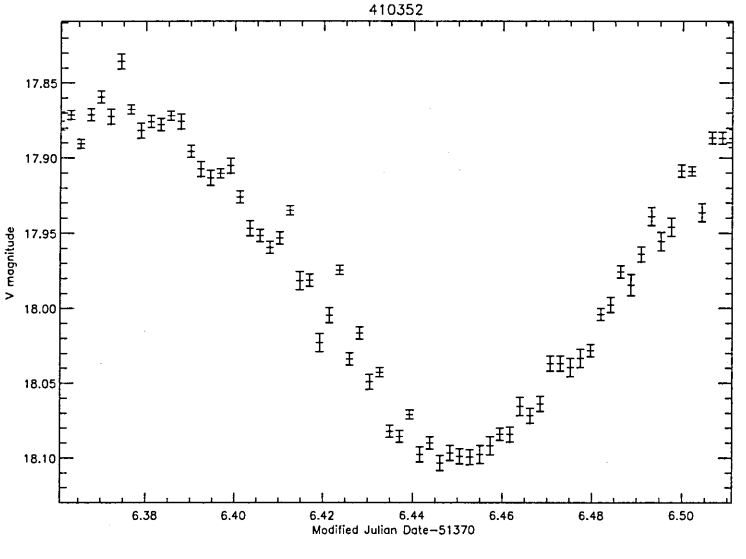
410352
V magnitude
17.85
17.90
17.95
18.00
18.05
18.10
6.38
6.40
6.42
6.44
6.46
6.48
6.50
Modified Julian Date−51370

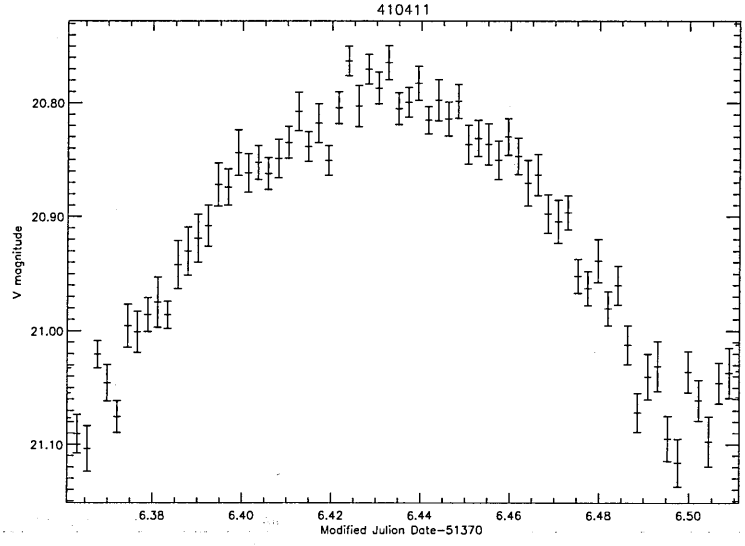
410411
20.80
20.90
21.00
21.10
V magnitude
6.38
6.40
6.42
6.44
6.46
6.48
6.50
Modified Julian Date−51370

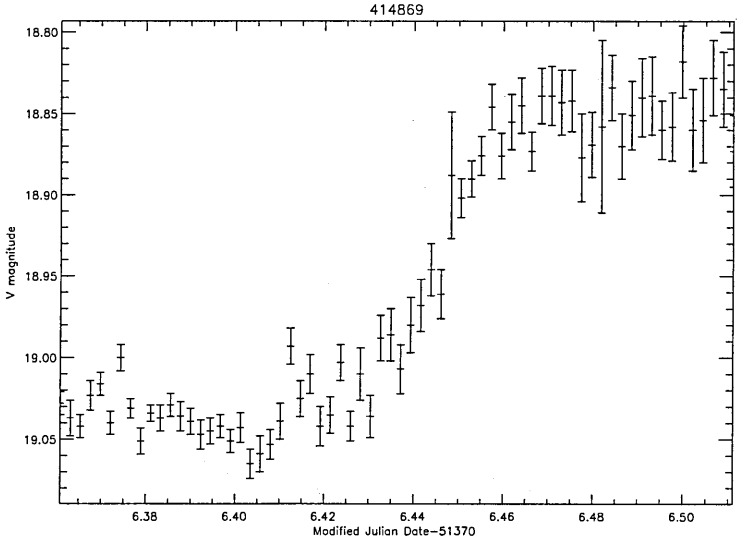
414869
18.80
18.85
18.90
18.95
19.00
19.05
V magnitude
6.38
6.40
6.42
6.44
6.46
6.48
6.50
Modified Julian Date−51370

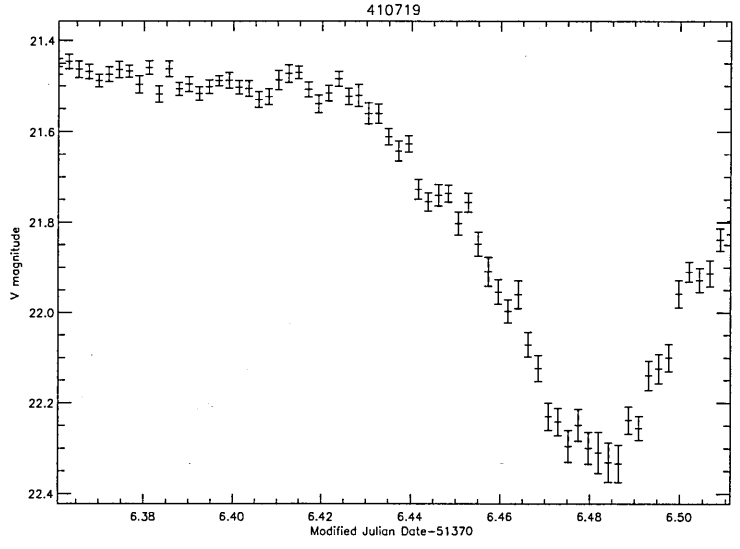
410719
21.4
21.6
21.8
22.0
22.2
22.4
V magnitude
6.38
6.40
6.42
6.44
6.46
6.48
6.50
Modified Julian Date−51370

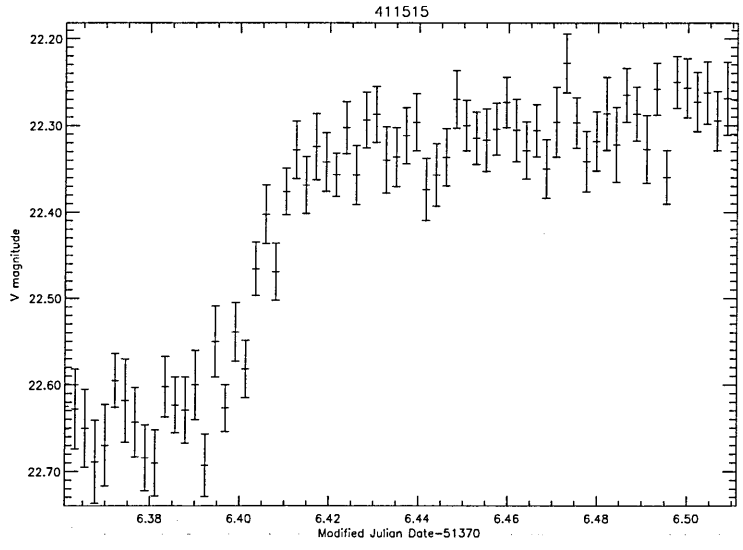
411515
22.20
22.30
22.40
22.50
22.60
22.70
V magnitude
6.38
6.40
6.42
6.44
6.46
6.48
6.50
Modified Julian Date−51370

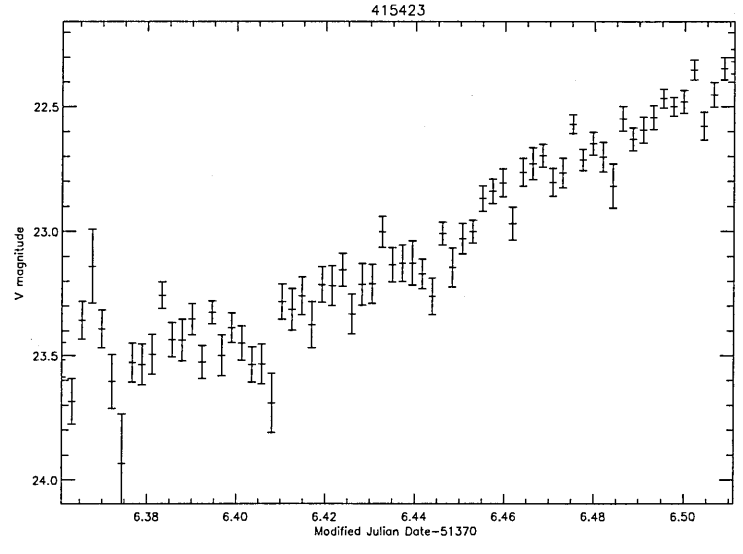
415423
22.5
23.0
23.5
24.0
V magnitude
6.38
6.40
6.42
6.44
6.46
6.48
6.50
Modified Julian Date−51370

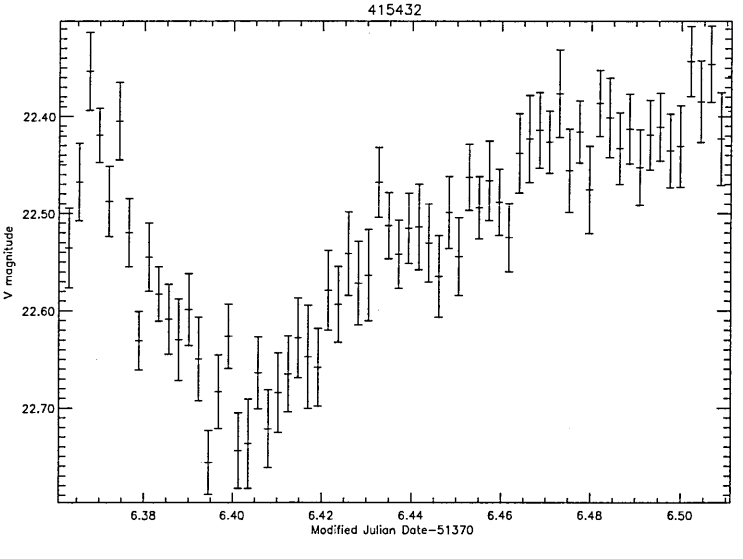
415432
22.40
22.50
22.60
22.70
V magnitude
6.38
6.40
6.42
6.44
6.46
6.48
6.50
Modified Julian Date−51370

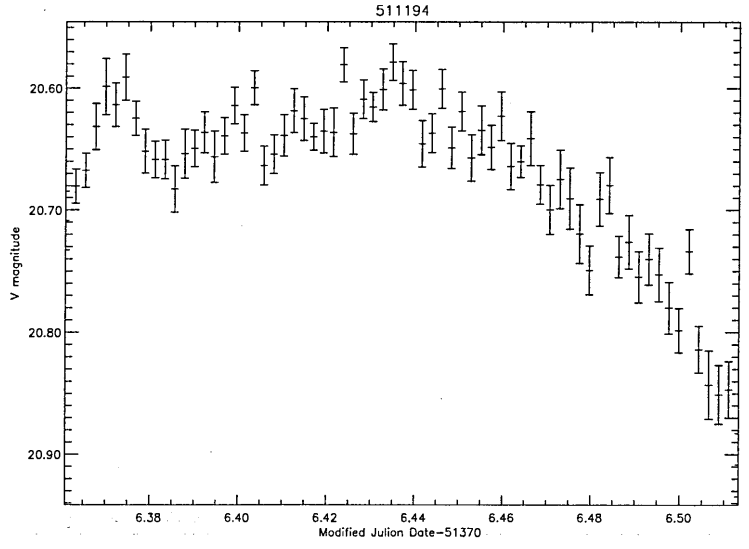
511194
20.60
20.70
20.80
20.90
V magnitude
6.38
6.40
6.42
6.44
6.46
6.48
6.50
Modified Julian Date−51370

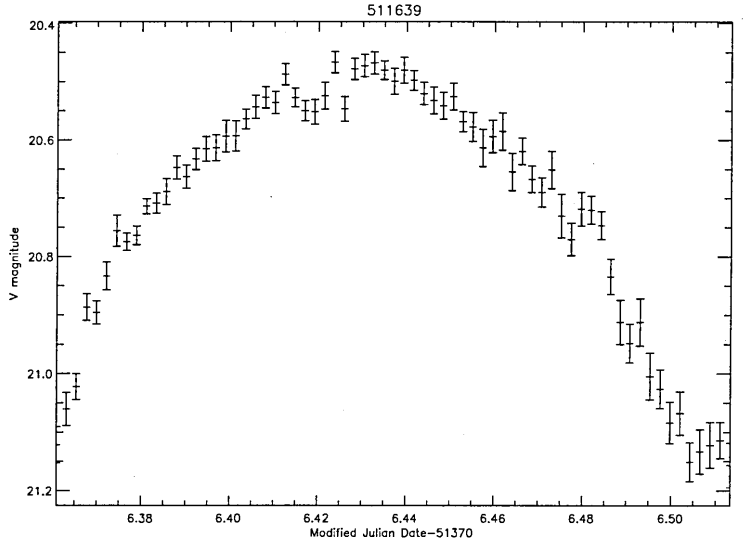
511639
20.4
20.6
20.8
21.0
21.2
V magnitude
6.38
6.40
6.42
6.44
6.46
6.48
6.50
Modified Julian Date−51370

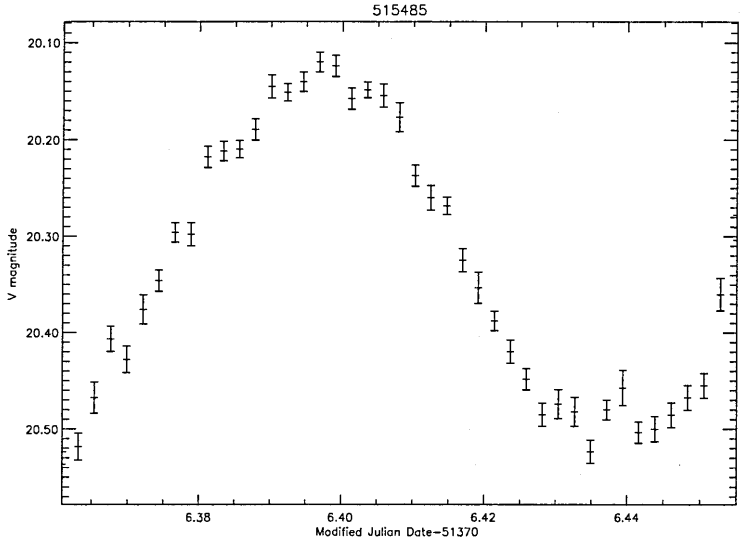
515485
20.10
20.20
20.30
20.40
20.50
V magnitude
6.38
6.40
6.42
6.44
Modified Julian Date−51370

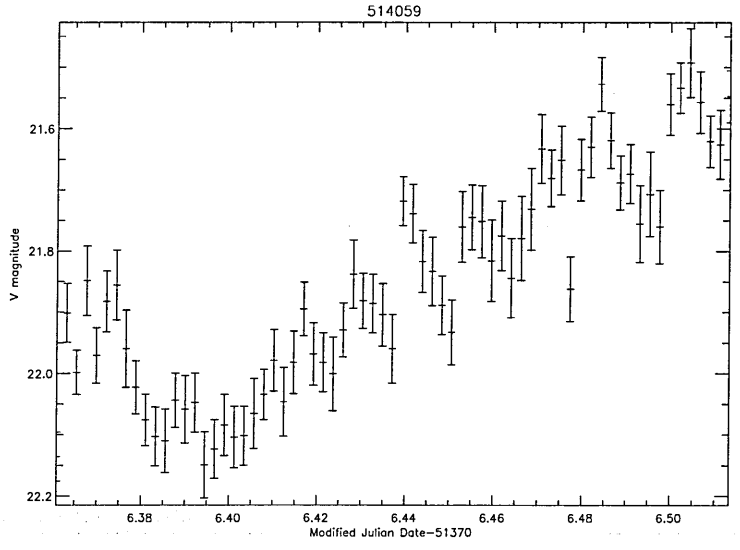
514059
V magnitude
21.6
21.8
22.0
22.2
6.38
6.40
6.42
6.44
6.46
6.48
6.50
Modified Julian Date−51370

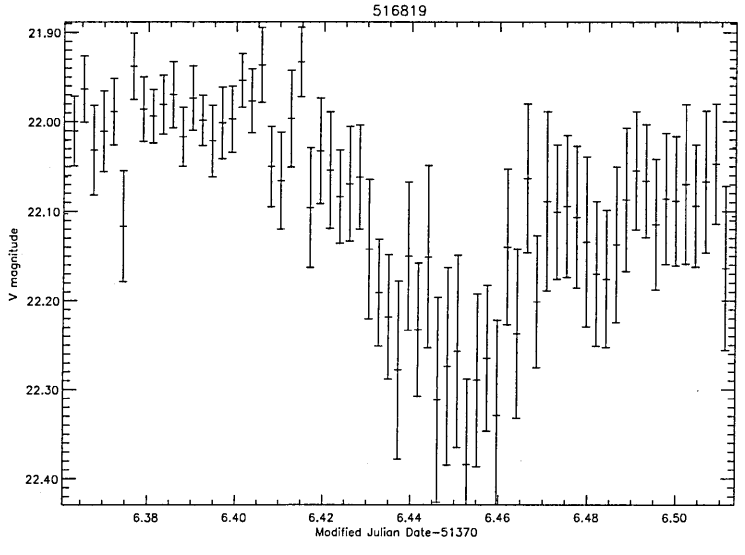
516819
V magnitude
21.90
22.00
22.10
22.20
22.30
22.40
6.38
6.40
6.42
6.44
6.46
6.48
6.50
Modified Julian Date−51370

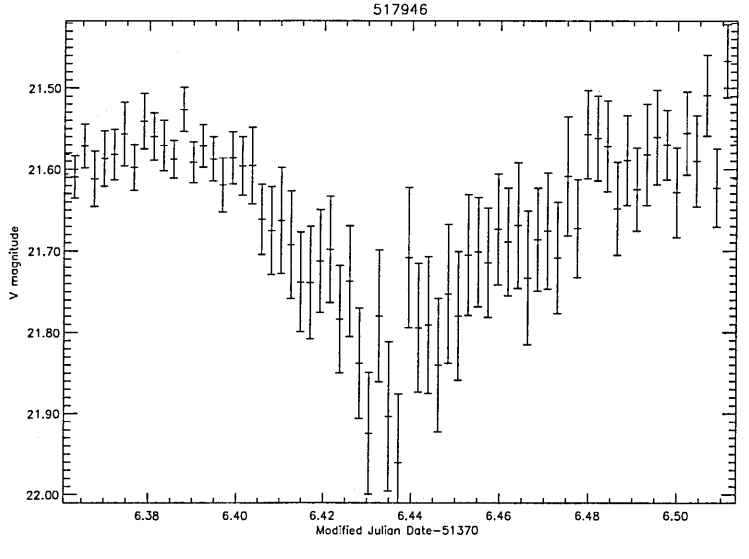
517946
V magnitude
21.50
21.60
21.70
21.80
21.90
22.00
6.38
6.40
6.42
6.44
6.46
6.48
6.50
Modified Julian Date−51370

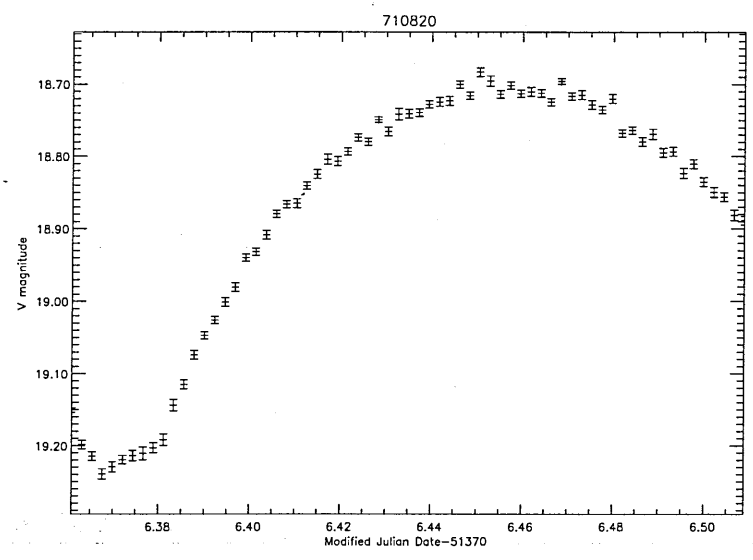
710820
18.70
18.80
18.90
19.00
19.10
19.20
V magnitude
6.38
6.40
6.42
6.44
6.46
6.48
6.50
Modified Julian Date−51370

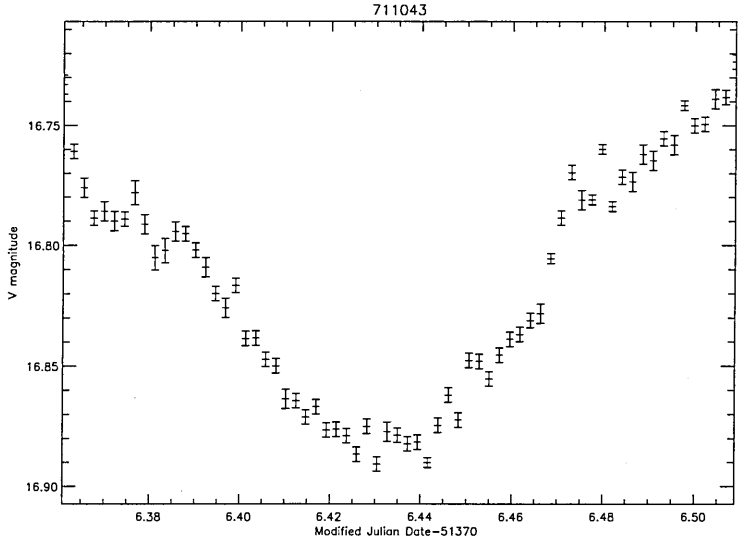
711043
16.75
16.80
16.85
16.90
V magnitude
6.38
6.40
6.42
6.44
6.46
6.48
6.50
Modified Julian Date−51370

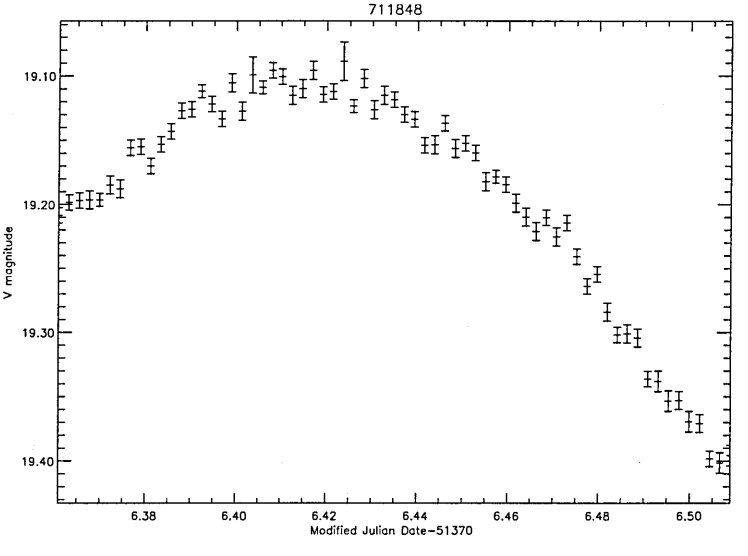
711848
19.10
19.20
19.30
19.40
V magnitude
6.38
6.40
6.42
6.44
6.46
6.48
6.50
Modified Julian Date−51370

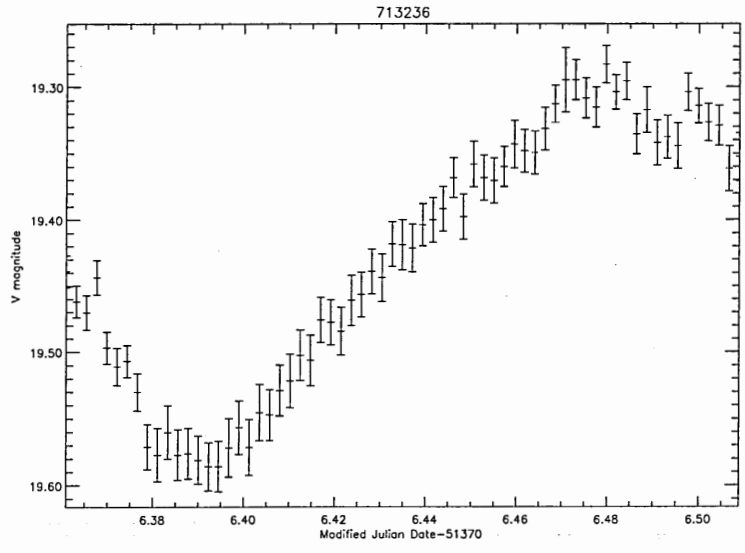
713236
V magnitude
19.30
19.40
19.50
19.60
6.38
6.40
6.42
6.44
6.46
6.48
6.50
Modified Julian Date−51370

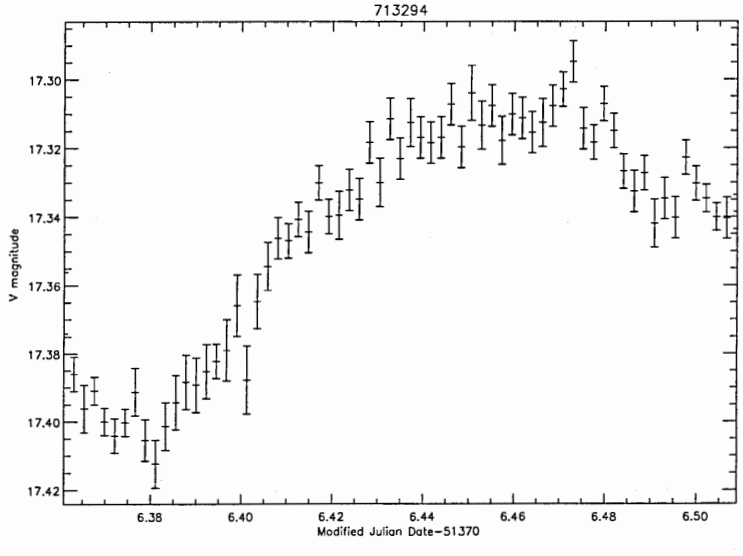
713294
V magnitude
17.30
17.32
17.34
17.36
17.38
17.40
17.42
6.38
6.40
6.42
6.44
6.46
6.48
6.50
Modified Julian Date−51370

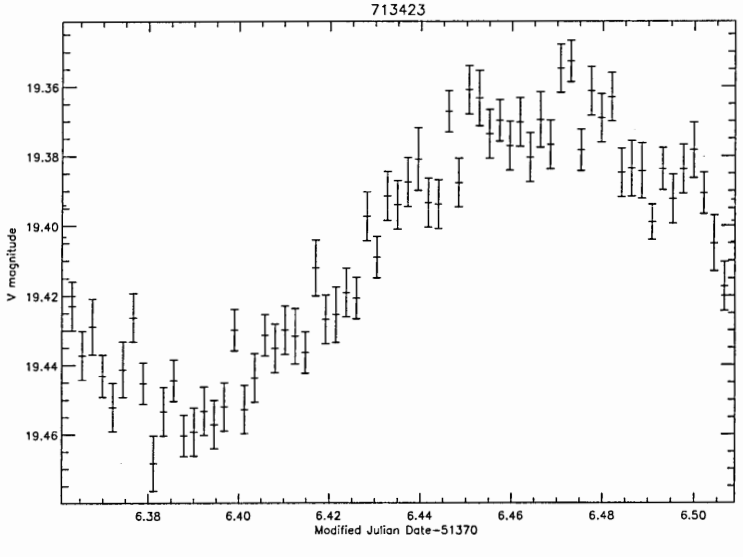
713423
V magnitude
19.36
19.38
19.40
19.42
19.44
19.46
6.38
6.40
6.42
6.44
6.46
6.48
6.50
Modified Julian Date−51370

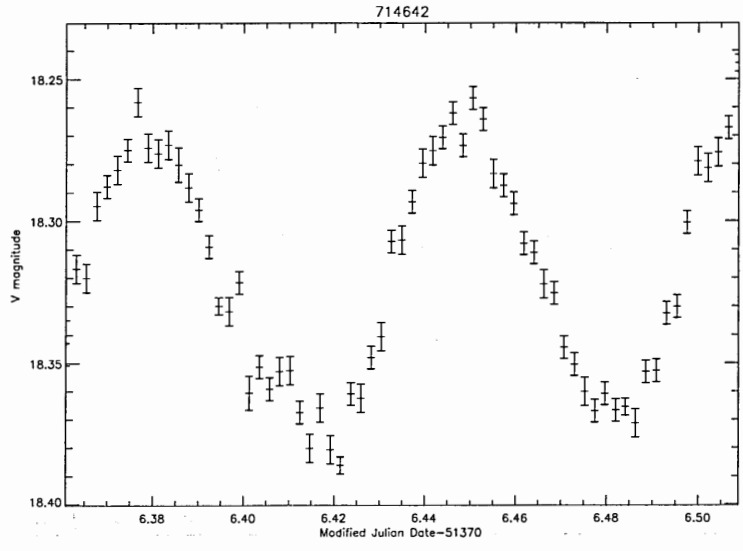
714642
18.25
18.30
18.35
18.40
V magnitude
6.38
6.40
6.42
6.44
6.46
6.48
6.50
Modified Julian Date−51370

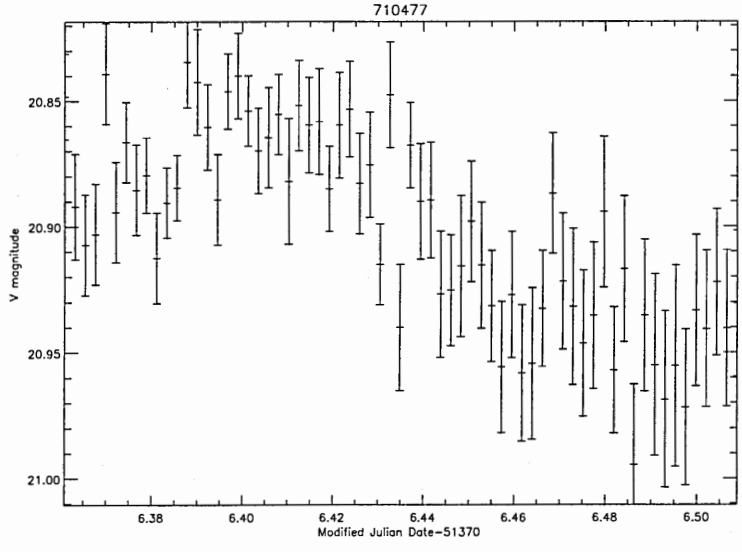
710477
20.85
20.90
20.95
21.00
V magnitude
6.38
6.40
6.42
6.44
6.46
6.48
6.50
Modified Julian Date−51370

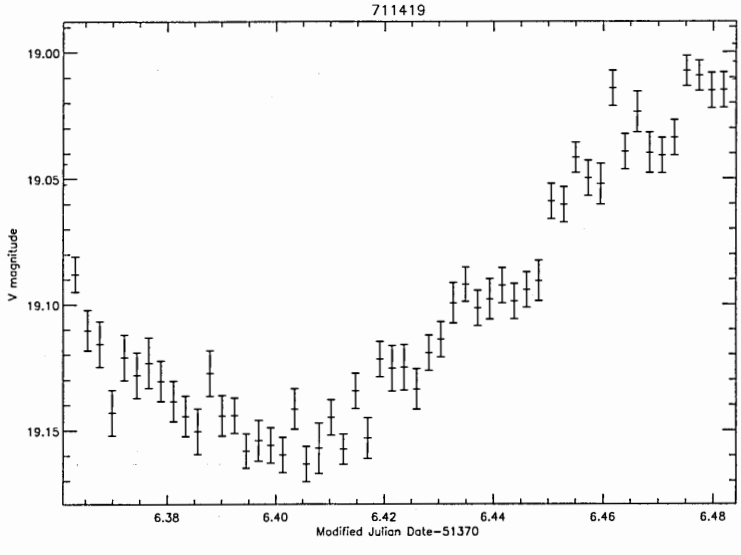
711419
19.00
19.05
19.10
19.15
V magnitude
6.38
6.40
6.42
6.44
6.46
6.48
Modified Julian Date−51370

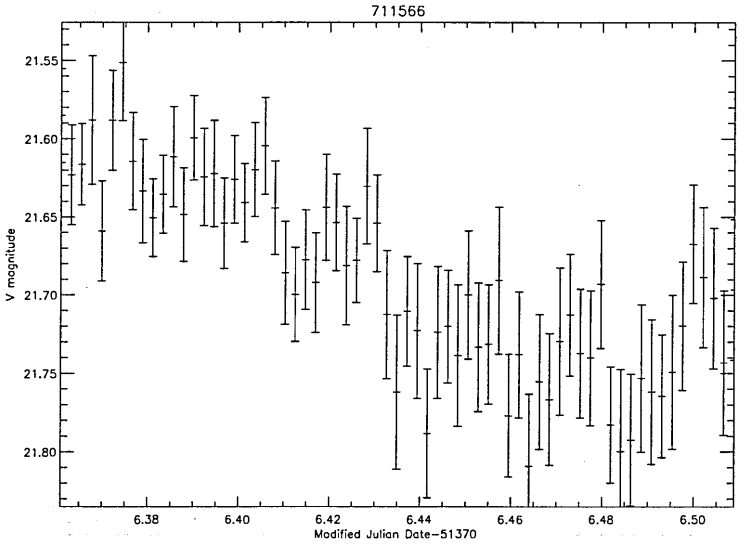
711566
V magnitude
21.55
21.60
21.65
21.70
21.75
21.80
6.38
6.40
6.42
6.44
6.46
6.48
6.50
Modified Julian Date−51370

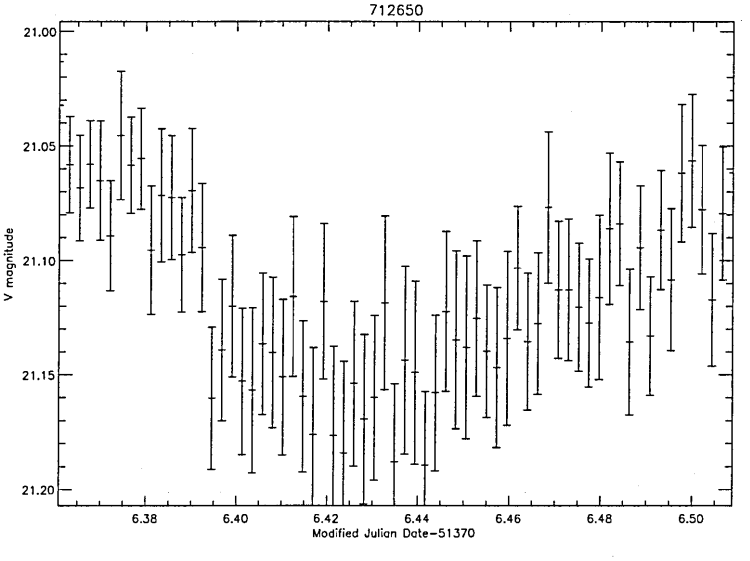
712650
V magnitude
21.00
21.05
21.10
21.15
21.20
6.38
6.40
6.42
6.44
6.46
6.48
6.50
Modified Julian Date−51370

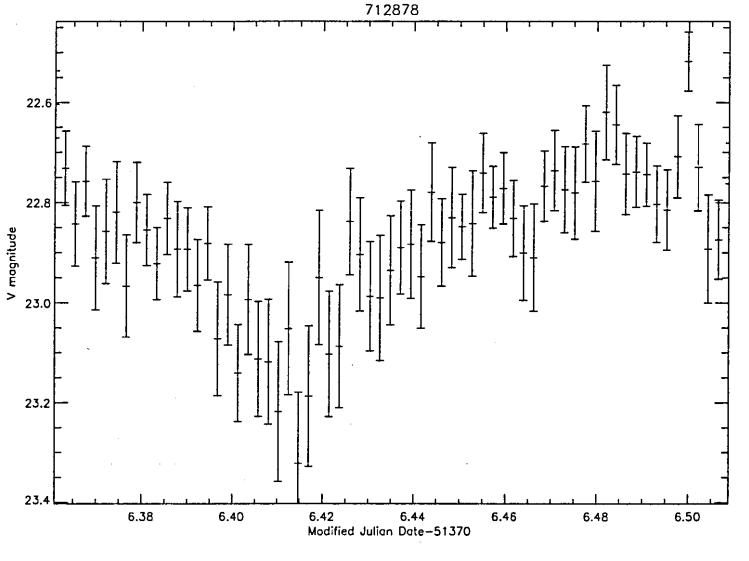
712878
V magnitude
22.6
22.8
23.0
23.2
23.4
6.38
6.40
6.42
6.44
6.46
6.48
6.50
Modified Julian Date−51370

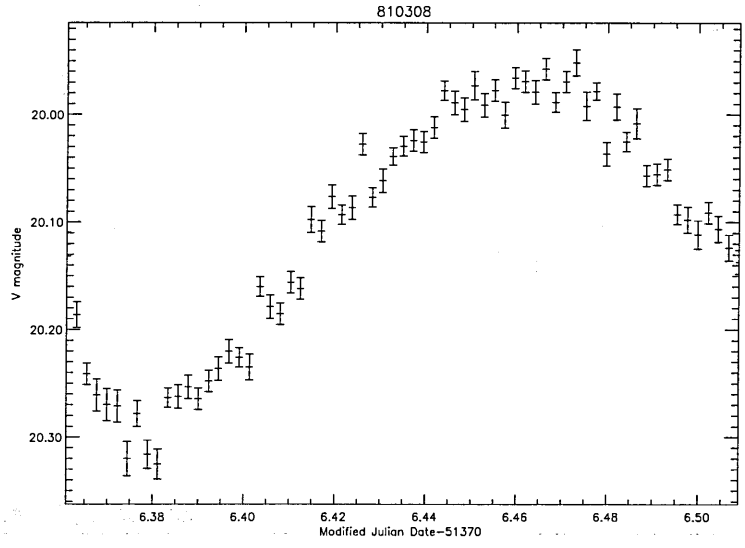
810308
V magnitude
20.00
20.10
20.20
20.30
6.38
6.40
6.42
6.44
6.46
6.48
6.50
Modified Julian Date−51370

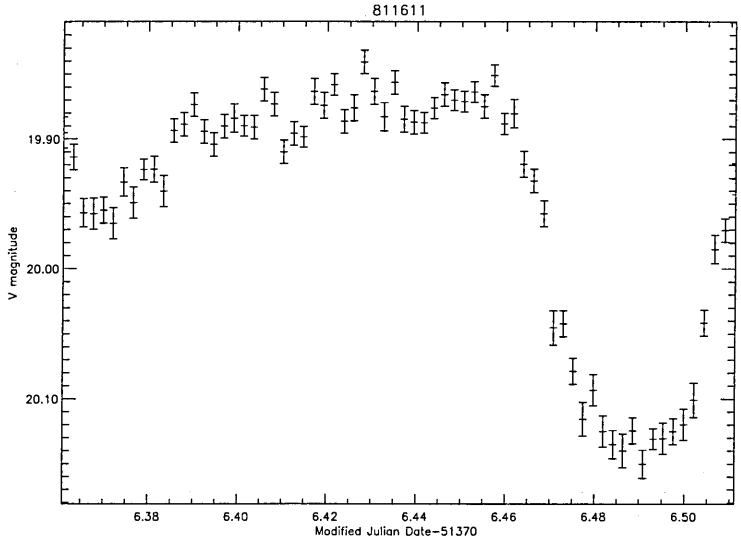
811611
V magnitude
19.90
20.00
20.10
6.38
6.40
6.42
6.44
6.46
6.48
6.50
Modified Julian Date−51370

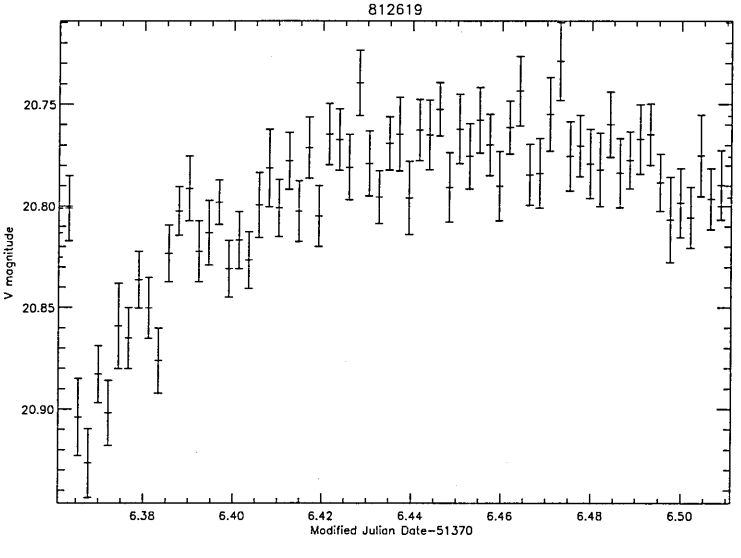
812619
V magnitude
20.75
20.80
20.85
20.90
6.38
6.40
6.42
6.44
6.46
6.48
6.50
Modified Julian Date−51370

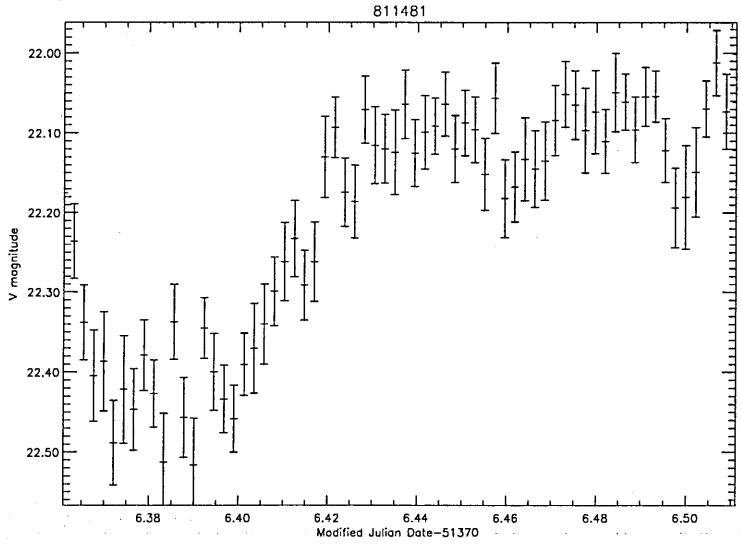
811481
22.00
22.10
22.20
22.30
22.40
22.50
V magnitude
6.38
6.40
6.42
6.44
6.46
6.48
6.50
Modified Julian Date−51370

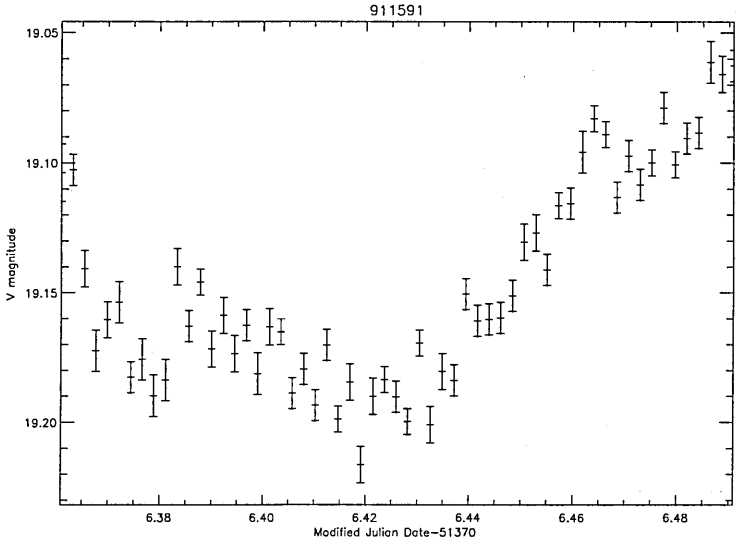
911591
19.05
19.10
19.15
19.20
V magnitude
6.38
6.40
6.42
6.44
6.46
6.48
Modified Julian Date−51370

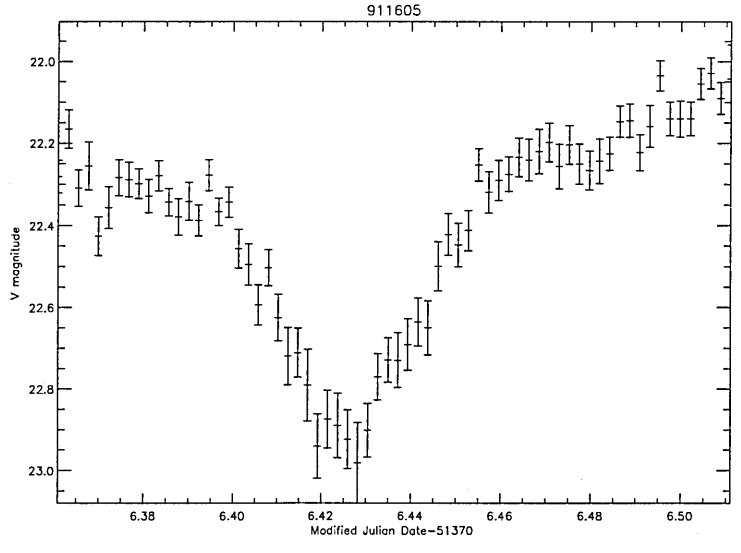
911605
22.0
22.2
22.4
22.6
22.8
23.0
V magnitude
6.38
6.40
6.42
6.44
6.46
6.48
6.50
Modified Julian Date−51370

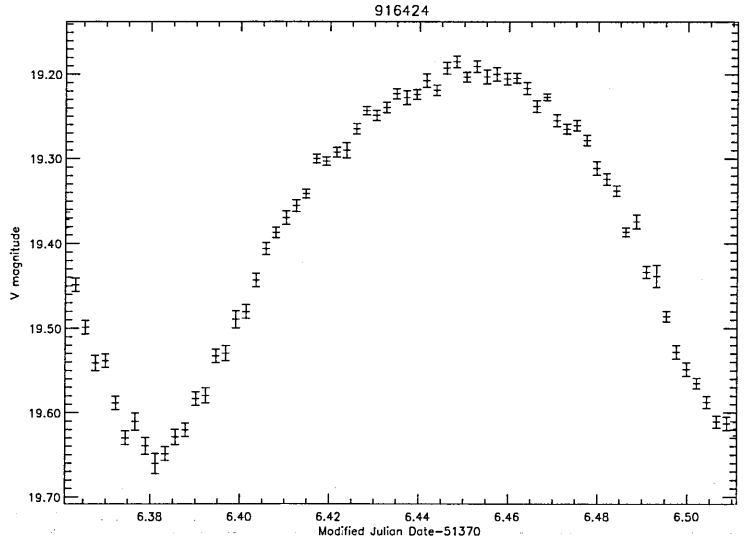
916424
V magnitude
19.20
19.30
19.40
19.50
19.60
19.70
6.38
6.40
6.42
6.44
6.46
6.48
6.50
Modified Julian Date−51370

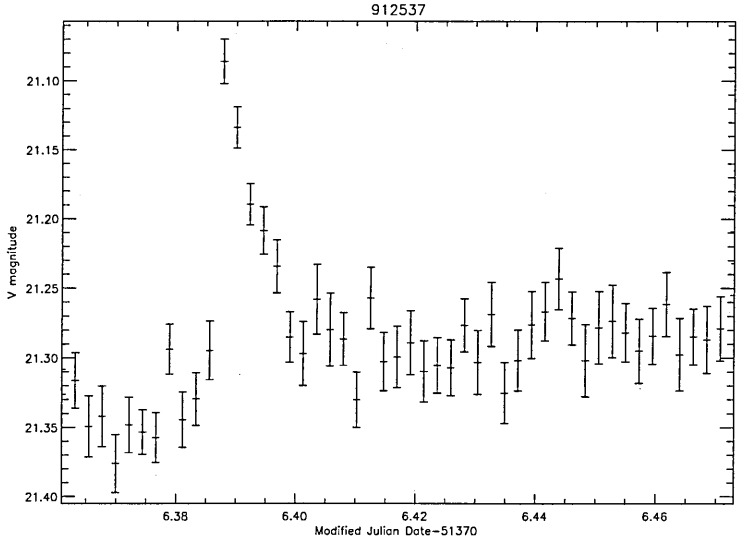
912537
V magnitude
21.10
21.15
21.20
21.25
21.30
21.35
21.40
6.38
6.40
6.42
6.44
6.46
Modified Julian Date−51370

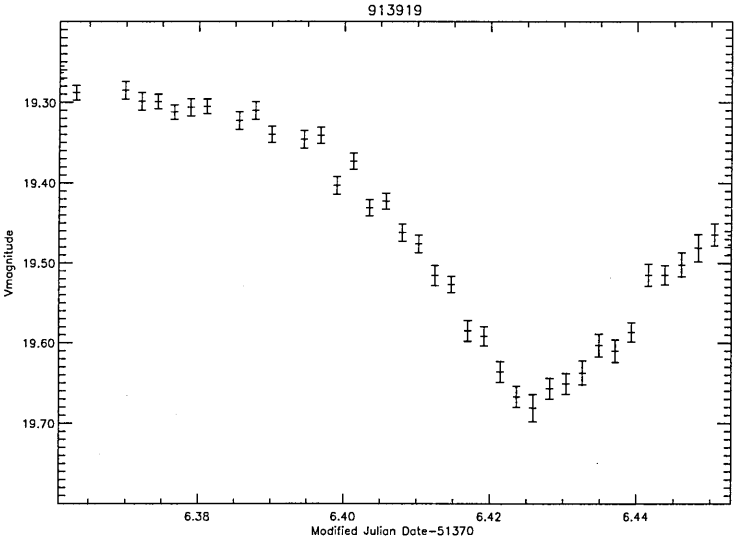
913919
Vmagnitude
19.30
19.40
19.50
19.60
19.70
6.38
6.40
6.42
6.44
Modified Julian Date−51370

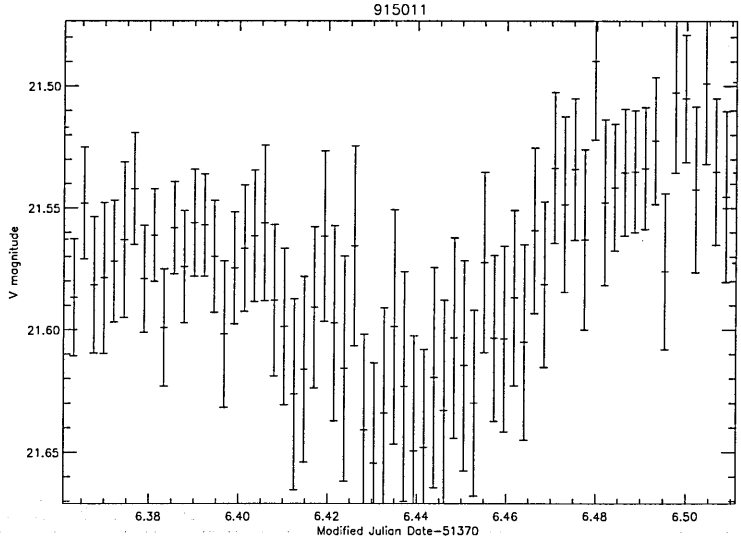
915011
21.50
21.55
21.60
21.65
V magnitude
6.38
6.40
6.42
6.44
6.46
6.48
6.50
Modified Julian Date−51370

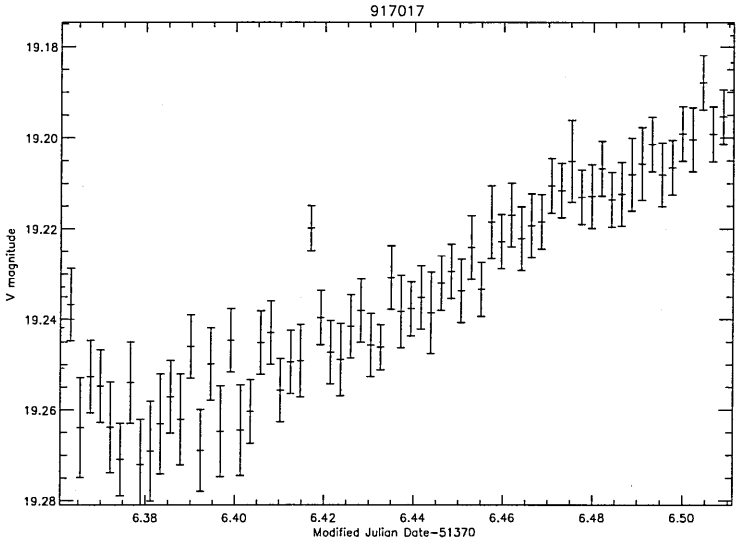
917017
19.18
19.20
19.22
19.24
19.26
19.28
V magnitude
6.38
6.40
6.42
6.44
6.46
6.48
6.50
Modified Julian Date−51370

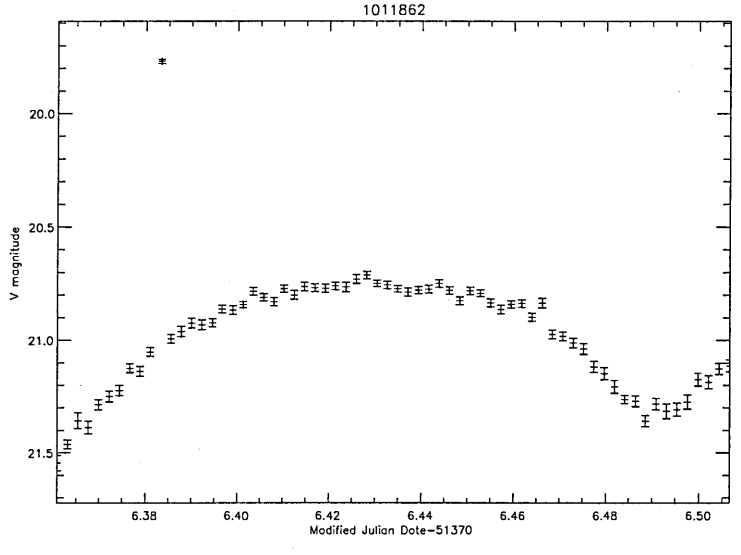
1011862
20.0
20.5
21.0
21.5
V magnitude
6.38
6.40
6.42
6.44
6.46
6.48
6.50
Modified Julian Date−51370

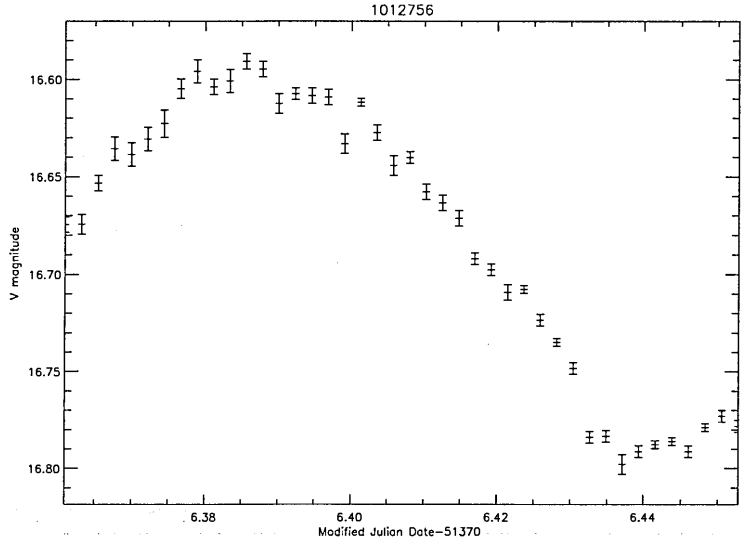
1012756
V magnitude
16.60
16.65
16.70
16.75
16.80
6.38
6.40
6.42
6.44
Modified Julian Date−51370

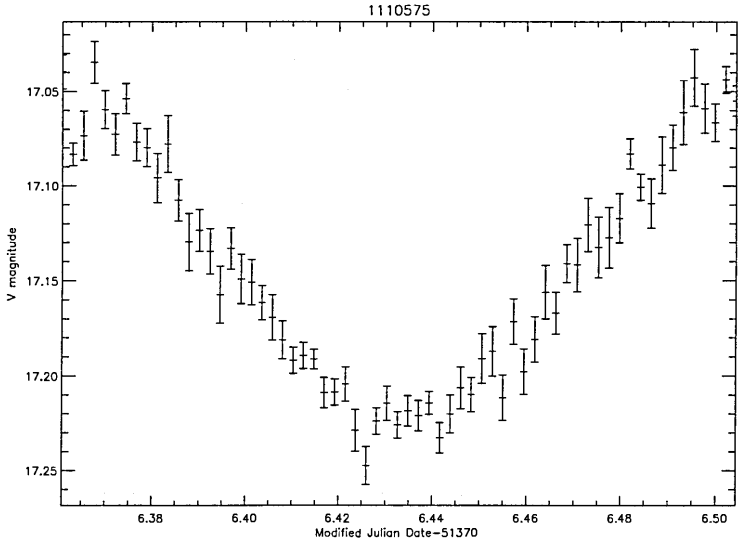
1110575
V magnitude
17.05
17.10
17.15
17.20
17.25
6.38
6.40
6.42
6.44
6.46
6.48
6.50
Modified Julian Date−51370

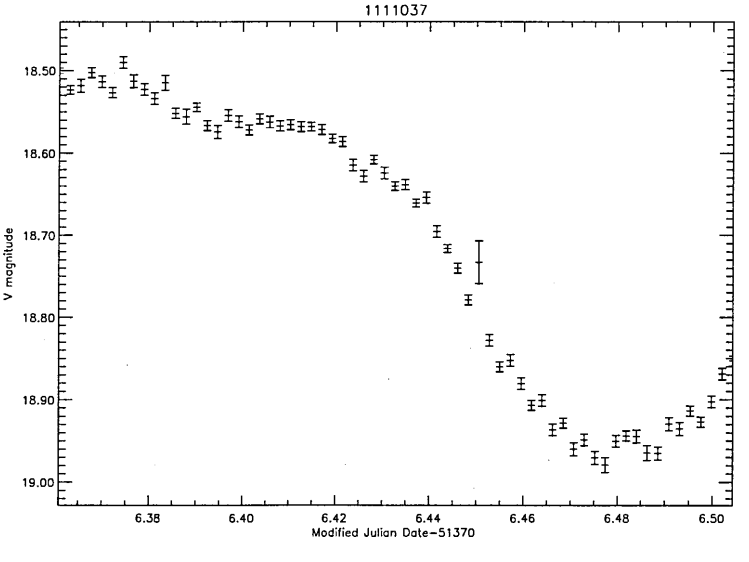
1111037
V magnitude
18.50
18.60
18.70
18.80
18.90
19.00
6.38
6.40
6.42
6.44
6.46
6.48
6.50
Modified Julian Date−51370

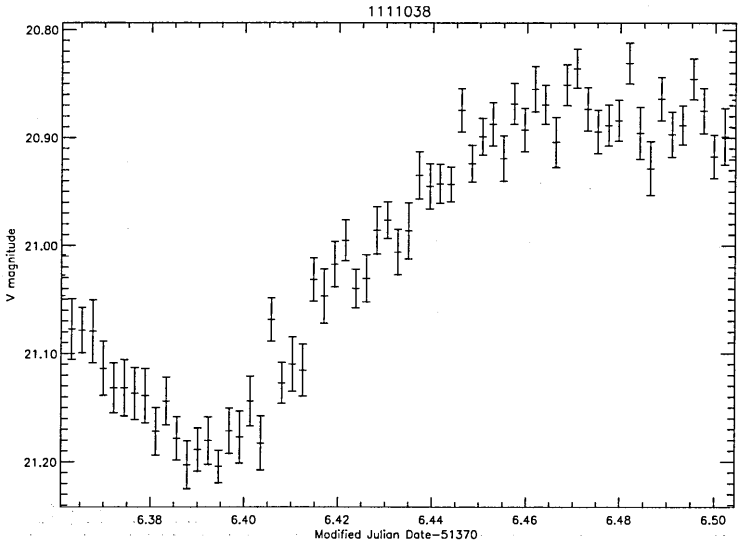
1111038
20.80
20.90
21.00
21.10
21.20
V magnitude
6.38
6.40
6.42
6.44
6.46
6.48
6.50
Modified Julian Date−51370

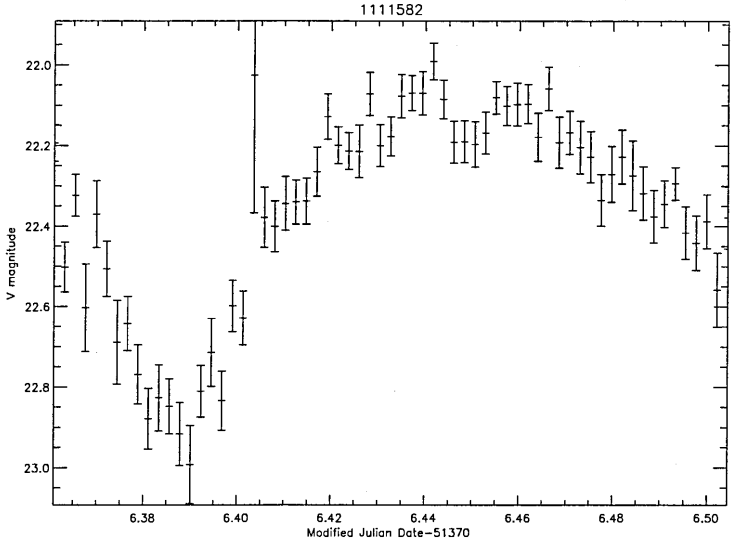
1111582
22.0
22.2
22.4
22.6
22.8
23.0
V magnitude
6.38
6.40
6.42
6.44
6.46
6.48
6.50
Modified Julian Date−51370

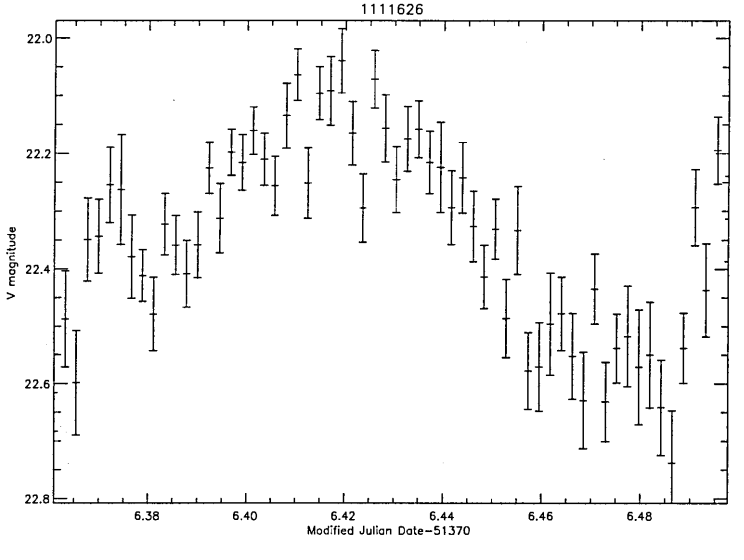
1111626
22.0
22.2
22.4
22.6
22.8
V magnitude
6.38
6.40
6.42
6.44
6.46
6.48
Modified Julian Date−51370

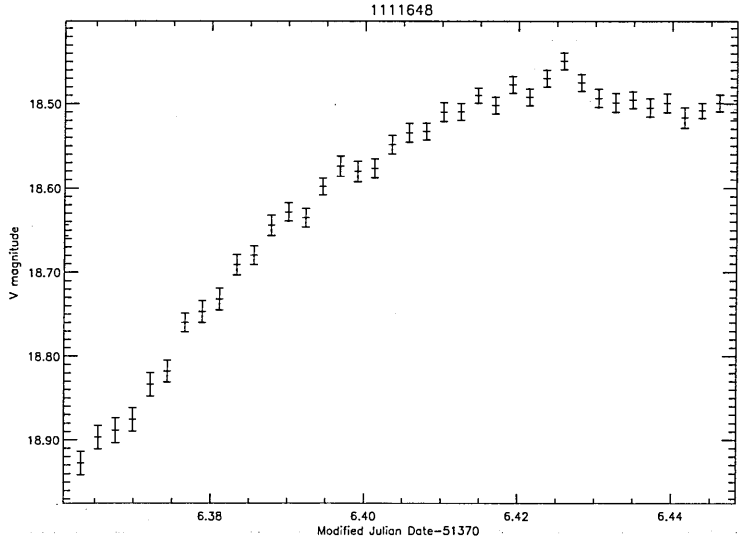
1111648
V magnitude
18.50
18.60
18.70
18.80
18.90
6.38
6.40
6.42
6.44
Modified Julian Date−51370

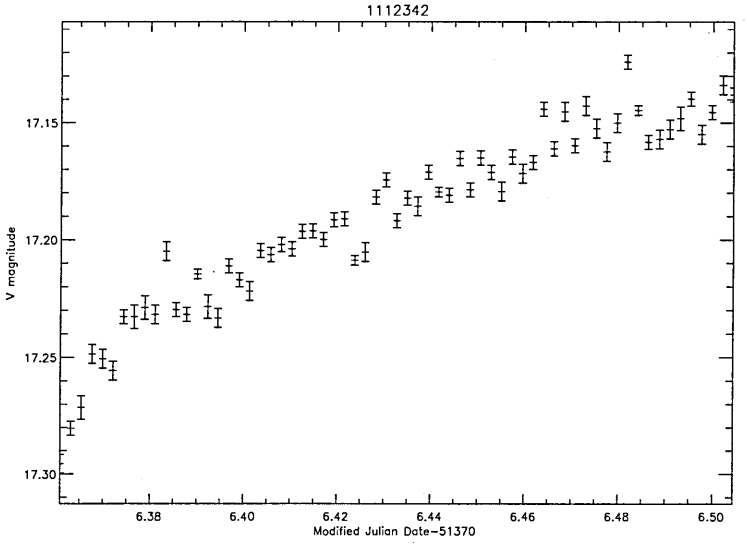
1112342
V magnitude
17.15
17.20
17.25
17.30
6.38
6.40
6.42
6.44
6.46
6.48
6.50
Modified Julian Date−51370

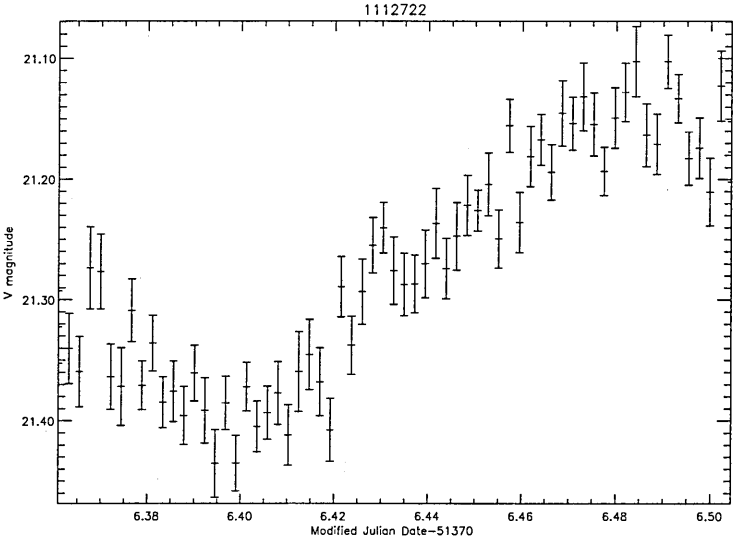
1112722
V magnitude
21.10
21.20
21.30
21.40
6.38
6.40
6.42
6.44
6.46
6.48
6.50
Modified Julian Date−51370

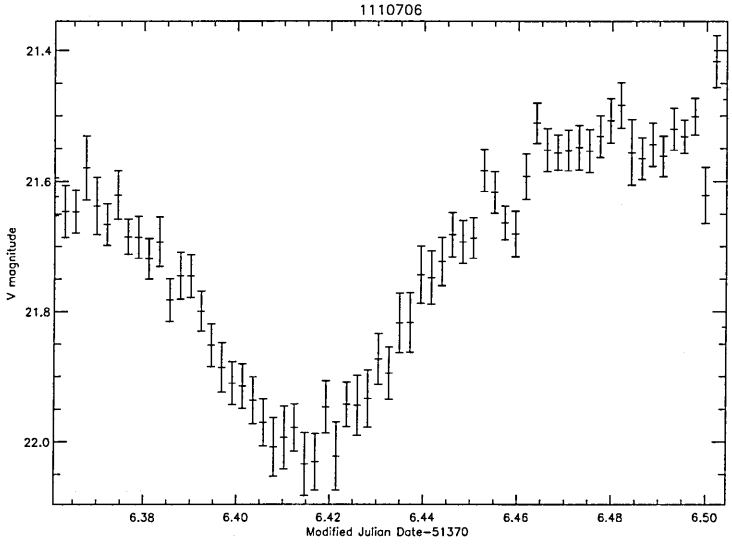
1110706
21.4
21.6
21.8
22.0
V magnitude
6.38
6.40
6.42
6.44
6.46
6.48
6.50
Modified Julian Date−51370

APPENDIX C

Lightcurves of variable objects observed on night two only

Table C.1: IDs and Positions Night Two Variables

ID	RA	DEC	Obs. V Max	Obs V Min
9923670	20h 25m 33.8	27h 50m 49.6	18.336 ± 0.010	19.195 ± 0.011
9920733	20h 25m 38.2	27h 58m 12.7	21.799 ± 0.039	22.661 ± 0.201
9925398	20h 25m 45.4	27h 46m 38.3	20.559 ± 0.021	20.738 ± 0.017
121830	20h 26m 17.3	27h 55m 1.9	19.657 ± 0.011	19.825 ± 0.019
123229	20h 26m 13.4	27h 52m 0.8	19.002 ± 0.006	19.101 ± 0.006
120754	20h 26m 24.0	27h 57m 55.4	18.859 ± 0.006	19.481 ± 0.009
122677	20h 26m 15.1	27h 53m 11.8	17.732 ± 0.003	18.250 ± 0.004
123169	20h 26m 25.9	27h 52m 8.4	20.493 ± 0.018	20.794 ± 0.015
124251	20h 26m 16.1	27h 50m 2.8	20.114 ± 0.008	20.361 ± 0.016
222584	20h 26m 45.8	27h 53m 27.2	18.686 ± 0.005	18.767 ± 0.008
222899	20h 26m 42.2	27h 52m 30.4	18.497 ± 0.005	18.819 ± 0.005
223345	20h 26m 45.4	27h 51m 15.1	19.364 ± 0.008	20.163 ± 0.017
223551	20h 26m 46.1	27h 50m 43.4	18.342 ± 0.014	19.585 ± 0.069
224858	20h 26m 37.9	27h 47m 21.1	16.469 ± 0.002	16.629 ± 0.008
224978	20h 26m 44.9	27h 46m 59.5	20.528 ± 0.016	20.731 ± 0.015
324293	20h 27m 17.8	27h 50m 1.0	20.656 ± 0.014	20.819 ± 0.019
321522	20h 27m 25.9	27h 56m 51.7	19.875 ± 0.014	19.998 ± 0.015

continued...

Table C.1: continued

320042	20h 27m 10.5	28h 00m 19.8	16.536 ± 0.013	16.961 ± 0.012
324886	20h 27m 3.8	27h 48m 32.4	19.232 ± 0.007	19.737 ± 0.010
424049	20h 27m 39.1	27h 50m 43.4	21.960 ± 0.084	23.209 ± 0.201
424233	20h 27m 46.1	27h 50m 17.2	19.171 ± 0.005	19.638 ± 0.012
424508	20h 27m 40.4	27h 43m 34.4	16.104 ± 0.014	16.381 ± 0.008
521150	20h 28m 23.8	27h 57m 29.5	21.466 ± 0.083	22.521 ± 0.254
521176	20h 28m 22.6	27h 57m 25.2	18.318 ± 0.016	18.432 ± 0.016
524898	20h 28m 23.8	27h 48m 27.0	20.169 ± 0.011	20.325 ± 0.014
520260	20h 28m 33.8	27h 59m 41.3	20.925 ± 0.038	21.877 ± 0.375
524006	20h 28m 24.0	27h 50m 42.0	21.613 ± 0.054	22.651 ± 0.063
524766	20h 28m 25.0	27h 48m 47.9	17.869 ± 0.008	18.294 ± 0.005
720134	20h 26m 26.2	27h 32m 42.0	18.377 ± 0.006	18.457 ± 0.006
720195	20h 26m 2.9	27h 32m 55.7	19.754 ± 0.011	19.854 ± 0.009
720553	20h 25m 57.6	27h 33m 57.6	18.306 ± 0.007	18.423 ± 0.012
720639	20h 26m 1.2	27h 34m 10.9	20.781 ± 0.026	20.973 ± 0.017
720911	20h 26m 19.7	27h 34m 59.9	21.739 ± 0.058	22.065 ± 0.047
721075	20h 26m 21.6	27h 35m 25.1	21.296 ± 0.024	21.564 ± 0.055
721327	20h 26m 7.7	27h 36m 10.1	21.708 ± 0.024	22.536 ± 0.059
721329	20h 26m 25.2	27h 36m 8.6	17.110 ± 0.004	17.202 ± 0.003
721426	20h 26m 18.7	27h 36m 25.6	19.431 ± 0.009	19.541 ± 0.015
722455	20h 26m 21.6	27h 39m 18.0	22.229 ± 0.092	22.913 ± 0.103
722785	20h 26m 20.6	27h 40m 7.7	21.738 ± 0.058	22.256 ± 0.086
723809	20h 26m 20.4	27h 42m 51.8	20.848 ± 0.028	20.993 ± 0.040
724012	20h 26m 06.6	27h 43m 21.2	19.287 ± 0.009	19.615 ± 0.012
720385	20h 26m 6.5	27h 33m 29.5	19.707 ± 0.007	19.902 ± 0.010
720868	20h 26m 20.4	27h 34m 50.9	19.564 ± 0.013	19.705 ± 0.029
721429	20h 26m 20.4	27h 36m 25.6	21.770 ± 0.042	22.060 ± 0.060
721846	20h 26m 20.4	27h 37m 34.3	21.687 ± 0.056	22.066 ± 0.049
723193	20h 26m 20.4	27h 41m 17.2	20.811 ± 0.029	21.032 ± 0.035
820051	20h 26m 55.2	27h 32m 28.3	19.659 ± 0.013	19.753 ± 0.011
820318	20h 26m 53.0	27h 33m 6.8	18.375 ± 0.007	18.519 ± 0.007

continued...

Table C.1: continued

821344	20h 26m 36.7	27h 35m 56.4	18.098 ± 0.005	18.154 ± 0.005
821760	20h 26m 44.2	27h 37m 3.7	19.885 ± 0.012	20.244 ± 0.009
823022	20h 26m 53.5	27h 40m 20.6	21.337 ± 0.025	21.547 ± 0.037
824576	20h 26m 45.8	27h 44m 20.0	21.602 ± 0.027	22.170 ± 0.079
824798	20h 26m 42.0	27h 44m 56.8	19.418 ± 0.009	19.838 ± 0.009
820163	20h 26m 44.6	27h 32m 43.4	18.997 ± 0.008	19.472 ± 0.008
920239	20h 27m 7.9	27h 32m 58.6	19.763 ± 0.010	19.912 ± 0.010
921760	20h 27m 0.7	27h 36m 55.1	21.07 ± 0.018	21.285 ± 0.019
922412	20h 27m 27.1	27h 38m 42.0	18.267 ± 0.005	18.400 ± 0.016
925132	20h 27m 27.4	27h 45m 18.7	21.339 ± 0.025	21.55 ± 0.037
925382	20h 27m 27.4	27h 45m 56.2	21.555 ± 0.046	21.788 ± 0.040
922754	20h 27m 16.1	27h 39m 37.1	22.087 ± 0.073	23.050 ± 0.117
925299	20h 27m 16.1	27h 39m 37.1	20.633 ± 0.014	21.112 ± 0.021
1020575	20h 27m 38.6	27h 33m 16.9	20.064 ± 0.017	20.529 ± 0.015
1020614	20h 27m 37.7	27h 33m 21.6	22.315 ± 0.051	23.055 ± 0.238
1020811	20h 27m 52.8	27h 33m 49.0	18.774 ± 0.007	19.014 ± 0.009
1020816	20h 27m 43.7	27h 33m 50.0	20.057 ± 0.017	20.878 ± 0.02
1021699	20h 27m 59.8	27h 35m 40.6	17.593 ± 0.009	18.145 ± 0.009
1021706	20h 27m 31.9	27h 35m 43.1	18.867 ± 0.008	19.195 ± 0.009
1021941	20h 27m 36.0	27h 36m 12.6	16.928 ± 0.003	17.125 ± 0.006
1021970	20h 27m 56.4	27h 36m 16.2	20.659 ± 0.025	21.435 ± 0.024
1023127	20h 27m 33.6	27h 38m 54.2	20.702 ± 0.027	21.594 ± 0.034
1120212	20h 28m 33.1	27h 32m 52.8	18.759 ± 0.013	19.322 ± 0.029
1120553	20h 28m 9.1	27h 33m 48.6	17.759 ± 0.005	17.953 ± 0.016
1122055	20h 28m 19.2	27h 37m 50.9	16.991 ± 0.004	17.245 ± 0.005
1122083	20h 28m 14.2	27h 37m 55.2	20.354 ± 0.011	21.545 ± 0.048
1122543	20h 28m 6.0	27h 39m 6.1	18.497 ± 0.008	18.893 ± 0.006
1122550	20h 28m 8.2	27h 39m 6.8	20.827 ± 0.02	21.216 ± 0.022
1122602	20h 28m 32.9	27h 39m 12.6	16.399 ± 0.004	16.485 ± 0.010
1123900	20h 28m 11.0	27h 42m 29.9	17.154 ± 0.003	17.309 ± 0.013
1124317	20h 28m 14.2	27h 43m 30.7	21.154 ± 0.207	21.447 ± 0.033

continued...

Table C.1: continued

1120387	20h 28m 16.8	27h 33m 21.2	22.164 ± 0.069	22.723 ± 0.073
1120794	20h 28m 14.6	27h 34m 28.6	21.636 ± 0.031	22.26 ± 0.109
1120804	20h 28m 18.7	27h 34m 29.6	21.062 ± 0.030	21.313 ± 0.024
1121781	20h 28m 28.1	27h 36m 06.4	18.699 ± 0.014	18.915 ± 0.024
1121811	20h 28m 6.5	27h 37m 12.0	17.800 ± 0.004	17.903 ± 0.006
1122288	20h 28m 26.6	27h 38m 30.5	20.624 ± 0.031	20.978 ± 0.018
1123123	20h 28m 11.8	27h 40m 28.6	21.438 ± 0.379	23.016 ± 0.102
1125498	20h 28m 24.7	27h 46m 8.4	18.449 ± 0.010	18.558 ± 0.022

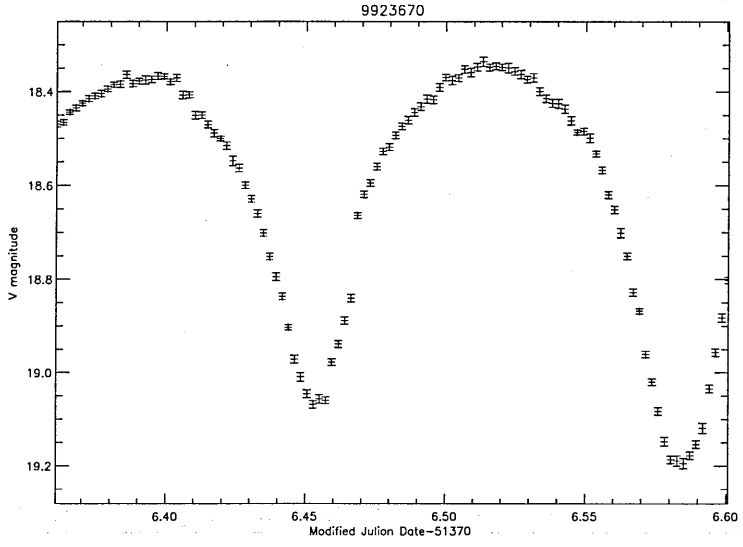
9923670
V magnitude
18.4
18.6
18.8
19.0
19.2
6.40
6.45
6.50
6.55
6.60
Modified Julian Date−51370

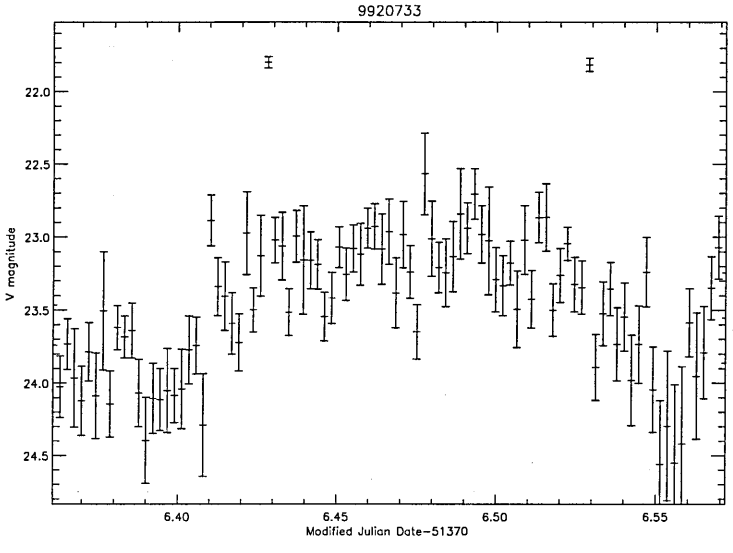
9920733
V magnitude
22.0
22.5
23.0
23.5
24.0
24.5
6.40
6.45
6.50
6.55
Modified Julian Date−51370

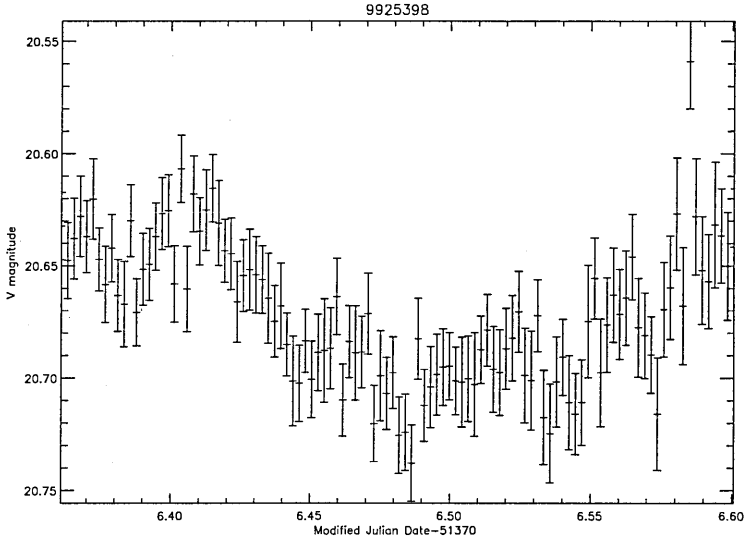
9925398
V magnitude
20.55
20.60
20.65
20.70
20.75
6.40
6.45
6.50
6.55
6.60
Modified Julian Date−51370

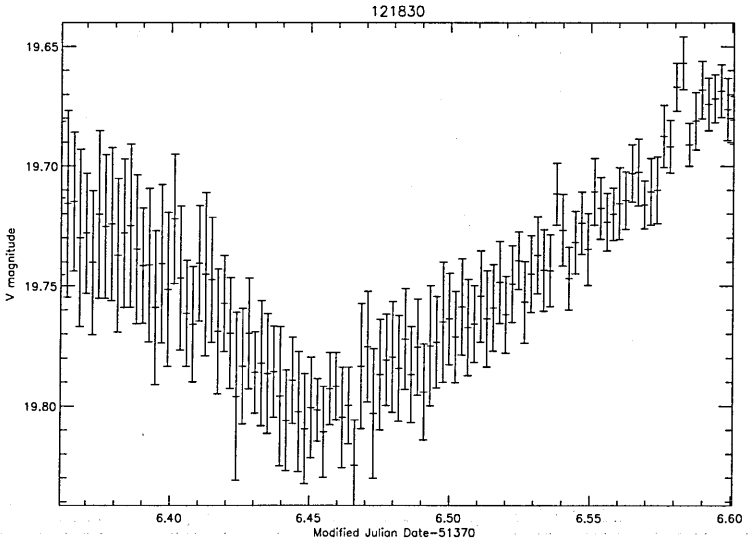
121830
19.65
19.70
19.75
19.80
V magnitude
6.40
6.45
6.50
6.55
6.60
Modified Julian Date−51370

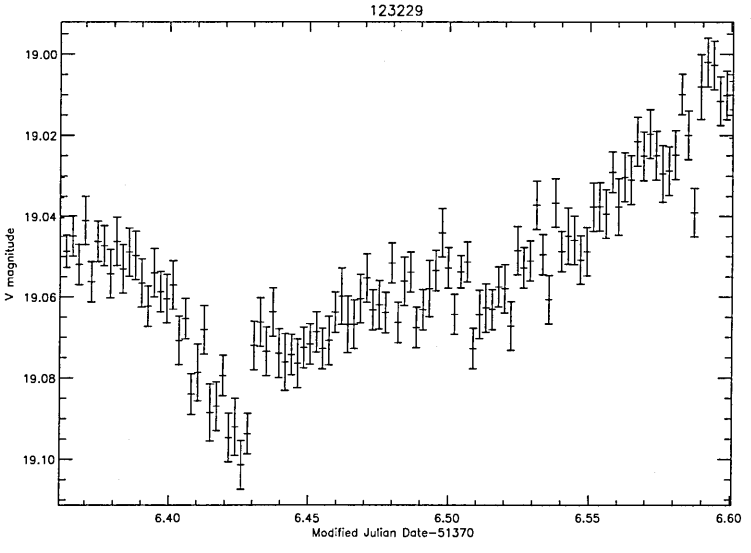
123229
19.00
19.02
19.04
19.06
19.08
19.10
V magnitude
6.40
6.45
6.50
6.55
6.60
Modified Julian Date−51370

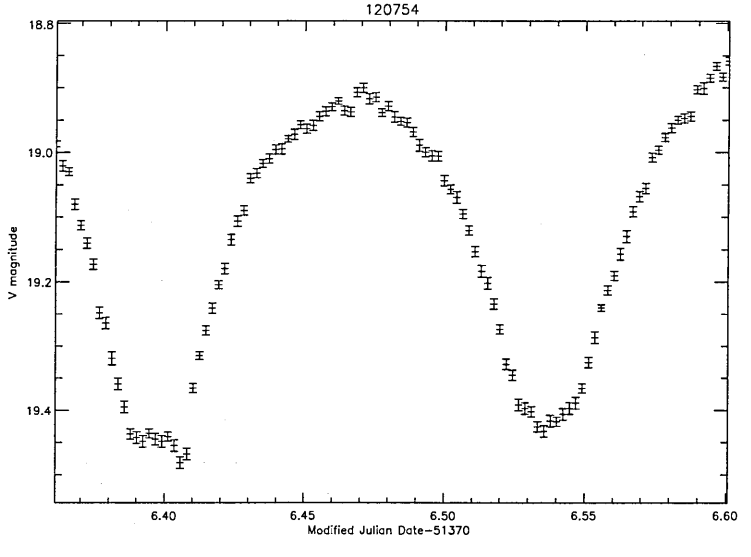
120754
18.8
19.0
19.2
19.4
V magnitude
6.40
6.45
6.50
6.55
6.60
Modified Julian Date−51370

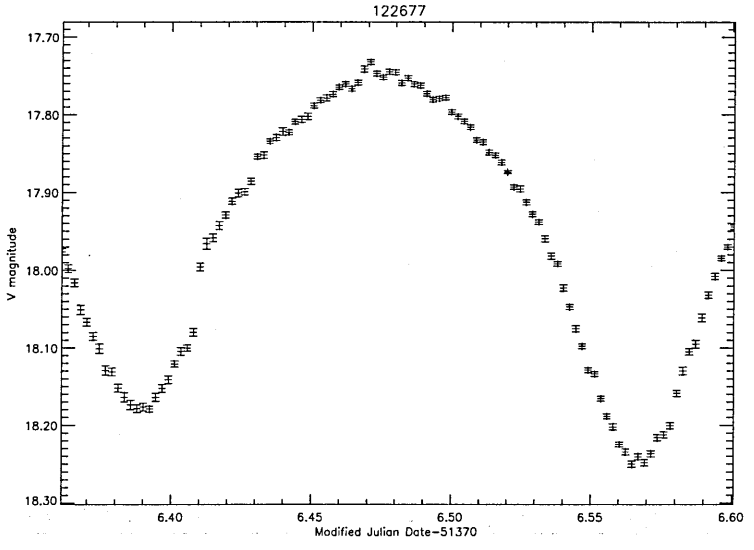
122677
17.70
17.80
17.90
18.00
18.10
18.20
18.30
V magnitude
6.40
6.45
6.50
6.55
6.60
Modified Julian Date−51370

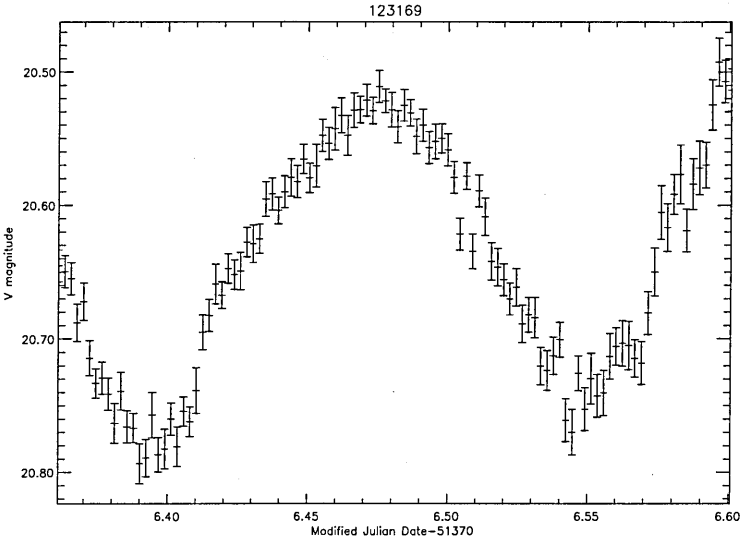
123169
20.50
20.60
20.70
20.80
V magnitude
6.40
6.45
6.50
6.55
6.60
Modified Julian Date−51370

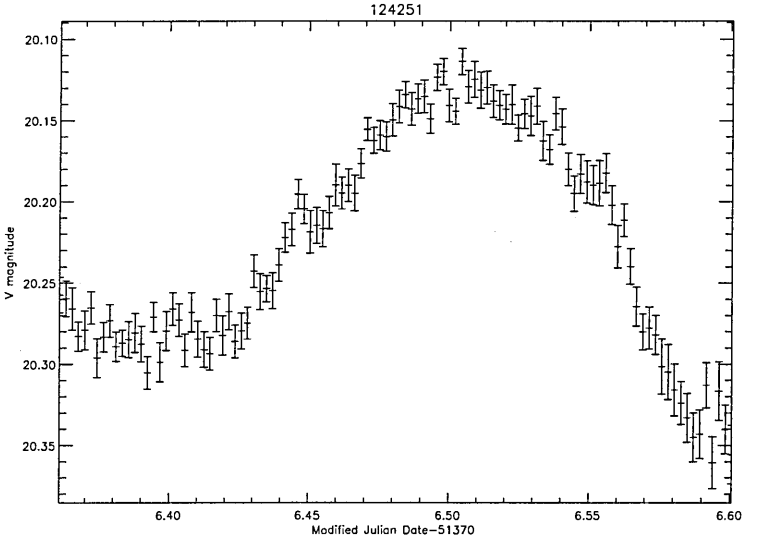
124251
20.10
20.15
20.20
20.25
20.30
20.35
V magnitude
6.40
6.45
6.50
6.55
6.60
Modified Julian Date−51370

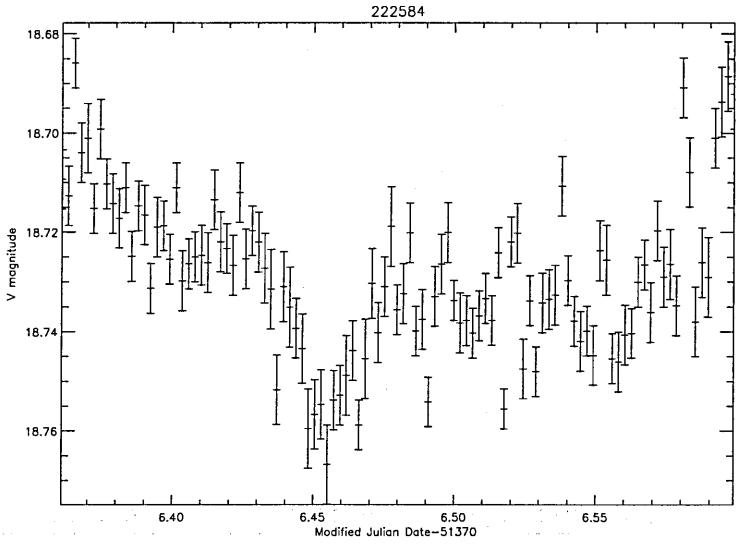
222584
18.68
18.70
18.72
18.74
18.76
V magnitude
6.40
6.45
6.50
6.55
Modified Julian Date−51370

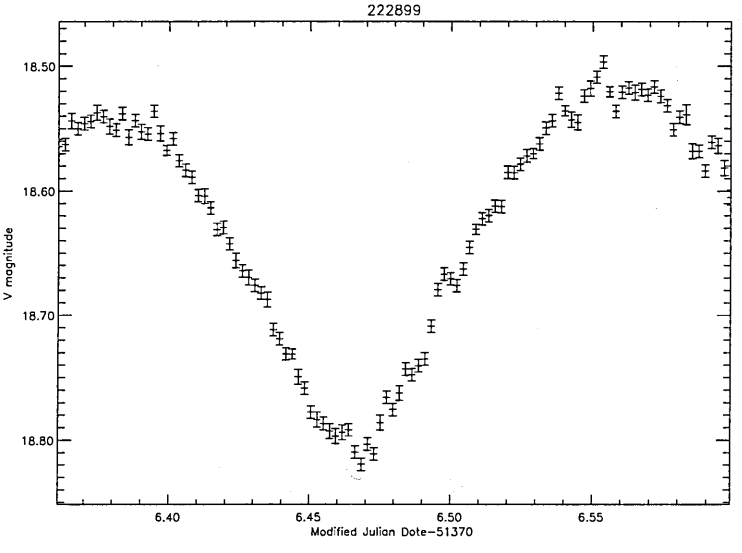
222899
18.50
18.60
18.70
18.80
V magnitude
6.40
6.45
6.50
6.55
Modified Julian Date−51370

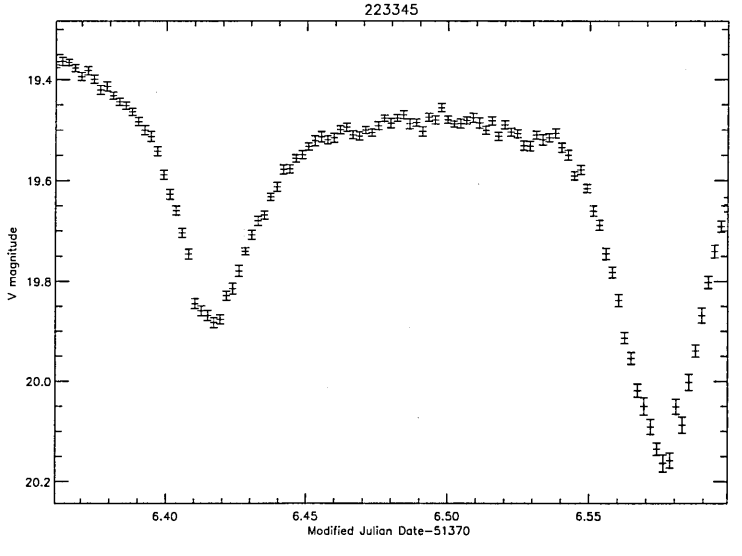
223345
19.4
19.6
19.8
20.0
20.2
V magnitude
6.40
6.45
6.50
6.55
Modified Julian Date−51370

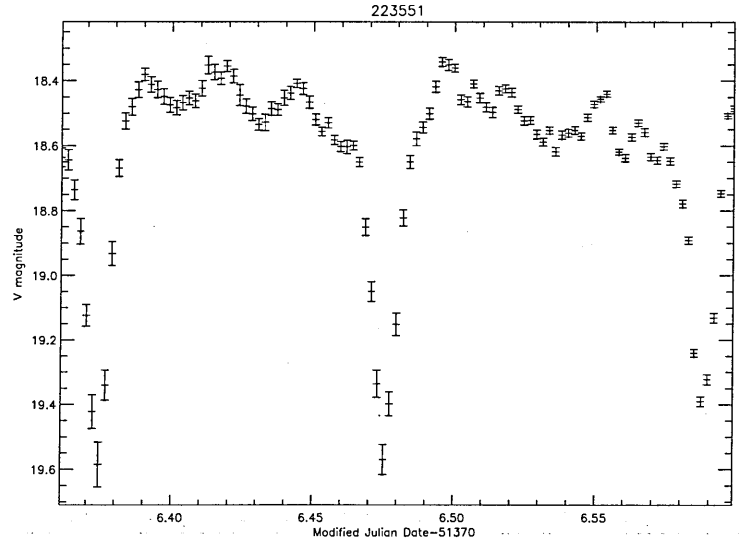
223551
V magnitude
18.4
18.6
18.8
19.0
19.2
19.4
19.6
6.40
6.45
6.50
6.55
Modified Julian Date−51370

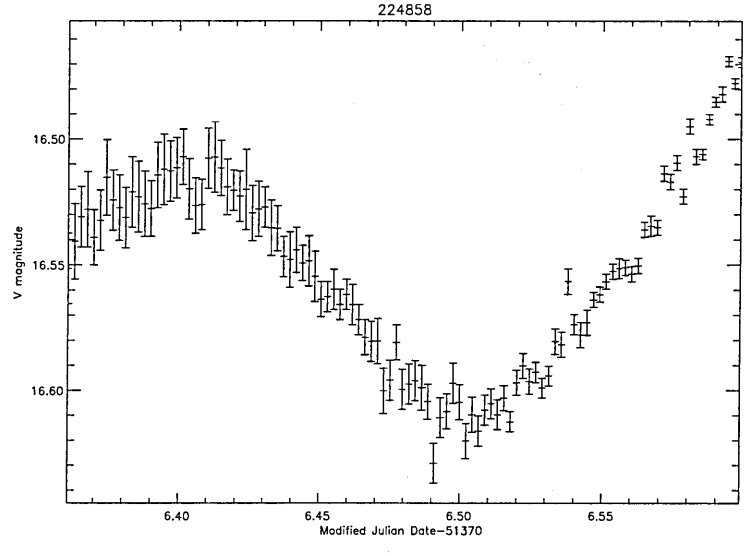
224858
V magnitude
16.50
16.55
16.60
6.40
6.45
6.50
6.55
Modified Julian Date−51370

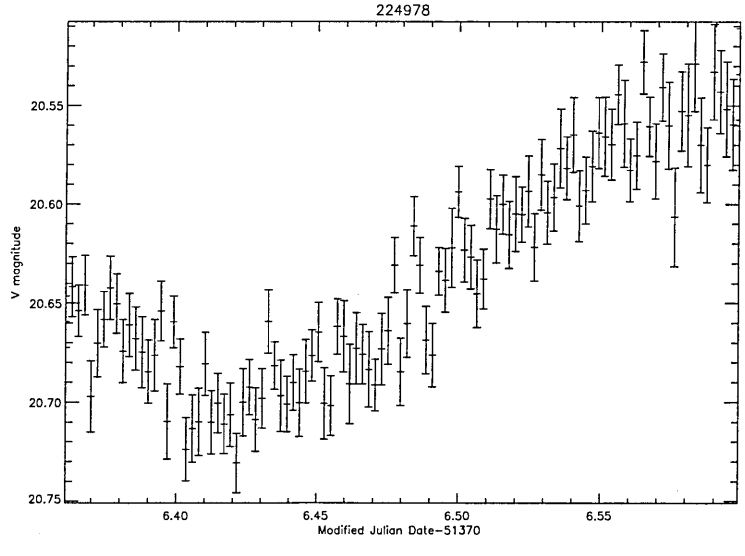
224978
V magnitude
20.55
20.60
20.65
20.70
20.75
6.40
6.45
6.50
6.55
Modified Julian Date−51370

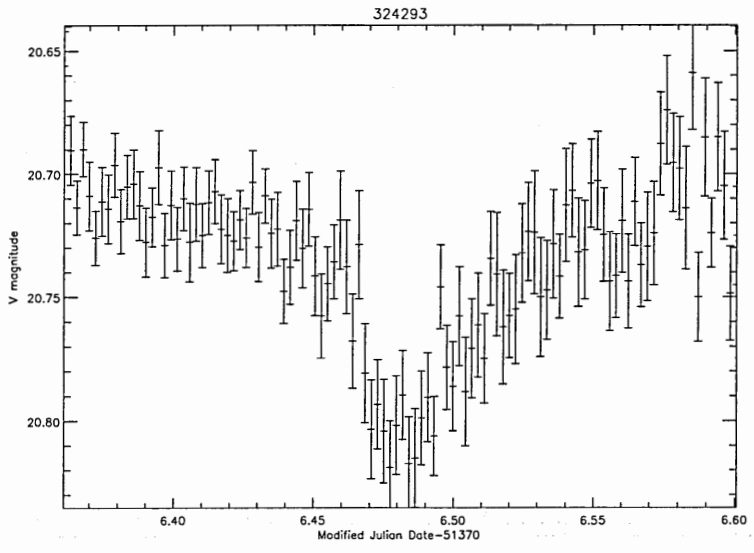
324293
20.65
20.70
20.75
20.80
V magnitude
6.40
6.45
6.50
6.55
6.60
Modified Julian Date−51370

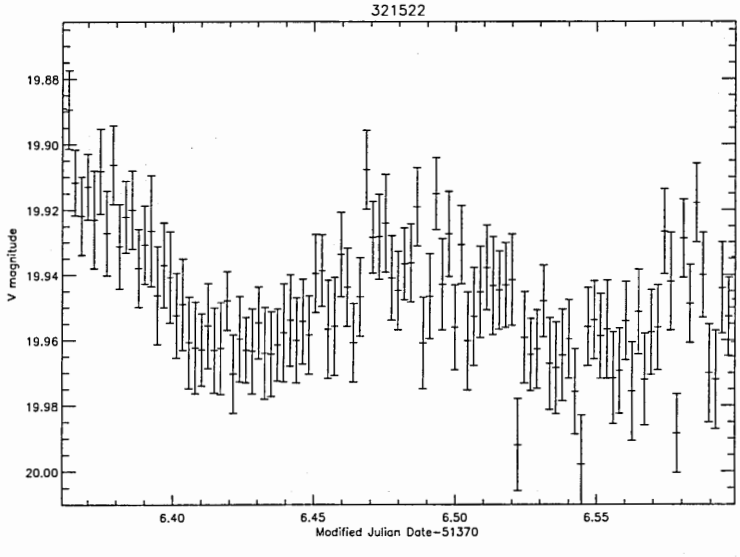
321522
19.88
19.90
19.92
19.94
19.96
19.98
20.00
V magnitude
6.40
6.45
6.50
6.55
Modified Julian Date−51370

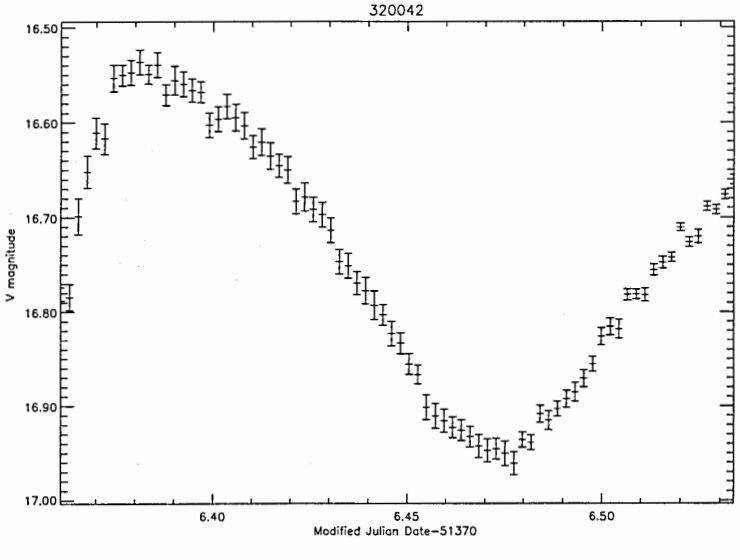
320042
16.50
16.60
16.70
16.80
16.90
17.00
V magnitude
6.40
6.45
6.50
Modified Julian Date−51370

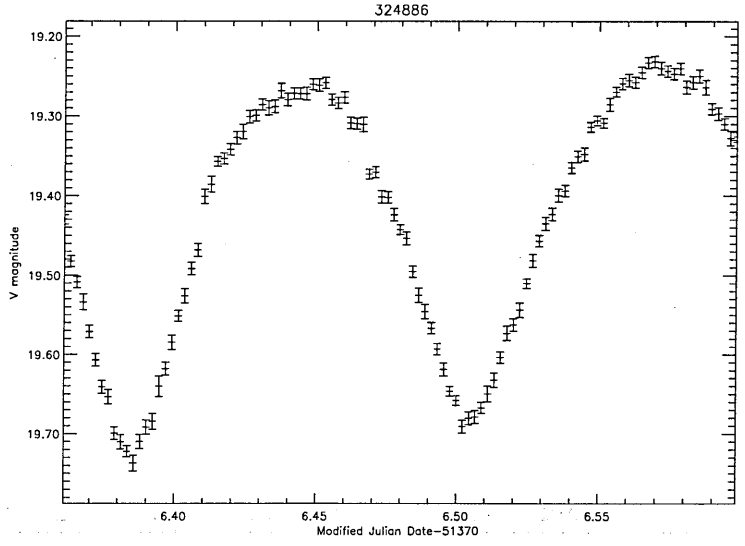
324886
19.20
19.30
19.40
19.50
19.60
19.70
V magnitude
6.40
6.45
6.50
6.55
Modified Julian Date−51370

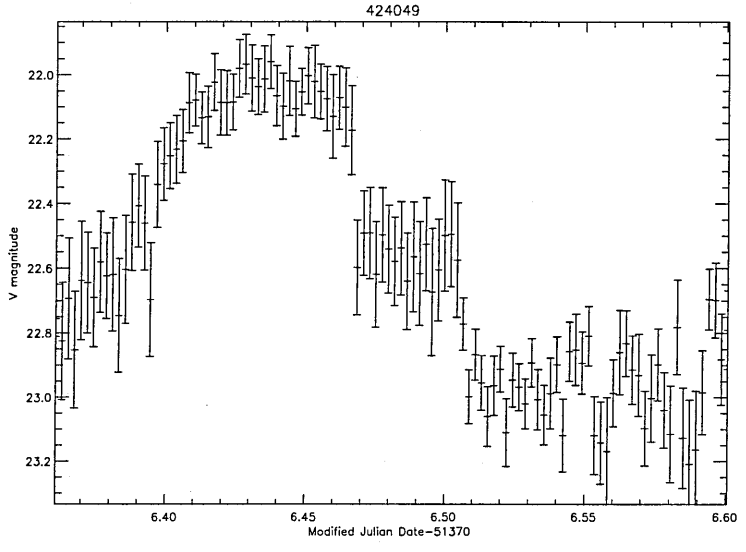
424049
22.0
22.2
22.4
22.6
22.8
23.0
23.2
V magnitude
6.40
6.45
6.50
6.55
6.60
Modified Julian Date−51370

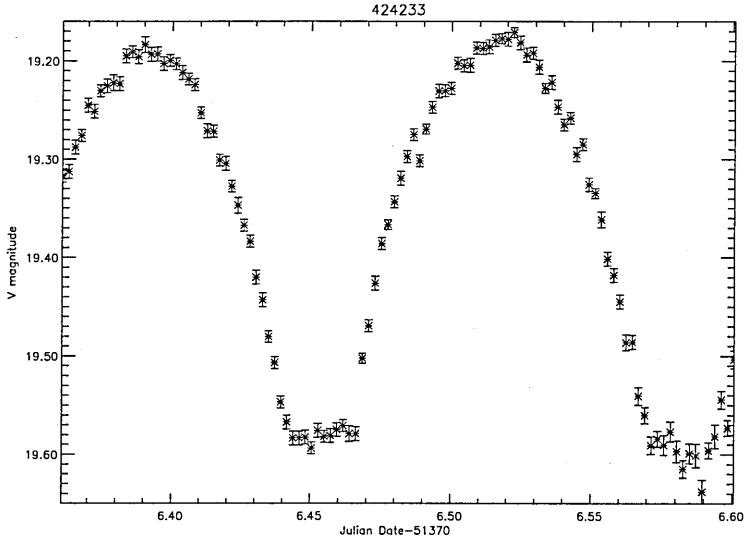
424233
19.20
19.30
19.40
19.50
19.60
V magnitude
6.40
6.45
6.50
6.55
6.60
Julian Date−51370

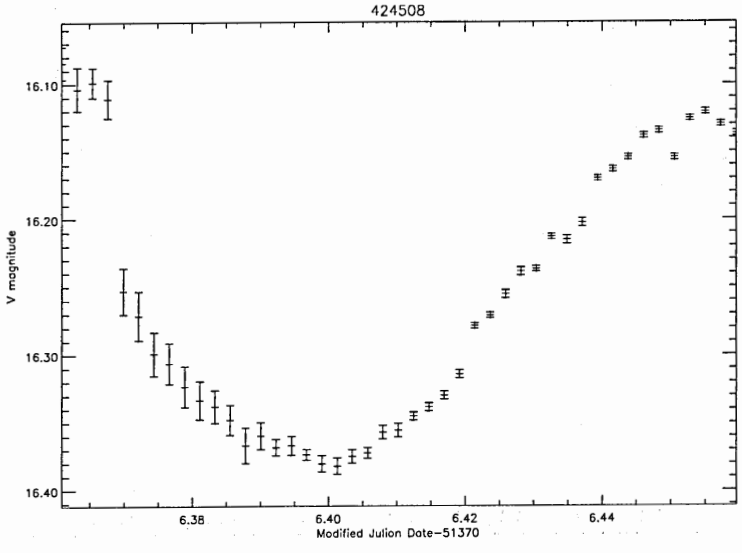
424508
16.10
16.20
16.30
16.40
V magnitude
6.38
6.40
6.42
6.44
Modified Julian Date−51370

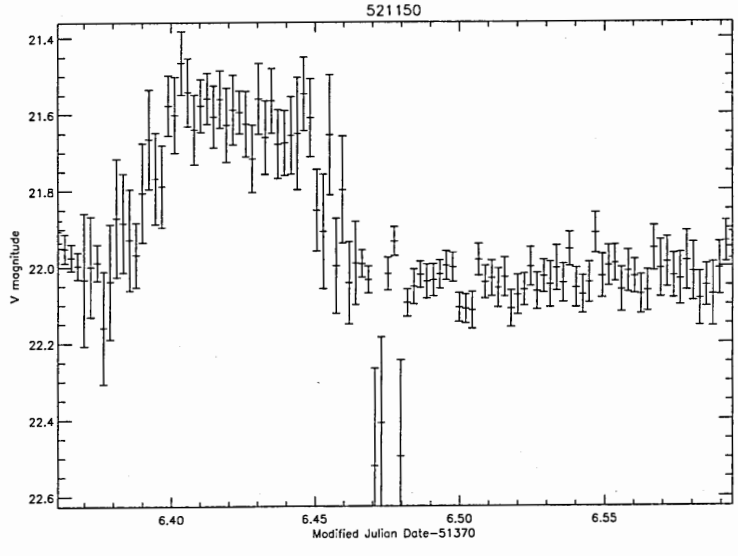
521150
21.4
21.6
21.8
22.0
22.2
22.4
22.6
V magnitude
6.40
6.45
6.50
6.55
Modified Julian Date−51370

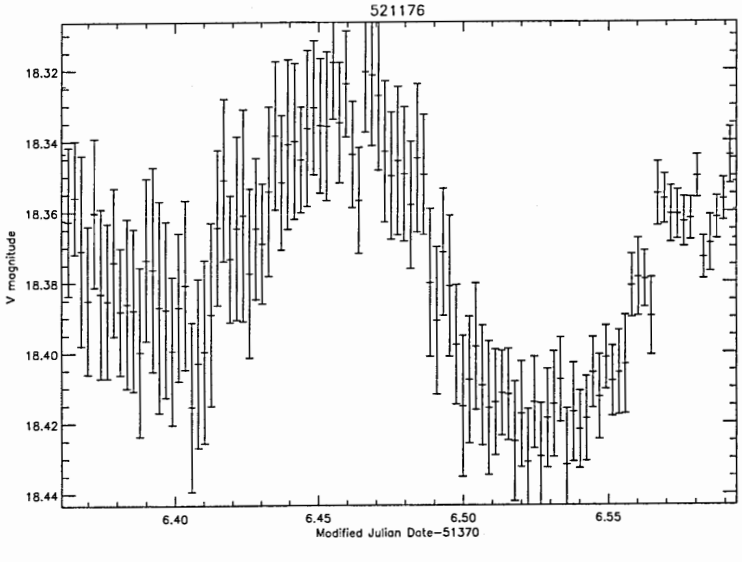
521176
18.32
18.34
18.36
18.38
18.40
18.42
18.44
V magnitude
6.40
6.45
6.50
6.55
Modified Julian Date−51370

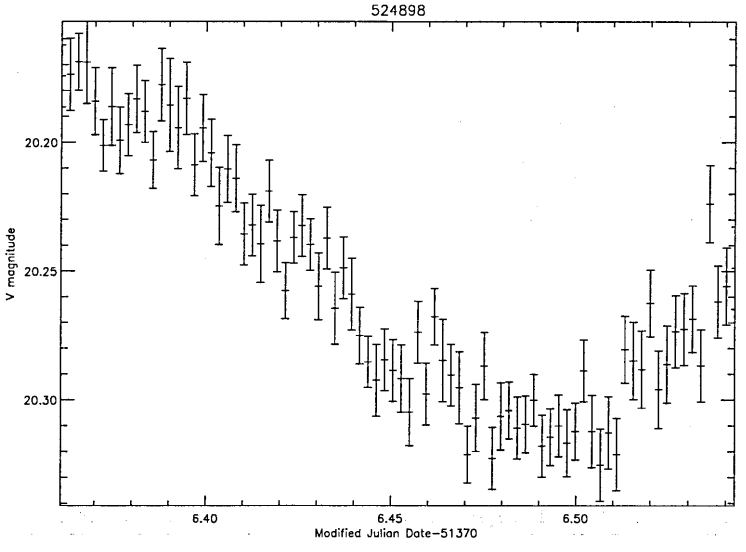
524898
20.20
20.25
20.30
V magnitude
6.40
6.45
6.50
Modified Julian Date−51370

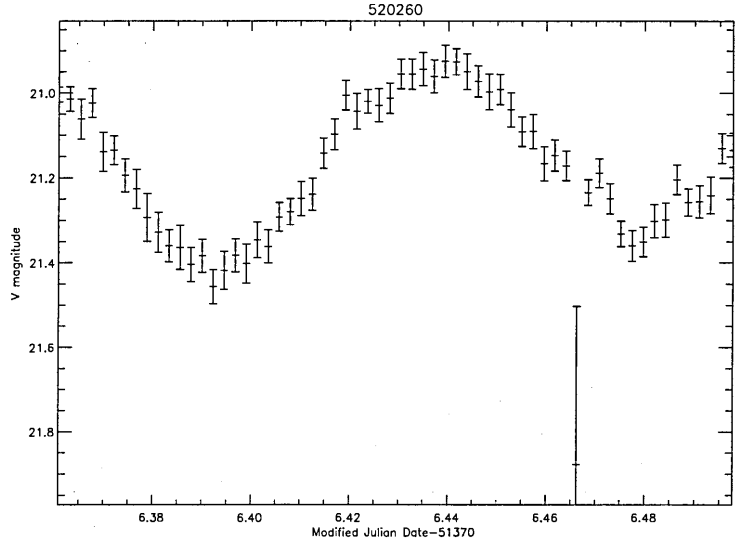
520260
21.0
21.2
21.4
21.6
21.8
V magnitude
6.38
6.40
6.42
6.44
6.46
6.48
Modified Julian Date−51370

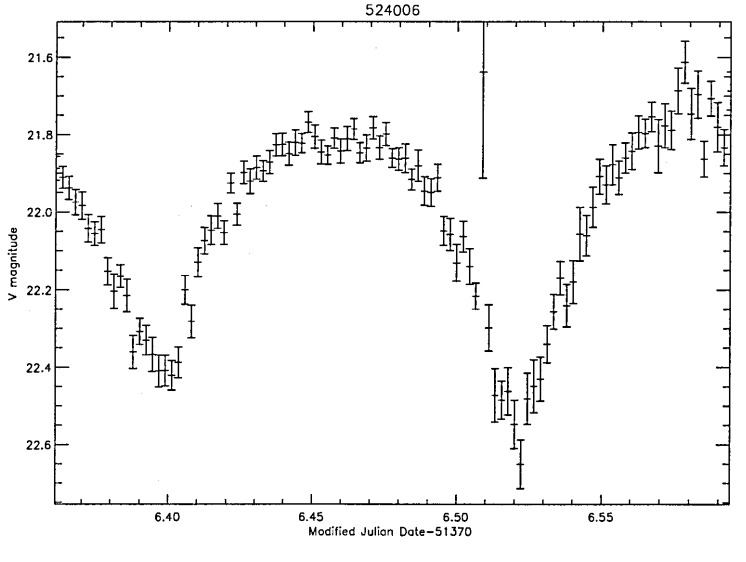
524006
21.6
21.8
22.0
22.2
22.4
22.6
V magnitude
6.40
6.45
6.50
6.55
Modified Julian Date−51370

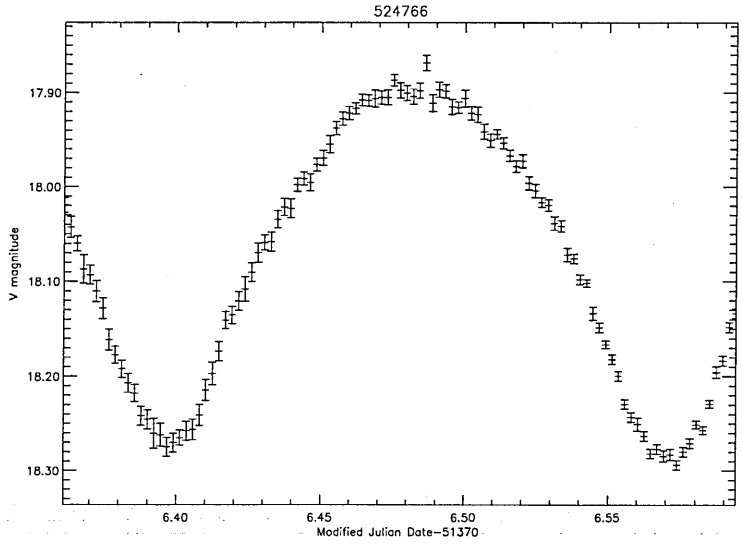
524766
17.90
18.00
18.10
18.20
18.30
V magnitude
6.40
6.45
6.50
6.55
Modified Julian Date−51370

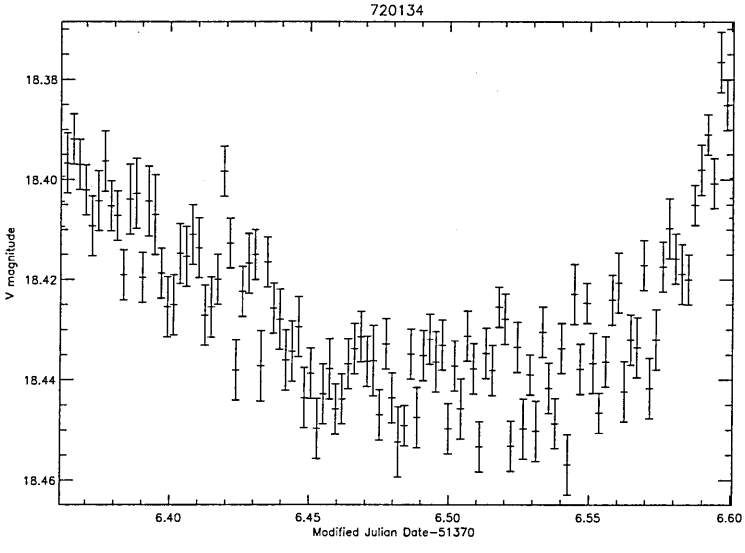
720134
18.38
18.40
18.42
18.44
18.46
V magnitude
6.40
6.45
6.50
6.55
6.60
Modified Julian Date−51370

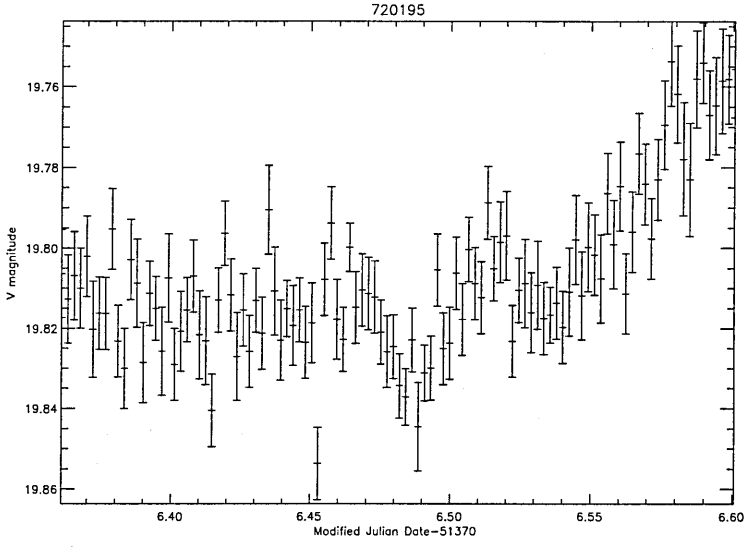
720195
19.76
19.78
19.80
19.82
19.84
19.86
V magnitude
6.40
6.45
6.50
6.55
6.60
Modified Julian Date−51370

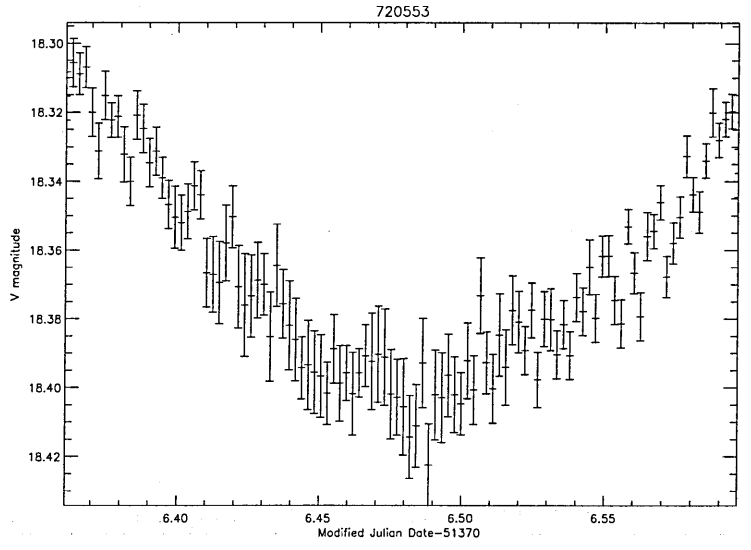
720553
18.30
18.32
18.34
18.36
18.38
18.40
18.42
V magnitude
6.40
6.45
6.50
6.55
Modified Julian Date−51370

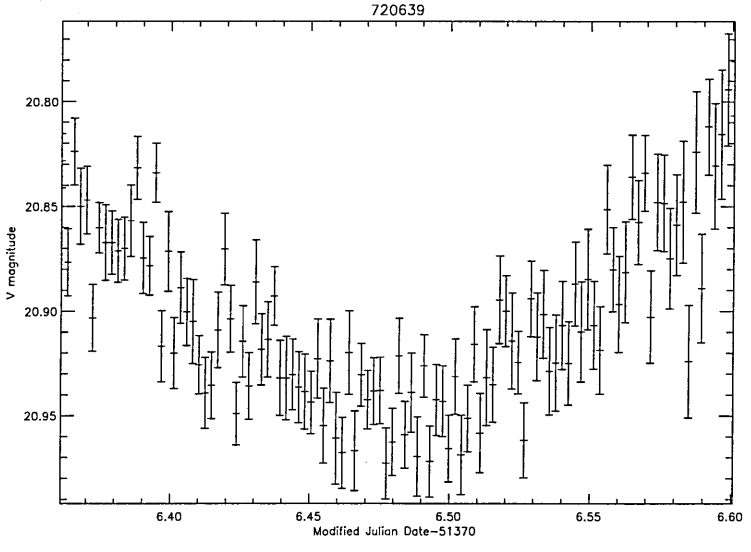
720639
20.80
20.85
20.90
20.95
V magnitude
6.40
6.45
6.50
6.55
6.60
Modified Julian Date−51370

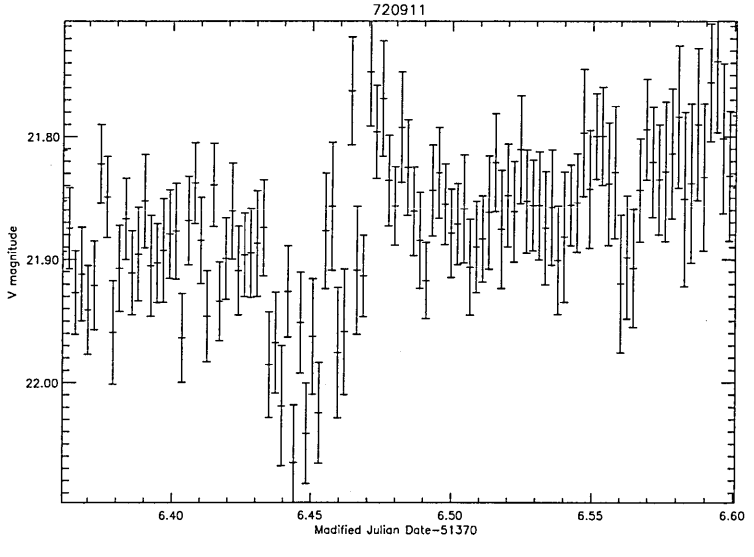
720911
21.80
21.90
22.00
V magnitude
6.40
6.45
6.50
6.55
6.60
Modified Julian Date−51370

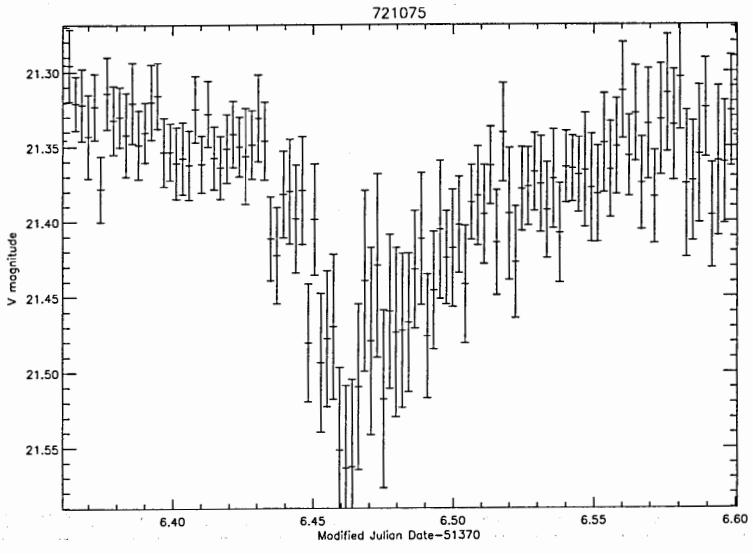
721075
V magnitude
21.30
21.35
21.40
21.45
21.50
21.55
6.40
6.45
6.50
6.55
6.60
Modified Julian Date−51370

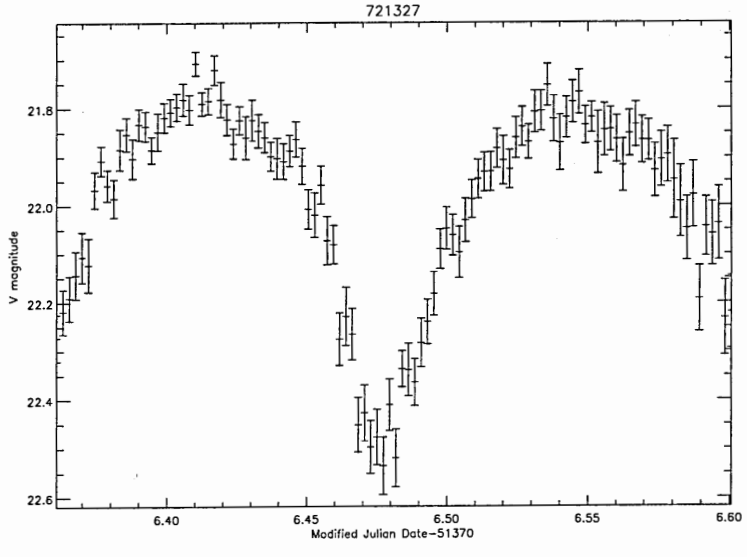
721327
V magnitude
21.8
22.0
22.2
22.4
22.6
6.40
6.45
6.50
6.55
6.60
Modified Julian Date−51370

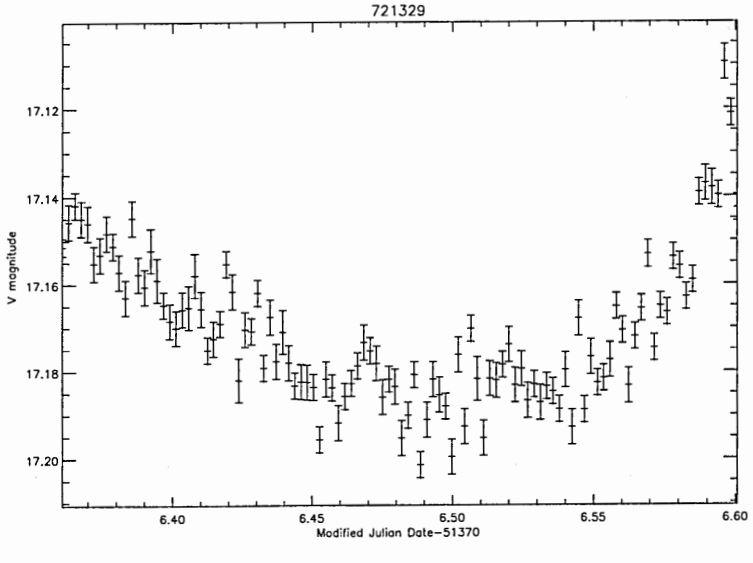
721329
V magnitude
17.12
17.14
17.16
17.18
17.20
6.40
6.45
6.50
6.55
6.60
Modified Julian Date−51370

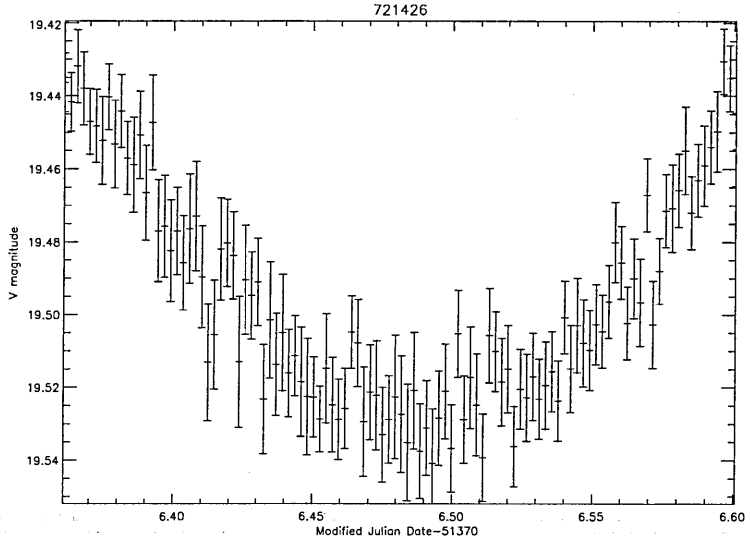
721426
19.42
19.44
19.46
19.48
19.50
19.52
19.54
V magnitude
6.40
6.45
6.50
6.55
6.60
Modified Julian Date−51370

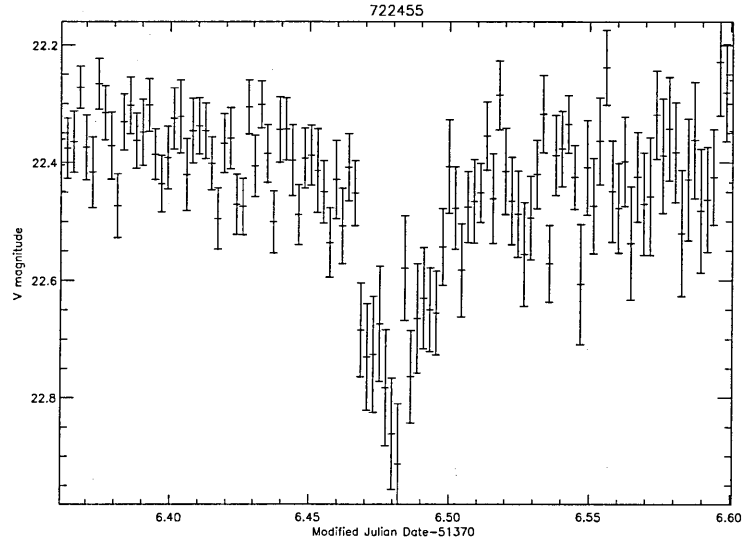
722455
22.2
22.4
22.6
22.8
V magnitude
6.40
6.45
6.50
6.55
6.60
Modified Julian Date−51370

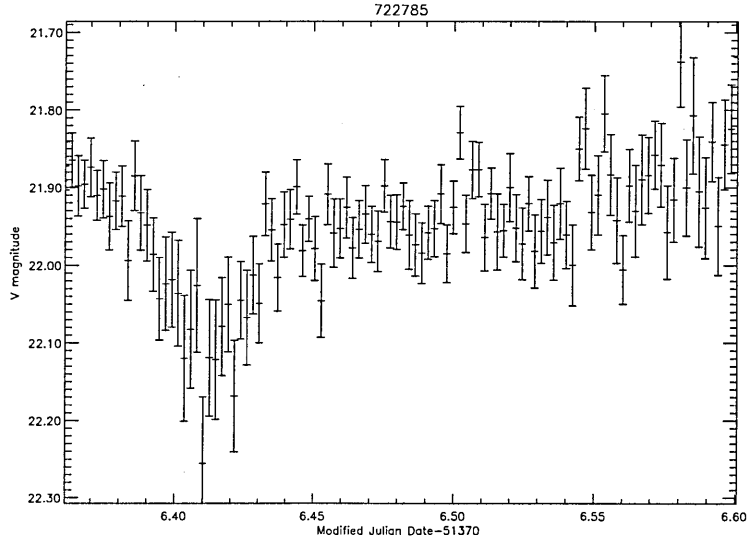
722785
21.70
21.80
21.90
22.00
22.10
22.20
22.30
V magnitude
6.40
6.45
6.50
6.55
6.60
Modified Julian Date−51370

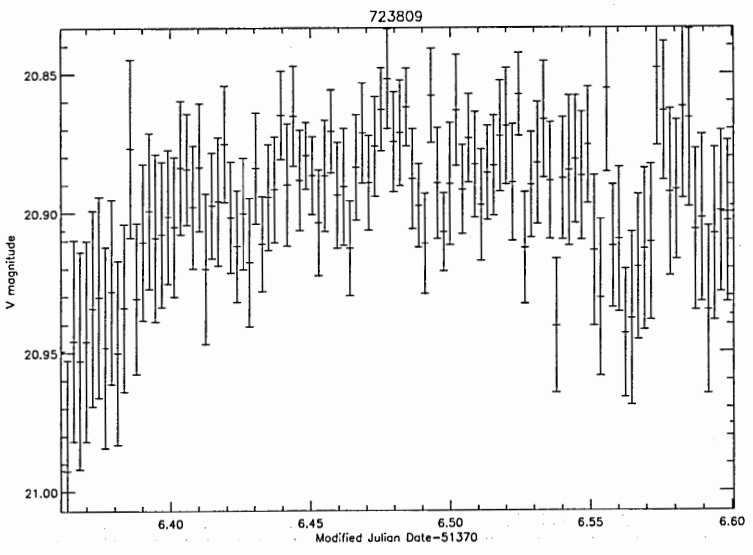
723809
20.85
20.90
20.95
21.00
V magnitude
6.40
6.45
6.50
6.55
6.60
Modified Julian Date−51370

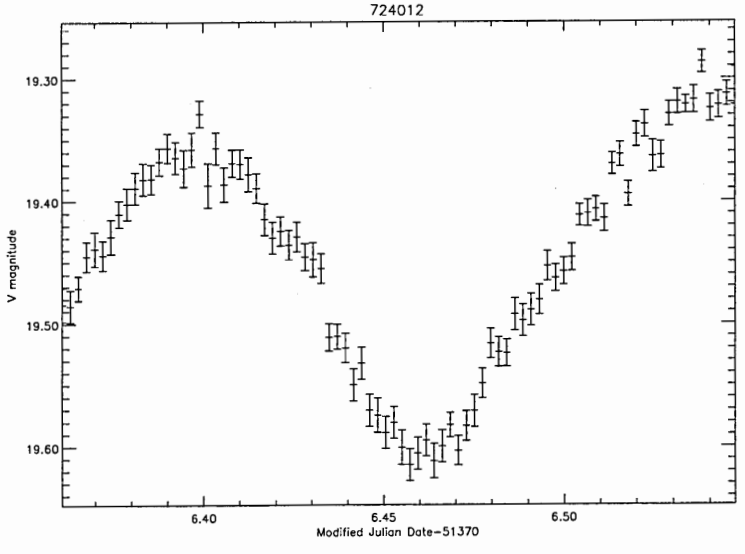
724012
19.30
19.40
19.50
19.60
V magnitude
6.40
6.45
6.50
Modified Julian Date−51370

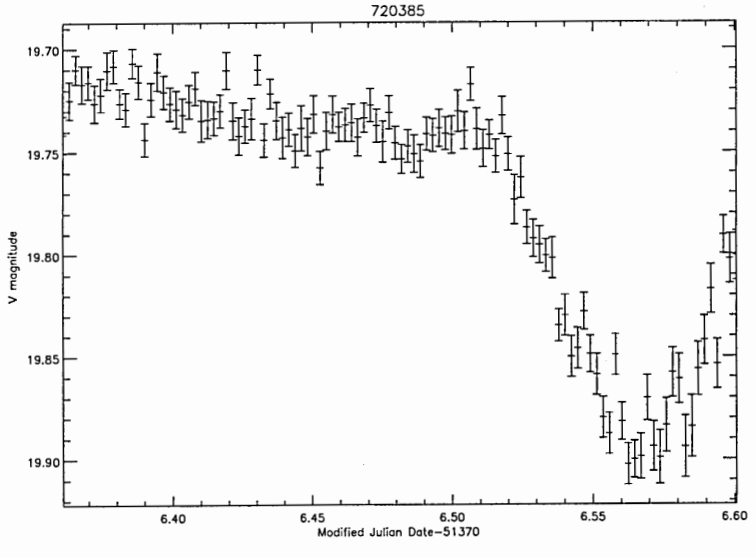
720385
19.70
19.75
19.80
19.85
19.90
V magnitude
6.40
6.45
6.50
6.55
6.60
Modified Julian Date−51370

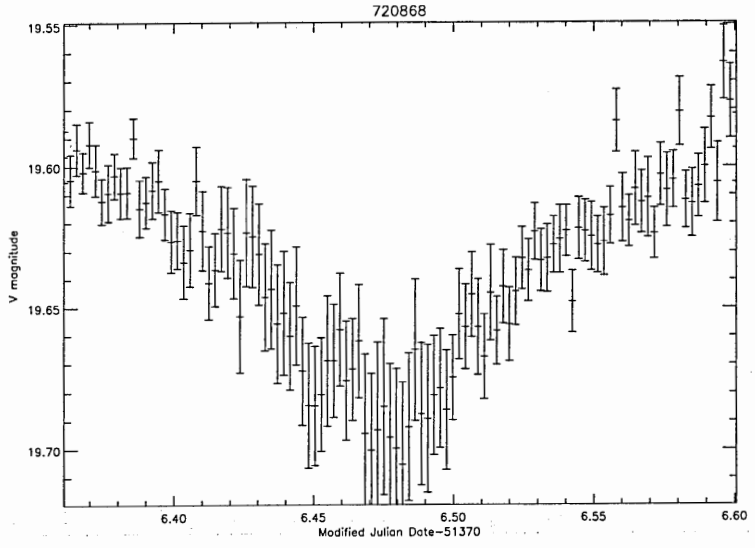
720868
19.55
19.60
19.65
19.70
V magnitude
6.40
6.45
6.50
6.55
6.60
Modified Julian Date−51370

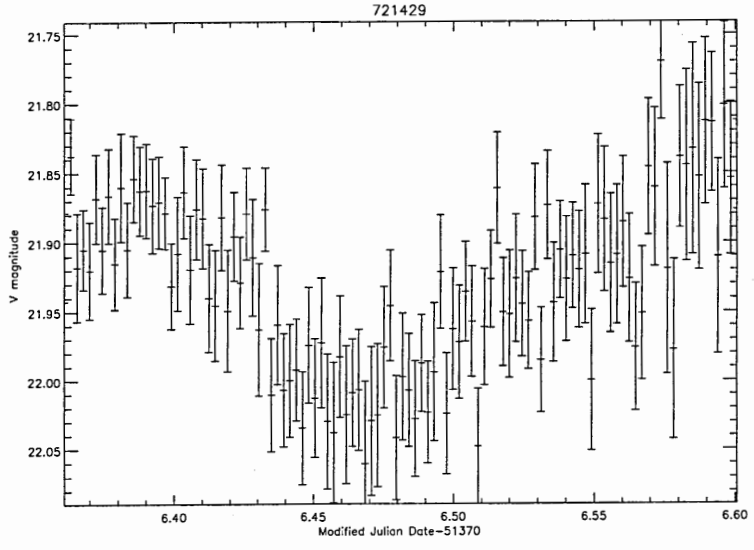
721429
21.75
21.80
21.85
21.90
21.95
22.00
22.05
V magnitude
6.40
6.45
6.50
6.55
6.60
Modified Julian Date−51370

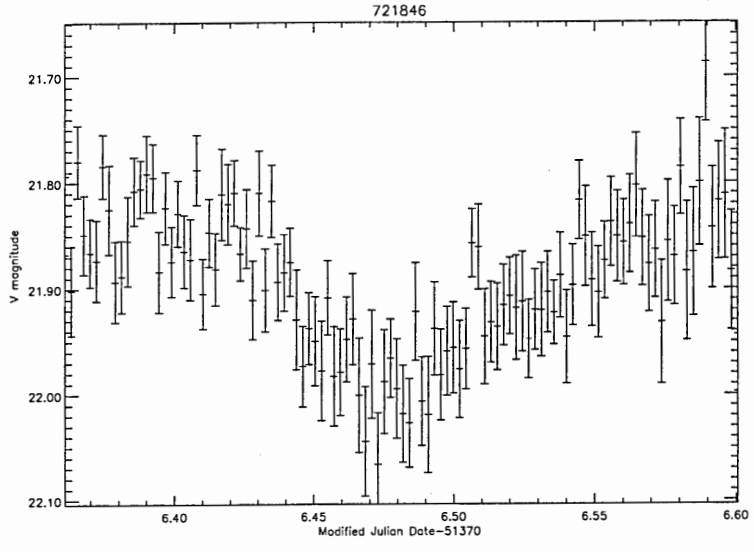
721846
21.70
21.80
21.90
22.00
22.10
V magnitude
6.40
6.45
6.50
6.55
6.60
Modified Julian Date−51370

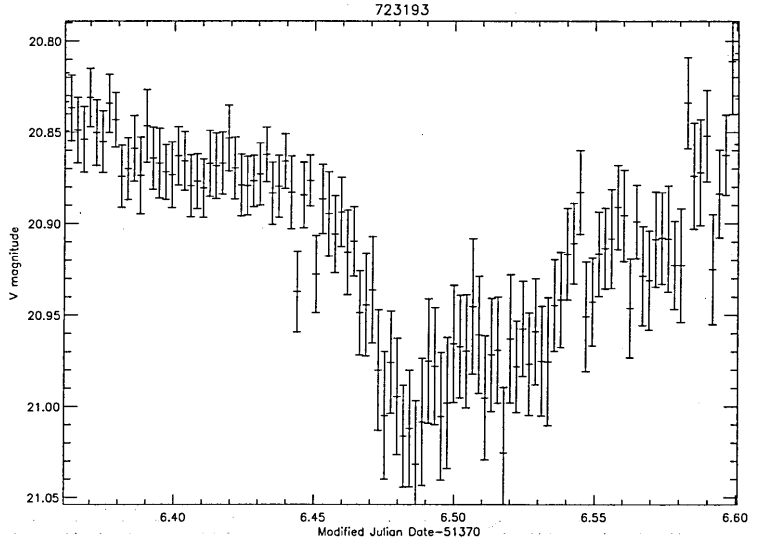
723193
20.80
20.85
20.90
20.95
21.00
21.05
V magnitude
6.40
6.45
6.50
6.55
6.60
Modified Julian Date−51370

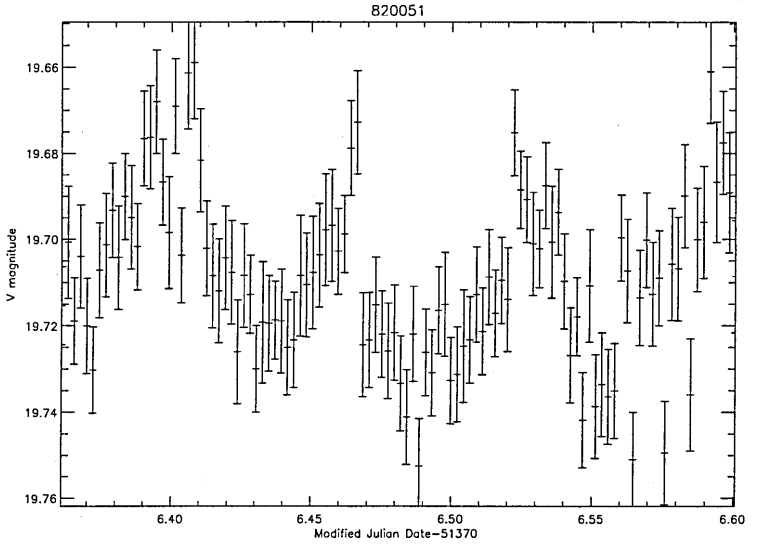
820051
19.66
19.68
19.70
19.72
19.74
19.76
V magnitude
6.40
6.45
6.50
6.55
6.60
Modified Julian Date−51370

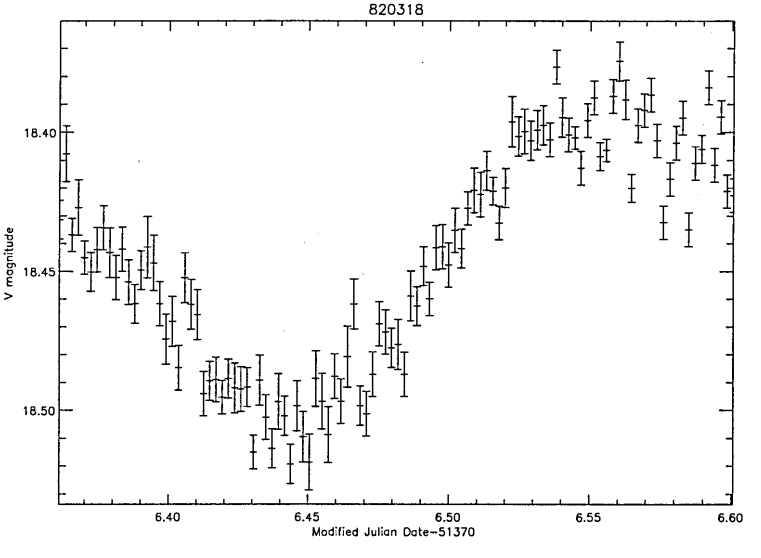
820318
18.40
18.45
18.50
V magnitude
6.40
6.45
6.50
6.55
6.60
Modified Julian Date−51370

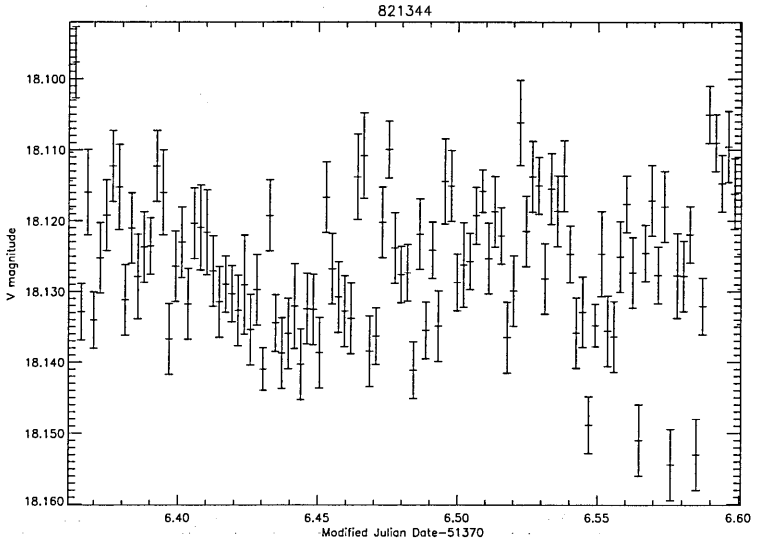
821344
V magnitude
18.100
18.110
18.120
18.130
18.140
18.150
18.160
6.40
6.45
6.50
6.55
6.60
Modified Julian Date−51370

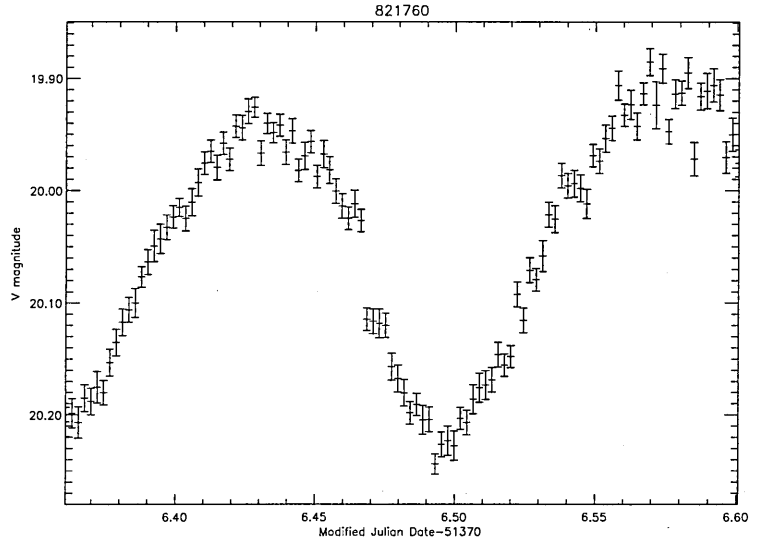
821760
V magnitude
19.90
20.00
20.10
20.20
6.40
6.45
6.50
6.55
6.60
Modified Julian Date−51370

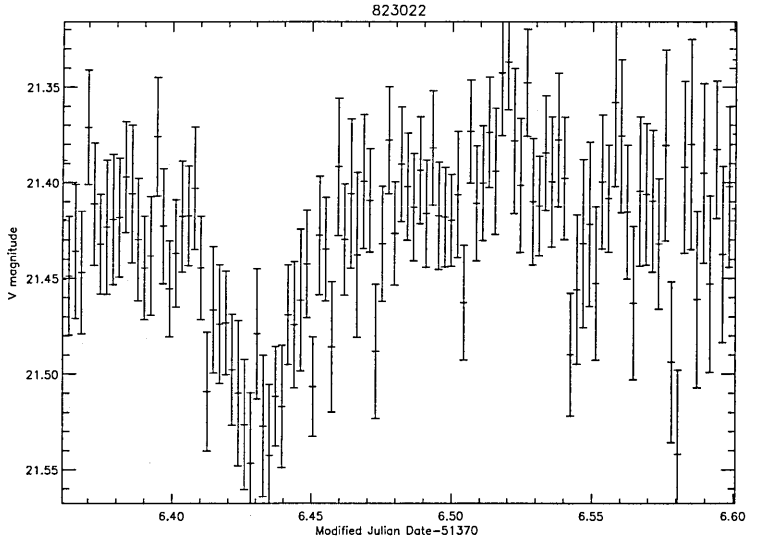
823022
V magnitude
21.35
21.40
21.45
21.50
21.55
6.40
6.45
6.50
6.55
6.60
Modified Julian Date−51370

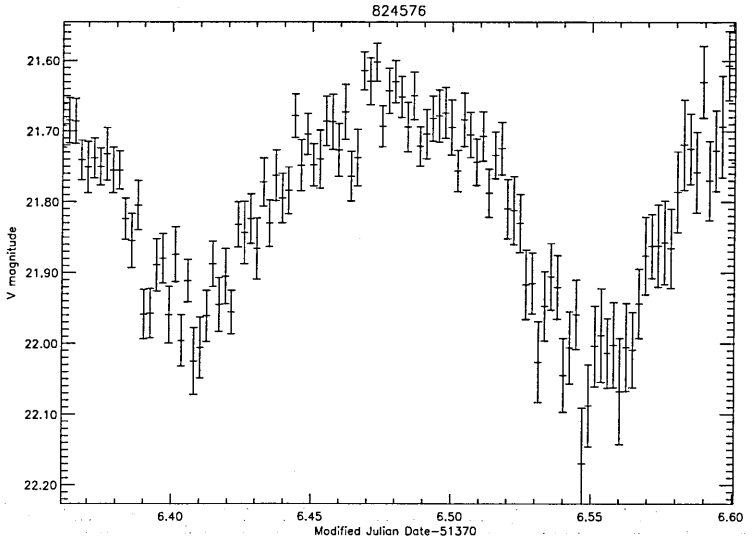
824576
V magnitude
21.60
21.70
21.80
21.90
22.00
22.10
22.20
6.40
6.45
6.50
6.55
6.60
Modified Julian Date−51370

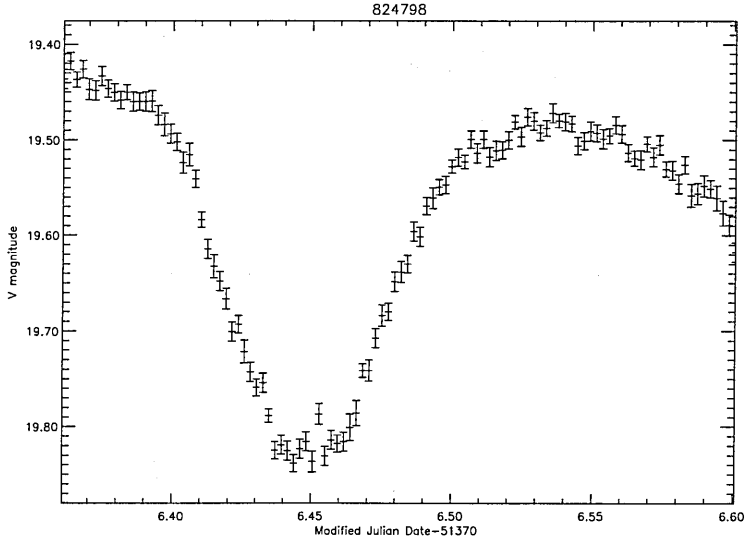
824798
V magnitude
19.40
19.50
19.60
19.70
19.80
6.40
6.45
6.50
6.55
6.60
Modified Julian Date−51370

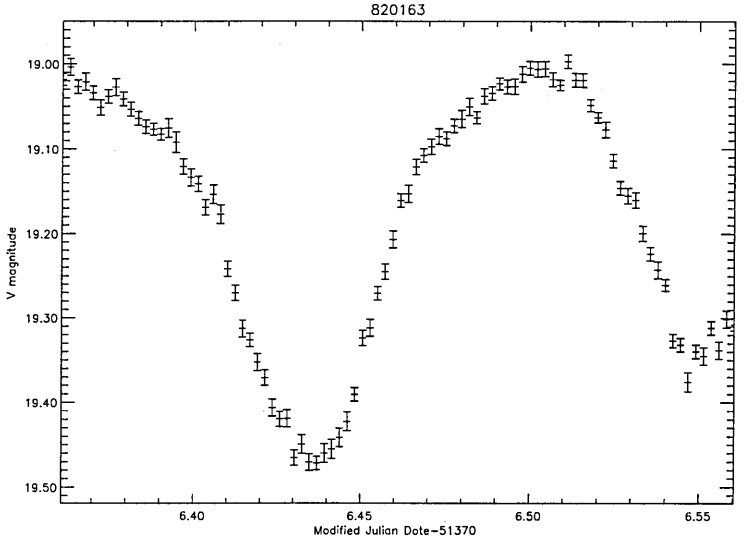
820163
V magnitude
19.00
19.10
19.20
19.30
19.40
19.50
6.40
6.45
6.50
6.55
Modified Julian Date−51370

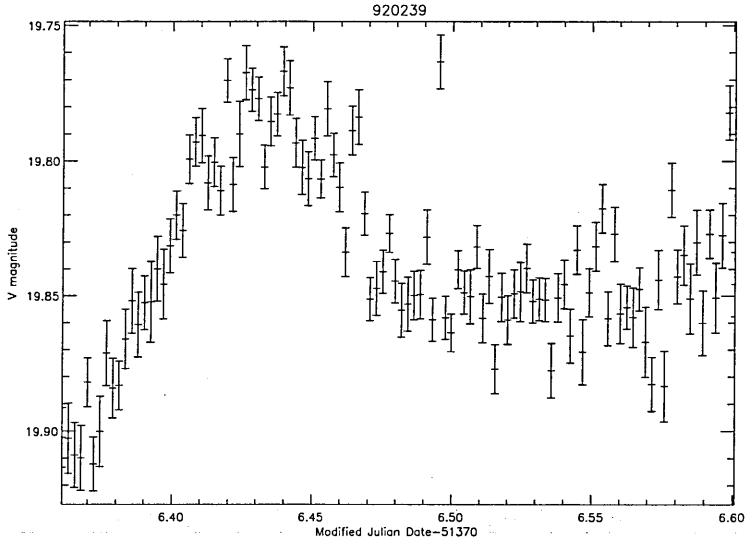
920239
19.75
19.80
19.85
19.90
V magnitude
6.40
6.45
6.50
6.55
6.60
Modified Julian Date−51370

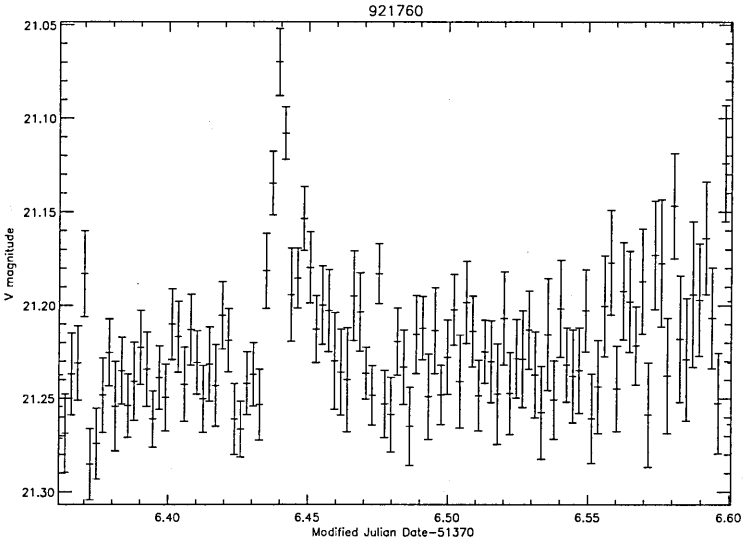
921760
21.05
21.10
21.15
21.20
21.25
21.30
V magnitude
6.40
6.45
6.50
6.55
6.60
Modified Julian Date−51370

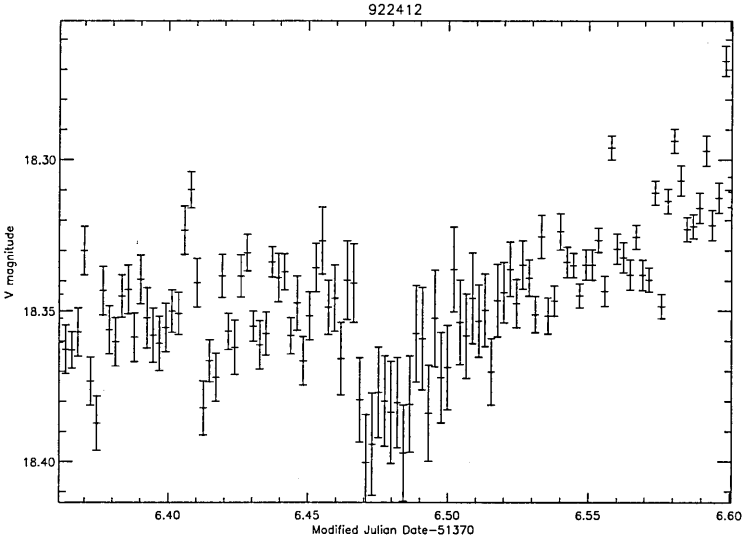
922412
18.30
18.35
18.40
V magnitude
6.40
6.45
6.50
6.55
6.60
Modified Julian Date−51370

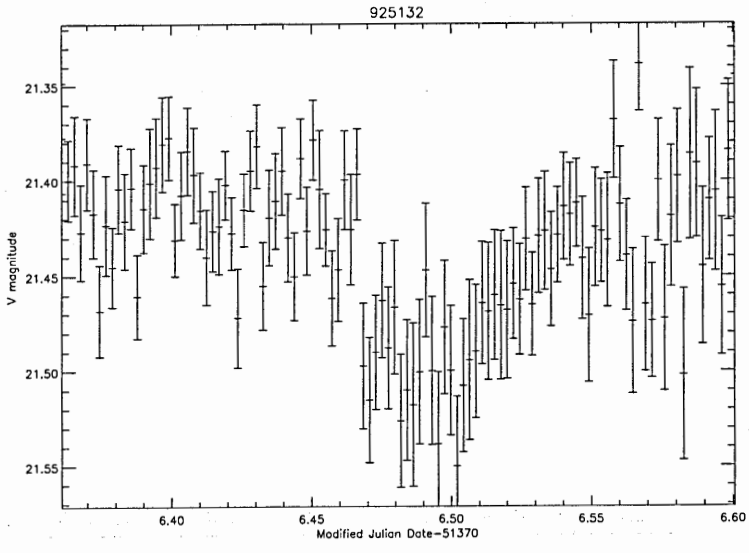
925132
V magnitude
21.35
21.40
21.45
21.50
21.55
6.40
6.45
6.50
6.55
6.60
Modified Julian Date−51370

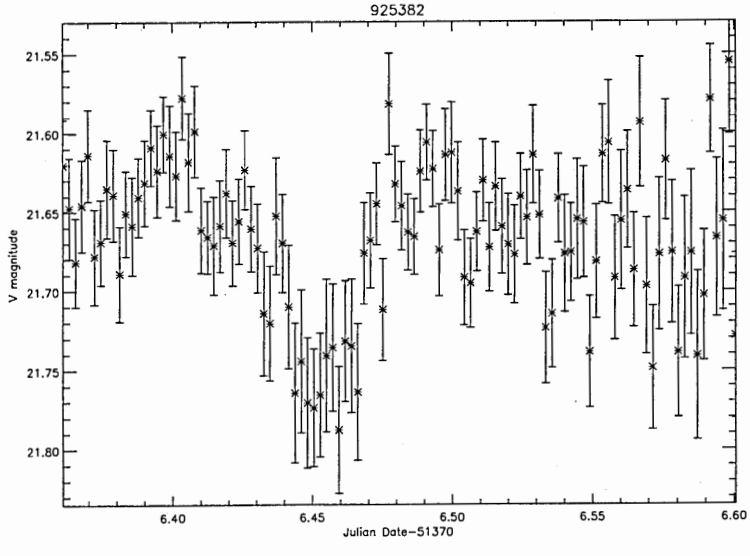
925382
V magnitude
21.55
21.60
21.65
21.70
21.75
21.80
6.40
6.45
6.50
6.55
6.60
Julian Date−51370

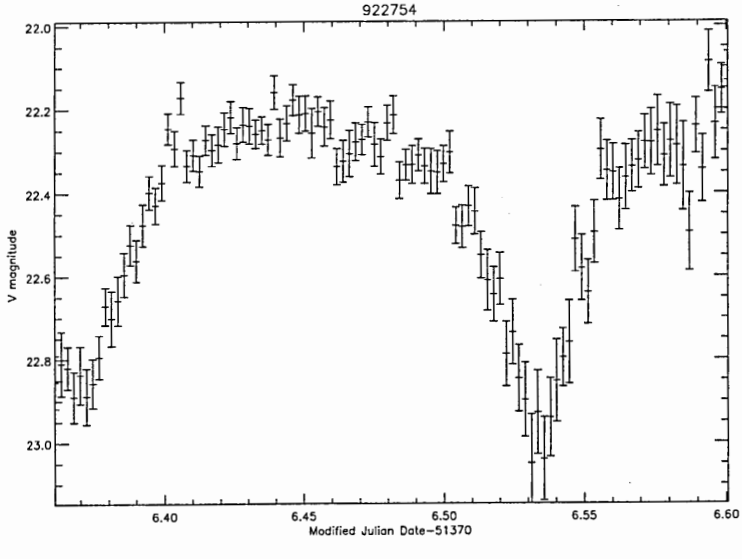
922754
V magnitude
22.0
22.2
22.4
22.6
22.8
23.0
6.40
6.45
6.50
6.55
6.60
Modified Julian Date−51370

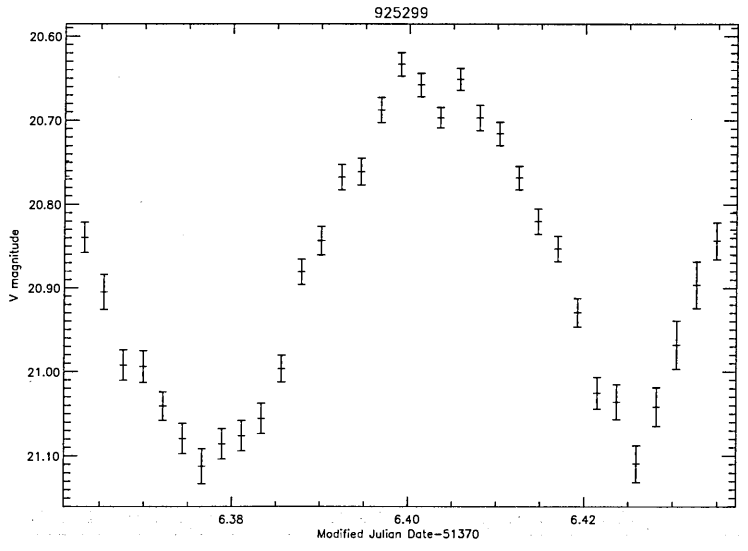
925299
20.60
20.70
20.80
20.90
21.00
21.10
V magnitude
6.38
6.40
6.42
Modified Julian Date−51370

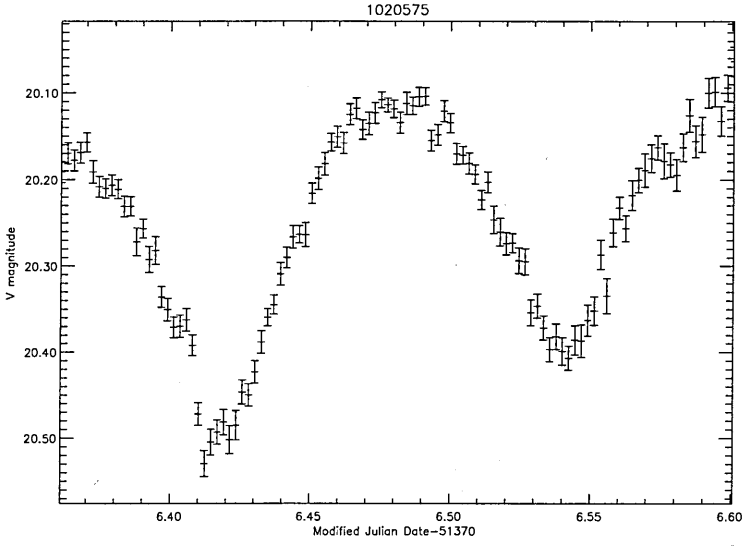
1020575
20.10
20.20
20.30
20.40
20.50
V magnitude
6.40
6.45
6.50
6.55
6.60
Modified Julian Date−51370

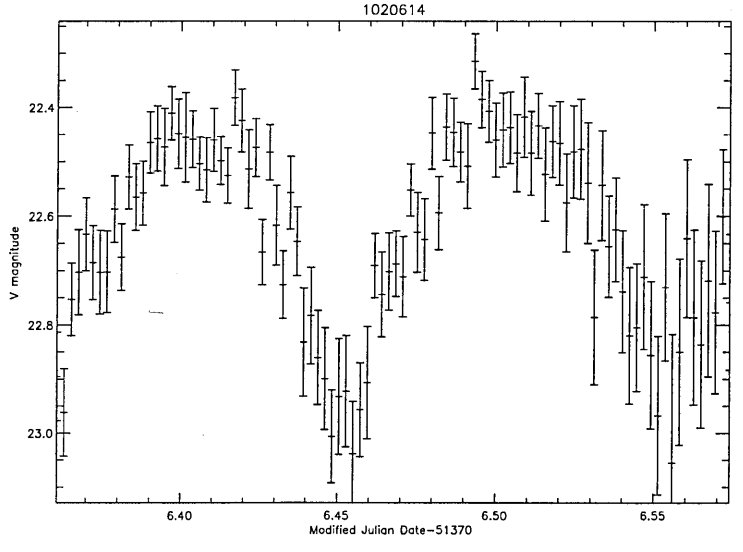
1020614
22.4
22.6
22.8
23.0
V magnitude
6.40
6.45
6.50
6.55
Modified Julian Date−51370

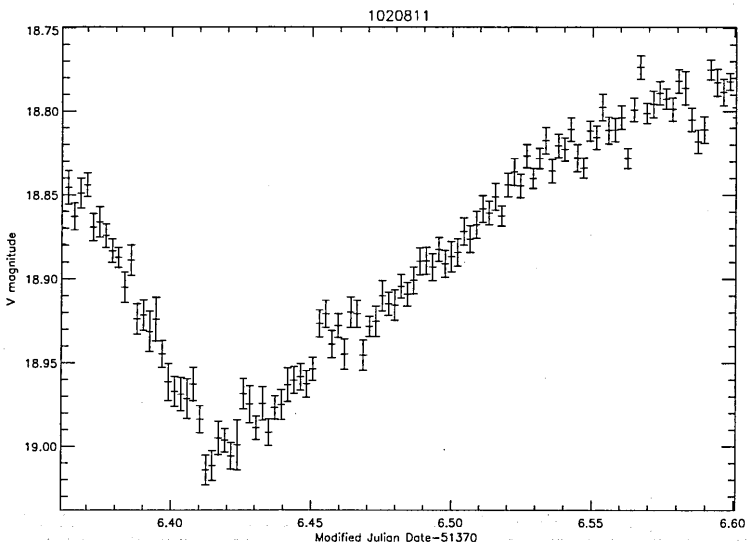
1020811
V magnitude
18.75
18.80
18.85
18.90
18.95
19.00
6.40
6.45
6.50
6.55
6.60
Modified Julian Date−51370

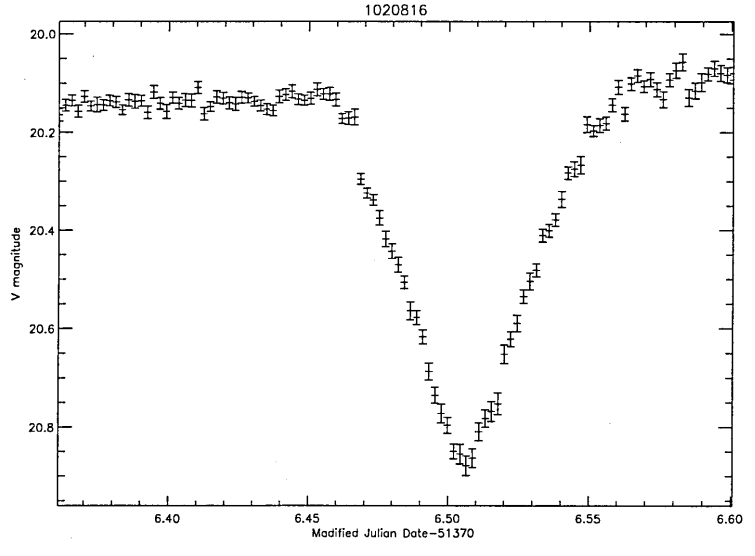
1020816
V magnitude
20.0
20.2
20.4
20.6
20.8
6.40
6.45
6.50
6.55
6.60
Modified Julian Date−51370

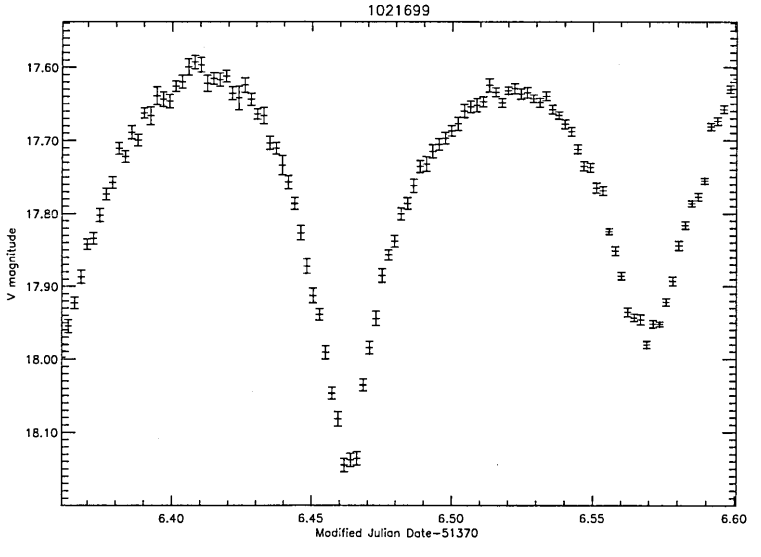
1021699
V magnitude
17.60
17.70
17.80
17.90
18.00
18.10
6.40
6.45
6.50
6.55
6.60
Modified Julian Date−51370

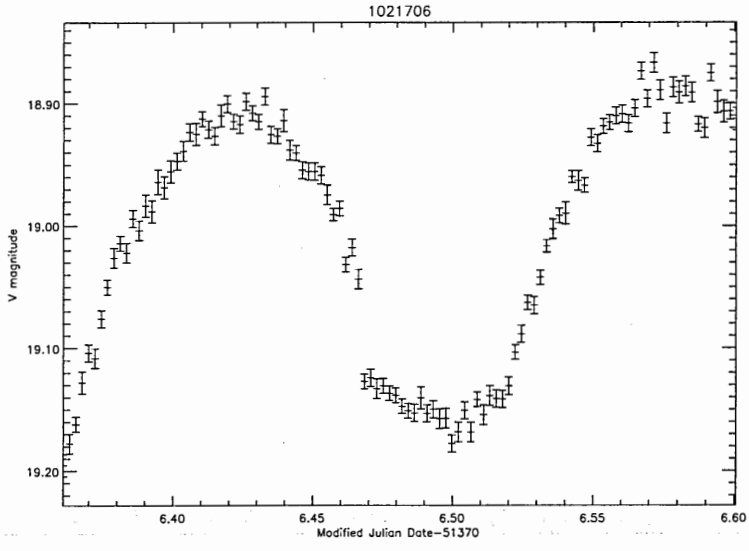
1021706
18.90
19.00
19.10
19.20
V magnitude
6.40
6.45
6.50
6.55
6.60
Modified Julian Date−51370

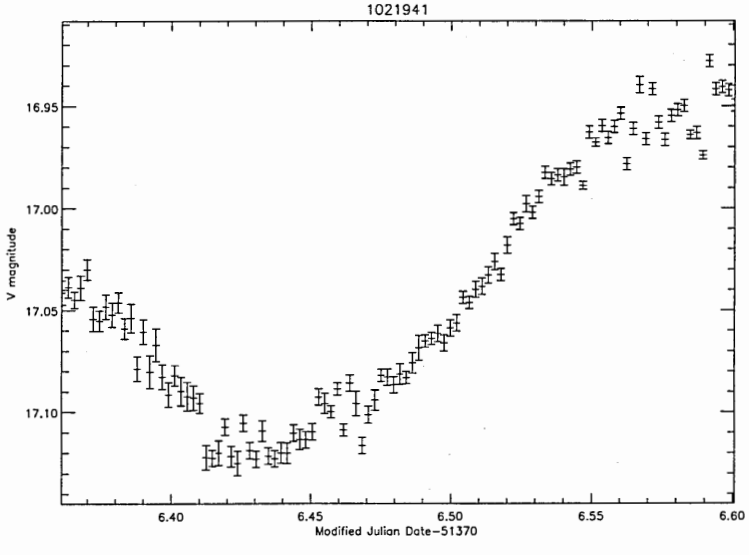
1021941
16.95
17.00
17.05
17.10
V magnitude
6.40
6.45
6.50
6.55
6.60
Modified Julian Date−51370

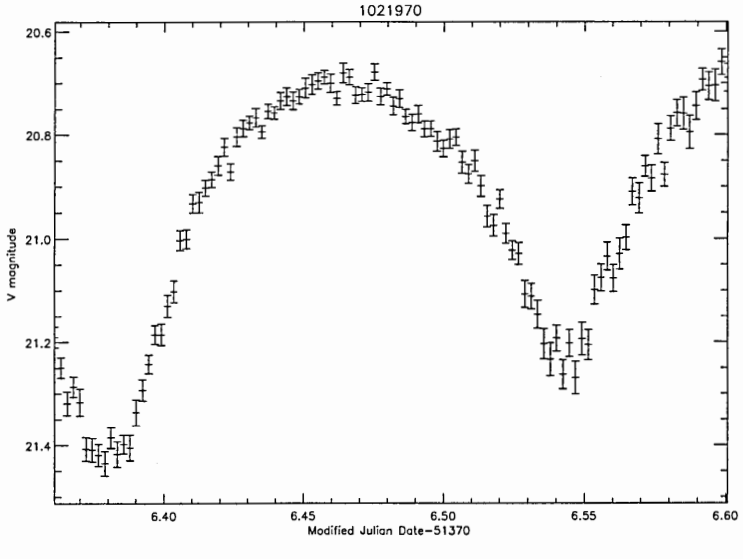
1021970
20.6
20.8
21.0
21.2
21.4
V magnitude
6.40
6.45
6.50
6.55
6.60
Modified Julian Date−51370

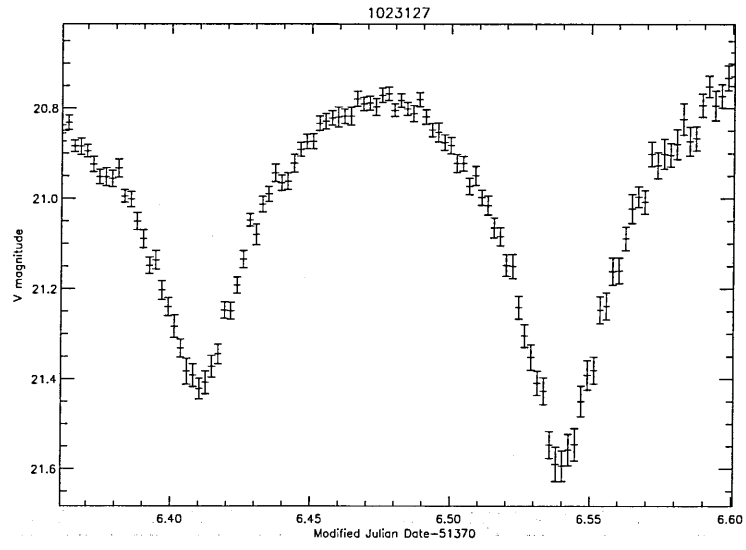
1023127
V magnitude
20.8
21.0
21.2
21.4
21.6
6.40
6.45
6.50
6.55
6.60
Modified Julian Date−51370

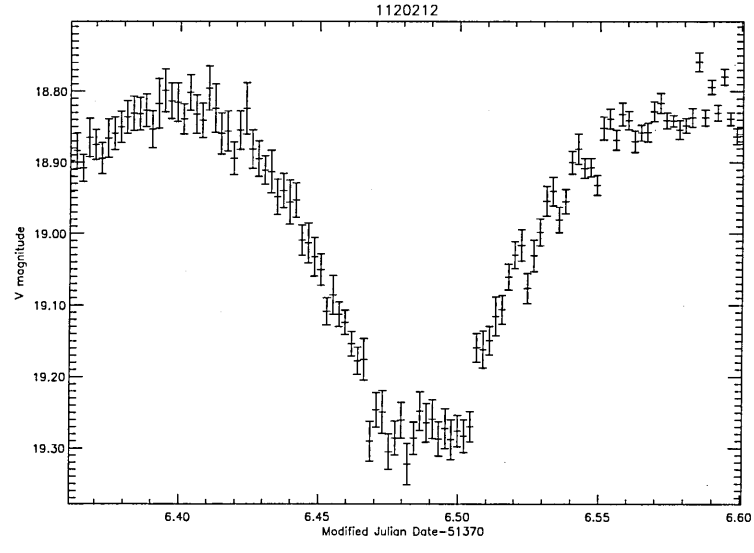
1120212
V magnitude
18.80
18.90
19.00
19.10
19.20
19.30
6.40
6.45
6.50
6.55
6.60
Modified Julian Date−51370

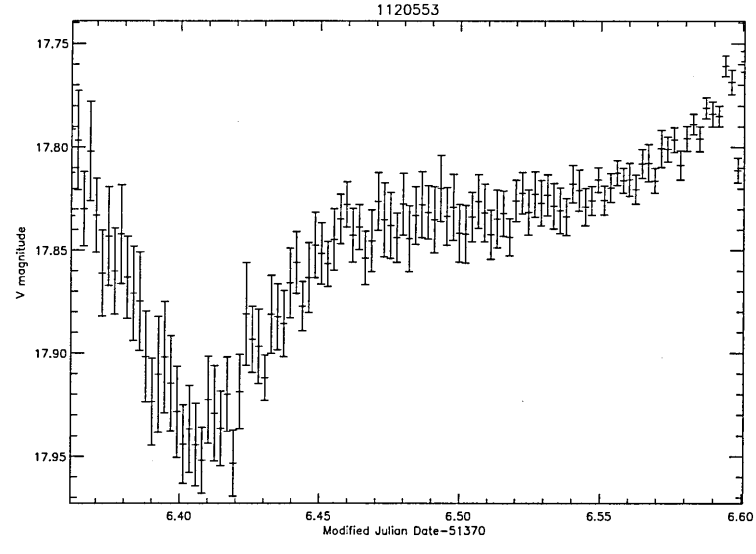
1120553
V magnitude
17.75
17.80
17.85
17.90
17.95
6.40
6.45
6.50
6.55
6.60
Modified Julian Date−51370

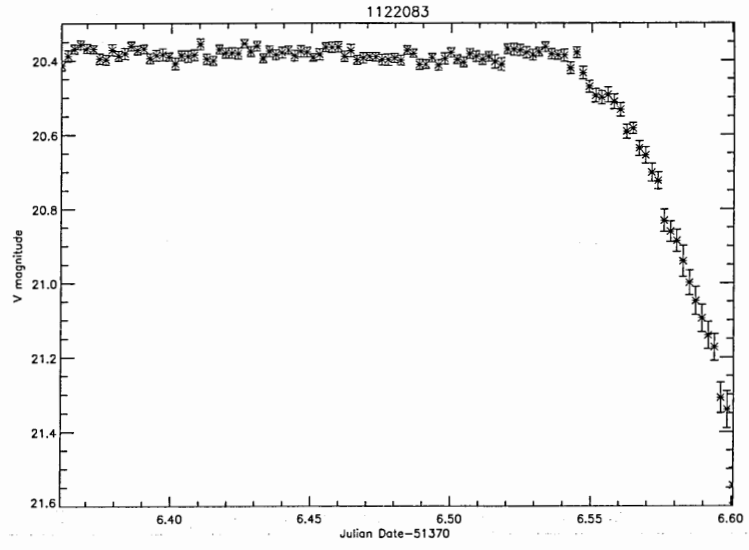
1122083
V magnitude
20.4
20.6
20.8
21.0
21.2
21.4
21.6
6.40
6.45
6.50
6.55
6.60
Julian Date−51370

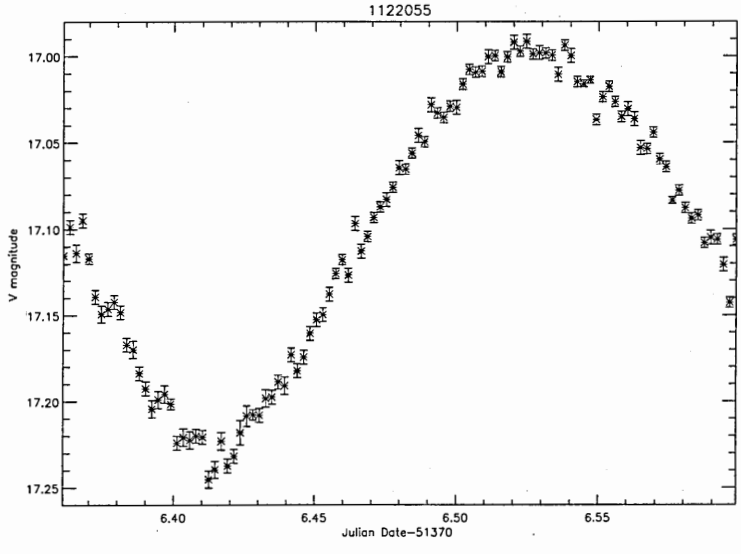
1122055
V magnitude
17.00
17.05
17.10
17.15
17.20
17.25
6.40
6.45
6.50
6.55
Julian Date−51370

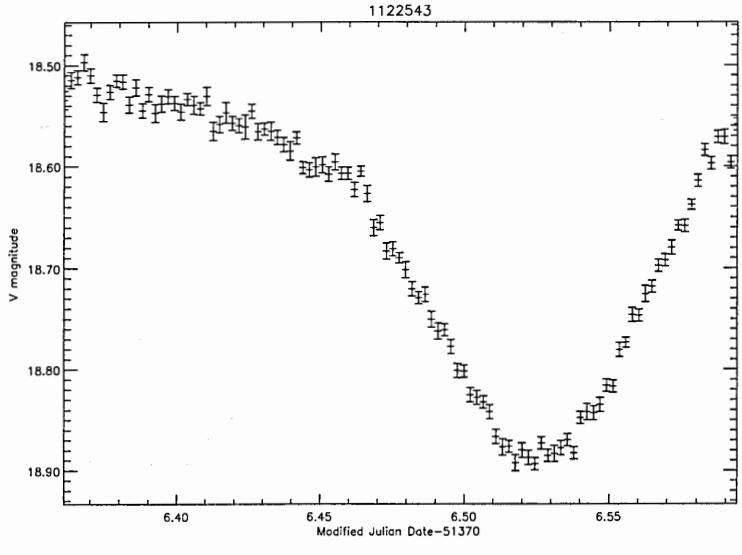
1122543
V magnitude
18.50
18.60
18.70
18.80
18.90
6.40
6.45
6.50
6.55
Modified Julian Date−51370

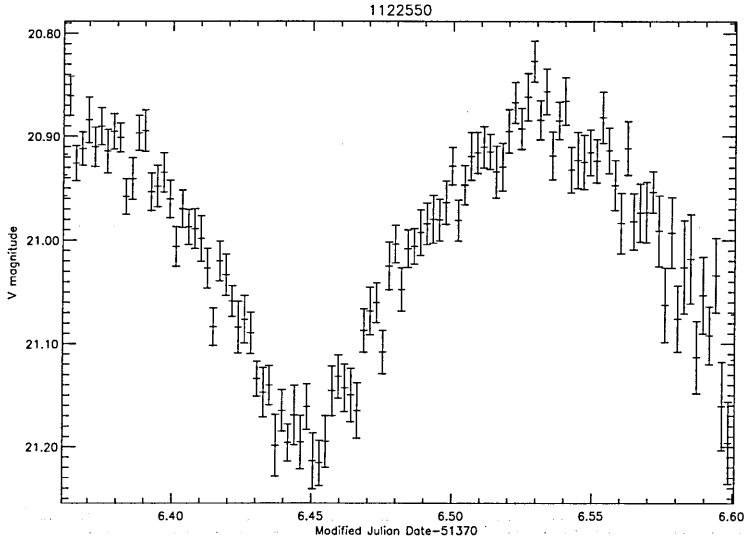
1122550
20.80
20.90
21.00
21.10
21.20
V magnitude
6.40
6.45
6.50
6.55
6.60
Modified Julian Date−51370

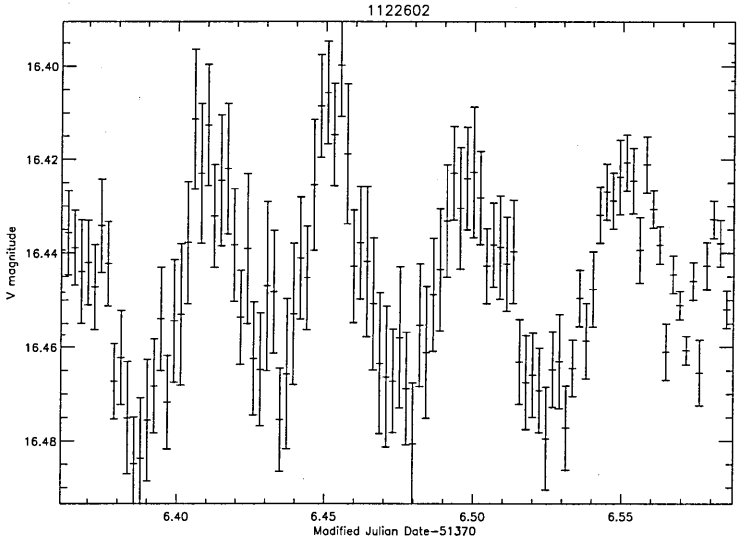
1122602
16.40
16.42
16.44
16.46
16.48
V magnitude
6.40
6.45
6.50
6.55
Modified Julian Date−51370

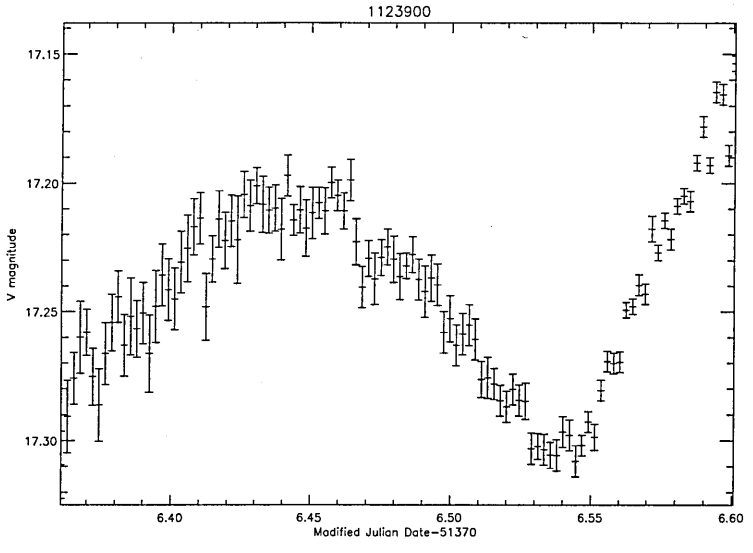
1123900
17.15
17.20
17.25
17.30
V magnitude
6.40
6.45
6.50
6.55
6.60
Modified Julian Date−51370

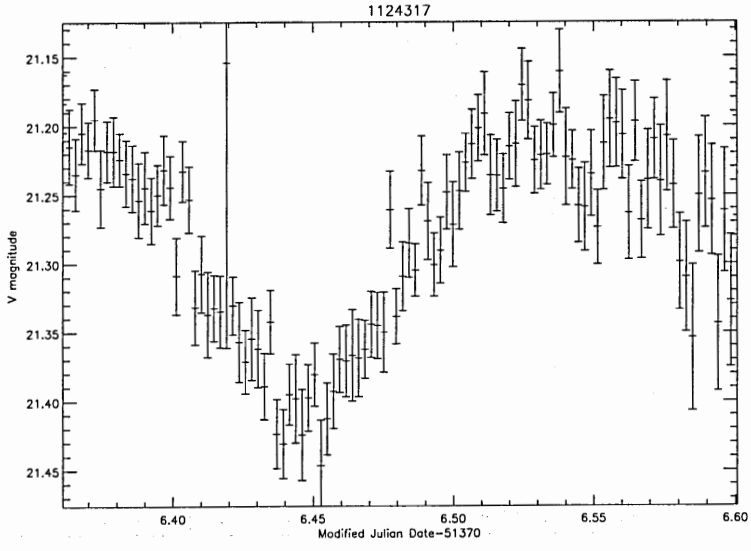
1124317
V magnitude
21.15
21.20
21.25
21.30
21.35
21.40
21.45
6.40
6.45
6.50
6.55
6.60
Modified Julian Date−51370

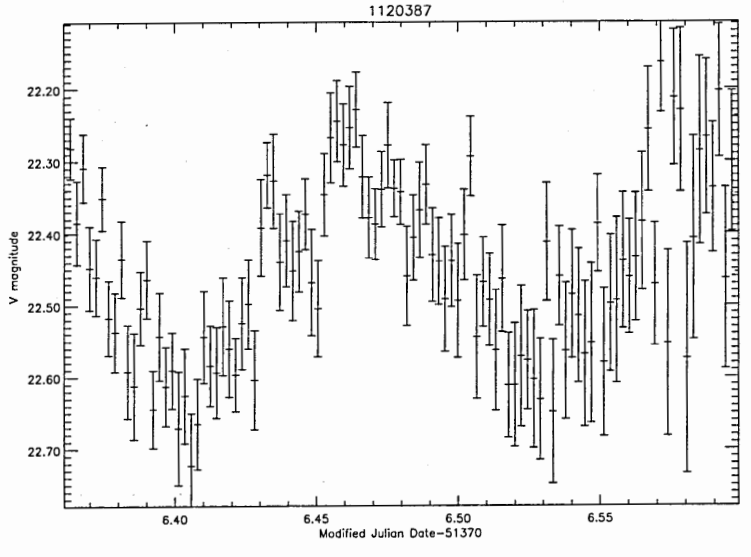
1120387
V magnitude
22.20
22.30
22.40
22.50
22.60
22.70
6.40
6.45
6.50
6.55
Modified Julian Date−51370

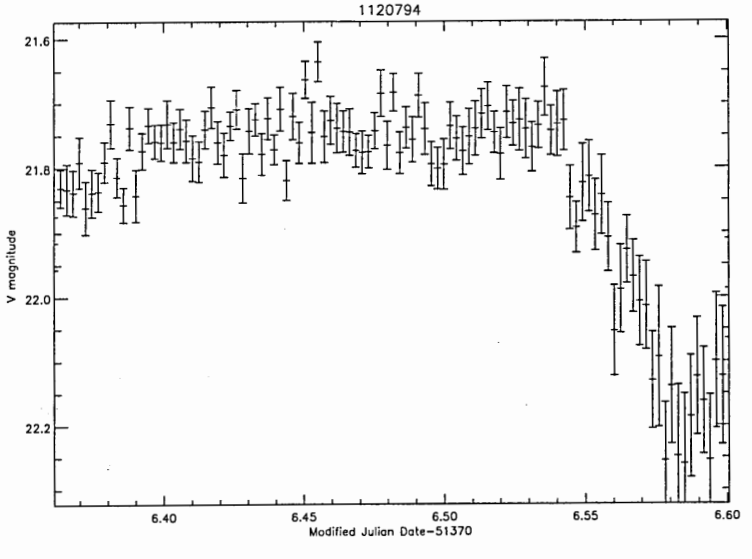
1120794
V magnitude
21.6
21.8
22.0
22.2
6.40
6.45
6.50
6.55
6.60
Modified Julian Date−51370

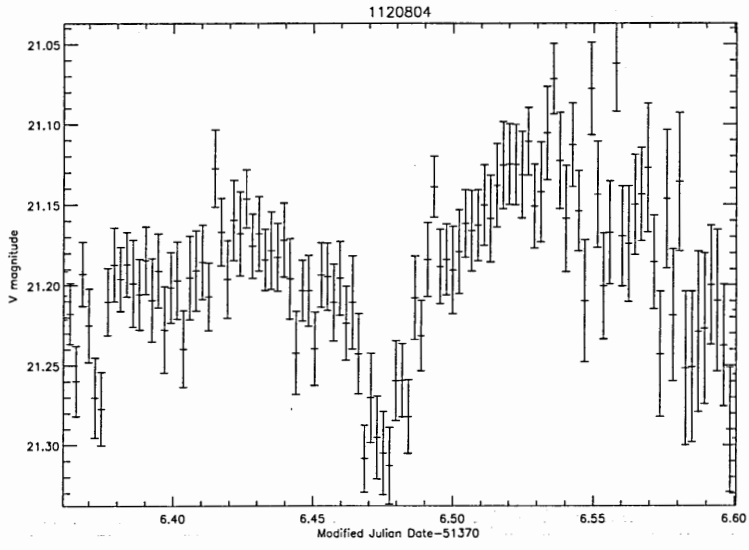
1120804
21.05
21.10
21.15
21.20
21.25
21.30
V magnitude
6.40
6.45
6.50
6.55
6.60
Modified Julian Date−51370

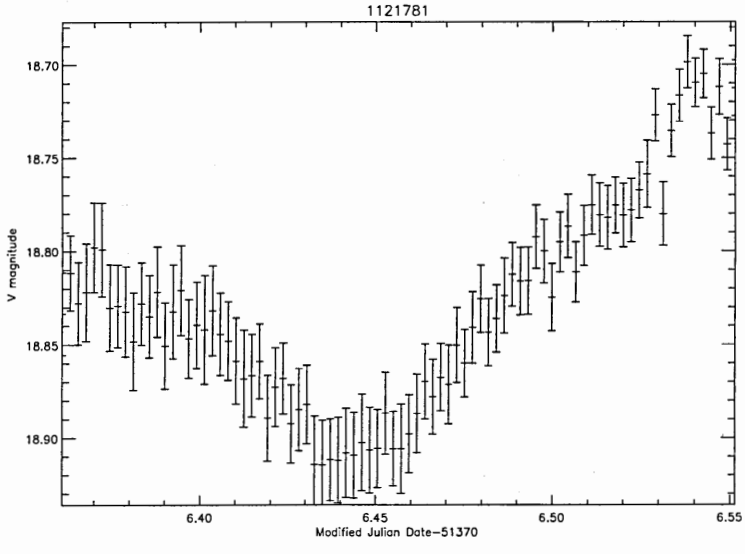
1121781
18.70
18.75
18.80
18.85
18.90
V magnitude
6.40
6.45
6.50
6.55
Modified Julian Date−51370

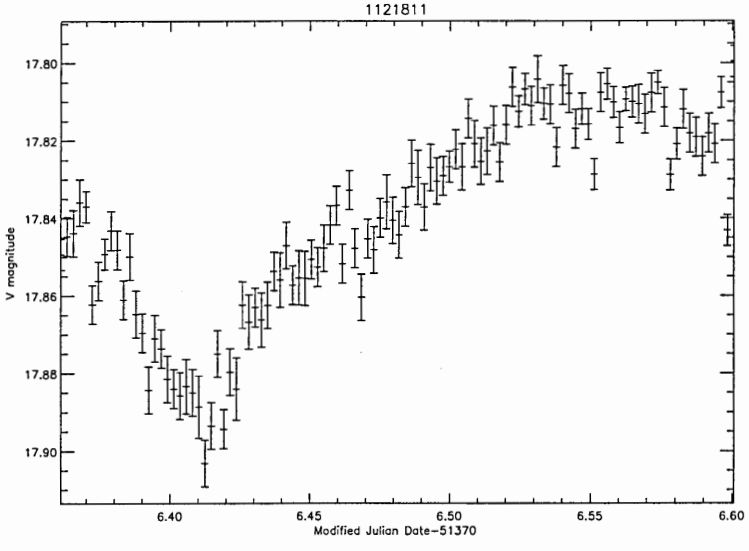
1121811
17.80
17.82
17.84
17.86
17.88
17.90
V magnitude
6.40
6.45
6.50
6.55
6.60
Modified Julian Date−51370

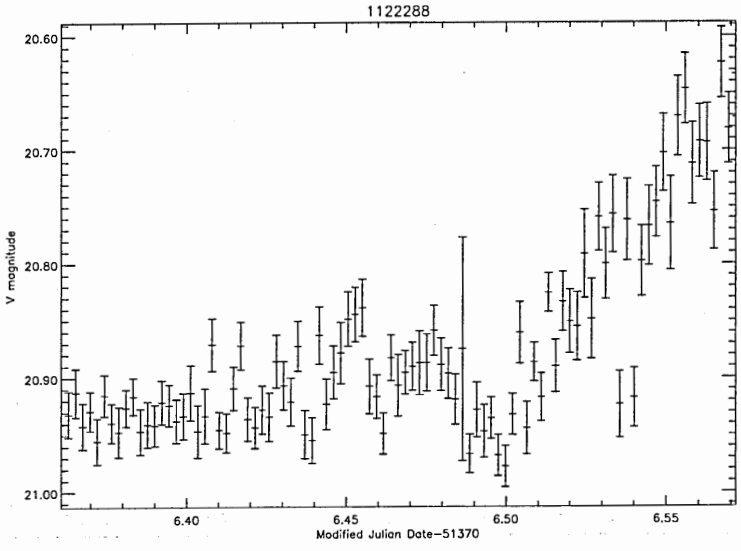
1122288
20.60
20.70
20.80
20.90
21.00
V magnitude
6.40
6.45
6.50
6.55
Modified Julian Date−51370

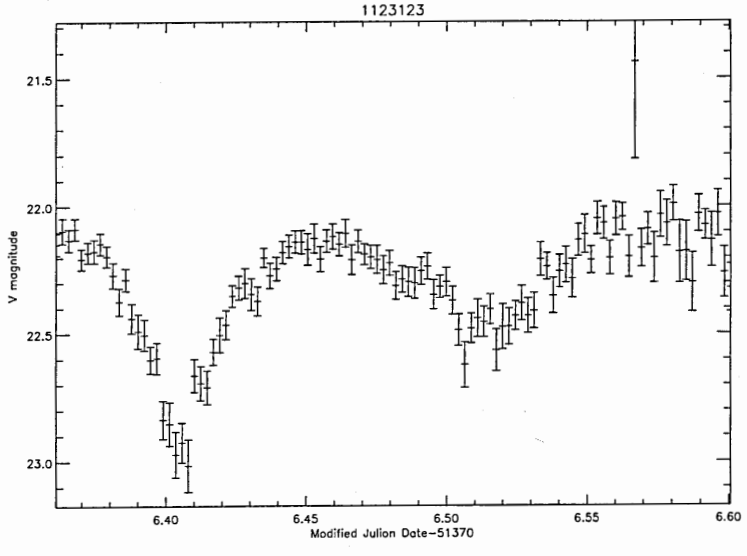
1123123
21.5
22.0
22.5
23.0
V magnitude
6.40
6.45
6.50
6.55
6.60
Modified Julian Date−51370

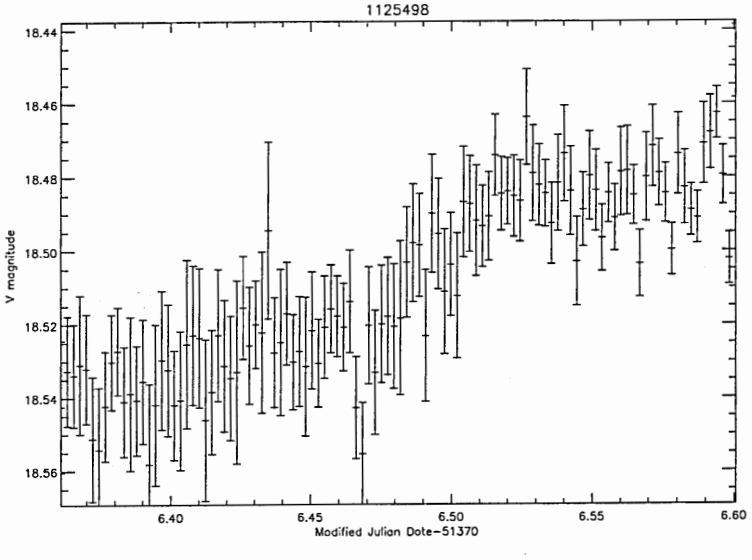
1125498
18.44
18.46
18.48
18.50
18.52
18.54
18.56
V magnitude
6.40
6.45
6.50
6.55
6.60
Modified Julian Date−51370

APPENDIX D

Bespoke code used in the WAVS project

D.1 IDL code

IDL routines created for use in the WAVS project.

D.1.1 differential.pro

```
;program to get average template lightcurves at a number of
different magnitude bins to use as standards for differential
photometry

mindices=n_elements(where(IDS eq 1))

for i=1,200 do begin
  indices=where(IDS eq i)
  nindices=n_elements(indices)
  mindices=[mindices,nindices]

endfor


max=max(mindices)
```

```
m14=intarr(max,1) m15=intarr(max,1) m16=intarr(max,1)
m17=intarr(max,1) m18=intarr(max,1) m19=intarr(max,1)
m20=intarr(max,1) m21=intarr(max,1) m22=intarr(max,1)
m23=intarr(max,1) m24=intarr(max,1)

e14=intarr(max,1) e15=intarr(max,1) e16=intarr(max,1)
e17=intarr(max,1) e18=intarr(max,1) e19=intarr(max,1)
e20=intarr(max,1) e21=intarr(max,1) e22=intarr(max,1)
e23=intarr(max,1) e24=intarr(max,1)

for j=0,10000 do begin

  curve=where(IDS eq j)


  if curve[0] ne -1 then begin
  if n_elements(MAGS[curve]) eq max then begin
    if stddev(MAGS[curve]) lt 3 then begin

      aver=mean(MAGS[curve])

      if aver lt 15 then m14=m14+MAGS[curve]
      if (aver gt 15) and (aver lt 16) then m15=m15+MAGS[curve]
      if (aver gt 16) and (aver lt 17) then m16=m16+MAGS[curve]
      if (aver gt 17) and (aver lt 18) then m17=m17+MAGS[curve]
      if (aver gt 18) and (aver lt 19) then m18=m18+MAGS[curve]
      if (aver gt 19) and (aver lt 20) then m19=m19+MAGS[curve]
      if (aver gt 20) and (aver lt 21) then m20=m20+MAGS[curve]
      if (aver gt 21) and (aver lt 22) then m21=m21+MAGS[curve]
      if (aver gt 22) and (aver lt 23) then m22=m22+MAGS[curve]
      if (aver gt 23) and (aver lt 24) then m23=m23+MAGS[curve]
      if aver gt 24 then m24=m24+MAGS[curve]
```

```
    if aver lt 15 then e14=e14+(MERRS[curve])^2
     if (aver gt 15) and (aver lt 16) then e15=e15+(MERRS[curve])^2
     if (aver gt 16) and (aver lt 17) then e16=e16+(MERRS[curve])^2
     if (aver gt 17) and (aver lt 18) then e17=e17+(MERRS[curve])^2
     if (aver gt 18) and (aver lt 19) then e18=e18+(MERRS[curve])^2
     if (aver gt 19) and (aver lt 20) then e19=e19+(MERRS[curve])^2
     if (aver gt 20) and (aver lt 21) then e20=e20+(MERRS[curve])^2
     if (aver gt 21) and (aver lt 22) then e21=e21+(MERRS[curve])^2
     if (aver gt 22) and (aver lt 23) then e22=e22+(MERRS[curve])^2
     if (aver gt 23) and (aver lt 24) then e23=e23+(MERRS[curve])^2
     if aver gt 24 then e24=e24+(MERRS[curve])^2

   endif
   endif
endif

   endfor

   e14=(sqrt(e14))/(mean(m14)/14)
   e15=(sqrt(e15))/(mean(m15)/15)
   e16=(sqrt(e16))/(mean(m16)/16)
   e17=(sqrt(e17))/(mean(m17)/17)
   e18=(sqrt(e18))/(mean(m18)/18)
   e19=(sqrt(e19))/(mean(m19)/19)
   e20=(sqrt(e20))/(mean(m20)/20)
   e21=(sqrt(e21))/(mean(m21)/21)
   e22=(sqrt(e22))/(mean(m22)/22)
   e23=(sqrt(e23))/(mean(m23)/23)
   e24=(sqrt(e24))/(mean(m24)/24)
```

```
m14=m14/(mean(m14)/14)
m15=m15/(mean(m15)/15)
m16=m16/(mean(m16)/16)
m17=m17/(mean(m17)/17)
m18=m18/(mean(m18)/18)
m19=m19/(mean(m19)/19)
m20=m20/(mean(m20)/20)
m21=m21/(mean(m21)/21)
m22=m22/(mean(m22)/22)
m23=m23/(mean(m23)/23)
m24=m24/(mean(m24)/24)

t=indgen(n_elements(m20))

for k=0,10000 do begin

  star=where(IDS eq k)

  if star[0] ne -1 then begin

    staver=mean(MAGS[star])
    staver=rnd(staver,/down)
    staver=trim(staver,2)

    if staver eq 14 then dm=m14
    if staver eq 15 then dm=m15
    if staver eq 16 then dm=m16
    if staver eq 17 then dm=m17
    if staver eq 18 then dm=m18
    if staver eq 19 then dm=m19
    if staver eq 20 then dm=m20
    if staver eq 21 then dm=m21
    if staver eq 22 then dm=m22
```

```
        if staver eq 23 then dm=m23
        if staver eq 24 then dm=m24



        if staver eq 14 then de=e14
        if staver eq 15 then de=e15
        if staver eq 16 then de=e16
        if staver eq 17 then de=e17
        if staver eq 18 then de=e18
        if staver eq 19 then de=e19
        if staver eq 20 then de=e20
        if staver eq 21 then de=e21
        if staver eq 22 then de=e22
        if staver eq 23 then de=e23
        if staver eq 24 then de=e24

      m=MAGS[star]
      e=MERRS[star]

      rm=m-dm

      me=sqrt((e^2)+(de^2))

      if  n_elements(NMAGS) eq 0 then NMAGS=rm else NMAGS=[NMAGS,rm]
      if n_elements(NIDS) eq 0 then NIDS=IDS[star] else NIDS=[NIDS,IDS[star]]
      if n_elements(NERRS) eq 0 then NERRS=me else NERRS=[NERRS,me]
    endif
  endfor
end
```

D.1.2 differential.pro (with colour separation)

```
;program to get average template lightcurves at a number of
different ;magnitude bins to use as standards for differential
photometry.  This ;version is an extension to differential.pro as
it creates ;differential lightcures on the basis of colour too.

readcol,'finalmagspro',f='(I,F,F,F)',CIDS,V,BV,VR

mindices=n_elements(where(IDS eq 1))

for i=1,200 do begin
  indices=where(IDS eq i)
  nindices=n_elements(indices)
  mindices=[mindices,nindices]
endfor

max=max(mindices)

;create arrays for blue data bm14=intarr(max,1) bm15=intarr(max,1)
bm16=intarr(max,1) bm17=intarr(max,1) bm18=intarr(max,1)
bm19=intarr(max,1) bm20=intarr(max,1) bm21=intarr(max,1)
bm22=intarr(max,1) bm23=intarr(max,1) bm24=intarr(max,1)


be14=intarr(max,1) be15=intarr(max,1) be16=intarr(max,1)
be17=intarr(max,1) be18=intarr(max,1) be19=intarr(max,1)
be20=intarr(max,1) be21=intarr(max,1) be22=intarr(max,1)
be23=intarr(max,1) be24=intarr(max,1)

;create arrays for middle data

mm14=intarr(max,1) mm15=intarr(max,1) mm16=intarr(max,1)
```

```
mm17=intarr(max,1) mm18=intarr(max,1) mm19=intarr(max,1)
mm20=intarr(max,1) mm21=intarr(max,1) mm22=intarr(max,1)
mm23=intarr(max,1) mm24=intarr(max,1)

me14=intarr(max,1) me15=intarr(max,1) me16=intarr(max,1)
me17=intarr(max,1) me18=intarr(max,1) me19=intarr(max,1)
me20=intarr(max,1) me21=intarr(max,1) me22=intarr(max,1)
me23=intarr(max,1) me24=intarr(max,1)

;create arrays for red data

rm14=intarr(max,1) rm15=intarr(max,1) rm16=intarr(max,1)
rm17=intarr(max,1) rm18=intarr(max,1) rm19=intarr(max,1)
rm20=intarr(max,1) rm21=intarr(max,1) rm22=intarr(max,1)
rm23=intarr(max,1) rm24=intarr(max,1)

re14=intarr(max,1) re15=intarr(max,1) re16=intarr(max,1)
re17=intarr(max,1) re18=intarr(max,1) re19=intarr(max,1)
re20=intarr(max,1) re21=intarr(max,1) re22=intarr(max,1)
re23=intarr(max,1) re24=intarr(max,1)

for j=0,10000 do begin


  curve=where(IDS eq j)
  col=where(CIDS eq j)
  if col[0] ne -1 then begin
  bcol=BV[col[0]]

  if curve[0] ne -1 then begin
  if n_elements(MAGS[curve]) eq max then begin
    if stddev(MAGS[curve]) lt 1 then begin
```

```
;begin blue if
if bcol lt 1 then begin

aver=mean(MAGS[curve])

if aver lt 15 then bm14=bm14+MAGS[curve]
if (aver gt 15) and (aver lt 16) then bm15=bm15+MAGS[curve]
if (aver gt 16) and (aver lt 17) then bm16=bm16+MAGS[curve]
if (aver gt 17) and (aver lt 18) then bm17=bm17+MAGS[curve]
if (aver gt 18) and (aver lt 19) then bm18=bm18+MAGS[curve]
if (aver gt 19) and (aver lt 20) then bm19=bm19+MAGS[curve]
if (aver gt 20) and (aver lt 21) then bm20=bm20+MAGS[curve]
if (aver gt 21) and (aver lt 22) then bm21=bm21+MAGS[curve]
if (aver gt 22) and (aver lt 23) then bm22=bm22+MAGS[curve]
if (aver gt 23) and (aver lt 24) then bm23=bm23+MAGS[curve]
if aver gt 24 then bm24=bm24+MAGS[curve]

if aver lt 15 then be14=be14+(MERRS[curve])^2
if (aver gt 15) and (aver lt 16) then be15=be15+(MERRS[curve])^2
if (aver gt 16) and (aver lt 17) then be16=be16+(MERRS[curve])^2
if (aver gt 17) and (aver lt 18) then be17=be17+(MERRS[curve])^2
if (aver gt 18) and (aver lt 19) then be18=be18+(MERRS[curve])^2
if (aver gt 19) and (aver lt 20) then be19=be19+(MERRS[curve])^2
if (aver gt 20) and (aver lt 21) then be20=be20+(MERRS[curve])^2
if (aver gt 21) and (aver lt 22) then be21=be21+(MERRS[curve])^2
if (aver gt 22) and (aver lt 23) then be22=be22+(MERRS[curve])^2
if (aver gt 23) and (aver lt 24) then be23=be23+(MERRS[curve])^2
if aver gt 24 then be24=be24+(MERRS[curve])^2
endif
                              ;begin middle if
```

```
 if (bcol gt 1) and (bcol lt 1.8) then begin
       aver=mean(MAGS[curve])
 if aver lt 15 then mm14=mm14+MAGS[curve]
 if (aver gt 15) and (aver lt 16) then mm15=mm15+MAGS[curve]
 if (aver gt 16) and (aver lt 17) then mm16=mm16+MAGS[curve]
 if (aver gt 17) and (aver lt 18) then mm17=mm17+MAGS[curve]
 if (aver gt 18) and (aver lt 19) then mm18=mm18+MAGS[curve]
 if (aver gt 19) and (aver lt 20) then mm19=mm19+MAGS[curve]
 if (aver gt 20) and (aver lt 21) then mm20=mm20+MAGS[curve]
 if (aver gt 21) and (aver lt 22) then mm21=mm21+MAGS[curve]
 if (aver gt 22) and (aver lt 23) then mm22=mm22+MAGS[curve]
 if (aver gt 23) and (aver lt 24) then mm23=mm23+MAGS[curve]
 if aver gt 24 then mm24=mm24+MAGS[curve]

if aver lt 15 then me14=me14+(MERRS[curve])^2
 if (aver gt 15) and (aver lt 16) then me15=me15+(MERRS[curve])^2
 if (aver gt 16) and (aver lt 17) then me16=me16+(MERRS[curve])^2
 if (aver gt 17) and (aver lt 18) then me17=me17+(MERRS[curve])^2
 if (aver gt 18) and (aver lt 19) then me18=me18+(MERRS[curve])^2
 if (aver gt 19) and (aver lt 20) then me19=me19+(MERRS[curve])^2
 if (aver gt 20) and (aver lt 21) then me20=me20+(MERRS[curve])^2
 if (aver gt 21) and (aver lt 22) then me21=me21+(MERRS[curve])^2
 if (aver gt 22) and (aver lt 23) then me22=me22+(MERRS[curve])^2
 if (aver gt 23) and (aver lt 24) then me23=me23+(MERRS[curve])^2
 if aver gt 24 then me24=me24+(MERRS[curve])^2

endif
                              ;begin red loop
if bcol gt 1.8 then begin
       aver=mean(MAGS[curve])
 if aver lt 15 then rm14=rm14+MAGS[curve]
 if (aver gt 15) and (aver lt 16) then rm15=rm15+MAGS[curve]
 if (aver gt 16) and (aver lt 17) then rm16=rm16+MAGS[curve]
```

```
      if (aver gt 17) and (aver lt 18) then rm17=rm17+MAGS[curve]
      if (aver gt 18) and (aver lt 19) then rm18=rm18+MAGS[curve]
      if (aver gt 19) and (aver lt 20) then rm19=rm19+MAGS[curve]
      if (aver gt 20) and (aver lt 21) then rm20=rm20+MAGS[curve]
      if (aver gt 21) and (aver lt 22) then rm21=rm21+MAGS[curve]
      if (aver gt 22) and (aver lt 23) then rm22=rm22+MAGS[curve]
      if (aver gt 23) and (aver lt 24) then rm23=rm23+MAGS[curve]
      if aver gt 24 then rm24=rm24+MAGS[curve]


     if aver lt 15 then re14=re14+(MERRS[curve])^2
      if (aver gt 15) and (aver lt 16) then re15=re15+(MERRS[curve])^2
      if (aver gt 16) and (aver lt 17) then re16=re16+(MERRS[curve])^2
      if (aver gt 17) and (aver lt 18) then re17=re17+(MERRS[curve])^2
      if (aver gt 18) and (aver lt 19) then re18=re18+(MERRS[curve])^2
      if (aver gt 19) and (aver lt 20) then re19=re19+(MERRS[curve])^2
      if (aver gt 20) and (aver lt 21) then re20=re20+(MERRS[curve])^2
      if (aver gt 21) and (aver lt 22) then re21=re21+(MERRS[curve])^2
      if (aver gt 22) and (aver lt 23) then re22=re22+(MERRS[curve])^2
      if (aver gt 23) and (aver lt 24) then re23=re23+(MERRS[curve])^2
      if aver gt 24 then re24=re24+(MERRS[curve])^2

     endif
   endif


    endif
    endif
  endif

    endfor

    ;create blue mean
```

```
be14=(sqrt(be14))/(mean(bm14)/14)
be15=(sqrt(be15))/(mean(bm15)/15)
be16=(sqrt(be16))/(mean(bm16)/16)
be17=(sqrt(be17))/(mean(bm17)/17)
be18=(sqrt(be18))/(mean(bm18)/18)
be19=(sqrt(be19))/(mean(bm19)/19)
be20=(sqrt(be20))/(mean(bm20)/20)
be21=(sqrt(be21))/(mean(bm21)/21)
be22=(sqrt(be22))/(mean(bm22)/22)
be23=(sqrt(be23))/(mean(bm23)/23)
be24=(sqrt(be24))/(mean(bm24)/24)


bm14=bm14/(mean(bm14)/14)
bm15=bm15/(mean(bm15)/15)
bm16=bm16/(mean(bm16)/16)
bm17=bm17/(mean(bm17)/17)
bm18=bm18/(mean(bm18)/18)
bm19=bm19/(mean(bm19)/19)
bm20=bm20/(mean(bm20)/20)
bm21=bm21/(mean(bm21)/21)
bm22=bm22/(mean(bm22)/22)
bm23=bm23/(mean(bm23)/23)
bm24=bm24/(mean(bm24)/24)

t=indgen(n_elements(bm20))

;create middle means

me14=(sqrt(me14))/(mean(mm14)/14)
me15=(sqrt(me15))/(mean(mm15)/15)
me16=(sqrt(me16))/(mean(mm16)/16)
me17=(sqrt(me17))/(mean(mm17)/17)
```

```
me18=(sqrt(me18))/(mean(mm18)/18)
me19=(sqrt(me19))/(mean(mm19)/19)
me20=(sqrt(me20))/(mean(mm20)/20)
me21=(sqrt(me21))/(mean(mm21)/21)
me22=(sqrt(me22))/(mean(mm22)/22)
me23=(sqrt(me23))/(mean(mm23)/23)
me24=(sqrt(me24))/(mean(mm24)/24)


mm14=mm14/(mean(mm14)/14)
mm15=mm15/(mean(mm15)/15)
mm16=mm16/(mean(mm16)/16)
mm17=mm17/(mean(mm17)/17)
mm18=mm18/(mean(mm18)/18)
mm19=mm19/(mean(mm19)/19)
mm20=mm20/(mean(mm20)/20)
mm21=mm21/(mean(mm21)/21)
mm22=mm22/(mean(mm22)/22)
mm23=mm23/(mean(mm23)/23)
mm24=mm24/(mean(mm24)/24)

                                ;create red means

re14=(sqrt(re14))/(mean(rm14)/14)
re15=(sqrt(re15))/(mean(rm15)/15)
re16=(sqrt(re16))/(mean(rm16)/16)
re17=(sqrt(re17))/(mean(rm17)/17)
re18=(sqrt(re18))/(mean(rm18)/18)
re19=(sqrt(re19))/(mean(rm19)/19)
re20=(sqrt(re20))/(mean(rm20)/20)
re21=(sqrt(re21))/(mean(rm21)/21)
re22=(sqrt(re22))/(mean(rm22)/22)
re23=(sqrt(re23))/(mean(rm23)/23)
```

```
re24=(sqrt(re24))/(mean(rm24)/24)


rm14=rm14/(mean(rm14)/14)
rm15=rm15/(mean(rm15)/15)
rm16=rm16/(mean(rm16)/16)
rm17=rm17/(mean(rm17)/17)
rm18=rm18/(mean(rm18)/18)
rm19=rm19/(mean(rm19)/19)
rm20=rm20/(mean(rm20)/20)
rm21=rm21/(mean(rm21)/21)
rm22=rm22/(mean(rm22)/22)
rm23=rm23/(mean(rm23)/23)
rm24=rm24/(mean(rm24)/24)


;begin loops to create new curves

for k=0,10000 do begin

  star=where(IDS eq k)
  scol=where(CIDS eq k)
  if scol[0] ne -1 then begin
  sbcol=BV[scol[0]]


  if star[0] ne -1 then begin


    staver=mean(MAGS[star])

    staver=rnd(staver,/down)
```

```
staver=trim(staver,2)

;rectify the blue lightcurves

if sbcol lt 1 then begin

if staver eq 14 then dm=bm14
if staver eq 15 then dm=bm15
if staver eq 16 then dm=bm16
if staver eq 17 then dm=bm17
if staver eq 18 then dm=bm18
if staver eq 19 then dm=bm19
if staver eq 20 then dm=bm20
if staver eq 21 then dm=bm21
if staver eq 22 then dm=bm22
if staver eq 23 then dm=bm23
if staver eq 24 then dm=bm24


if staver eq 14 then de=be14
if staver eq 15 then de=be15
if staver eq 16 then de=be16
if staver eq 17 then de=be17
if staver eq 18 then de=be18
if staver eq 19 then de=be19
if staver eq 20 then de=be20
if staver eq 21 then de=be21
if staver eq 22 then de=be22
if staver eq 23 then de=be23
if staver eq 24 then de=be24

m=MAGS[star]
e=MERRS[star]
```

```
rm=m-dm

me=sqrt((e^2)+(de^2))
endif

;rectify the middle lightcurves

if (sbcol gt  1) and (sbcol lt 1.8) then begin

  if staver eq 14 then dm=mm14
  if staver eq 15 then dm=mm15
  if staver eq 16 then dm=mm16
  if staver eq 17 then dm=mm17
  if staver eq 18 then dm=mm18
  if staver eq 19 then dm=mm19
  if staver eq 20 then dm=mm20
  if staver eq 21 then dm=mm21
  if staver eq 22 then dm=mm22
  if staver eq 23 then dm=mm23
  if staver eq 24 then dm=mm24


  if staver eq 14 then de=me14
  if staver eq 15 then de=me15
  if staver eq 16 then de=me16
  if staver eq 17 then de=me17
  if staver eq 18 then de=me18
  if staver eq 19 then de=me19
  if staver eq 20 then de=me20
  if staver eq 21 then de=me21
  if staver eq 22 then de=me22
  if staver eq 23 then de=me23
```

```
  if staver eq 24 then de=me24

m=MAGS[star]
e=MERRS[star]

rm=m-dm

me=sqrt((e^2)+(de^2))
endif

                              ;rectify the red curves

if sbcol gt  1.8 then begin

  if staver eq 14 then dm=rm14
  if staver eq 15 then dm=rm15
  if staver eq 16 then dm=rm16
  if staver eq 17 then dm=rm17
  if staver eq 18 then dm=rm18
  if staver eq 19 then dm=rm19
  if staver eq 20 then dm=rm20
  if staver eq 21 then dm=rm21
  if staver eq 22 then dm=rm22
  if staver eq 23 then dm=rm23
  if staver eq 24 then dm=rm24


  if staver eq 14 then de=re14
  if staver eq 15 then de=re15
  if staver eq 16 then de=re16
  if staver eq 17 then de=re17
  if staver eq 18 then de=re18
  if staver eq 19 then de=re19
```

```
        if staver eq 20 then de=re20
        if staver eq 21 then de=re21
        if staver eq 22 then de=re22
        if staver eq 23 then de=re23
        if staver eq 24 then de=re24

      m=MAGS[star]
      e=MERRS[star]

      rm=m-dm

      me=sqrt((e^2)+(de^2))
      endif

      ;create new 'N' arrays

      if  n_elements(NMAGS) eq 0 then NMAGS=rm else NMAGS=[NMAGS,rm]
      if n_elements(NIDS) eq 0 then NIDS=IDS[star] else NIDS=[NIDS,IDS[star]]
      if n_elements(NERRS) eq 0 then NERRS=me else NERRS=[NERRS,me]
    endif
  endif


  endfor

   end
```

D.1.3 diffchi.pro

```
;program to plot the chi squared values of my differential data

for i=0,6000 do begin

  indices=where((NIDS eq i) and finite(NMAGS))
  if indices[0] ne -1 then begin
    if NMAGS[indices[0]] ne -1 then begin

      a=n_elements(NMAGS[indices])
      if  a ge 30 then begin
        discrep=where(abs(NMAGS[indices[2:*]]-2*NMAGS[indices[1:*]]
        +NMAGS[indices]) gt 0.5)

        if discrep[0] eq 0 then begin
          NIDS[indices]=-NIDS[indices]
          discrep[0]=-1
        endif

        minim=Min(NMAGS[indices],/nan,max=maxim)
        range=maxim-minim
        frac=0.2;0<frac<0.5
        tester=(NMAGS[indices] gt (minim+frac*range))And(NMAGS[indices]
        Lt (maxim-frac*range))
        If Total(tester) Eq 0 Then Begin
          tester=(NMAGS[indices] lt (maxim-frac*range))
  NIDS[indices[Where(tester)]]=-NIDS[indices[Where(tester)]]

endif
indices=where((NIDS eq i) and finite(NMAGS)) if indices[0]
ne -1 then begin if n_elements(NIDS[indices] gt 0) gt 30 then
begin
```

```
discrep=where(abs(NMAGS[indices[2:*]]-2*NMAGS[indices[1:*]]
+NMAGS[indices])
gt 0.5)
        tindices=indices
        while discrep[0] ne -1 do begin

          NIDS[tindices[discrep[0]+2]]=-NIDS[tindices[discrep[0]+2]]

          if (discrep[0] eq n_elements(tindices)-3) then
           tindices=tindices[0:discrep[0]+1] else tindices=[tindices
           [0:discrep[0]+1],tindices[discrep[0]+3:*]]

discrep=where(abs(NMAGS[tindices[2:*]]-2*NMAGS[tindices[1:
*]]+NMAGS[tindices]) gt 0.5)

;NIDS[tindices[discrep[0]+2]]=-NIDS[tindices[discrep[0]+2]]

endwhile indices=where((NIDS eq i) and finite(NMAGS)) endif endif

 ;if discrep  eq 0 then begin

if indices[0] ne -1 then begin
    data=NMAGS[indices]
    mean=mean(data,/nan)
    dev=NERRS(indices)
    chi=rcs(data,dev,mean,dof=1)
    openw,1,'diffchitest',/append
    printf,1,NIDS[indices[0]],chi
    close,1

    if n_elements(chi2) eq 0 then chi2=chi else chi2=[chi2,chi]
    if n_elements(means) eq 0 then means=mean else means=[means,mean]
 endif
```

```
  endif
;endif endif

  endif
endfor end
```

D.1.4 curve.pro

```
;program to get lightcurves out of alslists
alllist=readlist('alslist') nfiles=n_elements(alllist)

  readcol,format='(I,F,F)',allist[0],ID,MAG,MERR
  time=replicate(0,n_elements(ID))
  ids=ID
  mags=MAG
  merrs=MERR
  times=time

for file=1,nfiles-1 do begin
  readcol,format='(I,F,F)',allist[file],ID,MAG,MERR
  time=replicate(file,n_elements(ID))
  ids=[ids,ID]
  mags=[mags,MAG]
  merrs=[merrs,MERR]
  times=[times,time]
end for
end
```

D.1.5 coefcols.pro

```
;program to apply the calculated b1 and b2 coefficients to allstar
;files to gain corrected colours


;get parameters

print,'input b1 B value' b1b='' read,b1b b1b=float(b1b)
;print,'input b2 B value' ;b2b='' ;read,b2b b2b=0.17 ;print,'input
B airmass' ;airb='' ;read,airb airb=1.105

print,'input b1 V value' b1v='' read,b1v b1v=float(b1v)

;print,'input b2 V value' ;b2v='' ;read,b2v b2V=0.12

;print,'input V airmass' ;airv='' ;read,airv airv=1.011
print,'input b1 R value' b1r='' read,b1r b1r=float(b1r)


;print,'input b2 R value' ;b2r='' ;read,b2r b2r=0.11

;print,'input R airmass' ;airr='' ;read,airr airr=1.171

;read in uncalibrated mag files

;print,'input uncalibrated B magnitude file' ;fileb='' ;read,fileb

readcol,'als17',f='(A,F,F)',IDB,MAGB,MERRB


;print,'input uncalibrated V magnitude file' ;filev='' ;read,filev

readcol,'als39',f='(A,F,F)',IDV,MAGV,MERRV
```

```
;print,'input uncalibrated R magnitude file' ;filer='' ;read,filer

readcol,'als12',f='(A,F,F)',IDR,MAGR,MERRR


;transform to correct mags

CMAGB=MAGB-b1b-(b2b*airb)
CMAGV=MAGV-b1v-(b2v*airv)
CMAGR=MAGR-b1r-(b2r*airr)


for i=0,n_elements(IDV)-1 do begin

  bindices=where(IDB eq IDV[i])
  rindices=where(IDR eq IDV[i])


  if bindices[0] ne -1 then begin
    if rindices[0] ne -1 then begin
;write out the new corrected magnitude lists

      BV=CMAGB[bindices[0]]-CMAGV[i]
      VR=CMAGV[i]-CMAGR[rindices[0]]

  openw,1,'finalmagspro',/append
  printf,1,string(IDV[i])+' '+string(CMAGV[i])+' '+string(BV)
  +'  '+string(VR)
  close,1

endif endif
```

```
endfor

;readcol,'finalmags',f='(I,F,F,F)',ID,NV,NBV,NVR ;print,mean(NBV)
;print,mean(NVR) end
```

D.1.6 docolextinct.pro

```
;Program to apply an extinction correction to the curve.dat files
;created previously.  In the first instance this program is only
;designed to work on the CCDs which do not have the correct
standards ;to be done in IRAF.

print,'restore which file?' curve='' read,curve

restore,filename=curve


airmass=readlist('airmasses')

print,'b1v value?' b1v='' read,b1v b1v=float(b1v)

print,'b3v value?' b3v='' read,b3v b3v=float(b3v)

b2v=0.12

print,'b1b value?' b1b='' read,b1b b1b=float(b1b)

print,'b3b value?' b3b='' read,b3b b3b=float(b3b)

b2b=0.17

bairmass=1.105

print,'B magnitude list?' bals='' read,bals

readcol,bals,format='(I,F,F)',BID,BMAG,BMERR
```

```
for i=1,10000 do begin

  indices=where(IDS eq i)
  bindices=where(BID eq i)
  if indices[0] ne -1 then begin
    if bindices[0] ne -1 then begin


  for j=0,n_elements(indices)-1 do begin

    binst=BMAG[bindices]
    vinst=MAGS[indices[j]]


    beta=(binst-b1b-(b2b*bairmass))
    nu=(vinst-b1v-(b2v*airmass[j]))

    left=(nu-((b3v*beta)/(1+b3b)))/(1-b3v)

    right=1+((b3v*b3b)/((1+b3b)*(1-b3v)))

    MAGS[indices[j]]=(left/right)

    ;MAGS[indices[j]]=MAGS[indices[j]]-b1v-(b2v*airmass[j])

  endfor
endif endif endfor

end
```

D.1.7 plotcurves.pro

```
 ;program to plot the curves that have been read in must run
 ;curve before this or load curve#.dat or diff#.dat.
 ;Classify.pro deals with the classification.

object=i

indices=where(ids eq object)
;begin loop to cycle through curves
if indices[0] eq -1 then i=i+1 else begin
  if n_elements(indices) lt 30 then i=i+1 else begin
    if i lt c then i=((i-(i-1))+c)

    t=times
m=mags[indices] e=merrs[indices] n=ids[indices]

w=string(n[0]) w=strcompress(w)

;bit to write out time, mags and errors if necessary
;openw,1,w ;printf,1,rotate([[t],[m],[e]],4) ;close,1

print,n[0] ploterror,t,m,e,psym=2;,xtickunits='time'

;call the classify program which deals with the keyboard inputs
 result=classify(n[0])

endelse
endelse

;bit to deal with quitting
if result eq 1 then stop,'done'
```

```
;bit to deal with keyboard input
if result eq 2 then begin
  b=''
  read,b

  nindices=where(ids eq b)

  if nindices[0] eq -1 then stop,''

  t=strtime(times)
  m=mags[nindices]
  e=merrs[nindices]
  n=ids[nindices]


  print,n[0]
  ploterror,t,m,e,psym=2,xticklength='time'
  result=classify(n[0])
  endif

  if result eq 4 then begin
    c=''
    read,c
  endif
endfor
end
```

D.1.8 classify.pro

```
function classify,n
;classify lightcurves, input e for eclipse, c for contaminated, n for
;normal,v for variable?,
;u for unusual,q to quit and now includes k ;for keyboard input.
;now if you press l you get the non-differential
light curve for the ; same star

  print,format='("classify lightcurve",$)'
  a=get_kbrd(1)
  print,''

  result=0

  if a eq 'e' then begin
    openw,1,'eclipselist',/append
    printf,1,n
    close,1
    print,'eclipse'
  endif

  if a eq 'v' then begin
    openw,2,'variablelist',/append
    printf,2,n
    close,2
    print,'variable'
  endif

  if a eq 'u' then begin
    openw,3,'unusuallist',/append
    printf,3,n
    close,3
    print,'unusual'
```

```
  endif


  if a eq 'c' then begin
    openw,4,'contaminatelist',/append
    printf,4,n
    close,4
    print,'contaminated'
  endif

  if a eq 'q' then begin
    print,'quitting'
    result=1

  endif
  if a eq 'n' then begin
    print,'normal'
  endif

  if a eq 'k' then begin
    print,'input ID number'
    result=2
  endif


  if a eq 'j' then begin
    print,'input point to jump to'
    result=4
  endif
  return,result

end
```

D.1.9 whyvar.pro

```
;program to show regions of images that contain stars which have
high ;chi2 and classify them according to what causes the high
chi2 value

;detect necessary elements and read them in if not there

if n_elements(image) eq 0 then begin
  print,'which image?'
  imchoose=''
  read,imchoose
  image=readfits(imchoose)
endif

if n_elements(NMAGS) eq 0 then begin
  print,'restore which diff file?'
  diffile=''
  read,diffile
  restore,filename=diffile
endif

if n_elements(IDC) eq 0 then
readcol,'sortchi',format='(A,F)',IDC,CHI

if n_elements(XCENTER) eq 0 then
readcol,'91.coo',format='(F,F,F,F,F,F,A)',XCENTER,
YCENTER,MAG,SHARPNESS,SROUND,GROUND,ID

;begin charting loop

for i=0,n_elements(IDC)-1 do begin

  indices=where(ID eq IDC[i])
```

```
if indices[0] ne -1 then begin
lowx=XCENTER[indices[0]]-50
if lowx lt 0 then begin
  lowx=0
  print,'edge'
endif

 highx=XCENTER[indices[0]]+50
 if highx gt 2041 then begin
   highx=2041
   print,'edge'
 endif

lowy=YCENTER[indices[0]]-50
if lowy lt 0 then begin
  lowy=0
  print,'edge'
endif

highy=YCENTER[indices[0]]+50
if highy gt 4091 then begin
  highy=4091
  print,'edge'
endif

tvzoom,image[lowx:highx,lowy:highy],perc=[5,95],zoo=5

print,IDC[i]
a=get_kbrd(1)

print,'Classify or plot'
;begin plotting options
```

```
if a eq 'n' then print,'next'
if a eq 'q' then stop,'quitting'

if a eq 'k' then begin


  print,'input number'
  numb=''
  read,numb

  kindices=where(ID eq numb)

  lowx=XCENTER[kindices[0]]-50
if lowx lt 0 then begin
  lowx=0
  print,'edge'
endif

 highx=XCENTER[kindices[0]]+50
 if highx gt 2041 then begin
   highx=2041
   print,'edge'
 endif


lowy=YCENTER[kindices[0]]-50
if lowy lt 0 then begin
  lowy=0
  print,'edge'
endif

highy=YCENTER[kindices[0]]+50
if highy gt 4091 then begin
```

```
   highy=4091
   print,'edge'
   endif

   tvzoom,image[lowx:highx,lowy:highy],perc=[5,95],zoo=5
print,IDC[i]

z=get_kbrd(1)

if z eq 'p' then begin
    nindices=where(NIDS eq numb)
   t=indgen(n_elements(NMAGS[nindices]))
   ploterr,t,NMAGS[nindices],NERRS[nindices],psym=3,xst=2,yst=2

   o=get_kbrd(1)

   endif

endif

if a eq 'p' then begin
   nindices=where(NIDS eq IDC[i])
   t=indgen(n_elements(NMAGS[nindices]))
   ploterr,t,NMAGS[nindices],NERRS[nindices],psym=3,xst=2,yst=2

   b=get_kbrd(1)
   cond=1
   while (cond ne 0) do begin

   b=get_kbrd(1)

   if b eq 'p' then ploterror,t,NMAGS[nindices],NERRS[nindices],psym=3,yst=2
   if b eq 'c' then tvzoom,image[lowx:highx,lowy:highy],perc=[5,95],zoo=5
```

```
    if b eq '!' then begin

      ploterr,t,NMAGS[nindices],NERRS[nindices],psym=3,xst=2,yst=2

m=NMAGS[nindices]

coords=select(x=2,y=2,sort=3,/box)

xmin=coords[0,0] xmax=coords[1,0] ymin=coords[0,1]
ymax=coords[1,1]

NMAGS[nindices[where((t gt xmin) and (t lt xmax) and (m gt ymin)
and(m lt ymax))]]=!values.f_nan

NERRS[nindices[where((t gt xmin) and (t lt xmax) and (m gt ymin)
and(m lt ymax))]]=!values.f_nan

t[nindices[where((t gt xmin) and (t lt xmax) and (m gt ymin) and(m
lt ymax))]]=!values.f_nan

endif
    if (b ne 'c') and (b ne 'p') then cond=0
  endwhile
  endif
  endif

                                ;begin classification options

  if a eq 'c' then begin
    print,'badcol'
    openw,1,'chireasons',/append
    printf,1,string(IDC[i])+'      '+'Bad column in field'
    close,1
```

```
endif

if a eq 'v' then begin
  print,'true variable'
endif

if a eq 's' then begin
  print,'loss of seeing'
  openw,1,'chireasons',/append
  printf,1,string(IDC[i])+'      '+'Bad seeing results in loss of star'
  close,1
endif

if a eq 'b' then begin
  print,'blooming'

  openw,1,'chireasons',/append
  printf,1,string(IDC[i])+'      '+'Severe blooming from saturated star'
  close,1
endif

if a eq 'e' then begin
  print,'edge image'

  openw,1,'chireasons',/append
  printf,1,string(IDC[i])+'      '+'Edge of image'
  close,1
endif

if a eq '?' then begin
  print,'plotting options: n=next, p=plot lightcurve
  (in plot mode press c to go back to chart) , q=stop.
  Classify options c=badcolumn, b=severe blooming, s=loss of
```

```
    star due to seeing change, e=edge of image, v=true variable'
  endif
endfor
end
```

D.1.10 allcurves.pro

```
;program to take individual curve.dat files
(named using the curve#n#.dat convention for ccd and night) and to
concatenate them into two large arrays, one for  either night

;read in the curve.dat files
for _a=1,2 do begin
 restore,filename='curve0n'+strtrim(_a,2)+'.dat'

;bit to change ids
 print,_a
ids='99'+strtrim(_a,2)+numtrim(ids,4)
 ids=long(ids)
print,ids[100]

if _a eq 1 then begin
 nids1=ids nmags1=mags nmerrs1=merrs
print,nids1[100] endif

if _a eq 2 then begin
 nids2=ids
  nmags2=mags
  nmerrs2=merrs
endif

for _b=1,11 do begin if _b eq 6 then continue

restore, filename='curve'+strtrim(_b,2)+'n'+strtrim(_a,2)+'.dat'

;bit to change ids

ids=strtrim(_b,2)+strtrim(_a,2)+numtrim(ids,4) ids=long(ids)
```

```
;it to concatinate all the stars into to big arrays (ids1 and ids2)

if _a eq 1 then begin
 nids1=[nids1,ids] nmags1=[nmags1,mags] nmerrs1=[nmerrs1,merrs]
endif

if _a eq 2 then begin
  nids2=[nids2,ids]
nmags2=[nmags2,mags] nmerrs2=[nmerrs2,merrs]
endif

print,ids[100]
endfor
endfor
end
```

D.1.11 matchstars.pro

```
 ;program to match up the identities of stars on the first
 and second nights using WCS information

;read in the list of night1 stars and night2 stars
 readcol,format='(F,F,I)','night1',RA2,DEC2,ID2
readcol,format='(F,F,I)','night2',RA1,DEC1,ID1
 ;set offset limit
limit=0.0005
 stars1=n_elements(RA1) stars2=n_elements(RA2)

;begin loop which compares position of one star in 1st night to
;positions of all stars in second

for i=0,stars1-1 do begin
  r=RA1[i]
  d=DEC1[i]
  rad=sqrt((r-RA2)^2+(d-DEC2)^2)
  rmin=min(rad)

;compare radial distance with offset limit

if rmin le limit then begin
 openw,1,'links',/append printf,1,ID1[i],ID2[(where(rad eq rmin))[0]] close,1
endif
endfor
end
```

D.1.12 combnights.pro

```
;program to combine the data from both nights with correct ids for each star
 ;read in the data from night1
restore,filename='~/curves/allnight1.dat'
;read data from night2
 restore,filename='~/curves/allnight2.dat'
;read in the links file
readcol,format='(L,L)','links',IDn2,IDn1
linked=n_elements(IDn2)

 object2=IDn2[0]
   object1=IDn1[0]

   indices2=where(ids2 eq object2)
   indices1=where(ids1 eq object1)

   numbs2=n_elements(indices2)
   numbs1=n_elements(indices1)
   numbs=(numbs1+numbs2)

   objarr=intarr(numbs)+object2

   nmags=[mags1[indices1],mags2[indices2]]
   nmerrs=[merrs1[indices1],merrs2[indices2]]
   nids=objarr

 for i=1,linked-1 do begin

   object2=IDn2[i]
   object1=IDn1[i]

   indices2=where(ids2 eq object2)
   indices1=where(ids1 eq object1)
```

```
   numbs2=n_elements(indices2)
   numbs1=n_elements(indices1)
   numbs=(numbs1+numbs2)

   if indices2[0] ne -1 then begin
     if indices1[0] ne -1 then begin

objarr=intarr(numbs)+object2

   nmags=[nmags,[mags1[indices1],mags2[indices2]]]
   nmerrs=[nmerrs,[merrs1[indices1],merrs2[indices2]]]
   nids=[nids,objarr]

   endif
   endif
 endfor

 ids=nids
 mags=nmags
 merrs=nmerrs
 end
```

D.1.13 allplot.pro

```
;smaller plotting program to deal with the new giant array.
 ;read in object number

print,'input number(1), see all? (2)or just large var(3)' w='' read,w

if w eq 1 then begin

while 1 do begin
  print,'input plot number'
  p=''
  read,p
  print,'input list number'
  l=''
  read,l

  if p eq 'quit' then break

  indices=where(ids eq p)
  if indices[0] eq -1 then begin
    print,'this is not a valid star number'
    continue
  endif

  ;plot the selected id number
  m=mags[indices]
  e=merrs[indices]
  times='timelist'+l
  t=readlist(times)
  ploterror,t,m,e,psym=1

;print out if need be
  print,'Filename for writing out'
```

```
  name=''
  read,name
 for prints=0,n_elements(t)-1 do begin
openw,1,name,/append printf,1,string(t[prints])+'  '
+string(m[prints]) +'  '+string(e[prints]) close,1
endfor
endwhile
endif

if w eq 2 then begin
  kept=readlist('keptvars')
  keepies=n_elements(kept)
  for j=0,keepies-1 do begin
    indices=where(ids eq kept[j])
    m=mags[indices]
    e=merrs[indices]
    t=readlist('timelist8')
    ploterror,t,m,e,psym=2

    key=''
    read,key

    if key eq 1 then begin
      openw,1,'goodvars',/append
      printf,1,kept[j]
      close,1
    endif
  endfor
endif

if w eq 3 then begin
   good=readlist('goodvars')
  keepies=n_elements(good)
```

```
  for j=0,keepies-1 do begin
    print,j
    indices=where(ids eq good[j])
    m=mags[indices]
    e=merrs[indices]
    t=readlist('timelist8')
    ploterror,t,m,e,psym=2,title=good[j]
    key=''
    read,key
  endfor
endif
end
```